Dissertation zur Erlangung des Doktorgrades

der Fakultät für Chemie und Pharmazie

der Ludwig-Maximilians-Universität München

Design Principles to Enhance Optoelectronic Properties in Oligothiophene-Based Covalent Organic Frameworks

Niklas David Keller

aus

Konstanz, Deutschland

2020

Erklärung

Diese Dissertation wurde im Sinne von § 7 der Promotionsordnung vom 28. November 2011 von Herrn Professor Dr. Thomas Bein betreut.

Eidesstattliche Versicherung

Diese Dissertation wurde eigenständig und ohne unerlaubte Hilfe bearbeitet.

München, 03.03.2020 Niklas Keller ……

Niklas D. Keller

Dissertation eingereicht am 16.01.2020

1. Gutachter: Prof. Dr. Thomas Bein
2. Gutachter: Prof. Dr. Konstantin Karaghiosoff

Mündliche Prüfung am 18.02.2020

Abstract

Covalent organic frameworks (COFs) have been established as a new class of porous and crystalline materials with promising properties resulting from their high degree of predetermined order. Benefitting from simple condensation reactions and the use of organic building blocks, a wide array of accessible structures, motifs and functionalization can be designed and realized. With this qualification building blocks can be chosen to assume different functions such as catalysis, redox activity, light harvesting, desirable host−guest interactions and many more. With these synthetic possibilities, the resulting crystalline scaffolds can be envisioned as potential materials not only for gas storage, separation and catalysis but also in photocatalysis, as photosensors or in supercapacitors to mention only a few examples.

Based on these promising features, the high interest in covalent organic frameworks has driven this work in order to study the impact of small and defined structural changes on optoelectronic properties in stable systems. The changes are generally of such a nature or scale that conclusive observations can be derived, but also small enough to retain the overall structural and chemical features of the system. This approach can enable crucial insights regarding basic design rules that may be generalized for many molecular frameworks. Up to now it has been challenging to construct general design strategies for COFs, since the investigated systems have very specific and unique properties and a direct comparison between different frameworks is difficult.

In the first part of this thesis (chapter 3 and 4), we will elucidate different stacking behavior of two-dimensional (2D) COFs (constructed from 2D polymer layers π-stacked in the third dimension) and its drastic influence on the optical properties of the corresponding COFs. Chapter 3 deals with the tetragonal node dibenzochrysene (DBC), which is a modified version of the 4,4',4",4"'-(ethene-1,1,2,2-tetrayl)tetraaniline (ETTA) or TPE node with only two additional C-C bonds leading to a more planar building block. The resulting structural changes in the COF are significant considering the much reduced stacking distance of the DBC-derived COF layers. In comparison to the related ETTA COFs, the reduced stacking distance of the DBC-derived COFs reveals intriguing optical properties such as greatly extended photoluminescence lifetimes.

Chapter 4 describes the implementation of porphyrin macrocycles in COFs and the resulting stacking behavior in the framework. We present a strategy to enforce self-assembled aggregation of the porphyrin moieties in a specific fashion by the solid COF matrix. The

resulting type of aggregation could be identified by structural and computational methods as extended solid-state J-aggregates of porphyrins within the stack created in the COF. The computational part was done in collaboration with the groups of Clark and Görling from the FAU Erlangen. Also, optical features typical for porphyrin J-aggregates could be achieved leading to drastically enhanced solar harvesting abilities. Finally, the stabilization of optically excited states in the framework could be an intriguing starting point for achieving more efficient charge separation in photovoltaic devices.

The second part of the thesis is dedicated to the investigation of oligothiophene-bridged COFs. Based upon the promising characteristics of (poly-)thiophenes such as high intrinsic charge carrier mobilities, favorable optical absorption throughout the visible spectrum and sufficient chemical stability, their ‘translation’ to COFs, where thiophenes or oligothiophenes could benefit from the highly ordered framework environment, was a focus of the second part of the thesis. However, the realization of such materials has remained challenging, in particular regarding laterally conjugated imine-linked 2D COFs. In chapter 5, we developed a new building block design employing an asymmetric modification on an otherwise symmetric backbone that allows us to construct highly crystalline quaterthiophene-derived COFs. Studying the optical response of these materials, we observed for the first time the formation of a charge transfer state between the COF subunits across the imine bond. We believe that our new building block design provides a general strategy for the construction of well-ordered COFs from various extended building blocks, thus greatly expanding the range of applicable molecules.

This concept was further investigated in chapter 6 to shed light on the structural and optical effects of different lengths of the oligothiophene bridges and of the attached alkyl chains. The frameworks were condensed to COFs with pyrene as a structurally stabilizing and guiding node to ensure facile formation of the COF series, where the observed changes of key features of the COF materials can be directly correlated with the pinpoint modification of the corresponding building blocks. We showed that stacking in the COF leads to drastic alterations regarding the investigated COF series. The oligothiophene-bridged COFs exhibit tunable optical properties and allow us to establish conclusive additional design rules. These findings might lead to an even more precise transfer from ideas on paper to realization of tailor-made materials in the laboratory.

To gain more insights on effects in COFs that are already known from the world of molecular chemistry, bithiophene derivatives with heavy atoms such as bromines were employed in COF synthesis via condensation with the pyrene node. It was expected that by insertion of heavy elements enhanced spin-orbit coupling leads to intensified intersystem crossing and hence to phosphorescence or at least to extended photoluminescence (PL) lifetimes. Indeed, the brominated COFs exhibit slightly extended PL decay lifetimes compared to the non-brominated analogous COF. Furthermore, structural changes resulting from the different stacking behavior of the brominated building blocks could be identified.

The third and last part of the thesis was elaborated in collaboration with the group of Paul Knochel (Department of Chemistry, LMU). The continuing search for new building blocks and synthesis routes has driven this work to gain new perspectives and broaden the horizon of applicable and promising molecules for integration into COFs. The investigation of a direct synthetic route to produce quinolines led to several new N-heterocyclic scaffolds which are of particular interest for organic light emitting diodes with their high photoluminescence quantum yields and long exciton lifetimes. This work led to additional molecular principles for the design of new building blocks for covalent organic frameworks.

Table of Contents

1 Introduction

This chapter is based on the manuscript:

Niklas Keller and Thomas Bein, Optoelectronic Processes in Covalent Organic Frameworks, *Chem. Soc. Rev.* **2020**, *to be submitted*.

Covalent organic frameworks are created through the condensation of molecular building blocks, resulting in crystalline porous materials with widely tunable channel systems. They have attracted great scientific interest since the first reports of their promising potential appeared in 2005.[1] Since then, thorough investigations have pointed towards a broad field of applications where covalent organic frameworks can be of great advantage. The porous and crystalline nature of these robust materials combined with the large structural diversity and the ability to fine-tune at an atomic scale makes them attractive candidates for applications in gas storage,[2-4] molecular separation[5-6] and energy storage.[7-9] Furthermore, their conductive properties and their optical behaviour in the visible and NIR region allow for applications as proton conducting materials,[10-13] in photocatalysis[14-17] or in optoelectronics, including sensors,[18-19] light-emitting diodes,[20-21] or photovoltaic devices.[22-24]

One of the attractive features of covalent organic frameworks is the diversity of the linker chemistry in combination with the vast choice of organic building blocks. The linkage motif can be chosen from non-conjugated bonds such as boronate esters to sp^2 carbon-conjugated frameworks.[25-27] Hence, one can not only decide if the linkers communicate over a conjugated bond but also adjust the degree of conjugation between the building units. With a view towards optoelectronics, the tunability of covalent organic frameworks allows for tailor-made absorption and photoluminescence behaviour of the building blocks by choosing from a whole range of chromophores.[28] Even sterically demanding side groups can be integrated into a framework by employing an asymmetric functionalization strategy.[29] Another parameter that can be adjusted to some degree is the stacking distance in two-dimensional (2D) covalent organic frameworks, which controls the nature and strength of the electronic overlap of adjacent layers and can promote the formation of long-lived excited species.[30]

In this review, we will discuss recent studies dealing with the optoelectronic properties of COFs, and explore their potential regarding key features such as efficient transport of excitons or

charge carriers, suitable absorption bands for harvesting the solar spectrum, or tunable emission for light-emitting devices.

1.1 Structural aspects – impact of different COF structures on electronic interaction

1.1.1 Linkage motif as a key feature controlling electronic interactions (conjugation)

A powerful approach towards tuning or controlling electronic interactions within the COF is to vary the linkage motif with which the building blocks are coupled. The first linkage motif leading to the family of crystalline covalent organic frameworks was the B-O bond, specifically involving boronate esters and boroxine rings.[1] This linkage motif is moderately stable and does not result in conjugated building blocks. It provides a suitable tool for generating non-conjugated heterojunctions, for example in a donor-acceptor COF.[23] However, the stability issue and the missing conjugation has limited applications in other optoelectronic fields.

Additional dynamic (slightly reversible) bond formation reactions have been implemented on the way towards new functional and stable COFs, such as the imine bond formed by the condensation of an aldehyde and an amine. In 2009, Yaghi and co-workers synthesized COF-300 from the condensation of tetra-(4-anilyl)methane and terephthalaldehyde, resulting in a 3D COF and the first COF using imine linkages as the connecting part.[31] This motif leads to conjugation throughout the frameworks across the linkage bonds. This has a direct impact on absorption and photoluminescence properties of the resulting imine linked COF, leading to larger conjugated, connected systems and hence to red-shifted optical features. Even though the stability of these (often) highly crystalline frameworks exceeds that of the boronate ester-linked COFs, imine bonds are still sensitive towards hydrolysis. Additional stability was built into COFs by employing a keto-enol-tautomerism occurring in building blocks with hydroxyl groups adjacent to the aldehyde function. The reversible condensation reaction of 1,3,5-triformylphloroglucinol and *p*-phenylenediamine or 2,5-dimethyl-*p*-phenylenediamine yielded the COFs TpPa-1 and TpPa-2, respectively. By means of an irreversible tautomerization, the COFs adopt a stable form that is prevented from undergoing the hydrolysis reaction in boiling water and acid, whereas the TpPa-2 even showed strong resistance against base.[32]

In general, a rotation around the imine bond is possible and occurs within the frameworks. This rotation of the building units, however, weakens the conjugation via the linking bond. Searching for a way to overcome this undesired rotation and to introduce an additional stability factor, the groups of Lotsch and Yaghi developed two different strategies towards locking the imine bond.

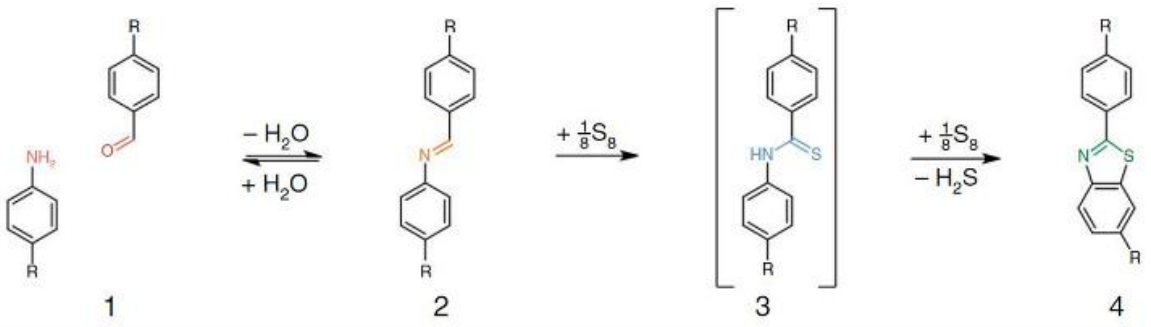

Figure 1.1: General scheme of the topochemical conversion of the imine bond into the thiazole linkage in TTT-COF. Reproduced with permission.[33] Copyright 2018, Nature Publishing Group.

In one approach, the TTI-COF (made of triazine triphenyl aldehyde and the respective amine) was treated post-synthetically with elemental sulfur at elevated temperatures. Under such conditions, aromatic imines oxidize to form a thioamide and then cyclize into a thiazole ring. The resulting TTT-COF showed high electron beam stability and provided a perfect system to study the local structure by TEM (Figure 1.1).[33] The group of Yaghi chose a different approach towards creating the thiazole (and oxazole) linkage. Using a linker exchange reaction followed by oxidative cyclization, ILCOF-1 was first synthesized from 1,3,6,8-tetrakis(4-formylphenyl)pyrene (1) and 1,4-phenylenediamine and then the substitution was carried out with 2,5-diaminobenzene-1,4-dithiol dihydrochloride and 2,5-diaminohydroquinone dihydrochloride to yield COF-921 and LZU-192, respectively.[34]

A long-standing aim of the COF research community has been to synthesize COFs purely based on sp^2-carbon conjugated bonds. That goal was achieved with the sp^2c-COF in 2017 by Jiang and co-workers. The sp^2c-COF was synthesized by polycondensation of 1,3,6,8-tetrakis(4-formylphenyl)pyrene as a tetravalent node and 1,4-phenylenediacetonitrile under solvothermal reaction conditions (Figure 1.2).[25] Based on these findings, other COFs linked by carbon-carbon double bonds followed, already indicating that not only the stability is of great advantage for further applications but also that the COFs demonstrate promising optoelectronic features such as tunable light emission with high PL quantum yields and photocatalytic activity for hydrogen evolution.[35-36]

A different approach towards accessing completely olefin-linked COFs was developed by Yaghi and co-workers in 2019. 2,4,6-trimethyl-1,3,5-triazine (TMT) and 4,4′-biphenyldicarbaldehyde undergo a trifluoroacetic acid catalyzed aldol condensation reaction to form COF-701 with high chemical robustness.[37] Shortly after, Acharjya *et al*. investigated a base-catalyzed aldol

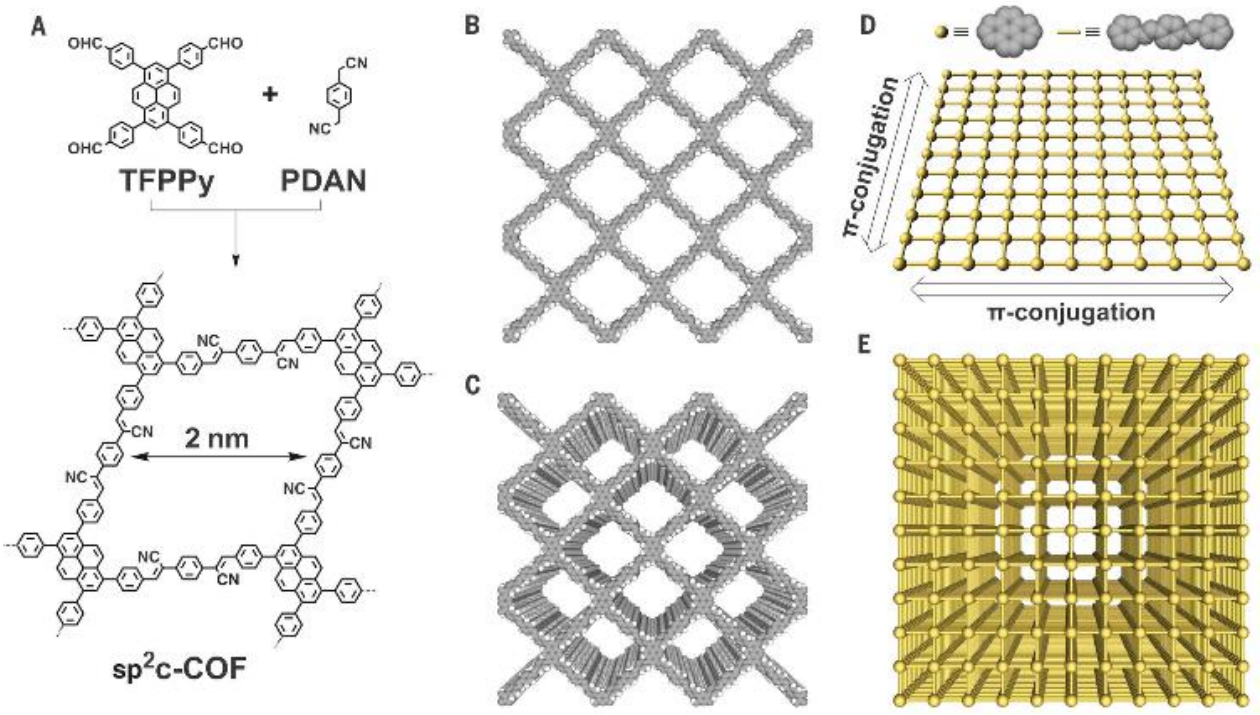

Figure 1.2: Scheme of sp^{2}c-COF synthesis (A). Crystal structures of a single layer (B) and many layers (C) of the sp^{2}c-COF exhibiting ordered pyrene π-stacks and 1D pores. Schematic overview of the intralayer π-conjugation of a single (D) and many layers (E). Reproduced with permission.[25] Copyright 2017, American Association for the Advancement of Science.

condensation of TMT with terephthalaldehyde and 1,3,5-tris(4-formyl)phenyl benzene leading to V-COF-1 and V-COF-2, respectively.[26]

The above examples illustrate the variety of bond formation reactions that are already available for constructing COFs, hence offering many options for tuning and controlling conjugation and stability of tailor-made COFs in optoelectronic devices.

1.1.2 π-Stacking – tuning by proximity effects

The mode of stacking and the stacking distance of the π-systems embedded in COFs is another means of adjusting their electronic properties. In the first semiconducting COF, discovered by the Jiang group in 2008, the prominent π-stacking of the TP-COF synthesized from 2,3,6,7,10,11-hexahydroxytriphenylene (HHTP) and pyrene-2,7-diboronic acid (PDBA) was seen as a promising characteristic for a semiconducting COF material. The electrical conductivity was measured applying a two-probe method, showing increased current for the stacked, covalently connected building blocks in the COF compared to the neat monomers.[38]

This publication point to the importance of stacking in COFs for optoelectronic applications. In

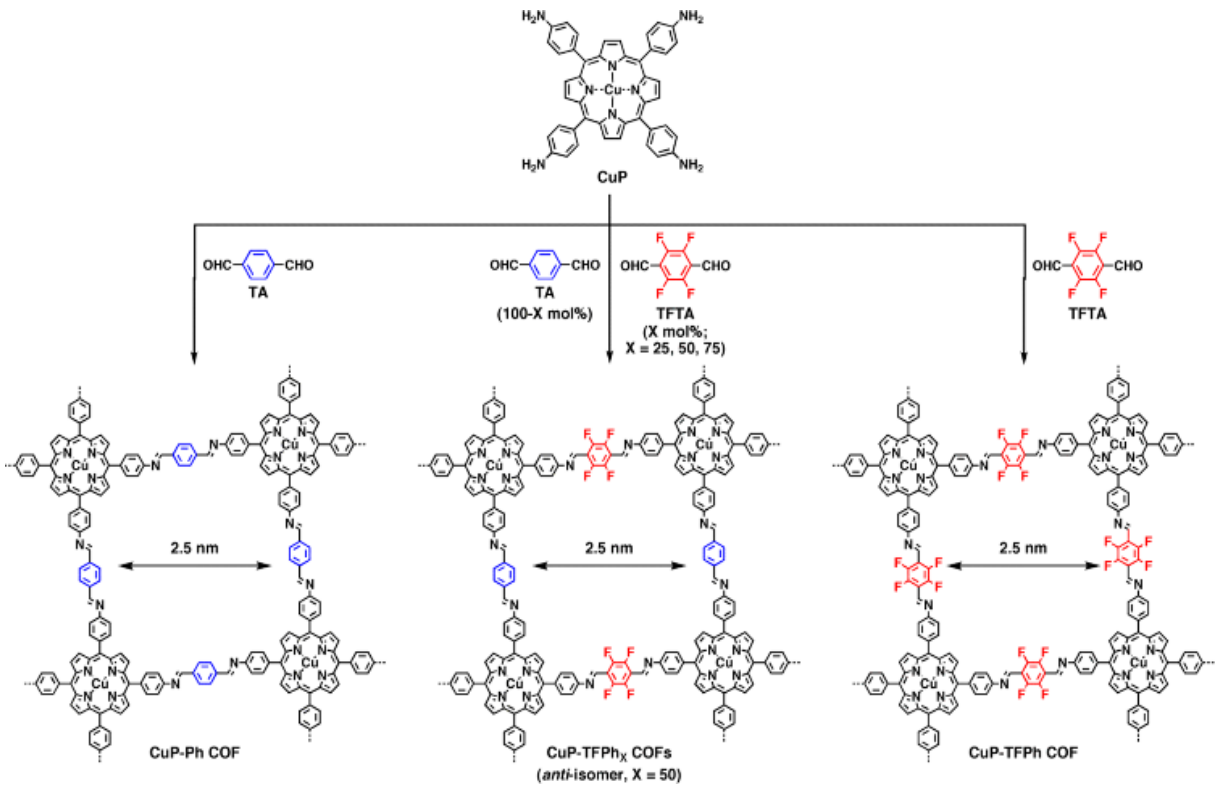

Figure 1.3: Scheme of a COF synthesis implementing self-complementary π-electronic interactions ($TFPh_{50}$) in the middle and the controls CuP-Ph COF and CuP-TFPh COF. Reproduced with permission.[39] Copyright 2013, American Chemical Society.

order to control the stacking of the COF layers and its effect on optoelectronic properties, many groups have investigated different approaches and designed concepts taking advantage of the modular system of COF synthesis. Chen *et al.* controlled the interlayer distance by inducing self-complementary π-electronic interactions. Partially replacing non-substituted arenes with fluoro-substituted arenes in a porphyrin-COF, the interlayer interactions and distances could be tuned (Figure 1.3). Along with the increased π-π interactions, the crystallinity was enhanced and the HOMO-LUMO gap was reduced, suggesting an enhanced ability for electron transfer.[39] Several concepts aiming at increased crystallinity by efficient and geometry-guided stacking were elaborated by our group. The studies highlight the significance of the interplay of propeller- and armchair-shaped tri- and tetradentate building blocks with their linear counterpart (1,1,2,2-tetrakis(4-formylphenyl)ethane (TPE) and pyrene, respectively).[40-41] Here, the often used tetraphenyl pyrene linker was intensively studied owing to the fact that pyrene serves as an important building block for several optoelectronic COF materials. The synchronized offset induced by the chair conformation of the pyrene unit provides optimum conditions for the formation of several highly crystalline, densely packed COFs (Figure 1.4).[41] Considerable delocalization of excitations along the close-packed, slip-stacked pyrene stacks was observed and it was also shown that charge-transfer excitations are possible across the imine bonds. This

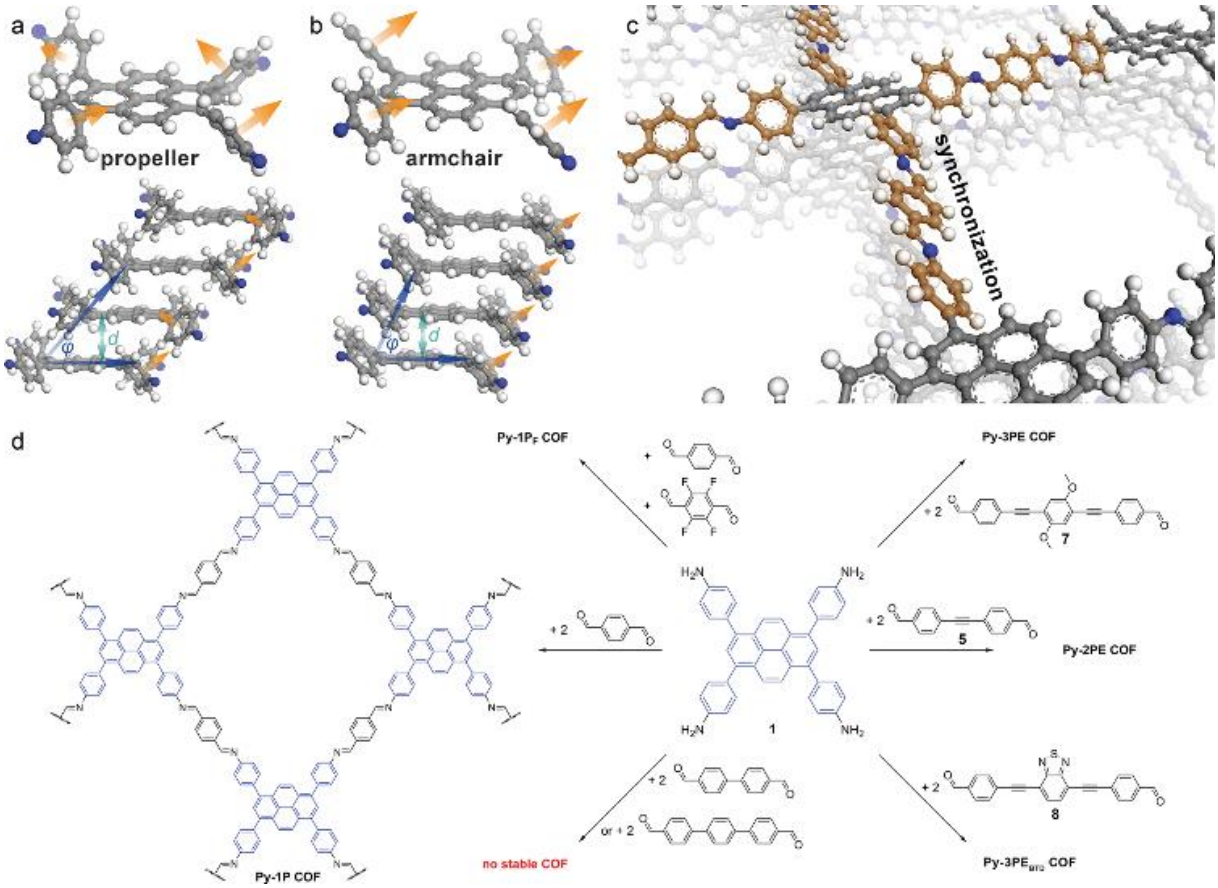

Figure 1.4: The structure of the different possible conformations of the pyrene molecule (a,b). The crystal structure of the Py-1P COF with pyrene in the armchair conformation allowing for closely stacked layers (c). Scheme of COF syntheses (d). Reproduced with permission.[41] Copyright 2016, American Chemical Society.

design concept allows for a broad range of tailor-made 2D COFs with extended π-conjugated building blocks for applications in photocatalysis and optoelectronics.

The group of Loh studied the photoluminescent properties of different 2D COFs and introduced approaches to overcome fluorescence quenching by strong *π-π* interactions and by locking-in imine bonds that could potentially rotate under excitation. In the first work,[42] the authors proposed that the *π-π* interlayer interactions in the stack are reduced when pyrene is combined with a non-planar building block such as TPE. In conjunction with the fabrication of spherical COF nanoparticles in which a curvature-induced strain might lead to restricted imine rotations and decreased *π-π* interactions, the aggregation-caused quenching (ACQ) mechanism was shown to be disabled.[42]

In the second work of the Loh group,[21] the imine bonds were locked-in by intramolecular hydrogen bonds to inhibit the rotationally labile linkage. Enabling a restriction of intramolecular bond rotations (RIR), the photoluminescence of the COFs could be enhanced. In addition, this RIR mechanism could be intensified by additional intermolecular hydrogen

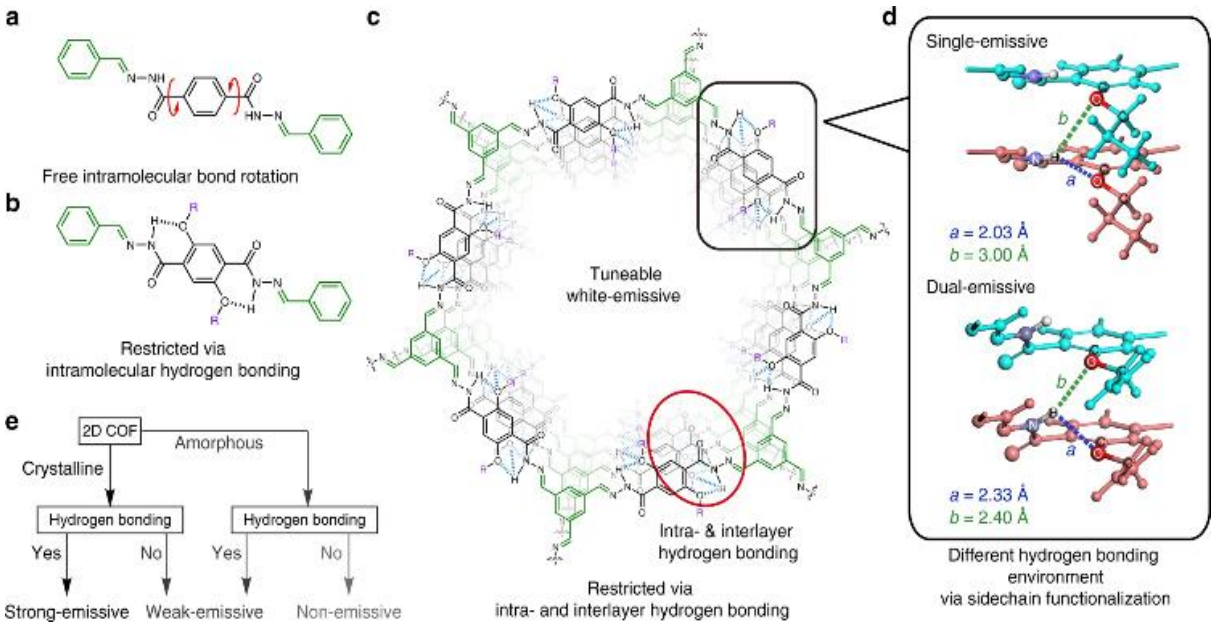

Figure 1.5: Intralayer hydrogen bonds restrict rotation leading to enhanced emission in the UV to violet range (a,b,c). The combination of intralayer and interlayer hydrogen bonds results in single- and dual emissive COFs (d) and the strategy to obtain strongly-emissive COFs. Reproduced with permission.[21] Copyright 2018, Nature Publishing Group.

bonds that occur in this eclipsed COF structure (Figure 1.5). Both kinds of hydrogen bonds could be used to tune the PL emission wavelength to gain almost white emission. In comparison, related eclipsed-stacked COFs without hydrogen bonding exhibited significantly weaker fluorescence.[21]

Recent work of the group of Zamora showed the effect of different stacking modes on the photoluminescence behavior of the COFs. By modifying the trigonal aldehyde linker to obtain 1,3,5 benzenetricarboxaldehyde or 2,4,6-triformylphloroglucinol, it was possible to shift the stacking from the staggered to the eclipsed form, respectively (Figure 1.6). As a consequence, this change turns on the fluorescence in the staggered-stacked IMDEA-COF-1 due to the decreased π-π interactions between the pyrene chromophores.[43] Another approach to influence the stacking mode is by steric tuning of the building blocks. Attaching alkyl chains to the core structure 1,3,5-tris(4-aminophenyl)benzene leads to different stacking behavior; whereas the absence of alkyl chains creates an AA stacking, ethyl and isopropyl chains induce an AB or ABC stacking. The study investigated binary, ternary and quaternary COFs with linear (terephthalaldehyde, 1,3,5-tris(4-aminophenyl)benzene, 4,4'-Biphenyldicarboxaldehyde and 2,2'-bipyridine-5,5'-dicarbaldehyde) and trigonal aldehydes (benzene-1,3,5-tricarbaldehyde and tris(4-formylphenyl)amine).[44]

In order to investigate the planarization of the well-known TPE building unit that adopts a propeller-like structure, recent work introduced a novel linker unit called dibenzo[*g*,*p*]chrysene (DBC). This chrysene unit features additional C-C bonds that cause a more planar and rigid tetradentate chromophore. The studies showed that the dibenzochrysene linker allows for closely packed docking, with the interlayer stacking distance reduced by almost 1 Å in comparison with analogous COFs embedding the TPE node.[30, 45] Furthermore, our group established the influence on the photoluminescence properties of the closer stacked DBC-COFs compared to the COFs using the propeller-shaped TPE. The enhanced PL lifetimes obtained in the DBC COF are postulated to be the consequence of a structurally induced stabilization of the photoexcited species across the DBC stacks.

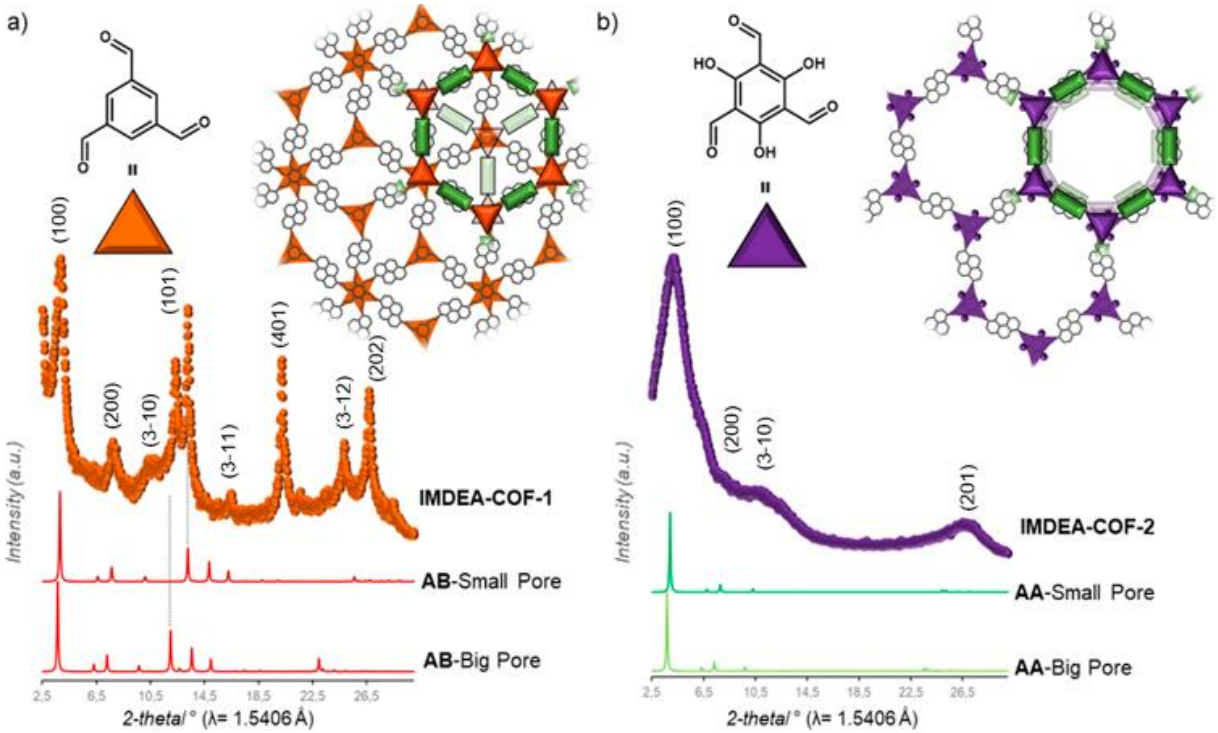

Figure 1.6: The crystal structure of IMDEA-COF-1 (a) and -2 (b) with AB- and AA-stacking, respectively, and the experimental diffraction data. Reproduced with permission.[43] Copyright 2018, American Chemical Society.

1.1.3 Self-assembled H- and J-aggregates

When a specific spatial stacking arrangement of chromophores is present in the COF, they can form H- or J-type aggregates within the framework of the COF. The different arrangements of the (transition)dipoles occur by either distinctly eclipsed alignment (H-aggregate) or a shifted (in the extreme case head-to-tail) alignment (J-aggregate). As a result, the optical features change and get blue-shifted for the H-aggregate and red-shifted for the J-aggregate.[28]

In the work of Ding *et al.*, the authors synthesized a metallophthalocyanine-based COF where the stacked phthalocyanines form an H-aggregate. Through the ordered, π-stacked columns of phthalocyanines the material exhibits enhanced intensity of the absorption bands in the visible and NIR light, is semiconducting and allows for an increased charge carrier transport in the COF.[46] Yaghi and co-workers were able to tune chromophore absorption spectra by fabricating H-aggregates of porphyrin units in COF-66 and COF-366.[47] Our group discovered that by the choice of the linear linker the nature of porphyrin aggregates could be switched to an extended J-aggregate (Figure 1.7). The solid COF matrix enforced the packing of the porphyrin units into J-aggregate formation, which led to strongly enhanced absorption into the IR region and stabilized photoexcited species with slower decay dynamics.[28]

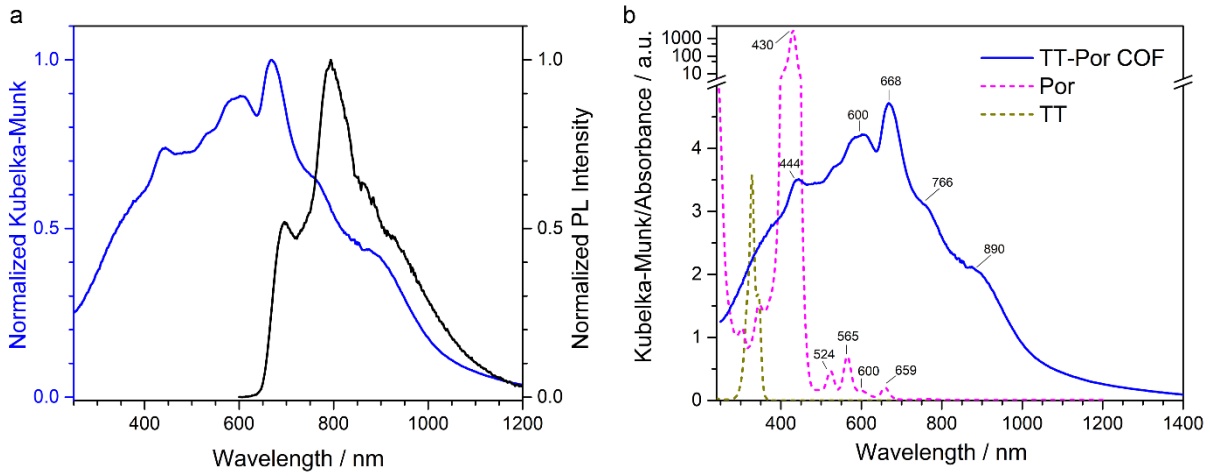

Figure 1.7: (a) Optical absorption (blue) spectrum of TT-Por COF measured as diffuse reflectance of the solid and converted with the Kubelka–Munk equation, and PL (λ_{exc} = 365 nm, black) spectrum of TT-Por COF. (b) Absorption spectra of the TT-Por COF (blue) compared to the monomers thienothiophene (TT) and porphyrin (Por) measured in diluted solution (50 µM, dioxane). Reproduced with permission.[28] Copyright 2018, American Chemical Society.

The formation of H-aggregates in boronate ester-based COFs was investigated by Spitler and Dichtel. They adapted a Lewis-acid catalysed procedure for protected catechols to overcome the issue of insoluble building blocks. This way, it was possible to synthesize a cofacially stacked phthalocyanine-based COF in which the phthalocyanine columns formed H-aggregates connected by 1,4-phenylenebis(boronic acid). This type of aggregation was indicated by the induced blue shift of the absorption maxima and a broadening into the NIR. Together with the non-emissive behaviour compared to the neat monomers, the H-aggregate stacking of the phthalocyanines could be confirmed.[48] Another study investigating COFs interlinked by boronate ester formation (made of 4,4′-benzildiboronic acid (BZLBA) and 2,3,6,7,10,11-hexahydroxytriphenylene (HHTP)) was performed by Wang *et al.*, who analysed the influence

of the interlayer distance on the phosphorescent properties of the eclipsed COFs. The authors show that next to the RIR mechanism and the H-aggregate formation the stacking distance is an important factor for tuning the photoluminescence in COFs (Figure 1.8).[49]

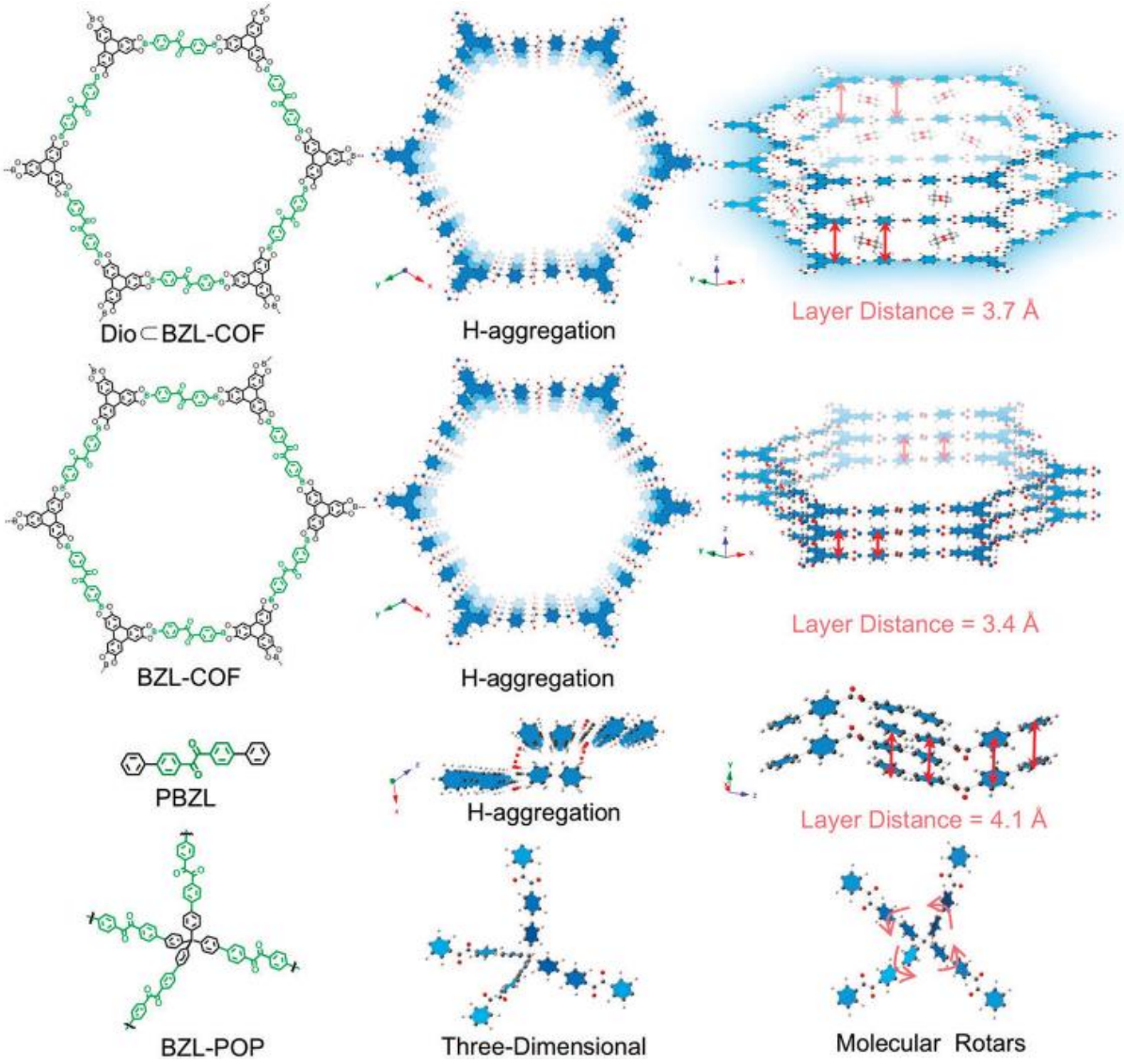

Figure 1.8: Structures of Dio BZL-COF, BZL-COF, PBZL and BZL POP and the corresponding interlayer distance. Reproduced with permission.[49] Copyright 2018, Royal Society of Chemistry.

1.1.4 Theoretical insights into stacking and growth behavior of COFs

First theoretical simulations based on DFT-B allowed for enhanced understanding of properties regarding structure and energy of the investigated boronate ester-based COFs. The stacking modes of the 2D COFs considered here were AA and AB stacking as well as low-symmetry versions such as serrated and inclined. It was found that the shifted layers such as AB, serrated and inclined lead to less repulsive interlayer interactions and subsequently to reduced stacking

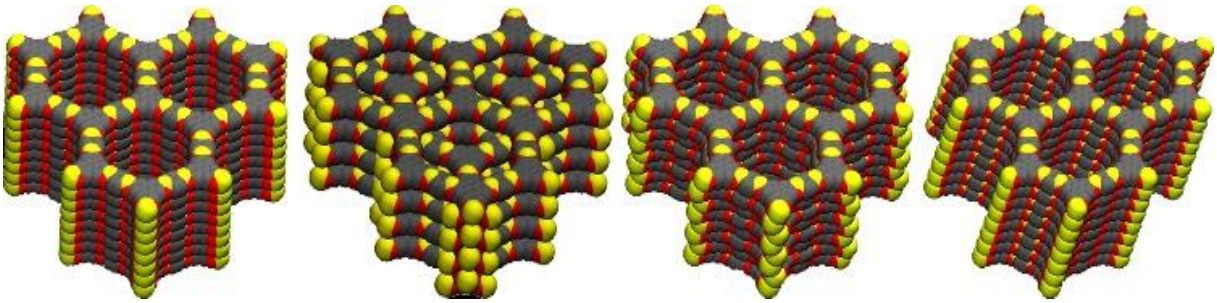

Figure 1.9: Calculated COF layer stackings AA, AB, serrated and inclined. Reproduced with permission.[50] Copyright 2010, Beilstein-Institut.

distances (Figure 1.9). However, the simulated XRD patterns for the respective stacking forms revealed that the AB stacking shows a distinct disagreement with experimental XRD data. Furthermore, the bandgaps of the respective boronate ester-based COFs were calculated to be between 1.7 eV and 4.0 eV, indicating that these COFs are semiconductors. It is important to note that the stacking mode as well as the distance of the adjacent layers greatly influence the bandgap.[50] This work was supported by another study that found the serrated and inclined stacking behavior in hexagonal COFs (COF-1, -5, -6 and -8) to be the energy minimum.[51] These results are in good agreement with the theoretical work of Spitler *et al.* showing that the hexagonal COF layers in HHTP-DPB COF (4,4′-diphenylbutadiynebis(boronic acid) (DPB)) are slightly offset by 1.7-1.8 Å.[52]

Another study showed that eclipsed stacking of triphenylenes leads to strong electronic coupling of the adjacent COF layers in HHTP-based COFs, thereby allowing for charge delocalization across the stack. The authors postulate band-like transport of delocalized charge carriers with promising mobility values for COFs.[53]

The effect of stacking was also investigated with regard to out-of-plane deformation and vacancy defects in the COF sheets. To investigate the influence of the stacking, the deformation and defects were studied for different number of layers in COF-5. It can be observed that the COF sheets in general exhibit large out-of-plane deformations in the range above 10 nm for isolated COF monolayers. If the COF layers are then stacked, the deformation decreases significantly and the role of defects diminishes. The defect concentration was found to be proportional to the out-of-plane deformation (Figure 1.10).[54]

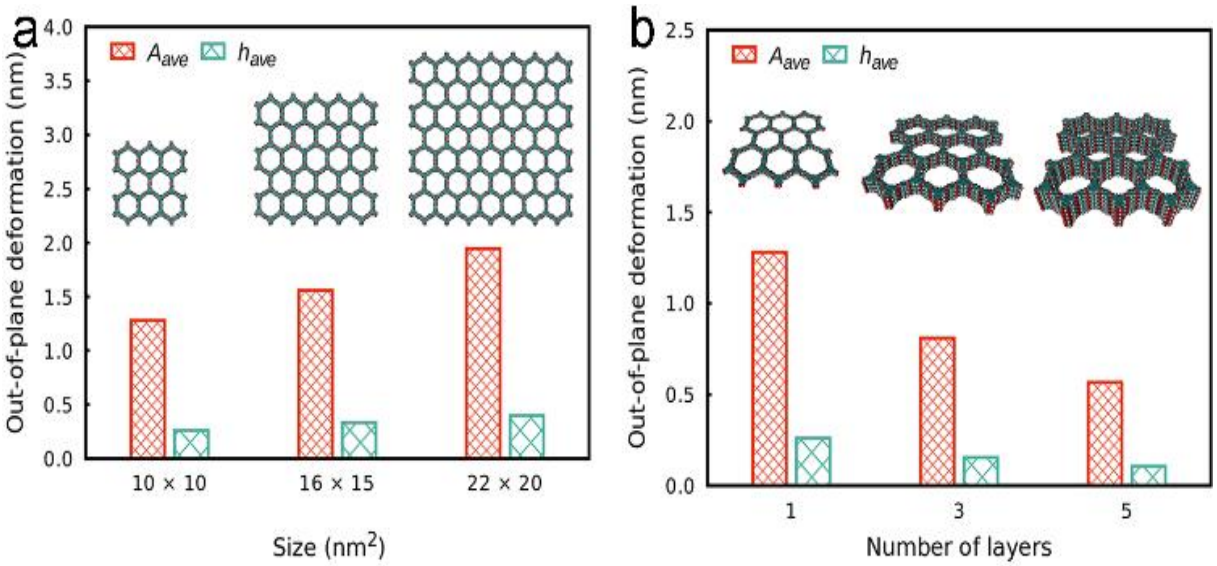

Figure 1.10: Out-of-plane deformation as a function of the COF sheet size (a) and of the number of stacked layers (b) in COF-5. Reproduced with permission.[54] Copyright 2018, American Chemical Society.

Furthermore, simulations of the crystallization process during the synthesis showed that enhanced stacking interactions of the building blocks in COF-5 lead to a rapid assembly of the monomers, accompanied by an increasing amount of defects causing poor crystallinity (Figure 1.11).[55] The authors suggest to use solvents that reduce the stacking interactions or nonplanar linker molecules with decreased stacking free energy.

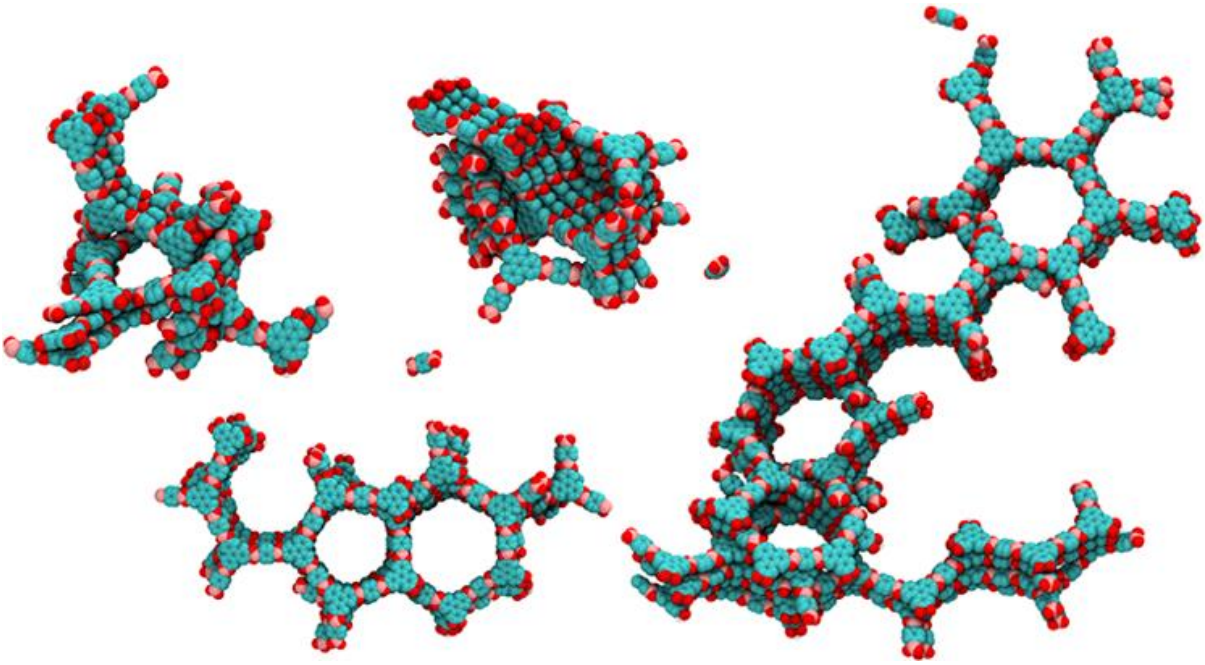

Figure 1.11: View of calculated clusters during synthesis with typical defects such as interpenetrating rings, five-membered rings and screw dislocations in COF-5. Reproduced with permission.[55] Copyright 2018, American Chemical Society.

1.1.5 Other approaches to structure COFs

Since there is a large pool of building blocks to choose from, not only the bond formation, conjugation or stacking can be varied, but other features such as the electronic nature of the building blocks can be designed and controlled as well. The combination of electron donor and electron acceptor units in the COF can lead to the formation of an intrinsic heterojunction of spatially separated donor and acceptor columns. The implementation of heterojunctions in the COF material is an attractive synthetic target for potential applications in organic electronics such as organic photovoltaics. Conceptually, this can be achieved by either inserting acceptor/donor molecules into the pores of an appropriate COF, or by tailoring the pore walls (in 2D COFs) such that donor and acceptor stacks are embedded in the COF structure, enabling charge separation and transport.

Hence, by modifying the fundamentally p-type NiPc COF made from 1,4-benzenediboronic acid and (2,3,9,10,16,17,23,24-octahydroxyphthalocyaninato)nickel(II)[46] with electron deficient linear units such as benzothiadiazole yielded an electron-conducting material.[56] This was elaborated further in the 2D D-A COF synthesized by Jiang and co-workers, where the triphenylene building block assumed the role of the donor and the benzothiadiazole building block represented the acceptor unit. This design allowed for significant charge carrier transport, electrons as well as holes, and photoconductivity.[57] Further studies showed that the charge

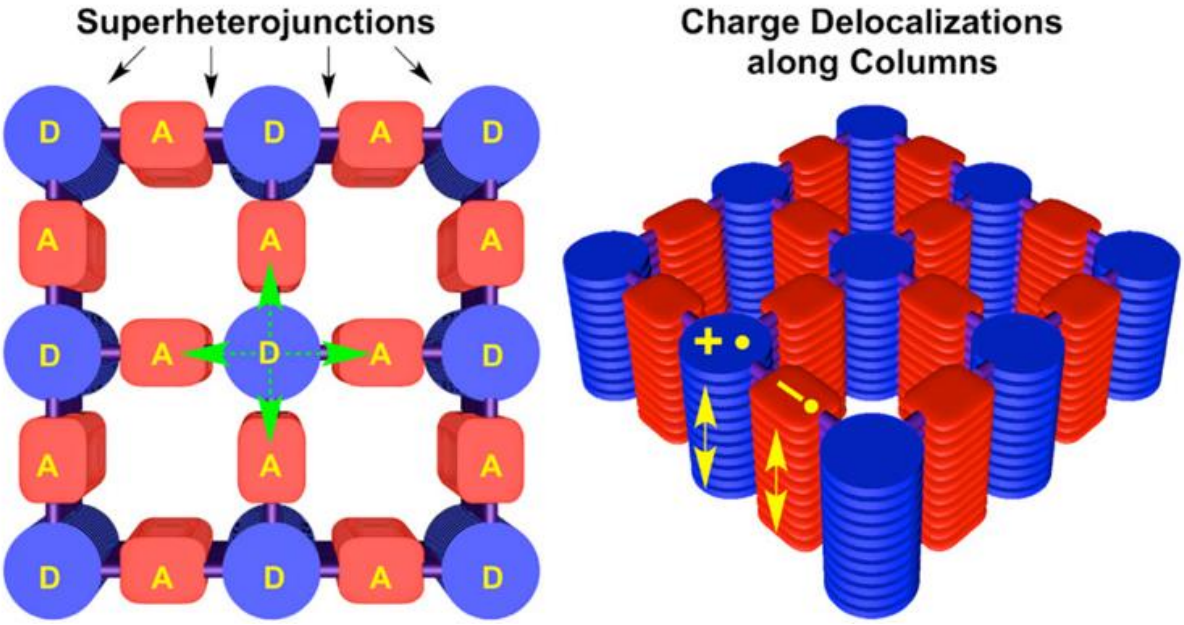

Figure 1.12: Illustration of segregated donor−acceptor columns in D_{MPc}-A_{DI}-COF. Photoinduced electron transfer occurs directly to the adjacent acceptor and also to diagonally disposed acceptors. Charge carrier migration is depicted as arrows along the columns. Reproduced with permission.[59] Copyright 2015, American Chemical Society.

generation and separation in these D-A frameworks occurs in the femto- and picosecond regime and that it leads to long-lived charge separation in the region of several microseconds (Figure 1.12).[58-60]

The design of D-A heterojunctions in COFs leads to broadband light absorption and photoconductivity, which allows for the design of a metal-free photocatalyst COF-JLU22 for reductive dehalogenation[61] or a photoinitiator TTT-DTDA and -BTDA COF for free radical polymerization.[62] Even the introduction of non-linear optical behavior is possible in the Sa-TAPA COF containing a donor-acceptor dyad.[63]

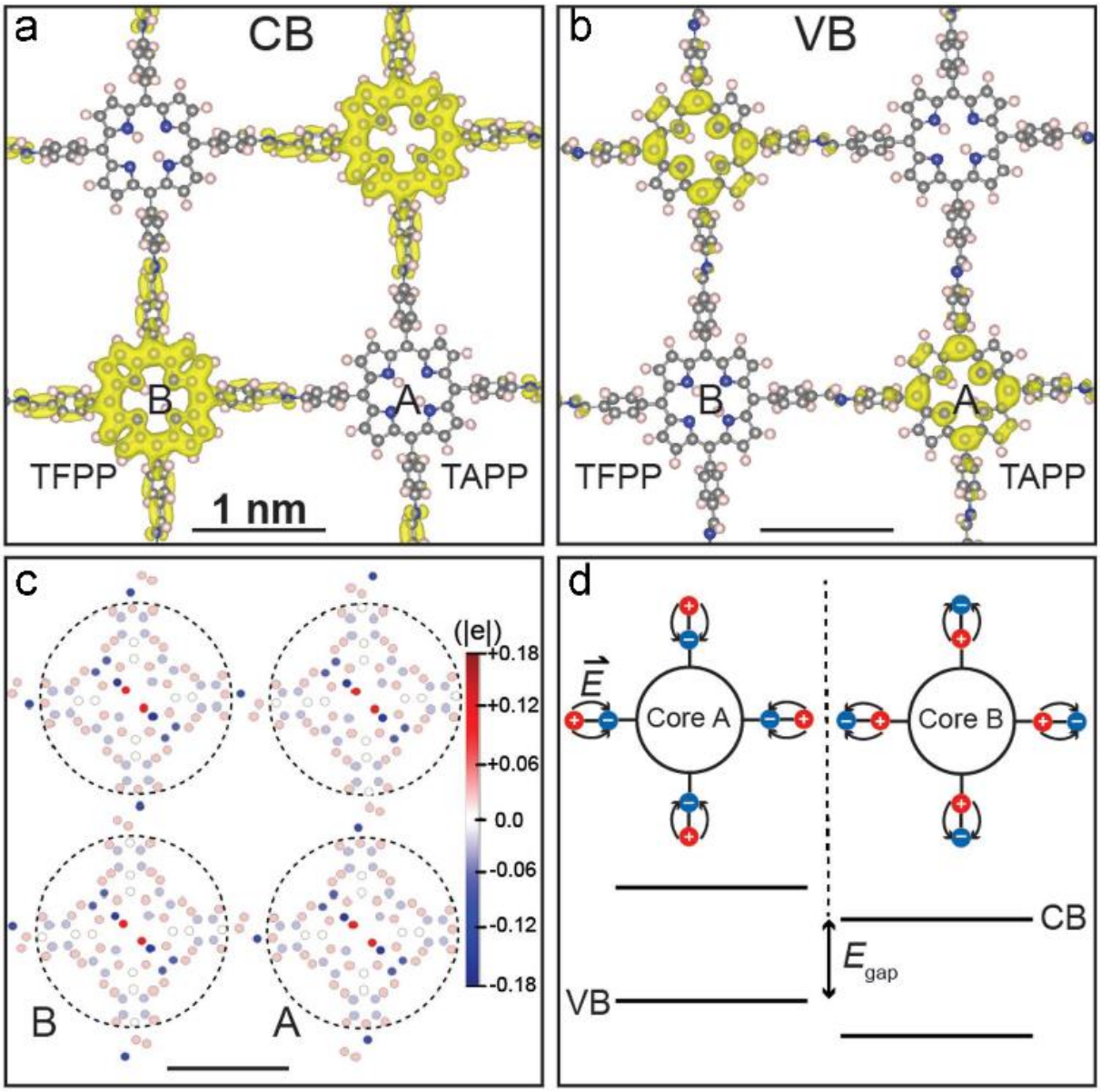

Figure 1.13: Charge density distribution for COF-420 at the conduction band minimum (a) and at the valence band maximum (b). (c) Hirshfeld population plot of COF-420 with local dipoles on nitrogen atoms (blue), and on carbon and hydrogen atoms (red). (d) Energy diagram with offset between core A and B. Reproduced with permission. Copyright 2019,[65] John Wiley and Sons.

Another approach to synthesize ordered donor-acceptor interfaces is by attaching azide groups to a fraction of the linear linkers in 2D COFs. These groups then operate as anchors in the pore walls for alkyne-modified fullerenes that can be attached by click chemistry. The electron-donating N_3-ZnPc COF is then precisely connected to the electron-accepting fullerene units in the channels.[64] Further, Crommie, Yaghi and Li developed a COF with a molecular heterojunction consisting of the same chromophores. The condensation of the porphyrin amine (core A) and the porphyrin aldehyde (core B) on a gold surface yielded the single-layer COF-420. Even though the COF consists solely of porphyrin-based building blocks, the donor-acceptor nature is induced by the asymmetric imine linkage bond causing the conduction band and valence band to localize onto different cores (Figure 1.13).[65]

With the two-in-one design strategy introduced by the group of Chen, an imine COF was synthesized by self-condensation of a pyrene bearing amine and aldehyde functions all in one building block (1,6-bis(4-formylphenyl)-3,8-bis(4-aminophenyl)pyrene (BFBAPy)). The resulting solvent-independent synthesis of the COF leads to simple handling and easy film synthesis. The films were investigated as a proof-of-principle in perovskite solar cells as hole transporting material.[66]

Gosh *et al.* developed a structure–property–activity relationship for the strategic development of novel COFs for efficient photocatalytic H_2 evolution. To elucidate the key factors for enhanced efficiency, the study compared experimental data from tailor-made COFs supported by calculations. From these studies it could be derived that the consideration of light absorption and charge carrier generation as well as transport is crucial for the design of photocatalytic water splitting of COFs.[67]

Further treatment methods such as pyrolysis and ionothermal transformation use the COF structure as a template. The resulting carbon-rich materials exhibit an increase of the conductivity.[68-69]

1.2 Interaction of light with COFs

Covalent organic frameworks can be designed to contain interconnected chromophore units that absorb visible light. Changing the size of the chromophore or introducing donor-acceptor features into the framework can enhance the absorption at lower energies. In addition, the degree of conjugation between the linked building units and the rotation of bonds within and between the linker molecules play an important role when it comes to absorbing visible light. With COFs, it is possible to tune these features and to synthesize strong absorbers not only in the visible but also in the (near) infrared (IR). The photoexcited states in the COF are then able to relax by emission or non-radiative decay. The emission can be of fluorescent or phosphorescent nature, depending on the spin relaxation pathways designed through the choice of linker molecules.

1.2.1 Photoemitting frameworks

The ability of COFs to serve as photoemitters was first reported in 2008, leading to an increased focus on optical properties.[38] Due to the aggregation-induced quenching effect of the π-stacked layers in 2D COFs, the PL emission is often reduced.[48] Furthermore, the popular imine bond formed during condensation of amine/aldehyde building blocks is also known to quench photoluminescence by temperature-dependent bond rotation.[70] These insights led to the development of first design principles for strongly emissive frameworks, by introducing building units that show aggregation-induced emission (AIE). For example, in a boronate ester-based COF propeller-shaped tetraphenylethylene (TPE) units were condensed with 1,2,4,5-tetrahydroxybenzene to obtain TPE-Ph COF. The PL properties of the resulting COF revealed fluorescence quantum yields of 32% in the solid COF material. When compared to a related model compound (tetraphenylethylenetetraboronic acid-pinacol ester), the PL quantum yield (QY) was enhanced in the COF implying that the stacking and interactions between the layers contribute to the higher PLQY values.[71] Another design strategy taking advantage of the AIE mechanism was based on mechanically entangling 1D organic strands with metal-coordinating phenanthroline building blocks. The interlocked 3D 'woven' COF-500 was found to be non-emissive in the metalated form where the ETTBA linker was spatially segregated from the adjacent linker, thus enabling rotation of the phenyl rings. After demetalation, the free rotation was restricted due to the non-coordinating phenanthroline units spatially approaching the

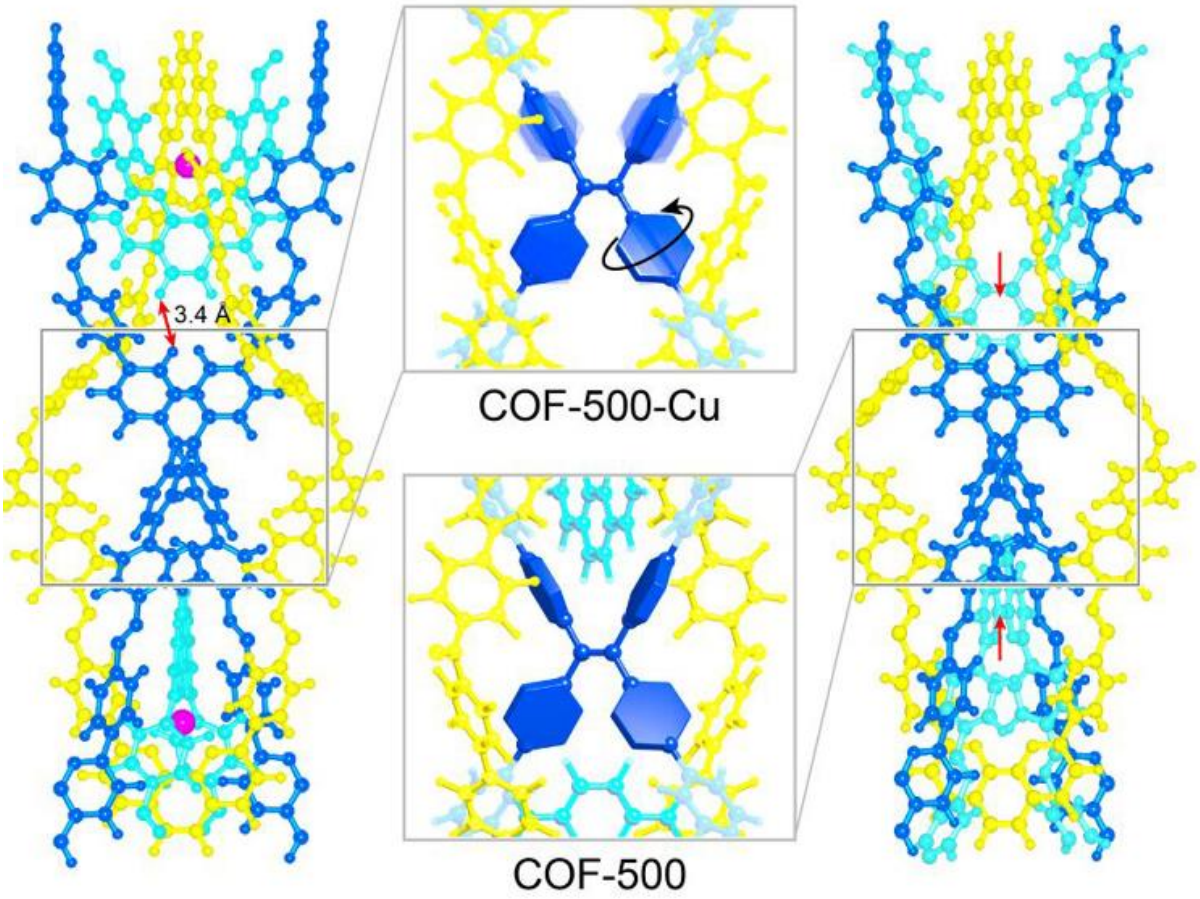

Figure 1.14: Motion of the phenylene groups of the tetraphenyleneethylene (TPE) core is restricted upon dematalation which enables the phenanthroline moieties (cyan) to move towards the TPE core in COF-500. Reproduced with permission.[72] Copyright 2018, American Chemical Society.

central ETTBA linker (Figure 1.14). This restriction of bond rotation led to aggregation-induced emission.[72]

We have recently developed a strategy allowing the construction of a quaterthiophene-based COF series by an asymmetric functionalization of the building blocks.[29] Using this approach, the steric repulsion was minimized enabling close face-on packing of the linear quaterthiophene (4T) units. The concept could also be transferred to optically interesting 4T-derived building blocks such as 3,3"-dibutyl-[2,2':5',5":2",2"'-quaterthiophene]-5,5"'-dicarbaldehyde (a4T), 4*H*-thieno[3,4-*c*]pyrrole-4,6(5*H*)-dione (TPD) and thieno[3,4-*b*]thiophene (TT) modified quaterthiophene ($4T_{TPD}$, $4T_{TT}$). It was shown that the optical properties of such oligothiophene COFs can be precisely tuned and tailored, resulting in COFs with optical absorption and emission far into the NIR region (Figure 1.15). Additionally, for the first time a charge transfer between the pyrene and the 4T units across the imine bond was observed.[29]

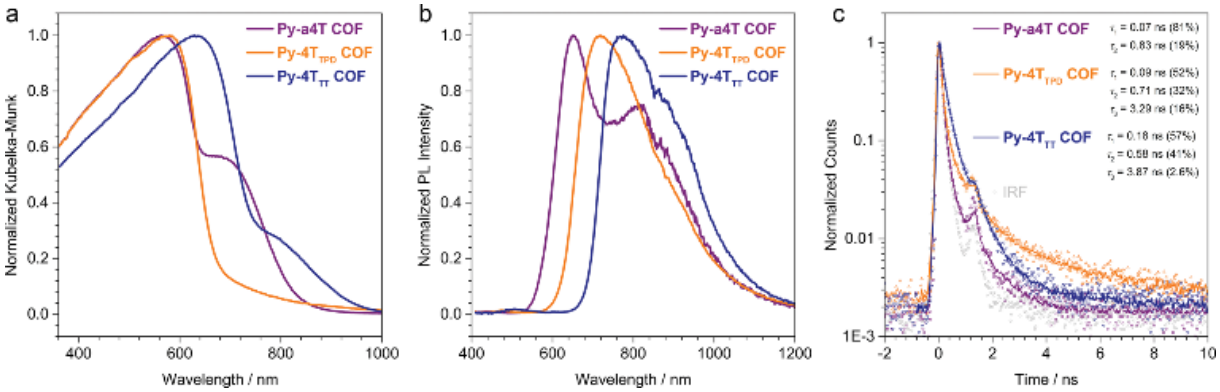

Figure 1.15: Optical properties of COFs built with quaterthiophene derivatives. Sterically demanding modifications on the backbone were enabled by an asymmetric functionalization approach. Reproduced with permission.[29] Copyright 2017, American Chemical Society.

Haldar *et al.* reported the first COF-LED with the IISERP-COF7 consisting of an anthracene and a triformyl resorcinol unit. The COF dispersed in N-methylpyrrolidone (NMP) showed a bright white emission. The source of the white light emission was attributed to the combination of the π-stacked anthracene units acting as a blue emitter and the resorcinol units contributing the red and green emission.[73] Approaching the white light emission challenge from a different angle, the first report on COFs grafted with lanthanides showed similar emission behavior. The COF was designed to bear coordination pockets for Eu^{3+} and Tb^{3+} that played an important role in complementing the blue emission feature of the COF with green and red emission from the lanthanides. The authors succeeded in synthesizing a solid-state white-light emitter, and by varying the excitation energy the emission could be tuned from orange over yellow to white light.[74]

Recently, a boroxine-linked COF series was synthesized in the form of stable colloidal suspensions. In this solution-based system, the emission of these highly photoluminescent COF colloids was suggested to originate from electronically communicating chromophores in the π-stacked COFs.[75]

Synthesizing COF single-crystals in sizes suitable for X-ray diffraction marked a big step forward for the structural and optical characterization of COFs (demonstrated for the imine-linked 3D COF-300, -303, LZU-79, and LZU-111 and for the boronate ester-based 2D COF-5 and COF-10).[76-77] Next to structural insights, the COF-5 colloids were investigated with transient absorption (TA) spectroscopy to identify the excitation dynamics dependent of the size of the crystallite. It was observed that for high photon fluence the exciton decay lifetimes drop with decreasing crystallite sizes. This behavior was postulated to occur due to exciton-exciton

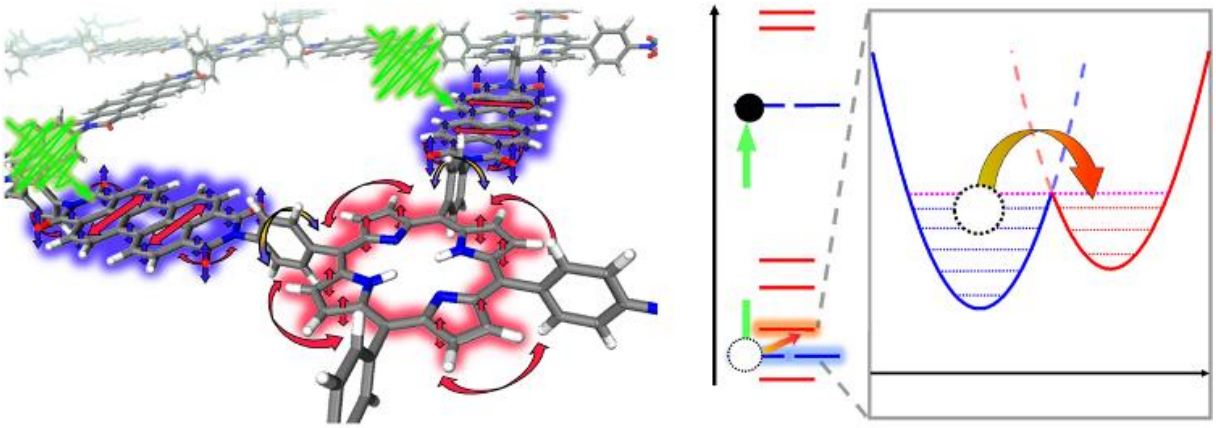

Figure 1.16: Schematic overview of phonon-assisted charge carrier dynamics in photo-excited COFs. The rotation of the phenyl ring correlates with the π-interactions between the PDI and the porphyrin linkers, leading to ultrafast hole transfer from PDI to the porphyrin macrocycle. Reproduced with permission.[60] Copyright 2019, Nature Publishing Group.

annihilation. The probability of excitons generated on smaller colloids to collide is higher than on larger crystallites where the crystallite size exceeds the diffusion length by far.[77]

Ultrafast charge transfer in a D-A COF, condensed from 3,4,9,10-perylenetetracarboxylic acid diimide (PDI) and porphyrin building blocks, could be observed with femtosecond TA spectroscopy and further studied by non-adiabatic molecular dynamics calculations. Photoexcitation of the PDI unit of the COF leads to charge generation, followed by hole injection from the PDI chromophore to the porphyrin ring resulting in polarons within the crystal lattice of the framework. The charge transfer with a time constant of 124 fs was phonon-assisted by the scaffold, especially by the motion of the phenyl rings connected to the porphyrin core (Figure 1.16).[60]

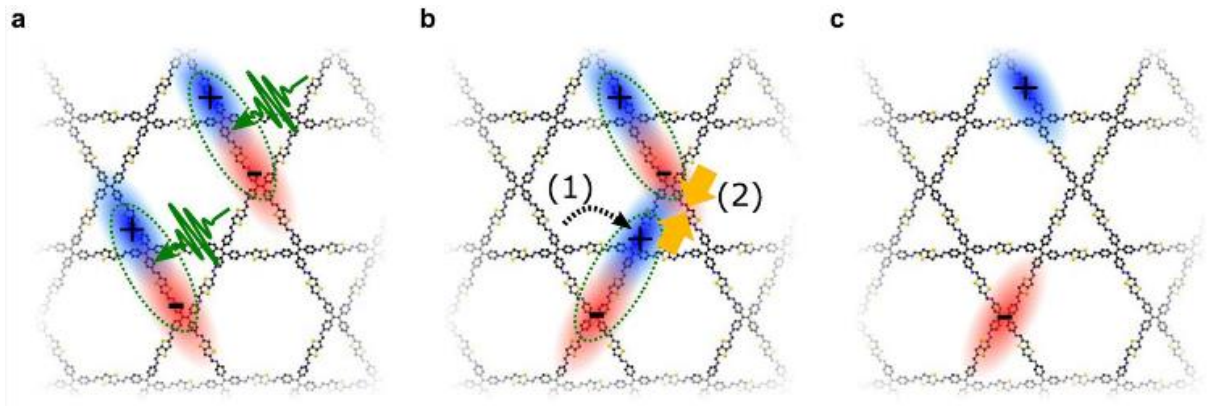

Figure 1.17: Illustration of the proposed photoinduced electronic processes in different imine-linked COFs (star-shaped COFs 4PE-TT and 4PE-BDT and hexagonal COF 3PB-BDT). (a) Photoexcitation leads to singlet excitons. (b) Diffusion and collision of generated singlet throughout the framework that leads to singlet−singlet annihilation. (c) Isolated free charges with lifetimes over tens of microseconds. Reproduced with permission.[78] Copyright 2019, American Chemical Society.

To study the excited-state dynamics in COFs grown as oriented thin films, Jakowetz *et al.* investigated a series of imine-linked COFs with TA spectroscopy. The measurements revealed similar dynamics independent of the COF topology and the authors proposed a standard model in which singlet excitons diffuse through the framework and possibly collide. Through these singlet−singlet annihilation events, charges are generated with lifetimes up to tens of microseconds, exceeding lifetimes of charges in classical polymer systems by orders of magnitude (Figure 1.17).[78]

1.2.2 Sensing ability

The ability to control the optical properties of COFs by various factors leading to different luminescence properties opens up the field of chemical sensing applications. The combination of the large surface area with pore channels accessible for small molecules and their delicate interplay with the photoluminescence properties of the framework makes COFs promising materials to sense and detect explosives, metal ions or even gases such as ammonia and HCl. The read-out of these COFs sensors occurs mostly via PL quenching of the material when interacting with guest molecules or ions.

With this in mind, one design of COFs requires functional sites in the pore walls for interacting with and sensing intruding molecules. This can be achieved by using azine-linked luminescent COFs in which the azine bridge acts as a possible docking site for hydrogen bonding. Such interactions with a trinitrophenol-type explosive led to sensitive and selective quenching of the photoluminescence of the azine-linked COF.[79] Adding hydroxyl groups as active sites in the framework allows for the detection of Cu^{2+} ions that bind to the nitrogen atoms of the azine linkage and the hydroxyl groups in the trigonal linker.[80] The chelating effect of a hydrazine-linked COF was used for the selective and sensitive detection of Fe^{3+} ions in water with a quenching constant of 2.3×10^4 M^{-1}. This method was facilitated by the geometrically precise design of the pockets with the suitable linker choice of benzene-1,3,5-tricarbohydrazide with 2,5-dihydroxyterephthal-aldehyde or 2,5-dimethoxyterephthalaldehyde.[81] Using DFT and TDDFT calculations, the influence of hydrogen bonding of simple formaldehyde on the emission profile of a representative boronate ester-based COF was elucidated. The analysis resulted in changes of the frontier molecular orbitals as well as electron configuration, which coincides with fluorescence quenching.[82]

Other docking sites for guest molecules can be thioether groups serving as receptor for the detection and removal of mercury. Again, the fluorescent COF (made from XXX) strongly interacts through its thioether arms with penetrating Hg^{2+} ions, which leads to a sensitive chelation-enhanced quenching effect. Additionally, the strong binding between the sulfur atoms and Hg^{2+} ions enables the efficient removal from mercury-containing solutions.[83] The same mechanism was applied for detecting Au^{3+} ions in water and successfully recovering metallic gold powder after reduction and pyrolysis treatments.[84]

Guest molecules such as ammonia can also form Lewis acid−base pairs with the boronate ester linkage in COFs. Elaborating this approach with the TPE-Ph, highly sensitive detection of ammonia with a fluorescence quenching rate constant of up to 6.3×10^{14} M^{-1} s^{-1} was enabled in solutions with ammonia gas at concentrations below the ppm range.[71] An alternative sensing mechanism for triacetone triperoxide (TATP) in *β*-ketoenamine COFs is suggested to occur by oxidation of the enamine moiety by TATP.[85]

In a straightforward approach, a *β*-ketoenamine-based COF known for its chemical stability was found to be applicable for HCl vapor detection. This sensing mechanism is based on the rapid change of UV-Vis absorption by protonation of the triazine ring. The induced electron enrichment in the triazine unit by protonation goes along with a conductivity increase by two orders of magnitude and PL quenching. The protonation can be reversed by deprotonation with ammonia or by physical treatments such as heating or vacuum.[86]

Exfoliation of an imide-based COF exhibited selective sensing of 2,4,6-trinitrophenol (TNP), whereas the fluorescence quenching constant was found to be higher than in the corresponding COF bulk material.[87] High selectivity towards TNP was also observed in a dual-pore COF (made from 4′-(bis(4-formylphenyl)amino)-[1,1′-biphenyl]-3,5-dicarboxaldehyde with diaminobenzene/benzidine) where the sensing event was visible to the naked eye as a rapid color change.[88] Organic pollutants and dyes could be detected with the exfoliated IMDEA-COF-1, a pyrene-containing imine-linked COF. The intercalated organic molecules were presumably responsible for fluorescence quenching, correlating with the surface area of the colloidal COF particles.[89]

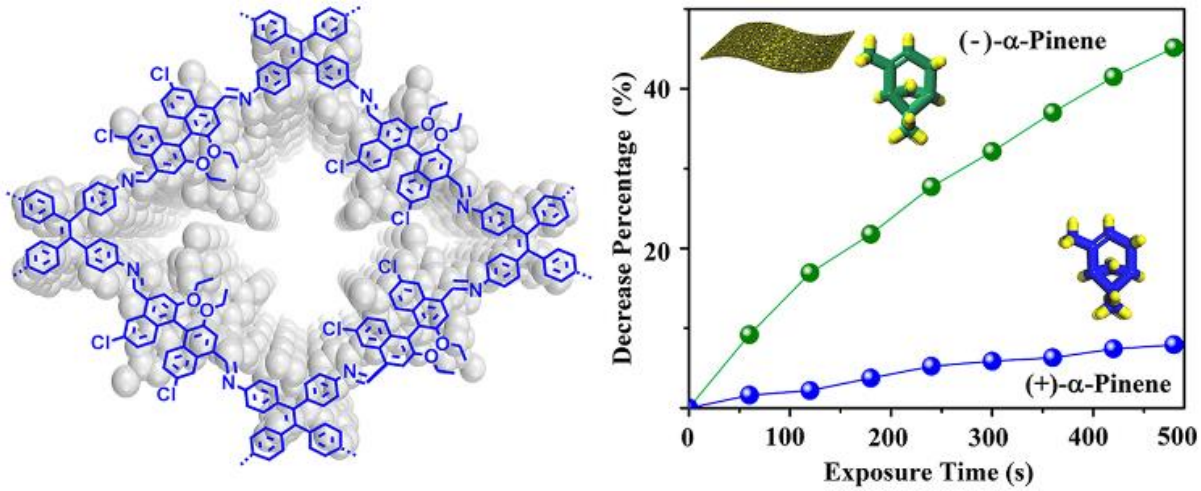

Figure 1.18: Structure of the chiral COF CCOF 7 and the observed selective fluorescence quenching of α-pinene. Reproduced with permission.[90] Copyright 2019, American Chemical Society.

By synthesizing highly fluorescent and chiral COF (CCOF) nanosheets, it was possible to achieve enantioselective sensing of chiral vapors in solution as well as in membranes (Figure 1.18). The selective fluorescence quenching was attributed to different binding energies of the enantiomers and a static enhancement due to the CCOF−vapor adduct, which may also lead to structural changes.[90]

Materials sensitive towards toxic pollutants such as perfluorooctane sulfonate (PFOS) are highly desirable. In this context, fluorescence quenching of a COF coated lanthanide-doped nanocrystal upon exposure to PFOS can function as an ultrasensitive detector with a detection limit as low as 0.15 pM. The detection mechanism was attributed to hydrogen bond formation or electrostatic interactions of the PFOS in the COF pores.[91]

1.2.3 Photoactive COFs – photoconductive and photocatalytic materials

The ordered structure of (2D) covalent organic frameworks allows for the modular assembly of building blocks in closely stacked columns with conjugated in-plane connections. This framework architecture with its intrinsic pathways for excitons and charge carriers is a determining characteristic pointing to the great potential of COFs as semiconducting materials. Considering the combination of these structural features with the properties of chromophores serving as building blocks in photoabsorbing COFs harvesting a large fraction of the solar spectrum, the leap to photoconductive materials is evident. The foundation for this strategy was

laid by Jiang's group with the report of the first COF showing semiconducting behavior due to its highly organized π-conjugated structure.[38]

It was again Jiang's group who designed the first photoconductive COF. The requirement of strong absorbance in the visible spectrum was fulfilled by the choice of pyrenediboronic acid that self-condensed to a crystalline COF leading to the essential order of the structure. The exciton migration in this single-component COF were found to occur within the COF layer as well as in the direction of stacking. The rapid photoresponse led to photocurrents with an on–off ratio of over 8.0×10^4. The ordered structure seemed to be key since the neat components showed almost no response when illuminated. Iodine doping led to an increased current in the hole-conducting COF material.[92] By utilizing Ni-phthalocyanine in an eclipsed framework coupled with BDBA, high hole mobility and strong light-harvesting result in a photocurrent of 3 μA at a bias voltage of 1 V and a photocarrier generation yield φ of 3.0×10^{-5}. In this COF the conducting species are holes with a mobility of 1.3 $cm^2\ V^{-1}\ s^{-1}$.[46] Switching from hole-conducting to an electron-conducting phthalocyanine-containing COF with the linear building unit benzothiadiazole broadened the absorption bands far into the IR with a high sensitivity towards near IR photons. Charge carrier generation upon illumination led to an increased photocurrent of up to 15 μA at a bias voltage of 1 V with a photocarrier generation yield of 9.2×10^{-4} measured by time-of-flight.[56] In order to harvest more light and to study the influence of the coordinated ions, the central metal in the phthalocyanine chromophore was exchanged by Co, Cu and Zn. The difference in electron density resulted in photocurrents ranging from 0.14 nA to 110 nA, which was attributed to a decrease of electron density in the metalated phthalocyanines.[93]

In order to increase the π-density of conjugated COF material at the expense of the pore size and volume, Jiang's group introduced two C_6-symmetric linkers, named hexaphenylbenzene and hexabenzocoronene, to form trigonal pores with a π-column density of 0.25 nm^{-2}. Time-of-flight measurements revealed a photocarrier generation yield φ of 2.1×10^{-5} for the hexabenzocoronene COF with a hole mobility of 0.7 $cm^2\ V^{-1}\ s^{-1}$.[94]

Orientation of COF films showed a significant difference in the generated photocurrent. The rapid photoresponse in oriented thin films varied by a factor of 5 compared to non-oriented TT-COF.[95] Photocurrent could be greatly enhanced after iodine doping of an azodioxy-linked porphyrin-containing COF, whereas the non-grafted COF showed hardly any photoresponse.[96]

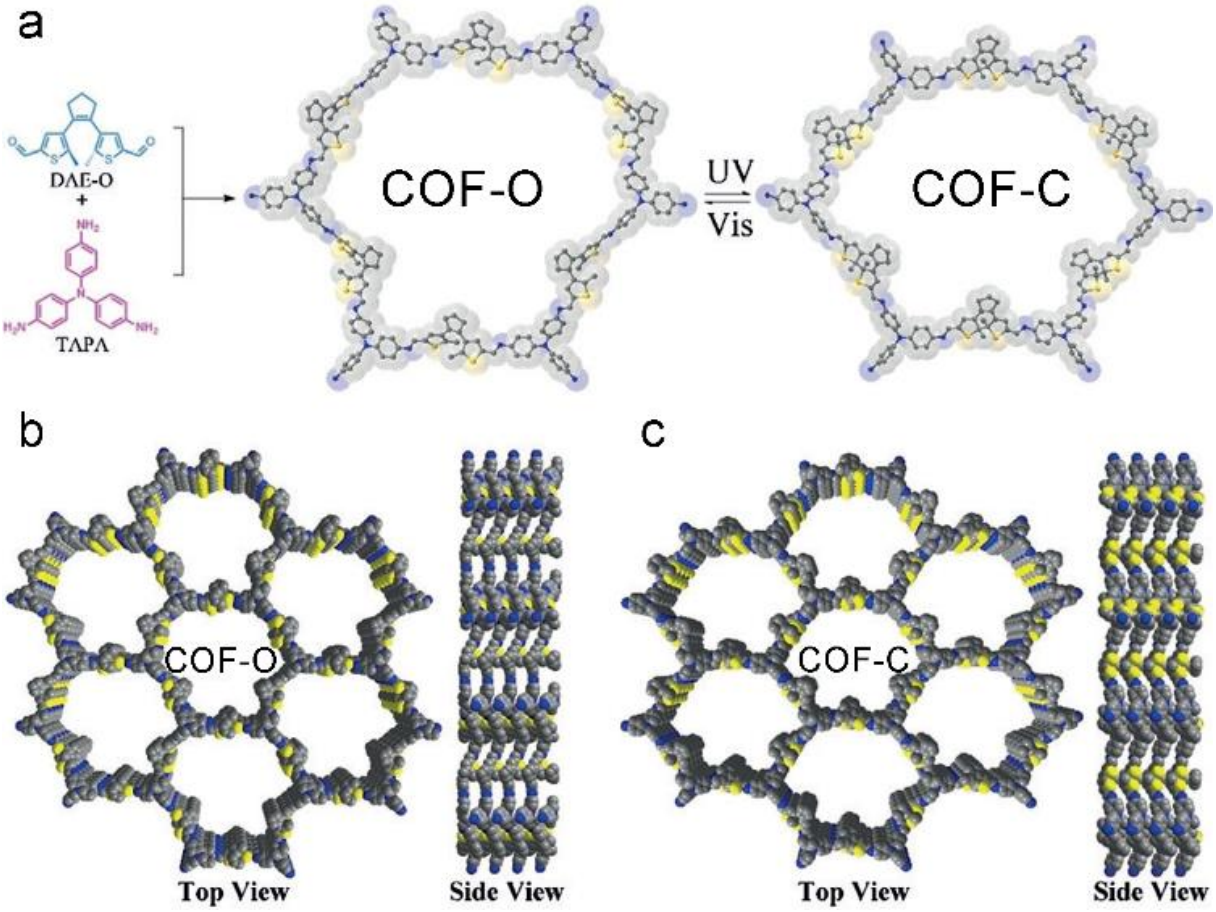

Figure 1.19: Synthesis and structure of COF-O and the corresponding photostimulated closed-ring state COF-C. Reproduced with permission. [97] Copyright 2019, John Wiley and Sons.

Upon implementation of photo-switchable molecules such as the dithienylethene moiety in COFs, it was possible to control the electrical conductivity by irradiation with UV or visible light. Upon UV irradiation at 365 nm the dithienylethene undergoes a ring closure which correlates with an increase in conductivity by the factor 200 to 2×10^{-5} S cm^{-1} compared to the open ring structure (Figure 1.19). The process is reversible by irradiating the material with light in the visible above 550 nm and was attributed to a smaller bandgap in the closed state.[97]

Since there is a great need for sustainable and effective energy sources, application in photocatalytic water splitting is an obvious step to take when considering the suitable characteristics of COFs. The photocatalytic activation of oxygen to singlet oxygen was already the first indication for the great potential. Jiang's group was able to implement a newly designed linkage motif for stable and conjugated COFs. The squaraine-linked porphyrin-containing COF showed excellent stability under the tested conditions and a reduced bandgap for enhanced absorption at lower energies. The stacking of the COF building blocks seems to be crucial since

the authors observed hardly any activity for the neat porphyrin monomer. The photoexcited states in the COF generate triplet states, which then activate molecular oxygen.[98]

In a further important development, Lotsch and co-workers reported the first COF applied as a photocatalyst for hydrogen evolution during the water splitting reaction. The authors designed a TFPT COF with hydrazone linkage for stability during catalytic operation and triazine units for achieving a bandgap suitable for light-harvesting as well as water splitting (Figure 1.20). Using sodium ascorbate as sacrificial donor and Pt as proton reduction catalyst led to a hydrogen evolution rate of 230 μmol h^{-1} g^{-1} (under visible light illumination >420 nm), whereas taking triethanolamine as sacrificial donor gave even higher values of 1970 μmol h^{-1} g^{-1}. This approach showed that the COF can clearly compare to other photocatalysts and laid the foundation for developing new types of organic materials for photocatalytic hydrogen evolution.[99]

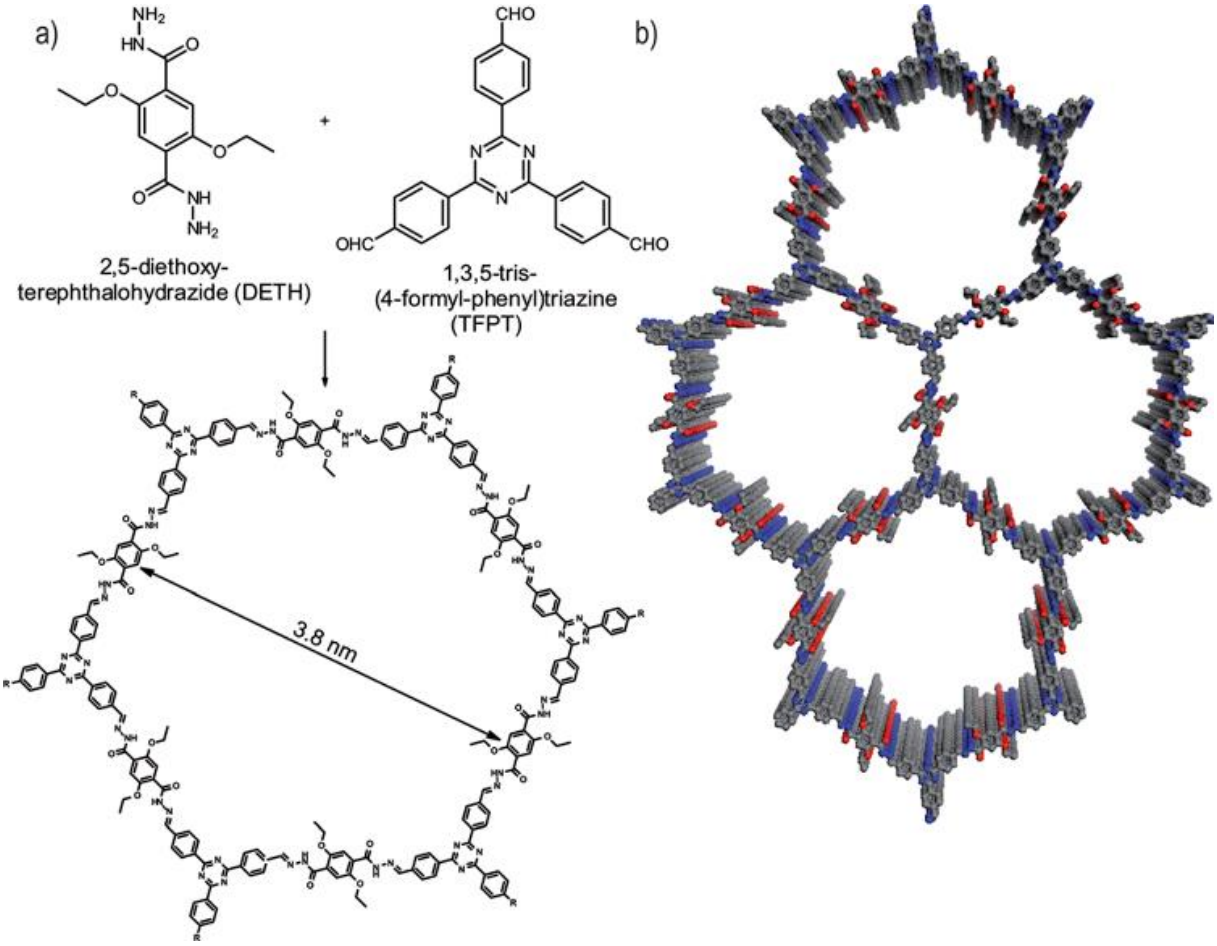

Figure 1.20: Hydrazone-linked TFPT-COF with a cofacial stacking of the layers exhibiting photocatalytic hydrogen evolution in the presence of a sacrificial agent and deposited Pt particles. Reproduced with permission.[99] Copyright 2014, Royal Society of Chemistry.

Extending the concepts for light-induced water splitting to photoelectrochemical designs, we developed the first photocathode based on a thin film of COFs. The oriented films of BDT-ETTA COF grown from propeller-shaped TPE also called ETTA and benzo[1,2-*b*:4,5-*b*′]dithiophene-2,6-dicarboxaldehyde on indium-doped tin oxide (ITO) revealed water splitting activity without the use of sacrificial donors and cocatalysts, which could be further increased by a factor of 4 using Pt nanoparticles as a cocatalyst. With the integration of a hydrogen sensor in the photoelectrochemical setup it could be shown that hydrogen is the evolving gas and that its evolution is directly correlated to the photocurrent. Under chopped illumination the COF system could repeatedly achieve photocurrent density of 0.9 μA cm^{-2} which indicates the stability of the photoelectrode.[14]

Further research and implementation of unsubstituted olefin linkages led to sp^2-carbon conjugated covalent organic frameworks with triazine cores allowing for bandgap tuning, high stability and accessibility through the pores. The n-type semiconductor exhibited photocurrents of up to 45 μA cm^{-2} and was applied as proof-of-principle in photocatalytic hydrogen evolution with ascorbic acid as sacrificial donor and deposited Pt on the COF material, resulting in promising results of 292 μmol h^{-1} g^{-1}.[100]

The high surface area and the tunable bandgap of COFs makes this new class of porous organic frameworks a promising metal-free platform for diverse photocatalytic applications beyond water splitting. One type of application involves the use of COFs as photocatalyst in selective organic transformations.

Introducing the benzoxazole linkage into COF systems not only increases their stability, chemically as well as physically, but also enhances their capability to harvest light at lower energies. Both characteristics made LZU-190, a COF consisting of 2,5-diamino-1,4-benzenediol dihydrochloride and 1,3,5-triformylbenzene, an excellent example of precise application-oriented tailoring of a photocatalytic COF. The COF achieved yields of up to 99% for the oxidative hydroxylation of arylboronic acids to phenols when illuminated and under air. The authors suggest a mechanism in which the photoexcited COF forms superoxide radical anions by single electron transfer. These events are followed by a rearrangement and hydrolysis step to yield the desired phenols.[101]

Another hydrazone-based COF made from 2,5-dimethoxyterephthalohydrazide and 1,3,5-triformylbenzene exhibited photoinduced catalytic activity with high yields for tandem radical addition–cyclization reactions of 2-aryl phenyl isocyanides. Mild conditions and recyclability of the COF as photosensitizer account for a metal-free and sustainable alternative for conventional catalysts. The proposed reaction mechanism includes the formation of radical anions and subsequent reduction of the COF to close the catalytic cycle.[102]

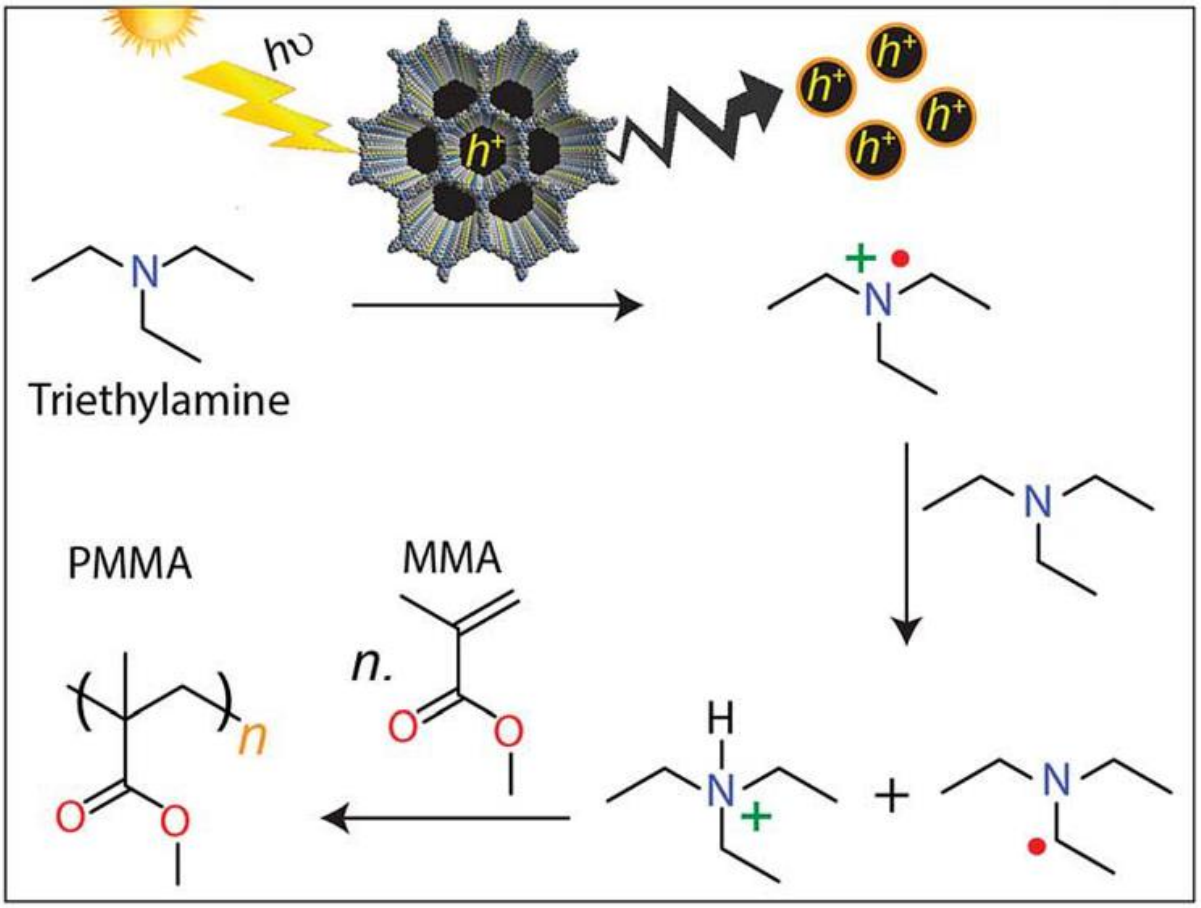

Figure 1.21: Illustration of proposed mechanism for the free radical polymerization of MMA to PMMA. Reproduced with permission.[62] Copyright 2019, Royal Society of Chemistry.

The design of donor-acceptor COFs with electron-deficient triazine units connected with electron-rich thiophene-based building blocks led to applications as photoinitiators for free radical polymerizations to generate poly(methyl methacrylate). Upon photoexcitation of the COF, generated holes oxidize triethylamine to form radical cations. Reaction with a second amine leads to amine radicals initiating the polymerization, which is not the case for reference systems without the COF initiator (Figure 1.21).[62]

The two-in-one linkage strategy introduced by Chen and co-workers led to various COFs that can photocatalyze organic transformations with high selectivity and efficiency. On the one

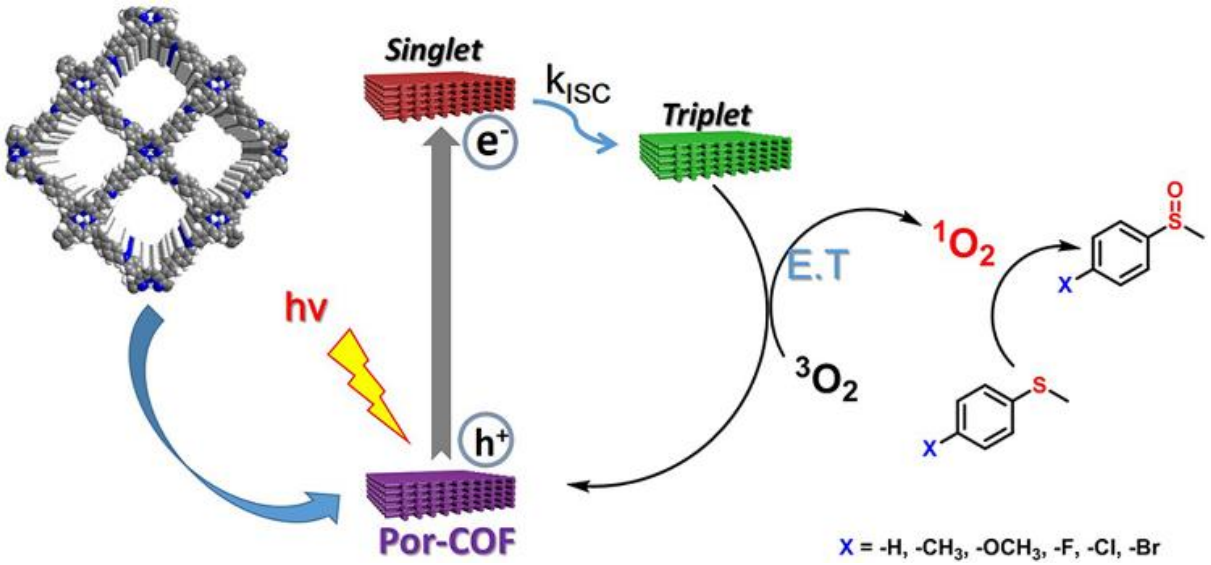

Figure 1.22: Illustration of proposed mechanism for the photocatalytic oxidation of thioanisole. Reproduced with permission.[103] Copyright 2019, American Chemical Society.

hand, the group developed a single component COF consisting of imine-linked porphyrin units, catalysing the oxidation of sulphides and Knoevenagel condensation reactions (Figure 1.22).[103] On the other hand, the group developed an benzoxazole-based COF with high photocatalytic performance for the oxidative hydroxylation of arylboronic acids.[104] This two-in-one linkage strategy seems to be promising for the efficient synthesis of a platform of photocatalytically active COFs existing of only a single component with two different linkage functionalities.

It is also possible to use MOF-COF hybrids covalently linked for the selective photocatalytic oxidation of alcohols. Here, TAPB-PDA (terephthalaldehyde, PDA) was grown on MIL-125 to form a hybrid structure. The proof-of-principle framework led to increased absorption and showed superior photocatalytic activity compared to related MOF-only catalysts.[105]

The π-conjugation in sp^2-carbon conjugated COFs allows for broadened solar light harvesting and enhanced photocatalytic activity. For example, the ability to photocatalyze the regeneration of the coenzyme in an artificial photosystem I (a COF made from 2,4,6-tris(4-formylphenyl)-1,3,5-triazine (TFPT) and 2,2′-(1,4-phenylene)diacetonitrile (PDAN)) boosted the conversion of the NADH-consuming L-glutamate dehydrogenase to 97 %, the highest value reported (Figure 1.23). Even without a mediator, the high efficiency was retained and attributed to a charge transfer complex of the COF and NAD^+ resulting from π-π interactions, amplifying electron transfer from the photoexcited COF.[106]

Benefitting from photothermal conversion, a porphyrin-containing chiral COF loaded with Pd or Au nanoparticles delivers the required thermal energy under visible light as well as the chiral

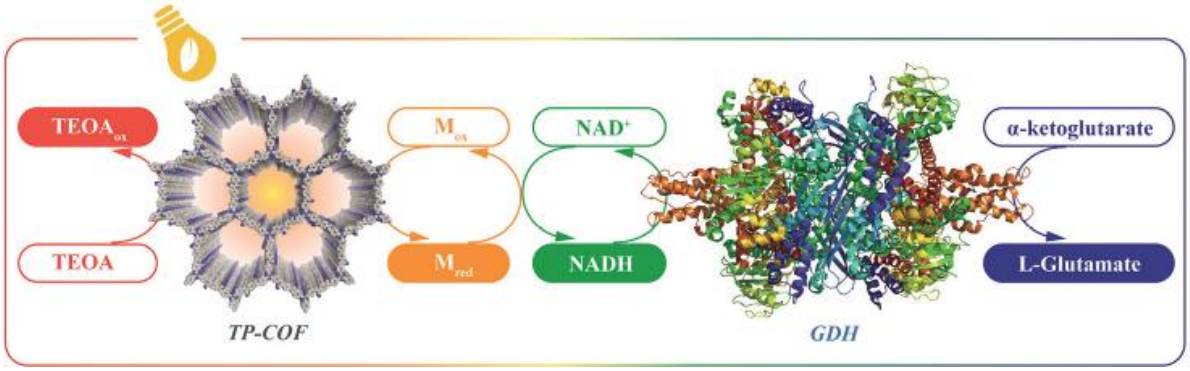

Figure 1.23: Illustration of the artificial photosystem-I-induced coenzyme regeneration and photoenzymatic synthesis of glutamate by glutamate dehydrogenase (GDH). Reproduced with permission.[106] Copyright 2019, John Wiley and Sons.

confinement to drive and catalyze asymmetric Henry and A^3-coupling reactions. The asymmetric catalysis showed not only high yields but also excellent enantiomeric excess.[107]

The application of COFs in the photoreduction of metal ions was demonstrated by Chen's group with a COF containing trigonal triazine units paired with benzothiadiazole via imine linkages. The authors were able to use the COF without sacrificial agent to achieve a photoreduction of Cr^{6+} to Cr^{3+} with 99% yield. The authors suggest an oxidation mechanism that is based on the oxidation of H_2O and OH-groups which further oxidize the framework or form oxygen.[108]

The photothermal effect has also been studied with respect to photothermal *in vitro* therapy of cancer cells. A pyrene-containing COF containing a stable radical cation in the linear linker exhibited high photothermal conversion upon irradiation with an IR laser, leading to enhanced cytotoxicity of the COF particles against A549 cancer cells. The radical cation was suggested to be stabilized as π-radical across the stacked COF layers and the broadened optical absorption spectrum allowed for enhanced IR sensitivity. Photoacoustic imaging with the irradiation of the same COF has been tested successfully in vivo.[109] Biomedical applications of photoactive COFs have also been investigated by Lang and co-workers. For example, coatings of porphyrin-containing COFs on polystyrene showed singlet oxygen production under illumination, which was shown to inactivate bacteria.[110]

A combined approach of photodynamic and photothermal therapy was reported for a hybrid material of COF-LZU-1 and Ag_2Se nanoparticles. *In vitro* and *in vivo* studies showed that the combined generation of singlet oxygen and increase in temperature led to highly efficient anticancer therapy.[111]

1.3 Electronic transport in COFs

The designed columnar pathways and the intralayer conjugation network in (2D) COFs allows for the migration of excitons or charge carriers, both holes and electrons. Studies have shown that ordering the building blocks in these frameworks and interconnecting them in-plane by covalent bonds shows superior behavior in charge carrier transport and separation in comparison to their neat monomer units. Charges can be generated by photoexcited states such as singlet excitons that spatially segregate at donor-acceptor interfaces within the framework, through host-guest interactions, or by singlet-singlet annihilation where the migration and collision of adjacent singlets leads to charge generation. Photoexcitation and subsequent charge separation in COFs have motivated investigations of photovoltaic devices or of photocatalysts for various reactions such as the hydrogen evolution reaction. In this context, the intrinsic high surface area of COFs and adjustment of both bandgap and band alignment are crucial for realizing efficient applications.

The theme of photoconductive COFs was already discussed in Chapter 1.2.3, and will now be extended to the whole field of conducting covalent organic frameworks.

1.3.1 Macroscopic and microscopic characterization techniques

Conductivity and mobility analysis techniques can differ regarding the observed parameters and the spatial extent of the relevant process, hence the meaning of the resulting data. Therefore, the results need careful consideration when compared to those obtained with other methods. For example, in a macroscopic technique, grain boundaries would strongly influence results, leading to reduced values compared to microscopic techniques where processes in single crystallites/domains may be probed.

A simple measurement setup is the two-contact probe for which the sample is contacted with two electrodes, or sandwiched in between two electrodes. By applying a voltage (and possibly illuminating the sample) a typical I-V curve is obtained from which the electrical conductivity can be retrieved. This macroscopic technique reflects the average conductivity of the gap in between the two contacts.

Based on a similar principle of a two-contact probe, time of flight (ToF) analysis with pulsed laser excitation can be used to obtain transient photocurrents and to reveal data such as nature and number of the generated charge carriers, the photocarrier generation yield φ, and the mobility.

Another macroscopic method is a four-electrode setup such as the van der Pauw method which can be applied to macroscopic COF samples such as thin films. The applied current between contact 1 and 2 induces a voltage which can be measured between contact 3 and 4 and converted to the resistivity. Together with the sample thickness the elucidation of the conductivity is possible. To retrieve more data such as charge carrier concentration and mobility, an external magnetic field affecting the moving charge carriers needs to be applied.

It is also possible to design devices in the form of a field-effect transistor with the COF serving as the active layer. By applying a gate voltage, the source-to-drain current initially increases linearly. This linear regime in the current vs. gate voltage plot is then used to calculate the mobility of the charge carriers on a macroscopic scale.

Going to smaller dimensions, time-resolved microwave conductivity (TRMC) is a non-destructive and non-contact method where the sample is exposed to microwave radiation in the GHz range and the transmitted or reflected microwave power is detected. After photoexcitation with a laser, charge carriers are generated on the surface or in the bulk material depending on the wavelength. The charge carriers then cause a change in the detected signal that can be related to the conductivity, photocarrier generation yield, carrier lifetime and mobility, and also allows for the determination of the nature of the carriers. The high frequency of the microwave radiation implies that the motion of the charge carriers only extends over microscopic length scales.[112]

If the frequency is further increased, we reach the optical pump terahertz probe spectroscopy (OPTP), which is also a non-contact method. The sample is optically pumped by a pulsed laser and then probed with a THz pulse. The photoexcited electron–hole pairs interact with the electric field of the terahertz pulse, leading to the photoinduced conductivity. From correlation with frequency and time after the optical pump, doping densities, carrier mobilities and lifetimes can be extracted. These features are again probed on a microscopic scale with a temporal resolution in the femtosecond region.[113]

For comparison reasons, in the following the conductivity will be given in S cm^{-1}.

1.3.2 Conducting COFs

In 2008, Jiang and co-workers reported the first semiconducting COF, made from 2,3,6,7,10,11-hexahydroxytriphenylene (HHTP) and pyrene-2,7-diboronic acid (PDBA). The stacked triphenylene and pyrene building blocks in the TP-COF led to an increased electric current of 4.3 nA at 2 V bias voltage compared to the neat monomer mixture. The measurements were performed with a two-contact probe across a 10 µm Pt gap under ambient conditions. The current could be increased by oxidative iodine doping allowing for the conclusion that the TP-COF is a p-type semiconductor.[38] It was again Jiang's group reporting the first n-type semiconducting COF, consisting of Ni-phthalocyanine units linked with electron-deficient benzothiadiazole bridges (Figure 1.24d,e). Flash-photolysis (FP) TRMC revealed a $\varphi\sum\mu$ of 5.8 $\times 10^{-4}$ cm^2 V^{-1} s^{-1}, with φ being the photocarrier generation yield and μ the carrier mobilities, for the 2D-NiPc-BTDA COF. In combination with time-of-flight measurements, a carrier mobility of 0.6 cm^2 V^{-1} s^{-1} was derived, which was attributed to the eclipsed stacking of the chromophore units.[56]

Yaghi and co-workers were then able to synthesize two porphyrin-containing COFs imine-linked by a phenyl ring (COF-366) and linked by boronate ester bonds with an anthracene unit (COF-66). Applying the FP-TRMC method, the associated COF/PMMA films revealed high charge carrier mobilities of 8.1 and 5.0 cm^2 V^{-1} s^{-1} for COF-366 and COF-66, respectively, which was two orders of magnitude higher than the values obtained from the contact-probed

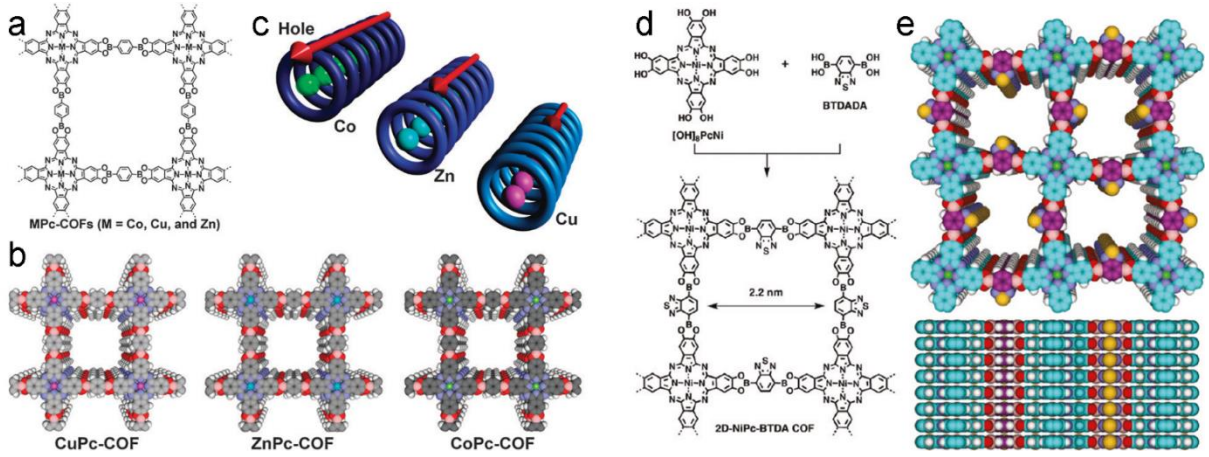

Figure 1.24: (a) Chemical structure of metalated phthalocyanine (MPc) COFs. (b) Slipped-AA stacking structure of MPc-COFs and (c) illustration of stacked phthalocyanine macrocycles allowing for hole transport. Reproduced with permission.[93] Copyright 2012, Royal Society of Chemistry. (d) Synthesis of the first n-type semiconducting COF and (e) eclipsed stacking mode of the resulting 2D-NiPc-BTDA COF. Reproduced with permission.[56] Copyright 2011, American Chemical Society.

TOF measurement. These mobilities exceed the values typical for many polymers and amorphous silicon and combined with the long carrier lifetime of around 80 μs, allow for promising charge carrier separation abilities of the two COFs.[47]

Notably, the nature of majority charge carriers in porphyrin COFs could be switched by introducing different central divalent metal centers. The free-base porphyrin COF exhibited a hole-conducting behavior with high charge carrier mobilities of 3.5 $cm^2\ V^{-1}\ s^{-1}$ measured by FP-TRMC. At the cost of reduced hole transport through the stacked macrocycles, the electron transport could be increased by inserting metal centers. Whereas Zn led to the first ambipolar conducting COF with mobility values μ_e and μ_h of 0.016 and 0.032 $cm^2\ V^{-1}\ s^{-1}$, the insertion of Cu led to an electron-transporting material with a carrier mobility of 0.19 $cm^2\ V^{-1}\ s^{-1}$. The combination of both transport channels, along the macrocycles and along the metals, also led to an increased photocurrent with a given electrode structure of 26.8 nA for the ZnP-COF with a high on–off ratio compared to 0.6 and 0.01 nA for the Cu-porphyrin and base-free porphyrin COF, respectively.[114]

Using the coordinating central metal in macrocycles such as porphyrins or phthalocyanines allows for tuning of the electron density in the macrocycles, thus influencing the photoelectric behavior. This was further shown by Ding *et al.* in a study where the influence of the central metal on photoelectric properties was investigated using FP-TRMC and by the conventional two-contact probe method where the metallophthalocyanine-based COFs was sandwiched between Al and Au electrodes. The TRMC results showed $\varphi\sum\mu$ values consistent with the electron densities of the metallophthalocyanines (CuPc-COF < ZnPc-COF < CoPc-COF) of 1.4×10^{-4}, 2.2×10^{-4} and 2.6×10^{-4} $cm^2\ V^{-1}\ s^{-1}$, respectively (Figure 1.24 a-c). The two-probe photocurrents of 110, 0.6 and 0.14 nA, respectively, differ from the trend of the $\varphi\sum\mu$ values and suggest the non-negligible influence of grain boundaries and morphologies of the COF material.[93]

Using femto- and nanosecond transient absorption spectroscopy, the charge dynamics in a donor–acceptor (D–A) COF with Zn-phthalocyanine nodes connected with naphthalenediimide (NDI) bridges were investigated. The authors suggested fast light-induced charge separation within 1.4 ps between the D–A pairs. The delocalization along the π-stacked arrays allowed for long lifetimes of the separated charges of up to 10 ns in benzonitrile suspension. Investigations of the solid COF material with time-resolved electron spin resonance spectroscopy confirmed the formation of charged D–A columns, with the donor phthalocyanine and the acceptor NDI.

The lifetimes of the separated charges were found to be 1.8 and 1500 µs at 280 and 80 K, respectively.[58]

Tetrathiafulvalene (TTF) is known for forming cation radicals and conducting charge-transfer salts. The introduction of the TTF unit into organic materials was therefore the focus of many studies. The charge carrier mobilities of phenyl- (TTF-Ph) and pyrene-containing (TTF-Py) TTF-COFs obtained with FP-TRMC were 0.2 and 0.08 $cm^2\ V^{-1}\ s^{-1}$, respectively. The higher mobility of the TTF-Ph-COF was attributed to the slightly tighter stacking behavior compared to the TTF-Py-COF. An increase of up to 6 orders of magnitude in electrical current was observed when the TTF unit was oxidized with iodine leading to a charge-transfer complex of the TTF radical cation and iodide radical anion. The conductivity of this oxidized COF was measured on pellets with a thickness of 0.5 mm and resulted in values of 10^{-5} and 10^{-6} S cm^{-1} for TTF-Ph and TTF-Py COF respectively.[115] A comparable electroactive behavior was also found by Zhang and co-workers, pointing out that the oxidized TTF-Ph COF retained the crystalline structure and showed a similar conductivity of 1.8×10^{-6} S cm^{-1}.[116]

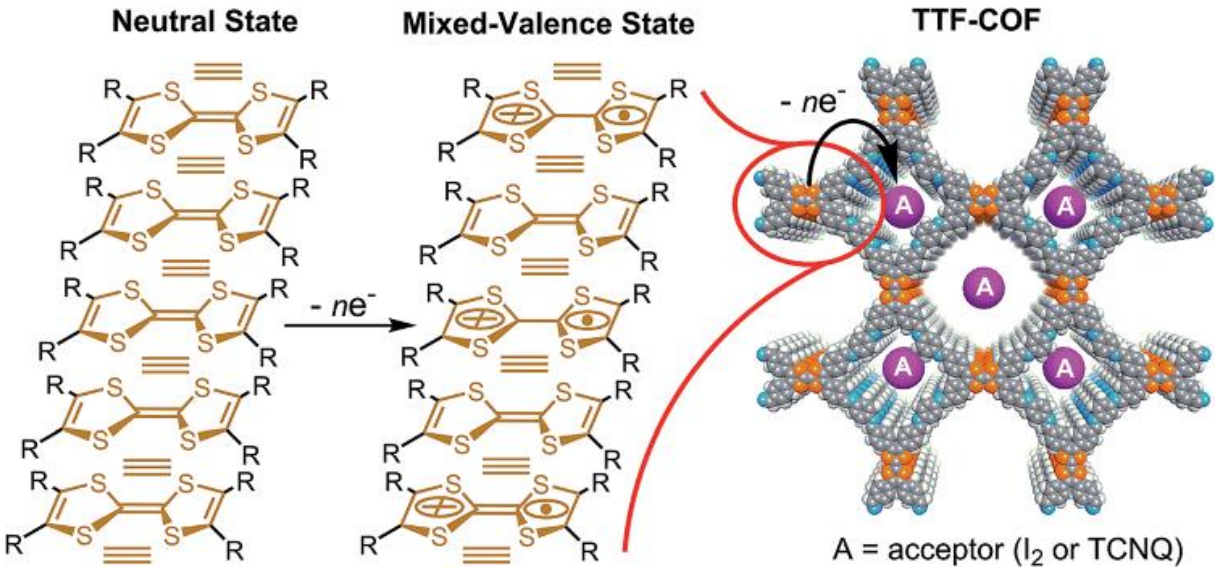

Figure 1.25: Scheme of the radical delocalization in the TTF-COF leading to mixed-valence state TTF species. Reproduced with permission.[117] Copyright 2014, Royal Society of Chemistry.

The conductivity of the TTF-Ph COF could be even more enhanced in iodine-doped oriented thin films, where the high resulting values of 2.8×10^{-3} S cm^{-1} were attributed to the delocalization of the radical across the mixed-valence TTF stacks (Figure 1.25).[117]

When aiming for high π-column density in COFs, the hexabenzocoronene (HBC) building block offers attractive features such as a large 'graphitic' coronene core, favorable stacking and multiple points for functionalization. A corresponding HBC-COF made from planar hexabenzocoronene and terephthalaldehyde shows a high hole mobility of 0.7 $cm^2\ V^{-1}\ s^{-1}$ determined by FP-TRMC. The $\varphi\sum\mu$ values of the HBC-COF were found to be 1.5×10^{-5} $cm^2\ V^{-1}\ s^{-1}$.[94] Further FP-TRMC investigations of a boronate ester-based COF containing non-planar hexabenzocoronene derivatives as linker molecules connected with pyrene units showed that the sum $\varphi\sum\mu$ of 0.6×10^{-4} $cm^2\ V^{-1}\ s^{-1}$ is not affected by the core-twisted structure of the building units, which induce a wavy 2D structure in the obtained COF (Figure 1.26).[118]

In a single component COF in which protected tetrakis(arylhydroxylamine)porphyrin units are fused by azodioxy bridges, the electrical conductivity could be enhanced by three orders of magnitude upon iodine doping to reach 1.52×10^{-7} S cm^{-1}. The increase is attributed to the decrease of the energy barrier for charge transport and to electron traps leading to better hole mobility due to the iodine doping.[96]

Our group studied directional charge transport in boronate ester-based COF thin films made from BDT and HHTP and showed a correlation between hole mobility and film thickness. The hole mobilities were measured for a hole-only device with MoOx serving as the hole-transporter and ITO and gold serving as the electrodes. For films with a thickness of around 80-90 nm, the hole mobility reached up to 3.0×10^{-7} $cm^2\ V^{-1}\ s^{-1}$ and turned out to be dependent on illumination, which was attributed to photoexcited charge carriers filling up electronic trap states. Furthermore, we observed an in-plane conductivity of up to 5×10^{-7} S cm^{-1} in oriented thin film devices, which exceeded the conductivity of non-oriented, pressed COF pellets.[119] For

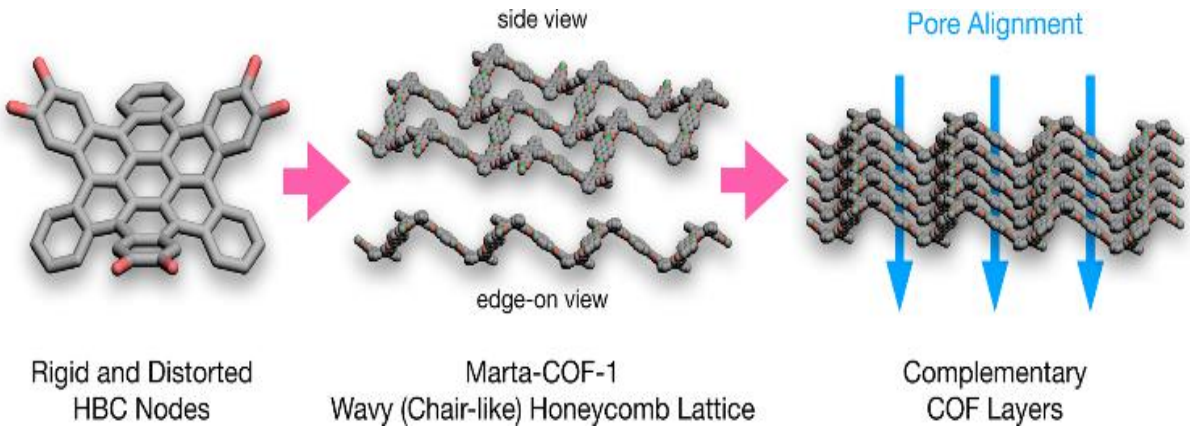

Figure 1.26: Schematic illustration of core-twisted HBC node inducing a wavy structure in Marta-COF-1 and guiding the layer stacking of the COF. Reproduced with permission.[118] Copyright 2019, American Chemical Society.

another boronate ester-based COF, the DPP2-HHTP-COF made from ((2,5-bis(2-ethylhexyl)-3,6-dioxo-2,3,5,6-tetrahydropyrrolo[3,4-c]-pyrrole-1,4-diyl)bis(thiophene-5,2-diyl))diboronic acid, we were able to induce diketopyrrolopyrrole stacks within the COF scaffold, which led to the highest conductivity (of up to 2.2×10^{-6} S cm^{-1}) found for boronate ester-linked COF bulk materials. The measurements were performed with a four-point probe Hall measurement providing macroscopic conductivity values.[120]

The application of COFs as bulk doping agent for perovskite solar cells (PSC) was investigated with 3D COFs bearing spirobifluorene units well known for their potential in optoelectronic devices. The power conversion efficiency (PCE) of the SP-3D-COF-1 and -2 doped PSCs could be increased by up to 18% and the electron mobility was almost doubled reaching 4.44×10^{-3} cm^2 V^{-1} s^{-1}. Based on computational studies, the mechanism could be attributed to the additional charge generation and the spatial separation of HOMO and LUMO in the COF preventing charge recombination.[121]

In a 3D-COF, a TTF-based building block was combined with an adamantane unit leading to a non-interpenetrated pts topology (Figure 1.27). The open pores and high surface areas allowed for efficient iodine doping and tunable electrical conductivity. The values could be enhanced up to 2.7×10^{-4} S cm^{-1} upon iodine doping for 48 h at 25 °C, measured with a two-probe method using gold paste as electrodes. Increasing the temperature to 120 °C led to a conductivity of 1.4×10^{-2} S cm^{-1}, which exceeds the value found for 2D TTF-COFs.[122]

To reach for even higher conductivity and mobility values, the conjugation across the bonds connecting the building blocks was increased by a pyrazine linkage motif. The hcc-COF consisting of pyrazine-linked benzene rings showed a conductivity, measured in a FET-type device of a COF film, of 4.0×10^{-3} S cm^{-1}. We note that this value was found for the pristine COF without any doping agents, and that the data do not allow conclusions regarding the orientation of the film. In the corresponding bulk material, conductivity values of up to 2.2×10^{-5} S cm^{-1} were obtained with a two-probe method.[123]

Mirica and co-workers used a pyrazine linkage to connect a Ni-phthalocyanine macrocycle with a pyrene unit to form a COF. Using a four-point probe method, the bulk conductivity of the COF was found to be 2.51×10^{-5} S cm^{-1}. Upon iodine doping of the COF device with interdigitated gold electrodes, the current increased by a factor of 10^3. DFT calculations suggest an eclipsed stacking of the building blocks and thus facilitated charge transport along the stacked macrocycles.[124]

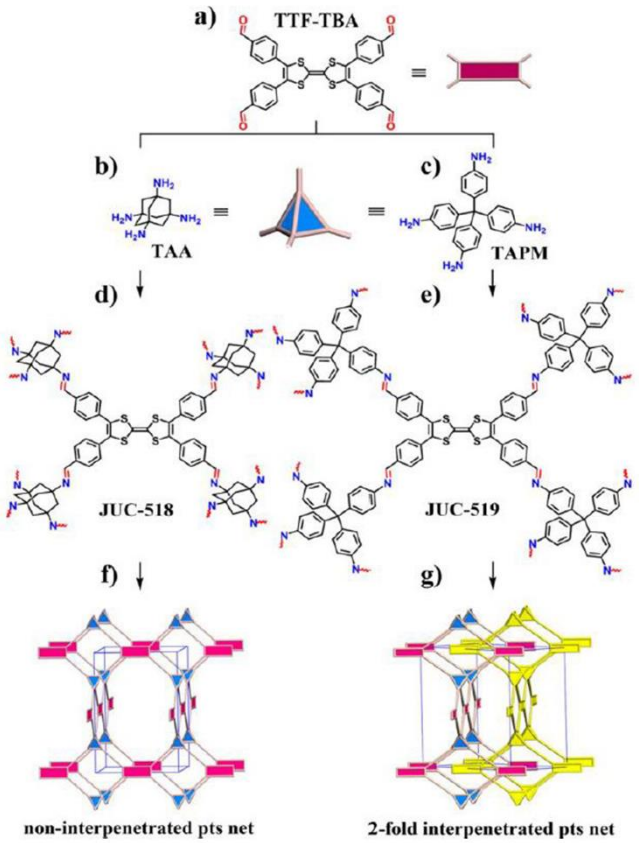

Figure 1.27: Synthesis of the 3D-TTF-COFs with a non-interpenetrated structure (f, JUC-518) and an interpenetrated structure (g, JUC-519). Reproduced with permission.[122] Copyright 2019, American Chemical Society.

Changing the metal center of the phthalocyanine unit to Zn and Cu and coupling with a *tert*-butylpyrene-tetraone via a pyrazine-linkage produced COFs with Hall mobilities of 4.8 $cm^2\ V^{-1}\ s^{-1}$ for the ZnPc-COF and 0.9 $cm^2\ V^{-1}\ s^{-1}$ for the CuPc-COF and conductivities of around 5×10^{-5} S cm^{-1}. Further investigation of these COFs with terahertz spectroscopy confirmed the above trend, revealing mobilities of 2.0 and 0.7 $cm^2\ V^{-1}\ s^{-1}$ for the Zn- and Cu-version, respectively. Notably, DFT calculations suggested that an influence of the metal centers on the hole mobilities could be excluded and that differences in boundary scattering led to the change in mobility. The boundary scattering is affected by depletion regions between the crystallites. In-plane charge carrier transport was calculated to be very low compared with the out-of-plane mobility (Figure 1.28).[125]

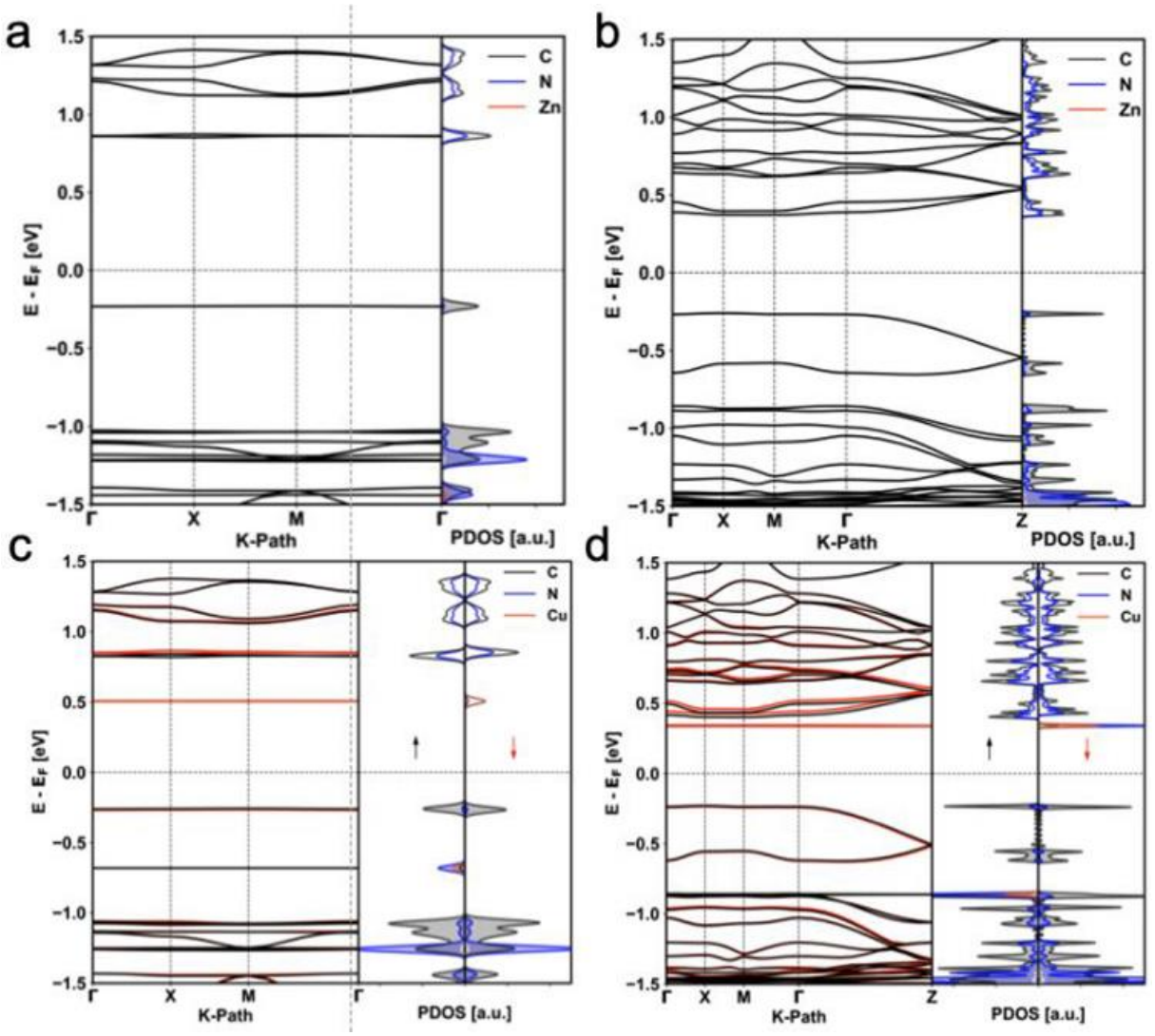

Figure 1.28: Electronic band structures and projected density of states (PDOS). (a) Monolayer and (b) serrated AA stacked multilayers of ZnPc-pz. (c) Monolayer and (d) serrated AA stacked multilayers of CuPc-pz. Reproduced with permission.[125] Copyright 2019, American Chemical Society.

To further evolve the level of conjugation, one can move from pyrazine-linked COFs to sp^2 carbon-conjugated linkage motifs to create a planar fully π-conjugated bridge between the aromatic building blocks. This is expected to allow for facilitated charge carrier transport, high stability and thus enhanced potential for application as semiconducting material. The group of Jiang was able to synthesize a fully sp^2 carbon-conjugated framework that was identified as an insulator with a conductivity of 6.1×10^{-16} S cm^{-1}. However, upon oxidation with iodine the conductivity could be immensely increased by a factor of 10^{12} to 7.1×10^{-4} S cm^{-1}. Furthermore, the spins of the generated radicals exhibit paramagnetic behavior but undergo a ferromagnetic phase transition below 10 K.[25] Based on computational analysis, a mechanism was proposed to explain the conducting behavior of the iodine-doped COF. Here, the large effective mass of carriers leads to low mobilities in the undoped framework whereas the iodine

oxidation leads to increased mobility values. In combination with the high conductivity calculated for the I_3^- anion in the channels of the framework, the authors propose that the increase in conductivity is based not only on the increased charge carrier mobilities in the framework but also aided by high ionic conductivity.[126]

Zhang, Bi and co-workers further developed this approach to study the abilities of semiconducting COFs and observed current densities of up to 45 μA cm^{-2} (with a COF made from 2,4,6-trimethyl-1,3,5-triazine and terephthalaldehyde) when applied as photoelectrodes in aqueous medium at 0.2 V vs RHE under conditions of photocatalytic hydrogen generation.[100]

In a computational study, C-C-bonded single component COFs containing pyrene, porphyrin and Zn-porphyrin building blocks were investigated regarding their charge carrier mobilities. The calculations predicted a carrier mobility of 66 $cm^2\ V^{-1}\ s^{-1}$ for holes and electrons in the pyrene COF and hole mobilities of 82 and 94 $cm^2\ V^{-1}\ s^{-1}$ in porphyrin and Zn-porphyrin COFs, respectively. Subsequently, a synthesized single component Zn-porphyrin COF with poor crystallinity revealed a mobility of 3.5×10^{-2} $cm^2\ V^{-1}\ s^{-1}$ with $\varphi\sum\mu$ of 3×10^{-5} $cm^2\ V^{-1}\ s^{-1}$.[127]

1.3.3 Energy storage with COFs

Their high surface area and the ability to combine a large variety of building units, including those with redox-active groups, makes covalent organic frameworks interesting for applications in energy storage, such as batteries, capacitors, supercapacitors or electrocatalysts.[128] The first COF showing reversible redox processes was reported by Dichtel and co-workers. Specifically, the ketoenamine-linked DAAQ-TFP COF bearing a redox-active 2,6-diaminoanthraquinone unit showed an initial capacitance of up to 48 F g^{-1} and even after 5000 cycles a stable capacitance of 40 F g^{-1} for COF bulk material mixed with carbon black. This work laid the foundation for future applications of COFs in pseudocapacitive energy storage.[129] It was again Dichtel's group that demonstrated the effect of oriented COF thin films on electrochemical behavior. Starting from non-oriented bulk material of the DAAQ-TFP COF with a charge storage ability of 0.4 mF cm^{-2}, this value was increased to 3 mF cm^{-2} by the enhanced access into the pores of oriented films, featuring high stability even after 5000 cycles.[7]

Staying with the same framework of ketoenamine-linked anthraquinone building units, Mulzer et al. and later Wu et al. constructed 'electron highways' in the COF pores by polymerization

of 3,4-ethylenedioxythiophene (EDOT) within the COF. The electropolymerization of EDOT occurred in COF thin films and led to a maximum capacitance of 350 F cm^{-2} but was limited to very low amounts of COF sample. The first step to scale up the amount of COF was achieved by a chemical polymerization (Figure 1.29).[130]

One step further was taken by Wu et al. with a solvent- and catalyst-free approach of solid-state polymerization of EDOT. With PEDOT strands winding through the pores, the COF reached a conductivity of up to 1.1 S cm^{-1} measured by two-probe and four-probe methods. Also, the

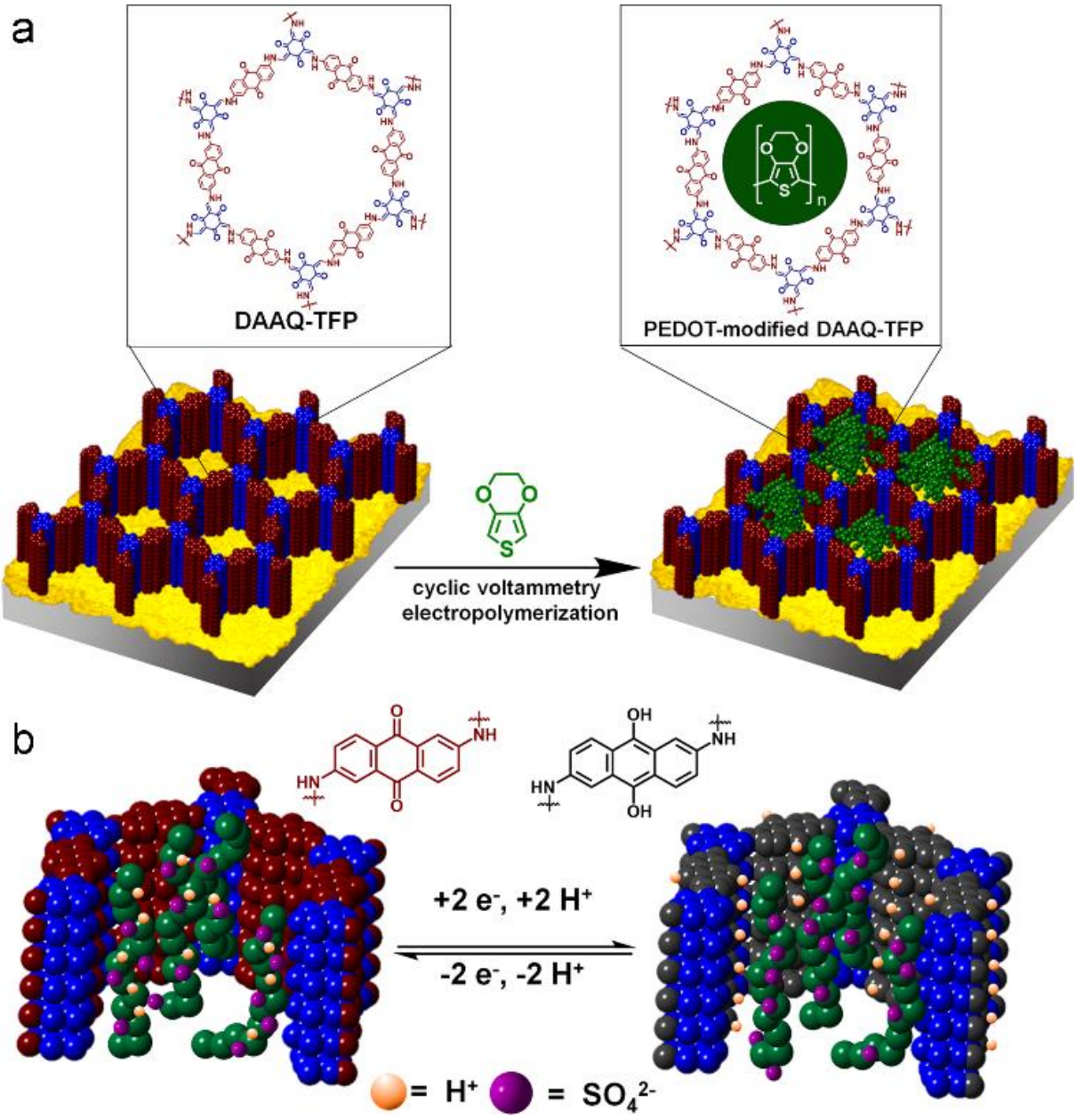

Figure 1.29: Schematic illustration of DAAQ-TFP films with incorporated PEDOT (a) and of corresponding oxidation and reduction of the DAAQ moieties in the COF. (b) Exemplary scheme of reduction and oxidation processes in the COF pores. Reproduced with permission.[130] Copyright 2016, American Chemical Society.

specific capacitance increased to 1663 F g^{-1} compared to the pristine DAAQ-TFP COF (see work of Dichtel above), exhibiting high stability and fast charge and discharge rates.[131]

Banerjee and co-workers combined the redox-active anthraquinone units with anthracene linkers embedded in the COF. This strategy allowed for the synthesis of flexible yet electrochemically active sheets. Their use in quasi-solid-state supercapacitors was investigated comparing anthraquinone-only COF (DqTp) sheets and mechanically more flexible COF sheets blended one-to-one with anthraquinone and anthracene bridges (Dq_1Da_1Tp). The highest energy density was 0.43 and 0.30 µW h cm^{-2} for the DqTp and Dq_1Da_1Tp COFs, respectively. Considering the power densities, the values were determined to be 980 and 960 µW cm^{-2}, respectively. The additional mechanical stability achieved by introducing the anthracene part led to a superior long-term stability compared to the DqTp COF.[132]

In order to further increase the electrochemical stability of the above COF, the hydroxy groups of 1,3,5-triformylphloroglucinol were substituted by methoxy groups to enable the formation of interlayer hydrogen bonds. As a result, instead of the ketoenamine linkage, imine bonds formed the COF in a condensation step with anthraquinone. Consequently, the COF sheets exhibited good performance when applied as supercapacitor in 3 M aqueous sulfuric acid with capacitance up to 1600 mF cm^{-2} and 169 F g^{-1}. The fabrication of a symmetric solid-state supercapacitor yielded a device with a capacitance of 84 mF cm^{-2} and energy and power densities of 2.9 µW h cm^{-2} and 61.8 µW cm^{-2}, respectively.[133]

The combination of the mechanically stable mixed one-to-one anthraquinone and anthracene COF (see work of Banerjee above) with carbon nanofibers increased the conductivity and led to outstanding performance in a quasi-solid-state supercapacitor with areal capacitance of 167 mF cm^{-2} (Figure 1.30). The energy and power density were determined to be 5.8 µW h cm^{-2} and 125 µW cm^{-2}, respectively. The supercapacitive capability of this device exceeds the values of MOF, COF and other carbon-based supercapacitors.[134]

Jiang and co-workers synthesized a COF consisting of a Ni-porphyrin framework connected by linear bridges with ethynyl groups attached. By click reaction, 4-azido-2,2,6,6-tetramethyl-1-piperidinyloxy groups were covalently bound to the framework leading to the radical-containing COF. This strategy led to enhanced capacitance compared to the corresponding non-radical COF scaffold.[135]

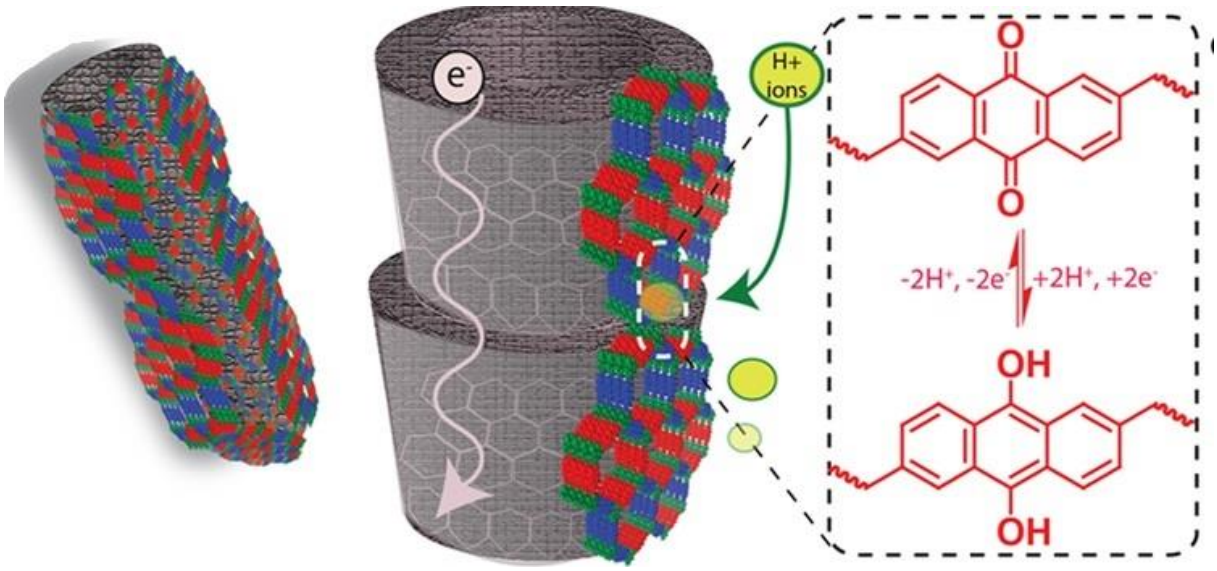

Figure 1.30: Illustration of supercapacitor material with carbon nanofiber as electron-conducting and COF as redoxactive compound with the scheme of oxidation and reduction in the enlarged area. Reproduced with permission.[134] Copyright 2019, American Chemical Society.

The influence of the morphology on the performance of a COF-based supercapacitor was established in a study investigating carbazole-based COFs. Even though Car-TPT COF showed the lowest BET surface area in this COF series and exhibited only a single redox-active site per building block, this COF featured the highest capacitance of 17.4 F g^{-1} due to its accessible microtubular structure.[136]

Recently, a series of pyridyl-functionalized COFs (made from tripyridine-triazine and different phenolic trialdehydes) was shown to exhibit high power density and stability over 10,000 cycles in supercapacitor applications. The redox-activity could be controlled by the number of hydroxyl groups attached to the trialdehyde linker. One attached hydroxyl group led to the largest BET surface and to a specific capacitance of 92 mF cm^{-2} (at 0.5 mA cm^{-2}) and a power density of 98 µW cm^{-2}.[137]

For applications of COFs in batteries, Jiang and co-workers proposed to combine COF material with carbon nanotubes. In their study, they investigated a boronate ester-based COF made from naphthalene diimide and triphenylene knots. The resulting accessible open pore structure of the COF was viewed as a key factor for efficient Li ion diffusion, redox-active COF architecture and facilitated electron conduction through the carbon nanotubes.[138] High Li ion conductivity of up to 0.26 mS cm^{-1} could be demonstrated in pressed COF samples inducing some orientation of the COF layers.[139] In a 3D cyclodextrin-based anionic COF (connected with trimethyl borate), Li^+ was chosen as a counterion resulting in Li channels along the framework.

The Li ion conductivity at 30 °C was determined to be 2.7 mS cm^{-1}, providing promising characteristics for Li-based batteries for energy storage.[140]

In order to trap polysulfides in COFs to make them applicable in Li-S batteries, a COF-net was synthesized on a carbon nanotube net creating an interlayer between COF and carbon nanotube. Here, boronate ester bonds in the COF served as adsorption sites for both Li ions and S_x^{2-}, showing promising results.[141-142] Further investigations established COFs (for example, made from pyrene and terephthalaldehyde, 4,4′,4″-(1,3,5-Triazine-2,4,6-triyl)trianiline and 2,3,5,6-tetrafluoroterephthalaldehyde, or TAPB and 2,5-divinylterephthalaldehyde) as potential cathode material in Li-S batteries with high capacity and cyclability.[143-145] It was also shown that COFs (for example, made from 1,3,5-tris(4-formylphenyl)benzene and DAAQ, or pyromellitic dianhydride and tris(4-aminophenyl)amine or TAPB) could serve as electrode material in Li ion batteries. Here, the Li-ion diffusion was facilitated by exfoliation of the COF material leading to few-layered COF sheets with superior performance compared to the bulk material, with promising capacities around 1000 mAh g^{-1}.[146-148]

The approach of using exfoliated COF nanosheets was also transferred to other alkali ion batteries, such as sodium and potassium ion batteries in which the COF served as anode material. The reversible capacities were found to be around 250 mAh g^{-1}.[149-151]

1.4 Charge separation in COF heterojunctions

In the chapters ahead, we will discuss charge separation in the COF as a crucial requirement for the envisioned applications of COF-based heterojunctions. Already having provided an overview of charge generation, charge transport, recombination processes and also charge separation and extraction to evolve hydrogen, reduce metals, or harvest solar energy, this chapter will briefly describe the different approaches towards structuring heterojunctions in COF devices.

Several sophisticated strategies for creating heterojunctions in COF materials have already been reported in the literature.

On the one hand, we can build up a heterojunction from molecular building blocks using the columnar arrays in the framework of 2D COFs in order to create separate donor and acceptor

stacks (named integrated heterojunction). The holes and electrons generated upon absorption of light in principle can then be spatially segregated onto the π-stacked donor or acceptor columns along which they can move and from where they can be extracted. By means of this arrangement and given a favorable band alignment, the charges can easily be separated due to a short diffusion distance to the heterojunction interface leading to ultrafast separation and an ambipolar conducting framework.[57]

It was already shown that in favorable cases these separated charges can have long lifetimes in the framework due to the delocalization across the π-stack.[152] This approach does not primarily depend on pore size or pore structure but on the energy levels of the COF building units. The energy alignment of the donor and acceptor is crucial for achieving an efficient driving force for separating the initially generated excitons. Following this principle, HOMO and LUMO of the COF structure should be spatially separated and located on different nodes serving as donor and acceptor.[59] If the driving force is too low, for example when coupling a weaker electron acceptor to the donor, one can face a situation where no charge separation occurs, as with D_{TP}-A_{PyrDI}-COF.[153]

Structuring the COF in this manner conceptually allows for its implementation in solar cell devices with ordered donor and acceptor columns. Challenges arising include loss mechanisms and conductivity issues occurring in the COF, thus impeding the extraction of charges.[23]

On the other hand, heterojunctions can be constructed by inserting an electron acceptor phase into the pore channels of a donor-type COF (or vice versa, inserting a donor phase into an acceptor-type COF), leading to an interpenetrated COF heterojunction. For this strategy to be realistic, the pore size needs to be in the mesoporous range to allow for the formation of a sufficiently large included phase consisting of guest molecules. This also requires good accessibility of the pores, whereas blocked pores by displaced COF layers or entrapped COF oligomers can significantly decrease the interface of the interpenetrated host-guest heterojunction.[154] Compared to the abovementioned concept, the travel distance of charge carriers might then be increased due to pore blocking or inadequate filling. Hence, if the scaffold serves as a hole-conducting material, the acceptor phase within the pores is expected to transport electrons. For example, in the TT-COF shown in Figure 1.31 (made from thienothiophene and HHTP), charge extraction could be achieved by inserting the soluble C_{60}

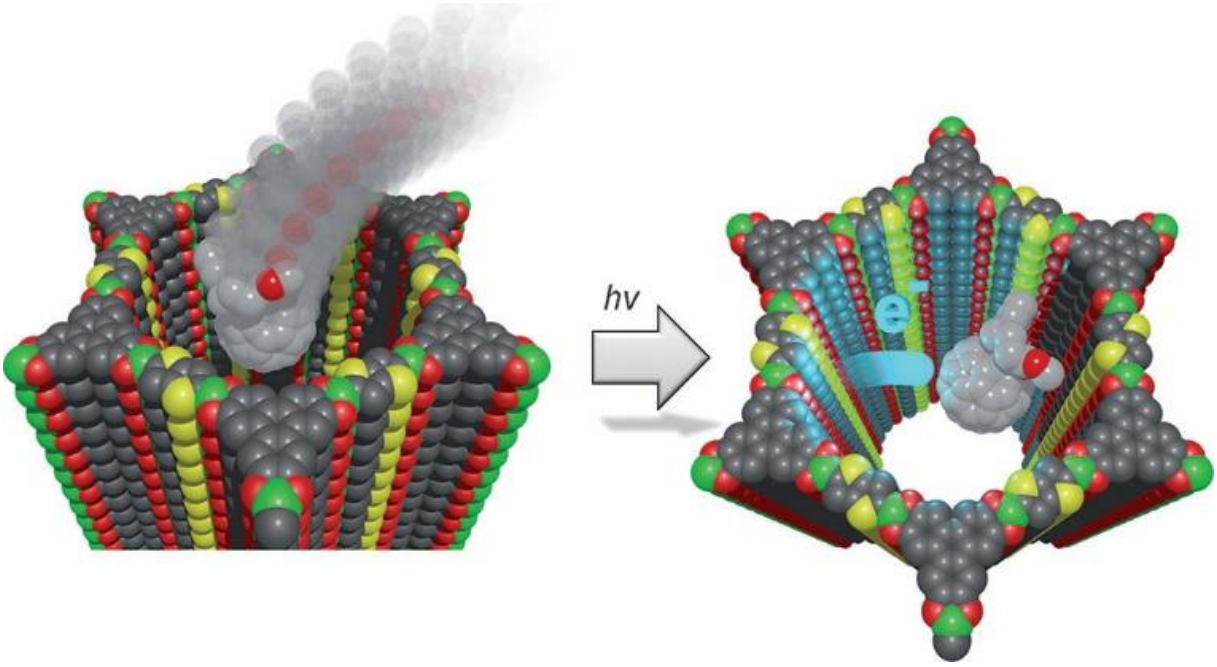

Figure 1.31: Schematic overview of fullerene insertion into COF pore and photo-induced electron transfer from the framework onto the electron-acceptor guest molecule. Reproduced with permission.[22] Copyright 2013, John Wiley and Sons.

derivative PCBM into the pores of the photoconductive thienothiophene-containing framework (Figure 1.31). The associated optoelectronic features allowed for the fabrication of a first heterojunction device based on the COF thin film grown on ITO and contacted with an aluminium top electrode. Under illumination, photovoltaic studies showed successful charge-transfer from the COF onto the PCBM, followed by charge separation and extraction.[22] Transient absorption spectroscopy revealed longer lifetimes of polarons, which can be attributed to the suitable interface created where charges dissociate and form polarons.[155]

Another elegant approach to create an ordered heterojunction with electron-accepting guest molecules includes the Huisgen cycloaddition between the azide-functionalized N_3-ZnPc-COF and fullerene units with an alkyne group attached (Figure 1.32). This allowed for controlled filling of the pores with fullerenes that could be easily observed in IR spectra. ESR data showed that an increase of fullerene content in the COF enhanced the signal intensity correlated with the amount of radical species. This indicated photo-induced charge generation and electron transfer to the electron-accepting fullerene units clicked to the framework.[64]

A different approach towards creating a heterojunction interface uses a liquid electrolyte which can serve as electron donor or acceptor. This is the case in photocatalytic water splitting where the hydrogen reduction or oxygen oxidation occurs on the interface benefitting from the large surface area which allows for short diffusion distances of the generated charges. Also, the

application of sacrificial electron donors (e.g., TEOA, ascorbic acid) or electron acceptors ($AgNO_3$) elucidates the advantage of this type of solid/liquid heterojunction.

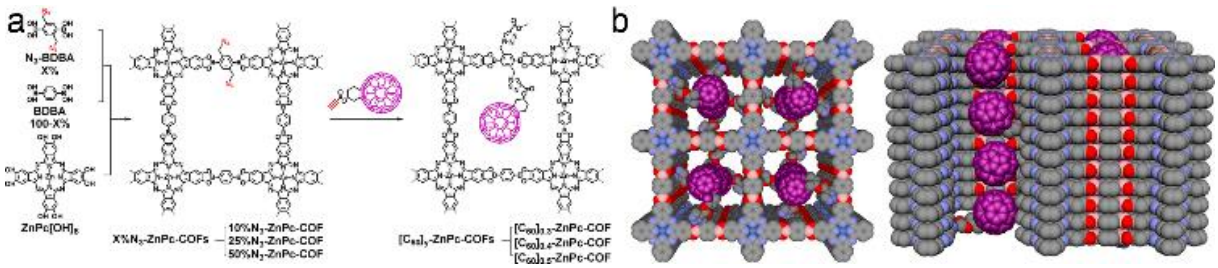

Figure 1.32: (a) Scheme of the synthetic route for a heterojunction COF and the subsequent functionalization of the pore walls with fullerene via Huisgen cycloaddition. (b) Top and side view of the resulting envisioned donor−acceptor structure. Reproduced with permission.[64] Copyright 2014, American Chemical Society.

1.5 From laboratory to application devices

With the ability to structure COF-based heterojunctions in various ways, they can be implemented in working devices requiring charge separation and related processes. Covering already some of the devices investigated for photocatalytic hydrogen evolution, solar cell or other optoelectronic devices such as sensors, this chapter will highlight the most promising examples.

1.5.1 Photovoltaic devices

In 2013, our group reported the construction of the first solar cell device with a COF acting as the photoactive layer. The oriented TT-COF thin film was spin-coated with a solution of PCBM serving as electron acceptor to achieve the desired heterojunction for charge separation. Sandwiched between ITO and aluminium, this photovoltaic device yielded a modest power conversion efficiency (PCE) of 0.053% with a V_{OC} of 622 mV, a J_{SC} of 0.213 mA cm^{-2}, and a fill factor 40%. These findings prove the conceptual feasibility of COFs integrated in photovoltaic applications, but also expose challenges regarding light harvesting and loss mechanisms limiting charge extraction.[22]

In related work, the group of Jiang chose a different approach with non-oriented COF bulk material, made from triphenylene hexamine (TPHA) and *tert*-butylpyrene tetraone. To insert the PCBM, thermal sublimation/diffusion at 400 °C was performed leading to a COF with fullerene inside the pores but also fullerene aggregates between COF particles. The fullerene content was 50 wt % and also acted as a glue which was additionally added in the spin-coating process. This composite material was spin-coated on ITO and contacted from the top with aluminium. The devices showed an increased performance compared to the oriented TT-COF film device above, leading to a power conversion efficiency (PCE) of 0.9 % with a V_{OC} of 980 mV, a J_{SC} of 1.7 mA cm^{-2}, and a fill factor of 54%. While the photovoltaic features could be enhanced, it is evident that extracting the photogenerated charges is still a challenge.[24]

The above examples are based on interpenetrated COF heterojunctions utilizing the COF pores to insert electron acceptors. The alternative approach relying on the combination of donor and acceptor building blocks to design an integrated COF heterojunction between the respective columns of donor and acceptor moieties, was reported by our group in 2014. In this Tp-Por

COF made from linear porphyrin units and HHTP, the electron transfer from the triphenylene unit to the porphyrin could be observed in photoinduced absorption (PIA) spectroscopy and led to the first working photovoltaic device using the COF donor−acceptor interface for charge separation. The device showed superior (but still moderate) performance compared to a device constructed from the simply mixed neat building blocks, with a V_{OC} of 312 mV and a J_{SC} of 0.045 mA cm^{-2} (Figure 1.33). The existence of severe loss processes was shown by the low external quantum efficiency of below 1%, which could be increased under reverse bias of 2 V to more than 30% at 350 nm.[23]

The challenge regarding efficient light harvesting has been greatly overcome in recent years. We reported several strategies to drastically increase absorption in the near IR (NIR) and IR. Connecting oligothiophene backbones with pyrene units lead to tunable optical absorption bands in the IR-region up to 1000 nm.[29] The absorption behavior of a thienoisoindigo-COF

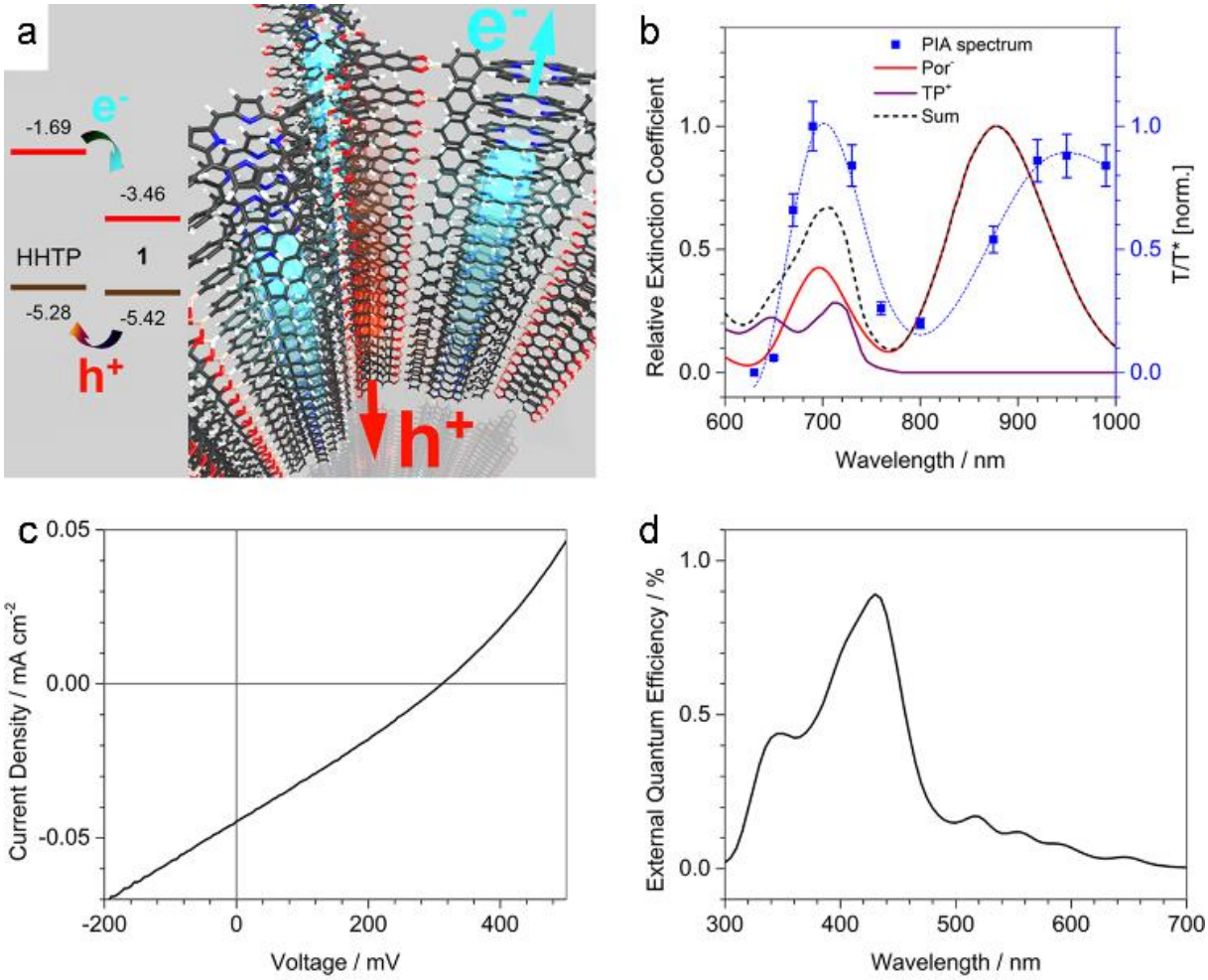

Figure 1.33: (a) Frontier orbital energies of both Tp-Por COF subunits and schematic illustration of the photogenerated charge separation. (b) PIA spectrum of the COF film together with radical ion absorption of the subunits. (c) *J-V* curve of the COF-based photovoltaic device and (d) the corresponding EQE spectrum. Reproduced with permission.[23] Copyright 2014, American Chemical Society.

could be applied in a NIR-responsive photodetector. The small bandgap was created by integrating electron-deficient isoindigo derivatives (such as 6,6′-bis(4-formylphenyl)-*N*,*N*′-dibutyl-isoindigo, 5,5′-bis(4-formylphenyl)-*N*,*N*′-dibutyl-thienoisoindigo and 5,5′-bis(2-formylthiophen-5-yl)-*N*,*N*′-dibutyl-thienoisoindigo) with electron-rich pyrene knots in a COF structure. Fabricating a heterojunction with PCBM as electron acceptor in the COF pores led to a spectrally switchable photodetector.[18] The matrix of a 2D COF made of porphyrin knots and linear thienothiophene enforced extended J-aggregate formation of the porphyrin macrocycles leading to enhanced light-harvesting in the near IR with strongly shifted peak ratios with much stronger absorption in the Q-bands.[28]

However, the extraction of the generated charges from the two different types of heterojunctions still remains a challenge and needs to be addressed for photovoltaic devices.

1.5.2 Photocatalytic water splitting

As mentioned in the chapter about the interactions of COFs with light, photocatalytic hydrogen evolution from water splitting reactions was first reported by the group of Lotsch in 2014. The respective COF (made from 1,3,5-tris-(4-formyl-phenyl)triazine and 2,5-diethoxy-terephthalohydrazide) was simply dispersed in water and in combination with platinum nanoparticles as proton reduction catalyst and triethanolamine as sacrificial donor the hydrogen evolution reached values as high as 1970 μmol h^{-1} g^{-1}, but degraded after 5 hours.[99]

This is a straightforward setup that can be applied since only one of the two half-reactions of water splitting occurs, otherwise the additional evolution of oxygen in the same chamber would create dangerous gas mixtures and limit scale-up. In the following publications, the stability of COFs in photocatalytic systems is often guaranteed by the use of 1,3,5-triformylphloroglucinol as building block leading to keto-enol tautomerism and stable linkages.

Further research on COFs as photocatalysts led to insights about the role of different linkers and functionalization. For example, an investigation of acetylene-functionalized COFs revealed the first operational COF photocatalyst without heteroaromatic building blocks as the active group. The catalytic activity was shown to be strongly dependent on the number of acetylene units in the COF. The TP-EDDA COF, made from 1,3,5-triformylphloroglucinol (TP) with 4,4′-(ethyne-1,2-diyl)dianiline (EDDA) with only one acetylene bridge in the linear linker exhibited

a hydrogen evolution rate (in the presence of TEOA and photodeposited Pt particles) of 30 μmol h^{-1} g^{-1}, which was enhanced compared to a COF with a linear linker of the same length but no acetylene moiety. Extending the acetylene bridge to a diacetylene bridge not only doubled the catalytic activity but led to a hydrogen evolution rate of 324 μmol h^{-1} g^{-1} which is one order of magnitude higher.[156] This positive impact of acetylene moieties in the COF on the HER was also observed in related computational studies, pointing to an enhanced diffusion of photogenerated excitons along the polyyne moieties in the COF.[157]

Changing the focus to a pyrene-based tetravalent linker containing phenyl rings with various nitrogen contents that are connected via acetylene bridges to the core, the impact of the nitrogen atoms in the ring on the photocatalytic hydrogen evolution was investigated. The experimental data in combination with quantum chemical calculations revealed the COF with the lowest number of nitrogen atoms to be the most efficient in water splitting, due to the highest driving force for the hydrogen evolution reaction (HER) of the more electron-rich framework. The hydrogen evolution rate was found to be 98 μmol h^{-1} g^{-1} for the COF with pure phenyl rings without nitrogen atoms, compared to 22 and 6 μmol h^{-1} g^{-1} for the COFs with pyridine and pyrimidine rings, respectively.[16]

Copolymers containing dibenzo[*b,d*]thiophene sulfone moieties are known to be highly active leading to significant hydrogen evolution rates. The experiments for the polymer P7 were performed in the presence of triethylamine and significant residues of Pd (from polymer synthesis).[158] This knowledge was transferred to COFs in order to investigate the impact of ordered crystalline and porous materials on the photocatalytic behavior on these moieties. The hydrogen evolution reaction induced by S-COF (made from 3,7-diaminodibenzo[*b*,*d*]thiophene sulfone and 1,3,5-triformylphloroglucinol) with a single sulfone group in the linear bridge already led to increased rates of up to 4.44 mmol h^{-1} g^{-1}, while the related FS-COF bearing two sulfone moieties doubled the rate to 10.1 mmol h^{-1} g^{-1} with a higher concentration of sacrificial donor ascorbic acid then for example Stegbauer *et al.*[99] and with deposited Pt nanoparticles (Figure 1.34). By adding a dye to enhance the optical absorption, the hydrogen evolution rate could be increased by another 60%, up to 16.3 mmol h^{-1} g^{-1}. Compared to the related polymer P7 (see work of Sprick *et al.* above), the dye-sensitized COF sample exceeded the values by one order of magnitude, showing the importance of crystallinity and accessible pore surface in these photocatalytic systems.[159]

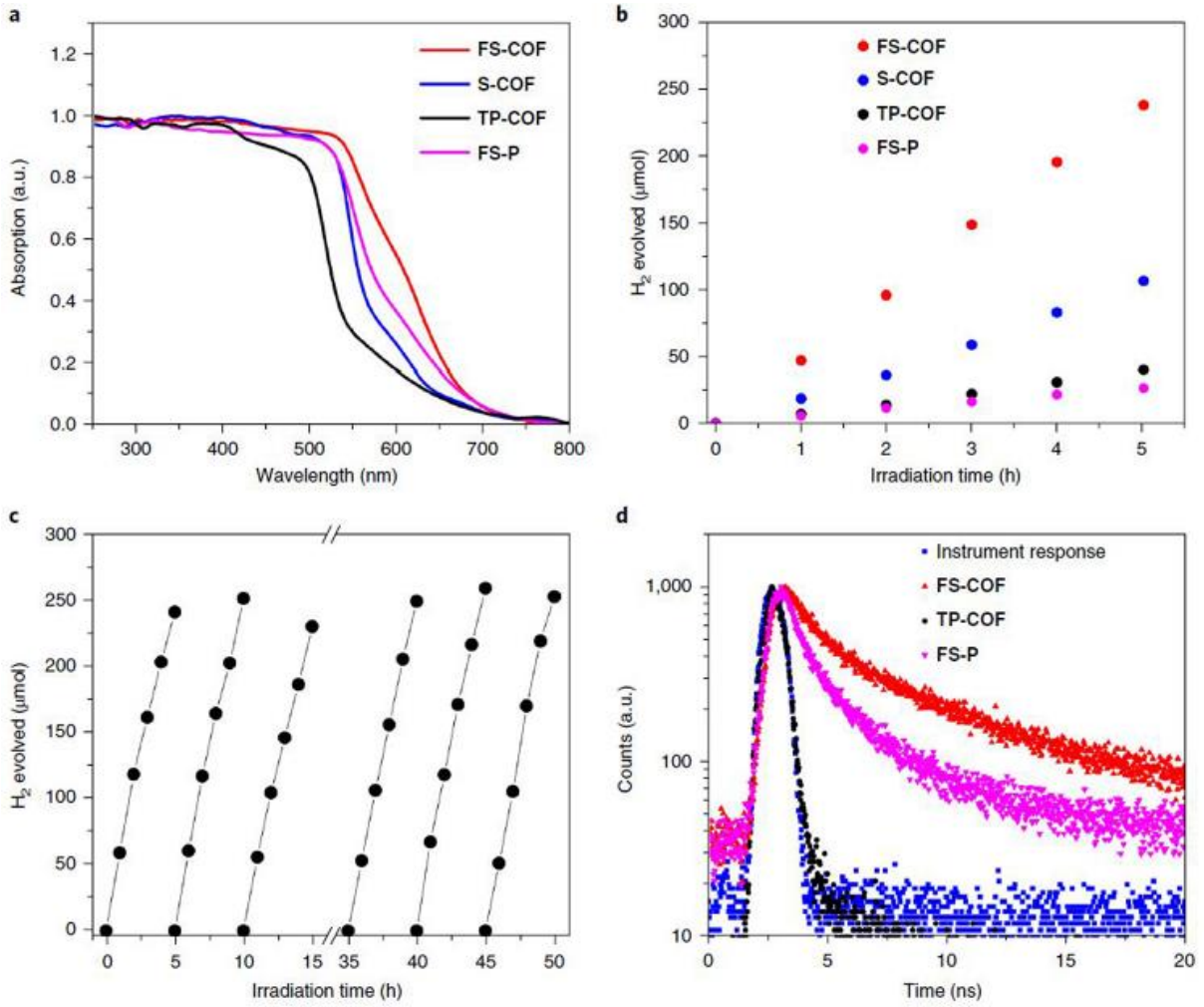

Figure 1.34: (a) Optical absorption and (b) photocatalytic H_2 production as a function of time of the FS-COF, S-COF, TP-COF (reference without sulfone moiety) and the FS-P (analogue amorphous polymer). (c) Stability tests of the catalytic activity of FS-COF and (d) time-correlated single photon counting traces of the FS-COF, reference TP-COF and amorphous FS-P. Reproduced with permission.[160] Copyright 2018, Nature Publishing Group.

Examining the possible replacement of Pt as co-catalyst for COF-catalysed hydrogen evolution reactions, it was found that $[Mo_3S_{13}]^{2-}$ clusters in the pores of a COF made from ethidium bromide and 1,3,5-triformylphloroglucinol exhibited great potential, delivering hydrogen at a stable rate of up to 13.2 mmol h^{-1} g^{-1} for 18 h. The highest values were measured using $Ru(bpy)_3Cl_2$ as a photosensitizer, ascorbic acid as a sacrificial donor and the MoS clusters loaded into the COF pores.[160] Alternatively, a combination of Eosin Y and triethanolamine (TEOA, sacrificial donor), with Pd^0 as co-catalyst reduced on site with EtOH also showed significant hydrogen evolution activity of up to10.4 mmol h^{-1} g^{-1} for at least 2 h with the COF TpPa-1 (made from 1,3,5-triformylphloroglucinol and *p*-phenylenediamine).[161]

Further research led to the substitution of Pt by Ni-based co-catalysts. The group of Lotsch reported the synthesis and successful application of a thiazolo[5,4-*d*]thiazole-bridged COF (with 1,3,5-triformylphloroglucinol knots) as the photoactive material. In photocatalysis

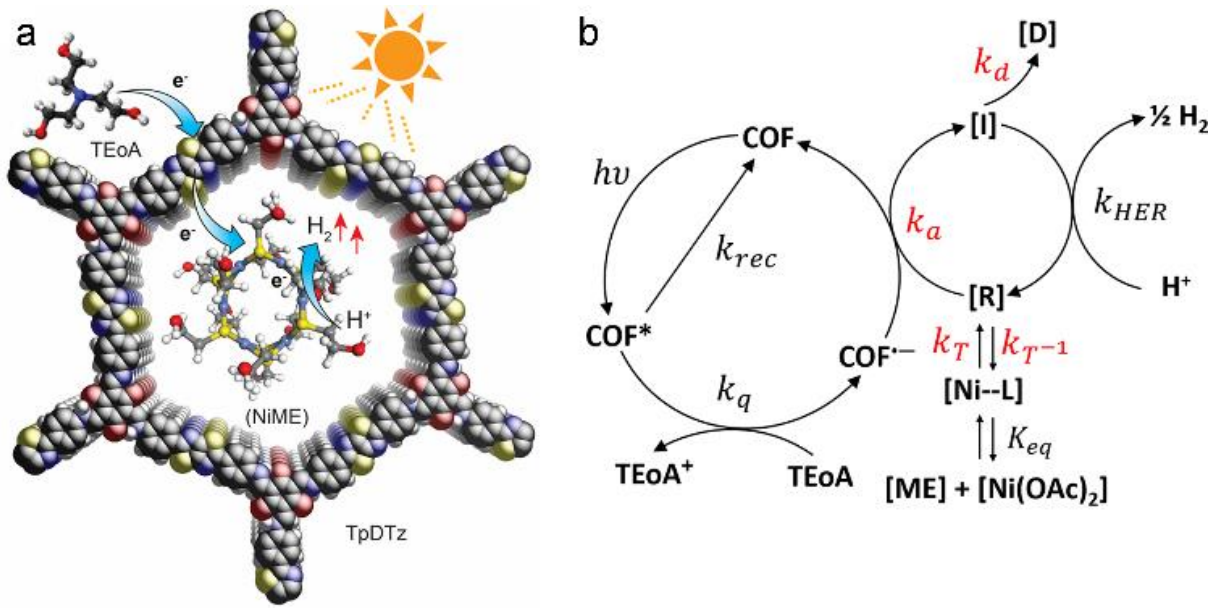

Figure 1.35: (a) Schematic representation of the proposed mechanism for the H_2 evolution. (b) Key steps of the photocatalysis: [R] active catalyst; [D] deactivated species [I] intermediate reduced catalyst species. Reproduced with permission.[17] Copyright 2019, American Chemical Society.

studies, a Ni-thiolate cluster was applied as co-catalyst and TEOA as a sacrificial electron donor (Figure 1.35). The system was able to deliver a hydrogen evolution rate of up to 941 μmol h^{-1} g^{-1} for at least 70 h. The Ni-thiolate cluster is known for efficiently catalyzing the HER in combination with erythrosin B as sensitizer with rates up to 49.3 mmol h^{-1} g^{-1}, but the catalyst fully degrades within 7 h resulting in a turnover number of Ni that is 12 times lower than for the stable COF system.[17]

Further research on noble metal alternatives showed that $Ni(OH)_2$ was efficient as co-catalyst in a COF photocatalytic system (made from 1,3,5-triformylphloroglucinol and 2,5-dimethyl-*p*-phenylenediamine), resulting in a hydrogen production rate of up to 1896 μmol h^{-1} g^{-1} for at least 5 h. The sacrificial donor in this case was sodium ascorbate.[162] Modifying a COF made from a triazine core and 1,3,5-triformylphloroglucinol with g-C_3N_4, graphitic carbon nitride which was recently reported to show significant activity in photocatalytic water splitting,[163-165] to form CN-COF, enhanced the photocatalytic performance to hydrogen evolution rates of up to 10.1 mmol h^{-1} g^{-1}, superior to any other g-C_3N_4-based photocatalyst reported (Figure 1.36).[166]

So far only photocatalytic hydrogen evolution with COFs has been extensively studied, while oxygen evolution seemed to be out of reach since the band alignment is crucial and the valence band needs to be below the energy level of the oxygen oxidation. However, in 2019 the group of Zhang synthesized the first COF (made from 3,5-dicyano-2,4,6-trimethylpyridine and 4,4″-

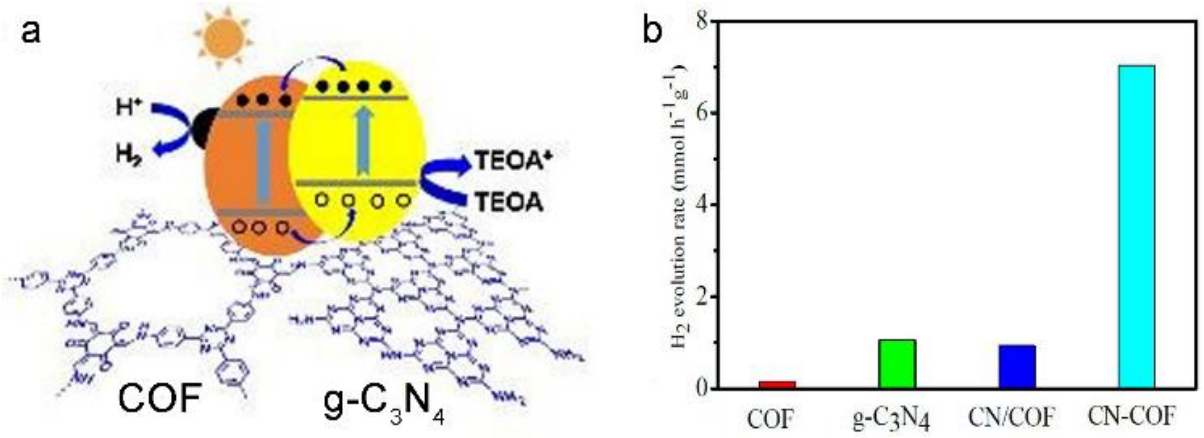

Figure 1.36: (a) Proposed photocatalytic mechanism for CN-COF. (b) H_2 production rate, whereby CN/COF is the physical mixture of g-C_3N_4 and COF. Reproduced with permission.[167] Copyright 2019, Royal Society of Chemistry.

diformyl-*p*-terphenyl) that was reported to be able to perform both half-reactions of water splitting (Figure 1.37). The sp^2 carbon-conjugated g-$C_{40}N_3$-COF revealed hydrogen production rates of 4120 μmol h^{-1} g^{-1} with TEOA and Pt, and also exhibited an oxygen production rate of 50 μmol h^{-1} g^{-1} with silver nitrate as electron acceptor and La_2O_3 as a pH buffer.[27]

With this work opening the field of COF-based photocatalytic OER, a first imine-linked COF constructed from TAPB knots and with a bipyridine bridge used to coordinate Co ions as co-catalyst showed oxygen evolving abilities, with an O_2-production rate of 152 μmol h^{-1} g^{-1}.[167]

Photoelectrochemistry (PEC) separates the light-induced oxidation- and reduction half-reactions from each other such that they occur at different electrodes and in different compartments if so desired. This can be beneficial if reaction products need to be separated (as hydrogen and oxygen in water splitting reactions). In this context, our group reported the first COF-based photocathode applicable for the HER in water splitting. Oriented BDT-ETTA COF thin films were grown on ITO and photoelectrochemically investigated in an aqueous 0.1 M Na_2SO_4 electrolyte without the use of a sacrificial donor or a co-catalyst. The hydrogen

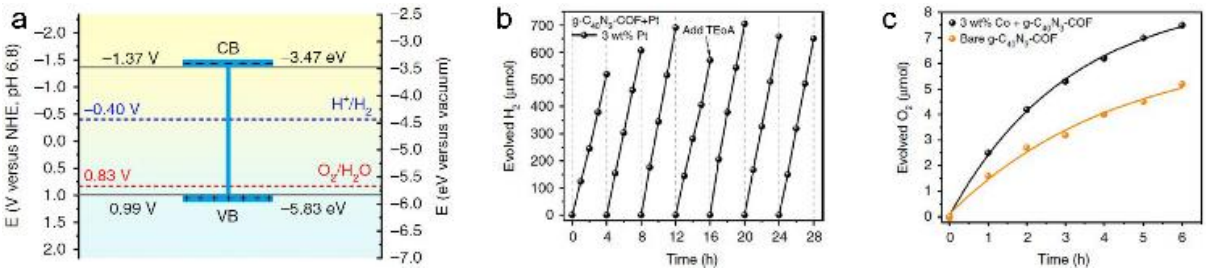

Figure 1.37: (a) Bandgap diagram with marked potential for HER and OER. (b) Hydrogen and (c) oxygen production during photocatalytic water splitting based on g-$C_{40}N_3$-COF. Reproduced with permission.[27] Copyright 2019, Nature Publishing Group.

reduction resulted in a photocurrent of 1.5 μA cm^{-2} at 0.2 V vs RHE, being strongly dependent of the film thickness. An increase of the photocurrent by the factor of 4 could be achieved by depositing Pt nanoparticles as co-catalysts.[14] The same COF system was used in a study addressing the importance of the COF morphology for catalytic applications. Using electrophoretic deposition (EPD), COF films can be easily prepared from COF suspensions within seconds, featuring textural porosity and thicknesses depending on the deposition time. Using such an EPD-based film of BDT-ETTA COF, the HER photocurrent density reached up to 21.1 μA cm^{-2} at 0.1 V vs RHE under otherwise the same conditions with illumination at AM1.5G (Figure 1.38). The EPD approach not only produces desirable textural porosity but also allows for the simultaneous co-deposition of a co-catalyst such as Pt nanoparticles. With such a co-catalyst, the photoelectrolysis of water resulted in a photocurrent density of 128.9 μA cm^{-2} at 0.1 V vs RHE, showing the vital role of both morphology and co-catalysts in the photocatalysis of water.[168]

The photoelectrochemical properties were also investigated for the sp^2 carbon-linked g-$C_{18}N_3$-COF (made from 2,4,6-trimethyl-1,3,5-triazine (TMTA) and terephthalaldehyde), which was drop-casted onto an ITO substrate. Linear sweep voltammetry in 0.2 M Na_2SO_4 exhibited a PEC current density of 45 μA cm^{-2} at 0.2 V vs RHE.[100]

The above examples show the great potential of COFs as photocatalytic and photoelectrochemical systems for the generation of hydrogen and increasingly also oxygen from water. Undoubtedly, this research will be further driven by the increasing knowledge about stabilizing highly conjugated COFs, controlling morphology and diffusion pathways, and embedding catalytic functionality and co-catalysts into these well-defined systems.

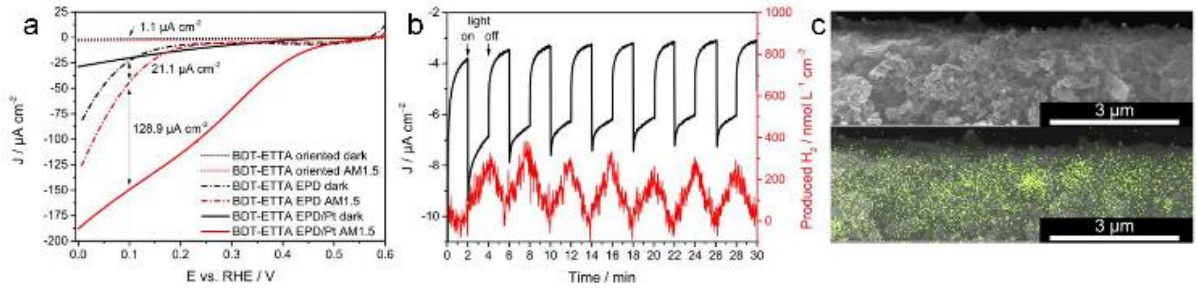

Figure 1.38: (a) PEC linear sweep voltammograms of electrodes coated with BDT-ETTA COF grown as an oriented film, a film prepared by EPD and a film with co-deposited Pt nanoparticles prepared by EPD. (b) Dynamic hydrogen evolution measurement under chopped illumination at 0.2 V vs RHE. (c) SEM cross-section of COF/Pt hybrid film with EDX mapping of Pt. Reproduced with permission.[156] Copyright 2019, American Chemical Society.

1.5.3 Photocatalytic CO_2 reduction

Converting solar energy with COFs into sustainable fuels can not only occur via photocatalytic hydrogen evolution but also by photocatalyzing CO_2 reduction. Notably, without the use of sacrificial agents and co-catalysts, the azine-linked COFs ACOF-1 (made from 1,3,5-triformylbenzene and hydrazine hydrate) and N_3-COF (made from 2,4,6-tris(4-formylphenyl)-1,3,5-triazine and hydrazine hydrate) could photocatalytically convert CO_2 in water to methanol, with a yield of 13.7 μmol g^{-1} within 24 h for the N_3-COF in a 100% CO_2 atmosphere. When the CO_2 concentration was reduced to 1%, the amount of methanol was still 9.9 μmol g^{-1} within 24 h for the N_3-COF. The presence of only traces of H_2 and O_2 illustrates the photocatalytic selectivity, which is attributed to the high selectivity of the nitrogen-rich COF systems.[169]

Enhancing the photocatalytic activity of the COFs can again be achieved by introducing metal-based co-catalysts into the framework. For example, when introducing bipyridine into a COF (connected with 4,4′,4″-(1,3,5-triazine-2,4,6-triyl) trianiline knots), the two neighboring nitrogen sites can coordinate a Re complex using a simple post-synthetic procedure. Here, the reduction of CO_2 yielded CO as a product at amounts of almost 15 mmol g^{-1} over the course of more than 20 h with the use of TEOA as sacrificial agent. The photocatalytic process is selective and shows recyclability for at least three cycles of 3 h each.[170] It was found that the efficiency is strongly dependent on the ordered structure in the COF.[171]

Notably, the rhenium in the above COF could also be substituted by Ni(II) ions coordinated by the bipyridine units. Connected via 1,3,5-triformylphloroglucinol nodes, the photocatalytically selective CO_2 reduction produced 811.4 μmol g^{-1} h^{-1} CO in the presence of TEOA as sacrificial electron donor. The synergistic combination of the COF and the single Ni-sites coordinated at the bipyridine linkers were experimentally and computationally found to be key for the high CO production rate.[172]

In a different study, several abundant metal ions such as Ni, Co and Zn coordinated to the quinone oxygens of adjacent layers in an anthraquinone-based COF (again linked with 1,3,5-triformylphloroglucinol) exhibited significant CO production rates, as high as 1020 μmol g^{-1} h^{-1} with TEOA for the Co-COF, whereas the Zn-coordinated COF selectively produced formic acid with a rate of 152.5 μmol g^{-1} h^{-1}, also in the presence of TEOA.[173]

A bottom-up approach for the synthesis of ultrathin COF (made from porphyrin and TAPB knots and terephthalaldehyde and 4,4′-biphenyldialdehyde bridges) nanosheets by adding 2,4,6-trimethylbenzaldehyde at high excess as modulator driving lateral growth due to steric hindrances between the layers led to promising photocatalytic performance for CO_2 reduction. The photocatalysis showed a high selectivity of 78% for the CO evolution compared to H_2 generation, with a CO production rate of 10.2 mmol g^{-1} h^{-1}. The reaction was performed in CO_2-saturated, 0.1 M $KHCO_3$ aqueous solution, with $[Ru(bpy)_3]Cl_2$ as photosensitizer and ascorbic acid as sacrificial electron donor. The nanosheet structures exhibited a superior catalytic activity towards CO_2 reduction than the bulk COF, showing a CO production rate of only 124 μmol g^{-1} h^{-1} and a selectivity of 13%.[174]

1.5.4 Sensors and detectors

The optoelectronic properties of COFs can also inspire new concepts aiming at applications in sensor or detector devices. For example, a popular approach has focused on luminescent COFs where the signal output consists of fluorescence enhancement or quenching in the presence of the detected species. Engaging electronic interactions such as charge transfer, the optical properties change and can even be detected conveniently with the naked eye upon illumination. As a result, complex device structures have typically not been established yet. Nevertheless, the development is rapidly progressing in this field, leading to insights regarding mechanisms and new detection systems.

The group of Banerjee reported highly emissive covalent organic nanosheets (CONs) exfoliated from TfpBDH bulk COF (made from 1,3,5-tris(4-formylphenyl)benzene and pyromellitic-*N*,*N*′-bisaminoimide), leading to the first turn-on/off sensing mechanism for nitroaromatics, especially 2,4,6-trinitrophenol (TNP). In solution, fluorescence quenching occurred by charge transfer from the nitroaromatic compound to the COF. In contrast, in the solid state the CON powders deposited on a paper strip exhibited fluorescence enhancement upon exposure to TNP. This effect was attributed to proton transfer from the TNP to the imine bond.[175]

A field-effect transistor (FET)-device for photo- and moisture-detection was built with an Lp-pi-COF thin film (made from TAPB and terephthalaldehyde), which was obtained by photon-assisted condensation of the building blocks on the water surface. The film was transferred to a SiO_2 substrate, then chromium and gold contacts (5 and 20 nm thickness, respectively) were deposited on top by electron beam metal evaporation. A current change by three orders of magnitude could be measured with the Lp-pi-COF-based FET-device upon water vapor exposure (Figure 1.39).[176]

Combining tetraphenylethylene monomers as photoactive component and triazine moieties as electron acceptor in a COF, COF-based photodetectors with high photoresponsivity of 3.2×10^7 A W^{-1} and fast response times of 1.14 ms could be realized. The device for the photoelectric measurements of the COF film on graphene was constructed on top of gold electrodes deposited on a Si/SiO_2 substrate. Due to the different electronic interactions with vapors of changing polarity, the photocurrent could be adjusted significantly.[177]

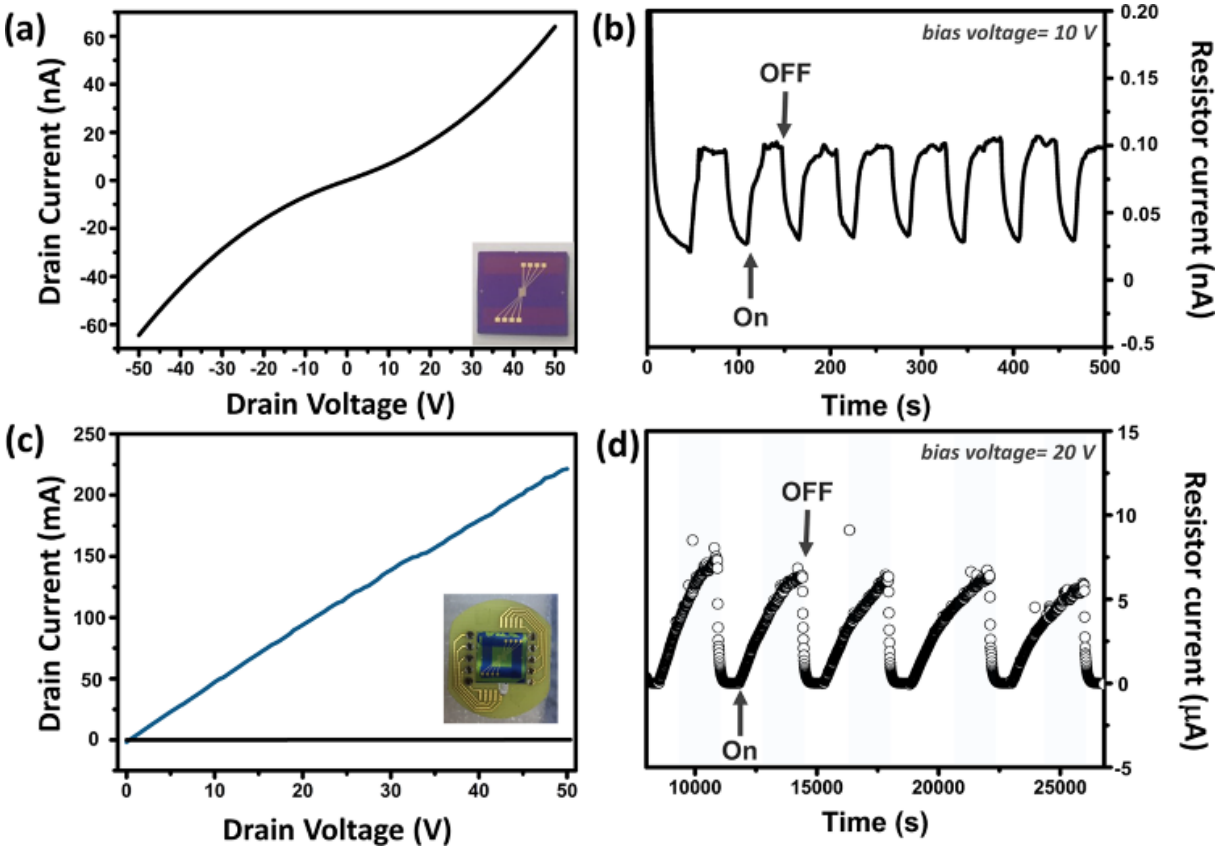

Figure 1.39: (a) I-V curve of the Lp-pi-COF film with tested device shown in photograph. (b) On−off switching behavior upon light irradiation of device from graph (a). (c) I-V curve of the Lp-pi-COF recorded in argon (black) and water vapor (blue) environment with tested device shown in photograph. (d) On−off switching behavior upon moisture exposure of device from graph (c). Reproduced with permission.[176] Copyright 2019, American Chemical Society.

A similar approach was already shown with a solvatochromic Py-TT COF, which proved to be a promising candidate for sensing of solvent or water vapors. The solvatochromism is based on electronic interactions between the solvent molecules and the COF, while excluding structural or chemical changes. In a sensor device, a COF thin film was grown, serving as an optical filter for an LED. As a result of the solvatochromic effects, the optical transmission of the COF at a specific wavelength was altered, thus inducing current changes in a photo-dependent resistor (Figure 1.40).[19] In a related study, imine-linked perylene-based COFs were applied as acid vapor sensors based on the ability to protonate and deprotonate their imine bonds, resulting in optical changes with high sensitivity. Additional information could be gained about the acid strength and concentration in non-aqueous solutions, which is enabled by the stepwise protonation of the two imine bonds connecting the linear bridges in the COF.[178]

The dual emission of COF-4-OH (made from 1,3,5-triformylphloroglucinol and 9,9-dibutyl-2,7-diaminofluorene) induced by the keto-enol tautomerism leading to an excited-state induced proton transfer was used as a sensing concept for water content in organic solvents and as pH

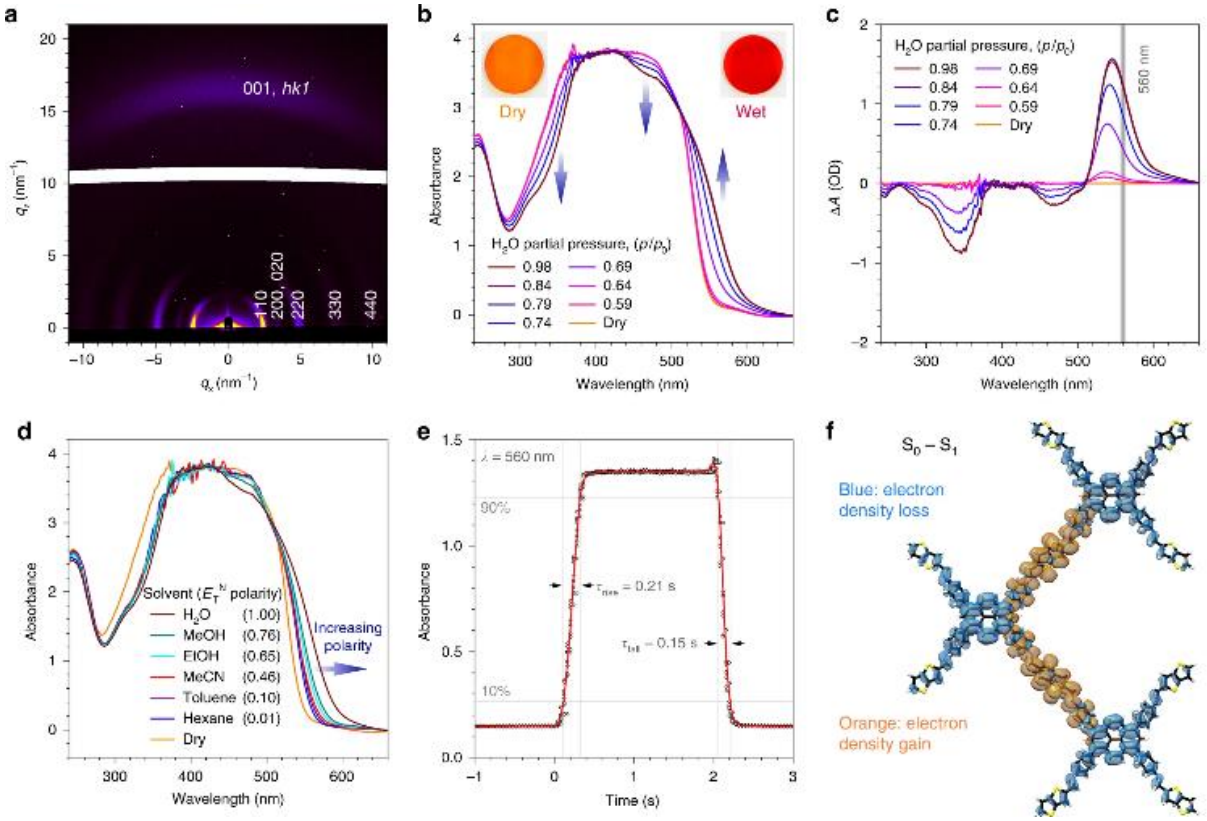

Figure 1.40: (a) GIWAXS pattern of oriented Py-TT COF film on sapphire. (b) UV-Vis absorption of COF film at different moisture contents. (c) Humidity-induced absorbance changes. (d) UV-Vis absorption of COF film in saturated solvent atmospheres. (e) Solvatochromic response of COF film to changes from dry to H_2O-saturated N_2-streams and back. (f) TD-DFT calculated electron density difference upon the one-electron excitation from ground state to the first singlet excited state showing a distinct charge-transfer character. Reproduced with permission.[19] Copyright 2018, Nature Publishing Group.

sensor. Furthermore, sterically demanding butyl chains were introduced to reduce aggregation-caused quenching (ACQ).[179]

The sensing abilities of COFs were also applied in biomedical systems, enabling the sensitive detection of methylglyoxal (MGO) for diabetes mellitus diagnosis in serum systems. Notably, the TpPa-1 COF could be deprotonated at the N-H bond leading to a 70-fold increased PL emission. Upon exposure to MGO, the excited, deprotonated COF forms an excited-state charge-transfer complex with MGO, also called an exciplex. By the implementation of two logic gates, the red-shifted fluorescence upon MGO exposure can directly be traced as an output signal, leading to an easy read-out diagnostic device.[180]

More examples of COFs as sensing material exhibit selective sensitivity towards analytes such as electron-rich arenes, proteins, or metal traces.

1.5.5 Light-emitting devices

The luminescent properties of COFs have been intensively studied. Various light-emitting COFs have been synthesized by implementing different strategies such as aggregation-induced emission (AIE) or restriction of intramolecular bond rotations (RIR) mechanisms.

The first COF-LED reported derived its white light from the blue emission of π-stacked anthracene units and the red and green emission from the resorcinol moieties in a COF, denoted as IISERP-COF7. It was even possible to fine tune the emission of this COF by the use of N-donor or O-donor solvents. Upon UV illumination, a film consisting of an IISERP-COF7-PMMA gel exhibited intense white light emission with a CIE coordinate of (0.35, 0.36). In a proof-of-principle COF-LED, poly(9-vinylcarbazole) served as the host for the same COF material, which was then implemented in an electroluminescent device (ITO, ZnO, polyethylenimine ethoxylated (PEIE), the hybrid material, MoO_3 and gold, Figure 1.41).[73]

Applying the principle of aggregation-induced emission (AIE), tetraphenylethylen, a known AIEgen, was used as a building block in a 3D COF (made from tetra(*p*-aminophenyl)methane and 1,1,2,2-tetrakis(4-formyl-(1,1′-biphenyl))ethene) that was found to be highly emissive with a CIE coordinate of (0.38,0.57). This COF was utilized as a yellow-emitting phosphor for a blue LED by coating the latter with the COF powder, obtaining a white light emission with CIE coordinate (0.30, 0.35).[20]

Since lanthanides have already shown their luminescent potential in conventional LEDs, a recent study explored their combination with the luminescence from a COF. The blue-emitting COF made from 4,4′4″-(1,3,5-triazine-2,4,6-triyl)trianiline and 2,6-diformylpyridine was hereby combined with the green and red emission from the lanthanides Eu^{3+} and Tb^{3+}, respectively, coordinated into nitrogen-rich pockets in the pore wall.[74] The combination with the COF resulted in a white light emitter upon excitation in the UV, with CIE coordinates (0.3636, 0.3355; 0.3636, 0.3355) for different ratios of the lanthanides.

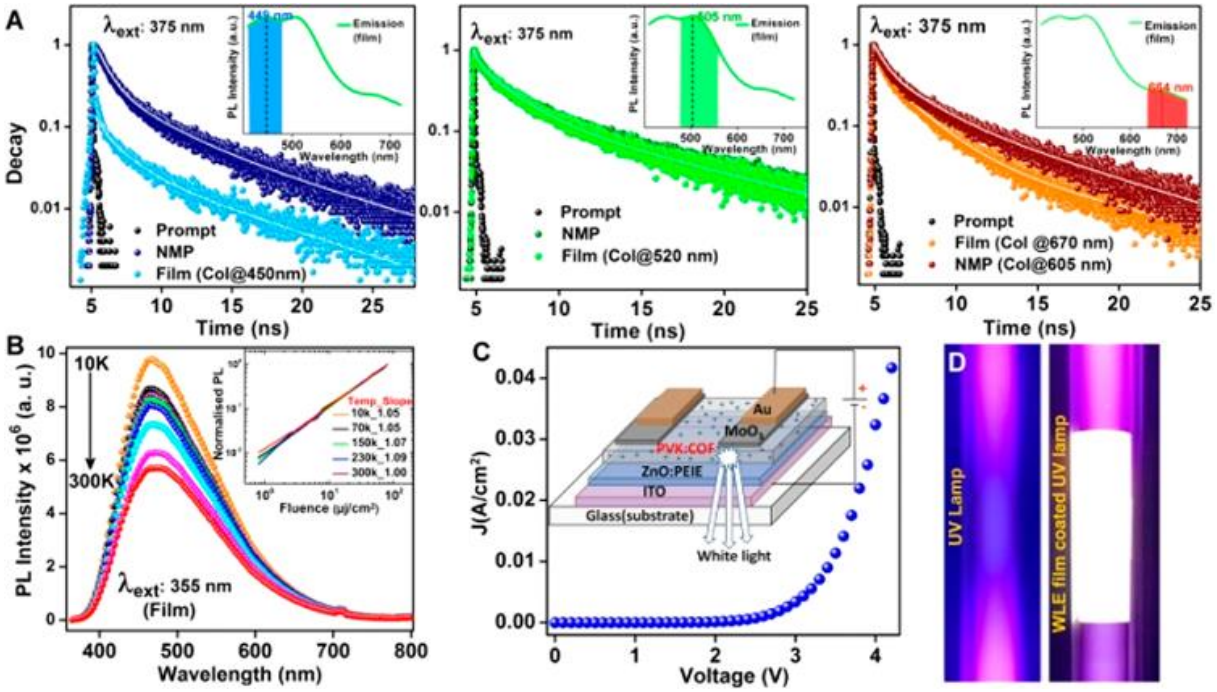

Figure 1.41: (a) PL lifetime traces of COF dispersion in NMP vs COF film recorded in the blue, green and red region. (b) Variable temperature PL spectra of the COF film. (c) J-V plot of the COF-based LED device using IISERP-COF7 with scheme showing device structure. (d) UV lamp emission without and with COF coating as phosphor. Reproduced with permission.[73] Copyright 2018, American Chemical Society.

1.6 Conclusions

In this review we have given an extensive overview about (opto)electronic properties and processes in covalent organic frameworks and their potential applications in various fields. Starting from luminescent and semiconducting frameworks, important insights into the impact of linkage motifs, stacking behavior, and functionalization on optoelectronic processes within the COF have been gathered over the last few years. The construction principles of COFs, based on the covalent coupling of molecular building blocks, allow for the design of diverse framework and pore topologies in combination with the properties of the building blocks themselves. Motivated by this potential, a large number of building blocks that can act as light-harvesters, semiconductors, ligands, binding sites or redox centers have been embedded in the frameworks of COFs. Coupled with the highly ordered structures and control of intrinsic and textural porosity, intriguing functionalities in the fields discussed in this review, i.e. defined donor−acceptor interfaces, batteries, supercapacitors, sensors, field-effect transistors, LEDs, photocatalysts and photovoltaic devices have recently been developed.

The chemical stability of COFs – a critical feature for several envisioned applications – has been greatly enhanced over the years by introducing new linkage motifs such as sp^2 carbon-conjugated bonds, intralayer/interlayer hydrogen bonds or the keto-enol tautomerism. It is anticipated that this progress will open access to applications where COFs need to overcome demanding conditions.

Controlling the stacking distances and stacking mode of 2D COF layers has been a powerful strategy to tune optical and electrical properties. However, challenges still remain regarding the rather modest electrical conductivity of these frameworks. The processes of charge carrier generation and diffusion should be further investigated to allow the development of design rules for further enhancing charge carrier mobilities and conductivity, for example *via* linker design or by creating suitable hybrid host-guest systems.

Embedding COFs into suitable device structures with morphologies optimised for desired applications will be key for the next generation of high-performance COFs. The solid foundation developed in the almost 15 years of COF science is an excellent basis for future developments focusing on specific demands and intriguing applications.

1.7 References

[1] Côté, A. P.; Benin, A. I.; Ockwig, N. W.; O'Keeffe, M.; Matzger, A. J.; Yaghi, O. M., Porous, Crystalline, Covalent Organic Frameworks. *Science* **2005,** *310* (5751), 1166-1170.

[2] Furukawa, H.; Yaghi, O. M., Storage of Hydrogen, Methane, and Carbon Dioxide in Highly Porous Covalent Organic Frameworks for Clean Energy Applications. *J. Am. Chem. Soc.* **2009,** *131* (25), 8875-8883.

[3] Doonan, C. J.; Tranchemontagne, D. J.; Glover, T. G.; Hunt, J. R.; Yaghi, O. M., Exceptional ammonia uptake by a covalent organic framework. *Nat. Chem.* **2010,** *2* (3), 235-238.

[4] Ding, S.-Y.; Wang, W., Covalent organic frameworks (COFs): from design to applications. *Chem. Soc. Rev.* **2013,** *42* (2), 548-568.

[5] Han, X.; Zhang, J.; Huang, J.; Wu, X.; Yuan, D.; Liu, Y.; Cui, Y., Chiral induction in covalent organic frameworks. *Nat. Commun.* **2018,** *9* (1), 1294.

[6] Guan, X.; Li, H.; Ma, Y.; Xue, M.; Fang, Q.; Yan, Y.; Valtchev, V.; Qiu, S., Chemically stable polyarylether-based covalent organic frameworks. *Nat. Chem.* **2019,** *11* (6), 587-594.

[7] DeBlase, C. R.; Hernández-Burgos, K.; Silberstein, K. E.; Rodríguez-Calero, G. G.; Bisbey, R. P.; Abruña, H. D.; Dichtel, W. R., Rapid and Efficient Redox Processes within 2D Covalent Organic Framework Thin Films. *ACS Nano* **2015,** *9* (3), 3178-3183.

[8] Yang, H.; Zhang, S.; Han, L.; Zhang, Z.; Xue, Z.; Gao, J.; Li, Y.; Huang, C.; Yi, Y.; Liu, H.; Li, Y., High Conductive Two-Dimensional Covalent Organic Framework for Lithium Storage with Large Capacity. *ACS Appl. Mater. Interfaces* **2016,** *8* (8), 5366-5375.

[9] Hu, Y.; Dunlap, N.; Wan, S.; Lu, S.; Huang, S.; Sellinger, I.; Ortiz, M.; Jin, Y.; Lee, S.-h.; Zhang, W., Crystalline Lithium Imidazolate Covalent Organic Frameworks with High Li-Ion Conductivity. *J. Am. Chem. Soc.* **2019,** *141* (18), 7518-7525.

[10] Chandra, S.; Kundu, T.; Kandambeth, S.; BabaRao, R.; Marathe, Y.; Kunjir, S. M.; Banerjee, R., Phosphoric Acid Loaded Azo (−N═N−) Based Covalent Organic Framework for Proton Conduction. *J. Am. Chem. Soc.* **2014,** *136* (18), 6570-6573.

[11] Shinde, D. B.; Aiyappa, H. B.; Bhadra, M.; Biswal, B. P.; Wadge, P.; Kandambeth, S.; Garai, B.; Kundu, T.; Kurungot, S.; Banerjee, R., A mechanochemically synthesized covalent organic framework as a proton-conducting solid electrolyte. *J. Mater. Chem. A* **2016,** *4* (7), 2682-2690.

[12] Xu, H.; Tao, S.; Jiang, D., Proton conduction in crystalline and porous covalent organic frameworks. *Nat. Mater.* **2016,** *15*, 722.

[13] Meng, Z.; Aykanat, A.; Mirica, K. A., Proton Conduction in 2D Aza-Fused Covalent Organic Frameworks. *Chem. Mater.* **2019,** *31* (3), 819-825.

[14] Sick, T.; Hufnagel, A. G.; Kampmann, J.; Kondofersky, I.; Calik, M.; Rotter, J. M.; Evans, A. M.; Döblinger, M.; Herbert, S.; Peters, K.; Boehm, D.; Knochel, P.; Medina, D. D.; Fattakhova-Rohlfing, D.; Bein, T., Oriented Films of Conjugated 2D Covalent Organic Frameworks as Photocathodes for Water Splitting. *J. Am. Chem. Soc.* **2017**.

[15] Banerjee, T.; Gottschling, K.; Savasci, G.; Ochsenfeld, C.; Lotsch, B. V., H2 Evolution with Covalent Organic Framework Photocatalysts. *ACS Energy Lett.* **2018**.

[16] Stegbauer, L.; Zech, S.; Savasci, G.; Banerjee, T.; Podjaski, F.; Schwinghammer, K.; Ochsenfeld, C.; Lotsch, B. V., Tailor-Made Photoconductive Pyrene-Based Covalent Organic Frameworks for Visible-Light Driven Hydrogen Generation. *Adv. Energy Mater.* **2018,** *8* (24), 1703278.

[17] Biswal, B. P.; Vignolo-González, H. A.; Banerjee, T.; Grunenberg, L.; Savasci, G.; Gottschling, K.; Nuss, J.; Ochsenfeld, C.; Lotsch, B. V., Sustained Solar H2 Evolution from a Thiazolo[5,4-d]thiazole-Bridged Covalent Organic Framework and Nickel-Thiolate Cluster in Water. *J. Am. Chem. Soc.* **2019,** *141* (28), 11082-11092.

[18] Bessinger, D.; Ascherl, L.; Auras, F.; Bein, T., Spectrally Switchable Photodetection with Near-Infrared-Absorbing Covalent Organic Frameworks. *J. Am. Chem. Soc.* **2017,** *139* (34), 12035-12042.

[19] Ascherl, L.; Evans, E. W.; Hennemann, M.; Di Nuzzo, D.; Hufnagel, A. G.; Beetz, M.; Friend, R. H.; Clark, T.; Bein, T.; Auras, F., Solvatochromic covalent organic frameworks. *Nat. Commun.* **2018,** *9* (1), 3802.

[20] Ding, H.; Li, J.; Xie, G.; Lin, G.; Chen, R.; Peng, Z.; Yang, C.; Wang, B.; Sun, J.; Wang, C., An AIEgen-based 3D covalent organic framework for white light-emitting diodes. *Nat. Commun.* **2018,** *9* (1), 5234.

[21] Li, X.; Gao, Q.; Wang, J.; Chen, Y.; Chen, Z.-H.; Xu, H.-S.; Tang, W.; Leng, K.; Ning, G.-H.; Wu, J.; Xu, Q.-H.; Quek, S. Y.; Lu, Y.; Loh, K. P., Tuneable near white-emissive two-dimensional covalent organic frameworks. *Nat. Commun.* **2018,** *9* (1), 2335.

[22] Dogru, M.; Handloser, M.; Auras, F.; Kunz, T.; Medina, D.; Hartschuh, A.; Knochel, P.; Bein, T., A Photoconductive Thienothiophene-Based Covalent Organic Framework Showing Charge Transfer Towards Included Fullerene. *Angew. Chem. Int. Ed.* **2013,** *52* (10), 2920-2924.

[23] Calik, M.; Auras, F.; Salonen, L. M.; Bader, K.; Grill, I.; Handloser, M.; Medina, D. D.; Dogru, M.; Löbermann, F.; Trauner, D.; Hartschuh, A.; Bein, T., Extraction of Photogenerated Electrons and Holes from a Covalent Organic Framework Integrated Heterojunction. *J. Am. Chem. Soc.* **2014,** *136* (51), 17802-17807.

[24] Guo, J.; Xu, Y.; Jin, S.; Chen, L.; Kaji, T.; Honsho, Y.; Addicoat, M. A.; Kim, J.; Saeki, A.; Ihee, H.; Seki, S.; Irle, S.; Hiramoto, M.; Gao, J.; Jiang, D., Conjugated organic framework with three-dimensionally ordered stable structure and delocalized pi clouds. *Nat. Commun.* **2013,** *4*, 2736.

[25] Jin, E.; Asada, M.; Xu, Q.; Dalapati, S.; Addicoat, M. A.; Brady, M. A.; Xu, H.; Nakamura, T.; Heine, T.; Chen, Q.; Jiang, D., Two-dimensional sp² carbon–conjugated covalent organic frameworks. *Science* **2017,** *357* (6352), 673-676.

[26] Acharjya, A.; Pachfule, P.; Roeser, J.; Schmitt, F.-J.; Thomas, A., Vinylene-Linked Covalent Organic Frameworks by Base-Catalyzed Aldol Condensation. *Angew. Chem. Int. Ed.* **2019**.

[27] Bi, S.; Yang, C.; Zhang, W.; Xu, J.; Liu, L.; Wu, D.; Wang, X.; Han, Y.; Liang, Q.; Zhang, F., Two-dimensional semiconducting covalent organic frameworks via condensation at arylmethyl carbon atoms. *Nat. Commun.* **2019,** *10* (1), 2467.

[28] Keller, N.; Calik, M.; Sharapa, D.; Soni, H. R.; Zehetmaier, P. M.; Rager, S.; Auras, F.; Jakowetz, A. C.; Görling, A.; Clark, T.; Bein, T., Enforcing Extended Porphyrin J-Aggregate Stacking in Covalent Organic Frameworks. *J. Am. Chem. Soc.* **2018,** *140* (48), 16544-16552.

[29] Keller, N.; Bessinger, D.; Reuter, S.; Calik, M.; Ascherl, L.; Hanusch, F. C.; Auras, F.; Bein, T., Oligothiophene-Bridged Conjugated Covalent Organic Frameworks. *J. Am. Chem. Soc.* **2017,** *139* (24), 8194-8199.

[30] Keller, N.; Sick, T.; Bach, N. N.; Koszalkowski, A.; Rotter, J. M.; Medina, D. D.; Bein, T., Dibenzochrysene Enables Tightly Controlled Docking and Stabilizes Photoexcited States in Dual-Pore Covalent Organic Frameworks. *ChemRxiv* **2019**.

[31] Uribe-Romo, F. J.; Hunt, J. R.; Furukawa, H.; Klöck, C.; O'Keeffe, M.; Yaghi, O. M., A Crystalline Imine-Linked 3-D Porous Covalent Organic Framework. *J. Am. Chem. Soc.* **2009,** *131* (13), 4570-4571.

[32] Kandambeth, S.; Mallick, A.; Lukose, B.; Mane, M. V.; Heine, T.; Banerjee, R., Construction of Crystalline 2D Covalent Organic Frameworks with Remarkable Chemical (Acid/Base) Stability via a Combined Reversible and Irreversible Route. *J. Am. Chem. Soc.* **2012,** *134* (48), 19524-19527.

[33] Haase, F.; Troschke, E.; Savasci, G.; Banerjee, T.; Duppel, V.; Dörfler, S.; Grundei, M. M. J.; Burow, A. M.; Ochsenfeld, C.; Kaskel, S.; Lotsch, B. V., Topochemical conversion of an imine- into a thiazole-linked covalent organic framework enabling real structure analysis. *Nat. Commun.* **2018,** *9* (1), 2600.

[34] Waller, P. J.; AlFaraj, Y. S.; Diercks, C. S.; Jarenwattananon, N. N.; Yaghi, O. M., Conversion of Imine to Oxazole and Thiazole Linkages in Covalent Organic Frameworks. *J. Am. Chem. Soc.* **2018**.

[35] Jin, E.; Li, J.; Geng, K.; Jiang, Q.; Xu, H.; Xu, Q.; Jiang, D., Designed synthesis of stable light-emitting two-dimensional sp2 carbon-conjugated covalent organic frameworks. *Nat. Commun.* **2018,** *9* (1), 4143.

[36] Jin, E.; Lan, Z.; Jiang, Q.; Geng, K.; Li, G.; Wang, X.; Jiang, D., 2D sp2 Carbon-Conjugated Covalent Organic Frameworks for Photocatalytic Hydrogen Production from Water. *Chem* **2019,** *5* (6), 1632-1647.

[37] Lyu, H.; Diercks, C. S.; Zhu, C.; Yaghi, O. M., Porous Crystalline Olefin-Linked Covalent Organic Frameworks. *J. Am. Chem. Soc.* **2019,** *141* (17), 6848-6852.

[38] Wan, S.; Guo, J.; Kim, J.; Ihee, H.; Jiang, D., A Belt-Shaped, Blue Luminescent, and Semiconducting Covalent Organic Framework. *Angew. Chem. Int. Ed.* **2008,** *47* (46), 8826-8830.

[39] Chen, X.; Addicoat, M.; Irle, S.; Nagai, A.; Jiang, D., Control of Crystallinity and Porosity of Covalent Organic Frameworks by Managing Interlayer Interactions Based on Self-Complementary π-Electronic Force. *J. Am. Chem. Soc.* **2013,** *135* (2), 546-549.

[40] Ascherl, L.; Sick, T.; Margraf, J. T.; Lapidus, S. H.; Calik, M.; Hettstedt, C.; Karaghiosoff, K.; Döblinger, M.; Clark, T.; Chapman, K. W.; Auras, F.; Bein, T., Molecular docking sites designed for the generation of highly crystalline covalent organic frameworks. *Nat. Chem.* **2016,** *8* (4), 310-316.

[41] Auras, F.; Ascherl, L.; Hakimioun, A. H.; Margraf, J. T.; Hanusch, F. C.; Reuter, S.; Bessinger, D.; Döblinger, M.; Hettstedt, C.; Karaghiosoff, K.; Herbert, S.; Knochel, P.; Clark, T.; Bein, T., Synchronized Offset Stacking: A Concept for Growing Large-Domain and Highly Crystalline 2D Covalent Organic Frameworks. *J. Am. Chem. Soc.* **2016,** *138* (51), 16703-16710.

[42] Gao, Q.; Li, X.; Ning, G.-H.; Leng, K.; Tian, B.; Liu, C.; Tang, W.; Xu, H.-S.; Loh, K. P., Highly photoluminescent two-dimensional imine-based covalent organic frameworks for chemical sensing. *Chem. Commun.* **2018,** *54* (19), 2349-2352.

[43] Albacete, P.; Martínez, J. I.; Li, X.; López-Moreno, A.; Mena-Hernando, S. a.; Platero-Prats, A. E.; Montoro, C.; Loh, K. P.; Pérez, E. M.; Zamora, F., Layer-Stacking-Driven Fluorescence in a Two-Dimensional Imine-Linked Covalent Organic Framework. *J. Am. Chem. Soc.* **2018,** *140* (40), 12922-12929.

[44] Wu, X.; Han, X.; Liu, Y.; Liu, Y.; Cui, Y., Control Interlayer Stacking and Chemical Stability of Two-Dimensional Covalent Organic Frameworks via Steric Tuning. *J. Am. Chem. Soc.* **2018,** *140* (47), 16124-16133.

[45] Xie, Z.; Wang, B.; Yang, Z.; Yang, X.; Yu, X.; Xing, G.; Zhang, Y.; Chen, L., Stable 2D Heteroporous Covalent Organic Frameworks for Efficient Ionic Conduction. *Angew. Chem. Int. Ed.* **2019,** *58* (44), 15742-15746.

[46] Ding, X.; Guo, J.; Feng, X.; Honsho, Y.; Guo, J.; Seki, S.; Maitarad, P.; Saeki, A.; Nagase, S.; Jiang, D., Synthesis of Metallophthalocyanine Covalent Organic Frameworks That Exhibit High Carrier Mobility and Photoconductivity. *Angew. Chem. Int. Ed.* **2011,** *50* (6), 1289-1293.

[47] Wan, S.; Gándara, F.; Asano, A.; Furukawa, H.; Saeki, A.; Dey, S. K.; Liao, L.; Ambrogio, M. W.; Botros, Y. Y.; Duan, X.; Seki, S.; Stoddart, J. F.; Yaghi, O. M., Covalent Organic Frameworks with High Charge Carrier Mobility. *Chem. Mater.* **2011,** *23* (18), 4094-4097.

[48] Spitler, E. L.; Dichtel, W. R., Lewis acid-catalysed formation of two-dimensional phthalocyanine covalent organic frameworks. *Nat. Chem.* **2010,** *2* (8), 672-677.

[49] Wang, S.; Ma, L.; Wang, Q.; Shao, P.; Ma, D.; Yuan, S.; Lei, P.; Li, P.; Feng, X.; Wang, B., Covalent organic frameworks: a platform for the experimental establishment of the influence of intermolecular distance on phosphorescence. *J. Mater. Chem. C* **2018**.

[50] Lukose, B.; Kuc, A.; Frenzel, J.; Heine, T., On the reticular construction concept of covalent organic frameworks. *Beilstein J. Nanotechnol.* **2010,** *1*, 60-70.

[51] Lukose, B.; Kuc, A.; Heine, T., The Structure of Layered Covalent-Organic Frameworks. *Chem. - Eur. J.* **2011,** *17* (8), 2388-2392.

[52] Spitler, E. L.; Koo, B. T.; Novotney, J. L.; Colson, J. W.; Uribe-Romo, F. J.; Gutierrez, G. D.; Clancy, P.; Dichtel, W. R., A 2D Covalent Organic Framework with 4.7-nm Pores and Insight into Its Interlayer Stacking. *J. Am. Chem. Soc.* **2011,** *133* (48), 19416-19421.

[53] Patwardhan, S.; Kocherzhenko, A. A.; Grozema, F. C.; Siebbeles, L. D. A., Delocalization and Mobility of Charge Carriers in Covalent Organic Frameworks. *J. Phys. Chem. C* **2011,** *115* (23), 11768-11772.

[54] Li, H.; Brédas, J.-L., Large Out-of-Plane Deformations of Two-Dimensional Covalent Organic Framework (COF) Sheets. *J. Phys. Chem. Lett.* **2018,** *9* (15), 4215-4220.

[55] Nguyen, V.; Grünwald, M., Microscopic Origins of Poor Crystallinity in the Synthesis of Covalent Organic Framework COF-5. *J. Am. Chem. Soc.* **2018,** *140* (9), 3306-3311.

[56] Ding, X.; Chen, L.; Honsho, Y.; Feng, X.; Saengsawang, O.; Guo, J.; Saeki, A.; Seki, S.; Irle, S.; Nagase, S.; Parasuk, V.; Jiang, D., An n-Channel Two-Dimensional Covalent Organic Framework. *J. Am. Chem. Soc.* **2011,** *133* (37), 14510-14513.

[57] Feng, X.; Chen, L.; Honsho, Y.; Saengsawang, O.; Liu, L.; Wang, L.; Saeki, A.; Irle, S.; Seki, S.; Dong, Y.; Jiang, D., An Ambipolar Conducting Covalent Organic Framework with Self-Sorted and Periodic Electron Donor-Acceptor Ordering. *Adv. Mater.* **2012,** *24* (22), 3026-3031.

[58] Jin, S.; Ding, X.; Feng, X.; Supur, M.; Furukawa, K.; Takahashi, S.; Addicoat, M.; El-Khouly, M. E.; Nakamura, T.; Irle, S.; Fukuzumi, S.; Nagai, A.; Jiang, D., Charge Dynamics in A Donor–Acceptor Covalent Organic Framework with Periodically Ordered Bicontinuous Heterojunctions. *Angew. Chem. Int. Ed.* **2013,** *52* (7), 2017-2021.

[59] Jin, S.; Supur, M.; Addicoat, M.; Furukawa, K.; Chen, L.; Nakamura, T.; Fukuzumi, S.; Irle, S.; Jiang, D., Creation of Superheterojunction Polymers via Direct Polycondensation: Segregated and Bicontinuous Donor–Acceptor π-Columnar Arrays in Covalent Organic Frameworks for Long-Lived Charge Separation. *J. Am. Chem. Soc.* **2015,** *137* (24), 7817-7827.

[60] Kim, T. W.; Jun, S.; Ha, Y.; Yadav, R. K.; Kumar, A.; Yoo, C.-Y.; Oh, I.; Lim, H.-K.; Shin, J. W.; Ryoo, R.; Kim, H.; Kim, J.; Baeg, J.-O.; Ihee, H., Ultrafast charge transfer coupled with lattice phonons in two-dimensional covalent organic frameworks. *Nat. Commun.* **2019,** *10* (1), 1873.

[61] Li, Z.; Zhi, Y.; Shao, P.; Xia, H.; Li, G.; Feng, X.; Chen, X.; Shi, Z.; Liu, X., Covalent organic framework as an efficient, metal-free, heterogeneous photocatalyst for organic transformations under visible light. *Appl. Catal., B* **2019,** *245*, 334-342.

[62] Pachfule, P.; Acharjya, A.; Roeser, J.; Sivasankaran, R. P.; Ye, M.-Y.; Brückner, A.; Schmidt, J.; Thomas, A., Donor–acceptor covalent organic frameworks for visible light induced free radical polymerization. *Chem. Sci.* **2019,** *10* (36), 8316-8322.

[63] Li, X.; Gao, Q.; Aneesh, J.; Xu, H.-S.; Chen, Z.; Tang, W.; Liu, C.; Shi, X.; Adarsh, K. V.; Lu, Y.; Loh, K. P., Molecular Engineering of Bandgaps in Covalent Organic Frameworks. *Chem. Mater.* **2018,** *30* (16), 5743-5749.

[64] Chen, L.; Furukawa, K.; Gao, J.; Nagai, A.; Nakamura, T.; Dong, Y.; Jiang, D., Photoelectric Covalent Organic Frameworks: Converting Open Lattices into Ordered Donor–Acceptor Heterojunctions. *J. Am. Chem. Soc.* **2014,** *136* (28), 9806-9809.

[65] Joshi, T.; Chen, C.; Li, H.; Diercks, C. S.; Wang, G.; Waller, P. J.; Li, H.; Bredas, J. L.; Yaghi, O. M.; Crommie, M. F., Local Electronic Structure of Molecular Heterojunctions in a Single-Layer 2D Covalent Organic Framework. *Adv. Mater.* **2019,** *31* (3).

[66] Li, Y.; Chen, Q.; Xu, T.; Xie, Z.; Liu, J.; Yu, X.; Ma, S.; Qin, T.; Chen, L., De Novo Design and Facile Synthesis of 2D Covalent Organic Frameworks: A Two-in-One Strategy. *J. Am. Chem. Soc.* **2019,** *141* (35), 13822-13828.

[67] Samrat, G.; Akinobu, N.; Maximilian A., S.; Takahiro, K.; Katsuaki, S.; Hironori, K.; Igor, B.; Agnieszka, K.; Thomas, H.; Ryu, A.; Shu, S., Identification of Prime Factors for Efficient Photocatalytic Hydrogen Evolution of Covalent Organic Frameworks via Molecular Engineering. *ChemRxiv* **2019**.

[68] Xu, Q.; Tang, Y.; Zhang, X.; Oshima, Y.; Chen, Q.; Jiang, D., Template Conversion of Covalent Organic Frameworks into 2D Conducting Nanocarbons for Catalyzing Oxygen Reduction Reaction. *Adv. Mater.* **2018**.

[69] Wei, H.; Ning, J.; Cao, X.; Li, X.; Hao, L., Benzotrithiophene-Based Covalent Organic Frameworks: Construction and Structure Transformation under Ionothermal Condition. *J. Am. Chem. Soc.* **2018,** *140* (37), 11618-11622.

[70] Dufresne, S.; Skene, W. G., Optoelectronic property tailoring of conjugated heterocyclic azomethines – the effect of pyrrole, thiophene and furans. *J. Phys. Org. Chem.* **2012,** *25* (3), 211-221.

[71] Dalapati, S.; Jin, E.; Addicoat, M.; Heine, T.; Jiang, D., Highly Emissive Covalent Organic Frameworks. *J. Am. Chem. Soc.* **2016,** *138* (18), 5797-5800.

[72] Liu, Y.; Diercks, C. S.; Ma, Y.; Lyu, H.; Zhu, C.; Alshmimri, S. A.; Alshihri, S.; Yaghi, O. M., 3D Covalent Organic Frameworks of Interlocking 1D Square Ribbons. *J. Am. Chem. Soc.* **2018**.

[73] Haldar, S.; Chakraborty, D.; Roy, B.; Banappanavar, G.; Rinku, K.; Mullangi, D.; Hazra, P.; Kabra, D.; Vaidhyanathan, R., Anthracene-Resorcinol Derived Covalent Organic Framework as Flexible White Light Emitter. *J. Am. Chem. Soc.* **2018,** *140* (41), 13367-13374.

[74] Krishnaraj, C.; Kaczmarek, A. M.; Jena, H. S.; Leus, K.; Chaoui, N.; Schmidt, J.; Van Deun, R.; Van Der Voort, P., Triggering White-Light Emission in a 2D Imine Covalent Organic Framework Through Lanthanide Augmentation. *ACS Appl. Mater. Interfaces* **2019**.

[75] Evans, A. M.; Castano, I.; Brumberg, A.; Parent, L. R.; Corcos, A. R.; Li, R. L.; Flanders, N. C.; Gosztola, D. J.; Gianneschi, N. C.; Schaller, R. D.; Dichtel, W. R., Emissive Single-Crystalline

Boroxine-Linked Colloidal Covalent Organic Frameworks. *J. Am. Chem. Soc.* **2019,** *141* (50), 19728-19735.

[76] Ma, T.; Kapustin, E. A.; Yin, S. X.; Liang, L.; Zhou, Z.; Niu, J.; Li, L.-H.; Wang, Y.; Su, J.; Li, J.; Wang, X.; Wang, W. D.; Wang, W.; Sun, J.; Yaghi, O. M., Single-crystal x-ray diffraction structures of covalent organic frameworks. *Science* **2018,** *361* (6397), 48-52.

[77] Evans, A. M.; Parent, L. R.; Flanders, N. C.; Bisbey, R. P.; Vitaku, E.; Kirschner, M. S.; Schaller, R. D.; Chen, L. X.; Gianneschi, N. C.; Dichtel, W. R., Seeded growth of single-crystal two-dimensional covalent organic frameworks. *Science* **2018,** *361* (6397), 52-57.

[78] Jakowetz, A. C.; Hinrichsen, T. F.; Ascherl, L.; Sick, T.; Calik, M.; Auras, F.; Medina, D. D.; Friend, R. H.; Rao, A.; Bein, T., Excited-State Dynamics in Fully Conjugated 2D Covalent Organic Frameworks. *J. Am. Chem. Soc.* **2019,** *141* (29), 11565-11571.

[79] Dalapati, S.; Jin, S.; Gao, J.; Xu, Y.; Nagai, A.; Jiang, D., An Azine-Linked Covalent Organic Framework. *J. Am. Chem. Soc.* **2013,** *135* (46), 17310-17313.

[80] Li, Z.; Zhang, Y.; Xia, H.; Mu, Y.; Liu, X., A robust and luminescent covalent organic framework as a highly sensitive and selective sensor for the detection of Cu2+ ions. *Chem. Commun.* **2016,** *52* (39), 6613-6616.

[81] Chen, G.; Lan, H.-H.; Cai, S.-L.; Sun, B.; Li, X.-L.; He, Z.-H.; Zheng, S.-R.; Fan, J.; Liu, Y.; Zhang, W.-G., Stable Hydrazone-Linked Covalent Organic Frameworks Containing O,N,O′-Chelating Sites for Fe(III) Detection in Water. *ACS Appl. Mater. Interfaces* **2019,** *11* (13), 12830-12837.

[82] Song, X.; Zhao, Z.; Si, D.; Wang, X.; Zhou, F.; Zhang, M.; Shi, Y.; Hao, C., Computational insights into the mechanism of formaldehyde detection by luminescent covalent organic framework. *J. Mol. Model.* **2019,** *25* (8), 248.

[83] Ding, S.-Y.; Dong, M.; Wang, Y.-W.; Chen, Y.-T.; Wang, H.-Z.; Su, C.-Y.; Wang, W., Thioether-Based Fluorescent Covalent Organic Framework for Selective Detection and Facile Removal of Mercury(II). *J. Am. Chem. Soc.* **2016,** *138* (9), 3031-3037.

[84] Zhou, Z.; Zhong, W.; Cui, K.; Zhuang, Z.; Li, L.; Li, L.; Bi, J.; Yu, Y., A covalent organic framework bearing thioether pendant arms for selective detection and recovery of Au from ultra-low concentration aqueous solution. *Chem. Commun.* **2018,** *54* (71), 9977-9980.

[85] Rao, M. R.; Fang, Y.; De Feyter, S.; Perepichka, D. F., Conjugated Covalent Organic Frameworks via Michael Addition–Elimination. *J. Am. Chem. Soc.* **2017,** *139* (6), 2421-2427.

[86] Kulkarni, R.; Noda, Y.; Kumar Barange, D.; Kochergin, Y. S.; Lyu, P.; Balcarova, B.; Nachtigall, P.; Bojdys, M. J., Real-time optical and electronic sensing with a β-amino enone linked, triazine-containing 2D covalent organic framework. *Nat. Commun.* **2019,** *10* (1), 3228.

[87] Zhang, C.; Zhang, S.; Yan, Y.; Xia, F.; Huang, A.; Xian, Y., Highly Fluorescent Polyimide Covalent Organic Nanosheets as Sensing Probes for the Detection of 2,4,6-Trinitrophenol. *ACS Appl. Mater. Interfaces* **2017,** *9* (15), 13415-13421.

[88] Zhu, M.-W.; Xu, S.-Q.; Wang, X.-Z.; Chen, Y.; Dai, L.; Zhao, X., The construction of fluorescent heteropore covalent organic frameworks and their applications in spectroscopic and visual detection of trinitrophenol with high selectivity and sensitivity. *Chem. Commun.* **2018,** *54* (18), 2308-2311.

[89] Albacete, P.; López-Moreno, A.; Mena-Hernando, S.; Platero-Prats, A. E.; Pérez, E. M.; Zamora, F., Chemical sensing of water contaminants by a colloid of a fluorescent imine-linked covalent organic framework. *Chem. Commun.* **2019,** *55* (10), 1382-1385.

[90] Wu, X.; Han, X.; Xu, Q.; Liu, Y.; Yuan, C.; Yang, S.; Liu, Y.; Jiang, J.; Cui, Y., Chiral BINOL-Based Covalent Organic Frameworks for Enantioselective Sensing. *J. Am. Chem. Soc.* **2019,** *141* (17), 7081-7089.

[91] Li, J.; Zhang, C.; Yin, M.; Zhang, Z.; Chen, Y.; Deng, Q.; Wang, S., Surfactant-Sensitized Covalent Organic Frameworks-Functionalized Lanthanide-Doped Nanocrystals: An Ultrasensitive Sensing Platform for Perfluorooctane Sulfonate. *ACS Omega* **2019,** *4* (14), 15947-15955.

[92] Wan, S.; Guo, J.; Kim, J.; Ihee, H.; Jiang, D., A Photoconductive Covalent Organic Framework: Self-Condensed Arene Cubes Composed of Eclipsed 2D Polypyrene Sheets for Photocurrent Generation. *Angew. Chem. Int. Ed.* **2009,** *48* (30), 5439-5442.

[93] Ding, X.; Feng, X.; Saeki, A.; Seki, S.; Nagai, A.; Jiang, D., Conducting metallophthalocyanine 2D covalent organic frameworks: the role of central metals in controlling π-electronic functions. *Chem. Commun.* **2012,** *48* (71), 8952-8954.

[94] Dalapati, S.; Addicoat, M.; Jin, S.; Sakurai, T.; Gao, J.; Xu, H.; Irle, S.; Seki, S.; Jiang, D., Rational design of crystalline supermicroporous covalent organic frameworks with triangular topologies. *Nat. Commun.* **2015,** *6*, 7786.

[95] Chen, Y.; Cui, H.; Zhang, J.; Zhao, K.; Ding, D.; Guo, J.; Li, L.; Tian, Z.; Tang, Z., Surface growth of highly oriented covalent organic framework thin film with enhanced photoresponse speed. *RSC Advances* **2015,** *5* (112), 92573-92576.

[96] Nath, B.; Li, W.-H.; Huang, J.-H.; Wang, G.-E.; Fu, Z.-h.; Yao, M.-S.; Xu, G., A new azodioxy-linked porphyrin-based semiconductive covalent organic framework with I2 doping-enhanced photoconductivity. *CrystEngComm* **2016,** *18* (23), 4259-4263.

[97] Yu, F.; Liu, W.; Li, B.; Tian, D.; Zuo, J. L.; Zhang, Q., Photostimulus-Responsive Large-Area Two-Dimensional Covalent Organic Framework Films. *Angew. Chem. Int. Ed.* **2019**.

[98] Nagai, A.; Chen, X.; Feng, X.; Ding, X.; Guo, Z.; Jiang, D., A Squaraine-Linked Mesoporous Covalent Organic Framework. *Angew. Chem. Int. Ed.* **2013,** *52* (13), 3770-3774.

[99] Stegbauer, L.; Schwinghammer, K.; Lotsch, B. V., A hydrazone-based covalent organic framework for photocatalytic hydrogen production. *Chem. Sci.* **2014,** *5* (7), 2789-2793.

[100] Wei, S.; Zhang, F.; Zhang, W.; Qiang, P.; Yu, K.; Fu, X.; Wu, D.; Bi, S.; Zhang, F., Semiconducting 2D Triazine-Cored Covalent Organic Frameworks with Unsubstituted Olefin Linkages. *J. Am. Chem. Soc.* **2019,** *141* (36), 14272-14279.

[101] Wei, P.-F.; Qi, M.-Z.; Wang, Z.-P.; Ding, S.-Y.; Yu, W.; Liu, Q.; Wang, L.-K.; Wang, H.-Z.; An, W.-K.; Wang, W., Benzoxazole-Linked Ultrastable Covalent Organic Frameworks for Photocatalysis. *J. Am. Chem. Soc.* **2018,** *140* (13), 4623-4631.

[102] Liu, S.; Pan, W.; Wu, S.; Bu, X.; Xin, S.; Yu, J.; Xu, H.; Yang, X., Visible-light-induced tandem radical addition–cyclization of 2-aryl phenyl isocyanides catalysed by recyclable covalent organic frameworks. *Green Chem.* **2019,** *21* (11), 2905-2910.

[103] Hao, W.; Chen, D.; Li, Y.; Yang, Z.; Xing, G.; Li, J.; Chen, L., Facile Synthesis of Porphyrin Based Covalent Organic Frameworks via an A2B2 Monomer for Highly Efficient Heterogeneous Catalysis. *Chem. Mater.* **2019,** *31* (19), 8100-8105.

[104] Yan, X.; Liu, H.; Li, Y.; Chen, W.; Zhang, T.; Zhao, Z.; Xing, G.; Chen, L., Ultrastable Covalent Organic Frameworks via Self-Polycondensation of an A2B2 Monomer for Heterogeneous Photocatalysis. *Macromolecules* **2019**.

[105] Lu, G.; Huang, X.; Li, Y.; Zhao, G.; Pang, G.; Wang, G., Covalently integrated core-shell MOF@COF hybrids as efficient visible-light-driven photocatalysts for selective oxidation of alcohols. *J. Energy Chem.* **2020,** *43*, 8-15.

[106] Zhao, Y.; Liu, H.; Wu, C.; Zhang, Z.; Pan, Q.; Hu, F.; Wang, R.; Li, P.; Huang, X.; Li, Z., Fully Conjugated Two-Dimensional sp2-Carbon Covalent Organic Frameworks as Artificial Photosystem I with High Efficiency. *Angew. Chem. Int. Ed.* **2019,** *58* (16), 5376-5381.

[107] Ma, H.-C.; Zhao, C.-C.; Chen, G.-J.; Dong, Y.-B., Photothermal conversion triggered thermal asymmetric catalysis within metal nanoparticles loaded homochiral covalent organic framework. *Nat. Commun.* **2019,** *10* (1), 3368.

[108] Chen, W.; Yang, Z.; Xie, Z.; Li, Y.; Yu, X.; Lu, F.; Chen, L., Benzothiadiazole functionalized D–A type covalent organic frameworks for effective photocatalytic reduction of aqueous chromium(vi). *J. Mater. Chem. A* **2019,** *7* (3), 998-1004.

[109] Mi, Z.; Yang, P.; Wang, R.; Unruangsri, J.; Yang, W.; Wang, C.; Guo, J., Stable Radical Cation-Containing Covalent Organic Frameworks Exhibiting Remarkable Structure-Enhanced Photothermal Conversion. *J. Am. Chem. Soc.* **2019**.

[110] Hynek, J.; Zelenka, J.; Rathouský, J.; Kubát, P.; Ruml, T.; Demel, J.; Lang, K., Designing Porphyrinic Covalent Organic Frameworks for the Photodynamic Inactivation of Bacteria. *ACS Appl. Mater. Interfaces* **2018,** *10* (10), 8527-8535.

[111] Hu, C.; Cai, L.; Liu, S.; Pang, M., Integration of a highly monodisperse covalent organic framework photosensitizer with cation exchange synthesized Ag2Se nanoparticles for enhanced phototherapy. *Chem. Commun.* **2019,** *55* (62), 9164-9167.

[112] Dicker, G.; de Haas, M. P.; Siebbeles, L. D. A.; Warman, J. M., Electrodeless time-resolved microwave conductivity study of charge-carrier photogeneration in regioregular poly(3-hexylthiophene) thin films. *Phys. Rev. B* **2004,** *70* (4), 045203.

[113] Boland, J. L.; Casadei, A.; Tütüncüoglu, G.; Matteini, F.; Davies, C. L.; Jabeen, F.; Joyce, H. J.; Herz, L. M.; Fontcuberta i Morral, A.; Johnston, M. B., Increased Photoconductivity Lifetime in GaAs Nanowires by Controlled n-Type and p-Type Doping. *ACS Nano* **2016,** *10* (4), 4219-4227.

[114] Feng, X.; Liu, L.; Honsho, Y.; Saeki, A.; Seki, S.; Irle, S.; Dong, Y.; Nagai, A.; Jiang, D., High-Rate Charge-Carrier Transport in Porphyrin Covalent Organic Frameworks: Switching from Hole to Electron to Ambipolar Conduction. *Angew. Chem. Int. Ed.* **2012,** *51* (11), 2618-2622.

[115] Jin, S.; Sakurai, T.; Kowalczyk, T.; Dalapati, S.; Xu, F.; Wei, H.; Chen, X.; Gao, J.; Seki, S.; Irle, S.; Jiang, D., Two-Dimensional Tetrathiafulvalene Covalent Organic Frameworks: Towards Latticed Conductive Organic Salts. *Chem. - Eur. J.* **2014,** *20* (45), 14608-14613.

[116] Ding, H.; Li, Y.; Hu, H.; Sun, Y.; Wang, J.; Wang, C.; Wang, C.; Zhang, G.; Wang, B.; Xu, W.; Zhang, D., A Tetrathiafulvalene-Based Electroactive Covalent Organic Framework. *Chem. - Eur. J.* **2014,** *20* (45), 14614-14618.

[117] Cai, S.-L.; Zhang, Y.-B.; Pun, A. B.; He, B.; Yang, J.; Toma, F. M.; Sharp, I. D.; Yaghi, O. M.; Fan, J.; Zheng, S.-R.; Zhang, W.-G.; Liu, Y., Tunable electrical conductivity in oriented thin films of tetrathiafulvalene-based covalent organic framework. *Chem. Sci.* **2014,** *5* (12), 4693-4700.

[118] Martínez-Abadía, M.; Stoppiello, C. T.; Strutynski, K.; Lerma-Berlanga, B.; Martí-Gastaldo, C.; Saeki, A.; Melle-Franco, M.; Khlobystov, A. N.; Mateo-Alonso, A., A Wavy Two-Dimensional Covalent Organic Framework from Core-Twisted Polycyclic Aromatic Hydrocarbons. *J. Am. Chem. Soc.* **2019,** *141* (36), 14403-14410.

[119] Medina, D. D.; Petrus, M. L.; Jumabekov, A. N.; Margraf, J. T.; Weinberger, S.; Rotter, J. M.; Clark, T.; Bein, T., Directional Charge-Carrier Transport in Oriented Benzodithiophene Covalent Organic Framework Thin Films. *ACS Nano* **2017,** *11* (3), 2706-2713.

[120] Rager, S.; Jakowetz, A. C.; Gole, B.; Beuerle, F.; Medina, D. D.; Bein, T., Scaffold-Induced Diketopyrrolopyrrole Molecular Stacks in a Covalent Organic Framework. *Chem. Mater.* **2019,** *31* (8), 2707-2712.

[121] Wu, C.; Liu, Y.; Liu, H.; Duan, C.; Pan, Q.; Zhu, J.; Hu, F.; Ma, X.; Jiu, T.; Li, Z.; Zhao, Y., Highly Conjugated Three-Dimensional Covalent Organic Frameworks Based on Spirobifluorene for Perovskite Solar Cell Enhancement. *J. Am. Chem. Soc.* **2018,** *140* (31), 10016-10024.

[122] Li, H.; Chang, J.; Li, S.; Guan, X.; Li, D.; Li, C.; Tang, L.; Xue, M.; Yan, Y.; Valtchev, V.; Qiu, S.; Fang, Q., Three-Dimensional Tetrathiafulvalene-Based Covalent Organic Frameworks for Tunable Electrical Conductivity. *J. Am. Chem. Soc.* **2019,** *141* (34), 13324-13329.

[123] Kim, S.; Choi, H. C., Light-promoted synthesis of highly-conjugated crystalline covalent organic framework. *Commun. Chem.* **2019,** *2* (1), 60.

[124] Meng, Z.; Stolz, R. M.; Mirica, K. A., Two-Dimensional Chemiresistive Covalent Organic Framework with High Intrinsic Conductivity. *J. Am. Chem. Soc.* **2019**.

[125] Wang, M.; Ballabio, M.; Wang, M.; Lin, H.-H.; Biswal, B. P.; Han, X.; Paasch, S.; Brunner, E.; Liu, P.; Chen, M.; Bonn, M.; Heine, T.; Zhou, S.; Canovas, E.; Dong, R.; Feng, X., Unveiling

Electronic Properties in Metal-Phthalocyanine-based Pyrazine-linked Conjugated Two-Dimensional Covalent Organic Frameworks. *J. Am. Chem. Soc.* **2019**.

[126] Zhang, Q.; Dai, M.; Shao, H.; Tian, Z.; Lin, Y.; Chen, L.; Zeng, X. C., Insights into High Conductivity of the Two-Dimensional Iodine-Oxidized sp2-c-COF. *ACS Appl. Mater. Interfaces* **2018,** *10* (50), 43595-43602.

[127] Thomas, S.; Li, H.; Dasari, R. R.; Evans, A. M.; Castano, I.; Allen, T. G.; Reid, O. G.; Rumbles, G.; Dichtel, W. R.; Gianneschi, N. C.; Marder, S. R.; Coropceanu, V.; Brédas, J.-L., Design and synthesis of two-dimensional covalent organic frameworks with four-arm cores: prediction of remarkable ambipolar charge-transport properties. *Mater. Horiz.* **2019**.

[128] DeBlase, C. R.; Hernández-Burgos, K.; Rotter, J. M.; Fortman, D. J.; dos S. Abreu, D.; Timm, R. A.; Diógenes, I. C. N.; Kubota, L. T.; Abruña, H. D.; Dichtel, W. R., Cation-Dependent Stabilization of Electrogenerated Naphthalene Diimide Dianions in Porous Polymer Thin Films and Their Application to Electrical Energy Storage. *Angew. Chem. Int. Ed.* **2015,** *54* (45), 13225-13229.

[129] DeBlase, C. R.; Silberstein, K. E.; Truong, T.-T.; Abruña, H. D.; Dichtel, W. R., β-Ketoenamine-Linked Covalent Organic Frameworks Capable of Pseudocapacitive Energy Storage. *J. Am. Chem. Soc.* **2013,** *135* (45), 16821-16824.

[130] Mulzer, C. R.; Shen, L.; Bisbey, R. P.; McKone, J. R.; Zhang, N.; Abruña, H. D.; Dichtel, W. R., Superior Charge Storage and Power Density of a Conducting Polymer-Modified Covalent Organic Framework. *ACS Cent. Sci.* **2016**.

[131] Wu, Y.; Yan, D.; Zhang, Z.; Matsushita, M. M.; Awaga, K., Electron Highways into Nanochannels of Covalent Organic Frameworks for High Electrical Conductivity and Energy Storage. *ACS Appl. Mater. Interfaces* **2019,** *11* (8), 7661-7665.

[132] Khayum M, A.; Vijayakumar, V.; Karak, S.; Kandambeth, S.; Bhadra, M.; Suresh, K.; Acharambath, N.; Kurungot, S.; Banerjee, R., Convergent Covalent Organic Framework Thin Sheets as Flexible Supercapacitor Electrodes. *ACS Appl. Mater. Interfaces* **2018,** *10* (33), 28139-28146.

[133] Halder, A.; Ghosh, M.; Khayum M, A.; Bera, S.; Addicoat, M.; Sasmal, H. S.; Karak, S.; Kurungot, S.; Banerjee, R., Interlayer Hydrogen-Bonded Covalent Organic Frameworks as High-Performance Supercapacitors. *J. Am. Chem. Soc.* **2018,** *140* (35), 10941-10945.

[134] Mohammed, A. K.; Vijayakumar, V.; Halder, A.; Ghosh, M.; Addicoat, M.; Bansode, U.; Kurungot, S.; Banerjee, R., Weak Intermolecular Interactions in Covalent Organic Framework-Carbon Nanofiber Based Crystalline yet Flexible Devices. *ACS Appl. Mater. Interfaces* **2019,** *11* (34), 30828-30837.

[135] Xu, F.; Xu, H.; Chen, X.; Wu, D.; Wu, Y.; Liu, H.; Gu, C.; Fu, R.; Jiang, D., Radical Covalent Organic Frameworks: A General Strategy to Immobilize Open-Accessible Polyradicals for High-Performance Capacitive Energy Storage. *Angew. Chem. Int. Ed.* **2015,** *54* (23), 6814-6818.

[136] El-Mahdy, A. F. M.; Young, C.; Kim, J.; You, J.; Yamauchi, Y.; Kuo, S.-W., Hollow Microspherical and Microtubular [3 + 3] Carbazole-Based Covalent Organic Frameworks and Their Gas and Energy Storage Applications. *ACS Appl. Mater. Interfaces* **2019,** *11* (9), 9343-9354.

[137] Haldar, S.; Kushwaha, R.; Maity, R.; Vaidhyanathan, R., Pyridine-Rich Covalent Organic Frameworks as High-Performance Solid-State Supercapacitors. *ACS Mater. Lett.* **2019,** *1* (4), 490-497.

[138] Xu, F.; Jin, S.; Zhong, H.; Wu, D.; Yang, X.; Chen, X.; Wei, H.; Fu, R.; Jiang, D., Electrochemically active, crystalline, mesoporous covalent organic frameworks on carbon nanotubes for synergistic lithium-ion battery energy storage. *Scientific Reports* **2015,** *5*, 8225.

[139] Vazquez-Molina, D. A.; Mohammad-Pour, G. S.; Lee, C.; Logan, M. W.; Duan, X.; Harper, J. K.; Uribe-Romo, F. J., Mechanically Shaped Two-Dimensional Covalent Organic Frameworks Reveal Crystallographic Alignment and Fast Li-Ion Conductivity. *J. Am. Chem. Soc.* **2016,** *138* (31), 9767-9770.

[140] Zhang, Y.; Duan, J.; Ma, D.; Li, P.; Li, S.; Li, H.; Zhou, J.; Ma, X.; Feng, X.; Wang, B., Three-Dimensional Anionic Cyclodextrin-Based Covalent Organic Frameworks. *Angew. Chem. Int. Ed.* **2017,** *56* (51), 16313-16317.

[141] Yoo, J.; Cho, S.-J.; Jung, G. Y.; Kim, S. H.; Choi, K.-H.; Kim, J.-H.; Lee, C. K.; Kwak, S. K.; Lee, S.-Y., COF-Net on CNT-Net as a Molecularly Designed, Hierarchical Porous Chemical Trap for Polysulfides in Lithium–Sulfur Batteries. *Nano Lett.* **2016,** *16* (5), 3292-3300.

[142] Ghazi, Z. A.; Zhu, L.; Wang, H.; Naeem, A.; Khattak, A. M.; Liang, B.; Khan, N. A.; Wei, Z.; Li, L.; Tang, Z., Efficient Polysulfide Chemisorption in Covalent Organic Frameworks for High-Performance Lithium-Sulfur Batteries. *Adv. Energy Mater.* **2016,** *6* (24).

[143] Meng, Y.; Lin, G.; Ding, H.; Liao, H.; Wang, C., Impregnation of sulfur into a 2D pyrene-based covalent organic framework for high-rate lithium–sulfur batteries. *J. Mater. Chem. A* **2018,** *6* (35), 17186-17191.

[144] Wang, D.-G.; Li, N.; Hu, Y.; Wan, S.; Song, M.; Yu, G.; Jin, Y.; Wei, W.; Han, K.; Kuang, G.-C.; Zhang, W., Highly Fluoro-Substituted Covalent Organic Framework and Its Application in Lithium–Sulfur Batteries. *ACS Appl. Mater. Interfaces* **2018,** *10* (49), 42233-42240.

[145] Jiang, Q.; Li, Y.; Zhao, X.; Xiong, P.; Yu, X.; Xu, Y.; Chen, L., Inverse-vulcanization of vinyl functionalized covalent organic frameworks as efficient cathode materials for Li–S batteries. *J. Mater. Chem. A* **2018,** *6* (37), 17977-17981.

[146] Wang, Z.; Li, Y.; Liu, P.; Qi, Q.; Zhang, F.; Lu, G.; Zhao, X.; Huang, X., Few layer covalent organic frameworks with graphene sheets as cathode materials for lithium-ion batteries. *Nanoscale* **2019,** *11* (12), 5330-5335.

[147] Wang, S.; Wang, Q.; Shao, P.; Han, Y.; Gao, X.; Ma, L.; Yuan, S.; Ma, X.; Zhou, J.; Feng, X.; Wang, B., Exfoliation of Covalent Organic Frameworks into Few-Layer Redox-Active Nanosheets as Cathode Materials for Lithium-Ion Batteries. *J. Am. Chem. Soc.* **2017**.

[148] Chen, X.; Li, Y.; Wang, L.; Xu, Y.; Nie, A.; Li, Q.; Wu, F.; Sun, W.; Zhang, X.; Vajtai, R.; Ajayan, P. M.; Chen, L.; Wang, Y., High-Lithium-Affinity Chemically Exfoliated 2D Covalent Organic Frameworks. *Adv. Mater.* **2019,** *31* (29).

[149] Kim, M.-S.; Lee, W.-J.; Paek, S.-M.; Park, J. K., Covalent Organic Nanosheets as Effective Sodium-Ion Storage Materials. *ACS Appl. Mater. Interfaces* **2018,** *10* (38), 32102-32111.

[150] Patra, B. C.; Das, S. K.; Ghosh, A.; Raj K, A.; Moitra, P.; Addicoat, M.; Mitra, S.; Bhaumik, A.; Bhattacharya, S.; Pradhan, A., Covalent organic framework based microspheres as an anode material for rechargeable sodium batteries. *J. Mater. Chem. A* **2018,** *6* (34), 16655-16663.

[151] Chen, X.; Zhang, H.; Ci, C.; Sun, W.; Wang, Y., Few-Layered Boronic Ester Based Covalent Organic Frameworks/Carbon Nanotube Composites for High-Performance K-Organic Batteries. *ACS Nano* **2019,** *13* (3), 3600-3607.

[152] Jin, S.; Ding, X.; Feng, X.; Supur, M.; Furukawa, K.; Takahashi, S.; Addicoat, M.; El-Khouly, M. E.; Nakamura, T.; Irle, S.; Fukuzumi, S.; Nagai, A.; Jiang, D., Charge Dynamics in A Donor–Acceptor Covalent Organic Framework with Periodically Ordered Bicontinuous Heterojunctions. *Angew. Chem. Int. Ed.* **2013,** *52* (7), 2017-2021.

[153] Jin, S.; Furukawa, K.; Addicoat, M.; Chen, L.; Takahashi, S.; Irle, S.; Nakamura, T.; Jiang, D., Large pore donor-acceptor covalent organic frameworks. *Chem. Sci.* **2013,** *4* (12), 4505-4511.

[154] Spitler, E. L.; Colson, J. W.; Uribe-Romo, F. J.; Woll, A. R.; Giovino, M. R.; Saldivar, A.; Dichtel, W. R., Lattice Expansion of Highly Oriented 2D Phthalocyanine Covalent Organic Framework Films. *Angew. Chem. Int. Ed.* **2012,** *51* (11), 2623-2627.

[155] Medina, D. D.; Werner, V.; Auras, F.; Tautz, R.; Dogru, M.; Schuster, J.; Linke, S.; Döblinger, M.; Feldmann, J.; Knochel, P.; Bein, T., Oriented Thin Films of a Benzodithiophene Covalent Organic Framework. *ACS Nano* **2014,** *8* (4), 4042-4052.

[156] Pachfule, P.; Acharjya, A.; Roeser, J.; Langenhahn, T.; Schwarze, M.; Schomaecker, R.; Thomas, A.; Schmidt, J., Diacetylene Functionalized Covalent Organic Framework (COF) for Photocatalytic Hydrogen Generation. *J. Am. Chem. Soc.* **2017**.

[157] Ma, H.; Wei, M.; Jin, F.; Chen, T.; Ma, Y., Two-Dimensional COF with Rather Low Exciton Binding Energies Comparable to 3D Inorganic Semiconductors in the Visible Range for Water Splitting. *J. Phys. Chem. C* **2019,** *123* (40), 24626-24633.

[158] Sprick, R. S.; Bonillo, B.; Clowes, R.; Guiglion, P.; Brownbill, N. J.; Slater, B. J.; Blanc, F.; Zwijnenburg, M. A.; Adams, D. J.; Cooper, A. I., Visible-Light-Driven Hydrogen Evolution Using Planarized Conjugated Polymer Photocatalysts. *Angew. Chem. Int. Ed.* **2016,** *55* (5), 1792-1796.

[159] Wang, X.; Chen, L.; Chong, S. Y.; Little, M. A.; Wu, Y.; Zhu, W.-H.; Clowes, R.; Yan, Y.; Zwijnenburg, M. A.; Sprick, R. S.; Cooper, A. I., Sulfone-containing covalent organic frameworks for photocatalytic hydrogen evolution from water. *Nat. Chem.* **2018,** *10* (12), 1180-1189.

[160] Cheng, Y.-J.; Wang, R.; Wang, S.; Xi, X.-J.; Ma, L.-F.; Zang, S.-Q., Encapsulating [Mo3S13]2− clusters in cationic covalent organic frameworks: enhancing stability and recyclability by converting a homogeneous photocatalyst to a heterogeneous photocatalyst. *Chem. Commun.* **2018,** *54* (96), 13563-13566.

[161] Ding, S.-Y.; Wang, P.-L.; Yin, G.-L.; Zhang, X.; Lu, G., Energy transfer in covalent organic frameworks for visible-light-induced hydrogen evolution. *Int. J. Hydrogen Energy* **2019,** *44* (23), 11872-11876.

[162] Dong, H.; Meng, X.-B.; Zhang, X.; Tang, H.-L.; Liu, J.-W.; Wang, J.-H.; Wei, J.-Z.; Zhang, F.-M.; Bai, L.-L.; Sun, X.-J., Boosting visible-light hydrogen evolution of covalent-organic frameworks by introducing Ni-based noble metal-free co-catalyst. *Chem. Eng. J.* **2020,** *379*, 122342.

[163] Wang, X.; Blechert, S.; Antonietti, M., Polymeric Graphitic Carbon Nitride for Heterogeneous Photocatalysis. *ACS Catal.* **2012,** *2* (8), 1596-1606.

[164] Chen, Y.; Lin, B.; Yu, W.; Yang, Y.; Bashir, S. M.; Wang, H.; Takanabe, K.; Idriss, H.; Basset, J.-M., Surface Functionalization of g-C3N4: Molecular-Level Design of Noble-Metal-Free Hydrogen Evolution Photocatalysts. *Chem. - Eur. J.* **2015,** *21* (29), 10290-10295.

[165] Cao, S.; Low, J.; Yu, J.; Jaroniec, M., Polymeric Photocatalysts Based on Graphitic Carbon Nitride. *Adv. Mater.* **2015,** *27* (13), 2150-2176.

[166] Luo, M.; Yang, Q.; Liu, K.; Cao, H.; Yan, H., Boosting photocatalytic H2 evolution on g-C3N4 by modifying covalent organic frameworks (COFs). *Chem. Commun.* **2019,** *55* (41), 5829-5832.

[167] Chen, J.; Tao, X.; Li, C.; Ma, Y.; Tao, L.; Zheng, D.; Zhu, J.; Li, H.; Li, R.; Yang, Q., Synthesis of bipyridine-based covalent organic frameworks for visible-light-driven photocatalytic water oxidation. *Appl. Catal., B* **2019**, 118271.

[168] Rotter, J. M.; Weinberger, S.; Kampmann, J.; Sick, T.; Shalom, M.; Bein, T.; Medina, D. D., Covalent Organic Framework Films through Electrophoretic Deposition - Creating Efficient Morphologies for Catalysis. *Chem. Mater.* **2019**.

[169] Fu, Y.; Zhu, X.; Huang, L.; Zhang, X.; Zhang, F.; Zhu, W., Azine-based covalent organic frameworks as metal-free visible light photocatalysts for CO2 reduction with H2O. *Appl. Catal., B* **2018,** *239*, 46-51.

[170] Yang, S.; Hu, W.; Zhang, X.; He, P.; Pattengale, B.; Liu, C.; Cendejas, M.; Hermans, I.; Zhang, X.; Zhang, J.; Huang, J., 2D Covalent Organic Frameworks as Intrinsic Photocatalysts for Visible Light-Driven CO2 Reduction. *J. Am. Chem. Soc.* **2018**.

[171] Li, S.-Y.; Meng, S.; Zou, X.; El-Roz, M.; Telegeev, I.; Thili, O.; Liu, T. X.; Zhu, G., Rhenium-functionalized covalent organic framework photocatalyst for efficient CO2 reduction under visible light. *Microporous Mesoporous Mater.* **2019,** *285*, 195-201.

[172] Zhong, W.; Sa, R.; Li, L.; He, Y.; Li, L.; Bi, J.; Zhuang, Z.; Yu, Y.; Zou, Z., A Covalent Organic Framework Bearing Single Ni Sites as a Synergistic Photocatalyst for Selective Photoreduction of CO2 to CO. *J. Am. Chem. Soc.* **2019,** *141* (18), 7615-7621.

[173] Lu, M.; Li, Q.; Liu, J.; Zhang, F.-M.; Zhang, L.; Wang, J.-L.; Kang, Z.-H.; Lan, Y.-Q., Installing earth-abundant metal active centers to covalent organic frameworks for efficient heterogeneous photocatalytic CO2 reduction. *Appl. Catal., B* **2019,** *254*, 624-633.

[174] Liu, W.; li, x.; Wang, C.; Pan, H.; Liu, W.; Wang, K.; Zeng, Q.; Wang, R.; Jiang, J., A Scalable General Synthetic Approach towards Ultrathin Imine-linked Two-dimensional Covalent Organic Framework Nanosheets for Photocatalytic CO2 Reduction. *J. Am. Chem. Soc.* **2019**.

[175] Das, G.; Biswal, B. P.; Kandambeth, S.; Venkatesh, V.; Kaur, G.; Addicoat, M.; Heine, T.; Verma, S.; Banerjee, R., Chemical sensing in two dimensional porous covalent organic nanosheets. *Chem. Sci.* **2015,** *6* (7), 3931-3939.

[176] Kim, S.; Lim, H.; Lee, J.; Choi, H. C., Synthesis of a Scalable Two-Dimensional Covalent Organic Framework by the Photon-Assisted Imine Condensation Reaction on the Water Surface. *Langmuir* **2018,** *34* (30), 8731-8738.

[177] Yifeng, X.; Liao, Q.-b.; Huang, Z.-p.; Huang, X.; Ke, C.; Zhu, H.-t.; Dong, C.-y.; Wang, H.-s.; Xi, K.; Zhan, P.; Xu, F.; Lu, Y.-q., Ultrahigh Responsivity Photodetectors of Two-dimensional Covalent Organic Frameworks Integrated on Graphene. *arXiv:1910.00088* **2019**.

[178] Ascherl, L.; Evans, E. W.; Gorman, J.; Orsborne, S.; Bessinger, D.; Bein, T.; Friend, R. H.; Auras, F., Perylene-Based Covalent Organic Frameworks for Acid Vapor Sensing. *J. Am. Chem. Soc.* **2019,** *141* (39), 15693-15699.

[179] Yin, H.-Q.; Yin, F.; Yin, X.-B., Strong Dual Emission in Covalent Organic Frameworks Induced by ESIPT. *Chem. Sci.* **2019**.

[180] Wang, J.; Yan, B., Improving Covalent Organic Frameworks Fluorescence by Triethylamine Pinpoint Surgery as Selective Biomarker Sensor for Diabetes Mellitus Diagnosis. *Anal. Chem.* **2019,** *91* (20), 13183-13190.

2 Characterization Methods

2.1 X-ray Diffraction (XRD)

X-ray diffraction (XRD) is an excellent technique to characterize the phase composition and to provide information on the crystallinity and structure of powders, films and single crystals of numerous types of compounds. The method is also extemely important for gathering structural information on covalent organic framework materials. The principle behind this technique is based on the scattering events of X-rays, which occur when interacting with crystallite lattice planes having a similar spacing as the X-ray wavelength. The scattered X-rays interfere, dependent on the lattice spacing and the scattering angle. The incident beam has to impinge under a certain angle, the so-called Bragg angle, on the sample to cause constructive interference. In a powder many crystals comply with this requirement due to the random order of crystallites. The occurring constructive interference of reflected X-rays can be observed as a peak in the one-dimensional diffraction pattern. The measured intensities of the so-called reflections are mainly dependent on the lattice atoms but can vary due to textural effects or disturbance by destructive interference of other lattice planes. The condition for constructive interference is given by Bragg's law:

$$n\,\lambda = 2d\,sin\theta \qquad (1)$$

where n is an integer, λ the X-ray wavelength, d the spacing between the lattice planes and θ the angle between the incident X-rays and the lattice planes.

The size of the crystallite domains has also an important effect on the diffraction data. For small domains the diffraction patterns show a broadening of the reflections compared to larger domains. Based on the peak broadening, which can be measured with the full width at half maximum (FWHM), the size of the crystallite domains can be determined. The correlation of the peak broadening and the size of the domains D is given in the Scherrer equation:

$$D = \frac{k\lambda}{\beta\,\cos\theta} \qquad (2)$$

where k is the form-dependent factor and β is the full width at half maximum of the reflection.

This method was used to determine the crystallinity of the samples and their crystal structure. The XRD measurements were performed with a Bruker D8 Discover with Ni-filtered Cu-Kα-radiation and a position-sensitive semiconductor detector (LynxEye).

2.2 Grazing-Incidence Wide-Angle X-ray Scattering (GIWAXS)

Based on X-ray scattering, a highly sensitive surface characterization technique can be obtained by illuminating a planar sample at grazing angle of incidence (grazing-incidence diffraction). This approach was first used in 1989 to investigate the structure of gold nanoparticles on silicon.[1] The grazing-incidence wide-angle X-ray scattering (GIWAXS) is an ideal method to characterize thin films or surfaces which would otherwise not be accessible to general X-ray scattering geometries resulting in poor information content due to the low sample thicknesses.

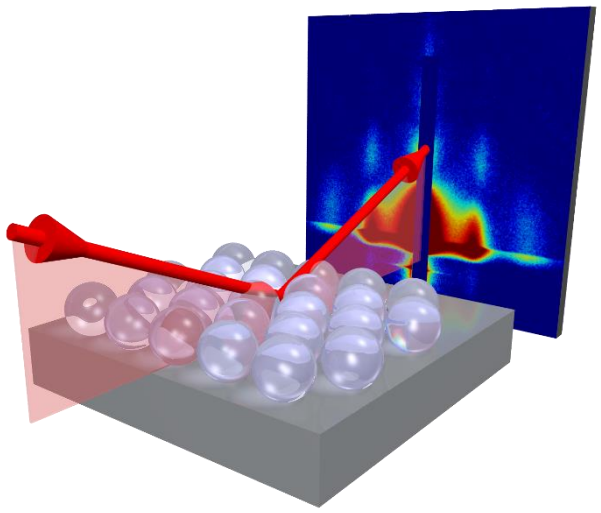

Figure 2.1: Simplified sketch of the GIWAXS method and the ability to study ultrathin films and surfaces.[2]

The importance for this measurement is that the angle of the incident beam is below the critical angle of the substrate. In this case, three factors lead to an enhancement of the intensity and thus the suitability of this measurement for ultrathin films or surfaces. The geometry of the grazing incidence angle leads to a larger irradiation area on the surface increasing the probe volume and additionally allows for more averaged data. Also, the small angle leads to a higher reflectivity coefficient that channels most of the scattered beams in direction of the detector. Moreover, by waveguiding features near to the critical angle the scattering events increase due to the reflection of the beam and thus expansion throughout the film.

The detected reflection peaks are given as the wavelength-independent scattering vector q which is related to 2θ angles by the following equation:

$$q = \frac{4\pi}{\lambda} \sin \frac{2\theta}{2} \qquad (3)$$

These features make GIWAXS a suitable instrument to study the structure and orientation of self-organized layers such as covalent organic frameworks on any flat substrate. The intensity enhancement leads to representative results on crystallinity and orientation for COF thin films which cannot be obtained by X-ray diffraction in normal reflection mode.

Two-dimensional grazing-incidence wide angle X-ray scattering (2D GIWAXS) data were collected using an Anton-Paar SAXSpace system equipped with a Cu Kα microfocus source operated at 50 kV and 1 mA and an Eiger Dectris R 1M 2D detector.

2.3 Gas Sorption

Gas sorption measurements represent a very convenient analytical technique to determine characteristic features of porous materials such as surface area, pore size, and pore volume. The method is based on physisorption, which implies that the inert gas molecules (adsorptive) are taken up by the sample surface (adsorbent) via physical, non-chemical interactions such as van der Waals forces. The adsorbed molecules, the adsorbate, is in a dynamic equilibrium with the adsorptive, which is the adsorbable gas, due to the reversible interactions between adsorptive and adsorbent. For porous materials, the adsorptive can cover two different surfaces of the sample. On the one hand, there is the external surface which is the surface outside of the pores and on the other hand, there is the internal surface which is the term for the surface of the pore walls inside the pores. The ratio of total pore volume to the particle volume or mass is defined as the porosity of the sample.[3]

Since the accessibility of the pore is amongst other factors dependent on the pore size, it is important to be able to distinguish and classify pores of different sizes. Hence, the recommendations developed in 1985 by IUPAC[4] are still useful and applied in the field of nanoporous materials:

(1) macropores (pores > 50 nm)

(2) mesopores (pores between 2 – 50 nm

(3) micropores (pores < 2 nm)

Plotting the relative pressure of adsorptive against the amount of adsorbed gas at standard pressure and constant temperature leads to typical isotherms that are classified according to IUPAC seen in Figure 2.2.

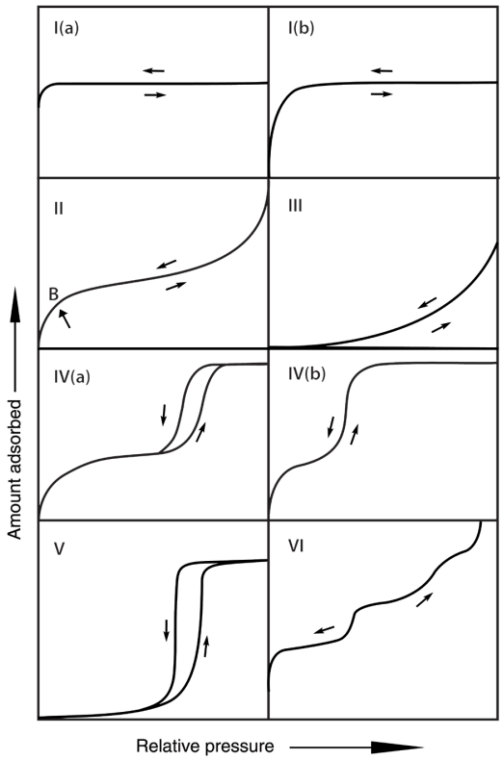

Figure 2.2: IUPAC classification of physisorption isotherms.[3]

Type I isotherms represent a reversible isotherm typical for microporous materials. The steep onset at low p/p^0 is due to the micropore filling which converges to a maximum that is defined by the accessible micropore volume. Type I isotherms can further be distinguished in I(a) for materials with narrow micropores (< ~ 1 nm) and in I(b) for materials with a range of wider micropores and narrow mesopores (< ~ 2.5 nm).

Type II isotherms show the reversible isotherm for nonporous or macroporous adsorbents. The first uptake displays monolayer adsorption which is then followed by unrestricted multilayer adsorption. The curvature in point B describes the transition between monolayer coverage and multilayer adsorption.

Type III isotherms are typical for nonporous or microporous materials that show weak interactions with the adsorbate. Hence, there is no point B which indicates the transition from monolayer to multilayer adsorption.

Type IV isotherms represent isotherms for mesoporous compounds. After the monolayer coverage and the multilayer adsorption, capillary condensation occurs leading then to a saturation of the amount adsorbed by pore filling. Type IV(a) isotherms are given for mesopores larger than ~ 4 nm, where the capillary condensation leads to hysteresis. The Type IV(b) isotherm shows no hysteresis but is fully reversible. This is typical for mesopores under the critical width of around 4 nm and for conical and cylindrical mesopores that are closed on one side.

Type V isotherms of mesoporous materials resemble the Type (III) isotherm due to weak adsorbate-adsorbent interactions. Here the pore filling is accompanied by hysteresis.

Type VI isotherm is reversible and typical for nonporous materials with a highly uniform surface. Each step in the uptake corresponds to an adsorbed monolayer on the adsorbent.

The Brunauer-Emmett-Teller model (BET) is the most common tool used for interpreting sorption isotherms in terms of surface area. BET is based on the Langmuir theory that is only considering monolayer adsorption but upgrades the model to multilayer adsorption by applying two assumptions:

(1) The adsorption enthalpy of the first monolayer differs from the adsorption enthalpy of the following layers whereby the layers above have the same adsorption enthalpy.

(2) Interactions do not occur between any adsorption layers.

Usually the BET equation is applied in the linear form:

$$\frac{p}{n \times (p^0 - p)} = \frac{1}{n_m \times C} + \frac{(C-1)}{n_m \times C}(p/p^0) \qquad (4)$$

where n is the amount adsorbed at p/p^0, p is the equilibrium pressure, p^0 the saturation pressure, n_m the monolayer capacity and C the BET constant.

A true value of n_m is only possible for the linear part of the equation which is typically restricted to relative pressures in the range of ~ 0.05 – 0.30. The total surface area a_s can now be determined by the following equation:

$$a_s(BET) = n_m \times N_A \times \sigma_m / m \qquad (5)$$

where N_A is the Avogadro constant, σ_m is the molecular cross-sectional area and m is the mass of the adsorbent.[3-4]

2.4 Electron Microscopy (EM)

Electron Microscopy is a highly accurate method to characterize the topography and the composition of a sample at the nanoscale. Due to the use of electrons with a de-Broglie-wavelength in the span of a few picometers the resolution is far better than the 200 nm spatial resolution of conventional light microscopy caused by the Abbe limit.[5] With the size of atoms in the same range as the wavelength, an electron microscope can easily image the well-defined pores and crystalline domains of covalent organic frameworks (provided beam damage can be controlled). The electron beam generation can occur by a heated tungsten filament and an applied extraction potential so the electrons can overcome the work function. Another possibility is the usage of the so-called cold or hot field electron emission, where very high potentials extract the electrons from a (heated) tungsten tip. This usually achieves higher resolution due to a smaller beam diameter, a more coherent beam and a higher brightness. Below the electron gun, the beam is then demagnified onto the sample by an array of electromagnetic lenses to achieve a highly focused beam with a spot size in the range of micrometers to Ångströms, depending on the operation mode of the microscope. The whole device is under high vacuum to maximize the mean free path of the electrons. Depending on the microscopy and operation mode different detector systems are needed. There are three main techniques for electron microscopy.

2.4.1 Scanning Electron Microscopy (SEM)

The scanning electron microscopy (SEM) uses a convergent electron beam at low acceleration voltages (typically 1 – 30 kV) which is able to scan the sample surface in a grid pattern to investigate the surface properties of the sample. The image arises by combining the beam's position with the detected signal. The detected signals consist of backscattered (BSE) and secondary electrons (SE), characteristic X-rays and cathodoluminescence whereby the method using the secondary electrons is the most common one. As the name already indicates BSE are primary electrons that scatter from the sample and SE are electrons with fewer energy as BSE ejected from the sample by the inelastic scattering of the primary beam. Therefore the Everhart-

Thornly-Detector is most suitable to achieve high-contrast images by applying a bias to attract low-energy electrons such as SE.

2.4.2 Transmission Electron Microscopy (TEM)

The information about the internal structure is obtained by the transmission electron microscopy (TEM) with resolutions in the sub-Ångstrom region. Together with the possibility to obtain data from the samples in reciprocal space by electron diffraction, this technique is very useful and applicable for various needs (see Figure 2.3 for detail).

Since the samples in TEM are studied at high voltages between 60 kV and 400 kV, potential degradation and decomposition of the sample during the measurement is an important factor which limits the spatial resolution and the ease of imaging, depending on the type of sample.

If the above techniques are combined, the resulting method is called scanning transmission electron microscopy (STEM) where a convergent electron beam scans the sample in a grid-like pattern. An annulus-shaped detector records the transmitted and scattered electrons at high angles, the so-called high-angle annular dark-field detector (HAADF detector). The advantage of HAADF STEM operation mode is that the image contrast is mainly formed by mass contrast (Z-contrast).[6]

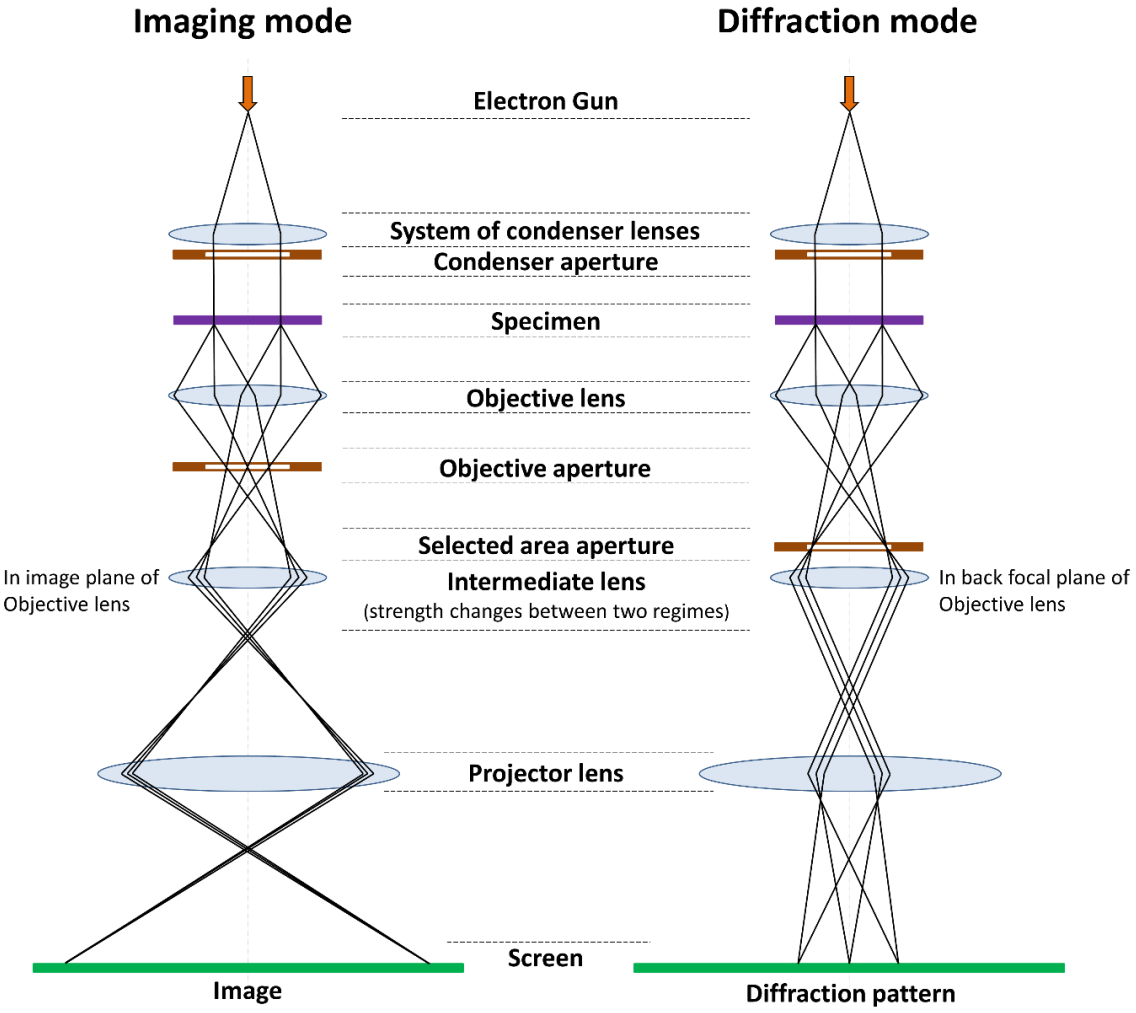

Figure 2.3: Schematic view of imaging and diffraction modes in TEM.[7]

For the measurements performed in this work JEOL JSM-6500F with a FEG and a secondary electron detector at an acceleration voltage of 5 kV and Thermo Fischer FEI Helios G3 UC Dual Beam Microscope with an acceleration voltage of 1 – 30 kV were used. High Resolution Transmission Electron Microscopy (HRTEM) and Scanning Transmission Electron Microscopy in High Angle Annular Dark Field mode (STEM-HAADF) were performed using an FEI Titan Themis 60-300 equipped with a field emission gun operated at 300 kV.

2.5 Infrared Spectroscopy (IR)

Molecular vibrations and rotations are excited by electromagnetic radiation in the infrared with a typical range between 4000 cm^{-1} and 400 cm^{-1}. These molecular vibrations and rotations can

be studied directly as absorption in the IR spectrum or indirectly as scattered radiation in a Raman spectrum. Since Raman spectroscopy was not performed during this work, this section will focus on IR spectroscopy. Many functional groups of organic molecules show characteristic vibrations that correspond to certain sections in the infrared spectrum (IR). Hence, IR spectroscopy is suitable to distinguish and identify defined functional groups and qualifies as a quantitative analytical technique. The method is based on the decrease of the intensity of the transmitted IR radiation by molecules absorbing radiation to excite vibrations. The measurements can be performed in solution or just as powder which can differ for the same molecules due to intermolecular interactions. If the analyzed molecules exhibit a changing dipole moment during the vibration process, the molecular vibration is called IR-active and thus can be excited. Vibrations of molecules with a center of symmetry are IR-inactive (forbidden) if the vibrations are symmetric to the center of symmetry. The occurring excited vibrations are categorized in stretching and deformation vibrations which are specified by their symmetric behavior in symmetric, antisymmetric and degenerate vibrations. The frequency of the IR radiation or the amount of energy required to excite vibrations depends on the bond strength and the atomic masses. Greater bond strength and lower atomic masses result in a higher vibrational frequency and thus more energy needed. The obtained spectrum is divided in the section above 1500 cm^{-1}, in which single assignable absorption bands may be frequently found, and in the section below 1500 cm^{-1}, which is sometimes called fingerprint region due to a large number of (overlapping) absorption bands that create a characteristic pattern.[8]

IR investigations were performed on a Perkin Elmer Spectrum BX FT-IR instrument in combination with an attenuated total reflection (ATR) accessory comprising an ATR diamond crystal.

2.6 Ultraviolet-Visible Spectroscopy (UV-Vis)

UV-Vis spectroscopy is a measurement of the absorption of ultraviolet (UV) and visible (Vis) light based on the interactions of radiation in the UV- and Vis-range with the sample. It is often applied to quantitatively analyze different compounds. The correlation between the measured intensity of transmitted light, the concentration of the absorbing sample and the path length is given in the Lambert-Beer law:

$$A = -\log_{10}\frac{I}{I_0} = \varepsilon \times c \times L \qquad (6)$$

where A is the absorbance, I the intensity of transmitted light, I_0 the intensity of incident light, ε the extinction coefficient, c the concentration of the absorbing sample and L the length in medium.

In both regions (UV and visible) the observed interactions are electronic transitions from the ground state to the electronically excited state. The absorbed photon has to provide the same amount of energy as the energy difference of the two energy levels HOMO (highest occupied molecule orbital) and LUMO (lowest unoccupied molecule orbital) to excite an electron from the HOMO to the LUMO. But when excited with more energy than the bandgap, excitation into higher vibrational states is possible (see Figure 2.4 for detail).

In order to measure the optical properties of thin films (which are often required to determine electronic properties and build solar devices) a different technique had to be developed because Lambert-Beer's law cannot fully capture the optical behavior of thin films. Photoactive films are often mounted on transparent substrates which cause reflection of the light on the interfaces between air, substrate and sample. For reliable absorbance data it is important to use a different procedure where the reflectance (and scattering) is not neglected. Therefore, the samples undergo transmittance and reflectance measurements whereby for the transmittance spectra the film is located inside an integrating sphere in front of the transmission hole. Contrary to that, for reflectance measurements the film has to be located outside of the integrating sphere. In order to obtain the absorbance with this method the assumption is made that the entire light is absorbed, reflected/scattered or transmitted. So, the following equation establishes the percentage absorbance %A.

$$\%T + \%R + \%A = 1 \qquad (7)$$

The percentage absorbance can now be converted into absolute absorbance by the relation:

$$A = -\log_{10}(1 - \%A) \qquad (8)$$

The absolute absorbance A is then utilized for optical bandgap calculations by Tauc plot formalism.

$$(\alpha h\nu)^{1/r} = A(h\nu - E_g) \qquad (9)$$

where α is the absorption coefficient or absolute absorbance, ν the frequency of light, E_g is the bandgap, h Planck's constant and A a proportionality constant.

Here, r depends on the type of transition and its value varies between 0.5, 1.5, 2 and 3 for direct allowed, direct forbidden, indirect allowed and indirect forbidden transitions, respectively. For the molecules and COFs investigated in this work the assumption of a direct bandgap was made to approximate the type of the existing bandgap. Therefore, the value of r = ½ was employed for the bandgap calculations. The resulting graph is characterized by a defined linear region just before y = 0 where the first absorption band is rising in the absorbance spectrum. Extrapolation of the linear region to the abscissa furnishes the energy of the optical bandgap of the material.

To study UV-Vis absorption on solid (powder) materials, the Kubelka-Munk (KM) theory is applied. The theory assumes that scattering is more likely than absorption and reflection on the surface is neglectable. The diffuse reflectance R of the compound is referenced to barium sulfate as white standard. The experimental data can be converted with the Kubelka-Munk equation into a spectrum that is approximating the absorption behavior:[9]

$$KM = \frac{(1-R)^2}{2R} \qquad (10)$$

UV-Vis-NIR spectra were recorded using a Perkin-Elmer Lambda 1050 spectrometer equipped with a 150 mm integrating sphere and photomultiplier tube (PMT) and InGaAs detectors. Diffuse reflectance spectra were collected with a Praying Mantis (Harrick) accessory and were referenced to barium sulfate powder as white standard.

2.7 Photoluminescence Spectroscopy (PL)

The counterpart to UV-Vis spectroscopy is photoluminescence (PL) spectroscopy, which examines transitions from optically excited states to the ground state. Photoluminescence is the spontaneous emission of radiation in the visible range by relaxation from the electronic excited state S_1 to the electronic ground state S_0. If the transition of the excited to the ground state occurs while maintaining the multiplicity, the fluorophore decays quickly whereby this phenomenon is called fluorescence. The emitted light is usually red-shifted due to non-radiative transitions which occur during collisions of excited-state molecules, also called vibrational

relaxations. During this process the excited-state molecules relax to the lowest vibrational state (ignoring rotational states here) of S_1 before they undergo fluorescence (see Figure 2.4).

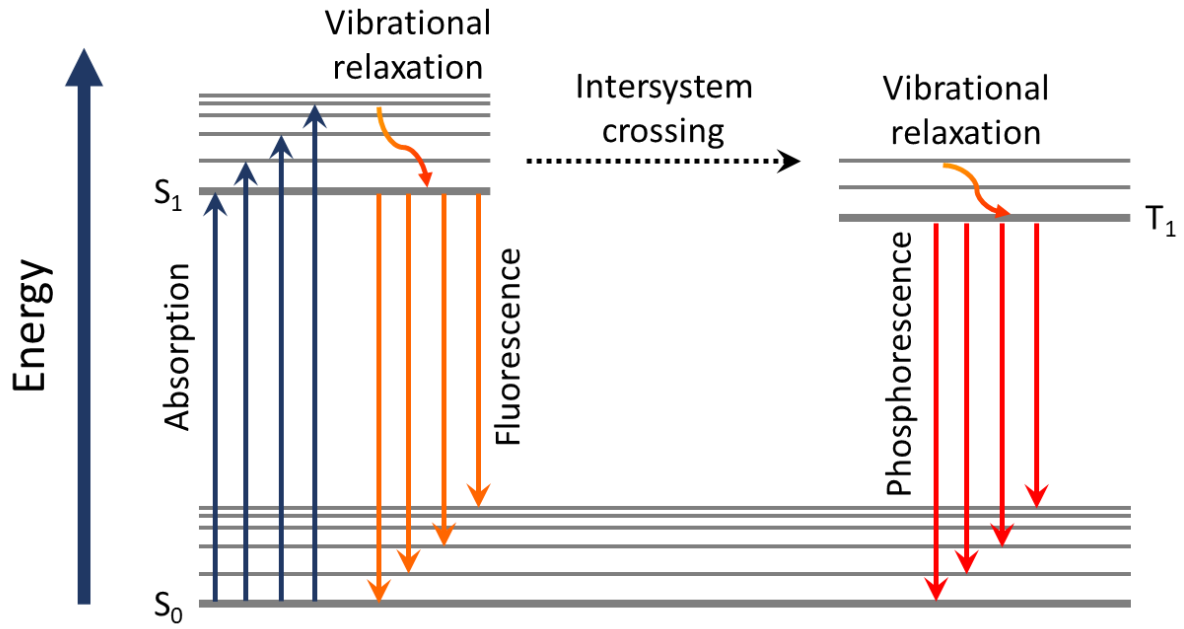

Figure 2.4: Simplified Jablonski diagram depicting possible transitions between ground and excited electronic states.

Instead of fluorescence, the system can undergo a non-radiative transition, which is called intersystem crossing (ISC), to a vibrationally excited triplet state. Transitions with a multiplicity change are forbidden, which drastically reduces the probability of this process. The triplet state then relaxes to the lowest vibrational state of T_1. From there it can decay to the ground state S_0 in a forbidden radiative transition called phosphorescence. Since the transition is forbidden and competes with non-radiative decay, phosphorescence is generally much less likely and the lifetime of the excited state T_1 is much longer compared to fluorescence. The probability of ISC can be enhanced by similar geometry of excited and ground state molecule and by stronger spin-orbit coupling with heavier elements.[10]

As seen in Figure 2.4, the spontaneous emission of a photon originates from the lowest excited state of the respective multiplicity. However, a molecule can also absorb photons of higher energy and thus is excited in any of the higher singlet states S_n where $n > 0$. This way internal conversion quickly leads to a non-radiative transition to a vibrationally excited state of the next lower excited state where due to vibrational relaxations the molecule reaches the lowest vibrational state. Kasha's rule says that these processes repeat until the excited molecules hit

the lowest excited state S_1. There the energy gap to S_0 is too large for an overlap of the vibrational wavefunctions and spontaneous emission occurs.

Quenching by internal conversion (non-radiative decay) or energy transfer to other molecules due to collisions or specific aggregation can interfere with the two phenomena and influence the intensity of the emitted light. When introducing electron acceptor molecules, the excited electron can be transferred to such an acceptor, leading to additional phenomena such as charge separation needed for applications in photovoltaics.[11]

Photoluminescence (PL) measurements were performed using a home-built setup consisting of a Horiba Jobin Yvon iHR 320 monochromator equipped with a photomultiplier tube and a liquid N_2-cooled InGaAs detector. The samples were illuminated with a 378 nm diode laser (pulse power 0.99 nJ cm^{-2}, pulse rate 40 MHz).

Steady-state PL measurements were also recorded on the TCSPC setup (see next chapter for details).

2.8 Time-Correlated Single Photon Counting (TCSPC)

Time correlated single photon counting (TCSPC) is a measurement to analyze low level light signals in the picosecond range. The technique is based on the same phenomenon as photoluminescence spectroscopy but instead of analyzing the absolute energy and the intensity of the emitted photons TCSPC gathers information about the time-resolved kinetics of the photoemission by the sample.

A pulsed laser excites the sample which can then emit a single photon. The detector records the signal periods, the so-called start-stop times, in which a single photon can be detected. It is significant to ensure that only a single or none photon is emitted during a single laser pulse cycle. The number of detected photons is plotted against the respective time difference from excitation to emission. As seen in Figure 2.5, this event is repeated multiple times to gather sufficient information for recording the fluorescence lifetimes.[12]

A pulsed laser with frequencies in the range of 100 kHz to 80 MHz is applied to achieve this highly repetitive registration of photons which leads to histograms displaying the exponential excitation decay and the corresponding lifetimes. The half-life of the excited species can be calculated based on the exponential decay shown in the following histogram (Figure 2.6).

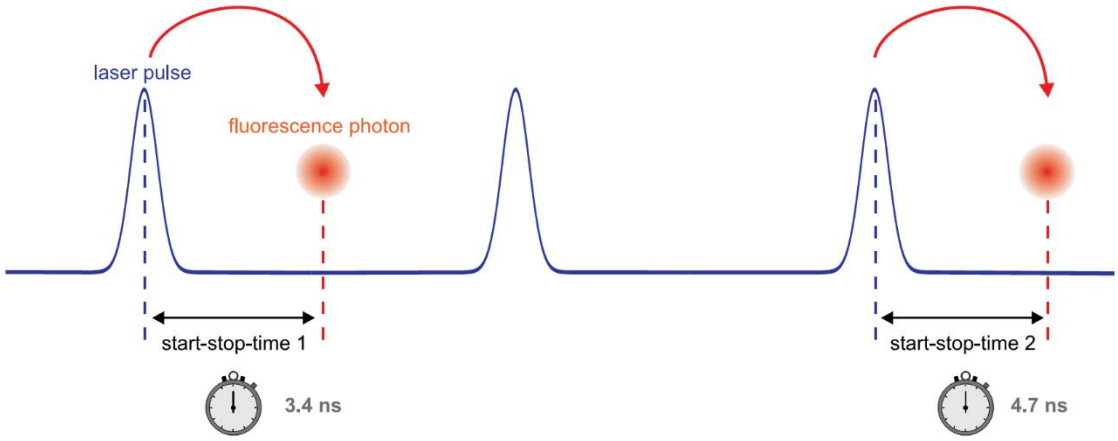

Figure 2.5: Measurement of start-stop times with TCSPC.[13]

Important applications of this technique are ultra-fast recording of optical waveforms, detection and identification of single molecules, DNA sequencing and optical tomography. Furthermore, and in this case very important was the fluorescence lifetime measurements for samples in solution or as solids (powder/film material).[12] For the highly sensitive single photon detection a Photomultiplier Tube (PMT), Hybrid PMT, Micro Channel Plate (MCP) or a Single Photon Avalanche Diode (SPAD) can be applied. For the exact determination of the time difference of the excitation and the fluorescence event each event will be converted into an electrical pulse. If the laser is not equipped with a synchronization pulse, the task is accomplished by a detector usually called trigger diode.[13]

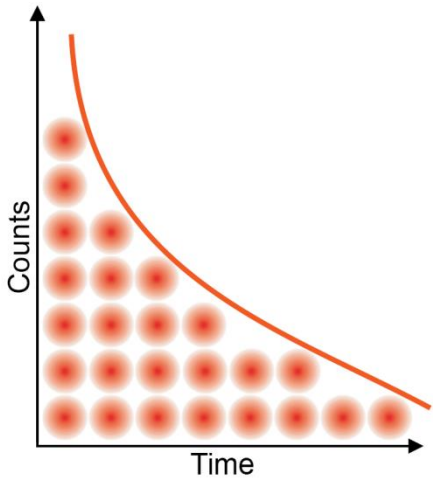

Figure 2.6: Histogram of start-stop times with TCSPC.[13]

Time-resolved PL measurements were acquired using a time-correlated single photon counting (TCSPC) setup (FluoTime 300, PicoQuant GmbH). The samples were photo-excited using

lasers with suitable wavelengths according to the sample absorption, i.e. 378 nm, 403 nm or 507 nm wavelength (LDH-P-C-375, LDH-P-C-405, and LDH-P-C-510, respectively, all from PicoQuant GmbH) pulsed at 500 kHz, with a pulse duration of ~100 ps and fluence of ~300 nJcm^{-2}/pulse. The samples were exposed to the pulsed light source set at 0.3 µJcm^{-2}/pulse fluence for ~10 minutes prior to measurement to ensure stable sample emission. The PL was collected using a high-resolution monochromator and photomultiplier detector assembly (PMA-C 192-N-M, PicoQuant GmbH).

2.9 Electrochemical Measurements

In order to investigate the energy levels of molecules, electrochemical measurements such as cyclic voltammetry (CV) and differential pulse voltammetry (DPV) were performed. These methods can be used to identify the energy level of the highest occupied molecular orbital (HOMO). Together with data from UV-Vis spectroscopy, where the bandgap can be obtained by application of the Tauc plot, the lowest unoccupied molecular orbital (LUMO) can be calculated.

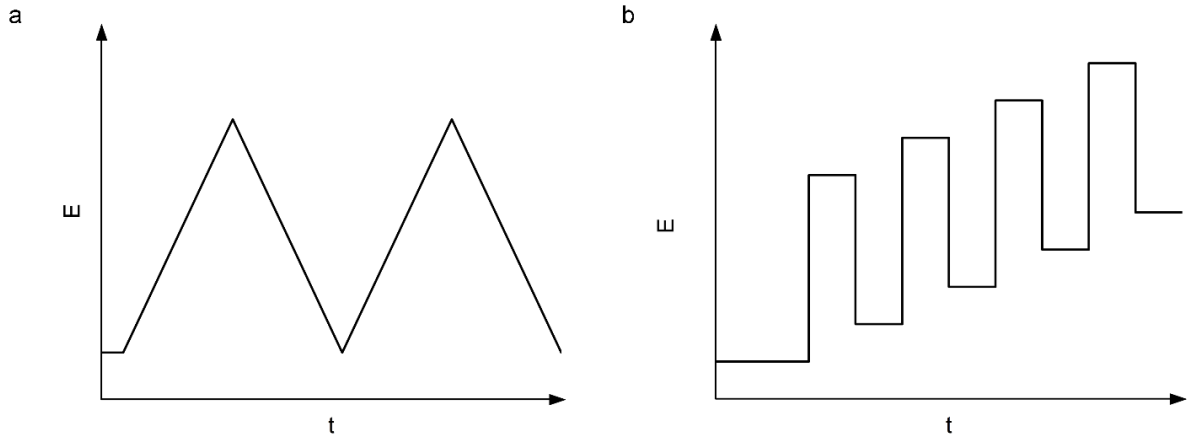

Figure 2.7: Change of potential during the measurements in (a) CV mode and (b) DPV mode.

Voltammetry, either CV or DPV, is an electroanalytical technique that is used to investigate the electrochemical properties of materials, as it can deliver information about fairly complicated electrode reactions. In a CV experiment, a linearly changing potential is applied to the electrode and the current during the potential scan is measured (see Figure 2.7). The resulting current-potential curve is called cyclic voltammogram or CV curve. The applied potential varies linearly over time with a certain scan or sweep rate [V s^{-1}] between an initial and a switching

potential where the potential direction is reversed until the starting potential is reached. The potential scan can be performed multiple times. In contrast, the DPV measurement is applied in small pulses with the same amplitude added to a staircase wave form (see Figure 2.7). Hence, in each pulse period the current is measured twice, before the pulse and at the end of the pulse. The difference between these currents is the data output in the obtained DPV curve. The advantage of DPV is hereby that even small current changes can be observed in the measurement.

A three-electrode arrangement is commonly used for these voltammetry measurements. A typical cell consists of a working electrode (WE), where the electrochemical process of interest occurs, a counter electrode (CE), and a reference electrode (RE) with a defined potential to control the potential of the WE. All three electrodes are electrically connected via an ionically conducting electrolyte which in this work was tetrabutylammonium hexafluorophosphate in acetonitrile. The current between the WE and the CE is recorded in dependence to the potential which is applied in the potential wave forms seen in Figure 2.7. During the measurement mass transport occurs by non-stationary diffusion, since the electrolyte is not stirred.

Measurements were performed with a Metrohm Autolab PGSTAT302N potentiostat, using Pt wires as the working electrode and counter electrode and an Ag wire as reference electrode with ferrocene as internal reference.

2.10 References

[1] Levine, J. R.; Cohen, J. B.; Chung, Y. W.; Georgopoulos, P., Grazing-incidence small-angle X-ray scattering: new tool for studying thin film growth. *J. Appl. Crystallogr.* **1989,** *22* (6), 528-532.

[2] Yager, K., http://gisaxs.com/index.php/File:Gisaxs_logo01.png. 2014.

[3] Thommes, M.; Kaneko, K.; Neimark, A. V.; Olivier, J. P.; Rodriguez-Reinoso, F.; Rouquerol, J.; Sing, K. S. W., Physisorption of gases, with special reference to the evaluation of surface area and pore size distribution (IUPAC Technical Report). *Pure Appl. Chem.* **2015,** *87* (9-10), 1051.

[4] Sing, K. S. W., Reporting physisorption data for gas/solid systems with special reference to the determination of surface area and porosity (Recommendations 1984). In *Pure Appl. Chem.*, 1985; Vol. 57, p 603.

[5] Williams, D. B.; Carter, C. B., *The Transmission Electron Microscope*. Springer: 1996.

[6] Goodhew, P. J.; Humphreys, J.; Beanland, R., *Electron microscopy and analysis*. Taylor & Francis Group: 2000; Vol. Third Edition.

[7] Tubus, B., https://commons.wikimedia.org/wiki/File:Schematic_view_of_imaging_and_diffraction_modes_in_TEM..tif. **2017**.

[8] Bienz, S.; Bigler, L.; Fox, T., Spektroskopische Methoden in der organischen Chemie. 8., überarbeitete und erweiterte Auflage ed.; Georg Thieme Verlag: Stuttgart, New York, 2012.

[9] Hecht, H. G., The Interpretation of Diffuse Reflectance Spectra. *J. Res. Natl. Bur. Stand., Sect. A* **1976,** *80A* (4), 567-583.

[10] Engel, T.; Reid, P., *Physical Chemistry*. Pearson Benjamin Cummings: San Francisco, 2006.

[11] Atkins, P. W.; Paula, J. d., *Physikalische Chemie*. Wiley VCH: Weinheim, 2013; Vol. 5.

[12] What Is Time Correlated Single Photon Counting.

[13] Wahl, M. Time-Correlated Single Photon Counting.

3 Dibenzochrysene Enables Tightly Controlled Docking and Stabilizes Photoexcited States in Dual-Pore Covalent Organic Frameworks

This chapter is published as:

Niklas Keller,‡ Torben Sick,‡ Nicolai N. Bach, Andreas Koszalkowski, Julian M. Rotter, Dana D. Medina and Thomas Bein, *Nanoscale* **2019**, *11*, pp 23338–23345.

‡ These authors contributed equally.

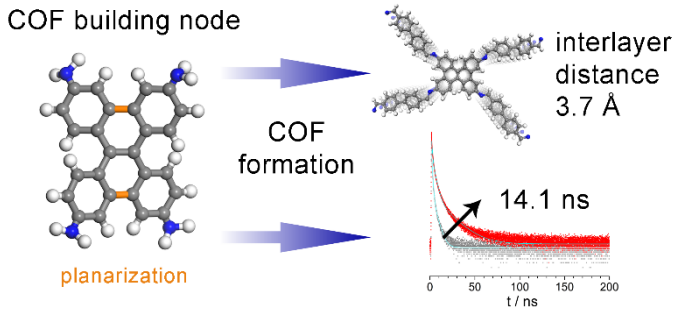

Covalent organic frameworks (COFs), consisting of covalently connected organic building units, combine attractive features such as crystallinity, open porosity and widely tunable physical properties. For optoelectronic applications, the incorporation of heteroatoms into a 2D COF has the potential to yield desired photophysical properties such as lower bandgaps, but can also cause lateral offsets of adjacent layers. Here, we introduce dibenzo[*g*,*p*]chrysene (DBC) as a novel building block for the synthesis of highly crystalline and porous 2D dual-pore COFs showing interesting properties for optoelectronic applications. The newly synthesized terephthalaldehyde (TA), biphenyl (Biph), and thienothiophene (TT) DBC-COFs combine conjugation in the *a*,*b*-plane with a tight packing of adjacent layers guided through the molecular DBC node serving as a specific docking site for successive layers. The resulting DBC-COFs exhibit a hexagonal dual-pore kagome geometry, which is comparable to COFs containing another molecular docking site, namely 4,4′,4″,4‴-(ethylene-1,1,2,2-tetrayl)-tetraaniline (ETTA). In this context, the respective interlayer distances decrease from about 4.6 Å in ETTA-COFs to about 3.6 Å in DBC-COFs, leading to well-defined hexagonally faceted single crystals sized about 50-100 nm. The TT DBC-COF feature broad light absorption covering large parts of the visible spectrum, while Biph DBC-COF shows extraordinary excited

state lifetimes exceeding 10 ns. In combination with the large number of recently developed linear conjugated building blocks, the new DBC tetra-connected node is expected to enable the synthesis of a large family of strongly π-stacked, highly ordered 2D COFs with promising optoelectronic properties.

3.1 Introduction

Covalent organic frameworks (COF) are crystalline polymers formed by covalently connecting relatively rigid and geometrically defined organic building blocks to form larger molecular components. Usually, the covalent linkages are achieved through slightly reversible condensation reactions such as boronic esters,[1] boroxines,[2] imines,[3] imides[4] or others.[5-7] The high porosity and great structural diversity and tunability and thermal stability of these frameworks make them attractive candidates for applications in energy storage,[8-10] gas storage,[11-13] proton conduction,[14-16] optoelectronics,[17-22] molecular separations[23-25] and catalysis.[26-28] While in 3D COFs the backbones consist of covalently connected building blocks in all dimensions, in 2D COFs individual polymer layers stack in a defined manner to form molecular columns and 1D pores. This mode of layer assembly is governed by weak dispersive π-stacking interactions between adjacent layers. These crystalline and porous materials offer numerous options regarding structural design, as tailoring of the pore size, shape and molecular interface is mainly governed by the selection of the building blocks. In the context of optoelectronics, this involves the potential ability to precisely manipulate the COFs' electronic properties such as the optical absorption, charge carrier mobility[29-33] or photoluminescence.[2, 7, 34-35] The incorporation of heteroatoms within the structures enables the chemical linkage of different building blocks via strong covalent bonds, for example boron atoms in the case of boronic esters and boroxines or nitrogen atoms in the case of imines, imides or others. However, heteroatoms exhibit electrostatic repulsion in an eclipsed stacking of adjacent layers, which results in slight lateral offsets.[36] Especially large and polarizable heteroatoms within adjacent COF layers prefer a stacking with lateral offsets with respect to one another.[37-38] This phenomenon can also have a strong effect on the stacking distance of adjacent layers and thereby the overall long-range order in the framework.[39] Furthermore, the polarization of certain chemical bonds may affect the stability of the frameworks.[40] Strategies aimed at controlling stacking interactions through steric considerations include the implementation of sterically demanding pyrene building blocks for enforcing predefined offset stacking angles[41] or the usage of propeller-like building blocks in imine-based frameworks.[42] In the latter case, the propeller-like building blocks define specific molecular docking sites for adjacent COF sheets, thereby enforcing a perfectly eclipsed stacking of adjacent layers. However, due to the steric demands of molecular docking sites such as 4,4′,4″,4‴-(ethylene-1,1,2,2-tetrayl)-tetraaniline (ETTA),[43] the stacking distance of adjacent layers of the resulting dual-pore kagome COF structures is comparably large. The enlarged stacking distance in combination with out-of-plane rotated

building blocks may have an influence on the π-electron overlap of adjacent COF layers and on the conjugation within each COF layer.

Dibenzochrysene (DBC) is a rigid molecular building block consisting of four benzene rings fused to a naphthyl unit. This molecular configuration can be envisioned as a fused ETTA analog which enables a more subtle rotation of the attached phenyl rings out of plane compared with ETTA.[44] Therefore, the incorporation of DBC into a framework is expected to drastically reduce the steric constraints for stacking, allowing for more closely packed molecular assemblies.[45] In addition, DBC and its derivatives exhibit attractive photophysical properties and charge carrier mobilities.[44, 46-47] This combination of properties is promising for the realization of highly ordered materials based on DBC nodes with features encoded for optoelectronic applications. In the context of framework materials, COF-based optoelectronic devices are still rare[48] and further breakthroughs in molecular design are anticipated to enable the construction of efficient devices.

Herein, we investigate the possibility to generate highly ordered COF structures by means of a molecular node intended to induce close π-stacking distances while providing specific docking sites for obtaining a high degree of order. For this purpose we utilized dibenzo[*g*,*p*]chrysene, DBC, as a structure-directing node. We synthesized a series of DBC-containing imine COFs with linear dialdehydes, namely terephthalaldehyde (TA), 4,4'-biphenyldicarbaldehyde (Biph) and thieno[3,2-*b*]thiophene-2,5-dicarboxaldehyde (TT). We present a detailed structural analysis showing the formation of highly crystalline and porous frameworks featuring outstanding crystal quality with hexagonal faceting. Furthermore, the photophysical properties of the DBC-based COFs namely UV-vis absorption as well as steady-state and time-resolved photoluminescence (PL) were studied. Here, TT DBC-COF featured broad light absorption covering large parts of the visible spectrum. Strikingly, the Biph DBC-COF powder showed extended PL lifetimes as high as 2-14 ns with 62% of the overall signal.

3.2 Results and Discussion

The DBC-based COF series was synthesized by the (slightly) reversible reaction of DBC with the respective linear dialdehydes TA, Biph, and TT to form imine-based COFs (Figure 3.15). Briefly, 30 µmol of the linear dialdehyde and 15 µmol of the fourfold amine functionalized DBC (DBCTA) were suspended in a mixture of benzyl alcohol and mesitylene (500 µL) in a culture tube. After the addition of 50 µL of acetic acid (6 M), the sealed tubes were kept in an oven at 120 °C for 72 h. The resulting precipitate was isolated by filtration, rinsed and finally Soxhlet extracted with anhydrous THF for 2 h. After vacuum-drying, the COF powders were examined concerning crystallinity, porosity and photophysical properties (for more details on the synthesis procedures see appendix).

X-ray diffraction (XRD) analysis of the obtained powders revealed highly crystalline materials with sharp and intense reflections at small diffraction angles and multiple additional high order reflections at higher diffraction angles (Figure 3.1b-d). To confirm the formation of a kagome dual-pore hexagonal structure, simulations of the possible crystal structures were carried out assuming an AA model layer arrangement in the hexagonal space group *P*6 (see section 3.5.7 in the appendix). Using this model, the experimental diffraction pattern was fully indexed and the observed reflections were attributed to *hkl* 100 110, 200, 210, 120, 300, 220, 310, 400 and 500 (by order of appearance) indicating the excellent crystallinity and the formation of a kagome structure in all the examined samples (Figure 3.1). For all the DBC-COFs, the observed reflection at around 23.9 °2θ is attributed to the 001 plane, which directly corresponds to the π-stacking distance. Accordingly, a similar *d*-spacing of about 3.6 Å was calculated for the examined DBC-COFs.

Nitrogen physisorption isotherms of the COFs exhibit a mixture of type I and type IVb isotherm shapes with two steep nitrogen uptakes, the one at low partial pressures indicating the presence of a microporous system and the one at relatively higher partial pressures characteristic for capillary condensation associated with mesoporous systems (< 5 nm) (Figure 3.2a and Figure 3.9-3.10).[49] This confirms that DBC-COFs adopt a dual-pore structure similar to their ETTA-COF analogs.[50] Pore size distributions based on carbon with a QSDFT kernel for cylindrical pores show excellent agreement with the structurally modeled pore sizes (Figure 3.9-3.10). The DFT-calculated pore sizes

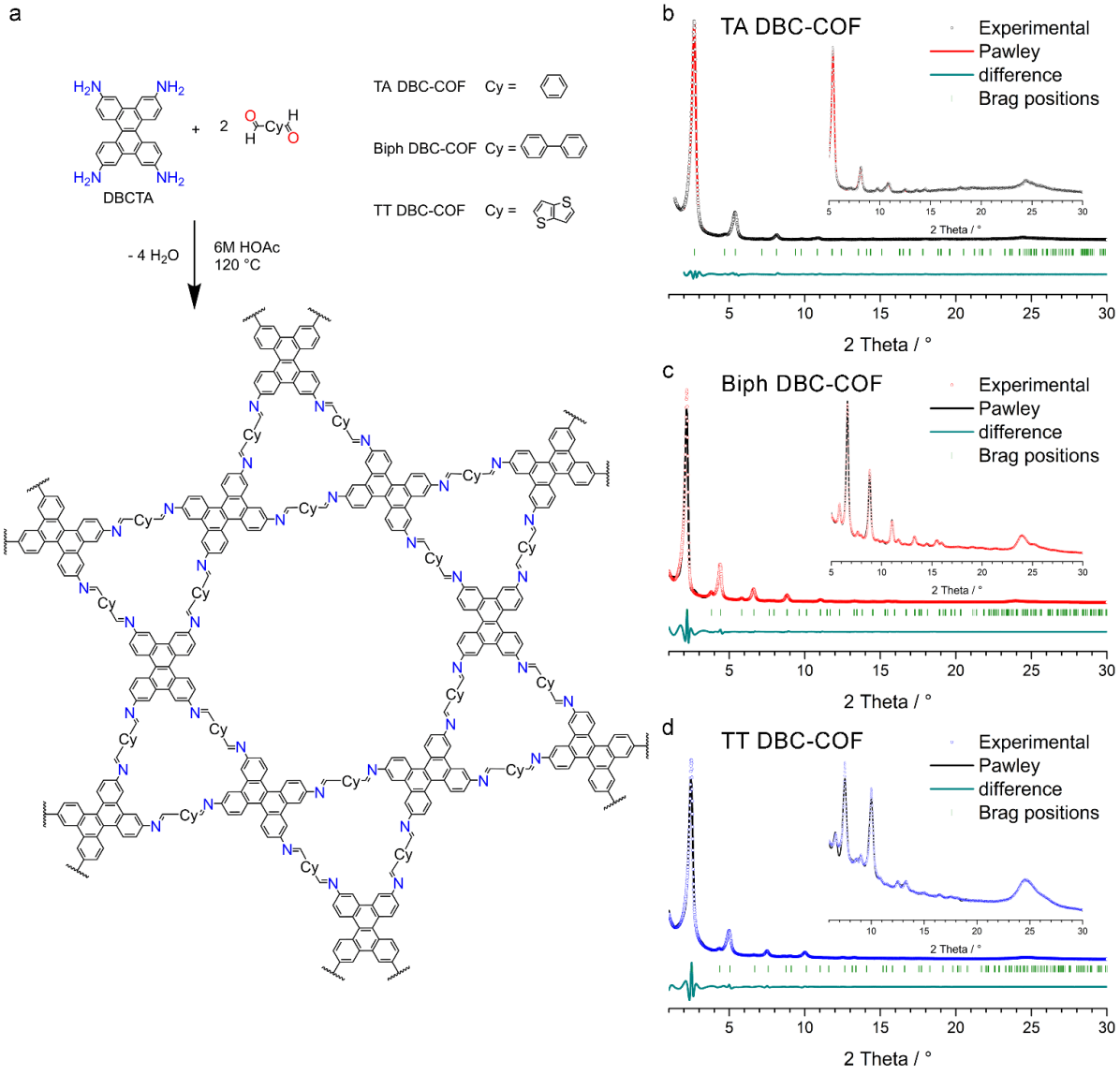

Figure 3.1: (a) Structure of the DBC-containing COFs (schematic). (b)-(d) PXRD patterns of the TA, Biph, and TT DBC-COFs with Pawley-refined simulations. The insets show higher order reflections in magnification.

were 1.50 nm and 2.89 nm (simulated 1.5 nm and 2.9 nm), 1.73 nm and 3.68 nm (simulated 1.7 nm and 3.7 nm) and 1.45 nm and 3.10 nm (simulated 1.5 nm and 3.1 nm) for TA DBC-COF, Biph DBC-COF, and TT DBC-COF, respectively. The BET surface areas and pore volumes of 2050 $m^2\ g^{-1}$ and 1.23 $cm^3\ g^{-1}$ (TA DBC-COF), 2170 $m^2\ g^{-1}$ and 1.39 $cm^3\ g^{-1}$ (Biph DBC-COF) as well as 1230 $m^2\ g^{-1}$ and 0.67 $cm^3\ g^{-1}$ (TT DBC-COF) can be compared to predicted accessible Connolly surface areas and pore volumes of 2090 $m^2\ g^{-1}$ and 0.90 $cm^3\ g^{-1}$ (TA DBC-COF), 2490 $m^2\ g^{-1}$ and 1.31 $cm^3\ g^{-1}$ (Biph DBC-COF) and 2260 $m^2\ g^{-1}$ and 1.12 $cm^3\ g^{-1}$ (TT DBC-COF), respectively.

Thermogravimetric analysis preformed under synthetic air flow revealed that DBC-COFs are thermally stable, while significant weight loss associated with structural degradation is detected

at around 450 °C, and the degradation process terminates at around 600 °C with a complete weight loss (Figure 3.23).

Morphological investigations of the DBC-COFs using scanning electron microscopy (SEM) revealed well-defined crystallites of different sizes, ranging from 10 to 150 nm, forming large intergrown objects (Figure 3.4). In the case of Biph DBC-COF, the agglomerated particles consist of faceted hexagonally shaped crystals. This is in excellent agreement with a parallel report illustrating the high crystallinity of Biph-DBC COF.[45, 51] Transmission electron microscopy (TEM) micrographs show the highly crystalline nature of the COFs (Figure 3.5). Strikingly, the Biph DBC-COF exhibits large numbers of hexagonally faceted single crystals sized about 50 to 100 nm throughout the sample (Figure 3.2).

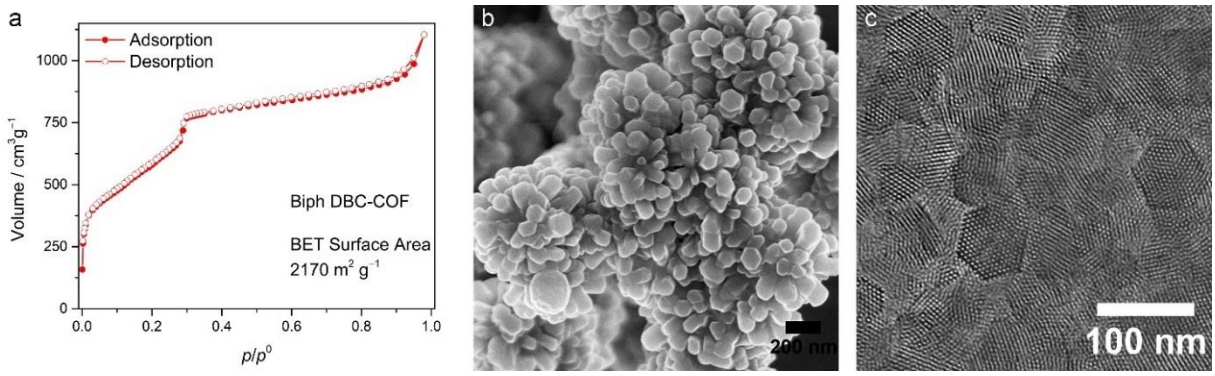

Figure 3.2: (a) Nitrogen physisorption isotherm of Biph DBC-COF. (b) SEM and (c) TEM micrographs of Biph DBC-COF.

In comparison to the previously reported ETTA systems with the same linear dialdehydes, namely TA, Biph, and TT, the reflections associated with the stacking distances in PXRD pattern are shifted from about 19.5 °2θ to 23.9 °2θ, corresponding to a reduction of stacking distances of about 4.6 Å (for TA ETTA-COF, Biph ETTA-COF, and TT ETTA-COF)[42] to 3.6 Å (TA and TT DBC-COFs), 3.7 Å (Biph DBC-COF). This drastically decreased stacking distance (by almost 1.0 Å) for each DBC-containing COFs is attributed to the more planar (gently curved) shape of the chrysene building block compared to the more sterically demanding ETTA node.[45] The influence of the linear dialdehyde on the stacking distance is apparently less dominant, though being still detectable.

Reported single crystal structures of the core elements of the different 4-connected COF building blocks, i.e., ETTA and DBC, clearly indicate the influence on the bond angles and steric requirements of the differently linked aromatic groups. In ETTA, an average dihedral angle of 47.3°[52] was determined, while in DBC the average angle reduces to 24.7°.[53] Here, the

angles were determined for two intersecting planes created, in ETTA, by the ethylene bond and the sequentially connected two carbon atoms in the aromatic substitution. The dihedral angle for the corresponding chrysene molecule was determined in the same manner by considering the same atom connectivity (Figure 3.12). Therefore, using a DBC node results in a COF kagome structure and connectivity similar to the ETTA-COF analogs, but the presence of a rigid naphthyl unit strongly reduces the torsion/rotation of the attached aromatic groups compared to the aromatic groups connected to the ethylene unit in ETTA. These findings are in line with the reported dihedral angles for ETTA and DBC.[45] As a result, the π-stacking distance between adjacent COF layers is expected to be reduced while the existing DBC torsion angle is still sufficient to act as a specific docking site for the successive layers. This is expected to enable defined π-π-interactions in the stacks and improved π-orbital overlap within the individual layers allowing for extended electron delocalization.

Next, we investigated the photophysical properties of the DBC-COFs by means of UV-vis, PL and TCSPC spectroscopies. The influence of the respective linear building block on the optical absorption can be clearly seen in the absorbance spectra recorded for the DBC-COF powders (see Figure 3.3 and Figure 3.16). While the phenyl-based linear linkers TA and Biph exhibit light brown color, comparable absorption features and absorption onsets at around 550 to 580 nm, the incorporation of the thiophene-based TT shifts the steep onset to longer wavelengths at around 650 nm. Consequently, the TT DBC-COF exhibits dark red color and a comparably smaller bandgap, which was calculated by Tauc plot. Assuming a direct optical bandgap for the DBC-COFs, we obtained a bandgap of 2.00 eV for the TT DBC-COF. In comparison, the direct optical bandgaps of TA DBC-COF and Biph DBC-COF were calculated to be 2.30 eV and 2.38 eV, respectively (Figure 3.17). In the context of extended conjugation within the COF layers, the TT DBC-COF exhibits a clear red-shifted absorption onset compared to its ETTA analogue. This extended absorbance can be attributed to the effect of closely packed molecular aggregates and larger π-electron delocalization attained by the geometry of the DBC node.

TA and Biph DBC-COFs exhibit similar PL spectra consisting of two distinct emission bands at around 640 and 720 nm, where the latter features stronger emission intensity. TT DBC-COF is slightly red-shifted and reveals a broader PL maximum at 760 nm with a slight shoulder at 660 nm. For all the investigated DBC-COFs, the PL covers a broad spectral range from the visible to the near-infrared (see Figure 3.3 and Figure 3.19). In comparison to the individual emission of the pristine, molecular components, the PL maxima of all DBC-COFs are

significantly red-shifted, which points toward the formation of new electronic structure through the framework chemistry (Figure 3.18).

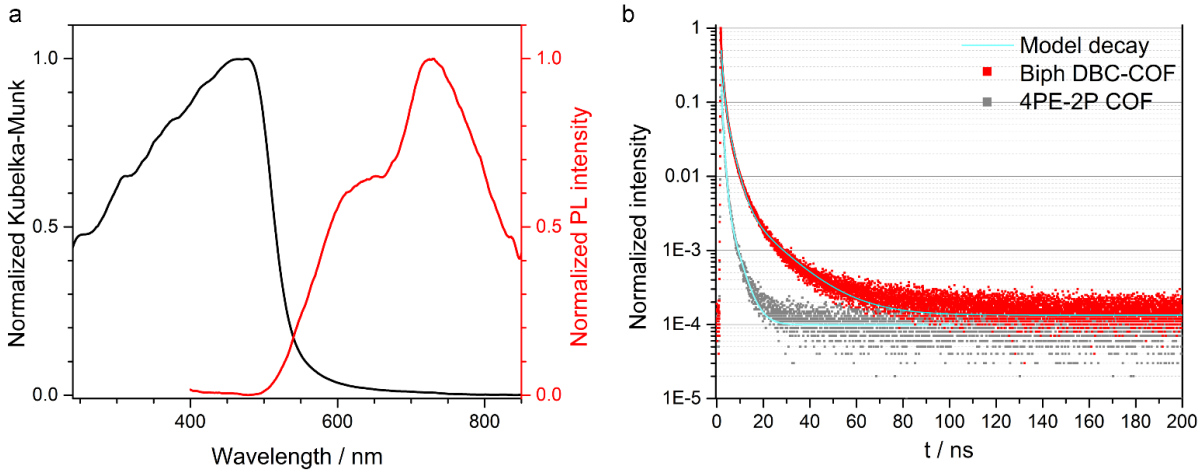

Figure 3.3: (a) Optical absorption spectrum (black) of Biph DBC-COF powder measured in diffuse reflectance mode, and PL (λ_{exc} = 378 nm, red) spectrum of Biph DBC-COF. (b) PL decay curve of Biph DBC-COF (red) and 4PE-2P COF (grey), the ETTA-based COF. The samples were illuminated at 378 nm with a pump fluence of ~0.99 nJ cm^{-2}; the emission was monitored at 724 and 643 nm, respectively (model decay in cyan).

To study the PL decay dynamics, time-correlated single photon counting (TCSPC) was employed using a pulsed 378 nm laser under nitrogen atmosphere (section 3.5.12 in the appendix), revealing the lifetimes of the photoexcited singlet states generated in the DBC-COF powders. The obtained decay curves were fitted with a tri-exponential function. The longest lifetimes were observed for the Biph DBC-COF, which features a long-time decay constant of 14.1 ns (12%) (see Figure 3.3). The additional two exponential time constants indicate 2.8 ns (50%) and 0.7 ns (38%). For the TA DBC-COF lifetimes of up to 7 ns were detected and the TT DBC-COF showed the fastest decay times for this series of DBC-COFs of up to 5 ns (for more details see appendix).

As illustrated, small modifications in the molecular structure of the building blocks can strongly impact the structural properties of the COF, here, a stacking distance reduced by about 1.0 Å was obtained with a DBC node. In addition, indications for enhanced photophysical properties in DBC-COF were observed. To study the differences in the photophysical properties of these two COF families, we compared the PL decay dynamics of DBC-COFs featuring tight molecular stacks with the ones of their ETTA-based COF analogues.[42] For all the examined COFs the decay profiles were fitted with tri-exponential decay functions. In general, the decay times obtained for the DBC-COFs were significantly longer, leading to overall longer PL lifetimes (see Figure 3.3 and section 3.5.12 in the appendix). The Biph DBC-COF exhibits the

longest lifetimes, of more than 10 ns longer compared to its corresponding 4PE-2P COF analog. 4PE-2P COF features PL decay times of 3.6 ns (11%) as the long-time constant, the rest of the PL signal (90%) arises from fast decay channels below 1 ns (0.8 ns (50%) and 0.14 ns (39%)). We postulate that in DBC-COFs the structural features greatly influence the PL decay and induce a stabilization of the photoexcited species in the COF. The proximity of the layers in the DBC-COFs may allow for delocalization of the excited state across the π-stacked chrysene columns. The closer stacking is also affecting the bandgap of the DBC-COFs compared to the analog ETTA-based COFs. A decrease in the bandgap for the DBC-COFs is observed which is attributed to the stronger π-π interactions between the tighter stacked chrysene docking sites and the potentially resulting band dispersions.[54] To further characterize the excited states and the processes involved, transient absorption or terahertz spectroscopy could be useful to stronger elucidate the PL dynamics in the DBC-COFs.

3.3 Conclusion

In this study, we have established dibenzo[*g*,*p*]chrysene (DBC) as a novel structural node for the construction of 2D COFs, serving as a specific docking site for the synthesis of flattened structural analogues of the well-studied ETTA-based COFs. Different DBC-COFs were synthesized with different linear linkers to not only vary the pore sizes but more importantly the photophysical properties. DBC-COFs show extraordinarily high crystallinity, porosity and structural precision, which is reflected in the formation of hexagonally faceted single crystals. Strikingly, in comparison with ETTA-based COF analogues the π-stacking distance of adjacent layers was drastically reduced by 1 Å, from about 4.6 Å in ETTA-COFs to about 3.6 Å in DBC-COFs. Among the newly synthesized, tightly π-stacked DBC-COFs, TT DBC-COF is viewed to be a promising candidate for photovoltaic applications, as it combines a relatively small bandgap and a steep absorption onset with a broad optical absorption ranging from the UV deep into the visible. The time-resolved photoluminescence profile of Biph DBC-COF shows remarkably long lifetimes, partially exceeding 10 ns. In general, the DBC-COFs showed significantly slower decay dynamics in contrast to their ETTA analogues. Further mechanistic investigations in our laboratories regarding the charge carrier dynamics in these intriguing molecular frameworks are expected to shed light on the impact of the building blocks and the nature of the layer stacking on the optoelectronic properties. In view of the above, dibenzochrysene-based COFs represent a promising platform of tuneable molecular framework materials with intriguing prospects for optoelectronic applications.

3.4 References

[1] Côté, A. P.; Benin, A. I.; Ockwig, N. W.; O'Keeffe, M.; Matzger, A. J.; Yaghi, O. M., Porous, Crystalline, Covalent Organic Frameworks. *Science* **2005,** *310* (5751), 1166-1170.

[2] Wan, S.; Guo, J.; Kim, J.; Ihee, H.; Jiang, D., A Photoconductive Covalent Organic Framework: Self-Condensed Arene Cubes Composed of Eclipsed 2D Polypyrene Sheets for Photocurrent Generation. *Angew. Chem. Int. Ed.* **2009,** *48* (30), 5439-5442.

[3] Uribe-Romo, F. J.; Hunt, J. R.; Furukawa, H.; Klöck, C.; O'Keeffe, M.; Yaghi, O. M., A Crystalline Imine-Linked 3-D Porous Covalent Organic Framework. *J. Am. Chem. Soc.* **2009,** *131* (13), 4570-4571.

[4] Fang, Q.; Zhuang, Z.; Gu, S.; Kaspar, R. B.; Zheng, J.; Wang, J.; Qiu, S.; Yan, Y., Designed synthesis of large-pore crystalline polyimide covalent organic frameworks. *Nat. Commun.* **2014,** *5*, 4503.

[5] Uribe-Romo, F. J.; Doonan, C. J.; Furukawa, H.; Oisaki, K.; Yaghi, O. M., Crystalline Covalent Organic Frameworks with Hydrazone Linkages. *J. Am. Chem. Soc.* **2011,** *133* (30), 11478-11481.

[6] Kuhn, P.; Antonietti, M.; Thomas, A., Porous, Covalent Triazine-Based Frameworks Prepared by Ionothermal Synthesis. *Angew. Chem. Int. Ed.* **2008,** *47* (18), 3450-3453.

[7] Dalapati, S.; Jin, S.; Gao, J.; Xu, Y.; Nagai, A.; Jiang, D., An Azine-Linked Covalent Organic Framework. *J. Am. Chem. Soc.* **2013,** *135* (46), 17310-17313.

[8] Yang, H.; Zhang, S.; Han, L.; Zhang, Z.; Xue, Z.; Gao, J.; Li, Y.; Huang, C.; Yi, Y.; Liu, H.; Li, Y., High Conductive Two-Dimensional Covalent Organic Framework for Lithium Storage with Large Capacity. *ACS Appl. Mater. Interfaces* **2016,** *8* (8), 5366-5375.

[9] DeBlase, C. R.; Hernández-Burgos, K.; Silberstein, K. E.; Rodríguez-Calero, G. G.; Bisbey, R. P.; Abruña, H. D.; Dichtel, W. R., Rapid and Efficient Redox Processes within 2D Covalent Organic Framework Thin Films. *ACS Nano* **2015,** *9* (3), 3178-3183.

[10] Hu, Y.; Dunlap, N.; Wan, S.; Lu, S.; Huang, S.; Sellinger, I.; Ortiz, M.; Jin, Y.; Lee, S.-h.; Zhang, W., Crystalline Lithium Imidazolate Covalent Organic Frameworks with High Li-Ion Conductivity. *J. Am. Chem. Soc.* **2019,** *141* (18), 7518-7525.

[11] Lee, G.-Y.; Lee, J.; Vo, H. T.; Kim, S.; Lee, H.; Park, T., Amine-Functionalized Covalent Organic Framework for Efficient SO2 Capture with High Reversibility. *Scientific Reports* **2017,** *7* (1), 557.

[12] Ding, S.-Y.; Wang, W., Covalent organic frameworks (COFs): from design to applications. *Chem. Soc. Rev.* **2013,** *42* (2), 548-568.

[13] Furukawa, H.; Yaghi, O. M., Storage of Hydrogen, Methane, and Carbon Dioxide in Highly Porous Covalent Organic Frameworks for Clean Energy Applications. *J. Am. Chem. Soc.* **2009,** *131* (25), 8875-8883.

[14] Shinde, D. B.; Aiyappa, H. B.; Bhadra, M.; Biswal, B. P.; Wadge, P.; Kandambeth, S.; Garai, B.; Kundu, T.; Kurungot, S.; Banerjee, R., A mechanochemically synthesized covalent organic framework as a proton-conducting solid electrolyte. *J. Mater. Chem. A* **2016,** *4* (7), 2682-2690.

[15] Xu, H.; Tao, S.; Jiang, D., Proton conduction in crystalline and porous covalent organic frameworks. *Nat. Mater.* **2016,** *15*, 722.

[16] Chandra, S.; Kundu, T.; Kandambeth, S.; BabaRao, R.; Marathe, Y.; Kunjir, S. M.; Banerjee, R., Phosphoric Acid Loaded Azo (−N═N−) Based Covalent Organic Framework for Proton Conduction. *J. Am. Chem. Soc.* **2014,** *136* (18), 6570-6573.

[17] Medina, D. D.; Werner, V.; Auras, F.; Tautz, R.; Dogru, M.; Schuster, J.; Linke, S.; Döblinger, M.; Feldmann, J.; Knochel, P.; Bein, T., Oriented Thin Films of a Benzodithiophene Covalent Organic Framework. *ACS Nano* **2014,** *8* (4), 4042-4052.

[18] Calik, M.; Auras, F.; Salonen, L. M.; Bader, K.; Grill, I.; Handloser, M.; Medina, D. D.; Dogru, M.; Löbermann, F.; Trauner, D.; Hartschuh, A.; Bein, T., Extraction of Photogenerated Electrons and Holes from a Covalent Organic Framework Integrated Heterojunction. *J. Am. Chem. Soc.* **2014,** *136* (51), 17802-17807.

[19] Bessinger, D.; Ascherl, L.; Auras, F.; Bein, T., Spectrally Switchable Photodetection with Near-Infrared-Absorbing Covalent Organic Frameworks. *J. Am. Chem. Soc.* **2017,** *139* (34), 12035-12042.

[20] Wuttke, S.; Medina, D. D.; Rotter, J. M.; Begum, S.; Stassin, T.; Ameloot, R.; Oschatz, M.; Tsotsalas, M., Bringing Porous Organic and Carbon-Based Materials toward Thin-Film Applications. *Adv. Funct. Mater.* **2018,** *28* (44), 1801545.

[21] Jakowetz, A. C.; Hinrichsen, T. F.; Ascherl, L.; Sick, T.; Calik, M.; Auras, F.; Medina, D. D.; Friend, R. H.; Rao, A.; Bein, T., Excited-State Dynamics in Fully Conjugated 2D Covalent Organic Frameworks. *J. Am. Chem. Soc.* **2019,** *141* (29), 11565-11571.

[22] Zhang, Y.; Hu, Y.; Zhao, J.; Park, E.; Jin, Y.; Liu, Q.; Zhang, W., Covalent organic framework-supported Fe–TiO2 nanoparticles as ambient-light-active photocatalysts. *J. Mater. Chem. A* **2019,** *7* (27), 16364-16371.

[23] Han, X.; Zhang, J.; Huang, J.; Wu, X.; Yuan, D.; Liu, Y.; Cui, Y., Chiral induction in covalent organic frameworks. *Nat. Commun.* **2018,** *9* (1), 1294.

[24] Liu, L.-H.; Yang, C.-X.; Yan, X.-P., Methacrylate-bonded covalent-organic framework monolithic columns for high performance liquid chromatography. *Journal of Chromatography A* **2017,** *1479*, 137-144.

[25] Guan, X.; Li, H.; Ma, Y.; Xue, M.; Fang, Q.; Yan, Y.; Valtchev, V.; Qiu, S., Chemically stable polyarylether-based covalent organic frameworks. *Nat. Chem.* **2019,** *11* (6), 587-594.

[26] Ding, S.-Y.; Gao, J.; Wang, Q.; Zhang, Y.; Song, W.-G.; Su, C.-Y.; Wang, W., Construction of Covalent Organic Framework for Catalysis: Pd/COF-LZU1 in Suzuki–Miyaura Coupling Reaction. *J. Am. Chem. Soc.* **2011,** *133* (49), 19816-19822.

[27] Han, X.; Xia, Q.; Huang, J.; Liu, Y.; Tan, C.; Cui, Y., Chiral Covalent Organic Frameworks with High Chemical Stability for Heterogeneous Asymmetric Catalysis. *J. Am. Chem. Soc.* **2017,** *139* (25), 8693-8697.

[28] Lu, S.; Hu, Y.; Wan, S.; McCaffrey, R.; Jin, Y.; Gu, H.; Zhang, W., Synthesis of Ultrafine and Highly Dispersed Metal Nanoparticles Confined in a Thioether-Containing Covalent Organic Framework and Their Catalytic Applications. *J. Am. Chem. Soc.* **2017,** *139* (47), 17082-17088.

[29] Medina, D. D.; Petrus, M. L.; Jumabekov, A. N.; Margraf, J. T.; Weinberger, S.; Rotter, J. M.; Clark, T.; Bein, T., Directional Charge-Carrier Transport in Oriented Benzodithiophene Covalent Organic Framework Thin Films. *ACS Nano* **2017,** *11* (3), 2706-2713.

[30] Cai, S.-L.; Zhang, Y.-B.; Pun, A. B.; He, B.; Yang, J.; Toma, F. M.; Sharp, I. D.; Yaghi, O. M.; Fan, J.; Zheng, S.-R.; Zhang, W.-G.; Liu, Y., Tunable electrical conductivity in oriented thin films of tetrathiafulvalene-based covalent organic framework. *Chem. Sci.* **2014,** *5* (12), 4693-4700.

[31] Patwardhan, S.; Kocherzhenko, A. A.; Grozema, F. C.; Siebbeles, L. D. A., Delocalization and Mobility of Charge Carriers in Covalent Organic Frameworks. *J. Phys. Chem. C* **2011,** *115*, 11768-11772.

[32] Wan, S.; Gándara, F.; Asano, A.; Furukawa, H.; Saeki, A.; Dey, S. K.; Liao, L.; Ambrogio, M. W.; Botros, Y. Y.; Duan, X.; Seki, S.; Stoddart, J. F.; Yaghi, O. M., Covalent Organic Frameworks with High Charge Carrier Mobility. *Chem. Mater.* **2011,** *23* (18), 4094-4097.

[33] Li, H.; Chang, J.; Li, S.; Guan, X.; Li, D.; Li, C.; Tang, L.; Xue, M.; Yan, Y.; Valtchev, V.; Qiu, S.; Fang, Q., Three-Dimensional Tetrathiafulvalene-Based Covalent Organic Frameworks for Tunable Electrical Conductivity. *J. Am. Chem. Soc.* **2019**.

[34] Wan, S.; Guo, J.; Kim, J.; Ihee, H.; Jiang, D., A Belt-Shaped, Blue Luminescent, and Semiconducting Covalent Organic Framework. *Angew. Chem. Int. Ed.* **2008,** *47* (46), 8826-8830.

[35] Dalapati, S.; Jin, E.; Addicoat, M.; Heine, T.; Jiang, D., Highly Emissive Covalent Organic Frameworks. *J. Am. Chem. Soc.* **2016,** *138* (18), 5797-5800.

[36] Lukose, B.; Kuc, A.; Frenzel, J.; Heine, T., On the reticular construction concept of covalent organic frameworks. *Beilstein J. Nanotechnol.* **2010,** *1*, 60-70.

[37] Haase, F.; Gottschling, K.; Stegbauer, L.; Germann, L. S.; Gutzler, R.; Duppel, V.; Vyas, V. S.; Kern, K.; Dinnebier, R. E.; Lotsch, B. V., Tuning the stacking behaviour of a 2D covalent organic framework through non-covalent interactions. *Materials Chemistry Frontiers* **2017,** *1* (7), 1354-1361.

[38] Lukose, B.; Kuc, A.; Heine, T., The Structure of Layered Covalent-Organic Frameworks. *Chem. - Eur. J.* **2011,** *17* (8), 2388-2392.

[39] Lohse, M. S.; Rotter, J. M.; Margraf, J. T.; Werner, V.; Becker, M.; Herbert, S.; Knochel, P.; Clark, T.; Bein, T.; Medina, D. D., From benzodithiophene to diethoxy-benzodithiophene covalent organic frameworks – structural investigations. *CrystEngComm* **2016,** *18* (23), 4295-4302.

[40] Xu, H.; Gao, J.; Jiang, D., Stable, crystalline, porous, covalent organic frameworks as a platform for chiral organocatalysts. *Nat. Chem.* **2015,** *7* (11), 905-912.

[41] Auras, F.; Ascherl, L.; Hakimioun, A. H.; Margraf, J. T.; Hanusch, F. C.; Reuter, S.; Bessinger, D.; Döblinger, M.; Hettstedt, C.; Karaghiosoff, K.; Herbert, S.; Knochel, P.; Clark, T.; Bein, T., Synchronized Offset Stacking: A Concept for Growing Large-Domain and Highly Crystalline 2D Covalent Organic Frameworks. *J. Am. Chem. Soc.* **2016,** *138* (51), 16703-16710.

[42] Ascherl, L.; Sick, T.; Margraf, J. T.; Lapidus, S. H.; Calik, M.; Hettstedt, C.; Karaghiosoff, K.; Döblinger, M.; Clark, T.; Chapman, K. W.; Auras, F.; Bein, T., Molecular docking sites designed for the generation of highly crystalline covalent organic frameworks. *Nat. Chem.* **2016,** *8* (4), 310-316.

[43] Zhou, T. Y.; Xu, S. Q.; Wen, Q.; Pang, Z. F.; Zhao, X., One-step construction of two different kinds of pores in a 2D covalent organic framework. *J Am Chem Soc* **2014,** *136* (45), 15885-8.

[44] Ueda, Y.; Tsuji, H.; Tanaka, H.; Nakamura, E., Synthesis, crystal packing, and ambipolar carrier transport property of twisted dibenzo[g,p]chrysenes. *Chem Asian J* **2014,** *9* (6), 1623-8.

[45] Xie, Z.; Wang, B.; Yang, Z.; Yang, X.; Yu, X.; Xing, G.; Zhang, Y.; Chen, L., Stable 2D Heteroporous Covalent Organic Frameworks for Efficient Ionic Conduction. *Angew. Chem. Int. Ed.* **2019,** *58* (44), 15742-15746.

[46] Khatua, R.; Sahoo, S. R.; Sharma, S.; Thangavel, R.; Sahu, S., Anisotropic charge transport properties of chrysene derivatives as organic semiconductor: A computational study. *Journal of Physical Organic Chemistry* **2018,** *31* (10), e3859.

[47] Liu, X.-Y.; Tang, X.; Zhao, Y.; Zhao, D.; Fan, J.; Liao, L.-S., Dibenzo[g,p]chrysene: A new platform for highly efficient red phosphorescent organic light-emitting diodes. *Dyes and Pigments* **2017,** *146*, 234-239.

[48] Medina, D. D.; Sick, T.; Bein, T., Photoactive and Conducting Covalent Organic Frameworks. *Adv. Energy Mater.* **2017,** *7* (16), 1700387-n/a.

[49] Thommes, M.; Kaneko, K.; Neimark, A. V.; Olivier, J. P.; Rodriguez-Reinoso, F.; Rouquerol, J.; Sing, K. S. W., Physisorption of gases, with special reference to the evaluation of surface area and pore size distribution (IUPAC Technical Report). *Pure Appl. Chem.* **2015,** *87* (9-10), 1051.

[50] Jin, Y.; Hu, Y.; Zhang, W., Tessellated multiporous two-dimensional covalent organic frameworks. *Nature Reviews Chemistry* **2017,** *1* (7), 0056.

[51] Keller, N.; Sick, T.; Bach, N. N.; Koszalkowski, A.; Rotter, J. M.; Medina, D. D.; Bein, T., Dibenzochrysene Enables Tightly Controlled Docking and Stabilizes Photoexcited States in Dual-Pore Covalent Organic Frameworks. *ChemRxiv* **2019**.

[52] Zhang, G.-F.; Chen, Z.-Q.; Aldred, M. P.; Hu, Z.; Chen, T.; Huang, Z.; Meng, X.; Zhu, M.-Q., Direct validation of the restriction of intramolecular rotation hypothesis via the synthesis of novel ortho-methyl substituted tetraphenylethenes and their application in cell imaging. *Chem. Commun.* **2014,** *50* (81), 12058-12060.

[53] Hatakeyama, T.; Hashimoto, S.; Seki, S.; Nakamura, M., Synthesis of BN-Fused Polycyclic Aromatics via Tandem Intramolecular Electrophilic Arene Borylation. *J. Am. Chem. Soc.* **2011,** *133* (46), 18614-18617.

[54] Wang, M.; Ballabio, M.; Wang, M.; Lin, H.-H.; Biswal, B. P.; Han, X.; Paasch, S.; Brunner, E.; Liu, P.; Chen, M.; Bonn, M.; Heine, T.; Zhou, S.; Cánovas, E.; Dong, R.; Feng, X., Unveiling Electronic Properties in Metal–Phthalocyanine-Based Pyrazine-Linked Conjugated Two-Dimensional Covalent Organic Frameworks. *J. Am. Chem. Soc.* **2019,** *141* (42), 16810-16816.

3.5 Appendix

3.5.1 Materials and Methods

All reagents and solvents were obtained from in house supply or commercial suppliers and used as received. Acetic acid (in house supply), benzyl alcohol (BnOH, anhydrous, Sigma-Aldrich), 4,4'-biphenyldicarboxaldehyde (Biph, >98%, TCI), 1,4-dioxane (anhydrous, Sigma Aldrich), dibenzo[*g*,*p*]chrysene (DBC, >98%, TCI), ethanol (anhydrous, Sigma Aldrich), hydrazine monohydrate (Sigma Aldrich), mesitylene (anhydrous, Sigma-Aldrich), nitrobenzene (anhydrous, Sigma Aldrich), Raney-Nickel slurry (Sigma Aldrich), terephthalaldehyde (TA, 99%, Sigma-Aldrich), tetrahydrofuran (THF, extra dry, stabilized, Acros Organics). Thieno[3,2-*b*]thiophene-2,5-dicarboxaldehyde (TT, >93%, TCI) was recrystallized from N,N-dimethylformamide (DMF, anhydrous, 99.8%, Sigma-Aldrich).

Nuclear magnetic resonance (NMR) spectra were recorded on Bruker AV 400 and AV 400 TR spectrometers. Proton chemical shifts are expressed in parts per million (δ scale) and are calibrated using residual non-deuterated solvent peaks as internal reference (e.g. DMSO-d_6: 2.50 ppm).

Infrared (IR) spectra were recorded on a Perkin Elmer Spectrum BX II FT-IR system and a Thermo Scientific Nicolet™ 6700 FT-IR spectrometer in transmission mode. IR data are reported in wavenumbers (cm^{-1}).

UV-Vis spectra were recorded using a Perkin-Elmer Lambda 1050 spectrometer equipped with a 150 mm integrating sphere. **Diffuse reflectance spectra** were collected with a Praying Mantis (Harrick) accessory and were referenced to barium sulfate powder as white standard.

Nitrogen sorption isotherms were recorded on a Quantachrome Autosorb 1 at 77 K within a pressure range of p/p^0 = 0.001 to 0.98. Prior to the measurement of the sorption isotherms the samples were heated for 24 h at 120 °C under turbo-pumped vacuum. For the evaluation of the surface area the BET model was applied between 0.05 and 0.3 p/p^0. Pore size distributions were calculated using the QSDFT equilibrium model (desorption branch) with a carbon kernel for cylindrical pores. Connolly surfaces were generated using an N_2-sized probe (r = 0.184 nm) at a 0.025 nm grid interval.

Thermogravimetric analysis (TGA) measurements were performed on a Netzsch Jupiter ST 449 C instrument equipped with a Netzsch TASC 414/4 controller. The samples were heated

from room temperature to 900 °C under a synthetic air flow (25 mL min^{-1}) at a heating rate of 10 K min^{-1}.

Powder X-ray diffraction (PXRD) measurements were performed using a Bruker D8 Discover with Ni-filtered Cu-Kα radiation and a LynxEye position-sensitive detector (scan speed of 4 s per 0.01 °2θ). Experimental XRD data were used for Pawley refinement to optimize the hypothetical structure.

The initial **structure models of the COFs** were built using the Forcite module of the Accelrys Materials Studio software package. We applied the space group with the highest possible symmetry, i.e. *P*6, considering the propeller-like conformation of the central building blocks. Using this coarse model, we determined the unit cell parameters via Pawley refinement of our PXRD data.

Transmission electron microscopy (TEM) was performed on an FEI Titan Themis equipped with a field emission gun operated at 300 kV.

Scanning electron microscopy (SEM) images were recorded with a JEOL 6500F and an FEI Helios NanoLab G3 UC scanning electron microscope equipped with a field emission gun operated at 3-5 kV.

Photoluminescence (PL) and **time-correlated single photon counting (TCSPC)** data were processed with a FluoTime 300 from PicoQuant GmbH. The samples were photo-excited using lasers with suitable wavelengths according to the sample absorption, i.e. 378 nm, 403 nm or 507 nm wavelength (LDH-P-C-375, LDH-P-C-405, and LDH-P-C-510, respectively, all from PicoQuant GmbH) pulsed at 500 kHz, with a pulse duration of ~100 ps and fluence of ~ 300 nJ cm^{-2}/pulse. The samples were exposed to the pulsed light source set at 3 μJ cm^{-2}/pulse fluence for ~10 minutes prior to measurement to ensure stable sample emission. The PL was collected using a high-resolution monochromator and photomultiplier detector assembly (PMA-C 192-N-M, PicoQuant GmbH).

3.5.2 Synthetic Procedures

Tetranitro-DBC

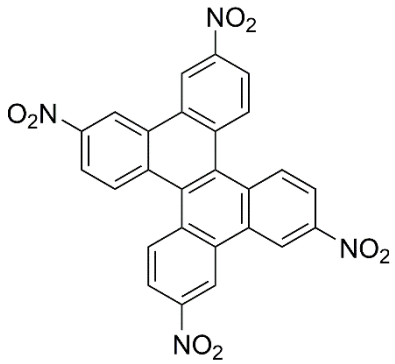

DBC (1.0 g, 3.0 mmol) was slowly added with stirring at 0 °C to a mixture of 10 mL nitric acid (≥ 99%) and 10 mL glacial acetic acid. After 10 min at 0 °C the solution was stirred at 100 °C for 2 h. The solution was poured into an ice-water mixture. The resulting precipitate was filtered, washed with 1,4-dioxane and recrystallized from nitrobenzene. After filtration and extensive washing with ethanol, 1.1 g of a yellow solid of tetranitro-DBC with 69% yield were obtained.

MS-EI: calculated (m/z): 508.066, measured (m/z): 508.065.

Tetraamino-DBC (adapted from Lu et al.[1])

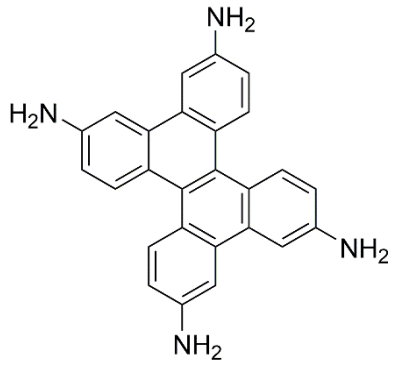

Under argon, tetranitro-DBC (500 mg, 0.98 mmol) was dissolved in 80 mL of anhydrous THF in a flame-dried 500 mL flask. Approximately 2.3 g of Raney-nickel catalyst slurry was added to the mixture with stirring. Hydrazine monohydrate (0.67 mL, 8.8 mmol) was added dropwise to the stirred mixture. The resulting solution was heated to reflux for two hours. The solution was allowed to cool to room temperature and filtered. The filtrate was dried under reduced pressure, giving 320 mg of a yellowish-greenish solid with 84% yield.

^{1}H NMR (400 MHz, DMSO-d_6) δ (ppm): 8.15 (d, J = 8.8 Hz, 4H, CH), 7.56 (d, J = 2.3 Hz, 4H, CH), 6.90 (dd, J = 8.8, 2.3 Hz, 4H, CH), 5.39 (s, 8H, NH_2). MS-EI: calculated (m/z): 388.169, measured (m/z): 388.168.

Synthesis of TA DBC-COF

In a 6 mL culture tube, terephthalaldehyde (4.02 mg, 30.0 µmol) and DBCA (5.83 mg, 15.0 µmol) were suspended in a mixture of BnOH and mesitylene (500 µL, v:v 9:1). After adding 50 µL of acetic acid (aqueous, 6 M) the tube was sealed and heated at 120 °C for 72 h. The resulting precipitate was filtered and rinsed with anhydrous THF before Soxhlet extraction with anhydrous THF for 12 h. The final product was vacuum-dried, to yield 5.07 mg (58%) as a light brown powder.

Synthesis of Biph DBC-COF

In a 6 mL culture tube, 4,4'-biphenyldicarboxaldehyde (6.31 mg, 30.0 µmol) and DBCA (5.83 mg, 15.0 µmol) were suspended in a mixture of BnOH and mesitylene (500 µL, v:v 1:1). After adding 50 µL of acetic acid (aqueous, 6 M) the culture tube was sealed and heated at 120 °C for 72 h. The resulting precipitate was filtered and rinsed with anhydrous THF before Soxhlet extraction with anhydrous THF for 12 h. The final product was vacuum-dried, to yield 5.47 mg (50%) as a brown powder.

Synthesis of TT DBC-COF

In a 6 mL culture tube, thieno[3,2-*b*]thiophene-2,5-dicarboxaldehyde (5.89 mg, 30.0 µmol) and DBCA (5.83 mg, 15.0 µmol) were suspended in a mixture of BnOH and mesitylene (500 µL, v:v 9:1). After adding 50 µL of acetic acid (aqueous, 6 M) the tube was sealed and heated at 120 °C for 72 h. The resulting precipitate was filtered and rinsed with anhydrous THF before Soxhlet extraction with anhydrous THF for 12 h. The final product was vacuum-dried, to yield 5.87 mg (55%) as a red powder.

Synthesis of analogue 4PE COFs

The ETTA-based COFs, 4PE-1P, 4PE-2P and 4PE-TT, are well-studied COF systems. Their synthesis here was carried out under the reported conditions previously reported in the literature.[2]

3.5.3 Electron Microscopy

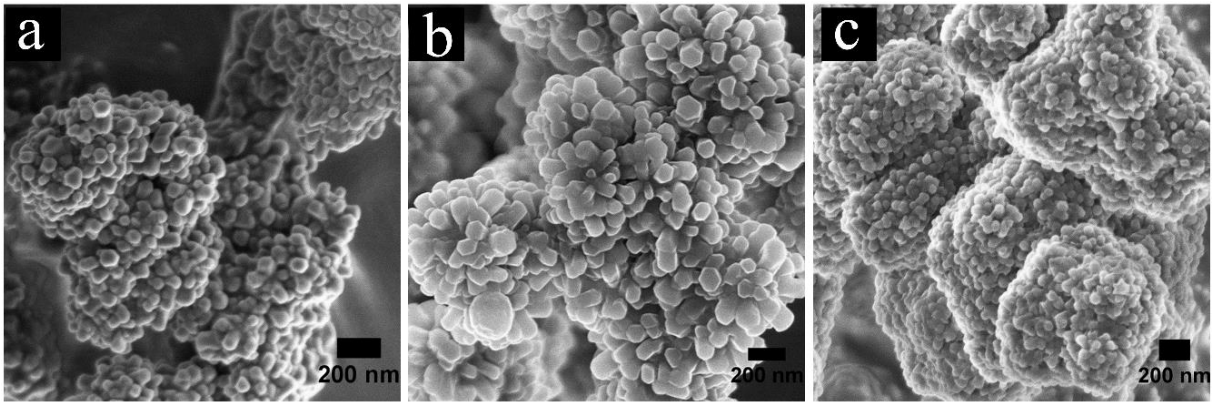

Figure 3.4: SEM images of TA DBC-COF (a), Biph DBC-COF (b) and TT DBC-COF (c). A hexagonal morphology is visible for many of the crystallites.

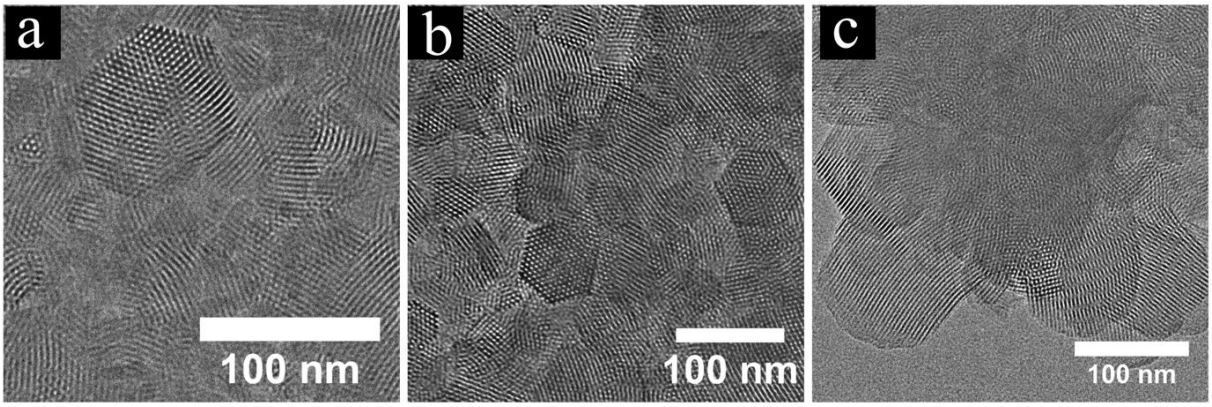

Figure 3.5: TEM images of TA DBC-COF (a), Biph DBC-COF (b) and TT DBC-COF (c). The long-range order of the hexagonal crystallites is apparent from the large domains of about 50 to 100 nm.

3.5.4 X-Ray Diffraction

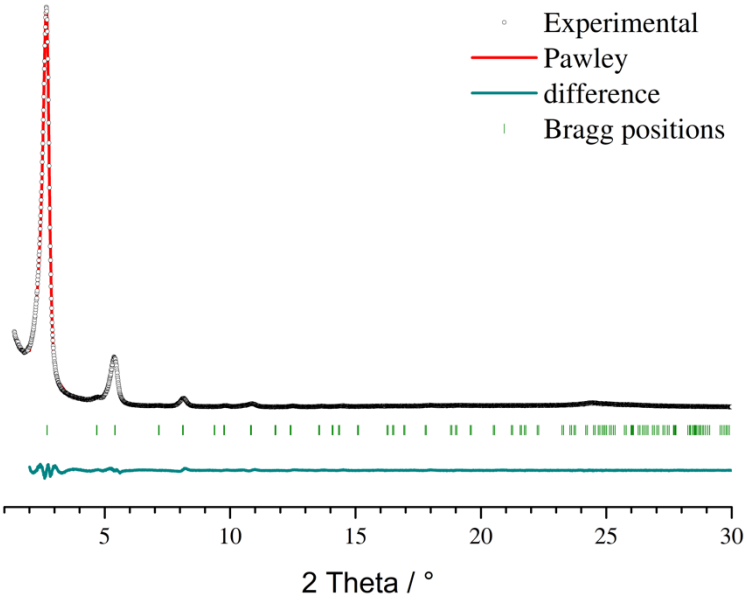

Figure 3.6: Pawley refinement of TA DBC-COF. Experimental (black), Pawley refined simulation (red), difference (navy) and Bragg positions (olive) show good agreement of experimental and simulated PXRD patterns.

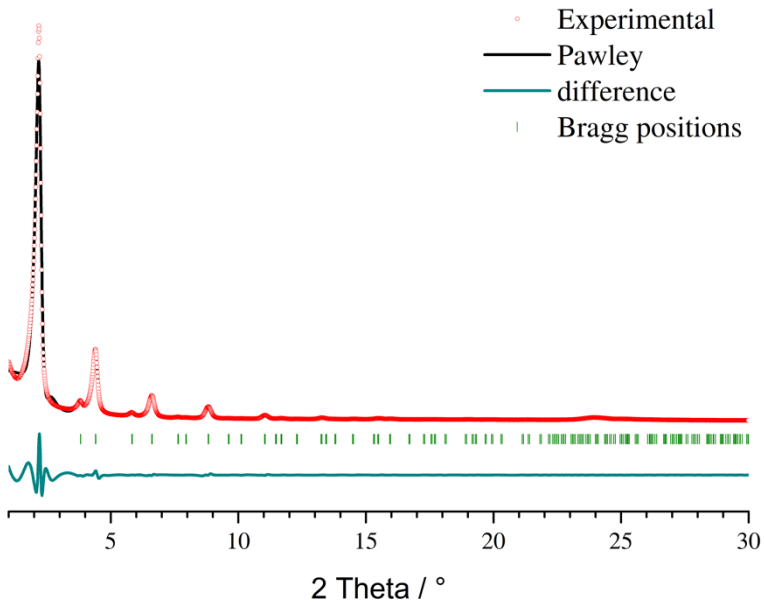

Figure 3.7: Pawley refinement of Biph DBC-COF. Experimental (red), Pawley refined simulation (black), difference (navy) and Bragg positions (olive) show good agreement of experimental and simulated PXRD patterns.

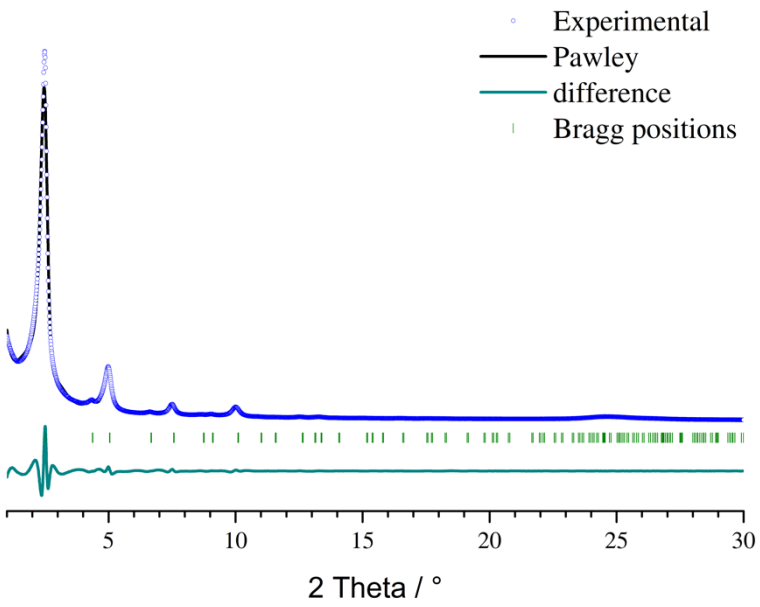

Figure 3.8: Pawley refinement of TT DBC-COF. Experimental (blue), Pawley refined simulation (black), difference (navy) and Bragg positions (olive) show good agreement of experimental and simulated PXRD patterns.

3.5.5 Sorption

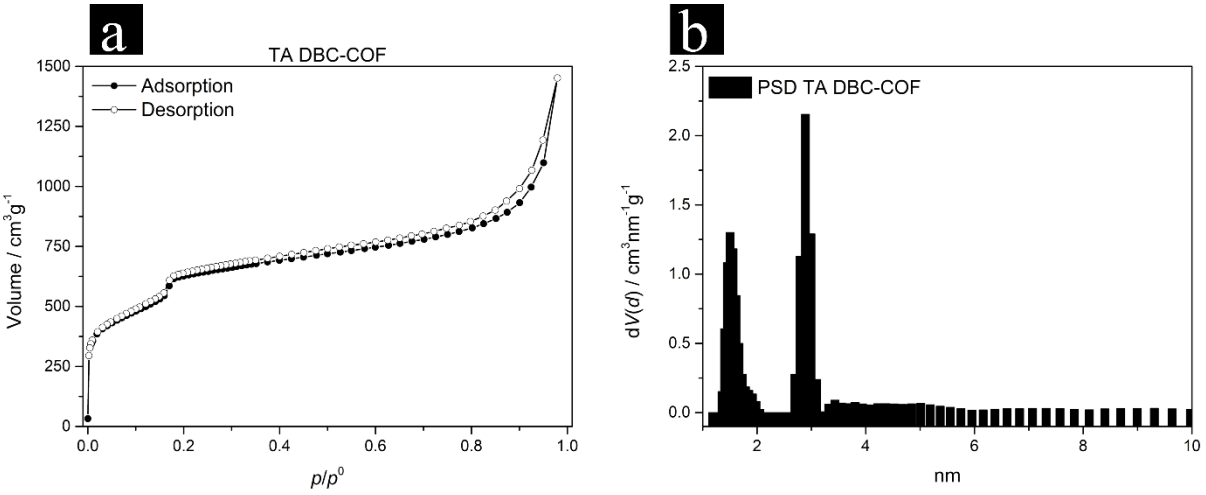

Figure 3.9: Nitrogen physisorption isotherm of TA DBC-COF (a) and the corresponding PSD with a QSDFT carbon equilibrium kernel for cylindrical pores reveal the dual-pore COF-structure (b).

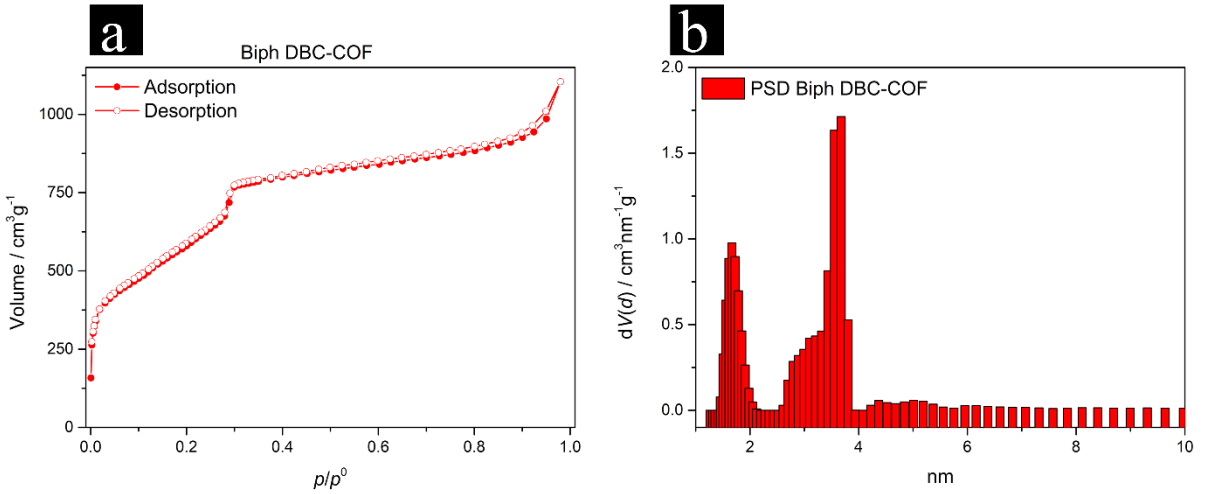

Figure 3.10: Nitrogen physisorption isotherm of Biph DBC-COF (a) and the corresponding PSD with a QSDFT carbon equilibrium kernel for cylindrical pores reveal the dual-pore COF-structure (b).

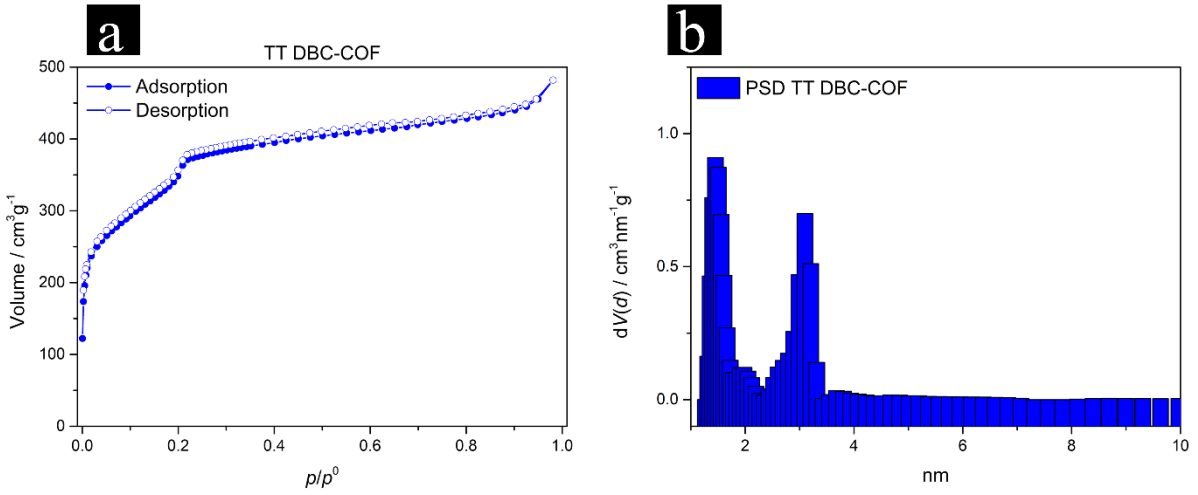

Figure 3.11: Nitrogen physisorption isotherm of TT DBC-COF (a) and the corresponding PSD with a QSDFT carbon kernel for cylindrical pores reveal the dual-pore COF-structure (b).

The first steep uptakes at very low p/p^0 in Figure 3.9-3.11 indicate the micropore filling, while the second one (p/p^0 = 0.15 to 0.35) represents the capillary condensation within the mesopores, respectively. Due to the comparably small size of the mesopores (≤ 4 nm), a type IVb physisorption isotherm without a hysteresis loop is obtained.[3] The pore size distribution was calculated from the equilibrium branch (desorption) with QSDFT with a carbon kernel for cylindrical pore geometry, respectively.

3.5.6 Structural Simulations of DBC-COFs

Space group: *P*6 with an AA-hexagonal eclipsed stacking (AA-H).

Table 3.1: Fractional atomic coordinates for the unit cell of AA-H calculated with Materials Studio v7.0 modeling program for TA DBC-COF.

P*6* (168) – hexagonal			
a = b = 347762(9) nm, c = 0.3611(6) nm			
α = β = 90°, γ = 120°			
Atom	**x/a**	**y/b**	**z/c**
C1	0.48191	0.48325	0.48052
C2	0.55441	0.51297	0.42694
C3	0.52066	0.55641	0.54156
C4	0.59020	0.54403	0.29244
C5	0.62475	0.54203	0.29230
C6	0.62425	0.50820	0.42101
C7	0.58821	0.47561	0.51286
C8	0.55272	0.47667	0.48965
C9	0.44374	0.40906	0.63294
C10	0.44115	0.37230	0.64931
C11	0.47408	0.36870	0.58695
C12	0.51035	0.40275	0.52521
C13	0.51377	0.44046	0.52582
N14	0.65911	0.50510	0.45965
N15	0.46921	0.32992	0.56729

C16	0.49663	0.32108	0.62398
C17	0.69535	0.53248	0.40083
Atom	**x/a**	**y/b**	**z/c**
H18	0.59210	0.57034	0.18775
H19	0.65141	0.56709	0.19352
H20	0.58881	0.44988	0.60748
H21	0.41715	0.40928	0.69160
H22	0.41317	0.34619	0.70662
H23	0.53515	0.39927	0.45855
H24	0.70243	0.56149	0.31031
C25	0.72818	0.52481	0.46130
C26	0.76693	0.55452	0.38691
C27	0.79842	0.54785	0.44169
C28	0.79169	0.51129	0.57228
C29	0.75295	0.48161	0.64787
C30	0.72145	0.48829	0.59315
H31	0.77280	0.58279	0.28273
H32	0.82803	0.57105	0.37785
H33	0.74708	0.45329	0.75074
H34	0.69183	0.46504	0.65574
H35	0.47430	0.65667	0.71292

Table 3.2: Fractional atomic coordinates for the unit cell of AA-H calculated with Materials Studio v7.0 modeling program for Biph DBC-COF.

P*6* (168) – hexagonal			
a = b = 4.6299(9) nm, c = 0.4017(6) nm			
α = β = 90°, γ = 120°			
Atom	**x/a**	**y/b**	**z/c**
C1	0.48657	0.48523	0.40595
C2	0.54747	0.51934	0.47987
C3	0.51209	0.54571	0.33928
C4	0.57621	0.54952	0.58548
C5	0.60724	0.55217	0.64763
C6	0.61072	0.52399	0.61072
C7	0.58252	0.49341	0.52786
C8	0.55050	0.48998	0.47046
C9	0.46428	0.42667	0.20464
C10	0.46592	0.39731	0.18524
C11	0.49474	0.39752	0.29305
C12	0.52262	0.42804	0.38814
C13	0.52182	0.45850	0.39736
N14	0.63973	0.52397	0.64491
Atom	**x/a**	**y/b**	**z/c**
N15	0.49293	0.36755	0.31443
C16	0.51695	0.35928	0.35322

C17	0.67165	0.54914	0.67079
C18	0.69733	0.54129	0.67394
C19	0.72920	0.56440	0.54611
C20	0.75392	0.55532	0.51221
C21	0.74763	0.52321	0.61062
C22	0.71632	0.50088	0.75625
C23	0.69152	0.50981	0.78764
C24	0.77174	0.51343	0.55738
C25	0.76261	0.48184	0.41627
C26	0.78678	0.47255	0.35085
C27	0.82080	0.49480	0.42288
C28	0.82988	0.52607	0.57053
C29	0.80569	0.53521	0.63833
H30	0.57550	0.57078	0.62568
H31	0.62702	0.57457	0.71974
H32	0.58659	0.47382	0.50670
H33	0.44290	0.42517	0.12112
H34	0.44592	0.37570	0.09814
H35	0.54311	0.42699	0.45890
H36	0.67735	0.57358	0.66739
H37	0.73437	0.58762	0.46757
H38	0.77636	0.57219	0.40737

H39	0.71121	0.47784	0.83934
H40	0.66899	0.49303	0.89182
H41	0.73825	0.46540	0.35523
H42	0.77938	0.44963	0.24633
H43	0.85426	0.54239	0.63296
H44	0.81311	0.55787	0.74889
H45	0.83795	0.46094	0.33347

Table 3.3: Fractional atomic coordinates for the unit cell of AA-H calculated with Materials Studio v7.0 modeling program for TT DBC-COF.

P*6* (168) – hexagonal			
a = b = 4.0444(2) nm, c = 0.3782(7) nm			
α = β = 90°, γ = 120°			
Atom	**x/a**	**y/b**	**z/c**
C1	0.0338	0.48331	0.55114
C2	0.03593	0.45208	0.66021
C3	0.06869	0.45123	0.67445
C4	0.10173	0.48243	0.58930
C5	0.10105	0.51468	0.51320
C6	0.06812	0.51646	0.51685
N7	0.13190	0.47895	0.58251
C8	0.16786	0.50433	0.56654
C9	0.19472	0.49415	0.53650

S10	0.18458	0.44890	0.46926
C11	0.23115	0.46555	0.45473
C12	0.25258	0.50249	0.50360
C13	0.23222	0.51956	0.55076
C14	0.25154	0.44857	0.40208
C15	0.28904	0.47401	0.41620
S16	0.29915	0.51912	0.49306
C17	0.31599	0.46407	0.37540
C18	0.48282	0.48310	0.49344
N19	0.44993	0.48486	0.43522
C20	0.44981	0.51846	0.47705
C21	0.41555	0.51758	0.48434
C22	0.38229	0.48620	0.40126
C23	0.38319	0.45469	0.30274
C24	0.41632	0.45455	0.31703
N25	0.35176	0.48897	0.42046
H26	0.06849	0.42769	0.74564
Atom	**x/a**	**y/b**	**z/c**
H27	0.12536	0.53671	0.44594
H28	0.17600	0.53155	0.57639
H29	0.24348	0.54707	0.58927
H30	0.24031	0.42112	0.35984

H31	0.30814	0.43753	0.31501
H32	0.41364	0.53983	0.55603
H33	0.35995	0.43173	0.22183
H34	0.41493	0.43116	0.23370
H35	0.01350	0.42866	0.73592

3.5.7 Crystallographic Data

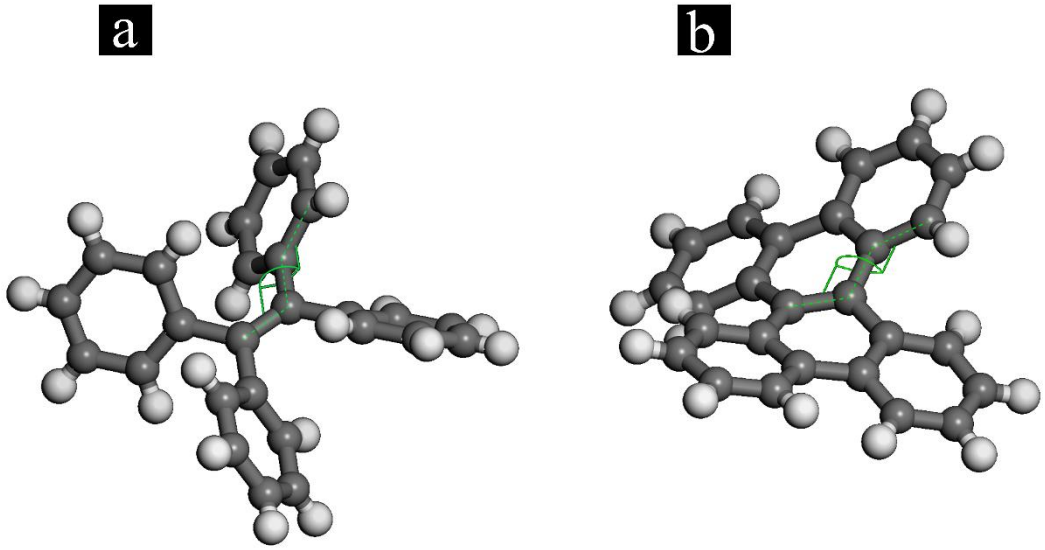

Figure 3.12: The calculated dihedral angle (green) of (a) ETTA and (b) DBC cores of the respective amine-functionalized building blocks. The molecular models are based on reported crystallographic data for the respective compounds, ETTA[4] and DBC.[5] It is evident that the dihedral angle of ETTA is much larger (47.3°) due to steric crowding caused by the phenyl-substituted ethylene moiety. In the case of DBC, the aromatic rings fused to the naphthalene core force the system to stay more planar (dihedral angle of 24.7°).

3.5.8 IR Spectroscopy

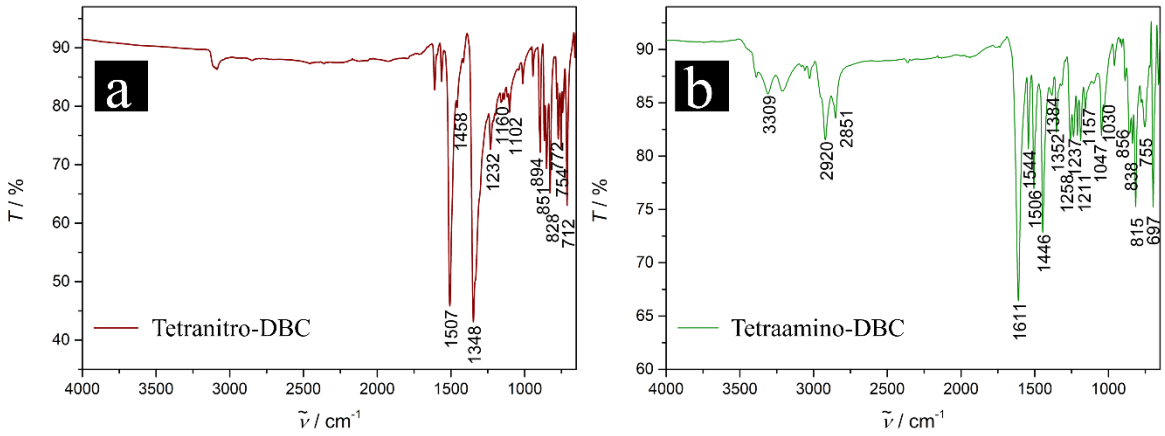

Figure 3.13: IR spectra of tetranitro- (a) and tetraamino-DBC (DBCA) (b).

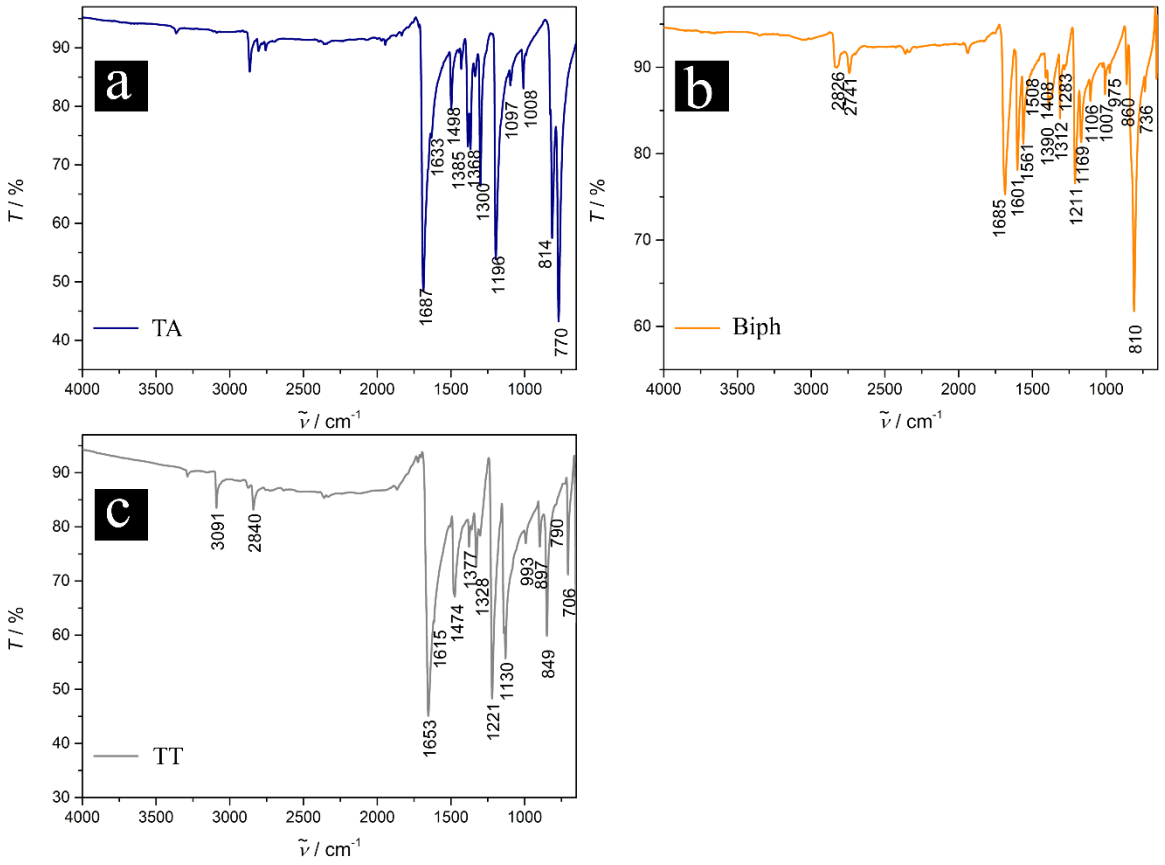

Figure 3.14: IR spectra of TA (a), Biph (b) and TT (c) precursors.

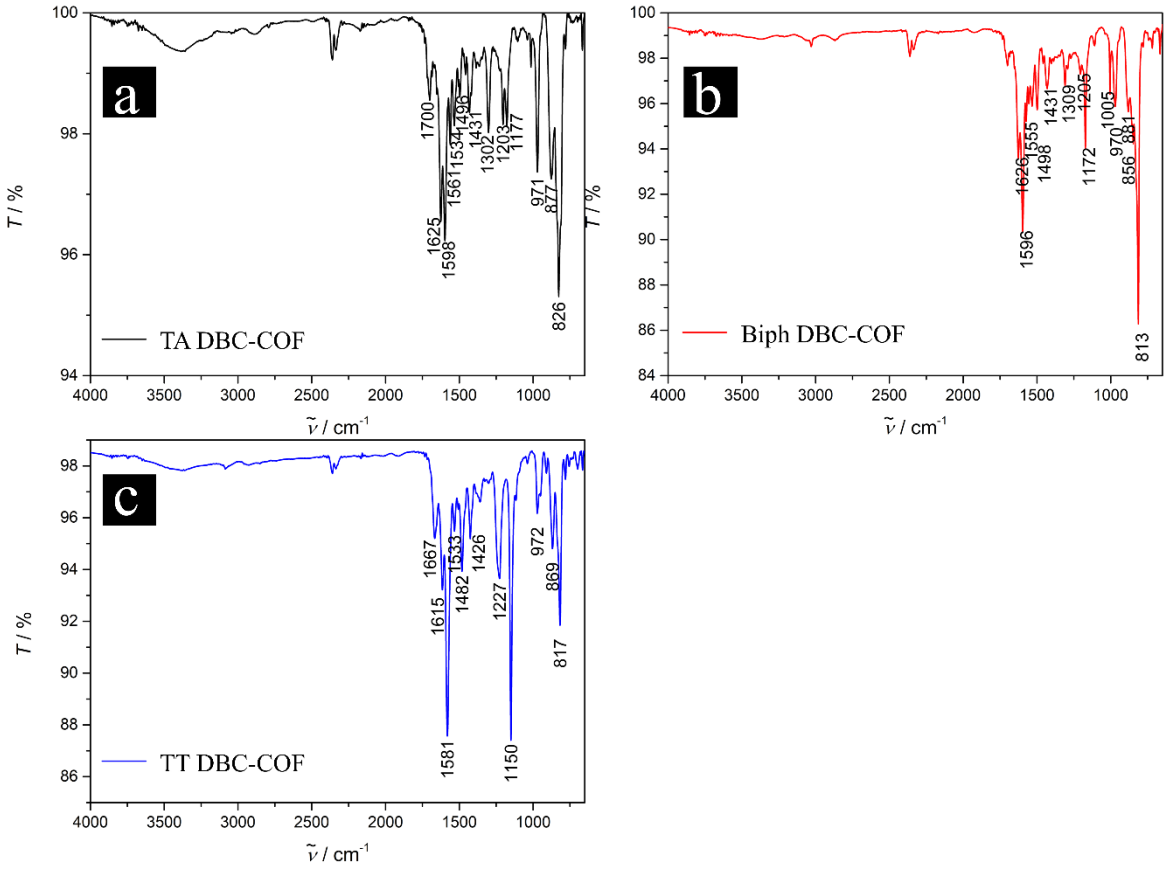

Figure 3.15: IR spectra of the synthesized DBC-COFs, namely TA DBC-COF (a), Biph DBC-COF (b) and TT DBC-COF (c).

3.5.9 UV-Vis Spectroscopy

Absorption spectra of the DBC-COFs were collected from solid samples in diffuse reflectance mode and transferred into absorption spectra by applying the Kubelka Munk equation.

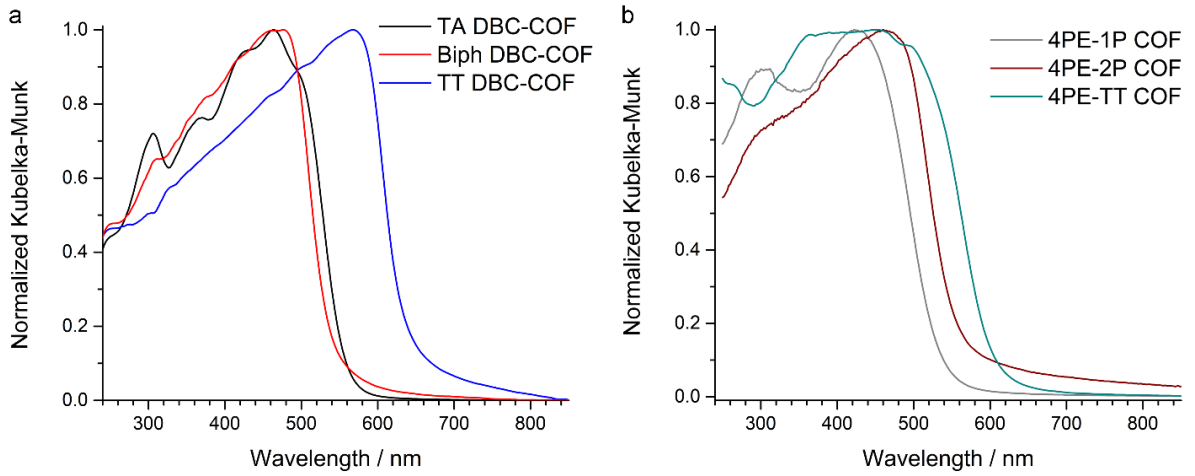

Figure 3.16: Optical absorption spectra of the DBC-COFs (a) vs. the analogue 4PE COFs (b) measured as diffuse reflectance spectra of the solid and converted with the Kubelka Munk equation.

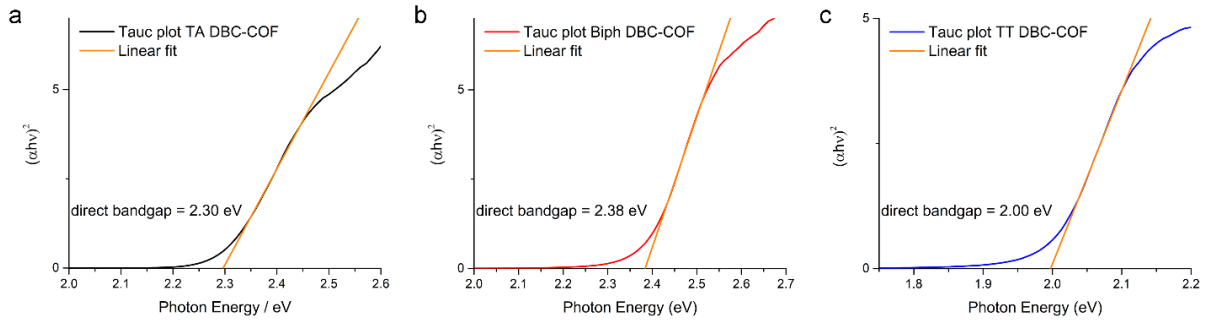

Figure 3.17: Tauc plots of the DBC-based COFs with a linear fit illustrated in orange.

3.5.10 Photoluminescence Spectroscopy

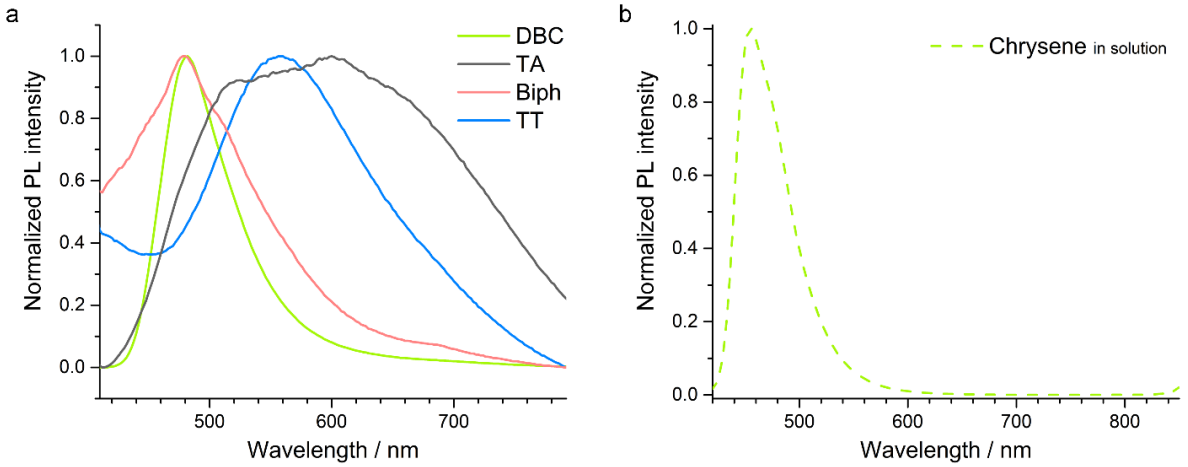

Figure 3.18: (a) Normalized PL spectra of the solid precursors tetraamino-DBC, TT, Biph and TA obtained with 378 nm excitation. By far the highest emission intensity resulted from excitation of DBC. (b) Normalized PL spectrum of DBC measured as solution in 1,4-dioxane (50 µM) and excited by a 378 nm laser. A strong emission could be detected at 480 nm.

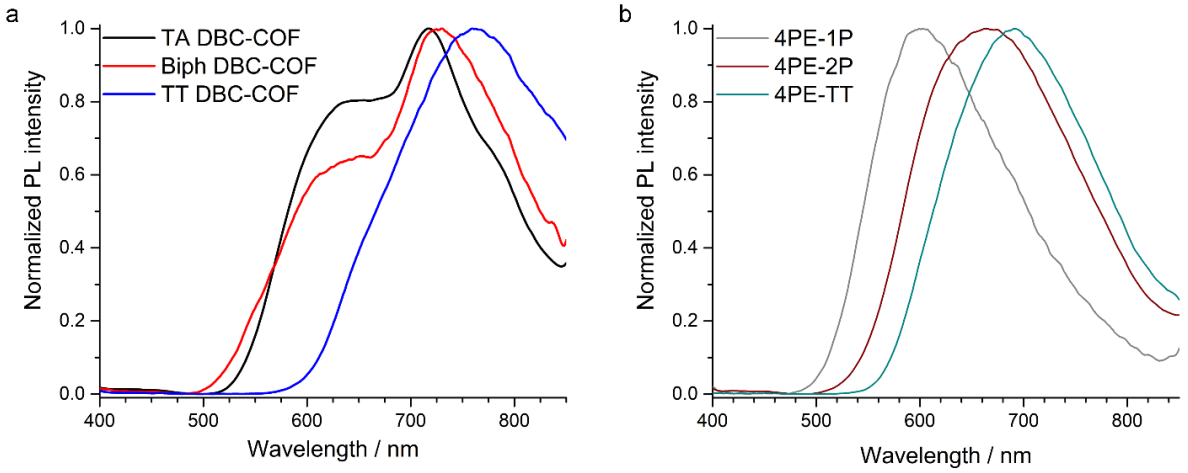

Figure 3.19: PL spectra of TA, Biph and TT DBC-COF (a) and of 4PE-1P, -2P and -TT COF (b). All compounds were measured as solids.

3.5.11 Time-Correlated Single Photon Counting

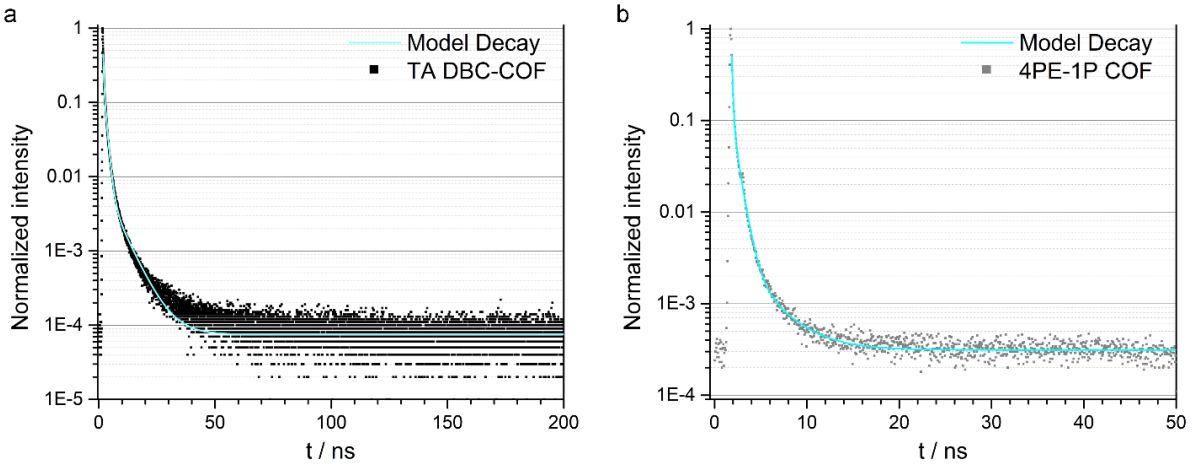

Figure 3.20: (a) PL decay of TA DBC-COF excited at 378 nm and measured at the maximum of the PL emission at 718 nm. (b) PL decay of 4PE-1P COF excited at 378 nm and measured at the maximum of the PL emission at 597 nm. Experimental decay: black (TA DBC-COF), grey (4PE-1P COF) dots, tri-exponential fit of the decay: cyan line.

Table 3.4: PL decay times of TA DBC-COF shown above. The given errors are uncertainties from the fit and hence do not reflect the real time-resolution of the setup. The latter is limited by the laser pulse duration of around 100 ps.

	τ / ns	error / ns	fractional intensity / %
τ_1	6.3	±0.2	15
τ_2	1.1	±0.02	65
τ_3	0.25	±0.01	20

Table 3.5: PL decay times of 4PE-1P COF shown above. The given errors are uncertainties from the fit and hence do not reflect the real time-resolution of the setup. The latter is limited by the laser pulse duration of around 100 ps.

	τ / ns	error / ns	fractional intensity / %
τ_1	3.2	±0.2	8
τ_2	0.66	±0.01	54
τ_3	0.12	±0.004	38

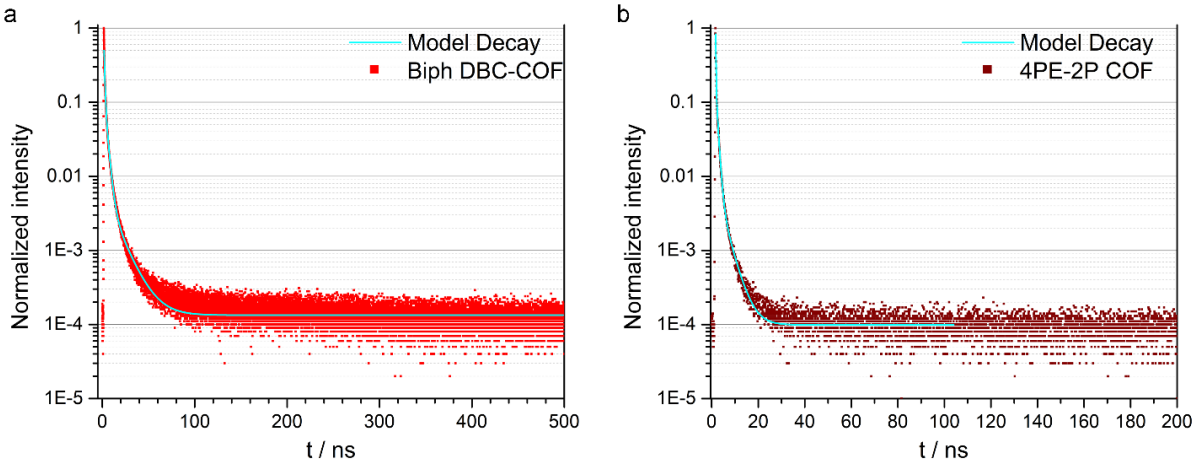

Figure 3.21: (a) PL decay of Biph DBC-COF excited at 378 nm and measured at the maximum of the PL emission at 724 nm. (b) PL decay of 4PE-2P COF excited at 378 nm and measured at the maximum of the PL emission at 643 nm. Experimental decay: red (Biph DBC-COF), wine-red (4PE-2P COF) dots, tri-exponential fit of the decay: cyan line.

Table 3.6: PL decay times of Biph DBC-COF shown above. The given errors are uncertainties from the fit and hence do not reflect the real time-resolution of the setup. The latter is limited by the laser pulse duration of around 100 ps.

	τ / ns	error / ns	fractional intensity / %
τ_1	14.1	±0.6	12
τ_2	2.8	±0.06	50
τ_3	0.71	±0.02	38

Table 3.7: PL decay times of 4PE-2P COF shown above. The given errors are uncertainties from the fit and hence do not reflect the real time-resolution of the setup. The latter is limited by the laser pulse duration of around 100 ps.

	τ / ns	error / ns	fractional intensity / %
τ_1	3.6	±0.1	11
τ_2	0.80	±0.01	50
τ_3	0.14	±0.003	39

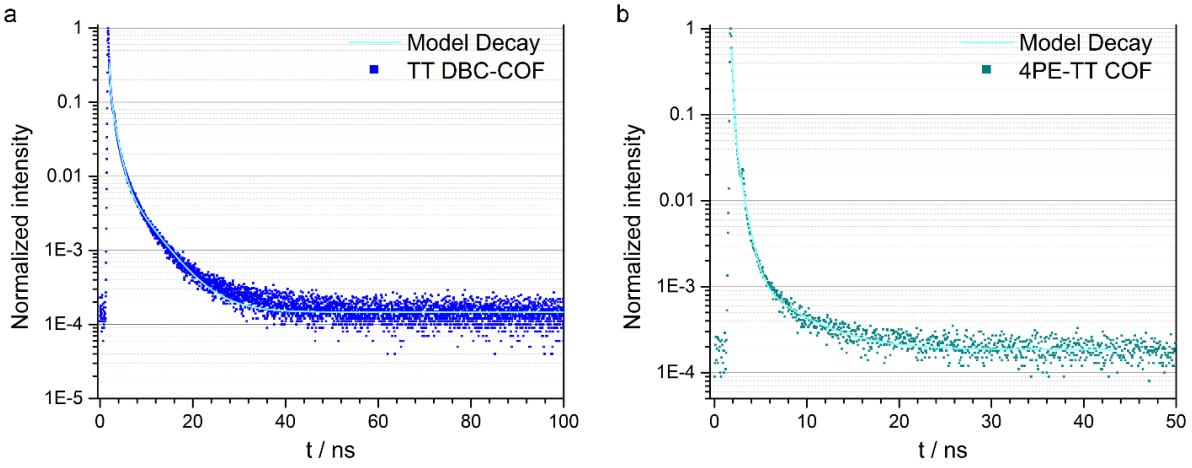

Figure 3.22: (a) PL decay of TT DBC-COF excited at 378 nm and measured at the maximum of the PL emission at 758 nm. (b) PL decay of 4PE-TT COF excited at 378 nm and measured at the maximum of the PL emission at 683 nm. Experimental decay: blue (TA DBC-COF), green (4PE-TT COF) dots, tri-exponential fit of the decay: cyan line.

Table 3.8: PL decay times of TT DBC-COF shown above. The given errors are uncertainties from the fit and hence do not reflect the real time-resolution of the setup. The latter is limited by the laser pulse duration of around 100 ps.

	τ / ns	error / ns	fractional intensity / %
τ_1	5.0	±0.1	25
τ_2	1.0	±0.02	60
τ_3	0.20	±0.01	15

Table 3.9: PL decay times of 4PE-TT COF shown above. The given errors are uncertainties from the fit and hence do not reflect the real time-resolution of the setup. The latter is limited by the laser pulse duration of around 100 ps.

	τ / ns	error / ns	fractional intensity / %
τ_1	4.5	±0.4	5
τ_2	0.65	±0.01	41
τ_3	0.14	±0.003	54

3.5.12 Thermogravimetric Analysis

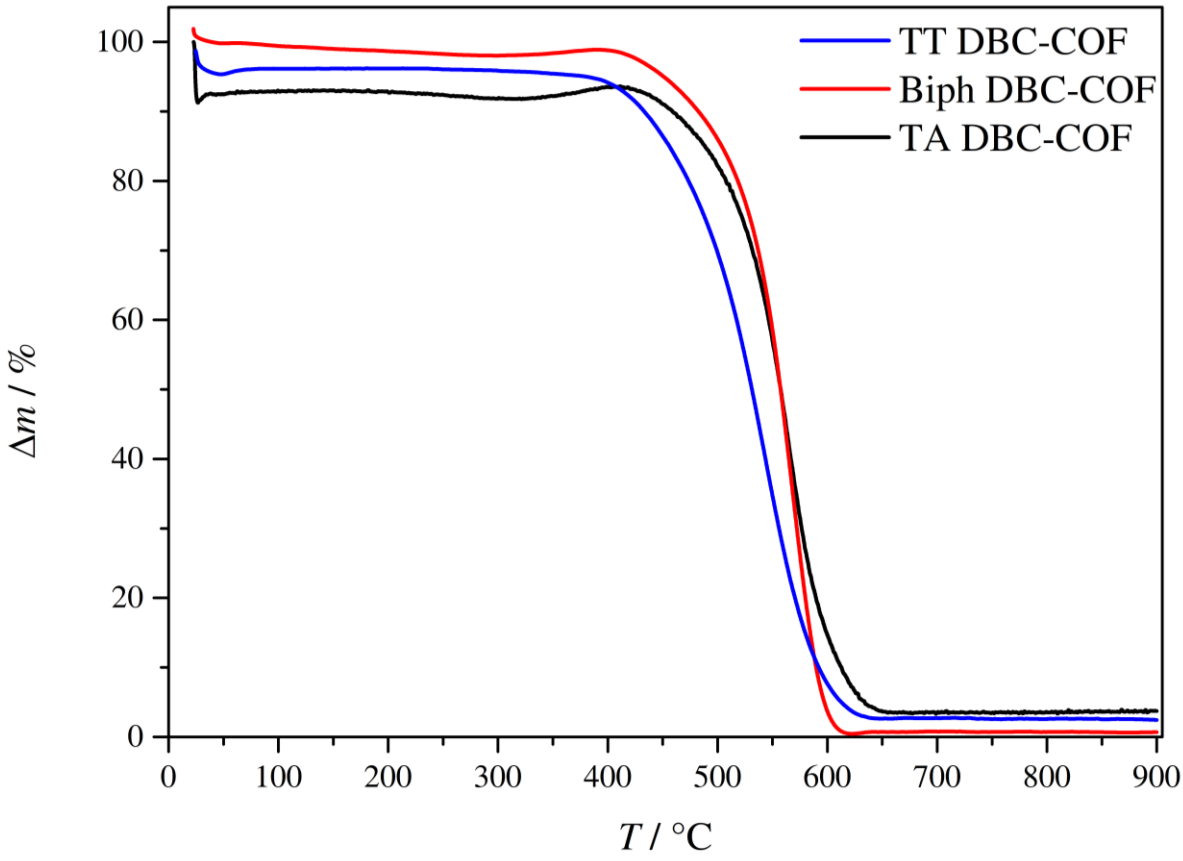

Figure 3.23: Thermogravimetric analysis of DBC COFs. TA DBC-COF (black), Biph DBC-COF (red) and TT DBC-COF (blue) are all stable until 350 °C under a heating rate of 10°C/min and under synthetic air (N_2/O_2 V/V 79.5/20.5, 25 mL min^{-1}).

3.5.13 Elemental Analysis

Table 3.10: Elemental analysis of TA DBC-COF bulk material compared with the calculated mass percentages.

	TA DBC-COF	
Element	Theoretical percentage	Measured percentage
N	9.58	8.49
C	86.28	77.68
H	4.14	4.70

Table 3.11: Elemental analysis of Biph DBC-COF bulk material compared with the calculated mass percentages.

	Biph DBC-COF	
Element	Theoretical percentage	Measured percentage
N	7.60	7.63
C	88.02	83.35
H	4.38	4.59

Table 3.12: Elemental analysis of TT DBC-COF bulk material compared with the calculated mass percentages.

	TT DBC-COF	
Element	Theoretical percentage	Measured percentage
N	7.90	7.01
C	71.16	65.73
H	2.84	3.19
S	18.09	16.64

3.5.14 NMR Spectroscopy

^{1}H, 400 MHz, DMSO-d_6

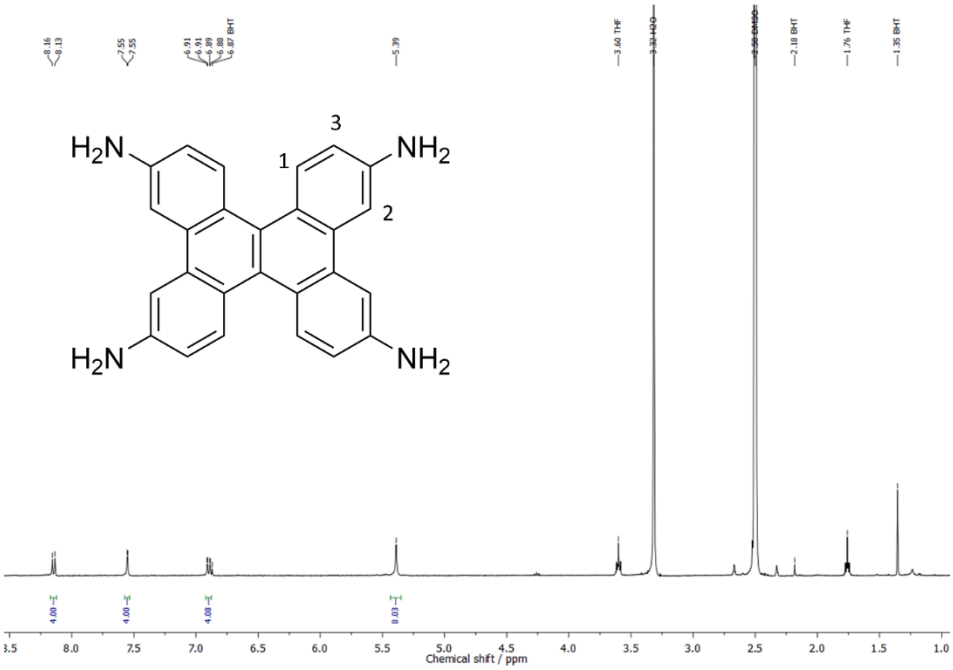

^{13}C, 100 MHz, DMSO-d_6

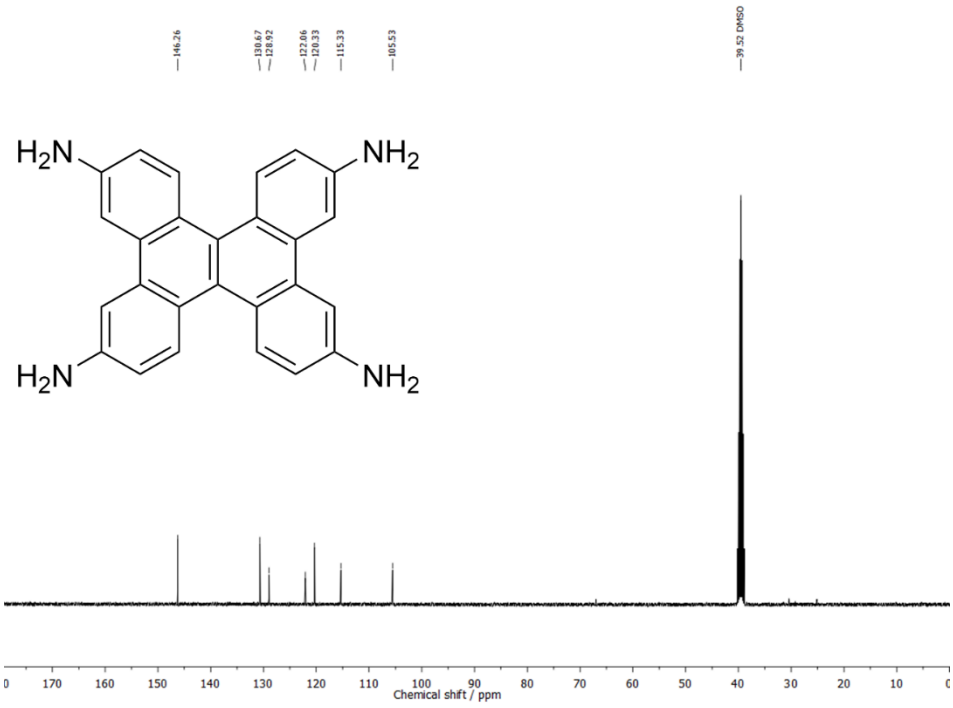

3.5.15 References

[1] Lu, J.; Zhang, J., Facile synthesis of azo-linked porous organic frameworks via reductive homocoupling for selective CO2 capture. *J. Mater. Chem. A* **2014,** *2* (34), 13831-13834.

[2] Ascherl, L.; Sick, T.; Margraf, J. T.; Lapidus, S. H.; Calik, M.; Hettstedt, C.; Karaghiosoff, K.; Döblinger, M.; Clark, T.; Chapman, K. W.; Auras, F.; Bein, T., Molecular docking sites designed for the generation of highly crystalline covalent organic frameworks. *Nat. Chem.* **2016,** *8* (4), 310-316.

[3] Thommes, M.; Kaneko, K.; Neimark, A. V.; Olivier, J. P.; Rodriguez-Reinoso, F.; Rouquerol, J.; Sing, K. S. W., Physisorption of gases, with special reference to the evaluation of surface area and pore size distribution (IUPAC Technical Report). *Pure Appl. Chem.* **2015,** *87* (9-10), 1051.

[4] Zhang, G.-F.; Chen, Z.-Q.; Aldred, M. P.; Hu, Z.; Chen, T.; Huang, Z.; Meng, X.; Zhu, M.-Q., Direct validation of the restriction of intramolecular rotation hypothesis via the synthesis of novel ortho-methyl substituted tetraphenylethenes and their application in cell imaging. *Chem. Commun.* **2014,** *50* (81), 12058-12060.

[5] Hatakeyama, T.; Hashimoto, S.; Seki, S.; Nakamura, M., Synthesis of BN-Fused Polycyclic Aromatics via Tandem Intramolecular Electrophilic Arene Borylation. *J. Am. Chem. Soc.* **2011,** *133* (46), 18614-18617.

4 Enforcing Extended Porphyrin J-Aggregate Stacking in Covalent Organic Frameworks

This chapter is published as:

Niklas Keller, Mona Calik, Dmitry Sharapa, Himadri R. Soni, Peter M. Zehetmaier, Sabrina Rager, Florian Auras, Andreas C. Jakowetz, Andreas Görling, Timothy Clark, and Thomas Bein, *J. Am. Soc. Chem.* **2018**, *140*, pp 16544–16552.

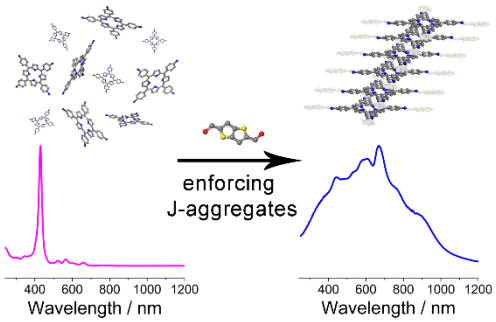

The potential of covalent organic frameworks (COFs) for realizing porous, crystalline networks with tailored combinations of functional building blocks has attracted considerable scientific interest in the fields of gas storage, photocatalysis, and optoelectronics. Porphyrins are widely studied in biology and chemistry and constitute promising building blocks in the field of electroactive materials, but they reveal challenges regarding crystalline packing when introduced into COF structures due to their nonplanar configuration and strong electrostatic interactions between the heterocyclic porphyrin centers. A series of porphyrin-containing iminelinked COFs with linear bridges derived from terephthalaldehyde, 2,5-dimethoxybenzene-1,4-dicarboxaldehyde, 4,4′-biphenyldicarboxaldehyde and thieno[3,2-*b*]thiophene-2,5-dicarboxaldehyde, were synthesized, and their structural and optical properties were examined. By combining X-ray diffraction analysis with density-functional theory (DFT) calculations on multiple length scales, we were able to elucidate the crystal structure of the newly synthesized porphyrin-based COF containing thieno[3,2-*b*]thiophene-2,5-dicarboxaldehyde as linear bridge. Upon COF crystallization, the porphyrin nodes lose their 4-fold rotational symmetry, leading to the formation of extended slipped J-aggregate stacks. Steady-state and time-resolved optical spectroscopy techniques confirm the realization of the first porphyrin J-aggregates on a > 50 nm length scale with strongly red-shifted Q-bands and increased absorption strength. Using the COF as a structural template, we were thus able to

force the porphyrins into a covalently embedded J-aggregate arrangement. This approach could be transferred to other chromophores; hence, these COFs are promising model systems for applications in photocatalysis and solar light harvesting, as well as for potential applications in medicine and biology.

4.1 Introduction

Inspired by numerous natural examples, the self-assembly of molecules has attracted increasing attention as these evolving aggregates often exhibit unique electronic and spectroscopic characteristics. For example, self-assembled derivatives of tetrapyrrole macrocycles of the porphyrin family are of vital importance for natural light-harvesting and electron transfer processes. Thus, understanding and controlling the aggregation of supramolecular structures enables important insights in natural processes such as photosynthesis and in the context of synthetic optoelectronic systems including organic photovoltaics or photodynamic therapy (PDT).[1-2] Here, molecular assembly leads to emergent new features compared to the monomers such as excitonic coupling,[3] photoinduced electrontransfer,[4] nonlinear optics,[5] and activation of molecular oxygen.[6-7]

In addition to their enormous importance in natural systems, their extended π-electron system and semiconducting and photoconducting capabilities make porphyrins the most widely studied conjugated macrocycles.[5, 8-11] They exhibit high extinction coefficients in the visible and near-infrared (NIR) regions, where the maximum of the solar flux occurs, rendering them interesting candidates for solar light-harvesting.[12] Moreover, porphyrins can act as model systems in medicine and biology due to their close relationship to structures such as heme and chlorophyll. The latter is found in light-harvesting complexes present in plants and bacteria.[13-16]

Artificial aggregates of porphyrins have been the focus of many studies, and H-aggregates as well as J-aggregates have been obtained. While both types exhibit a parallel stacking of monomers, in H-aggregates, the monomer centers are aligned on top of each other. In contrast, the centers are offset in a “head-to-tail” fashion in J-aggregates. The resulting aggregate transition dipole moment, taking into account the possible parallel or antiparallel dipole moments on the individual monomers, is shifted to higher (H-type) or lower (J-type) energies, as described in the literature.[17-19] Therefore, controlling the stacking can directly influence the optical properties of a material. So far porphyrin J-aggregates have been synthesized as thin molecular films or dispersed in solutions (dependent on pH), thus limiting the versatility.[20-22]

In principle, this issue could be overcome by fixing chromophores in a solid matrix in a highly ordered structure, hence enforcing the system to aggregate in the desired fashion.

Here, we address this challenge by integrating two photoactive units, a tetragonal aminophenyl porphyrin linked to a thieno[3,2-*b*]thiophene-2,5-dicarboxaldehyde (TT) unit, through chemical bonds into a covalent organic framework. To the best of our knowledge, this is the first report on such an ordered porphyrin J-aggregate embedded in a solid matrix with novel optical characteristics, especially in the NIR region, that have not been observed with porphyrins to date. In contrast, H-aggregate formation has been observed in the porphyrin-containing COF-366 (see below).[23] Through targeted selection of molecular units, our synthetic strategy presents a new paradigm for creating highly crystalline solid-state J-aggregates, directed through the structural templating power of a covalent molecular framework.

Ordered in a COF structure, the combination of the above two building blocks leads to a reduction in local symmetry, which is caused by a staircase-like stacking behavior of the porphyrin-COF that causes a splitting of reflections in the X-ray diffraction pattern. This stacking motif results in the strong J-aggregate behavior within the porphyrin stack, which is locked by the surrounding framework structure and drastically changes the optoelectronic properties of the porphyrin moiety. The Q-bands in the absorption spectrum are not only red-shifted compared to the monomer in solution but also gain in transition dipole moment compared to the Soret band, while at the same time the fluorescence lifetime is strongly enhanced as compared to molecular porphyrin crystals.

The extended lattices of highly ordered and tightly packed chromophores in COFs combine novel optical behavior with the unique molecular accessibility of the porous network. Both are promising properties for applications in photovoltaic cells, optoelectronic devices, and could also be of great interest for chemical, medical, and biological applications.[24] For example, photodynamic therapy in medicine could be strongly enhanced by the nonlinear multiphoton absorption of aggregated chromophores and the open architecture of frameworks enabling the efficient conversion of $^3O_2$ to $^1O_2$ at the reactive porphyrin centers.

4.2 Results and Discussion

The new 2D TT-Por COF was synthesized by combining 5,10,15,20−tetrakis(4-aminophenyl)porphyrin (1) with thieno[3,2-*b*]thiophene-2,5-dicarboxaldehyde (TT) in a 1:2 molar ratio. The solvothermal reaction was carried out in a solvent mixture of benzyl alcohol, dichlorobenzene and 6 molar acetic acid (30:10:4, *v*:*v*:*v*) for 3 days at 120 °C, identified to be the optimal conditions following comprehensive screening of reaction parameters (Figure 4.1a, see appendix for experimental details). The porphyrin units, located at the corners, are linked by the linear TT to form an ordered structure with open channels (Figure 4.1b). Porphyrins have been integrated into various COF structures.[25-35] The resulting frameworks, with metallo- as well as free-base porphyrins, were found to exhibit an eclipsed structure, meaning that the 2D sheets lie on top of each other in an AA-stacking arrangement, while AB-stacking simulations did not agree with the experimental XRD patterns.[23, 30, 36-40] However, density-functional theory (DFT) calculations performed by different groups suggest that truly eclipsed structures are energetically disfavored in most frameworks and that COFs rather adopt structures with slightly offset layers.[41-43]

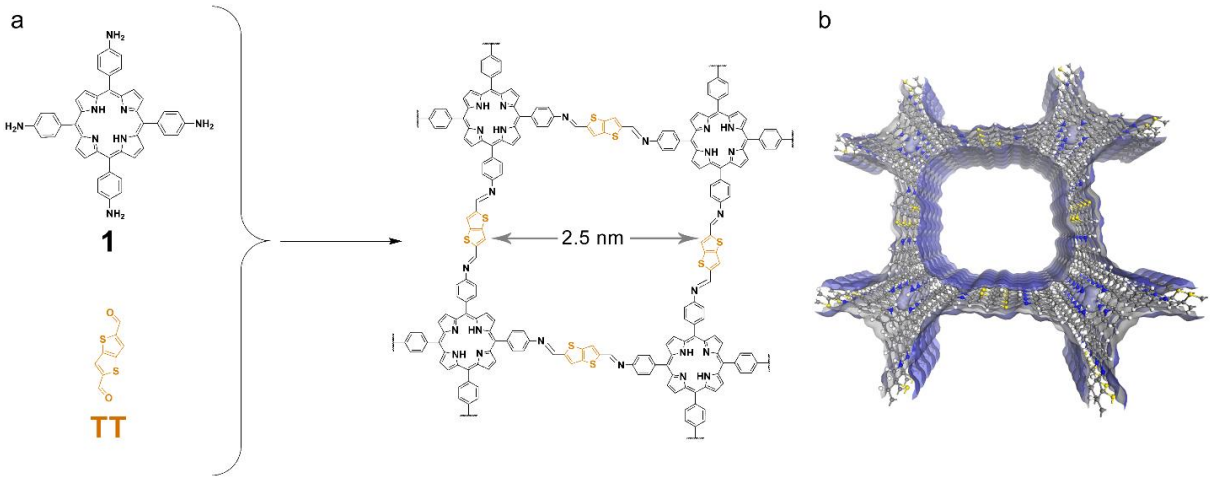

Figure 4.1: (a) Co-condensation reaction of 5,10,15,20−tetrakis(4-aminophenyl)porphyrin (1) and thieno[3,2-*b*]thiophene-2,5-dicarboxaldehyde (TT) in a 1:2 molar ratio to form the TT-Por COF, featuring tetragonal pores with a diameter of 2.5 nm. (b) Illustration of the TT-Por COF, showing the extended, 3-dimensional structure along the c-axis.

In a two-layer system, the offset can occur with the same probability in all symmetry-equivalent directions. However, only if the geometric conformation of this initial bilayer can be conveyed to the growing framework, translational symmetry is generated throughout the COF domain and can be observed via diffraction techniques.[44] While synchronizing the layer offset has become a very effective COF construction principle with C_2-symmetric building blocks,[44-46]

this has not been observed experimentally for building blocks of higher rotational symmetry.[41] In the case of the C_4-symmetric tetraphenyl porphyrin, generating an offset-stacked translational symmetry would require breaking the rotational symmetry of each porphyrin node.

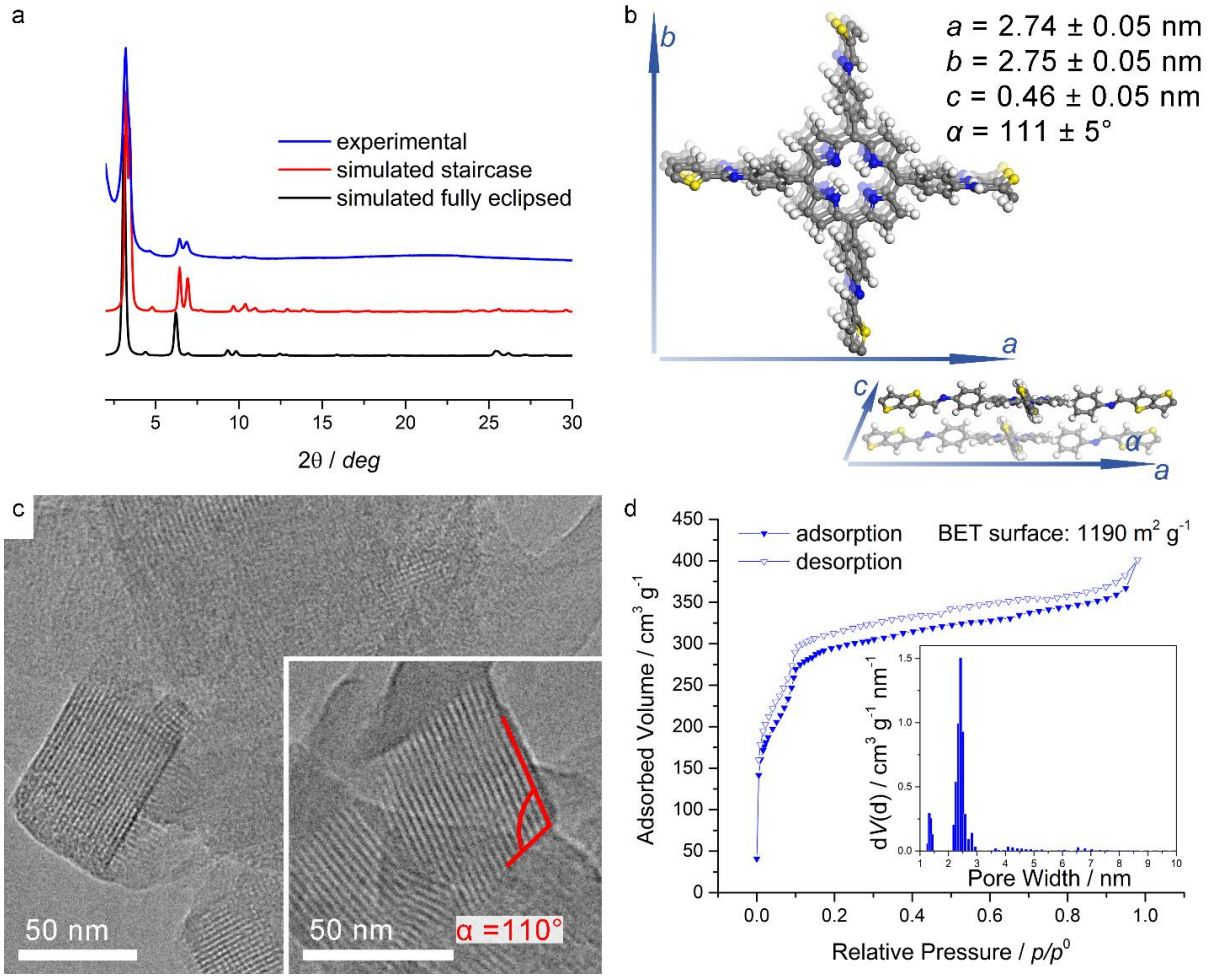

Figure 4.2: (a) Experimental PXRD data (blue) vs simulated patterns (red and black) for a fully eclipsed and (b) staircase arrangement of the 2D layers of TT-Por COF calculated by AM1. The theoretical XRD patterns were simulated for a crystallite size of 50 nm. (c) Transmission electron micrographs of TT-Por COF bulk material showing the rectangular pore structure with defined crystal facets (bottom left) and the staircase arrangement of the COF with an angle between adjacent layers of 110° (inset bottom right). (d) Nitrogen sorption isotherm of a TT-Por COF powder sample measured at 77 K. The corresponding pore size distribution (inset) with an average pore size of 2.4 nm was obtained by fitting the experimental data using an NLDFT adsorption branch model.

Powder X-ray diffraction (PXRD) measurements of the synthesized bulk material confirmed the formation of a crystalline porphyrin COF. To identify the structure, the calculated pattern of an eclipsed P_4-symmetric AA-stacking arrangement was compared to experimental data but did not match (Figure 4.2a). The size of the unit cell, given by the position of the 100 reflection, however, is in good agreement with the experimental data, suggesting only slight deviations in the unit cell. Both a shoulder on the 100 reflection and a splitting of the 200 reflection into two new distinct peaks indicate a loss in symmetry of the unit cell. Optimizing the geometry,

including all unit cell parameters and using a periodic force-field treatment resulted in a simulated pattern that matches the experimental one. In order to produce the correct pattern without neglecting the geometry of the building blocks, the unit cell parameter γ must deviate from 90°, resulting in an offset of the adjacent layers (Figure 4.2a,b). This offset results in a staircase-like stacking behavior, which is prevalent in one direction and can be distinctly recognized in the PXRD pattern (Figure 4.2a).

Computer simulations were performed at three different levels of theory: DFT to obtain accurate intermolecular interactions, semiempirical molecular-orbital theory on large periodic systems to investigate bulk electronic properties, and molecular mechanics (classical force field) simulations to compute X-ray diffraction patterns for large models to compare with experimental data.

Periodic DFT calculations were carried out with the VASP[47] code. The calculations employed the semilocal exchange-correlation functional due to Perdew, Burke, and Ernzerhof[48] supplemented with the D3 van der Waals correction[49] (including Becke–Johnson damping[50]) to take into account dispersion interactions, see the SI for further details. The unit cell as well as the positions of all atoms within the unit cell were optimized starting from the geometry obtained from AM1 calculations (see below). The obtained lattice parameters, see Table 4.1 in appendix, are in very good agreement with the XRD data and confirm the suggested staircase geometry. To examine whether other geometries represent local energy minima, we flipped the thiophene units bridging porphyrin rings in the obtained structure and reoptimized again. This optimization, however, led back to the same structure as before.

In order to identify the driving force for creating the staircase geometry, we carried out a geometry optimization in which the interlayer spacing of the COFs was initially set to 15 Å and the unit cell volume was kept fixed. This way the structure of an isolated COF sheet could relax while the interlayer spacing remained at a large distance such that the COF sheets remained isolated. It turned out that in an isolated COF sheet the lateral, i.e., in-plane, unit cell is almost perfectly quadratic with in-plane unit cell vectors of length a = 27.39 Å and b = 27.33 Å and an angle γ = 90.97° between them, see Table 4.4 in appendix. In the crystalline three-dimensional (3D) material the corresponding in-plane geometry data are a = 27.41 Å, b = 27.46 Å, and γ = 94.34° and an offset angle of α = 111.41°, see Table 4.1 in appendix. These results show that the formation of the staircase geometry goes along with a certain distortion of the quadratic lateral unit cell of an isolated single sheet of the COF. The calculated formation energy of the

3D material with respect to single sheets is 1.81 eV per unit cell (compare total energies of three-dimensional crystalline material and single sheets, Table 4.1 and Table 4.4 in appendix) with a van der Waals contribution of 2.13 eV. The finding that the van der Waals contribution to the formation energy is higher than the total formation energy means that packing effects lead to distortions that lower the covalent binding energy of the COF network. This raising of the energy upon formation of the 3D-material is, however, overcompensated by van der Waals interactions. This identifies the latter as the driving force for the formation of the observed staircase structure.

In the periodic semiempirical calculations the MNDO,[51-52] MNDO/d,[53] AM1,[54] and AM1*[55] Hamiltonians were tested with and without Grimme D3-dispersion corrections[49] using the EMPIRE program.[56-57] Minimal unit cells and supercells up to 2 × 2 × 4 (>1600 atoms) were used in the simulations. AM1 was found to be most reliable, correctly describing that aromatic delocalization and π–π stacking are preferred to hydrogen-bond formation. The Grimme corrections are very important for reproducing the interlayer distance and for the energy difference between the eclipsed and staircase arrangements. Several different staircase stacking-patterns were found, including one with unit cell parameters very close to those observed experimentally, while eclipsed stacking was not found to be stable with any of the Hamiltonians investigated. Optimized geometries and unit cell parameters can be found in the appendix, Table 4.1.

A periodic system with 1000 unit cells was subjected to force-field-based simulated annealing (see appendix for details). This procedure resulted in significantly distorted layers, which, however, retained the staircase shifted pattern. PXRD patterns predicted for idealized and annealed supercells (see appendix for details) fit the experimental curve very well (Figure 4.3).

The transmission electron microscopy (TEM) images of the TT-Por COF confirmed the successful formation of a crystalline and ordered material. Domain sizes of up to 100 nm and the formation of defined rectangular crystal facets could be observed (Figure 4.2c). Depending on the orientation of the crystallites, the rectangular porous network can be seen from the top or the porous channels from the side. Some facets are oriented such that the staircase stacking arrangement of the sheets is evident and can directly be seen (Figure 4.2c, inset bottom right). The measured angle between the adjacent layers is 110° which is in excellent agreement with the angle of 111.41° in the DFT-simulated structure (compare Figure 4.2b,c, see appendix, Table 4.1).

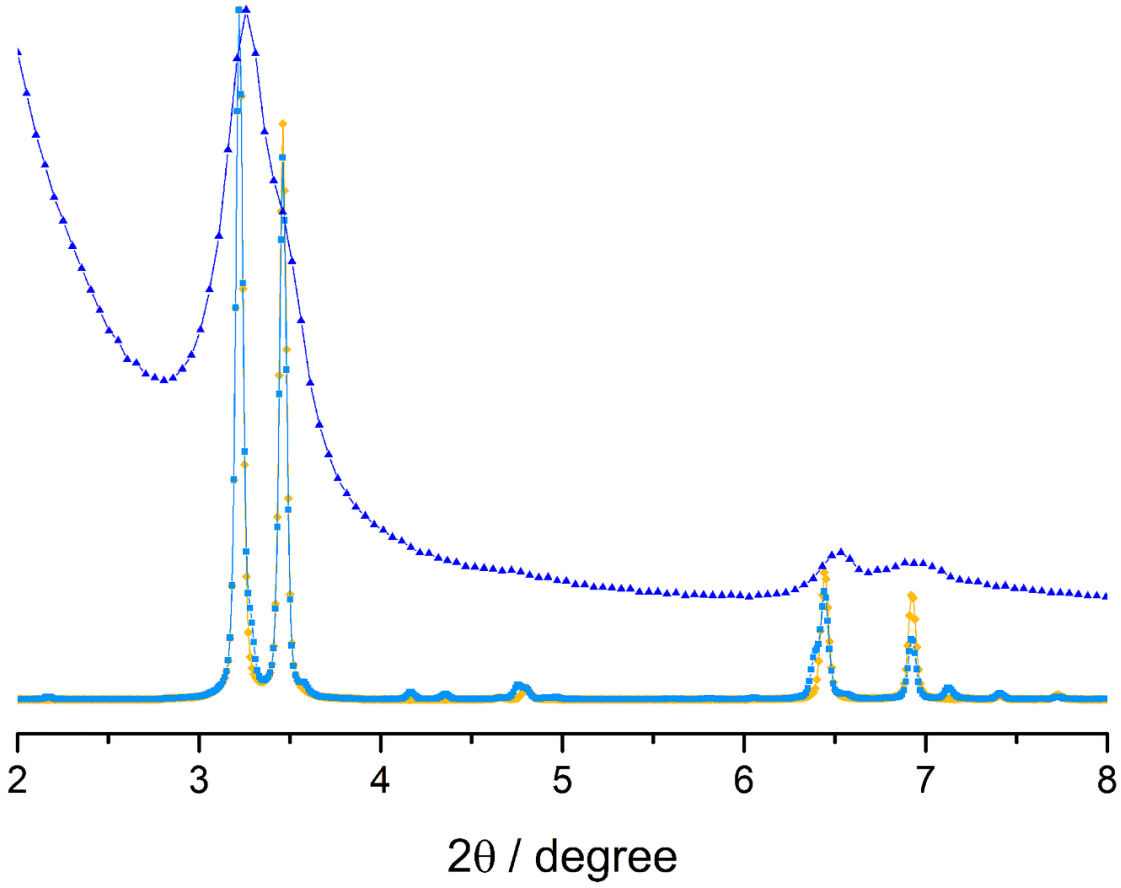

Figure 4.3: Experimental (blue) and calculated PXRD patterns, ideal (yellow) and annealed (light blue).

Nitrogen sorption measurements reveal the typical shape of a type IV isotherm with a steep increase in adsorbed volume at 0.09 p/p_0 (Figure 4.2d). The calculated Brunauer−Emmett−Teller (BET) surface area is 1190 $m^2\ g^{-1}$ with a pore volume of 0.56 $cm^3\ g^{-1}$. This corresponds to 57% of the predicted Connolly surface of 2095 $m^2\ g^{-1}$, which can be possibly explained by defects, displacement of COF layers or adsorbed molecular fragments. Nevertheless, similar surface areas have been reported for other porphyrin-containing COFs (see appendix for more details).[23] The pore size shows a very narrow distribution with an average pore size of 2.4 nm (Figure 4.2d inset) with a fitting error of 0.7%. This is in good agreement with the theoretical pore size of 2.5 nm.

The newly synthesized TT-Por COF shows a strong absorbance throughout the UV and visible spectral range, tailing far into the infrared region with distinct features (Figure 4.4a, blue). Peak absorption is at 668 nm with two more distinct peaks at 444 and 600 nm. The peak at 444 nm corresponds to the Soret band (S2 ← S0), as it can be easily observed in the absorption spectrum

of porphyrin monomers in solution (Figure 4.4b). The two peaks at 600 and 668 nm can be attributed to the Q-bands of the porphyrin J-aggregate, together with the two shoulders at around 766 and 890 nm. The strong red-shift with respect to the monomer in solution indicates a large length scale of ordered J-aggregate-like staircase stacking, which is in good agreement with the PXRD data showing distinctly split peaks as well as the structural modeling. Furthermore, by comparing the COF absorption spectrum with neat porphyrin in powder form (see Figure 4.12a in appendix), a strong dominance of the porphyrin features is observed and considering the ratio of 2:1 between TT and porphyrin units, the TT absorption is small (overall <30% in the region of TT powder absorption). Direct comparison between COF and porphyrin solid monomer absorption shows no new absorption features arising in the COF and the overall absorption can be described, at least in terms of feature location, by a superposition of both neat material absorptions. However, as mentioned above, peak ratios strongly shift with much stronger absorption in the Q-bands due to the J-aggregate arrangement.[58] With little shift of the absorption features and no new ones emerging upon COF formation, we conclude that the aromatic system is essentially nonconjugated (Figure 4.4b), which can be explained by a 90° rotated phenylene ring between TT and the porphyrin core. We note that all absorption spectra from solid samples are obtained in reflection mode and converted with the Kubelka−Munk equation. The optical bandgap of the COF, estimated from the corresponding Tauc plot for direct and allowed transitions, is 1.25 eV (appendix, Figure 4.13). With this small bandgap, TT-Por COF is an excellent candidate for a photoactive material, since its optical absorption covers almost the complete visible spectrum.

Upon excitation of the TT-Por COF at 365 nm, a distinct fluorescence occurs at 794 nm with a second smaller peak at 696 nm (Figure 4.4a, black). The position of the latter peak is possibly obscured by self-absorption of the COF. Comparing the emission of COF and aggregated monomers (see appendix, Figure 4.14), the spectral shape does not correlate to a superposition of the neat monomer emissions. The strong overlap between absorption and emission of the COF is not clear but similar optical behavior has been observed for porphyrins in the literature before.[10, 20-23, 59]

Electrochemical measurements provide insights into the oxidation and reduction potentials of the electroactive linker molecules. In order to determine the exact energy level of the highest occupied molecular orbital (HOMO), differential pulse voltammetry (DPV) was applied in dilute solutions in which the samples exist as single molecules. Ferrocene was used as internal reference and a potential of $E(Fc/Fc^{+}) = -4.80$ eV vs E_{vac} was assumed.[60] The sum of the

HOMO and the bandgap energy, which was obtained from the Tauc plot, yielded the position of the lowest unoccupied molecular orbital (LUMO) and the energy levels of the bandgap with $E_{HOMO}(TT) = -5.40$ eV, $E_{LUMO}(TT) = -1.92$ eV, $E_{HOMO}(Por) = -5.01$ eV, and $E_{LUMO}(Por) = -3.27$ eV (Figure 4.4c). We note that since the connecting building blocks rotate out of the plane (Figure 4.2b), overlap between the orbitals of the aromatic linker molecules is restricted, reducing the effective conjugation of the resulting COF as confirmed by UV−vis measurements.

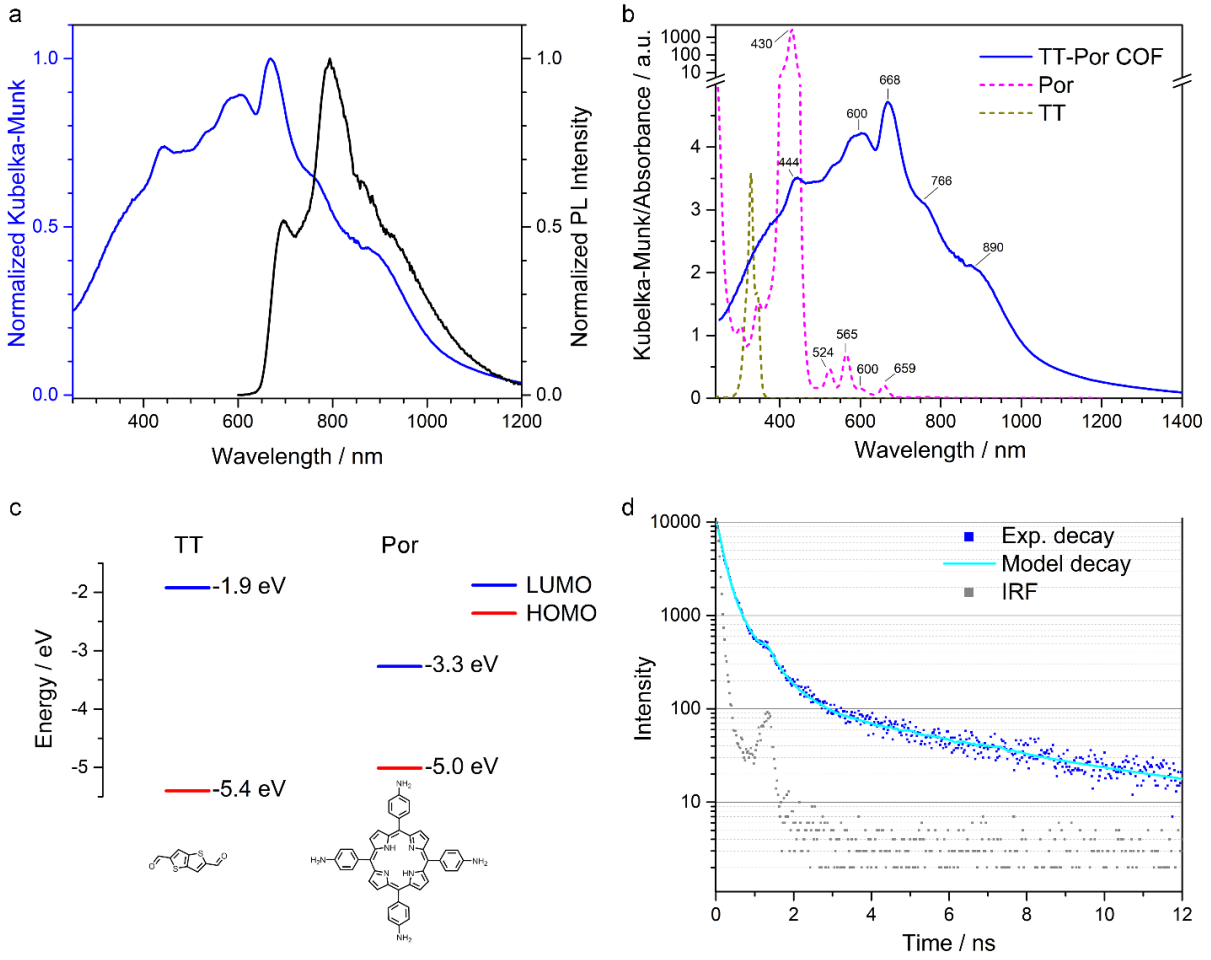

Figure 4.4: (a) Optical absorption (blue) spectrum of TT-Por COF measured as diffuse reflectance of the solid and converted with the Kubelka−Munk equation, and PL (λ_{exc} = 365 nm, black) spectrum of TT-Por COF, respectively. (b) Absorption spectra of the TT-Por COF measured in diffuse reflectance (blue) compared to the monomers (given in c; TT: dark yellow, dashed; Por: magenta, dashed) measured in diluted solution (50 µM, dioxane). (c) Relevant energy levels of the monomers with HOMO (red) and LUMO (blue), which were determined by combining differential pulse voltammetry measurements and UV−vis data. (d) Photoluminescence (PL) decay curve for TT-Por COF. The sample was illuminated at 378 nm with a pump fluence of ~0.99 nJ cm^{-2}; the emission was monitored at 800 nm (model decay in cyan).

Photoluminescence (PL) dynamics provide important information on the lifetime of the initially generated singlet. To determine the PL dynamics, time-correlated single photon counting

(TCSPC) was applied using a pulsed 378 nm laser (see appendix for method). The PL decay of TT-Por COF was measured at 800 nm and the resulting histogram was fitted with the sum of three exponentials (see appendix for full set of parameters). The long-time decay constant is 4.90 ns (Figure 4.4d) which is among the longest lifetimes for COF PL reported in the literature.[38, 44] This decay time is somewhat shorter than that of the monomers in solution, which show PL decays on a time scale of 4 and 9 ns, as has been observed in the literature.[59] However, the pure solid starting materials TT and (1) exhibit average lifetimes of 1.12 and 0.67 ns, respectively (appendix, Figure 4.18). Hence, the results show a significant increase of singlet lifetime within the COF compared to the neat solids, which we attribute to a stabilization of the singlet state within the well-defined spatial molecular arrangements within the COF lattice.

To investigate the influence of the TT building block on the excited state lifetimes, three additional porphyrin COFs were synthesized from compound (1) and different linear building blocks (for more details, see appendix). As the first example, 2,5-dimethoxybenzene-1,4-dicarboxaldehyde (OMe) was used as bridging unit between the four-armed porphyrin molecules.[39] The PL decay of the resulting OMe- Por COF structure was analyzed by TCSPC and the lifetimes of the excited species were found to be merely the sum of the lifetimes of its two components, without any noticeable impact due to embedding in the COF lattice (for more information see appendix). As a second example COF-366 was chosen, formed by combining compound (1) with terephthalaldehyde (1P; for experimental details see appendix) as reported in the literature.[23] It showed a fluorescence lifetime of less than 1 ns, suggesting the occurrence of processes analogous to those within the starting materials. Comparing optical absorption and PXRD data between the three different COFs, TT-Por shows the strongest aggregation, as derived from the most pronounced red-shift of the optical absorption and splitting of PXRD peaks. This indicates that the extended lifetime of the fluorescent species within the TT-Por COF compared to its components is a result of the J-aggregate formation, allowing for a better delocalization of the singlet across the porphyrin units. This delocalization throughout the COF structure causes a stabilization of the excited species and prolonged lifetimes. With the weaker aggregation arising within the OMe-Por and COF-366 structures, singlets are more localized and hence resemble the behavior on solid monomers. As a result, no prolonged lifetimes of the excited species could be observed in these COFs.

4.3 Conclusion

In this study we have developed a new offset-stacked imine-linked COF comprising tetragonal porphyrin and linear thienothiophene building blocks, resulting in the formation of J-aggregate stacks of unprecedented spatial extension. This aggregation enables substantially prolonged lifetimes of the singlet excitons compared to the solid starting materials, as indicated by the PL dynamics. Hence, covalently embedding the chromophore building blocks in the COF forces the formation of aggregates and facilitates exciton delocalization throughout the framework as well as stabilization of the excited species. Through careful covalent framework design, this directed stacking arrangement could potentially be transferred to other chromophore systems as well, allowing for specific utilization of the aggregate benefits. This aggregation-based spectral tuning of (sustainable) chromophores can lead to materials with appealing bandgaps in the NIR region. Moreover, we believe that the insights gained from these well-defined model systems can be transferred to currently used organic photovoltaic devices and help to understand and optimize these systems. Specifically, the strong absorption of the TT-Por COF in the visible is desirable for harvesting a large fraction of the solar spectrum, and the prolonged singlet lifetime would be beneficial for charge separation and ultimately collecting the energy of these excitations. Applications in photovoltaics would require the design of appropriate heterojunctions providing efficient exciton diffusion and dissociation as well as efficient charge carrier transport.

Moreover, the solid COF matrix in which these J-aggregates are incorporated enables efficient molecular access through the porous framework for interactions with liquids and gases. This would allow valuable insights and open up a new basis for experiments with porphyrin aggregates without the need of aqueous environments and pH restrictions. Here, especially the close relation to molecules occurring in nature such as chlorophyll could be of interest, and possibly similar COFs enforcing J-aggregates can be built with metal-containing porphyrins. Thus, this type of COF could be used as a model system for biological, chemical, and medical applications. Recently, porphyrin aggregates have attracted great interest due to their increased two-photon absorption cross-section that can be used to selectively target tumor cells in human tissue with photodynamic therapy (PDT).[61-64] Due to the use of NIR light, high spatial resolution, deep tissue penetration depths (of around 2 cm) and selective excitation can be achieved, which is of great advantage in PDT.[1] Furthermore, this architecture could lead to new materials for the photodynamic inactivation of bacteria due to enhanced absorption by the

enforced J-aggregate stacking of porphyrins within the COF.[65] The entire set of special features of such COFs, i.e., the high density of chromophores, intrinsic porosity and crystallinity, as well as intriguing optical characteristics, are expected to open a vast field of new opportunities where highly ordered aggregates yield new insights and functionalities.

4.4 References

[1] Shen, Y.; Shuhendler, A. J.; Ye, D.; Xu, J.-J.; Chen, H.-Y., Two-photon excitation nanoparticles for photodynamic therapy. *Chem. Soc. Rev.* **2016,** *45* (24), 6725-6741.

[2] Satake, A.; Kobuke, Y., Artificial photosynthetic systems: assemblies of slipped cofacial porphyrins and phthalocyanines showing strong electronic coupling. *Org. Biomol. Chem.* **2007,** *5* (11), 1679-1691.

[3] Kasha, M.; Rawls, H. R.; El-Bayoumi, M. A., The Exciton Model in Molecular Spectroscopy. *Pure Appl. Chem.* **1965,** *11*, 371-392.

[4] Wasielewski, M. R., Photoinduced electron transfer in supramolecular systems for artificial photosynthesis. *Chem. Rev.* **1992,** *92* (3), 435-461.

[5] L. Anderson, H., Building molecular wires from the colours of life: conjugated porphyrin oligomers. *Chem. Commun.* **1999,** (23), 2323-2330.

[6] Chen, L.; Yang, Y.; Guo, Z.; Jiang, D., Highly Efficient Activation of Molecular Oxygen with Nanoporous Metalloporphyrin Frameworks in Heterogeneous Systems. *Adv. Mater.* **2011,** *23* (28), 3149-3154.

[7] Chen, L.; Yang, Y.; Jiang, D., CMPs as Scaffolds for Constructing Porous Catalytic Frameworks: A Built-in Heterogeneous Catalyst with High Activity and Selectivity Based on Nanoporous Metalloporphyrin Polymers. *J. Am. Chem. Soc.* **2010,** *132* (26), 9138-9143.

[8] Li, Y.; Auras, F.; Löbermann, F.; Döblinger, M.; Schuster, J.; Peter, L.; Trauner, D.; Bein, T., A Photoactive Porphyrin-Based Periodic Mesoporous Organosilica Thin Film. *J. Am. Chem. Soc.* **2013,** *135* (49), 18513-18519.

[9] Luo, L.; Lin, C.-J.; Hung, C.-S.; Lo, C.-F.; Lin, C.-Y.; Diau, E. W.-G., Effects of potential shift and efficiency of charge collection on nanotube-based porphyrin-sensitized solar cells with conjugated links of varied length. *Phys. Chem. Chem. Phys.* **2010,** *12* (40), 12973-12977.

[10] Maiti, N. C.; Mazumdar, S.; Periasamy, N., J- and H-Aggregates of Porphyrin−Surfactant Complexes: Time-Resolved Fluorescence and Other Spectroscopic Studies. *J. Phys. Chem. B* **1998,** *102* (9), 1528-1538.

[11] Li, L.; Huang, Y.; Peng, J.; Cao, Y.; Peng, X., Highly responsive organic near-infrared photodetectors based on a porphyrin small molecule. *J. Mater. Chem. C* **2014,** *2* (8), 1372-1375.

[12] Martinez-Diaz, M. V.; de la Torre, G.; Torres, T., Lighting porphyrins and phthalocyanines for molecular photovoltaics. *Chem. Commun.* **2010,** *46* (38), 7090-7108.

[13] Scholes, G. D.; Fleming, G. R.; Olaya-Castro, A.; van Grondelle, R., Lessons from nature about solar light harvesting. *Nat. Chem.* **2011,** *3* (10), 763-74.

[14] Sundström, V.; Pullerits, T.; van Grondelle, R., Photosynthetic Light-Harvesting: Reconciling Dynamics and Structure of Purple Bacterial LH2 Reveals Function of Photosynthetic Unit. *J. Phys. Chem. B* **1999,** *103* (13), 2327-2346.

[15] van Grondelle, R., Excitation energy transfer, trapping and annihilation in photosynthetic systems. *Biochim. Biophys. Acta, Rev. Bioenerg.* **1985,** *811* (2), 147-195.

[16] Michel, H.; Deisenhofer, J., Relevance of the photosynthetic reaction center from purple bacteria to the structure of photosystem II. *Biochemistry* **1988,** *27* (1), 1-7.

[17] Jelley, E. E., Spectral Absorption and Fluorescence of Dyes in the Molecular State. *Nature* **1936,** *138*, 1009.

[18] Jelley, E. E., Molecular, Nematic and Crystal States of I: I-Diethyl--Cyanine Chloride. *Nature* **1937,** *139*, 631.

[19] Kasha, M., Energy Transfer Mechanisms and the Molecular Exciton Model for Molecular Aggregates. *Radiat. Res.* **1963,** *20* (1), 55-70.

[20] Egawa, Y.; Hayashida, R.; Anzai, J.-I., pH-Induced Interconversion between J-Aggregates and H-Aggregates of 5,10,15,20-Tetrakis(4-sulfonatophenyl)porphyrin in Polyelectrolyte Multilayer Films. *Langmuir* **2007,** *23* (26), 13146-13150.

[21] Kano, H.; Kobayashi, T., Time-resolved fluorescence and absorption spectroscopies of porphyrin J-aggregates. *J. Chem. Phys.* **2002,** *116* (1), 184.

[22] Ohno, O.; Kaizu, Y.; Kobayashi, H., J-aggregate formation of a water-soluble porphyrin in acidic aqueous media. *J. Chem. Phys.* **1993,** *99* (5), 4128.

[23] Wan, S.; Gándara, F.; Asano, A.; Furukawa, H.; Saeki, A.; Dey, S. K.; Liao, L.; Ambrogio, M. W.; Botros, Y. Y.; Duan, X.; Seki, S.; Stoddart, J. F.; Yaghi, O. M., Covalent Organic Frameworks with High Charge Carrier Mobility. *Chem. Mater.* **2011,** *23* (18), 4094-4097.

[24] Giovannetti, R., *The Use of Spectrophotometry UV-Vis for the Study of Porphyrins, Macro To Nano Spectroscopy*. InTech: 2012.

[25] Saptal, V.; Shinde, D. B.; Banerjee, R.; Bhanage, B. M., State-of-the-art catechol porphyrin COF catalyst for chemical fixation of carbon dioxide via cyclic carbonates and oxazolidinones. *Catal. Sci. Technol.* **2016,** *6* (15), 6152-6158.

[26] Liao, H.; Wang, H.; Ding, H.; Meng, X.; Xu, H.; Wang, B.; Ai, X.; Wang, C., A 2D porous porphyrin-based covalent organic framework for sulfur storage in lithium-sulfur batteries. *J. Mater. Chem. A* **2016,** *4* (19), 7416-7421.

[27] Lin, S.; Diercks, C. S.; Zhang, Y.-B.; Kornienko, N.; Nichols, E. M.; Zhao, Y.; Paris, A. R.; Kim, D.; Yang, P.; Yaghi, O. M.; Chang, C. J., Covalent organic frameworks comprising cobalt porphyrins for catalytic CO2 reduction in water. *Science* **2015,** *349* (6253), 1208-1213.

[28] Chen, X.; Addicoat, M.; Jin, E.; Zhai, L.; Xu, H.; Huang, N.; Guo, Z.; Liu, L.; Irle, S.; Jiang, D., Locking Covalent Organic Frameworks with Hydrogen Bonds: General and Remarkable Effects on Crystalline Structure, Physical Properties, and Photochemical Activity. *J. Am. Chem. Soc.* **2015,** *137* (9), 3241-3247.

[29] Calik, M.; Auras, F.; Salonen, L. M.; Bader, K.; Grill, I.; Handloser, M.; Medina, D. D.; Dogru, M.; Löbermann, F.; Trauner, D.; Hartschuh, A.; Bein, T., Extraction of Photogenerated Electrons

and Holes from a Covalent Organic Framework Integrated Heterojunction. *J. Am. Chem. Soc.* **2014,** *136* (51), 17802-17807.

[30] Feng, X.; Liu, L.; Honsho, Y.; Saeki, A.; Seki, S.; Irle, S.; Dong, Y.; Nagai, A.; Jiang, D., High-Rate Charge-Carrier Transport in Porphyrin Covalent Organic Frameworks: Switching from Hole to Electron to Ambipolar Conduction. *Angew. Chem. Int. Ed.* **2012,** *51* (11), 2618-2622.

[31] Xu, H.; Chen, X.; Gao, J.; Lin, J.; Addicoat, M.; Irle, S.; Jiang, D., Catalytic covalent organic frameworks via pore surface engineering. *Chem. Commun.* **2014,** *50* (11), 1292-1294.

[32] Hou, Y.; Zhang, X.; Sun, J.; Lin, S.; Qi, D.; Hong, R.; Li, D.; Xiao, X.; Jiang, J., Good Suzuki-coupling reaction performance of Pd immobilized at the metal-free porphyrin-based covalent organic framework. *Microporous Mesoporous Mater.* **2015,** *214*, 108-114.

[33] Huang, N.; Chen, X.; Krishna, R.; Jiang, D., Two-Dimensional Covalent Organic Frameworks for Carbon Dioxide Capture through Channel-Wall Functionalization. *Angew. Chem. Int. Ed.* **2015,** *54* (10), 2986-2990.

[34] Hou, Y.; Zhang, X.; Wang, C.; Qi, D.; Gu, Y.; Wang, Z.; Jiang, J., Novel Imine-linked Porphyrin Covalent Organic Frameworks with Good Adsorption Removing Property of RhB. *New J. Chem.* **2017**.

[35] Wang, K.; Qi, D.; Li, Y.; Wang, T.; Liu, H.; Jiang, J., Tetrapyrrole macrocycle based conjugated two-dimensional mesoporous polymers and covalent organic frameworks: From synthesis to material applications. *Coord. Chem. Rev.* **2017**.

[36] Feng, X.; Chen, L.; Dong, Y.; Jiang, D., Porphyrin-based two-dimensional covalent organic frameworks: synchronized synthetic control of macroscopic structures and pore parameters. *Chem. Commun.* **2011,** *47* (7), 1979-1981.

[37] Jin, S.; Ding, X.; Feng, X.; Supur, M.; Furukawa, K.; Takahashi, S.; Addicoat, M.; El-Khouly, M. E.; Nakamura, T.; Irle, S.; Fukuzumi, S.; Nagai, A.; Jiang, D., Charge Dynamics in A Donor–Acceptor Covalent Organic Framework with Periodically Ordered Bicontinuous Heterojunctions. *Angew. Chem. Int. Ed.* **2013,** *52* (7), 2017-2021.

[38] Jin, S.; Furukawa, K.; Addicoat, M.; Chen, L.; Takahashi, S.; Irle, S.; Nakamura, T.; Jiang, D., Large pore donor-acceptor covalent organic frameworks. *Chem. Sci.* **2013,** *4* (12), 4505-4511.

[39] Kandambeth, S.; Shinde, D. B.; Panda, M. K.; Lukose, B.; Heine, T.; Banerjee, R., Enhancement of Chemical Stability and Crystallinity in Porphyrin-Containing Covalent Organic Frameworks by Intramolecular Hydrogen Bonds. *Angew. Chem. Int. Ed.* **2013,** *52* (49), 13052-13056.

[40] Neti, V. S. P. K.; Wu, X.; Deng, S.; Echegoyen, L., Synthesis of a phthalocyanine and porphyrin 2D covalent organic framework. *CrystEngComm* **2013,** *15* (35), 6892-6895.

[41] Spitler, E. L.; Koo, B. T.; Novotney, J. L.; Colson, J. W.; Uribe-Romo, F. J.; Gutierrez, G. D.; Clancy, P.; Dichtel, W. R., A 2D Covalent Organic Framework with 4.7-nm Pores and Insight into Its Interlayer Stacking. *J. Am. Chem. Soc.* **2011,** *133* (48), 19416-19421.

[42] Zhou, W.; Wu, H.; Yildirim, T., Structural stability and elastic properties of prototypical covalent organic frameworks. *Chem. Phys. Lett.* **2010,** *499* (1–3), 103-107.

[43] Ascherl, L.; Sick, T.; Margraf, J. T.; Lapidus, S. H.; Calik, M.; Hettstedt, C.; Karaghiosoff, K.; Döblinger, M.; Clark, T.; Chapman, K. W.; Auras, F.; Bein, T., Molecular docking sites designed for the generation of highly crystalline covalent organic frameworks. *Nat. Chem.* **2016,** *8* (4), 310-316.

[44] Auras, F.; Ascherl, L.; Hakimioun, A. H.; Margraf, J. T.; Hanusch, F. C.; Reuter, S.; Bessinger, D.; Döblinger, M.; Hettstedt, C.; Karaghiosoff, K.; Herbert, S.; Knochel, P.; Clark, T.; Bein, T., Synchronized Offset Stacking: A Concept for Growing Large-Domain and Highly Crystalline 2D Covalent Organic Frameworks. *J. Am. Chem. Soc.* **2016,** *138* (51), 16703-16710.

[45] Keller, N.; Bessinger, D.; Reuter, S.; Calik, M.; Ascherl, L.; Hanusch, F. C.; Auras, F.; Bein, T., Oligothiophene-Bridged Conjugated Covalent Organic Frameworks. *J. Am. Chem. Soc.* **2017,** *139* (24), 8194-8199.

[46] Bessinger, D.; Ascherl, L.; Auras, F.; Bein, T., Spectrally Switchable Photodetection with Near-Infrared-Absorbing Covalent Organic Frameworks. *J. Am. Chem. Soc.* **2017,** *139* (34), 12035-12042.

[47] Kresse, G.; Furthmüller, J., Efficiency of ab-initio total energy calculations for metals and semiconductors using a plane-wave basis set. *Comput. Mater. Sci.* **1996,** *6* (1), 15-50.

[48] Perdew, J. P.; Burke, K.; Ernzerhof, M., Generalized Gradient Approximation Made Simple. *Phys. Rev. Lett.* **1996,** *77* (18), 3865-3868.

[49] Grimme, S.; Antony, J.; Ehrlich, S.; Krieg, H., A consistent and accurate ab initio parametrization of density functional dispersion correction (DFT-D) for the 94 elements H-Pu. *J. Chem. Phys.* **2010,** *132* (15), 154104.

[50] Grimme, S.; Ehrlich, S.; Goerigk, L., Effect of the damping function in dispersion corrected density functional theory. *J. Comput. Chem.* **2011,** *32* (7), 1456-1465.

[51] Dewar, M. J. S.; Thiel, W., Ground states of molecules. 38. The MNDO method. Approximations and parameters. *J. Am. Chem. Soc.* **1977,** *99* (15), 4899-4907.

[52] Dewar, M. J. S.; Yuan, Y. C., AM1 parameters for sulfur. *Inorg. Chem.* **1990,** *29* (19), 3881-3890.

[53] Thiel, W.; Voityuk, A. A., Extension of MNDO to d Orbitals: Parameters and Results for the Second-Row Elements and for the Zinc Group. *J. Phys. Chem.* **1996,** *100* (2), 616-626.

[54] Dewar, M. J. S.; Zoebisch, E. G.; Healy, E. F.; Stewart, J. J. P., Development and use of quantum mechanical molecular models. 76. AM1: a new general purpose quantum mechanical molecular model. *J. Am. Chem. Soc.* **1985,** *107* (13), 3902-3909.

[55] Winget, P.; Horn, A. H. C.; Selçuki, C.; Martin, B.; Clark, T., AM1* parameters for phosphorus, sulfur and chlorine. *J. Mol. Model.* **2003,** *9* (6), 408-414.

[56] Hennemann, M.; Clark, T., EMPIRE: a highly parallel semiempirical molecular orbital program: 1: self-consistent field calculations. *J. Mol. Model.* **2014,** *20* (7), 2331.

[57] Margraf, J. T.; Hennemann, M.; Meyer, B.; Clark, T., EMPIRE: a highly parallel semiempirical molecular orbital program: 2: periodic boundary conditions. *J. Mol. Model.* **2015,** *21* (6), 144.

[58] Zimmermann, J.; Siggel, U.; Fuhrhop, J.-H.; Röder, B., Excitonic Coupling between B and Q Transitions in a Porphyrin Aggregate. *J. Phys. Chem. B* **2003,** *107* (25), 6019-6021.

[59] Verma, S.; Ghosh, A.; Das, A.; Ghosh, H. N., Ultrafast Exciton Dynamics of J- and H-Aggregates of the Porphyrin-Catechol in Aqueous Solution. *J. Phys. Chem. B* **2010,** *114* (25), 8327-8334.

[60] Frost, J. M.; Faist, M. A.; Nelson, J., Energetic Disorder in Higher Fullerene Adducts: A Quantum Chemical and Voltammetric Study. *Adv. Mater.* **2010,** *22* (43), 4881-4884.

[61] Secret, E.; Maynadier, M.; Gallud, A.; Chaix, A.; Bouffard, E.; Gary-Bobo, M.; Marcotte, N.; Mongin, O.; El Cheikh, K.; Hugues, V.; Auffan, M.; Frochot, C.; Morère, A.; Maillard, P.; Blanchard-Desce, M.; Sailor, M. J.; Garcia, M.; Durand, J.-O.; Cunin, F., Two-Photon Excitation of Porphyrin-Functionalized Porous Silicon Nanoparticles for Photodynamic Therapy. *Adv. Mater.* **2014,** *26* (45), 7643-7648.

[62] Mauriello-Jimenez, C.; Henry, M.; Aggad, D.; Raehm, L.; Cattoen, X.; Wong Chi Man, M.; Charnay, C.; Alpugan, S.; Ahsen, V.; Tarakci, D. K.; Maillard, P.; Maynadier, M.; Garcia, M.; Dumoulin, F.; Gary-Bobo, M.; Coll, J.-L.; Josserand, V.; Durand, J.-O., Porphyrin- or phthalocyanine-bridged silsesquioxane nanoparticles for two-photon photodynamic therapy or photoacoustic imaging. *Nanoscale* **2017,** *9* (43), 16622-16626.

[63] Mauriello-Jimenez, C.; Croissant, J.; Maynadier, M.; Cattoen, X.; Wong Chi Man, M.; Vergnaud, J.; Chaleix, V.; Sol, V.; Garcia, M.; Gary-Bobo, M.; Raehm, L.; Durand, J.-O., Porphyrin-functionalized mesoporous organosilica nanoparticles for two-photon imaging of cancer cells and drug delivery. *J. Mater. Chem. B* **2015,** *3* (18), 3681-3684.

[64] Biswas, S.; Ahn, H.-Y.; Bondar, M. V.; Belfield, K. D., Two-Photon Absorption Enhancement of Polymer-Templated Porphyrin-Based J-Aggregates. *Langmuir* **2012,** *28* (2), 1515-1522.

[65] Hynek, J.; Zelenka, J.; Rathouský, J.; Kubát, P.; Ruml, T.; Demel, J.; Lang, K., Designing Porphyrinic Covalent Organic Frameworks for the Photodynamic Inactivation of Bacteria. *ACS Appl. Mater. Interfaces* **2018,** *10* (10), 8527-8535.

4.5 Appendix

4.5.1 Materials and Methods

Unless stated otherwise, all reactions were performed in oven-dried glassware under a positive pressure of Ar. All reagents and solvents were sourced from commerical suppliers and used without further purification. Solvents were, unless provided under inert gas, degassed and saturated with argon prior to use. Thieno[3,2-*b*]thiophene-2,5-dicarboxaldehyde (TT) and 5,10,15,20-tetrakis(4-aminophenyl)porphyrin (compound 1) were acquired from Sigma Aldrich and PorphyChem, respectively.

Magic angle spinning (MAS) solid state nuclear magnetic resonance (ssNMR) spectra were recorded using a Bruker Avance III 500 spectrometer.

Infrared (IR) spectra were recorded on a Perkin Elmer Spectrum BX II FT-IR system and a Thermo Scientific Nicolet™ 6700 FT-IR spectrometer in transmission mode. IR data are reported in wavenumbers (cm^{-1}).

The **nitrogen sorption** isotherm was recorded on a Quantachrome Autosorb 1 at 77 K in a pressure range from $p/p_0 = 0.001$ to 0.98. Prior to the measurement of the sorption isotherm, the sample was heated for 24 h at 120 °C under turbomolecular pump vacuum. For the evaluation of the surface area, the BET model was applied between 0.05 and 0.2 p/p_0. The calculation of the pore size distribution was done using the QSDFT equilibrium model with a carbon kernel for cylindrical pores on the adsorption branch. The Connolly surface area differs from the experimental data usually due to the non-ideal composition and structure of the COF sample. Grain boundaries and the displacement of COF layers may lead to defects in the crystalline structure and to blocked pores and thus lower experimental values. Adsorbed molecular fragments may also decrease the accessible surface area.

Powder X-ray diffraction (PXRD) measurements were performed using a Bruker D8 Discover with Ni-filtered Cu K_α radiation and a LynxEye position-sensitive detector.

Transmission electron microscopy (TEM) measurements were performed on a probe-corrected FEI Titan Themis 60-300 kV (FEI Company/Thermo Fisher Scientic Inc., USA) electron microscope equipped with a Super-X windowless EDX (four quadrant SDD EDX detection) and a X-FEG high-brightness gun with monochromator (energy spread <0.2 eV). **Scanning electron microscopy (SEM)** measurements were performed on a FEI Helios

NanoLab G3 UC electron microscope (FEI Company/Thermo Fisher Scientic Inc., USA) with a X-MaxN EDX detector (Oxford Instruments, UK). The samples were mounted on sample carriers with a sticky carbon support and sputtered with carbon on a Bal-Tec MED 020 coating system.

UV-Vis spectra were recorded using a Perkin-Elmer Lambda 1050 spectrometer equipped with a 150 mm integrating sphere. **Diffuse reflectance spectra** were collected with a Praying Mantis (Harrick) accessory and were referenced to barium sulfate powder as white standard.

Photoluminescence (PL) measurements were performed using a home-built setup consisting of a Horiba Jobin Yvon iHR 320 monochromator equipped with a photomultiplier tube and a liquid N_2-cooled InGaAs detector. The samples were illuminated with a pulsed (83 Hz) 365 nm or 405 nm LED at a light intensity of 500 mW cm^{-2}.

Time-resolved PL measurements were acquired using a **time-correlated single photon counting (TCSPC)** setup (FluoTime 300, PicoQuant GmbH). The samples were photo-excited using lasers with suitable wavelengths according to the sample absorption, i.e. 378 nm, 403 nm or 507 nm wavelength (LDH-P-C-375, LDH-P-C-405, and LDH-P-C-510, respectively, all from PicoQuant GmbH) pulsed at 500 kHz, with a pulse duration of ~100 ps and fluence of ~300 nJcm^{-2}/pulse. The samples were exposed to the pulsed light source set at 3 μJcm^{-2}/pulse fluence for ~10 minutes prior to measurement to ensure stable sample emission. The PL was collected using a high-resolution monochromator and photomultiplier detector assembly (PMA-C 192-N-M, PicoQuant GmbH).

Differential pulse voltammetry (DPV) was measured using 50 μM solutions of the starting materials in acetonitrile or in a mixture of acetonitrile and dioxane (8 Vol%), with 0.1 M tetrabutylammonium hexafluorophosphate as electrolyte and 0.1 mM ferrocene as internal reference. Measurements were performed with a Metrohm Autolab PGSTAT302N potentiostat, using Pt wires as the working electrode and counter electrode and a saturated Ag/AgCl reference electrode (Sigma Aldrich, 0.197 V vs. SHE). The potential window was from −1.8 V up to 1.4 V with a modulation amplitude of 0.005 V, modulation time of 0.05 s and an interval time of 0.5 s.

4.5.2 Syntheses

The reaction conditions for all COF syntheses were optimized in a screening program concerning solvents, solvent ratio, concentration and volume of the acid, temperature and reaction time.

TT-Por COF

For the synthesis of TT-Por COF, 13.5 mg of 5,10,15,20-(tetra-4-aminophenyl)porphyrin, further mentioned as compound 1 (0.02 mmol, 1 equiv.) and 7.9 mg of thieno[3,2-*b*]thiophene-2,5-dicarboxaldehyde, further referred to as TT (0.04 mmol, 2 equiv.) were added to a 10 mL Schott culture tube with screw cap and dispersed in a solvent mixture of benzyl alcohol, o-dichlorobenzene and 6 M acetic acid (30:10:4 *v*:*v*:*v*, 550 µL). The tube was placed in an oven at 120 °C for 72 h. After the time had elapsed, the reaction mixture was allowed to cool down to room temperature and the resulting powder was then collected by filtration through a Hirsch funnel. After washing the product three times with dry 1,4-dioxane, it was dried under vacuum, followed by CO_2-extraction to furnish TT-Por COF as a black powder at a high yield of 75%.

Elemental analysis (calculated, found for $C_{60}H_{89}N_8S_4$): C (72.41, 68.68), H (3.44, 3.86), N (11.26, 10.14), S (12.89, 11.12).

COF-366

13.5 mg compound 1 (0.02 mmol, 1 equiv.) and 5.36 mg of terephthalaldehyde (0.04 mmol, 2 equiv.) were dispersed in a solvent mixture of benzyl alcohol, mesitylene and 6 M acetic acid (10:20:3 *v*:*v*:*v*, 550 µL) in a 10 mL Schott culture tube with screw cap. The tube was heated in an oven at 120 °C for 72 h. After cooling down, the product was isolated by filtration, followed by three washing cycles with 1,4-dioxane. The dark purple product was dried under reduced pressure, followed by CO_2-extraction to furnish COF-366 as a brownish, black powder at a high yield of 76%.

Elemental analysis (calculated, found for $C_{60}H_{38}N_8$): C (82.74, 79.99), H (4.40, 4.73), N (12.86, 12.81).

OMe-Por COF

6.74 mg compound 1 (0.01 mmol, 1 equiv.) and 5.82 mg of 2,5-dimethoxybenzene-1,4-dicarboxaldehyde (0.02 mmol, 2 equiv.) were dispersed in a solvent mixture of benzyl alcohol, mesitylene and 6 M acetic acid (49:49:2 *v*:*v*:*v*, 510 µL) in a 10 mL Schott culture tube with screw cap. The tube was heated in an oven at 100 °C for 2 h and then heated at 120 °C for 72 h. After cooling down, the product was isolated by filtration, followed by CO_2-extraction to furnish OMe-Por as a brownish, black powder at a high yield of 71%.

Elemental analysis (calculated, found for $C_{64}H_{46}N_8O_4$): C (77.56, 77.22), H (4.68, 4.96), N (11.31, 11.90).

2P-Por COF

6.74 mg compound 1 (0.01 mmol, 1 equiv.) and 4.20 mg of 4,4'-biphenyldicarboxaldehyde (0.02 mmol, 2 equiv.) were dispersed in a solvent mixture of 1,4-dioxane, mesitylene and 6 M acetic acid (58:29:12 *v*:*v*:*v*, 570 µL) in a 10 mL Schott culture tube with screw cap. The tube was heated in an oven at 70 °C for 2 h and then heated at 120 °C for 72 h. After cooling down, the product was isolated by filtration, followed by three washing cycles with mesitylene. The dark purple product was dried under reduced pressure, followed by CO_2-extraction to furnish 2P-Por COF as a brownish, black powder at a high yield of 69%.

Elemental analysis (calculated, found for $C_{72}H_{46}N_8$): C (84.52, 82.40), H (4.53, 4.70), N (10.95, 9.58).

4.5.3 Simulations

To determine the crystal structure of the obtained products, a powder diffraction pattern was calculated based on a simulated crystal structure. The unit cell was constructed using the Materials Studio software and optimized by force field calculations. Due to the non-planar porphyrin building block, the unit cell is limited to a triclinic P_1 symmetry in the case of a stacked staircase structure and to P_4 symmetry for an eclipsed arrangement. The comparison of the calculated pattern with the experimental data identified the obtained structure as staircase stacked TT-Por COF.

DFT calculations were performed using Vienna Ab initio Simulation Package (VASP)[1] code, which employs a plane-wave basis set and the projector augmented-wave method.[2] The applied Perdew-Burke-Ernzerhof exchange-correlation functional[3] was supplemented by the D3 van der Waals correction[4] (including Becke−Johnson damping)[5] to take dispersive forces into account. The energy cutoff for the plane-wave basis-set was set to 415 eV. The Brillouin zone (BZ) was sampled by 2×2×6 Monkhorst-Pack k-point grids.[6] Electronic structures and geometries converged below 1×10^{-7} eV and 0.01 eV $Å^{-1}$ with respect to total energies and forces acting on ions, respectively.

All semiempirical calculations were performed in the EMPIRE program. The unit cell was optimized in the way of manual scan over each of 6 transition vectors while the structure was optimized within each point of this scan. The last 3 vectors are particularly important, as they are defining interlayer distance and a split visible in XRD data. These values are also affected the strongest by varying of Hamiltonian and switching the Grimme correction on and off.

Optimized structures within the optimized unit cell are listed in Table 4.1 and Table 4.3.

Force-field-based simulated annealing was performed using Dreiding force-field[7] in LAMMPS computational package.[8] Supercells were built as 10×10×10 and 5×5×40 unit cells. Calculations included relaxation, MD at constant temperature 300 K for 1 nanosecond (timestep 1 femtosecond) and 5 times gradual heating and cooling from 300 K to 800 K and back in 2 milions steps during 2 nanoseconds. Thus, the total length of the annealing simulation is 10 nanoseconds. Each of the annealed structures was kept one nanosecond longer in MD simulation under the constant temperature to ensure that total energy did not decrease or significant geometry shifts did not occur, respectively. XRD data for these structures were computed with 2Theta values in the range from 2.0° to 45°, with the most interesting area (2-

8°) plotted in the main text of the article. Heating to higher temperature as well as more rapid cooling were tested on the smaller supercells. Among the obtained snapshots we found structures with very significant slicing of one layer or blocking of few layers with respect to the rest of the layers. This results in additional XRD peaks that are different for each structure with this kind of defects and do not occur in experimental patterns. However, experimental spectra have a significantly higher level of noise than predicted from simulation described above, thus this kind of defects has not to be excluded.

Table 4.1: Cell parameters from experiment and different levels of simulation.

Cell parameter	X-Ray	DFT	Semiempirics
a (Å)	27.96	27.41	27.20
b (Å)	27.92	27.46	27.17
c (Å)	4.51	4.57	4.48
α (°)	113.83	111.41	115.39
β (°)	79.04	80.85	79.71
γ (°)	96.0	94.34	95.70

Table 4.2: Calculated energies of optimized TT-Por COF.

Total energy	−750.82 eV
D3 energy	−7.37 eV

Table 4.3: xyz-coordinates of optimized structures.

PBE-D3				AM1-D3			
Atom	x	y	z	Atom	x	y	z
H	3.513296467	24.902945380	2.806906687	S	12.385892	1.426674	−0.738334
H	5.964908645	24.976642310	2.818532626	H	6.129112	−1.614292	1.521637
H	2.344030758	4.759690262	0.258639937	H	8.600958	−1.747574	1.483074
H	4.368252224	2.997818029	0.208028521	C	5.908459	0.417300	−1.557691
H	5.072492748	1.421852919	1.959057529	C	7.295666	0.304167	−1.556452
H	7.564502464	1.489186068	1.990638234	C	8.045982	0.486495	−0.376668

H	15.204610095	1.300373056	1.963935190	N	9.449759	0.554377	−0.501375
H	22.208335619	1.180761128	1.513031013	H	12.269826	−1.560714	1.307655
H	19.756693626	1.105966127	1.503455336	C	11.683415	0.294879	0.279628
H	23.376433073	21.324614406	4.058775672	C	12.585214	−0.601586	0.877838
H	21.352252806	23.086452618	4.110671115	C	−13.293181	−0.310566	0.401888
H	20.647007535	24.662866388	2.360175082	H	5.424270	0.913259	1.785517
H	18.155001447	24.594412120	2.330692422	H	7.907646	0.840000	1.780968
H	10.516211526	24.779877213	2.360871739	C	7.351263	0.679328	0.843324
H	1.656861610	3.767908453	2.694151605	C	5.962269	0.779453	0.832306
H	1.368940329	6.192105100	2.844988626	C	10.244482	0.184306	0.453124
H	23.470786778	1.049701542	3.519617379	H	9.961917	−0.239197	1.452373
H	25.218522015	3.085972295	3.571547263	C	5.232486	0.638488	−0.345620
H	25.647386832	5.263607290	1.650622181	H	−2.004652	7.129603	−1.989874
H	25.347897619	7.727994051	1.809804630	H	−1.673085	7.721628	1.929600
H	24.115747293	15.337876908	1.336456252	C	−1.012949	7.276397	1.166137
H	2.249480233	25.034455797	0.799654874	C	−0.725717	5.900153	1.235366
H	0.501738869	22.998234049	0.746298145	C	−0.537322	10.290421	−0.774221
H	0.073249707	20.821063252	2.666260974	C	−0.858469	11.681378	−0.505335
H	0.372859263	18.356703998	2.506641962	C	−0.570292	12.772874	−1.309970
H	1.605216175	10.746414132	2.979676605	H	0.056404	10.108396	−1.693631
H	24.063898079	22.316073615	1.622701866	H	0.663684	8.042587	−1.748237
H	24.351963674	19.891894646	1.471463801	H	0.979038	5.586964	−1.706840
H	24.228233485	26.892996568	0.144142579	H	0.715574	10.878112	1.711136
H	1.492390295	−0.808769212	4.173452662	S	−1.514533	12.100153	0.998195
H	8.009597873	25.283249401	2.972767486	C	−0.067008	5.294439	0.151281
H	17.711696949	0.797271311	1.351334260	C	0.416939	6.076382	−0.895822
H	24.406897022	17.887666416	0.842035223	C	0.165820	7.444038	−0.970933
H	1.314051667	8.196513956	3.474189410	C	−0.553328	8.065350	0.094397
C	5.419552583	25.449439537	3.636703098	N	−0.867500	9.418088	0.132249
C	4.030731449	25.405549912	3.625211610	C	1.344454	−13.304039	0.701322
C	8.324963903	25.727177821	3.933981437	H	−4.070748	−2.581373	−0.031608
C	9.745398431	25.793402398	4.136245524	H	−2.014731	−4.391815	−0.134968
C	10.737603187	25.286077288	3.299462303	H	−0.104198	−7.311931	1.826448
C	12.025587377	25.531592085	3.815634633	H	−0.359462	−4.847847	1.767761

C	1.039533775	2.951024245	0.090227549	C	−3.148410	0.149822	0.290817
C	2.751792445	1.459646141	0.088820000	C	−2.425532	−1.089298	0.216486
C	2.270175508	3.680846214	0.183741193	C	−3.005037	−2.386898	0.054755
C	3.307465413	2.778631658	0.162722953	C	−1.948397	−3.314360	−0.011709
C	4.948515937	0.320837908	0.109604000	C	0.190882	−5.359482	0.960618
C	5.640947848	0.975664260	1.142665371	C	0.402263	−6.732950	1.039509
C	7.031052562	1.012609997	1.166318873	C	1.093269	−7.380847	−0.029468
C	7.796720250	0.408548035	0.150165445	N	1.379842	−8.738821	−0.057090
C	−0.268476416	3.480049104	0.071461366	C	−4.617062	0.053065	0.333192
C	20.301601987	0.633595825	0.684732941	H	−11.652531	2.042739	−1.410416
C	21.690415243	0.678124782	0.695050195	H	−4.764409	−0.241512	−1.802840
C	17.395935890	0.353850936	0.390014266	H	−7.248982	−0.256443	−1.829228
C	15.975424012	0.287144128	0.188356035	N	−1.043017	−1.236828	0.257769
C	14.983229171	0.794231137	1.025306978	C	−0.723102	−2.581505	0.101253
C	13.695229527	0.548776970	0.509115012	C	0.692071	−4.599454	−0.093762
C	25.989022018	22.604234948	4.245642347	C	0.600238	−3.132271	−0.035291
C	24.681013026	23.133240129	4.227093065	C	−6.712845	−0.077476	−0.882870
C	22.968766631	24.624628523	4.229436145	C	−5.321356	−0.120325	−0.856496
C	23.450337817	22.403435495	4.133876312	C	−9.623707	0.323200	−0.533593
C	22.413052073	23.305650396	4.155551383	C	−11.062800	0.191335	−0.376701
C	20.772028832	25.763305415	4.209930962	C	−11.965947	1.083006	−0.980330
C	20.079042071	25.108564595	3.177183244	C	−13.287734	0.788359	−0.508217
C	18.688941795	25.070985547	3.154696599	H	−0.389061	−0.499900	0.385981
C	17.923869348	25.674318199	4.171737765	H	−9.336381	0.748927	−1.530524
C	0.882144160	5.557656782	3.587486166	H	3.331080	−4.055535	−0.219917
C	1.042417467	4.180046731	3.495074511	H	5.077326	−1.938118	−0.421570
C	0.430105760	8.404526978	4.104656053	C	3.166409	−0.696132	−0.262442
C	0.079605538	9.790939138	4.217000502	C	3.126206	−2.987686	−0.242583
C	0.733531375	10.868174598	3.620679363	C	3.995048	−1.942138	−0.326746
C	0.114236518	12.090949698	3.939576822	H	1.796612	−4.628112	−1.973436
C	25.316899040	−0.216541567	3.893577795	H	2.199758	−7.080302	−1.880486
C	26.738626285	1.441318636	3.954140552	C	1.558950	−6.613081	−1.113677
C	24.539848201	1.001546806	3.698119054	C	1.313499	−5.228148	−1.185269
C	25.423833758	2.032578938	3.730582670	C	1.753862	−2.407270	−0.129831

C	−0.413164205	4.955616074	0.176684365	N	1.867708	−0.986057	−0.139105
C	26.157647913	5.919603224	0.944605549	H	−0.227407	−10.190709	−1.624592
C	25.991210120	7.296251823	1.041428003	H	−5.556441	2.273601	−1.530523
C	26.658068066	8.176353699	0.165479072	H	−8.030763	2.303818	−1.523956
C	22.259514886	25.842936316	4.231943060	C	1.841636	−13.045618	−0.614522
C	3.461035482	0.241331765	0.086729155	S	2.003561	−11.415384	−0.912503
C	0.403613766	26.300816594	0.424821350	S	−11.765524	−0.945607	0.634807
C	−1.018117597	24.642991148	0.363325142	N	−1.212500	1.724440	0.193504
C	1.180530092	25.082676700	0.620521502	C	−5.314500	0.232106	1.538087
C	0.296549977	24.051672636	0.587368611	C	−6.705294	0.283726	1.520286
C	26.133791473	21.128691800	4.140164394	C	−7.431163	0.082913	0.328264
C	−0.436987425	20.164909854	3.372149077	N	−8.834043	−0.028120	0.432271
C	−0.270470873	18.788281534	3.275098439	H	−2.660804	4.758070	0.151852
C	−0.937239482	17.907997209	4.150952942	H	−4.468586	2.691194	0.343577
C	24.838686388	20.526501151	0.729056673	C	−1.125199	3.058265	0.162213
C	24.678314386	21.904084852	0.821679341	C	−2.595890	1.396042	0.272377
C	25.290846007	17.679763409	0.211545492	C	−2.486118	3.686665	0.208583
C	25.641354550	16.293366941	0.099110115	C	−3.383357	2.665595	0.286412
C	24.987395662	15.216119188	0.695390227	N	1.668063	1.934454	−0.154395
C	25.606662621	13.993340179	0.376457127	C	0.087773	3.838502	0.093772
N	−0.650886527	16.547749500	4.006103997	H	1.016169	1.205672	−0.318029
N	−0.149023008	24.353938476	4.482145783	H	4.723214	3.313683	−0.064649
N	26.371778748	9.536629008	0.310158052	H	2.653536	5.127379	0.104630
N	25.869581672	1.730382340	−0.164423292	C	3.061706	1.781971	−0.194472
N	16.534094409	25.600159967	4.025038476	C	1.336476	3.291344	−0.040395
N	24.337678685	24.467798530	4.277243013	C	3.646785	3.150295	−0.090273
N	9.186417432	0.481985852	0.298043163	C	2.625755	4.043751	0.001996
N	1.382900134	1.616463299	0.040415214	C	3.766927	0.615890	−0.287963
S	12.080060299	0.898446767	1.020222770	C	1.039514	−9.600462	0.856495
S	13.640729463	25.182328329	3.304250860	C	1.349419	−10.995139	0.592340
S	25.320094361	12.334086549	0.766175526	C	1.058952	−12.086062	1.396698
S	0.400870567	13.750212823	3.549929935	H	0.445811	−9.406248	1.773193
27.4056368719	0.3950908088	−0.2140880635	27.200	0.000	0.000		

−2.4679791106	27.3456216629	0.3456654297	−2.699	27.036	0.000
0.7836107729	−1.6575373609	4.1873291534	0.800	−1.85	4.000

Table 4.4: Calculated total energy and lattice parameters of TT-Por COF in a geometry with an initial interlayer spacing of 15 Å and fixed unit cell volume.

Total energy	−749.01 eV
D3 energy	−5.14 eV
Cell parameters	a = 27.39 Å
	b = 27.33 Å
	c = 15.13 Å
	α = 95.33
	β = 89.91
	γ = 90.97

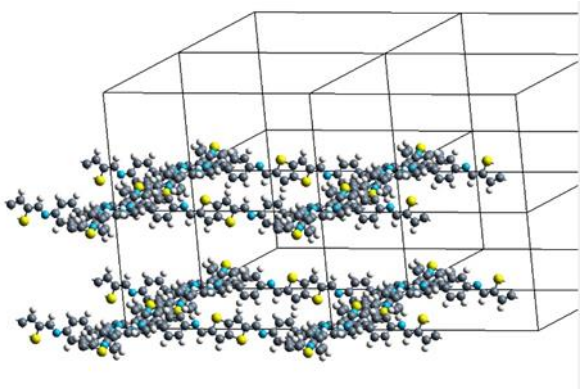

Table 4.5: xyz-coordinates of optimized TT-Por COF with an initial interlayer spacing of 15 Å and fixed unit cell volume.

Atom	x	y	z
H	4.086719378	24.974673068	13.657355127
H	6.552029911	25.073286238	13.763414277
H	2.303563290	4.764899127	0.192741405
H	4.354965306	3.032670135	0.035755019
H	5.008682382	1.383198924	1.954315181
H	7.496477123	1.488642858	2.063566559
H	15.278989379	0.568933542	1.932382834
H	22.080276764	1.894045991	1.122464308
H	19.614897566	1.795883601	1.016710743
H	23.863019134	22.103757903	14.586350353
H	21.811590102	23.836020471	14.743680850
H	21.157451389	25.485641279	12.825351894
H	18.669606278	25.380730860	12.716381480
H	10.887595358	26.300624025	12.847981684
H	0.972905928	3.728810433	13.376932064
H	0.669239273	6.178374713	13.524831991

H	23.074892774	1.910096076	14.127298548
H	24.831483555	3.939418804	14.233771217
H	25.919480088	6.066576001	1.462480206
H	25.607848385	8.536625442	1.614591191
H	24.361452514	16.259526173	0.565129553
H	3.091691726	24.958481587	0.651674474
H	1.335136126	22.929189329	0.544807097
H	0.246802161	20.802437141	13.316121031
H	0.558278376	18.332364264	13.163574359
H	1.804456768	10.609170955	14.212289774
H	25.193618770	23.139596009	1.401766504
H	25.497085745	20.690024354	1.253372780
H	25.436439027	26.050479391	14.746457767
H	0.730149493	0.818184830	0.032885014
H	10.072568304	−0.978132856	13.301843735
H	16.094147254	27.847456101	1.478331913
H	24.902113784	18.794378292	0.130609134
H	1.264018957	8.074310254	14.647097032
C	5.960706780	25.538941200	14.553675526
C	4.572380693	25.470078800	14.499938760
C	10.441226707	−1.013084427	14.343879790
C	11.868778403	−1.011578757	14.496193541
C	11.156724381	26.283514698	13.902989575
C	12.467882487	26.277511757	14.416967591
C	1.027257242	2.931866274	0.114437311
C	2.756150547	1.470287937	0.032975113
C	2.248109593	3.683535605	0.134135956
C	3.296510260	2.797960360	0.063600845
C	4.959040354	0.361187038	0.053035638
C	5.608893340	0.977328777	1.138359951
C	6.995731416	1.035408347	1.206957244
C	7.792557644	0.504686357	0.174391908
C	27.070477544	4.655369391	−0.535908933
C	20.206085586	1.330151246	0.226333077

C	21.594463273	1.398719739	0.279892074
C	15.725410375	27.882599858	0.436378611
C	14.297854799	27.881170619	0.284098047
C	15.009858738	0.586084449	0.877298651
C	13.698646277	0.592126455	0.363367788
C	−0.903900708	22.213305320	15.314886826
C	25.139342857	23.936819090	14.664740271
C	23.410433610	25.398400525	14.746470471
C	23.918468676	23.185159459	14.645054971
C	22.870072118	24.070762174	14.715785712
C	21.207546065	26.507541600	14.726665313
C	20.557432172	25.891572840	13.641421271
C	19.170617175	25.833801005	13.572977779
C	18.373949921	26.364592269	14.605628040
C	0.351164045	5.543565713	14.354000213
C	0.512765269	4.163805142	14.266172317
C	0.306955956	8.359149758	15.122887093
C	0.038265299	9.768690908	15.182720057
C	0.848276851	10.792509622	14.700016864
C	0.269383054	12.056536311	14.924840182
C	24.930386076	0.623843778	14.386153830
C	25.884065811	3.887463511	−0.577282166
C	24.149678988	1.849967874	14.268449382
C	25.038595027	2.877360545	14.321246747
C	26.929408641	6.134308026	−0.442988463
C	26.288781751	6.715260905	0.666546439
C	26.113434885	8.090818309	0.756795699
C	26.596970282	8.945261287	−0.252339535
C	22.690345046	26.607878898	14.774749801
C	3.476186549	0.260743219	0.004753447
C	1.236242899	26.244764014	0.393162740
C	0.282529776	22.981221874	15.356330122
C	2.016931589	25.018668989	0.510607173
C	1.128034590	23.991285422	0.457593263

C	−0.762939166	20.734403122	15.221740055
C	−0.122422840	20.153619916	14.112018455
C	0.052809340	18.778016927	14.021500717
C	−0.430677148	17.923423272	15.030559401
C	25.815214389	21.324969982	0.424289280
C	25.653741509	22.704697449	0.512404351
C	25.859130844	18.509575967	−0.345151797
C	26.127698572	17.100051697	−0.405287758
C	25.317616003	16.076168896	0.077280441
C	25.896464355	14.812092117	−0.147639360
N	−0.197400221	16.554493921	14.889561225
N	0.369996165	24.350847563	15.331555743
N	26.363566087	10.314255952	−0.111594330
N	25.796583804	2.517832581	−0.552271668
N	16.988613366	26.288902878	14.451427879
N	24.781404233	25.265751514	14.727375113
N	9.177885794	0.580670926	0.328719438
N	1.385180036	1.602911543	0.051938061
S	12.112636043	0.573239863	1.049393164
S	14.054013678	26.296360574	13.730918783
S	25.441828346	13.178624228	0.185850480
S	0.724068631	13.690059338	14.591470175

27.3522114645	1.2093273530	−0.6872402161
−1.6593806253	27.2731628462	0.4267892610
0.4741983004	−1.6140519556	15.0395126815

4.5.4 X-Ray Diffraction

COF-366 was analyzed via PXRD, revealing a crystalline framework.

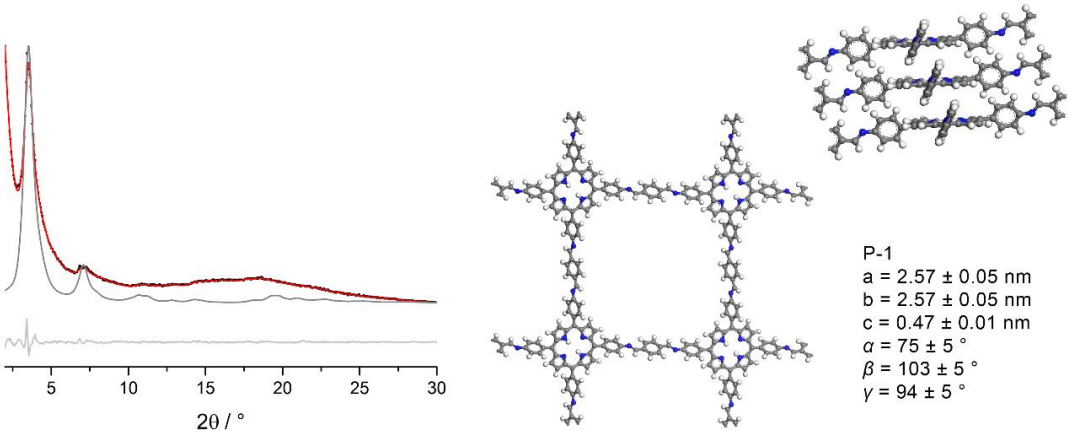

Figure 4.5: Experimental PXRD data (black dots) of the COF-366. Pawley refinement (red line) using the P1 symmetric structure model shown on the right provides a very good fit to the experimental pattern (difference shown in light grey). The simulated crystal structure of COF-366 (grey line) is in good agreement with the experimental and the refined data, respectively. Differences in the peak intensities, in particular the altered intensity ratios between lower- and higher-angle reflections, may be caused by small oligomeric fragments trapped in the large COF pores (the attenuation of peak intensities due to this will be strongest at small 2θ angles).

OMe-Por COF and 2P-Por COF was analyzed via PXRD, revealing a crystalline framework.

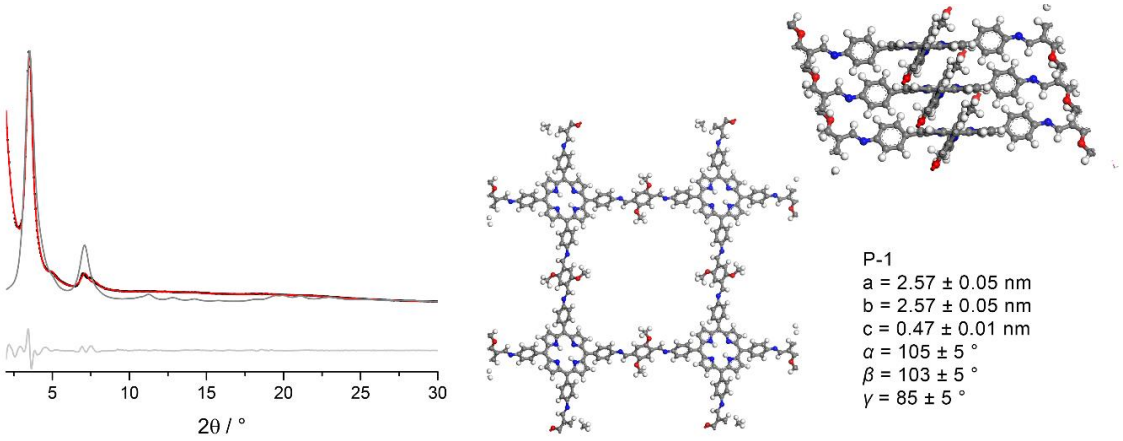

Figure 4.6: Experimental PXRD data (black dots) of the OMe-Por COF. Pawley refinement (red line) using the P1 symmetric structure model shown on the right provides a very good fit to the experimental pattern (difference shown in light grey). The simulated crystal structure of OMe-Por COF (grey line) is in good agreement with the experimental and the refined data, respectively. Differences in the peak intensities, in particular the altered intensity ratios between lower- and higher-angle reflections, may be caused by small oligomeric fragments trapped in the large COF pores (the attenuation of peak intensities due to this will be strongest at small 2θ angles).

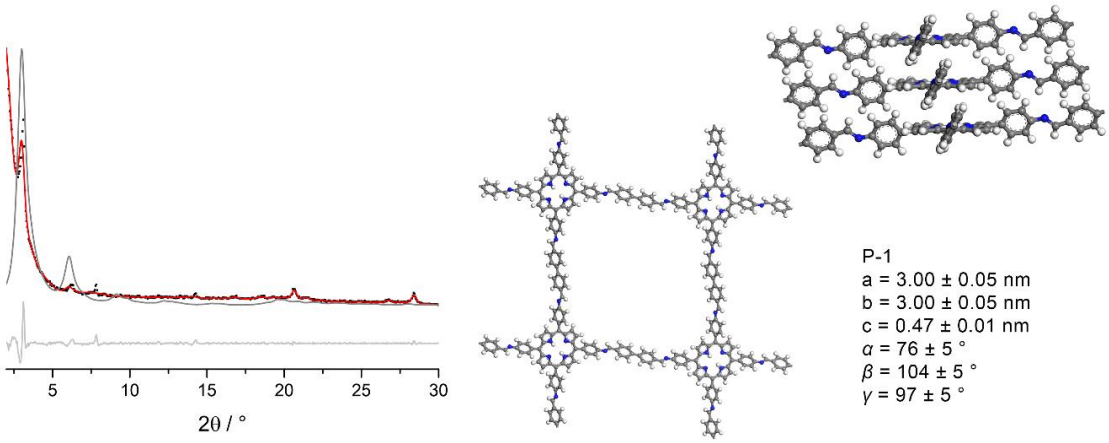

Figure 4.7: Experimental PXRD data (black dots) of the 2P-Por COF. Pawley refinement (red line) using the P1 symmetric structure model shown on the right provides a good fit to the experimental pattern (difference shown in light grey). The simulated crystal structure of 2P-Por COF (grey line) is in reasonable agreement with the experimental and the refined data. Differences in the peak intensities, in particular the altered intensity ratios between lower- and higher-angle reflections, may be caused by small oligomeric fragments trapped in the large COF pores (the attenuation of peak intensities due to this will be strongest at small 2θ angles).

4.5.5 IR Spectroscopy

The successful formation of the imine-linked TT-Por COF was confirmed by Fourier transform infrared (FTIR) spectroscopy. Consistent with previously reported COFs, the appearance of the characteristic C=N stretching mode at 1581 cm^{-1} indicates the coupling of the monomers via imine bonds (Figure 4.8). The lack of the aldehyde Fermi double resonance at 2841 and 2755 cm^{-1} as well as the aldehyde C=O stretching vibration at 1652 cm^{-1} suggests the complete consumption of the starting material TT-dialdehyde. Furthermore, the attenuation of the characteristic C-N stretching mode at 1285 cm^{-1} indicates the absence of the second starting material porphyrin-tetraphenylamine.[9-10]

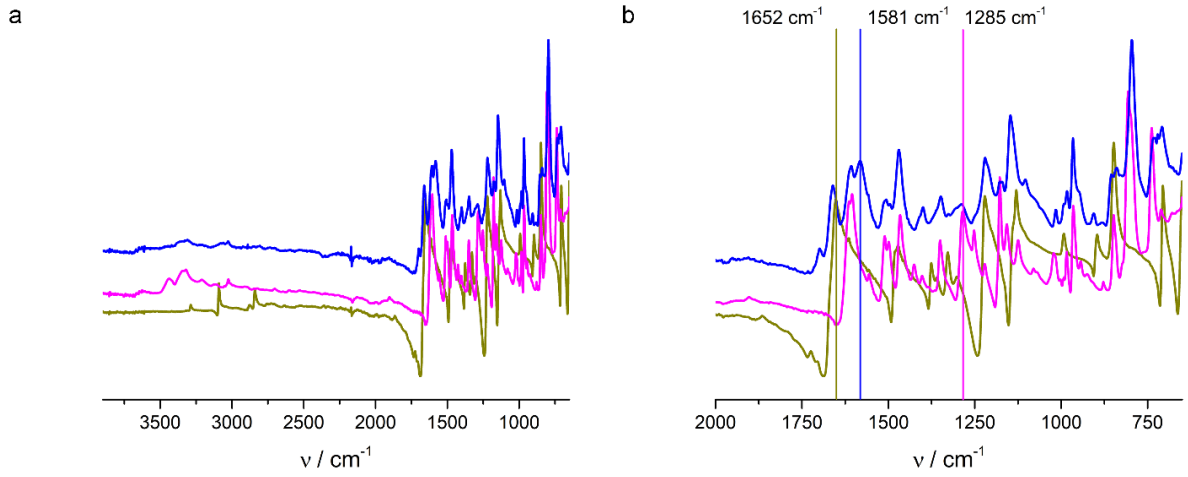

Figure 4.8: (a) IR spectra of TT-Por COF (blue), thienothiophene monomer (dark yellow) and porphyrin monomer (magenta), measured as powder. (b) Enlargement of the region of interest.

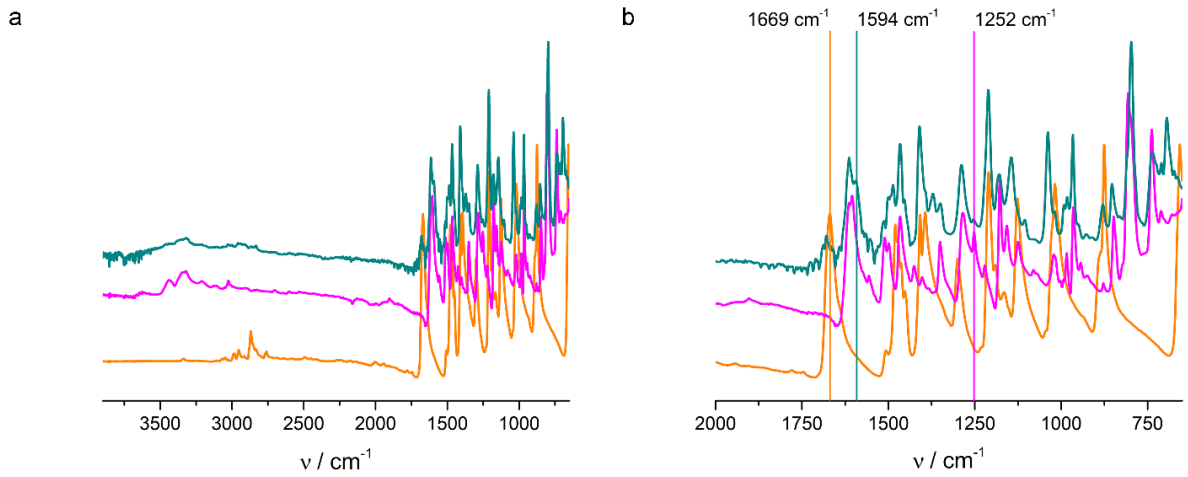

Figure 4.9: (a) IR spectra of OMe-Por COF (cyan), porphyrin monomer (magenta) and 2,5-dimethoxybenzene-1,4-dicarboxaldehyde (orange). (b) Enlargement of the region of interest.

Furthermore, the successful synthesis of OMe-Por COF, COF-366 and 2P-Por COF was confirmed by FTIR spectroscopy. As seen in the spectra (Figure 4.9-Figure 4.11), the lack of the aldehyde Fermi double resonance between 2750 cm^{-1} and 2850 cm^{-1} as well as the aldehyde C=O stretching vibration at 1669 cm^{-1}, 1686 cm^{-1} and 1686 cm^{-1}, respectively, suggests the complete consumption of the starting dialdehyde material (terephthalaldehyde, 2,5-dimethoxybenzene-1,4-dicarboxaldehyde and 4,4'-biphenyldicarboxaldehyde, respectively). Additionally, the attenuation of the characteristic C-N stretching mode at 1252 cm^{-1}, 1285 cm^{-1}, and 1284 cm^{-1}, respectively, indicates the absence of the second starting material compound 1. The appearance of the C=N stretching mode at 1594 cm^{-1}, 1564 cm^{-1}, and 1572 cm^{-1}, respectively, is characteristic for the formation of imine bonds within the COF material and indicates the successful Schiff base reaction of the monomers.[9-10]

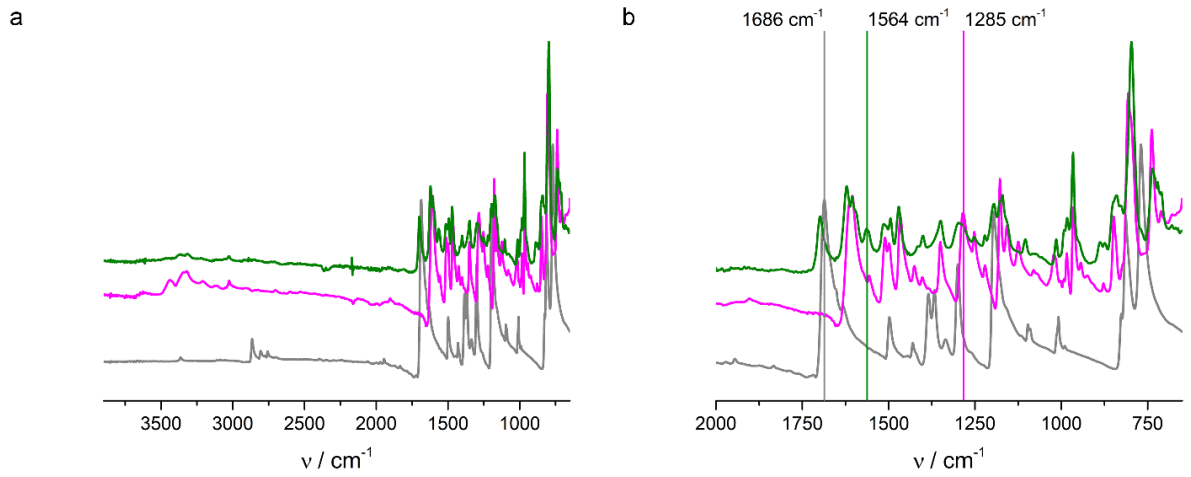

Figure 4.10: (a) IR spectra of COF-366 (green), porphyrin monomer (magenta) and terephthalaldehyde (gray). (b) Enlargement of the region of interest.

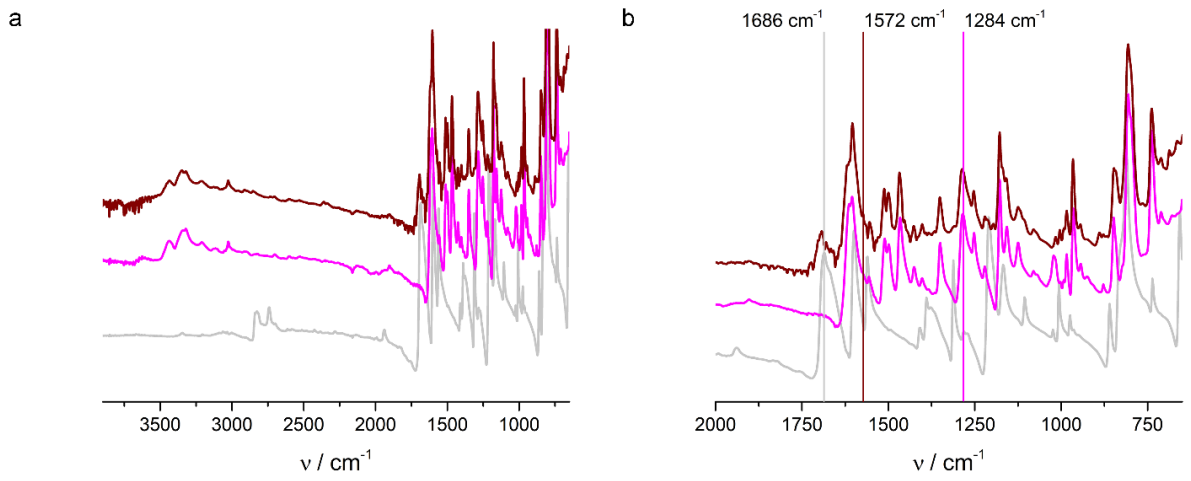

Figure 4.11: (a) IR spectra of 2P-Por COF (red), porphyrin monomer (magenta) and 4,4'-biphenyldicarboxaldehyde (light gray). (b) Enlargement of the region of interest.

4.5.6 UV-vis and Fluorescence Spectroscopy

Absorption spectra of the starting materials, TT-Por COF, COF-366, OMe-Por COF and 2P-Por COF (Figure 4.12) were collected from solid samples in diffuse reflection mode and transferred into absorption spectra by applying the Kubelka Munk equation:

$$\frac{K}{S} = \frac{(1 - R_\infty)^2}{2R_\infty}$$

with K = Absorption Coefficient, S = Scattering Coefficient, R_∞ = reflectance of sample with infinite thickness.

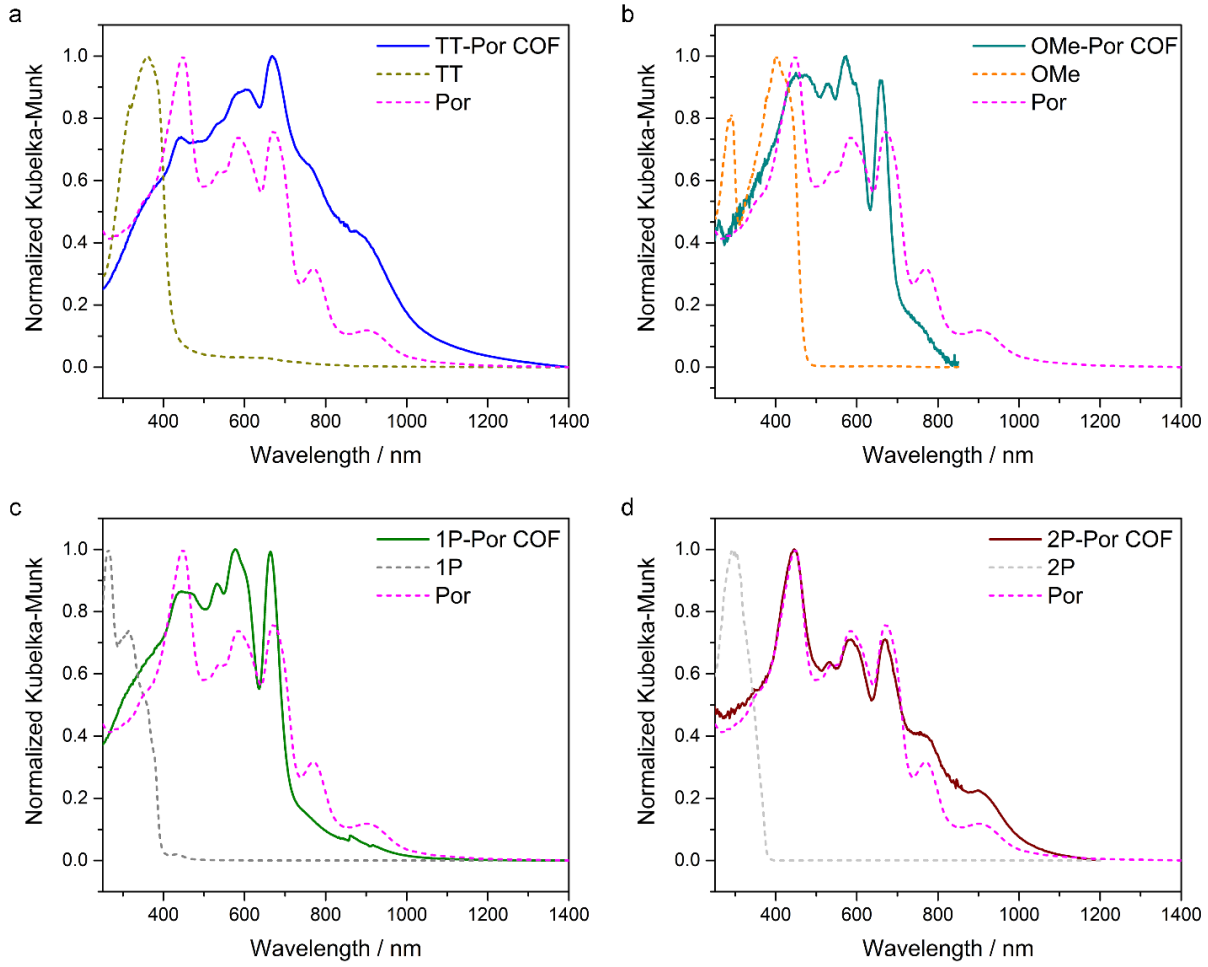

Figure 4.12: (a) UV-Vis spectra of TT-Por COF (blue) and the corresponding starting materials compound 1 (Por, magenta) and thienothiophene (TT, dark yellow). (b) UV-Vis spectra of OMe-Por COF (cyan) and the corresponding starting materials compound 1 (Por, magenta) and 2,5-dimethoxybenzene-1,4-dicarboxaldehyde (OMe, orange). (c) UV-Vis spectra of COF-366 (green) and the corresponding starting materials compound 1 (Por, magenta) and terephthalaldehyde (1P, gray). (d) UV-Vis spectra of 2P-Por COF (red) and the corresponding starting materials compound 1 (Por, magenta) and 4,4'-biphenyldicarboxaldehyde (2P, light gray). Diffuse reflectance spectra measured for the respective powders dispersed in $BaSO_4$.

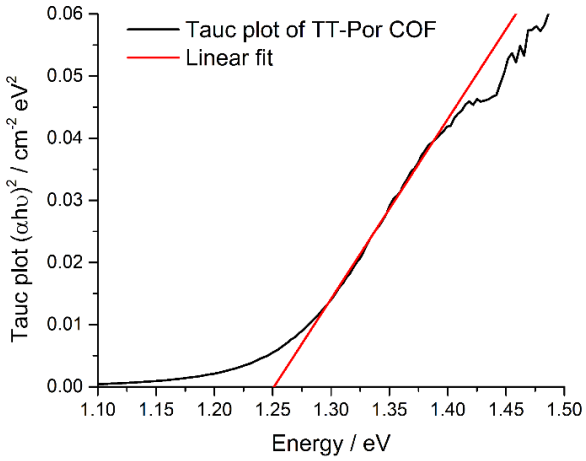

Figure 4.13: Tauc plot for absorption spectra (black) obtained with Kubelka-Munk function of the TT-Por COF and the linear fit for a direct bandgap (red).

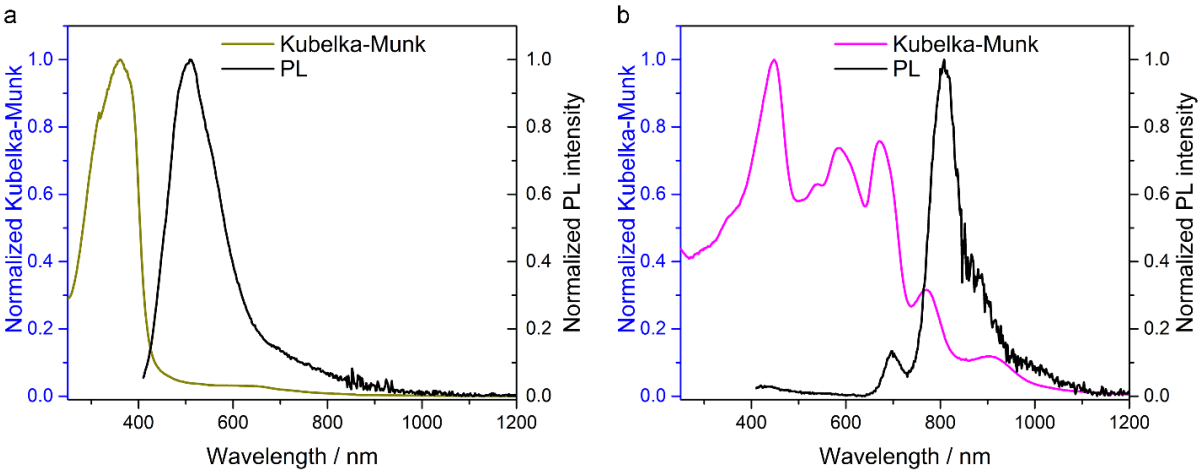

Figure 4.14: (a) Absorption (dark yellow) and PL (λ_{exc} = 365 nm, black) spectra of the TT starting material measured as solid. (b) Absorption (magenta) and PL (λ_{exc} = 365 nm, black) spectra of compound 1 measured as solid. Diffuse reflectance spectra measured for the respective powders dispersed in $BaSO_4$.

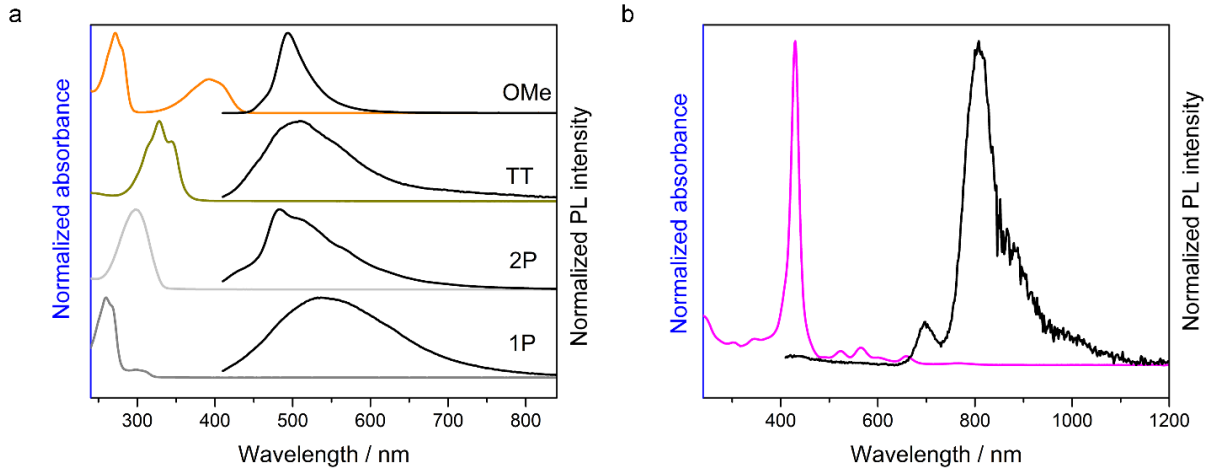

Figure 4.15: (a) Optical absorption (OMe: orange, TT: dark yellow, 2P: light gray, 1P: gray) and PL (λ_{exc} = 365 nm, black) spectra of the starting materials. (b) Absorption (magenta) and PL (λ_{exc} = 365 nm, black) spectra of the compound 1. The absorbance of the compounds was measured in a 50 µM solution in dioxane.

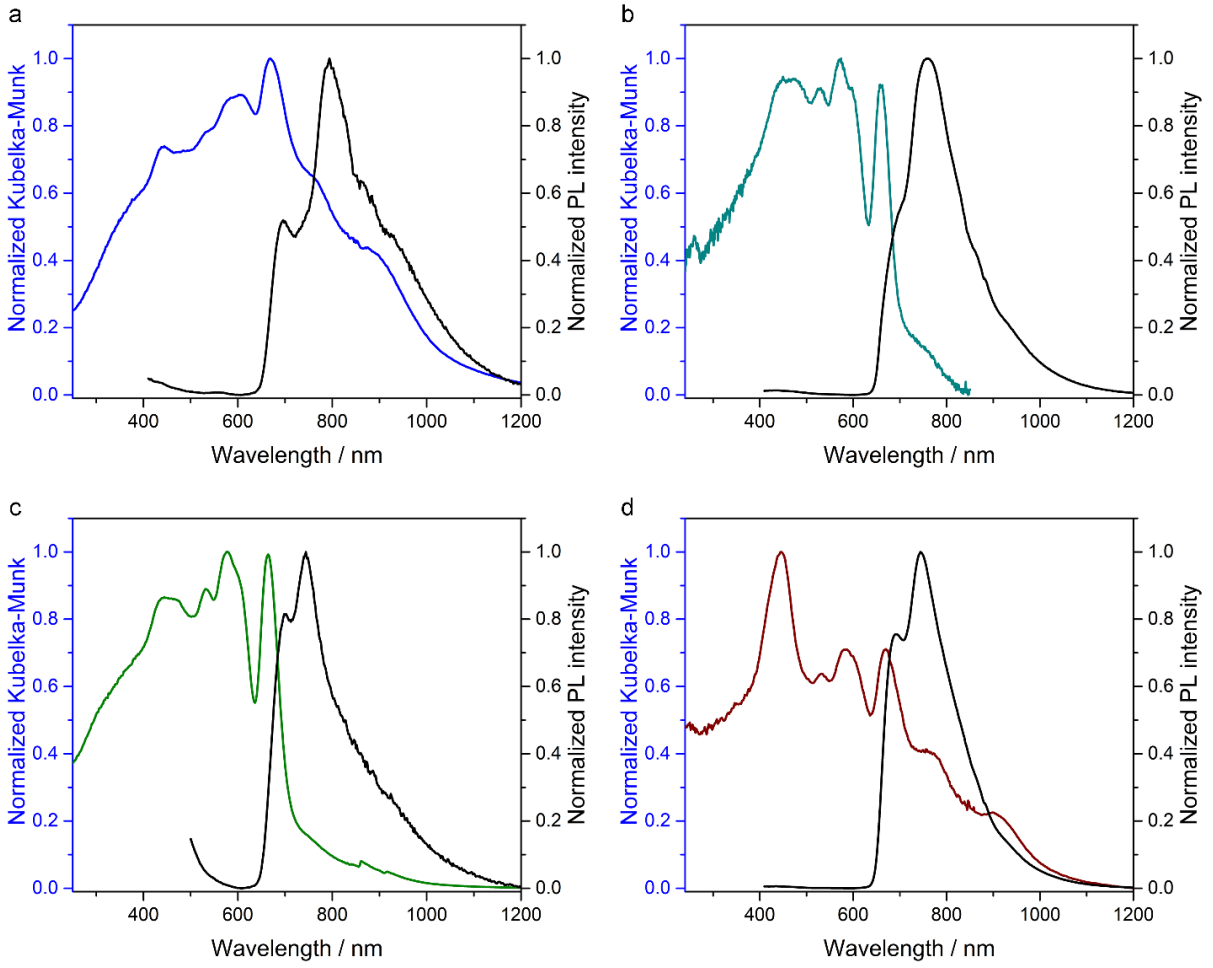

Figure 4.16: Optical absorption spectra measured as diffuse reflectance of the solid and converted with the Kubelka Munk equation, and PL (λ_{exc} = 365 nm, black) spectra of TT-Por COF (a), OMe-Por COF (b), COF-366 (c) and 2P-Por COF (d).

4.5.7 Time-Correlated Single Photon Counting

The tri-exponential fit of the TCSPC histogram for TT-Por COF revealed long decay times of 4.90 ns (16.4%) and also two fast components with lifetimes of 0.55 ns (38.1%) and 0.15 ns (45.5%). Quenching by the imine bond weakens the PL intensity compared to the starting materials. Internal conversion involving bond rotation results in the deactivation of the singlet excited state which is primarily the reason for PL quenching in imines.[11-12]

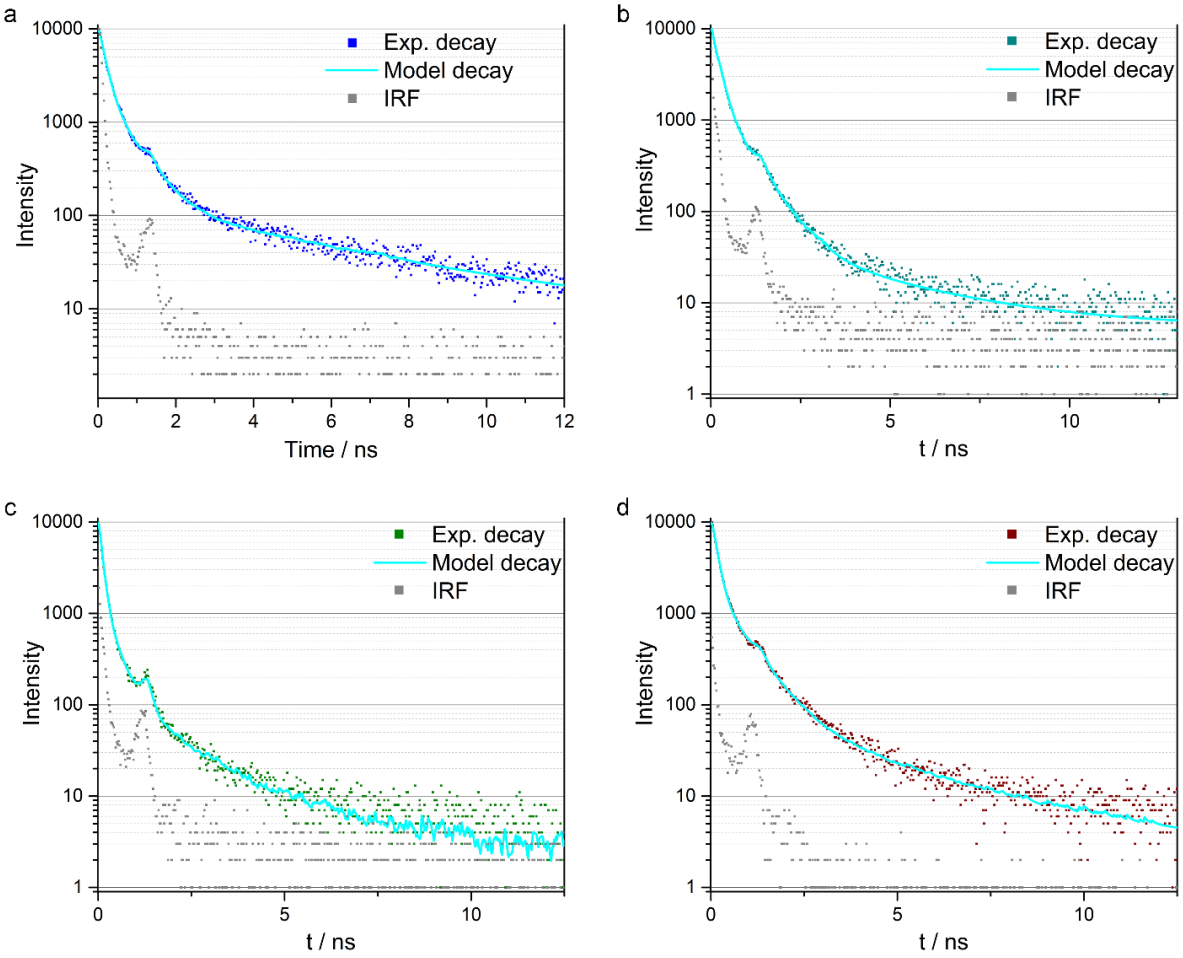

Figure 4.17: (a) PL decay of TT-Por COF excited at 378 nm and measured at the maximum of the PL emission at 800 nm. (b) PL decay of OMe-Por COF excited at 408 nm and measured at the maximum of the PL emission at 735 nm. (c) PL decay of COF-366 excited at 378 nm and measured at the maximum of the PL emission at 735 nm. (d) PL decay of 2P-Por COF excited at 408 nm and measured at the maximum of the PL emission at 743 nm. Experimental decay: blue (TT-Por), dark cyan (OMe-Por), green (1P-Por) and red (2P-Por) dots, tri-exponential fit of the decay: cyan line, instrument response function: gray dots.

When comparing the lifetimes, it is obvious that the TT-Por COF reveals the longest PL decay. In addition, the fractional intensity of the longest lifetimes is, with 16.4%, significantly higher

for the TT-Por COF than the fractional intensities of OMe-Por COF, COF-366 and 2P-Por COF. Hence, the optoelectronic behavior of the TT-Por COF seems to be substantially different, which is attributed to different structural features indicated by the distinct peak splitting in the XRD data for the TT-Por COF compared to the other three COFs.

Table 4.6: PL decay times of TT-Por COF, OMe-Por COF, COF-366 and 2P-Por COF. The given errors are uncertainties from the fit and hence do not reflect the real time-resolution of the setup. The latter is limited by the laser pulse duration of around 100 ps.

		τ / ns	error / ns	fractional intensity / %
TT-Por	τ_1	4.9	±0.3	16.4
	τ_2	0.55	±0.02	38.1
	τ_3	0.150	±0.006	45.5
OMe-Por	τ_1	3.2	±0.2	5.5
	τ_2	0.60	±0.01	37.9
	τ_3	0.175	±0.003	56.6
COF-366	τ_1	1.74	±0.09	6.5
	τ_2	0.31	±0.01	19.1
	τ_3	0.066	±0.001	74.4
2P-Por	τ_1	2.9	±0.2	7.5
	τ_2	0.63	±0.01	35.1
	τ_3	0.121	±0.003	57.4

The PL lifetime was also measured for the two starting materials TT and (1) by illumination at 405 nm and 508 nm, respectively, with a pump fluence of ~0.99 nJcm^{-2}; the emission was monitored at the maximum of the PL emission at 550 nm for TT and at 800 nm for (1).

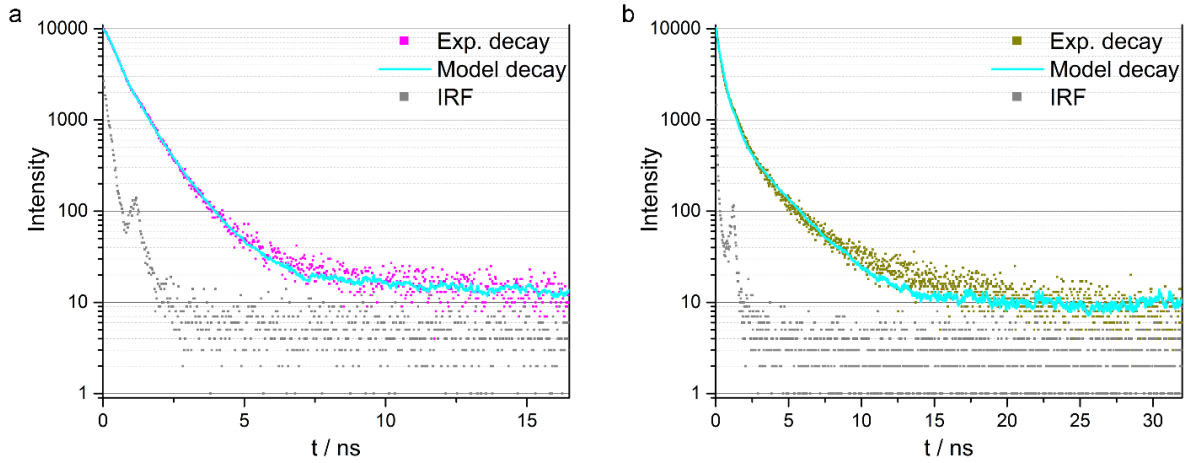

Figure 4.18: (a) PL decay of compound (1) excited at 508 nm and measured at the PL maximum at 800 nm. (b) PL decay of TT linker excited at 405 nm and measured at the PL maximum at 550 nm. All samples were measured as solids. Experimental decay: black dots, tri-exponential fit of the decay: red line, instrument response function: gray line.

Table 4.7: PL decay times of the starting materials (1) and TT, measured as solids. The given errors are uncertainties from the fit and hence do not reflect the real time-resolution of the setup. The latter is limited by the laser pulse duration of around 100 ps.

		τ / ns	error / ns	fractional intensity / %
Compound (1)	τ_1	1.01	±0.02	47.7
	τ_2	0.365	±0.006	52.3
TT	τ_1	2.31	±0.06	37.3
	τ_2	0.42	±0.01	62.7

Furthermore, TCSPC measurements were performed for the starting materials in dilute solutions of dioxane (50 µM), in which the monomers exist as individual molecules and intermolecular interactions can be neglected. It can be observed that the two starting materials TT and (1) observed as solvated molecules in dilute solutions have very long PL decay times, which when aggregated in a solid reduce to the order of 1 ns. This was also reported for porphyrin derivatives, which reveal shorter lifetimes when a J-aggregate behavior of the porphyrin stacks in the solid phase exists.[13] When embedding (1) in a COF, the decay lifetimes far exceed those of the solid compound (1), but do not reach the PL lifetimes of the individual molecules in dilute solution.

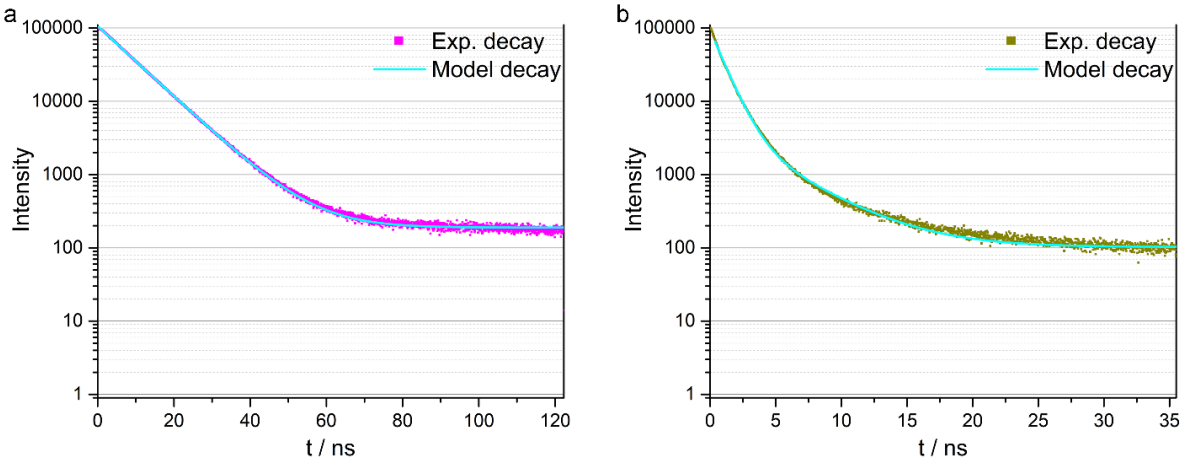

Figure 4.19: (a) PL decay of compound (1) in dilute solutions of dioxane (50 µM) excited at 508 nm and measured at the maximum of the PL emission at 680 nm. (b) PL decay of TT in in dilute solutions of dioxane (50 µM) excited at 378 nm and measured at the maximum of the PL emission at 495 nm. Experimental decay: black dots, tri-exponential fit of the decay: red line.

Table 4.8: PL decay times of the COF starting materials (1) and TT in dilute solutions of dioxane (50 µM). The given errors are uncertainties from the fit and hence do not reflect the real time-resolution of the setup. The latter is limited by the laser pulse duration of around 100 ps.

		τ / ns	error / ns	fractional intensity / %
Compound (1)	τ_1	9.05	±0.02	100.0
TT	τ_1	4.04	±0.06	21.1
	τ_2	0.987	±0.007	78.9

4.5.8 Differential Pulse Voltammetry and Optical HOMO-LUMO Gap of the Starting Materials

Differential pulse voltammetry was performed to obtain the energy levels of the HOMO from the different starting materials (Figure 4.20). The monomers were analyzed in dilute solutions of dioxane (50 µM) such that the starting materials exist as individual molecules, and interactions with other molecules are minimized. As a result, the measurement reveals the HOMO level of the solvated molecule. To identify the LUMO, Tauc plots were generated from the UV-Vis spectra (Figure 4.21) leading to the energy levels displayed in Figure 4.22.

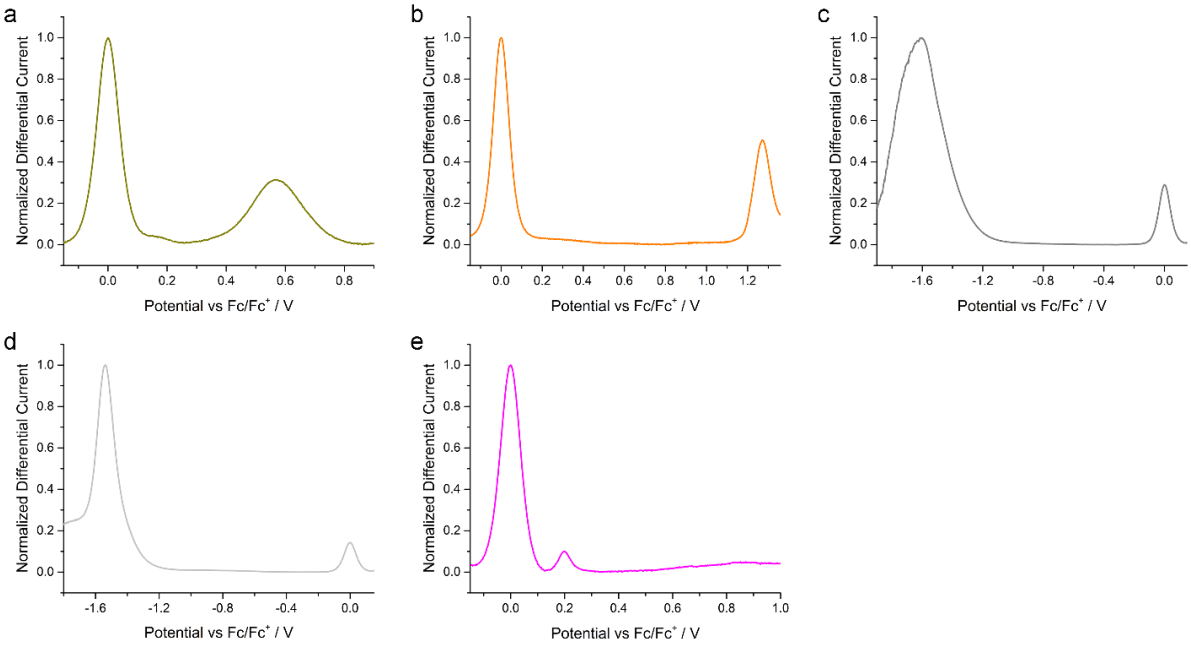

Figure 4.20: DPV measurements of the starting materials referenced to ferrocene (at 0.0 V). (a) TT, (b) OMe, (c) 1P, (d) 2P and (e) compound 1 (Por).

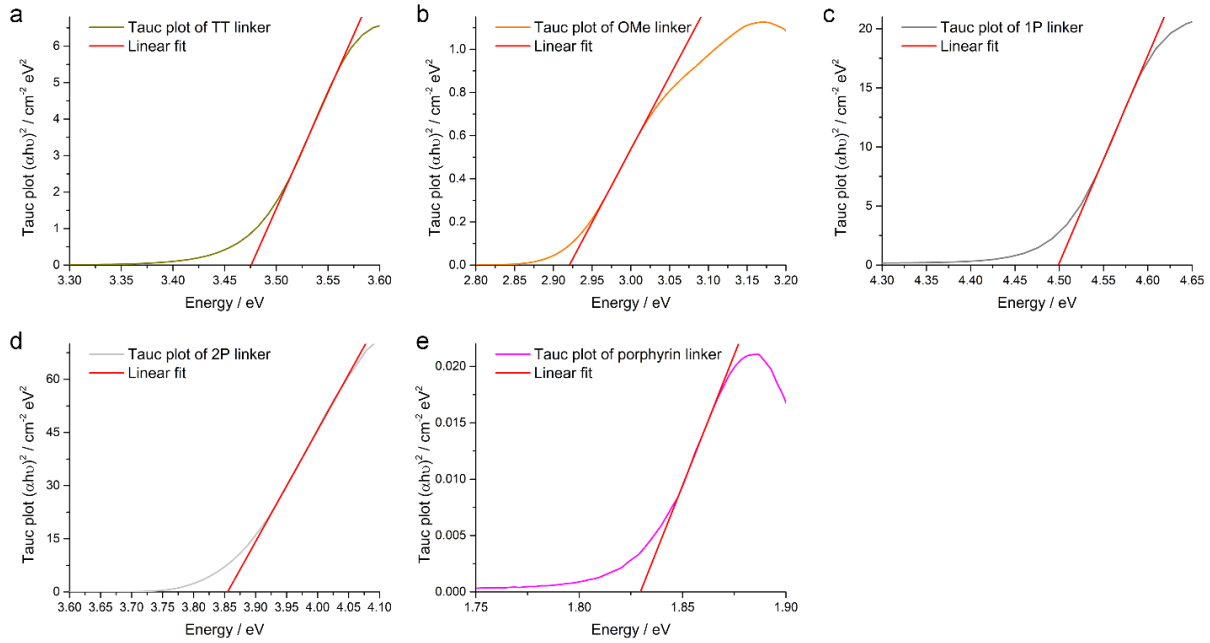

Figure 4.21: Tauc plots generated from optical absorption spectra obtained with Kubelka-Munk data of the starting materials and linear fits for direct bandgaps (red). (a) TT, (b) OMe, (c) 1P, (d) 2P and (e) compound 1 (Por).

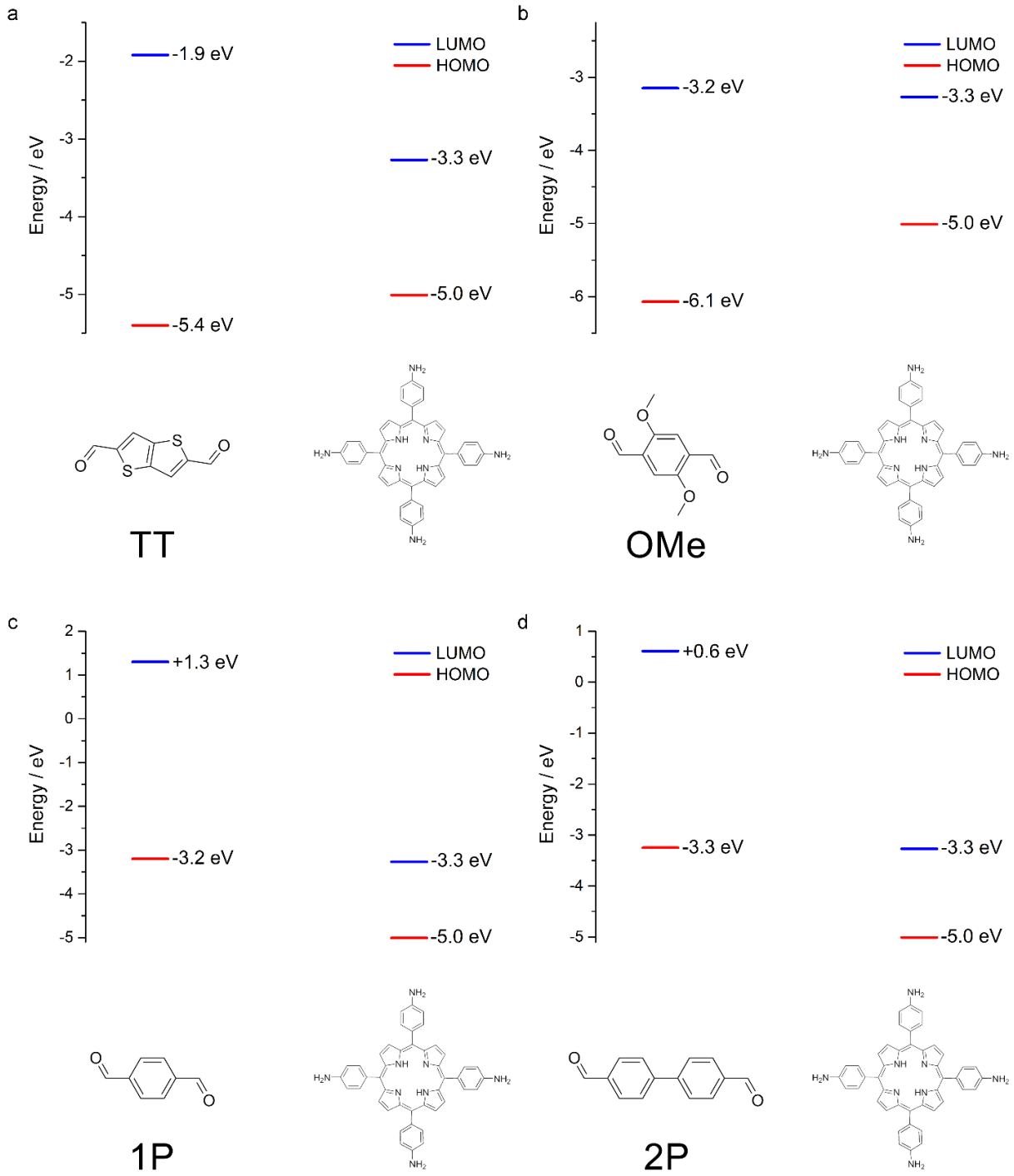

Figure 4.22: DPV measurements of the starting materials and the corresponding HOMO-LUMO gaps lead to the exact positions of the HOMO (red) and LUMO (blue) of the monomers. The linear monomers (a) TT, (b) OMe, (c) 1P and (d) 2P are compared to the tetragonal porphyrin unit (compound 1, Por).

4.5.9 Solid-State Nuclear Magnetic Resonance

The formation of the imine bonds in the COF can be confirmed by solid-state nuclear magnetic resonance (ssNMR). In the ^{13}C solid-state NMR only the carbons next to protons can be seen due to the cross-polarization. In the spectrum only four main broad peaks are clearly visible but there are some shoulders that can be attributed to other signals (Figure 4.23). The peak at 146 ppm can be attributed to C4 in the imine bonds arising from COF formation.

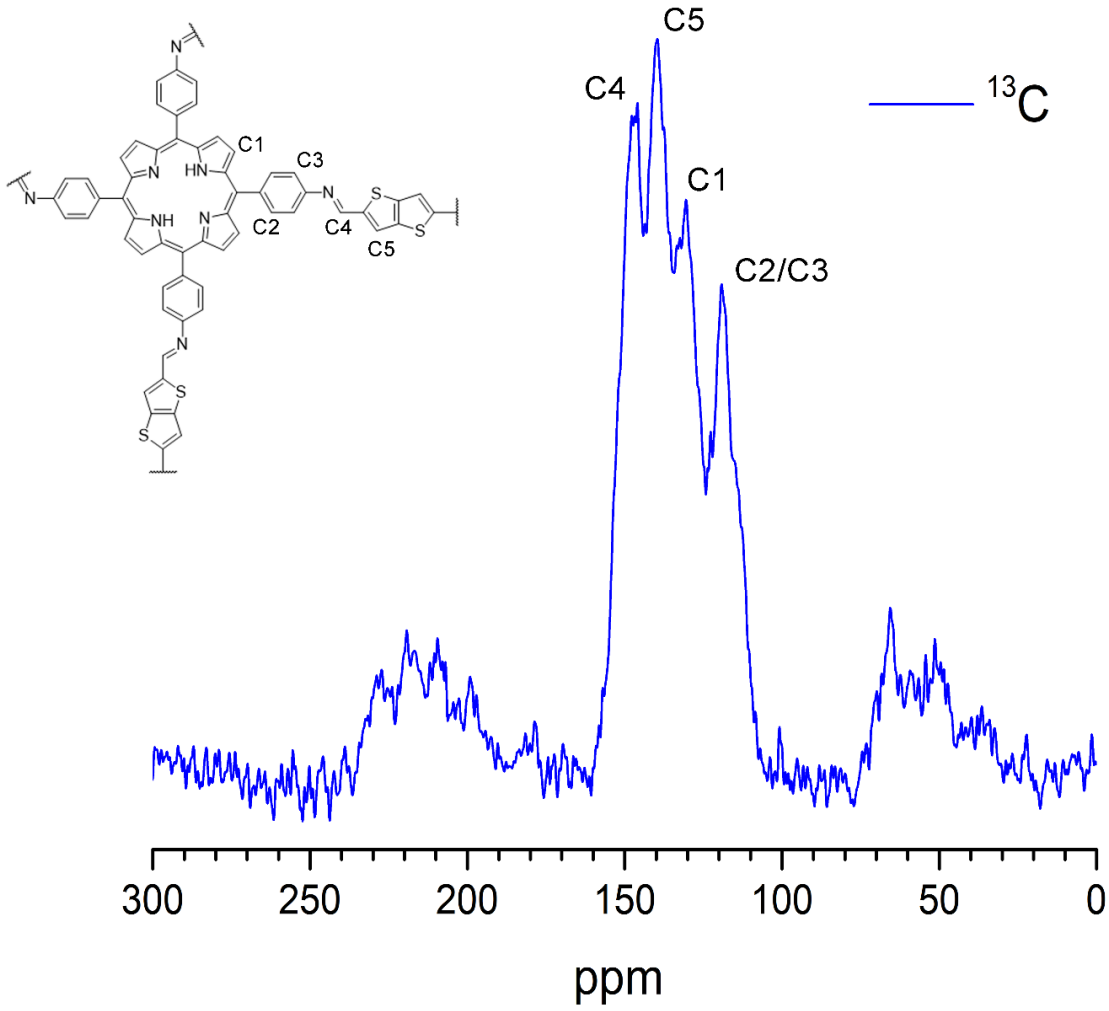

Figure 4.23: ^{13}C ssNMR of TT-Por COF measured with cross polarization to enhance signal from ^{13}C. Inset visualizes the different carbon species in the framework.

For the TT unit only C5 is visible, appearing in the spectrum at 140 ppm. Furthermore, the phenyl carbons C2 and C3 are observed around 119 ppm and the side peak at 123 ppm. The carbons of the tetrapyrrole subunit are summarized under C1 and can be found at 131 ppm and the shoulder at 133 ppm.

4.5.10 References

[1] Kresse, G.; Furthmüller, J., Efficiency of ab-initio total energy calculations for metals and semiconductors using a plane-wave basis set. *Comput. Mater. Sci.* **1996,** *6* (1), 15-50.

[2] Blöchl, P. E., Projector augmented-wave method. *Phys. Rev. B* **1994,** *50* (24), 17953-17979.

[3] Perdew, J. P.; Burke, K.; Ernzerhof, M., Generalized Gradient Approximation Made Simple. *Phys. Rev. Lett.* **1996,** *77* (18), 3865-3868.

[4] Grimme, S.; Antony, J.; Ehrlich, S.; Krieg, H., A consistent and accurate ab initio parametrization of density functional dispersion correction (DFT-D) for the 94 elements H-Pu. *J. Chem. Phys.* **2010,** *132* (15), 154104.

[5] Grimme, S.; Ehrlich, S.; Goerigk, L., Effect of the damping function in dispersion corrected density functional theory. *J. Comput. Chem.* **2011,** *32* (7), 1456-1465.

[6] Monkhorst, H. J.; Pack, J. D., Special points for Brillouin-zone integrations. *Phys. Rev. B* **1976,** *13* (12), 5188-5192.

[7] Mayo, S. L.; Olafson, B. D.; Goddard, W. A., DREIDING: a generic force field for molecular simulations. *J. Phys. Chem.* **1990,** *94* (26), 8897-8909.

[8] Plimpton, S., Fast Parallel Algorithms for Short-Range Molecular Dynamics. *J. Comput. Phys.* **1995,** *117*, 1-19.

[9] Uribe-Romo, F. J.; Hunt, J. R.; Furukawa, H.; Klöck, C.; O'Keeffe, M.; Yaghi, O. M., A Crystalline Imine-Linked 3-D Porous Covalent Organic Framework. *J. Am. Chem. Soc.* **2009,** *131* (13), 4570-4571.

[10] Stegbauer, L.; Schwinghammer, K.; Lotsch, B. V., A hydrazone-based covalent organic framework for photocatalytic hydrogen production. *Chem. Sci.* **2014,** *5* (7), 2789-2793.

[11] Dufresne, S.; Skene, W. G., Optoelectronic property tailoring of conjugated heterocyclic azomethines – the effect of pyrrole, thiophene and furans. *J. Phys. Org. Chem.* **2012,** *25* (3), 211-221.

[12] Barik, S.; Skene, W. G., A fluorescent all-fluorene polyazomethine-towards soluble conjugated polymers exhibiting high fluorescence and electrochromic properties. *Polymer Chemistry* **2011,** *2* (5), 1091-1097.

[13] Verma, S.; Ghosh, A.; Das, A.; Ghosh, H. N., Ultrafast Exciton Dynamics of J- and H-Aggregates of the Porphyrin-Catechol in Aqueous Solution. *J. Phys. Chem. B* **2010,** *114* (25), 8327-8334.

LAMMPS WWW Site: http://lammps.sandia.gov.

5 Oligothiophene-Bridged Conjugated Covalent Organic Frameworks

This chapter is published as:

Niklas Keller, Derya Bessinger, Stephan Reuter, Mona Calik, Laura Ascherl, Fabian C. Hanusch, Florian Auras, and Thomas Bein, *J. Am. Soc. Chem.* **2017**, *139*, pp 8194–8199.

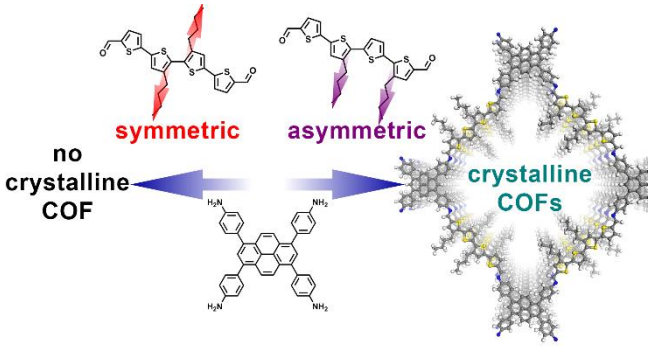

Two-dimensional covalent organic frameworks (2D-COFs) are crystalline, porous materials comprising aligned columns of π-stacked building blocks. With a view toward the application of these materials in organic electronics and optoelectronics, the construction of oligothiophene-based COFs would be highly desirable. The realization of such materials, however, has remained a challenge, in particular with respect to laterally conjugated imine-linked COFs. We have developed a new building block design employing an asymmetric modification on an otherwise symmetric backbone that allows us to construct a series of highly crystalline quaterthiophene-derived COFs with tunable electronic properties. Studying the optical response of these materials, we have observed for the first time the formation of a charge transfer state between the COF subunits across the imine bond. We believe that our new building block design provides a general strategy for the construction of well-ordered COFs from various extended building blocks, thus greatly expanding the range of applicable molecules.

5.1 Introduction

Since the development of the first covalent organic frameworks (COFs) in 2005,[1] these materials have attracted considerable scientific interest for applications in gas storage and separation,[2-3] in photocatalysis,[4-5] as proton conducting materials,[6-7] and in optoelectronics.[8-9] Cross-linking multidentate organic building blocks via reversible covalent bond formation into a crystalline porous framework allows for the construction of robust materials with tunable functionality based on the selection of their building blocks.[10-16] This way, a great variety of highly ordered materials can be realized having specific combinations of properties that can offer advantages over already established materials, such as zeolites or conductive polymers. With a view on optoelectronic properties, sheet-like 2D-COFs are of particular interest.[17] In these materials, the covalently linked layers are tightly π-stacked, thus forming columns with significant electronic overlap that enable efficient migration of excitations and charge carriers.[18-20]

Oligo- and polythiophene-based materials, such as 2,2′:5′,2″:5″,2‴-quaterthiophene (4T), α-sexithiophene (6T), and poly(3-hexylthiophene-2,5-diyl) (P3HT), are among the most prominent molecular semiconductors in organic field effect transistors (OFETs) and organic photovoltaics (OPV).[21-23] These materials benefit from high intrinsic charge carrier mobilities of both electrons and holes, typically broad optical absorption throughout the visible spectrum, and good chemical stability.[24-26]

The incorporation of this important class of molecular semiconductors into a COF, however, has remained a challenge. Only the smallest thiophene-based building blocks, i.e., thiophene, bithiophene (2T),[27] and small fused thiophenes such as thieno[3,2-*b*]thiophene (TT)[8, 11] and benzo[1,2-*b*:4,5-*b*′]dithiophene (BDT),[28-30] have been applied as COF building blocks to date, and mostly in boronate-linked COFs that lack electronic conjugation within the COF layers.

With a view on COFs for optoelectronics, it would thus be highly desirable to develop a method to integrate larger oligothiophenes (nT, $n \geq 4$) that allow for significant π-overlap and spectral coverage into a conjugated COF.

As flat, extended conjugated building blocks typically suffer from very low solubility in all common solvents, solubilizing groups such as alkyl chains are required for tuning the solubility into the optimal regime for COF growth.[30-31] However, even short alkyl chains can severely

impede the close face-on oriented packing that is a prerequisite for the formation of conductive 2D-COFs.

In this work, we have developed a building block design concept that allows us to overcome these limitations through an asymmetric functionalization of an otherwise C_2-symmetric 4T backbone. This way, we can incorporate solubilizing alkyl chains and allow them to integrate into the COF lattice at sufficiently large distances, while maintaining the desirable close contacts between the thiophene layers. We then extended this concept to electronic modifications of the backbone via the incorporation of thiophene-based acceptor units, such as 4*H*-thieno[3,4-*c*]pyrrole-4,6(5*H*)-dione (TPD) and thieno[3,4-*b*]thiophene (TT). Combining these modified 4T building blocks with pyrene-based moieties, we synthesized a first series of highly crystalline quaterthiophene-linked COFs with tunable optical absorption and emission properties.

5.2 Results and Discussion

Starting from commercially available 3-bromothiophene, we synthesized the quaterthiophene (4T) dialdehyde building blocks via Ni- and Pd-catalyzed Kumada and Suzuki cross-coupling reactions [see appendix for details]. In order to study the effect of the configuration of the alkyl chains, we synthesized a symmetric and an asymmetric version of the dibutyl-4T, in which the alkyl chains are attached to the 3-positions of the second and third (s4T) and the first and third thiophene units (a4T), respectively (Figure 5.1a).

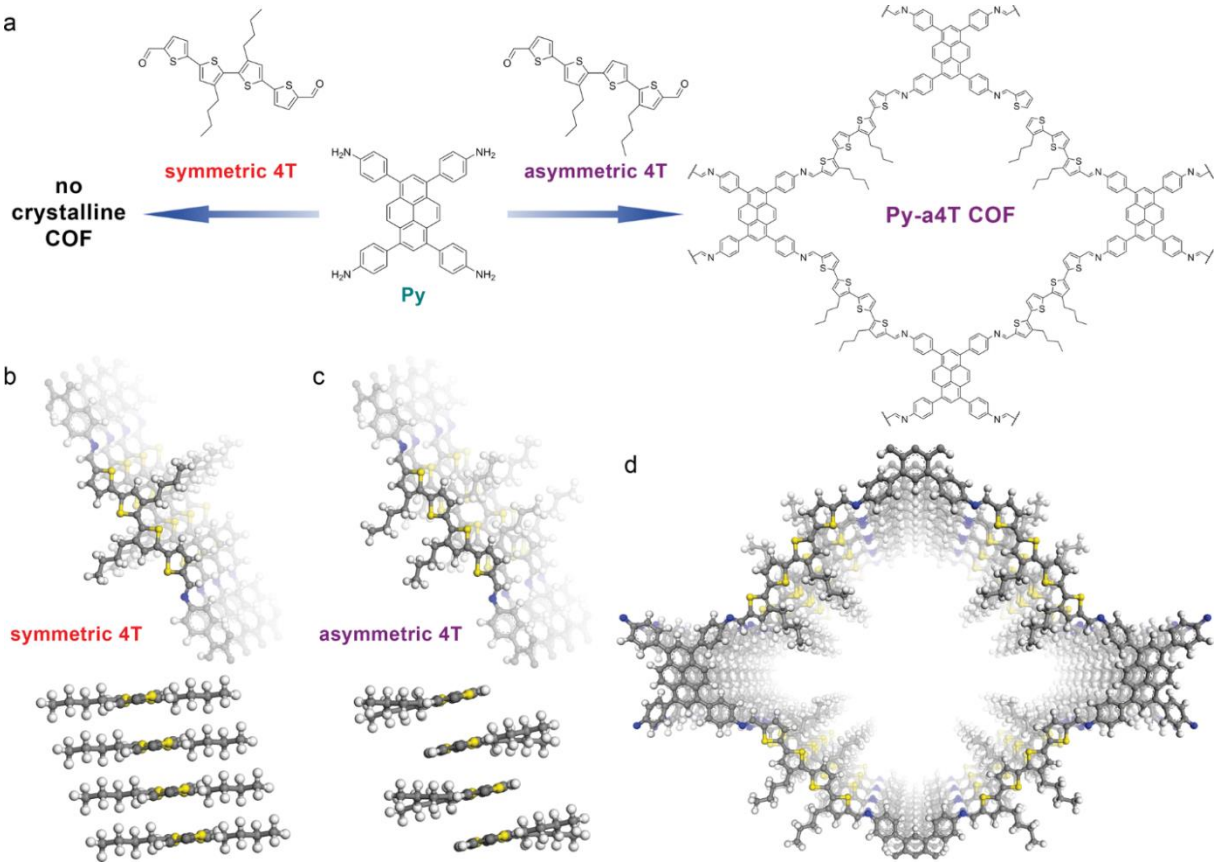

Figure 5.1: (a) Co-condensation of 1,3,6,8-tetrakis(4-aminophenyl)pyrene (Py) with 2 equiv of the quaterthiophene dialdehyde bearing asymmetric butyl chains (a4T) leads to the formation of the Py-a4T COF. When employing a quaterthiophene dialdehyde with a symmetric configuration of the alkyl chains (s4T), however, no crystalline material can be obtained. (b) Cut-out of the DFT-optimized hypothetical Py-s4T COF structure. Slipped cofacial stacking of the s4T building block would place the alkyl chains of adjacent layers in close vicinity, causing considerable steric repulsion and impeding the close packing required for 2D-COF formation. (c) This steric repulsion can be avoided by attaching the alkyl chains to the first and third thiophene unit (a4T) instead, allowing for sufficiently spaced alternating alkyl chains while a close-packed cofacial arrangement of the thiophene backbone is supported. (d) DFT-optimized structure of the Py-a4T COF with alternating orientation of the alkyl chains viewed along the pseudoquadratic pore.

For constructing the imine-linked COFs, we followed a synchronized offset stacking approach.[15] This COF design uses geometrically interlocked layers for superior crystallinity

while enabling close-packed arrangements of both subunits and is perfectly compatible with the quasi C2-symmetric flat geometry of the 4T bridges. The quaterdentate 1,3,6,8-tetrakis(4-aminophenyl)pyrene (Py) has previously been applied in the synthesis of several imine-linked frameworks and has proven to generate stable and exceptionally crystalline 2D-COFs.[15, 32-33] Pyrene-based frameworks feature a quasi-quadratic geometry comprising close-packed, slightly slip-stacked pyrene columns and equally close-packed, slip-stacked linear bridges, thus providing the ideal geometric environment for our new 4T building blocks.

On the basis of published pyrene COF structures and density functional theory (DFT) simulations, we expect the 4T unit to be incorporated as face-on oriented stacks, whereby each layer is slipped by about 0.1 nm, mainly perpendicular to the 4T axis (Figure 5.1b,c). In the case of s4T, this would bring the alkyl chains of adjacent layers very close together and most likely cause considerable steric repulsion, forcing the framework into a less closely stacked conformation and sacrificing in part the π- overlap between the thiophenes. On the other hand, a4T can stack with the butyl chains alternating on both sides of the stack, thus allowing for much larger spacing between these alkyl chains while maintaining a close-packed face-on orientation of the 4T backbone (Figure 5.1c,d).

Acid-catalyzed solvothermal synthesis using a4T and Py in a 2:1 molar ratio yielded the anticipated Py-a4T COF as a dark red powder (see appendix for details). The successful formation of a crystalline material was confirmed by powder X-ray diffraction (PXRD; Figure 5.2a). The presence of multiple higher-order reflections reveals the high degree of long-range order present in this new COF. Pawley refinement using a force-field- optimized *C*2/*m* symmetric structure model (Figure 5.2b) provides a very good fit to the experimental data and produced the lattice parameters a = 4.80 ± 0.05 nm, b = 5.14 ± 0.05 nm, c = 0.388 ± 0.01 nm, and β = 72° ± 5°. From the above discussion and the computational modeling, we anticipate an alternating sequence of the alkyl chains as the predominant stacking motif within a single a4T stack. The four a4T stacks that constitute the walls of a COF pore, however, are separated well enough such that they will not form an ordered superstructure. We thus treated the alkyl chains in the Pawley refinement and the simulation of the PXRD pattern as a superposition of both possible orientations with 50% occupancy each.

The formation of an ordered porous framework was further confirmed by transmission electron microscopy (TEM) (appendix, Figure 5.15). The contrast of the pore channels is visible for a number of crystallites with a projected periodicity of 3.4 nm, which corresponds very well to

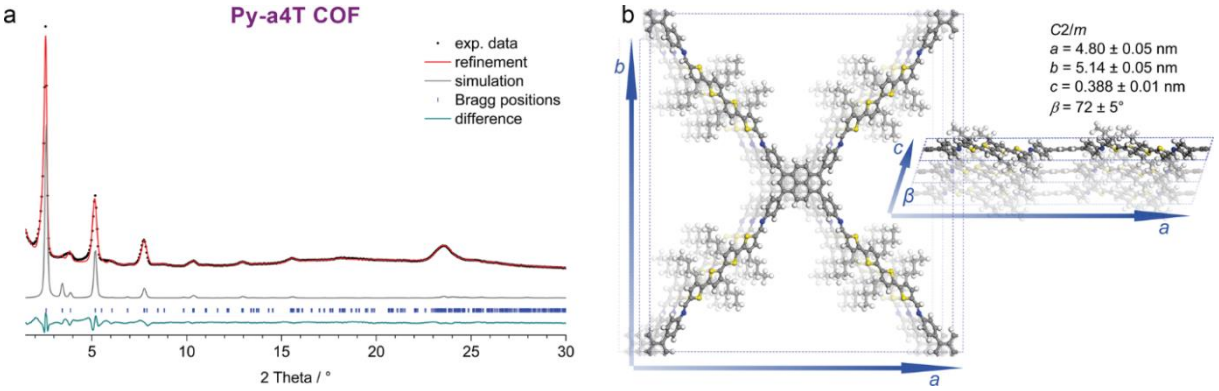

Figure 5.2: (a) Experimental PXRD data (black dots) of Py-a4T COF. Pawley refinement (red line) using the *C*2/*m* symmetric structure model shown in part b provides a very good fit to the experimental pattern with only minimal differences (the green line shows the difference plot between the experimental and refined patterns; R_{wp} = 7.5%, R_p = 13.4%). Bragg positions are indicated with blue ticks. The alkyl chains of the a4T building block were treated in the refinement as a superposition of both possible orientations with 50% occupancy each (both shown in the figure). The simulated PXRD pattern based on the *C*2/*m* symmetric unit cell (gray line) is in very good agreement with the experimental and the refined pattern. Differences in the peak intensities, in particular the altered intensity ratios between lower- and higher-angle reflections, might stem from small oligomeric fragments that are trapped in the large COF pores (the attenuation of peak intensities due to this will be strongest at small 2θ angles).

the channel repeat distance of 3.45 nm in the refined structure.

In order to probe the influence of the alkyl chain length on the resulting framework, we synthesized a short-chain analogue of the a4T building block bearing two methyl groups instead of the butyl chains. Due to the significantly lower solubility of this a4TMe building block, the COF synthesis required a 2.5 times more dilute reaction mixture. The resulting framework is isostructural to the original a4T COF, with a slightly smaller unit cell (appendix, Figure 5.16).

Under identical synthetic conditions as those chosen for the Py-a4T COF and under all other solvent combinations and concentrations tested, the reaction between Py and 2 equiv of s4T yielded only orange-red, fully amorphous networks. This observation confirms our above conclusions drawn from the structure modeling and highlights the importance of the building block design.

The asymmetric modification strategy also allows us to extend one of the thiophene units into a more-electron- deficient fused heterocycle, thus forming a donor−acceptor (D−A) building block with modified optical and electronic properties while retaining the overall geometry of the 4T backbone.

Incorporation of a single 4*H*-thieno[3,4-*c*]pyrrole-4,6(5*H*)-dione (TPD) or thieno[3,4-*b*]thiophene (TT) via sequential Stille coupling reactions yielded the $4T_{TPD}$ and $4T_{TT}$ building blocks, respectively (Figure 5.3a; see appendix for experimental details). For the best possible

crystallinity, the $4T_{TT}$ building block was synthesized as an isomer-pure material with the orientation of the TT subunit as shown in Figure 5.3a. In both cases, the asymmetric incorporation enables the 4T derivatives to stack in a close-packed alternating sequence despite the sterically demanding acceptor moieties (Figure 5.3b,c).

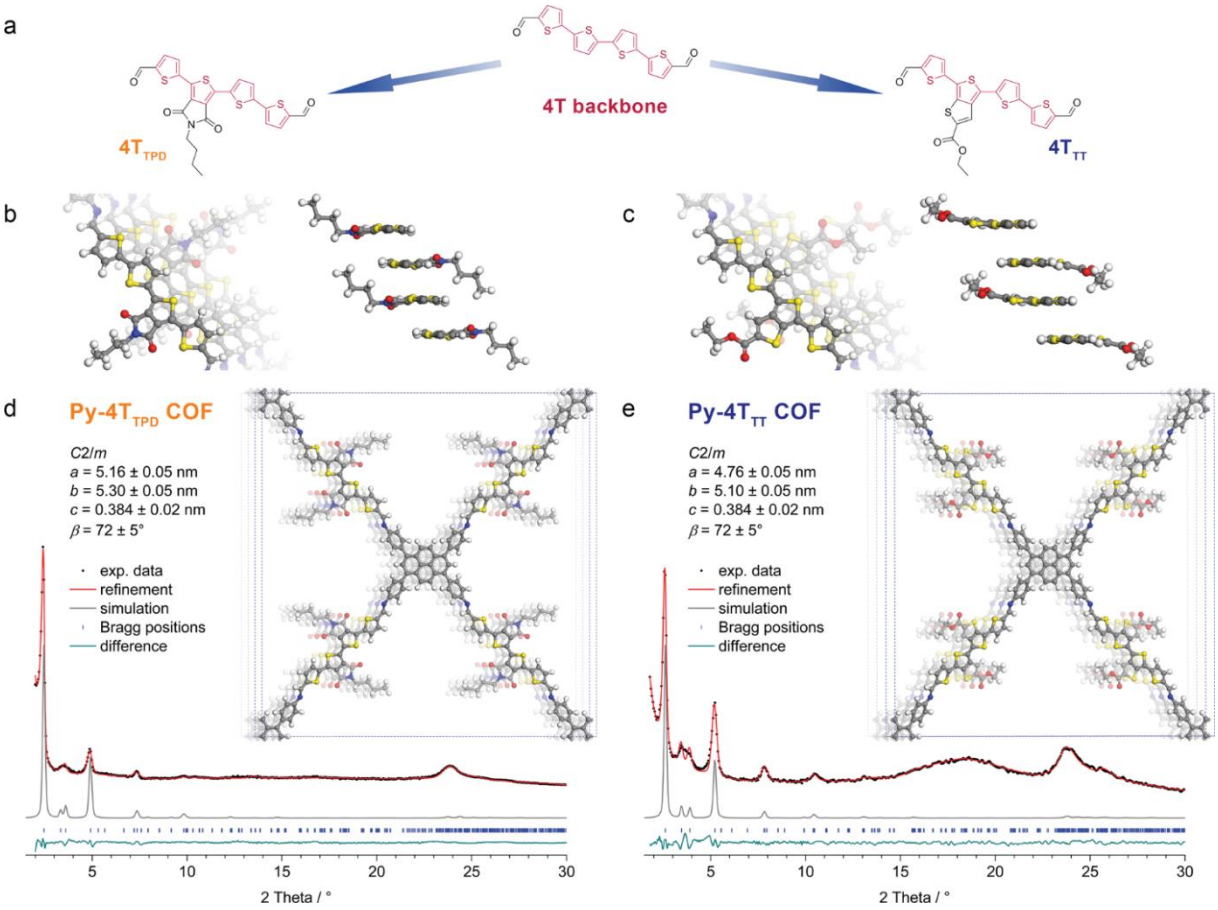

Figure 5.3: (a) The asymmetric modification approach can also be used to construct quaterthiophene-based donor–acceptor building blocks, in which one thiophene is replaced by an electron-deficient 3,4-extended thiophene. (b, c) Despite the increased steric demands of these subunits, a close- packed cofacial arrangement of the asymmetric building blocks is possible via alternating orientation of the electron-deficient moieties. (d, e) Experimental PXRD data (black dots) of the Py-$4T_{TPD}$ and Py-$4T_{TT}$ COFs, respectively, and corresponding Pawley-refined patterns (red lines) and difference plots (green lines; R_{wp} = 5.2%, R_p = 14.3% and R_{wp} = 9.3%, R_p = 16.1%, respectively). Bragg positions are indicated with blue ticks. The acceptor moieties (TPD and TT) were treated in the refinements as a superposition of both possible orientations with 50% occupancy each (both shown in the representations of the unit cells). The simulated PXRD patterns (gray lines) based on the *C*2/*m* symmetric unit cells (insets) agree very well with the experimental and refined patterns of the respective frameworks. Differences in the peak intensities, in particular the altered intensity ratios between lower- and higher-angle reflections, might stem from unreacted precursor materials or small fragments adsorbed in the COF pores (the attenuation of peak intensities due to this is strongest at small 2θ angles).

The acid-catalyzed reaction of Py with 2 equiv of the modified 4T building blocks under solvothermal conditions yielded the Py-$4T_{TPD}$ and Py-$4T_{TT}$ COFs, respectively. The formation of crystalline frameworks was confirmed by PXRD analysis (Figure 5.3d,e). Pawley refinements of the Py-$4T_{TPD}$ and Py-$4T_{TT}$ COFs using the force-field-optimized structure

models displayed as insets in Figure 3d,e reproduced the experimental patterns very well. Following the same reasoning as for the simulation and refinement of the Py-a4T COF (see above), the asymmetric $4T_{TPD}$ and $4T_{TT}$ building blocks were approximated as a superposition of both possible orientations with 50% occupancy each. The refined unit cell parameters are a = 5.16 ± 0.05 nm, b = 5.30 ± 0.05 nm, c = 0.384 ± 0.02 nm, and β = 72° ± 5° for the Py-$4T_{TPD}$ COF and a = 4.76 ± 0.05 nm, b = 5.10 ± 0.05 nm, c = 0.384 ± 0.02 nm, and β = 72°± 5° for the Py- $4T_{TT}$ COF. The longer pore diagonals a and b in these COFs compared to the Py-a4T COF can be attributed to a slight variation in the optimal stacking offset perpendicular to the 4T axis and the resulting differences in the tilt of the 4T columns versus the pyrene core. The length of the crystallographic c axis, on the other hand, is dominated by the stacking of the pyrene units and, thus, hardly affected by the tilt of the 4T bridge.

The new 4T-based COFs are intensely colored powders that are capable of absorbing most of the visible spectrum (Figure 5.4a). The optical bandgaps estimated from Tauc plots are 1.57, 1.17 (indirect), and 1.40 eV for the Py-a4T, Py-$4T_{TPD}$, and Py- $4T_{TT}$ COFs, respectively (appendix, Figure 5.9). Electronic integration of the 4T subunit is apparent from the strong red-shift of the absorption in comparison to previously reported pyrene COFs with small acene bridges. Furthermore, the increased absorption capabilities of the D−A building blocks (appendix, Figure 5.7 and Figure 5.8) translate to red-shifted absorption maxima of the corresponding COFs (Py-a4T COF, 563 nm; Py-$4T_{TPD}$ COF, 580 nm; Py-$4T_{TT}$ COF, 638 nm). All three COFs feature an additional absorption band below the energy of the main π–π^* transition that is relatively weak for the Py-$4T_{TPD}$ and strongest for the Py-a4T COF. This might indicate the formation of a charge transfer state between the electron-rich pyrene and the slightly electron-deficient 4T subunits (see below).

The photoluminescence (PL) spectra follow the same trends as the absorption spectra with emission maxima of the COFs at 654, 718, and 773 nm, respectively (Figure 5.4b and appendix, Figure 5.10 and Figure 5.11).

The hypothesis of a photoinduced charge transfer between the two imine-linked building blocks is supported by the time- correlated single photon counting (TCSPC) traces of the COFs (Figure 5.4c). Dilute solutions of the 4T building blocks exhibit monoexponential decay curves with lifetimes of about 0.5 ns (a4T, $4T_{TT}$) or 1 ns ($4T_{TPD}$) (appendix, Figure 5.13 and Figure 5.14). In the solid state, the PL lifetimes of the pure building blocks are increased to $\tau_1 \sim 0.5$ ns and $\tau_2 \sim 1$ ns (biexponential decays). The Py building block shows even longer lifetimes of above

2 ns in solution and a main component of >1 ns in the solid state. If integrated into a COF, however, the PL lifetimes are drastically reduced. The fastest component, which represents more than 50% of the emitted photons, drops to below 200 ps (Py-4T$_{TT}$) or even below 100 ps (Py-a4T, Py- 4T$_{TPD}$). This indicates that the imine-linked pairing with the tetraphenylpyrene has opened up a new pathway for fast and efficient conversion of the COF π* excited state, potentially via electron transfer to the quaterthiophenes and hole transfer to the pyrene. This is further supported by comparison with the PL lifetimes reported for electron-rich acene-bridged pyrene COFs that do not enable strong intramolecular charge transfer.[15] In these materials, the lifetimes are much longer, ranging from 0.35 ns to well above 1 ns.

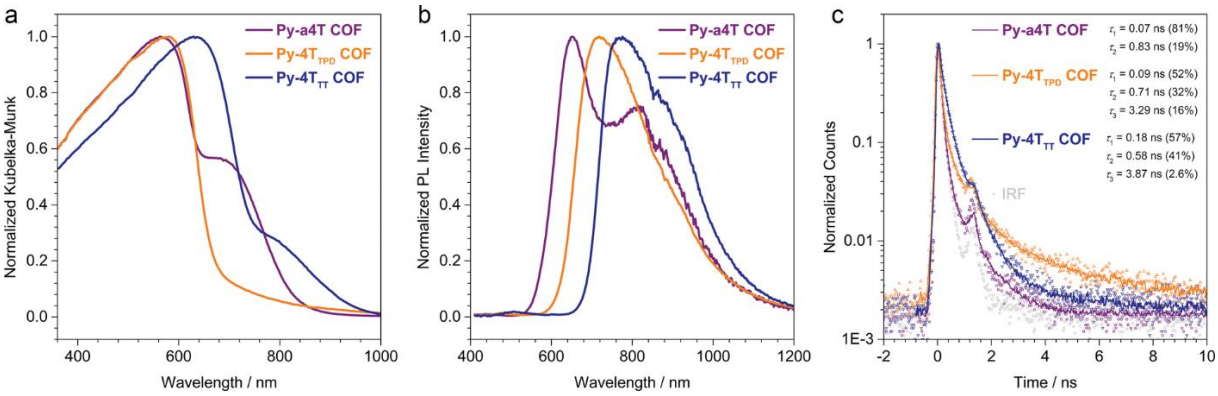

Figure 5.4: (a) UV−vis−NIR absorption of the three thiophene-bridged COFs, calculated from the diffuse reflectance spectra of the COF powders dispersed in $BaSO_4$. (b) PL spectra measured with pulsed 378 nm excitation and (c) the corresponding TCSPC traces recorded at the respective emission maximum of each COF. The lines represent exponential deconvolution fits taking into account the instrument response function and scattering (see the SI for details; the rise at 1.35 ns originates from the diode laser). The COFs exhibit fast biexponential (Py-a4T) or triexponential (Py-4T$_{TPD}$ and Py-4T$_{TT}$) decays with sub-nanosecond components. The fractional intensities, i.e., the fractions of collected photons corresponding to the respective lifetimes, are stated in brackets.

The existence of an efficient charge transfer pathway that competes effectively with the radiative recombination of the COF π* excited state is additionally supported by the quenching of the 4T PL upon incorporation into the COF (appendix, Figure 5.12). This effect is most significant for the Py-a4T COF, which is consistently the material that exhibits the strongest charge transfer absorption band in the diffuse reflectance spectrum. To the best of our knowledge, this is the first observation of the formation of a charge transfer state between the subunits of an imine-linked COF.

5.3 Conclusion

In this work, we have developed the first quaterthiophene-based 2D covalent organic frameworks comprising ordered π-stacked columns of 4T and pyrene moieties. Following an asymmetric functionalization strategy of the otherwise C_2–symmetric 4T backbone allowed us to incorporate alkyl chains for optimized solubility while fully retaining the ability of the building blocks to form close-packed face-on stacked thiophene columns. We demonstrate that this strategy also provides a facile route for modifying the electronic properties of the 4T backbone via incorporation of electron-deficient subunits, thus forming donor−acceptor type molecules. The absorption and emission spectra confirm that the 4T-based building blocks are electronically integrated into the framework. Spectral features below the energy of the π–π* transition and the analysis of the corresponding emission decay time traces reveal the fast and efficient formation of a charge transfer state between the imine-linked pyrene and quaterthiophene subunits. We believe that our new asymmetric building block design provides a general strategy for the construction of well-ordered COFs from various extended building blocks. This will greatly expand the range of applicable molecules for realizing frameworks with tailor-made optoelectronic properties.

5.4 References

[1] Côté, A. P.; Benin, A. I.; Ockwig, N. W.; O'Keeffe, M.; Matzger, A. J.; Yaghi, O. M., Porous, Crystalline, Covalent Organic Frameworks. *Science* **2005,** *310* (5751), 1166-1170.

[2] Furukawa, H.; Yaghi, O. M., Storage of Hydrogen, Methane, and Carbon Dioxide in Highly Porous Covalent Organic Frameworks for Clean Energy Applications. *J. Am. Chem. Soc.* **2009,** *131* (25), 8875-8883.

[3] Doonan, C. J.; Tranchemontagne, D. J.; Glover, T. G.; Hunt, J. R.; Yaghi, O. M., Exceptional ammonia uptake by a covalent organic framework. *Nat. Chem.* **2010,** *2* (3), 235-238.

[4] Stegbauer, L.; Schwinghammer, K.; Lotsch, B. V., A hydrazone-based covalent organic framework for photocatalytic hydrogen production. *Chem. Sci.* **2014,** *5* (7), 2789-2793.

[5] Lin, S.; Diercks, C. S.; Zhang, Y.-B.; Kornienko, N.; Nichols, E. M.; Zhao, Y.; Paris, A. R.; Kim, D.; Yang, P.; Yaghi, O. M.; Chang, C. J., Covalent organic frameworks comprising cobalt porphyrins for catalytic CO2 reduction in water. *Science* **2015,** *349* (6253), 1208-1213.

[6] Chandra, S.; Kundu, T.; Kandambeth, S.; BabaRao, R.; Marathe, Y.; Kunjir, S. M.; Banerjee, R., Phosphoric Acid Loaded Azo (−N═N−) Based Covalent Organic Framework for Proton Conduction. *J. Am. Chem. Soc.* **2014,** *136* (18), 6570-6573.

[7] Shinde, D. B.; Aiyappa, H. B.; Bhadra, M.; Biswal, B. P.; Wadge, P.; Kandambeth, S.; Garai, B.; Kundu, T.; Kurungot, S.; Banerjee, R., A mechanochemically synthesized covalent organic framework as a proton-conducting solid electrolyte. *J. Mater. Chem. A* **2016,** *4* (7), 2682-2690.

[8] Dogru, M.; Handloser, M.; Auras, F.; Kunz, T.; Medina, D.; Hartschuh, A.; Knochel, P.; Bein, T., A Photoconductive Thienothiophene-Based Covalent Organic Framework Showing Charge Transfer Towards Included Fullerene. *Angew. Chem. Int. Ed.* **2013,** *52* (10), 2920-2924.

[9] Guo, J.; Xu, Y.; Jin, S.; Chen, L.; Kaji, T.; Honsho, Y.; Addicoat, M. A.; Kim, J.; Saeki, A.; Ihee, H.; Seki, S.; Irle, S.; Hiramoto, M.; Gao, J.; Jiang, D., Conjugated organic framework with three-dimensionally ordered stable structure and delocalized pi clouds. *Nat. Commun.* **2013,** *4*, 2736.

[10] Calik, M.; Sick, T.; Dogru, M.; Döblinger, M.; Datz, S.; Budde, H.; Hartschuh, A.; Auras, F.; Bein, T., From Highly Crystalline to Outer Surface-Functionalized Covalent Organic Frameworks—A Modulation Approach. *J. Am. Chem. Soc.* **2016,** *138* (4), 1234-1239.

[11] Ascherl, L.; Sick, T.; Margraf, J. T.; Lapidus, S. H.; Calik, M.; Hettstedt, C.; Karaghiosoff, K.; Döblinger, M.; Clark, T.; Chapman, K. W.; Auras, F.; Bein, T., Molecular docking sites designed for the generation of highly crystalline covalent organic frameworks. *Nat. Chem.* **2016,** *8* (4), 310-316.

[12] Bunck, D. N.; Dichtel, W. R., Internal Functionalization of Three-Dimensional Covalent Organic Frameworks. *Angew. Chem. Int. Ed.* **2012,** *51* (8), 1885-1889.

[13] Shinde, D. B.; Kandambeth, S.; Pachfule, P.; Kumar, R. R.; Banerjee, R., Bifunctional covalent organic frameworks with two dimensional organocatalytic micropores. *Chem. Commun.* **2015,** *51* (2), 310-313.

[14] Chen, L.; Furukawa, K.; Gao, J.; Nagai, A.; Nakamura, T.; Dong, Y.; Jiang, D., Photoelectric Covalent Organic Frameworks: Converting Open Lattices into Ordered Donor–Acceptor Heterojunctions. *J. Am. Chem. Soc.* **2014,** *136* (28), 9806-9809.

[15] Auras, F.; Ascherl, L.; Hakimioun, A. H.; Margraf, J. T.; Hanusch, F. C.; Reuter, S.; Bessinger, D.; Döblinger, M.; Hettstedt, C.; Karaghiosoff, K.; Herbert, S.; Knochel, P.; Clark, T.; Bein, T., Synchronized Offset Stacking: A Concept for Growing Large-Domain and Highly Crystalline 2D Covalent Organic Frameworks. *J. Am. Chem. Soc.* **2016,** *138* (51), 16703-16710.

[16] Lin, G.; Ding, H.; Yuan, D.; Wang, B.; Wang, C., A Pyrene-Based, Fluorescent Three-Dimensional Covalent Organic Framework. *J. Am. Chem. Soc.* **2016,** *138* (10), 3302-3305.

[17] Wan, S.; Gándara, F.; Asano, A.; Furukawa, H.; Saeki, A.; Dey, S. K.; Liao, L.; Ambrogio, M. W.; Botros, Y. Y.; Duan, X.; Seki, S.; Stoddart, J. F.; Yaghi, O. M., Covalent Organic Frameworks with High Charge Carrier Mobility. *Chem. Mater.* **2011,** *23* (18), 4094-4097.

[18] Jin, S.; Ding, X.; Feng, X.; Supur, M.; Furukawa, K.; Takahashi, S.; Addicoat, M.; El-Khouly, M. E.; Nakamura, T.; Irle, S.; Fukuzumi, S.; Nagai, A.; Jiang, D., Charge Dynamics in A Donor–Acceptor Covalent Organic Framework with Periodically Ordered Bicontinuous Heterojunctions. *Angew. Chem. Int. Ed.* **2013,** *52* (7), 2017-2021.

[19] Calik, M.; Auras, F.; Salonen, L. M.; Bader, K.; Grill, I.; Handloser, M.; Medina, D. D.; Dogru, M.; Löbermann, F.; Trauner, D.; Hartschuh, A.; Bein, T., Extraction of Photogenerated Electrons and Holes from a Covalent Organic Framework Integrated Heterojunction. *J. Am. Chem. Soc.* **2014,** *136* (51), 17802-17807.

[20] Cai, S.-L.; Zhang, Y.-B.; Pun, A. B.; He, B.; Yang, J.; Toma, F. M.; Sharp, I. D.; Yaghi, O. M.; Fan, J.; Zheng, S.-R.; Zhang, W.-G.; Liu, Y., Tunable electrical conductivity in oriented thin films of tetrathiafulvalene-based covalent organic framework. *Chem. Sci.* **2014,** *5* (12), 4693-4700.

[21] Kim, J. Y.; Kim, S. H.; Lee, H.-H.; Lee, K.; Ma, W.; Gong, X.; Heeger, A. J., New Architecture for High-Efficiency Polymer Photovoltaic Cells Using Solution-Based Titanium Oxide as an Optical Spacer. *Adv. Mater.* **2006,** *18* (5), 572-576.

[22] Irwin, M. D.; Buchholz, D. B.; Hains, A. W.; Chang, R. P. H.; Marks, T. J., p-Type semiconducting nickel oxide as an efficiency-enhancing anode interfacial layer in polymer bulk-heterojunction solar cells. *Proceedings of the National Academy of Sciences* **2008,** *105* (8), 2783-2787.

[23] Cnops, K.; Rand, B. P.; Cheyns, D.; Verreet, B.; Empl, M. A.; Heremans, P., 8.4% efficient fullerene-free organic solar cells exploiting long-range exciton energy transfer. *Nat. Commun.* **2014,** *5*, 3406.

[24] Kan, B.; Li, M.; Zhang, Q.; Liu, F.; Wan, X.; Wang, Y.; Ni, W.; Long, G.; Yang, X.; Feng, H.; Zuo, Y.; Zhang, M.; Huang, F.; Cao, Y.; Russell, T. P.; Chen, Y., A Series of Simple Oligomer-like Small Molecules Based on Oligothiophenes for Solution-Processed Solar Cells with High Efficiency. *J. Am. Chem. Soc.* **2015,** *137* (11), 3886-3893.

[25] Li, Z.; He, G.; Wan, X.; Liu, Y.; Zhou, J.; Long, G.; Zuo, Y.; Zhang, M.; Chen, Y., Solution Processable Rhodanine-Based Small Molecule Organic Photovoltaic Cells with a Power Conversion Efficiency of 6.1%. *Adv. Energy Mater.* **2012,** *2* (1), 74-77.

[26] Zhang, Q.; Kan, B.; Liu, F.; Long, G.; Wan, X.; Chen, X.; Zuo, Y.; Ni, W.; Zhang, H.; Li, M.; Hu, Z.; Huang, F.; Cao, Y.; Liang, Z.; Zhang, M.; Russell, T. P.; Chen, Y., Small-molecule solar cells with efficiency over 9%. *Nature Photonics* **2014,** *9*, 35.

[27] Bertrand, G. H. V.; Michaelis, V. K.; Ong, T.-C.; Griffin, R. G.; Dincă, M., Thiophene-based covalent organic frameworks. *Proceedings of the National Academy of Sciences* **2013,** *110* (13), 4923-4928.

[28] Medina, D. D.; Werner, V.; Auras, F.; Tautz, R.; Dogru, M.; Schuster, J.; Linke, S.; Döblinger, M.; Feldmann, J.; Knochel, P.; Bein, T., Oriented Thin Films of a Benzodithiophene Covalent Organic Framework. *ACS Nano* **2014,** *8* (4), 4042-4052.

[29] Medina, D. D.; Rotter, J. M.; Hu, Y.; Dogru, M.; Werner, V.; Auras, F.; Markiewicz, J. T.; Knochel, P.; Bein, T., Room Temperature Synthesis of Covalent–Organic Framework Films through Vapor-Assisted Conversion. *J. Am. Chem. Soc.* **2015,** *137* (3), 1016-1019.

[30] Feldblyum, J. I.; McCreery, C. H.; Andrews, S. C.; Kurosawa, T.; Santos, E. J. G.; Duong, V.; Fang, L.; Ayzner, A. L.; Bao, Z., Few-layer, large-area, 2D covalent organic framework semiconductor thin films. *Chem. Commun.* **2015,** *51* (73), 13894-13897.

[31] Lohse, M. S.; Rotter, J. M.; Margraf, J. T.; Werner, V.; Becker, M.; Herbert, S.; Knochel, P.; Clark, T.; Bein, T.; Medina, D. D., From benzodithiophene to diethoxy-benzodithiophene covalent organic frameworks – structural investigations. *CrystEngComm* **2016,** *18* (23), 4295-4302.

[32] Rabbani, M. G.; Sekizkardes, A. K.; Kahveci, Z.; Reich, T. E.; Ding, R.; El-Kaderi, H. M., A 2D Mesoporous Imine-Linked Covalent Organic Framework for High Pressure Gas Storage Applications. *Chem. - Eur. J.* **2013,** *19* (10), 3324-3328.

[33] Chen, X.; Huang, N.; Gao, J.; Xu, H.; Xu, F.; Jiang, D., Towards covalent organic frameworks with predesignable and aligned open docking sites. *Chem. Commun.* **2014,** *50* (46), 6161-6163.

5.5 Appendix

5.5.1 Methods

Nuclear magnetic resonance (NMR) spectra were recorded on Bruker AV 400 and AV 400 TR spectrometers. Chemical shifts are expressed in parts per million (δ scale) and are calibrated using residual (undeuterated) solvent peaks as an internal reference (^{1}H-NMR: $CDCl_3$: 7.26, DMSO-d_6: 2.50, DMF-d_7: 8.03; ^{13}C-NMR: $CDCl_3$: 77.16, DMSO-d_6: 39.52, DMF-d_7: 163.15). Data for ^{1}H NMR spectra are reported in the following way: chemical shift (δ ppm) (multiplicity, coupling constant/Hz, integration). Multiplicities are reported as follows: s = singlet, d = doublet, t = triplet, q = quartet, m = multiplet, or combinations thereof.

High resolution electron ionization (EI) **mass spectra** (MS) were recorded with a Thermo Finnigan MAT 95 instrument.

Powder X-ray diffraction (PXRD) measurements were performed using a Bruker D8 Discover with Ni-filtered Cu K_α radiation and a LynxEye position-sensitive detector.

The **structure models of the COFs** were built using the Forcite module of the Accelrys Materials Studio software package. For each COF structure, we applied the space group with the highest possible symmetry, taking into account the rotation of the phenylenes versus the pyrene core. Structure refinements using the Pawley method were carried out as implemented in the Reflex module of the Materials Studio software. Pseudo-Voigt peak profiles were used, and peak asymmetry was corrected using the Finger-Cox-Jephcoat method. A crystallite domain size of 100 nm along a, b and c, and lattice strain parameters of 0.5%, 0.5% and 0.2% along a, b, c, respectively, were assumed throughout the refinements. The asymmetric linear building blocks were treated as a superposition of both possible orientations, both having 50% occupancy.

DFT-based geometry optimizations were performed with the CASTEP code using the generalized-gradient-approximation PBE functional. The energy cutoff for the planewave basis set was set to 310.0 eV, ions were represented with ultra-soft pseudopotentials and k-point sampling was performed with a 1x1x4 Monkhorst-Pack grid (1x1x2 for the Py-a4T COF double layer). The correction scheme of Tkatchenko and Scheffler was used to account for dispersion interactions.

The **nitrogen sorption isotherms** were recorded on a Quantachrome Autosorb 1 at 77 K in a pressure range from p/p_0 = 0.001 to 0.999. For the evaluation of the surface area, the BET model was applied between 0.069 and 0.132 p/p_0. The pore size distribution was calculated from the adsorption branch using a QSDFT model with a carbon kernel for cylindrical pores.

Transmission electron microscopy (TEM) was performed on an FEI Titan Themis instrument equipped with a field emission gun operated at 300 kV.

Infrared (IR) spectra were recorded on a Perkin Elmer Spectrum BX II FT-IR system equipped with a diamond attenuated total reflection unit.

UV-VIS-NIR spectra were recorded using a Perkin-Elmer Lambda 1050 spectrometer equipped with a 150 mm integrating sphere and photomultiplier tube (PMT) and InGaAs detectors. **Diffuse reflectance** spectra were collected with a Praying Mantis (Harrick) accessory and were referenced to barium sulfate powder as white standard. The specular reflection of the sample surface was removed from the signal using apertures that allow only light scattered at angles > 20° to pass.

Photoluminescence (PL) measurements were performed using a home-built setup consisting of a Horiba Jobin Yvon iHR 320 monochromator equipped with a photomultiplier tube and a liquid N_2-cooled InGaAs detector. The samples were illuminated with a 378 nm diode laser (pulse power 0.99 nJ cm^{-2}, pulse rate 40 MHz).

Time-correlated single photon counting (TCSPC) measurements were performed using a PicoQuant FluoTime 300 spectrometer equipped with a 378 nm picosecond diode laser (pulse power 0.99 nJ cm^{-2}, pulse rate 40 MHz).

5.5.2 Building Block Syntheses

All reactions were performed in oven-dried glassware under argon atmosphere using standard Schlenk techniques. Reagents and solvents were obtained in high purity grades from commercial suppliers and used as received.

Scheme 5.1: Synthesis of the s4T, a4T and $a4T_{Me}$ building blocks.

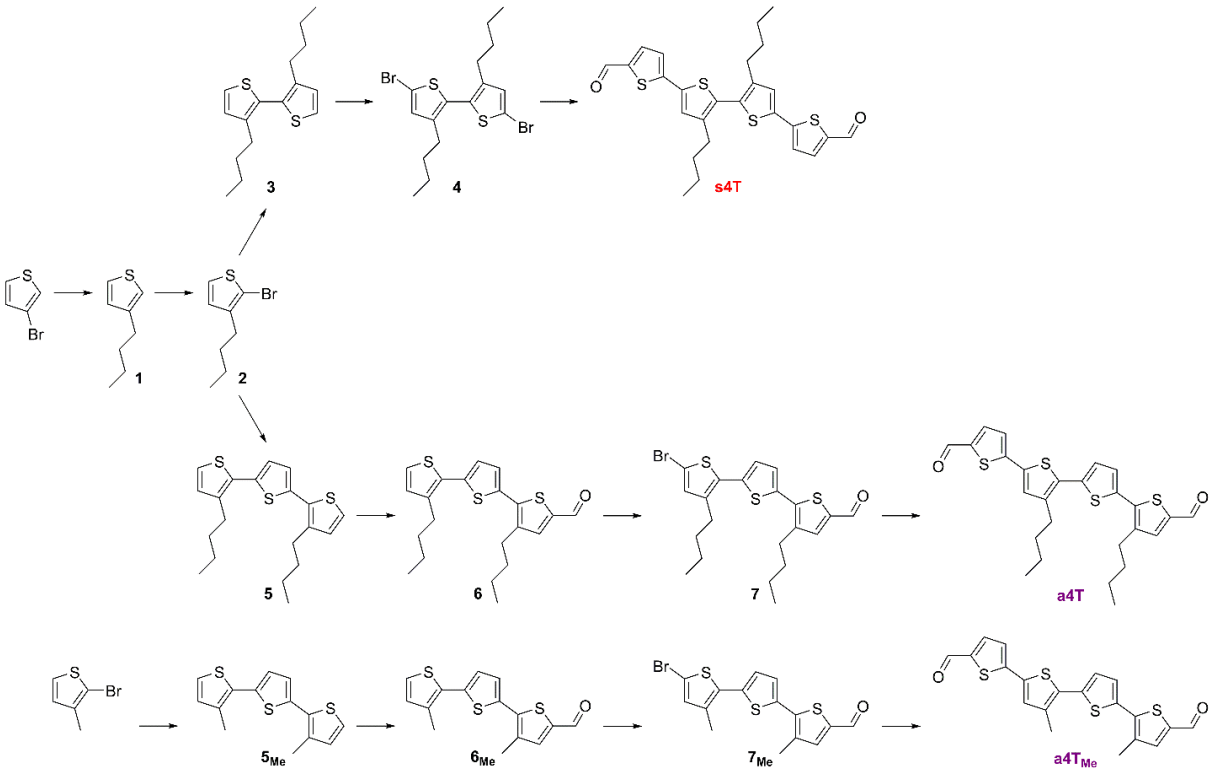

3-butylthiophene (1)

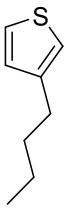

A solution of BuMgCl (2.0 M in THF, 100 mmol, 1.25 eq.) was slowly added to a solution of 3-bromothiophene (13.0 g, 80 mmol, 1.0 eq.) and $Ni(dppp)Cl_2$ (867 mg, 1.6 mmol, 2 mol%) in 120 mL THF. During the addition, the reaction mixture was maintained at room temperature by a water bath. After stirring at 30 °C overnight, the reaction mixture was quenched by the addition of 50 mL of 2 M HCl, extracted with Et_2O, washed with brine, dried over $MgSO_4$, and

concentrated under reduced pressure. Vacuum distillation (10^{-1} mbar, 35 °C) furnished the title compound as a colorless liquid (8.02 g, 57.2 mmol, 71%).

^{1}H NMR (400 MHz, $CDCl_3$): 7.24 (dd, J = 4.9, 2.9 Hz, 1H), 6.94 (dd, J = 4.9, 1.3 Hz, 1H), 6.93 – 6.91 (m, 1H), 2.67 – 2.62 (m, 2H), 1.66 – 1.57 (m, 2H), 1.42 – 1.31 (m, 2H), 0.93 (t, J = 7.3 Hz, 3H).

2-bromo-3-butylthiophene (2)

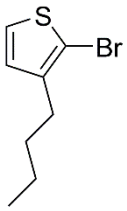

N-bromosuccinimide (10.7 g, 60 mmol, 1.05 eq.) was added to a solution of compound 1 (8.02 g, 57.2 mmol, 1.0 eq.) in 60 mL $CHCl_3$. The reaction mixture was cooled to 0 °C, followed by the addition of 60 mL glacial acetic acid. The solution was allowed to warm to room temperature over the course of several hours and stirred for 2 d in the dark. The slightly yellow solution was poured onto 200 mL H_2O, extracted with DCM, washed with saturated $NaHCO_3$ solution, dried over $MgSO_4$, and concentrated under reduced pressure. High vacuum distillation (10^{-3} mbar, 33 °C) furnished the title compound as a colorless liquid (11.2 g, 51.1 mmol, 89%).

1H NMR (400 MHz, CDCl3): 7.18 (d, J = 5.6 Hz, 1H), 6.80 (d, J = 5.6 Hz, 1H), 2.60 – 2.55 (m, 2H), 1.61 – 1.52 (m, 2H), 1.41 – 1.31 (m, 2H), 0.94 (t, J = 7.3 Hz, 3H).

3,3'-dibutyl-2,2'-bithiophene (3)[1]

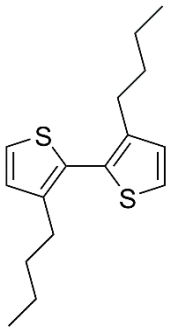

A Grignard reagent, prepared by sonication of compound **2** (1.10 g, 5.0 mmol, 1.1 eq.), 1,2-dibromoethane (939 mg, 5.0 mmol, 1.1 eq.) and Mg (243 mg, 10 mmol, 2.2 eq.) in 14 mL of dry Et_2O, was slowly added to a solution containing compound **2** (986 mg, 4.5 mmol, 1.0 eq.) and Ni(dppp)Cl_2 (81 mg, 0.15 mmol, 3 mol%) in 21 mL of dry Et_2O. The reaction mixture was heated to reflux for 20 h. Upon completion, the reaction was quenched by the addition of EtOH and a few droplets of 2 M HCl, and concentrated under reduced pressure. The crude product was purified via column chromatography (silica gel, heptane), yielding the title compound as a colorless oil (772 mg, 2.77 mmol, 62%).

^{1}H NMR (400 MHz, $CDCl_3$): 7.29 (d, J = 5.2 Hz, 2H), 6.97 (d, J = 5.2 Hz, 2H), 2.53 – 2.48 (m, 4H), 1.58 – 1.49 (m, 4H), 1.34 – 1.23 (m, 4H), 0.86 (t, J = 7.3 Hz, 6H).

^{13}C NMR (101 MHz, $CDCl_3$): 142.4, 128.9, 125.4, 33.0, 28.6, 22.6, 14.1.

5,5'-dibromo-3,3'-dibutyl-2,2'-bithiophene (4)

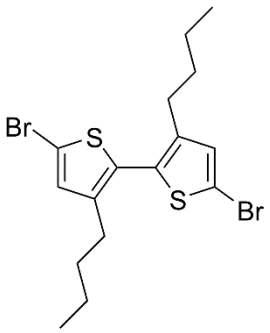

Compound **3** (772 mg, 2.77 mmol, 1.0 eq.) was dissolved in 6 mL $CHCl_3$ and cooled to 0 °C. *N*-bromosuccinimide (1.04 g, 5.82 mmol, 2.1 eq.) and glacial acetic acid (6 mL) were added and the solution was allowed to slowly warm up to room temperature. After stirring at room

temperature for 2 d in the dark, the reaction mixture was poured onto H_2O, extracted with DCM, washed with saturated $NaHCO_3$ solution, dried over $MgSO_4$, and concentrated under reduced pressure. The crude product was purified by column chromatography (silica gel, cyclohexane), yielding a colorless oil (1.17 g, 2.68 mmol, 97%).

^{1}H NMR (400 MHz, $CDCl_3$): 6.91 (s, 2H), 2.47 – 2.41 (m, 4H), 1.54 – 1.44 (m, 4H), 1.33 – 1.22 (m, 4H), 0.86 (t, J = 7.3 Hz, 6H).

^{13}C NMR (101 MHz, $CDCl_3$): 143.9, 131.6, 129.0, 112.5, 32.8, 28.6, 22.5, 14.0.

3',3''-dibutyl-[2,2':5',5'':2'',2'''-quaterthiophene]-5,5'''-dicarbaldehyde (s4T)

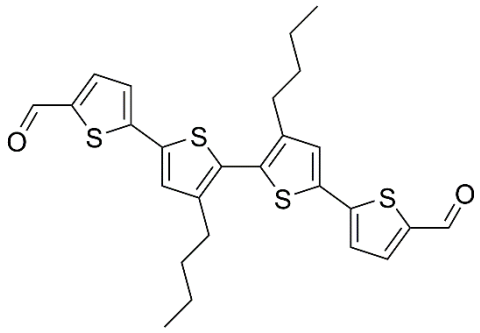

Following a procedure by Yang *et al.*,[2] compound **4** (1.08 g, 2.48 mmol, 1.0 eq.) was stirred with Pd(OAc)2 (23 mg, 0.10 mmol, 4 mol%) and XPhos (57 mg, 0.12 mmol, 4.8 mol%) in 14 mL n-butanol until complete dissolution of the solids (ca. 15 min). Next, a solution containing $CsOH{\cdot}H_2O$ (1.42 g, 8.43 mmol, 3.4 eq.) in 3.5 mL H_2O was added, followed by the addition of 5-formyl-2-thienylboronic acid (1.16 g, 7.44 mmol, 3.0 eq.). The resulting mixture was stirred for 2 d at 35 °C. After completion, H_2O was added and the product was extracted with DCM, dried over $MgSO_4$ and concentrated under reduced pressure. Purification via column chromatography (silica gel, DCM) furnished the title compound as a bright red powder (697 mg, 1.40 mmol, 56%).

^{1}H NMR (400 MHz, $CDCl_3$): 9.86 (s, 2H), 7.67 (d, J = 4.0 Hz, 2H), 7.24 (d, J = 3.9 Hz, 2H), 7.23 (s, 2H), 2.59 – 2.51 (m, 4H), 1.63 – 1.52 (m, 4H), 1.38 – 1.27 (m, 4H), 0.89 (t, J = 7.3 Hz, 6H).

^{13}C NMR (101 MHz, $CDCl_3$): 182.6, 146.9, 144.4, 141.9, 137.4, 136.1, 129.8, 127.8, 124.3, 32.8, 28.8, 22.6, 14.0.

HR-EI-MS: *m/z* 498.74 (M^+, calculated for $C_{26}H_{26}O_2S_4$: 498.75).

3,3''-dibutyl-2,2':5',2''-terthiophene (5)[1]

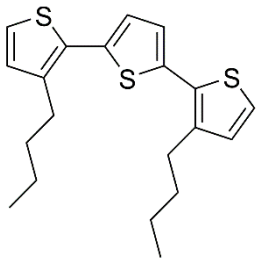

A Grignard reagent, prepared by sonication of compound **2** (4.38 g, 20 mmol, 2.9 eq.), 1,2-dibromoethane (3.76 g, 20 mmol, 2.9 eq.) and Mg (972 mg, 40 mmol, 5.7 eq.) in 56 mL of dry Et_2O, was slowly added to a solution containing 2,5-dibromothiophene (1.69 g, 7.0 mmol, 1.0 eq.) and Ni(dppp)Cl_2 (325 mg, 0.6 mmol, 3 mol%) in 50 mL dry Et_2O. The reaction mixture was heated to reflux for 40 h. Upon completion, the reaction was quenched by the addition of 1 M HCl (50 mL), extracted with DCM, washed with H_2O, dried over $MgSO_4$, and concentrated under reduced pressure. The crude product was purified via column chromatography (silica gel, heptane), yielding the title compound as a slightly yellow oil (2.47 g, 6.84 mmol, 98%).

^{1}H NMR (400 MHz, $CDCl_3$): 7.18 (d, J = 5.2 Hz, 2H), 7.06 (s, 2H), 6.94 (d, J = 5.2 Hz, 2H), 2.79 (t, J = 7.8 Hz, 4H), 1.69 – 1.59 (m, 4H), 1.46 – 1.35 (m, 4H), 0.94 (t, J = 7.3 Hz, 6H).

3,3''-dibutyl-5-formyl-2,2':5',2''-terthiophene (6)

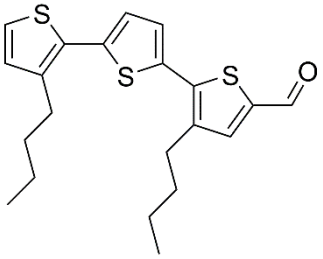

A Vilsmeier reagent, prepared by the addition of $POCl_3$ (1.57 g, 10.3 mmol, 1.5 eq.) to 6.5 mL of dry DMF at 0 °C, was added to a solution of compound **5** (2.47 g, 6.84 mmol, 1.0 eq.) in 96 mL DCE at 0 °C. The reaction mixture was stirred overnight at 70 °C. Subsequently, H_2O was added and the pH was adjusted to 8.5-9 with 1 M NaOH. The product was extracted with

DCM, dried over $MgSO_4$ and concentrated under reduced pressure. Purification via column chromatography (silica gel, DCM/n-hexane 3:2) furnished the product as a slightly yellow solid (1.95 g, 5.02 mmol, 73%).

^{1}H NMR (400 MHz, $CDCl_3$): 9.83 (s, 1H), 7.60 (s, 1H), 7.24 (d, J = 3.8 Hz, 1H), 7.22 (d, J = 5.2 Hz, 1H), 7.11 (d, J = 3.8 Hz, 1H), 6.96 (d, J = 5.2 Hz, 1H), 2.87 – 2.81 (m, 2H), 2.82 – 2.76 (m, 2H), 1.73 – 1.60 (m, 4H), 1.49 – 1.36 (m, 4H), 0.97 (t, J = 7.4 Hz, 3H), 0.94 (t, J = 7.3 Hz, 3H).

^{13}C NMR (101 MHz, $CDCl_3$): 182.7, 141.3, 140.5, 140.4, 140.4, 139.2, 138.6, 134.6, 130.4, 129.9, 127.9, 126.5, 124.6, 33.0, 32.6, 29.3, 29.2, 22.8, 22.7, 14.1, 14.1.

5-bromo-3,3''-dibutyl-5''-formyl-2,2':5',2''-terthiophene (7)

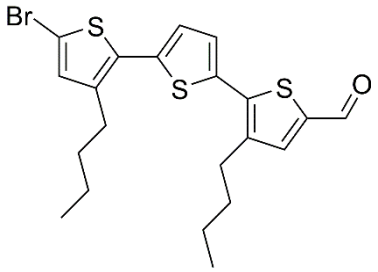

Compound **6** (1.95 g, 5.02 mmol, 1.0 eq.) was dissolved in 15 mL $CHCl_3$ and cooled to 0 °C. NBS (938 mg, 5.27 mmol, 1.05 eq.) and glacial acetic acid (15 mL) were added and the solution was allowed to slowly warm up to room temperature. After stirring at room temperature for 2 d in the dark, the reaction mixture was poured onto H_2O, extracted with DCM, washed with saturated $NaHCO_3$ solution, dried over $MgSO_4$, and concentrated under reduced pressure. The crude product was purified by column chromatography (silica gel, DCM/cyclohexane 3:2), yielding an orange solid (2.20 g, 4.71 mmol, 94%).

^{1}H NMR (400 MHz, $CDCl_3$): 9.83 (s, 1H), 7.60 (s, 1H), 7.22 (d, J = 3.8 Hz, 1H), 7.05 (d, J = 3.8 Hz, 1H), 6.92 (s, 1H), 2.85 – 2.79 (m, 2H), 2.76 – 2.70 (m, 2H), 1.73 – 1.56 (m, 4H), 1.49 – 1.33 (m, 4H), 0.96 (t, J = 7.3 Hz, 3H), 0.94 (t, J = 7.3 Hz, 3H).

^{13}C NMR (101 MHz, $CDCl_3$): 182.7, 141.1, 140.9, 140.6, 140.6, 139.1, 137.1, 135.2, 133.0, 131.4, 127.9, 126.9, 111.4, 32.9, 32.6, 29.3, 29.2, 22.7, 22.7, 14.0, 14.0.

3,3''-dibutyl-[2,2':5',5'':2'',2'''-quaterthiophene]-5,5'''-dicarbaldehyde (a4T)

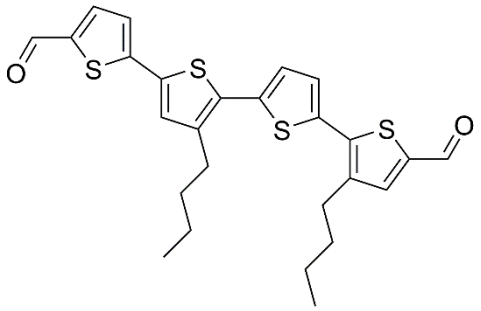

Following a procedure by Yang et al.,[2] compound 7 (2.20 g, 4.71 mmol, 1.0 eq.) was stirred with $Pd(OAc)_2$ (21 mg, 0.094 mmol, 2 mol%) and XPhos (54 mg, 0.113 mmol, 2.4 mol%) in 26.4 mL n-butanol until complete dissolution of the solids (ca. 15 min). Next, a solution containing $CsOH{\cdot}H_2O$ (1.58 g, 9.42 mmol, 2.0 eq.) in 6.6 mL H_2O was added. Subsequently, 5-formyl-2-thienylboronic acid (1.32 g, 8.48 mmol, 1.8 eq.) was added and the resulting mixture was stirred for 18 h at room temperature. After completion, H_2O was added and the product was extracted with $CHCl_3$, dried over $MgSO_4$ and concentrated under reduced pressure. Purification via column chromatography (silica gel, $CHCl_3$), followed by recrystallization from hot DCE furnished the title compound as a dark red microcrystalline powder (2.15 g, 4.29 mmol, 91%).

^{1}H NMR (400 MHz, $CDCl_3$): 9.86 (s, 1H), 9.84 (s, 1H), 7.67 (d, J = 4.0 Hz, 1H), 7.60 (s, 1H), 7.26 (d, J = 3.8 Hz, 1H), 7.24 (d, J = 4.0 Hz, 1H), 7.20 (s, 1H), 7.16 (d, J = 3.9 Hz, 1H), 2.86 – 2.82 (m, 2H), 2.82 – 2.77 (m, 2H), 1.74 – 1.63 (m, 4H), 1.50 – 1.39 (m, 4H), 0.97 (t, J = 7.4 Hz, 3H), 0.97 (t, J = 7.3 Hz, 3H).

^{13}C NMR (101 MHz, $CDCl_3$): 182.6, 182.5, 146.7, 142.0, 141.6, 140.7, 140.7, 140.7, 139.1, 137.4, 137.4, 135.5, 134.3, 131.9, 129.3, 128.0, 126.9, 124.4, 32.8, 32.6, 29.4, 29.3, 22.8, 22.7, 14.1, 14.0.

HR-EI-MS: *m/z* 498.73 (M^+, calculated for $C_{26}H_{26}O_2S_4$: 498.75).

3,3''-dimethyl-2,2':5',2''-terthiophene (5_{Me})

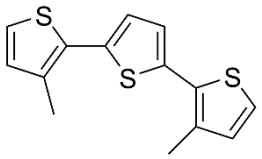

A Grignard reagent, prepared by sonication of 2-bromo-3-methylthiophene (1.126 mL, 10.0 mmol, 2.9 eq.), 1,2-dibromoethane (0.862 mL, 10.0 mmol, 2.9 eq.), and Mg (477.7 mg, 19.6 mmol, 5.7 eq.) in 30 mL dry Et_2O was slowly added to a solution containing 2,5-dibromothiophene (389 µL, 3.5 mmol, 1.0 eq.) and $Ni(dppp)Cl_2$ (162.6 mg, 0.3 mmol, 3 mol%) in 20 mL dry Et_2O. The reaction mixture was heated to reflux for 40 h. Upon completion, the reaction was quenched by the addition of 30 mL 1 M HCl, extracted with DCM and washed with H_2O. The organic phase was then dried over $MgSO_4$ and concentrated under reduced pressure. The crude product was purified via column chromatography (silica gel, pentane), yielding the title compound as a slightly yellow oil, which crystallized slowly (492 mg, 1.78 mmol, 51%).

^{1}H NMR (400 MHz, $CDCl_3$): 7.15 (d, J = 5.1 Hz, 2H), 7.08 (s, 2H), 6.89 (d, J = 5.1 Hz, 2H), 2.42 (s, 6H).

^{13}C NMR (101 MHz, $CDCl_3$): 136.7, 134.5, 131.9, 131.3, 126.2, 123.8, 15.9.

5-formyl-3,3''-dimethyl-2,2':5',2''-terthiophene (6_{Me})

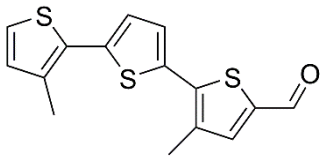

A Vilsmeier reagent, prepared by the addition of $POCl_3$ (283 mg/ 168 µL, 1.8 mmol, 1.3 eq.) to 1.343 mL of dry DMF, was added to a solution of compound **5_{Me}** (391.8 mg, 1.4 mmol, 1.0 eq.) in 28 mL DCE. The reaction mixture was stirred overnight at 70 °C. Subsequently, 50 mL H_2O was added and the pH was adjusted to 8.5-9 with 1 M NaOH. The product was extracted with DCM, dried over $MgSO_4$ and concentrated under reduced pressure. Purification via column chromatography (silica gel, chloroform) furnished the product as a slightly yellow solid (397 mg, 1.3 mmol, 92%).

^{1}H NMR (400 MHz, $CDCl_3$): 9.82 (s, 1H), 7.54 (s, 1H), 7.28 (d, J = 3.9 Hz, 1H), 7.19 (d, J = 5.1 Hz, 1H), 7.13 (d, J = 3.9 Hz, 1H), 6.91 (d, J = 5.1 Hz, 1H), 2.48 (s, 3H), 2.43 (s, 3H).

^{13}C NMR (101 MHz, $CDCl_3$): 182.5, 141.7, 140.5, 139.8, 139.0, 134.9, 134.9, 134.8, 131.8, 130.4, 127.8, 126.1, 124.2, 16.0, 15.7.

5-bromo-5''-formyl-3,3''-dimethyl-2,2':5',2''-terthiophene (7$_{Me}$)

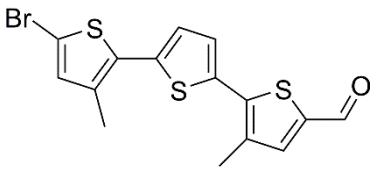

Compound **6$_{Me}$** (397 mg, 1.3 mmol, 1.0 eq.) was dissolved in a mixture of 12.5 mL $CHCl_3$ and 12.5 mL glacial acetic acid and cooled to 0 °C. *N*-bromosuccinimide (255 mg, 1.4 mmol, 1.1 eq.) was added in the dark and the solution was allowed to slowly warm up to room temperature. After stirring at room temperature for 3 d in the dark, the reaction mixture was poured onto H_2O, extracted with DCM, washed with brine, dried over $MgSO_4$, and concentrated under reduced pressure. The crude product was purified by column chromatography (silica gel, gradient eluent: n-hexane with 2% - 25% EtOAc), yielding a bright yellow solid (438 mg, 1.14 mmol, 90%).

^{1}H NMR (400 MHz, $CDCl_3$): 9.82 (s, 1H), 7.54 (s, 1H), 7.26 (d, J = 4.0 Hz, 1H), 7.07 (d, J = 3.9 Hz, 1H), 6.88 (s, 1H), 2.47 (s, 3H), 2.37 (s, 3H).

^{13}C NMR (101 MHz, $CDCl_3$): 182.5, 141.3, 140.4, 140.1, 137.5, 135.4, 135.4, 135.0, 134.3, 131.9, 127.7, 126.5, 111.0, 16.0, 15.6.

3,3''-dimethyl-[2,2':5',5'':2'',2'''-quaterthiophene]-5,5'''-dicarbaldehyde (a4T$_{Me}$)

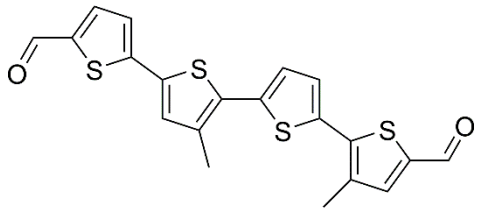

Following a procedure by Yang et al.,[2] compound **7$_{Me}$** (232 mg, 0.6 mmol, 1.0 eq.) was stirred with $Pd(OAc)_2$ (2.71 mg, 0.012 mmol, 2 mol%) and XPhos (6.91 mg, 0.015 mmol, 2.4 mol%) in 3.4 mL n-butanol (ca. 15 min). Next, a solution containing $CsOH \cdot H_2O$ (203 mg, 1.21 mmol, 2.0 eq.) in 846 µL H_2O was added, followed by the addition of 5-formyl-2-thienylboronic acid (170 mg, 1.09 mmol, 1.8 eq.). The resulting mixture was stirred for 2 d at room temperature and 1 d at 50 °C. After completion, H_2O was added and the product was extracted with $CHCl_3$, washed with brine 3 times, dried over $MgSO_4$, and concentrated under reduced pressure. Purification via column chromatography (silica gel, chloroform/EtOAc 99:1) furnished the title compound as a bright red powder (205 mg, 0.494 mmol, 82%).

^{1}H NMR (400 MHz, $CDCl_3$): 9.86 (s, 1H), 9.83 (s, 1H), 7.67 (d, J = 4.0 Hz, 1H), 7.55 (s, 1H), 7.30 (d, J = 3.9 Hz, 1H), 7.23 (d, J = 4.0 Hz, 1H), 7.19 (d, J = 3.9 Hz, 1H), 7.18 (s, 1H), 2.49 (s, 3H), 2.45 (s, 3H).

^{13}C NMR (101 MHz, $CDCl_3$): 182.5, 146.6, 142.0, 141.2, 140.4, 140.2, 137.8, 137.5, 136.0, 135.8, 135.1, 133.9, 132.4, 130.6, 127.9, 126.7, 124.4, 16.1, 15.9.

HR-EI-MS: *m/z* 414.56 (M^+, calculated for $C_{20}H_{14}O_2S_4$: 414.57).

Scheme 5.2: Synthesis of the $4T_{TPD}$ building block.

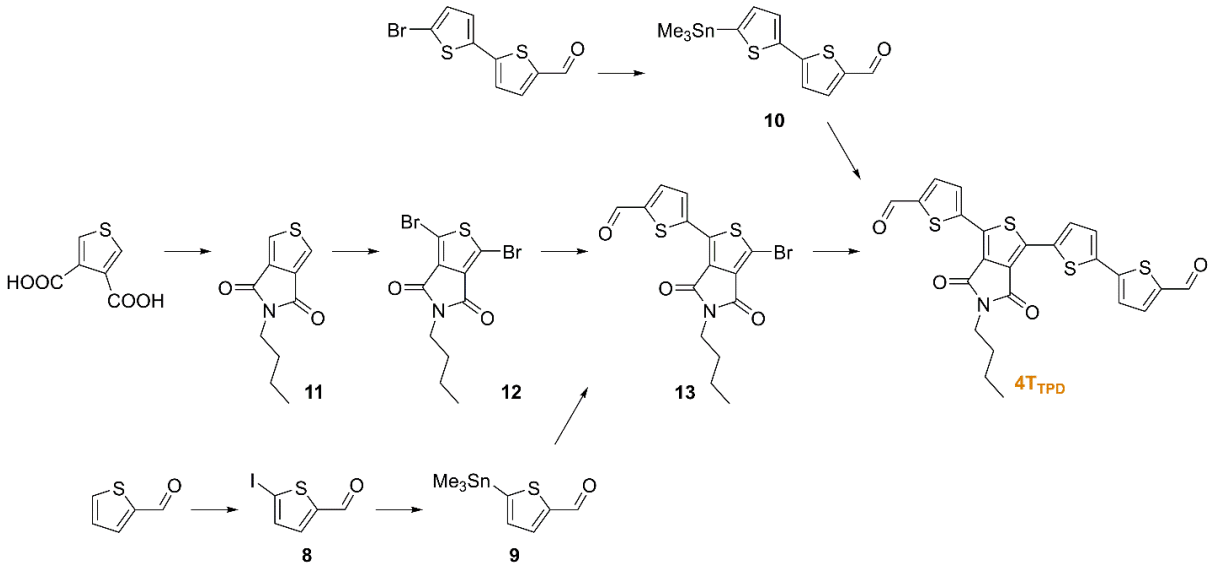

5-iodothiophene-2-carbaldehyde (8)[3]

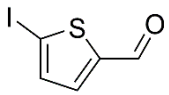

Thiophene-2-carbaldehyde (2.24 g, 20 mmol, 1.0 eq.) was dissolved in 40 mL EtOH and heated to 50 °C. *N*-iodosuccinimide (4.95 g, 22 mmol, 1.1 eq.) and *p*-toluenesulfonic acid monohydrate (380 mg, 2 mmol, 10 mol%) were added and the resulting mixture was stirred at 50 °C in the dark for 10 min. After completion, 20 mL of 1 M aqueous HCl and 20 mL EtOAc were added. The organic layer was extracted with EtOAc, washed with saturated aqueous $Na_2S_2O_3$ and Na_2CO_3 solutions, dried over $MgSO_4$, and filtered through a cotton plug. All volatiles were removed under high vacuum, yielding a slightly yellow solid (4.57 g, 19.2 mmol, 96%).

^{1}H NMR (400 MHz, $CDCl_3$): 9.77 (s, 1H), 7.39 (s, 2H).

^{13}C NMR (101 MHz, $CDCl_3$): 181.3, 149.8, 138.4, 137.1, 87.9.

5-(trimethylstannyl)thiophene-2-carbaldehyde (9)

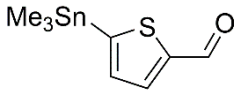

A reaction mixture containing compound **8** (472 mg, 2.0 mmol, 1.0 eq.), hexamethylditin (786 mg, 2.4 mmol, 1.2 eq.), and $Pd(PPh_3)_4$ (116 mg, 0.1 mmol, 5 mol%) in 10 mL of dry toluene was heated to 85 °C for 24 h. After completion, the solution was concentrated under reduced pressure at room temperature to remove the solvent and most of the by-product. The product was purified by sublimation (10^{-3} mbar, 60 °C), yielding the title compound as a white crystalline solid (264 mg, 0.96 mmol, 48%).

^{1}H NMR (400 MHz, $CDCl_3$): 9.94 (s, 1H), 7.83 (d, J = 3.5 Hz, 1H), 7.28 (d, J = 3.5 Hz, 1H), 0.42 (s, with Sn coupling, 9H).

5'-(trimethylstannyl)-[2,2'-bithiophene]-5-carbaldehyde (10)

A reaction mixture containing 5'-bromo-[2,2'-bithiophene]-5-carbaldehyde (1.00 g, 3.66 mmol, 1.0 eq.), hexamethylditin (1.44 g, 4.4 mmol, 1.2 eq.), and $Pd(PPh_3)_4$ (208 mg, 0.18 mmol, 5 mol%) in 20 mL of dry toluene was heated to 85 °C for 24 h. After completion, all volatiles were removed under high vacuum at 40 °C. The brown residue was dissolved in toluene, washed with saturated aqueous KCl, dried over Na_2SO_4, passed through a neutral alumina plug and evaporated to dryness, yielding a yellow solid (920 mg, 2.58 mmol, 70%), which was used in the next step without further purification.

^{1}H NMR (400 MHz, $CDCl_3$): 9.85 (s, 1H), 7.66 (d, J = 4.0 Hz, 1H), 7.45 (d, J = 3.4 Hz, 1H), 7.24 (d, J = 4.0 Hz, 1H), 7.14 (d, J = 3.4 Hz, 1H), 0.41 (s, with Sn coupling, 9H).

5-butyl-4*H*-thieno[3,4-*c*]pyrrole-4,6(5*H*)-dione (11)[4-5]

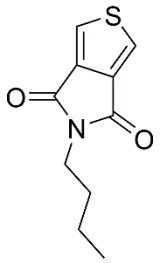

Thiophene-3,4-dicarboxylic acid (3.29 g, 19.1 mmol, 1.0 eq.) and 3 Å molecular sieve (~200 mg) were dispersed in 40 mL acetic anhydride and heated to 140 °C for 24 h. After cooling to room temperature, the solution was decanted and evaporated to dryness. The resulting light grey solid was dried under high vacuum and re-dissolved in 60 mL of dry toluene. Butylamine (2.01 g, 28.7 mmol, 1.5 eq.) was added, and the solution was heated to reflux for 24 h. All volatiles were removed under high vacuum, yielding a faint brownish powder. $SOCl_2$ (120 mL) was added and the mixture was heated to reflux (88 °C) overnight. The $SOCl_2$ was distilled off at ambient pressure, leaving behind a dark crystalline solid. Purification via column chromatography (silica gel, DCM), followed by recrystallization from Et_2O afforded the title compound as colorless platelets (3.06 g, 14.6 mmol, 77%).

^{1}H NMR (400 MHz, $CDCl_3$): 7.80 (s, 2H), 3.67 – 3.57 (m, 2H), 1.67 – 1.58 (m, 2H), 1.41 – 1.30 (m, 2H), 0.94 (t, J = 7.4 Hz, 3H).

^{13}C NMR (101 MHz, $CDCl_3$): 162.8, 136.9, 125.6, 38.4, 30.7, 20.2, 13.8.

1,3-dibromo-5-butyl-4*H*-thieno[3,4-*c*]pyrrole-4,6(5*H*)-dione (12)[6]

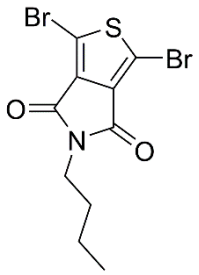

Compound **11** (2.64 g, 12.6 mmol, 1.0 eq.) was dissolved in a mixture of conc. H_2SO_4 (18.9 mL) and trifluoroacetic acid (63 mL) at 0 °C. *N*-bromosuccinimide (6.73 g, 37.8 mmol, 3.0 eq.) was added and the reaction mixture was allowed to slowly warm to room temperature.

After stirring in the dark for 2 d, the solution was poured onto H_2O, extracted with $CHCl_3$, dried over $MgSO_4$, and concentrated under reduced pressure. The product was purified by column chromatography (silica gel, toluene/DCM/heptane 3:1:1), yielding a slightly yellow solid (3.18 g, 8.65 mmol, 69%).

^{1}H NMR (400 MHz, $CDCl_3$): 3.60 (t, J = 7.2 Hz, 2H), 1.66 – 1.57 (m, 2H), 1.40 – 1.29 (m, 2H), 0.94 (t, J = 7.3 Hz, 3H).

^{13}C NMR (101 MHz, $CDCl_3$): 160.5, 135.0, 113.1, 38.7, 30.5, 20.2, 13.7.

compound 13

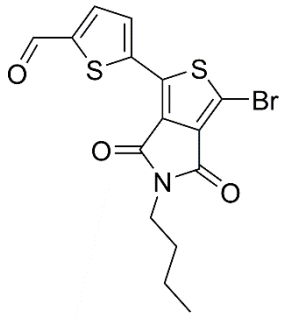

A reaction mixture containing compound **12** (602 mg, 1.64 mmol, 1.0 eq.), compound **9** (451 mg, 1.64 mmol, 1.0 eq.), $Pd(dba)_2$ (47 mg, 0.082 mmol, 5 mol%), and tri(2-furyl)phosphine (47 mg, 0.20 mmol, 12 mol%) in 20 mL dry toluene was heated to 85 °C for 48 h. After completion, all volatiles were removed under high vacuum at 50 °C. Purification via column chromatography (silica gel, $CHCl_3$) yielded the title compound as a yellow solid (171 mg, 0.43 mmol, 26%).

^{1}H NMR (400 MHz, $CDCl_3$): 9.94 (s, 1H), 8.08 (d, J = 4.0 Hz, 1H), 7.75 (d, J = 4.1 Hz, 1H), 3.66 (t, J = 7.2 Hz, 2H), 1.71 – 1.60 (m, 2H), 1.42 – 1.32 (m, 2H), 0.95 (t, J = 7.4 Hz, 3H).

TPD-modified quaterthiophene (4T$_{TPD}$)

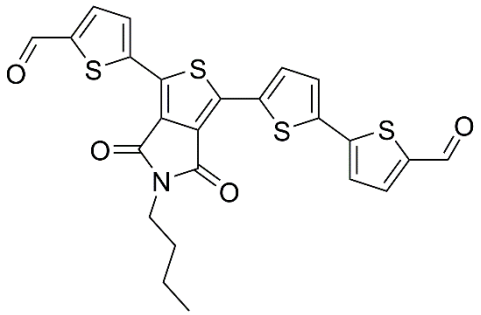

A reaction mixture containing compound **13** (80 mg, 0.20 mmol, 1.0 eq.), compound **10** (86 mg, 0.24 mmol, 1.2 eq.), $Pd(dba)_2$ (12 mg, 0.020 mmol, 10 mol%), and tri(2-furyl)phosphine (12 mg, 0.050 mmol, 25 mol%) in 2 mL dry toluene was heated to 85 °C for 24 h. After completion, all volatiles were removed under high vacuum at 50 °C. Purification via column chromatography (silica gel, DCM), followed by recrystallization from DCE/Et_2O afforded the title compound as an orange solid (89 mg, 0.174 mmol, 87%).

^{1}H NMR (400 MHz, $CDCl_3$): 9.94 (s, 1H), 9.90 (s, 1H), 8.19 (d, J = 4.0 Hz, 1H), 7.98 (d, J = 4.0 Hz, 1H), 7.77 (d, J = 4.0 Hz, 1H), 7.71 (d, J = 4.0 Hz, 1H), 7.36 (d, J = 4.0 Hz, 2H), 3.70 (t, J = 7.3 Hz, 2H), 1.74 – 1.64 (m, 2H), 1.46 – 1.35 (m, 2H), 0.97 (t, J = 7.4 Hz, 3H).

^{13}C NMR (101 MHz, $CDCl_3$): 182.7, 182.6, 162.5, 162.3, 145. 5, 144.9, 143.0, 140.6, 139.8, 137.3, 137.2, 136.8, 134.8, 133.1, 131.8, 131.6, 130.6, 129.8, 127.2, 125.6, 38.7, 30.7, 20.3, 13.8.

HR-EI-MS: *m/z* 511.63 (M^+, calculated for $C_{24}H_{17}NO_4S_4$: 511.64).

Scheme 5.3: Synthesis of the $4T_{TT}$ building block.

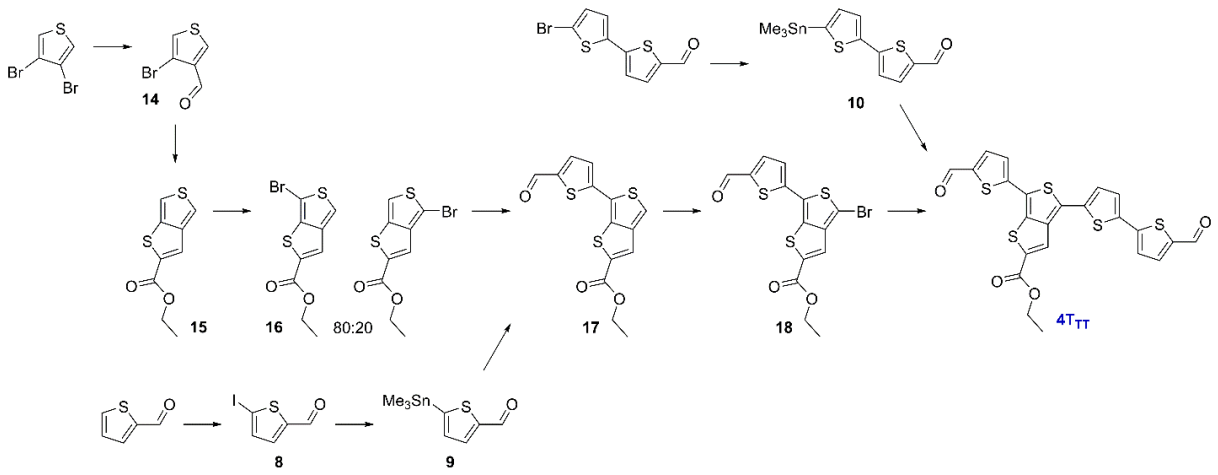

4-bromothiophene-3-carbaldehyde (14)

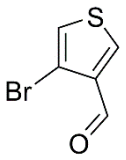

A solution of 3,4-dibromothiophene (5.4 g, 22.3 mmol, 1.0 eq.) in 15 mL of dry Et_2O was cooled to −78 °C and n-BuLi (2.0 M in cyclohexane, 22.3 mmol, 1.0 eq.) was slowly added. After stirring for 15 min, DMF (1.63 g, 22.3 mmol, 1.0 eq.) was added. The reaction mixture was stirred for 3 h at −78 °C and then allowed to slowly warm to room temperature. H_2O was added to quench the reaction, and the solution was extracted with DCM, dried over Na_2SO_4, and evaporated to dryness. Purification via high vacuum distillation (10^{-3} mbar, 65 °C) afforded the title compound as a faint yellowish, air-sensitive liquid (2.29 g, 12.0 mmol, 54%).

^{1}H NMR (400 MHz, $CDCl_3$): 9.95 (s, 1H), 8.15 (d, J = 3.4 Hz, 1H), 7.36 (d, J = 3.4 Hz, 1H).

^{13}C NMR (101 MHz, $CDCl_3$): 184.8, 137.7, 134.7, 125.2, 111.5.

ethyl thieno[3,4-*b*]thiophene-2-carboxylate (15)[7]

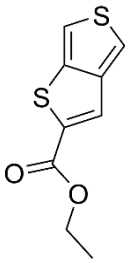

Ethyl mercaptoacetate (1.59 g, 13.2 mmol, 1.1 eq.) was added dropwise to a solution of compound **14** (2.29 g, 12.0 mmol, 1.0 eq.), K_2CO_3 (2.49 g, 18.0 mmol, 1.5 eq.), and CuO nanopowder (< 50 nm particle size, 28 mg, 0.36 mmol, 3 mol%) in 24 mL DMSO at 60 °C. The reaction mixture was stirred overnight at 60 °C. After completion, H_2O and brine were added, and the product was extracted with DCM. The combined organic phase was washed with brine, dried over Na_2SO_4, and concentrated under reduced pressure. Purification via column chromatography (silica gel, DCM/heptane 2:1) yielded the title compound as a slightly yellowish powder (1.50 g, 7.08 mmol, 59%).

^{1}H NMR (400 MHz, $CDCl_3$): 7.70 (d, J = 0.8 Hz, 1H), 7.59 (d, J = 2.6 Hz, 1H), 7.28 (dd, J = 2.7, 0.8 Hz, 1H), 4.38 (q, J = 7.1 Hz, 2H), 1.39 (t, J = 7.1 Hz, 3H).

^{13}C NMR (101 MHz, $CDCl_3$): 163.3, 146.1, 140.0, 140.0, 123.6, 116.7, 111.5, 61.8, 14.5.

ethyl 6-bromothieno[3,4-*b*]thiophene-2-carboxylate (16)[8]

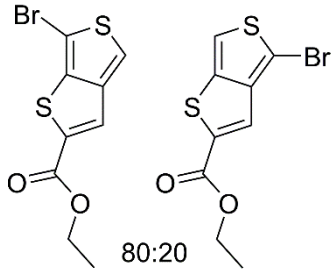

Compound **15** (1.34 g, 6.31 mmol, 1.0 eq.) was dissolved in 45 mL DMF and stirred at 0 °C in the dark. A solution of *N*-bromosuccinimide (1.12 g, 6.31 mmol, 1.0 eq.) in 45 mL DMF was added over the course of 6 h via an addition funnel (approximately one drop every 10 s). Upon completion, the reaction mixture was allowed to warm up to room temperature over the course of 12 h. All volatiles were removed under reduced pressure. Purification via column

chromatography (silica gel, CHCl3/cyclohexane 1:1) afforded a slightly pink solid (1.68 g, 5.78 mmol, 92%). The product was found to be a 80:20 mixture of the 6-bromo- and the 4-bromothieno[3,4-*b*]thiophene-2-carboxylate that could not be separated at this stage.

^{1}H NMR (400 MHz, $CDCl_3$): 7.56 (d, J = 0.9 Hz, 1H), 7.24 (d, J = 0.9 Hz, 1H), 4.38 (q, J = 7.1 Hz, 2H), 1.41 (t, J = 7.1 Hz, 3H).

Isomer: 7.66 (s, 1H), 7.52 (s, 1H), 4.38 (q, J = 7.1 Hz, 2H), 1.39 (t, J = 7.1 Hz, 3H).

^{13}C NMR (101 MHz, $CDCl_3$): 162.7, 145.9, 140.8, 138.9, 122.5, 112.6, 102.8, 61.9, 14.3.

Isomer: 162.7, 145.3, 140.4, 124.2, 123.2, 118.0, 97.9, 61.8, 14.3.

compound 17

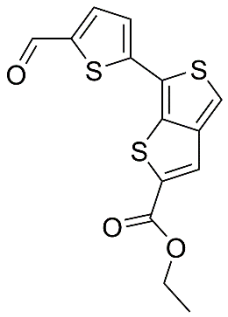

A reaction mixture containing compound **16** (730 mg, 2.5 mmol, 1.0 eq.), compound **9** (825 mg, 3.0 mmol, 1.2 eq.), $Pd(dba)_2$ (144 mg, 0.25 mmol, 10 mol%), and tri(2-furyl)phosphine (145 mg, 0.625 mmol, 25 mol%) in 25 mL dry toluene was heated to 85 °C for 20 h. After completion, all volatiles were removed under high vacuum at 50 °C. Purification via column chromatography (silica gel, DCM/cyclohexane 5:1) afforded the title compound as a yellow-green solid (470 mg, 1.46 mmol, 58%). The product was found to be a 90:10 mixture of the 6-thienyl and 4-thienyl isomers.

^{1}H NMR (400 MHz, $CDCl_3$): 9.90 (s, 1H), 7.99 (d, J = 0.8 Hz, 1H), 7.73 (d, J = 4.0 Hz, 1H), 7.36 (d, J = 4.0 Hz, 1H), 7.33 (d, J = 0.8 Hz, 1H), 4.42 (q, J = 7.1 Hz, 2H), 1.43 (t, J = 7.1 Hz, 3H).

^{13}C NMR (101 MHz, $CDCl_3$): 182.4, 162.6, 145.3, 143.2, 142.4, 142.3, 141.3, 137.1, 126.8, 124.8, 122.9, 112.8, 62.0, 14.3.

compound 18

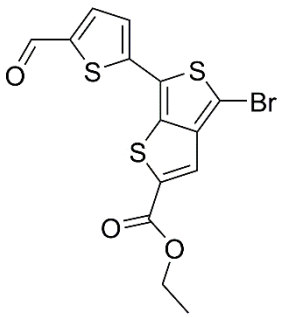

Compound **17** (470 mg, 1.46 mmol, 1.0 eq.) was dissolved in 30 mL $CHCl_3$. *N*-bromosuccinimide (312 mg, 1.75 mmol, 1.2 eq.) was added and the resulting mixture was stirred at room temperature in the dark for 2 d. After completion, the solution was poured onto H_2O and extracted with DCM. The organic phase was dried over Na_2SO_4 and concentrated under reduced pressure. Purification via column chromatography (silica gel, DCM/cyclohexane 4:1) afforded the isomer-pure title compound as an orange solid (501 mg, 1.25 mmol, 86%). The 4-thienyl isomer is slightly slower on the column and thus could be fully removed from the product.

^{1}H NMR (400 MHz, $CDCl_3$): 9.91 (s, 1H), 7.96 (s, 1H), 7.71 (d, J = 4.0 Hz, 1H), 7.28 (d, J = 4.0 Hz, 1H), 4.42 (q, J = 7.1 Hz, 2H), 1.43 (t, J = 7.1 Hz, 3H).

^{13}C NMR (101 MHz, $CDCl_3$): 182.5, 162.4, 144.3, 143.0, 142.9, 142.8, 142.4, 137.2, 128.3, 125.2, 123.8, 100.1, 62.4, 14.5.

TT-modified quaterthiophene ($4T_{TT}$)

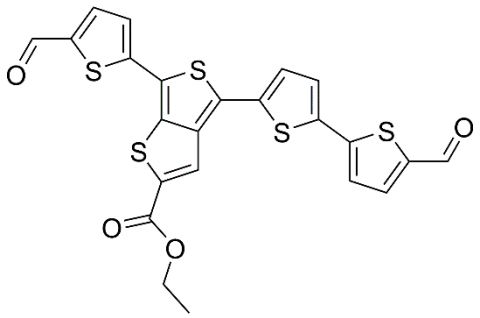

A reaction mixture containing compound **18** (321 mg, 0.8 mmol, 1.0 eq.), compound **10** (343 mg, 0.96 mmol, 1.2 eq.), $Pd(dba)_2$ (46 mg, 0.08 mmol, 10 mol%), and tri(2-furyl)phosphine (46 mg, 0.20 mmol, 25 mol%) in 8 mL dry toluene was heated to 85 °C for

20 h. After completion, all volatiles were removed under high vacuum at 50 °C. Purification via column chromatography (silica gel, DCM), followed by precipitation from $CHCl_3$/Et_2O afforded the title compound as a deep red solid (266 mg, 0.517 mmol, 65%).

^{1}H NMR (400 MHz, $CDCl_3$): 9.92 (s, 1H), 9.89 (s, 1H), 8.03 (s, 1H), 7.75 (d, J = 4.1 Hz, 1H), 7.71 (d, J = 4.1 Hz, 1H), 7.39 (d, J = 3.8 Hz, 1H), 7.38 (d, J = 3.8 Hz, 1H), 7.32 (d, J = 4.1 Hz, 1H), 7.29 (d, J = 4.0 Hz, 1H), 4.46 (q, J = 7.1 Hz, 2H), 1.46 (t, J = 7.2 Hz, 3H).

^{13}C NMR data could not be recorded for this compound due to its low solubility.

HR-EI-MS: *m/z* 514.61 (M^+, calculated for $C_{23}H_{14}O_4S_5$: 514.61).

1,3,6,8-tetrakis(4-aminophenyl)pyrene (Py)[9-10]

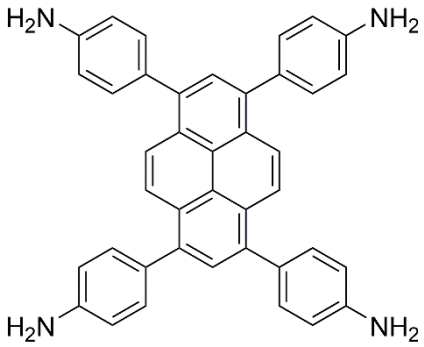

A reaction mixture containing 1,3,6,8-tetrabromopyrene (1482 mg, 2.86 mmol, 1.0 eq.), 4-aminophenylboronic acid pinacol ester (3010 mg, 13.7 mmol, 4.8 eq.), K_2CO_3 (2175 mg, 15.7 mmol, 5.5 eq.), and $Pd(PPh_3)_4$ (330 mg, 0.29 mmol, 10 mol%) in 32 mL 1,4-dioxane and 8 mL H_2O was heated to reflux (115 °C) for 3 d. After cooling to room temperature, H_2O was added. The resulting precipitate was collected via filtration and was washed with H_2O and MeOH. Recrystallization from 1,4-dioxane, followed by drying under high vacuum furnished the title compound, co-crystallized with approximately 1.5 dioxane molecules per formula unit, as a bright yellow powder (1792 mg, 2.56 mmol, 90%).

^{1}H NMR (400 MHz, DMSO-d_6): 8.13 (s, 4 H), 7.79 (s, 2 H), 7.34 (d, J = 8.4 Hz, 8 H), 6.77 (d, J = 8.5 Hz, 8 H), 5.30 (s, 8 H), 3.56 (s, 12 H, dioxane).

^{13}C NMR (100 MHz, DMSO-d_6): 148.2, 137.1, 131.0, 129.0, 127.6, 126.7, 126.1, 124.4, 113.9, 66.3 (dioxane).

5.5.3 COF Syntheses

All COF syntheses were performed under argon atmosphere in PTFE-sealed glass reaction tubes (6 mL volume). Solvents and acetic acid were obtained in high purity grade from commercial suppliers and were, unless shipped under argon, degassed and saturated with argon prior to use.

Py-a4T COF

1,3,6,8-tetrakis(4-aminophenyl)pyrene dioxane adduct (Py; 14.0 mg, 20 µmol, 1.0 eq.) and 3,3"-dibutyl-[2,2':5',5":2",2"'-quaterthiophene]-5,5"'-dicarbaldehyde (a4T; 20 mg, 40 µmol, 2.0 eq.) were filled into a reaction tube, followed by the addition of mesitylene (133 µL), BnOH (67 µL), and 6 M acetic acid (20 µL). The tube was sealed and the reaction mixture was heated at 120 °C for 4 d. After cooling to room temperature, the precipitate was collected by filtration and slowly dried in air for 24 h, yielding the Py-a4T COF as a dark red powder (19 mg, 64%).

Following the same synthesis protocol, but employing the s4T building block instead, did not lead to the formation of a crystalline network. Other solvent mixtures (mesitylene/dioxane, mesitylene/BnOH, DCB/dioxane, DCB/BnOH; ratios from 2:1 to 1:9) and concentrations were tested as well, but the resulting solids did not show any sign of long-range order.

Py-a4T$_{Me}$ COF

1,3,6,8-tetrakis(4-aminophenyl)pyrene dioxane adduct (Py; 14.0 mg, 20 µmol, 1.0 eq.) and 3,3"-dimethyl-[2,2':5',5":2",2"'-quaterthiophene]-5,5"'-dicarbaldehyde (a4T$_{Me}$; 17 mg, 40 µmol, 2.0 eq.) were filled into a reaction tube, followed by the addition of mesitylene (333 µL), BnOH (167 µL), and 6 M acetic acid (50 µL). The tube was sealed and the reaction mixture was heated at 120 °C for 4 d. After cooling to room temperature, the precipitate was collected by filtration, slowly dried in an argon atmosphere overnight, and extracted with supercritical CO_2 for 2 h, yielding the Py-a4T$_{Me}$ COF as a dark red powder.

Py-4T$_{TPD}$ COF

Py (7.0 mg, 10 µmol, 1.0 eq.) and the TPD-modified quaterthiophene (4T$_{TPD}$; 10.2 mg, 20 µmol, 2.0 eq.) were filled into a reaction tube, followed by the addition of mesitylene (167 µL), 1,4-dioxane (333 µL), and 6 M acetic acid (50 µL). The tube was sealed and the reaction mixture was heated at 120 °C for 4 d. After cooling to room temperature, the precipitate was collected by filtration and slowly dried in air, yielding the Py-4T$_{TPD}$ COF as an orange powder.

Py-4T$_{TT}$ COF

Py (14.0 mg, 20 µmol, 1.0 eq.) and TT-modified quaterthiophene (4T$_{TT}$; 20.6 mg, 40 µmol, 2.0 eq.) were filled into a reaction tube, followed by the addition of mesitylene (667 µL), BnOH (333 µL), and 6 M acetic acid (100 µL). The tube was sealed and the reaction mixture was heated at 120 °C for 4 d. After cooling to room temperature, the precipitate was collected by filtration and slowly dried in air for 24 h, yielding the Py-4T$_{TT}$ COF as a very dark purple powder (26 mg, 85%).

5.5.4 NMR Spectroscopy

^{1}H and ^{13}C NMR spectra. Residual (undeuterated) solvent peaks are marked with asterisks.

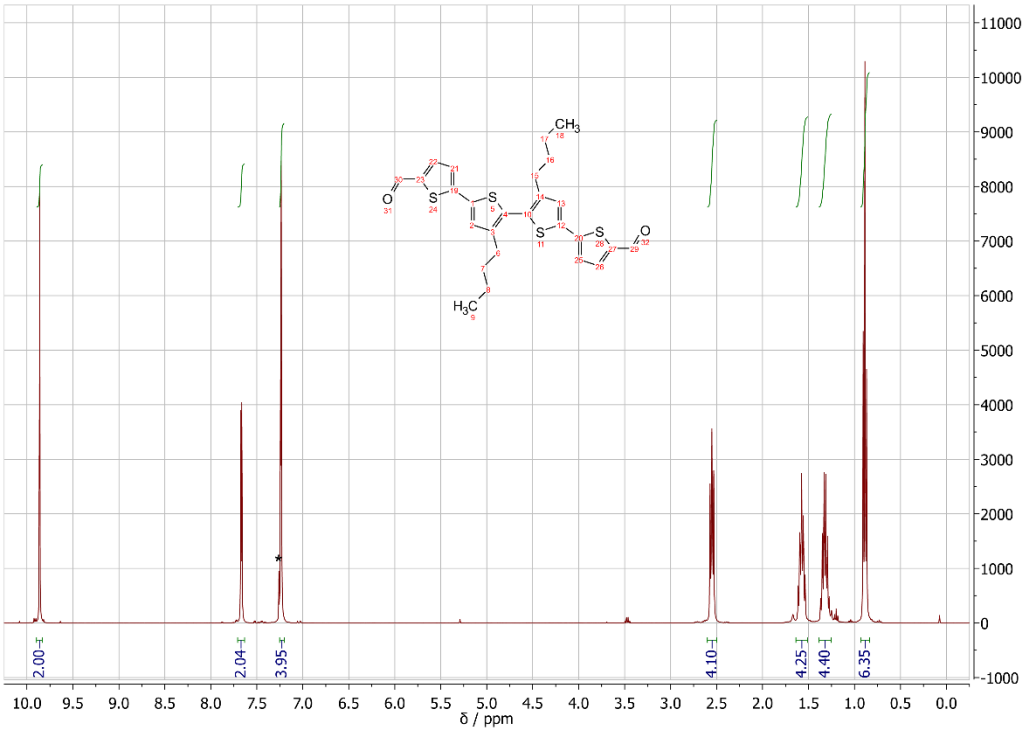

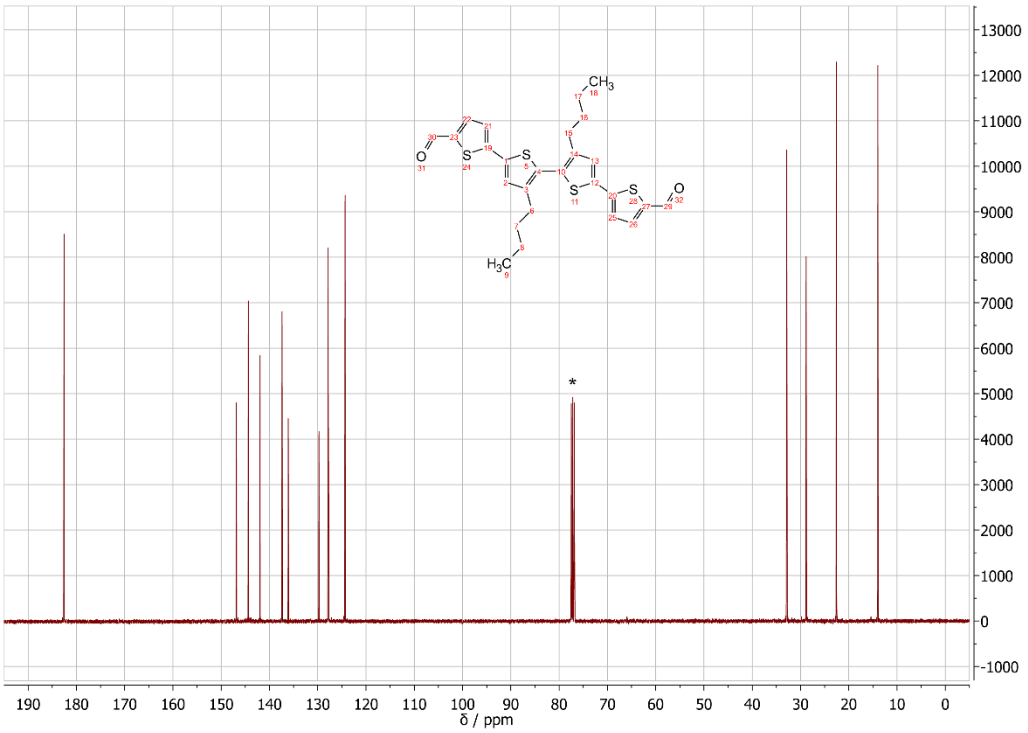

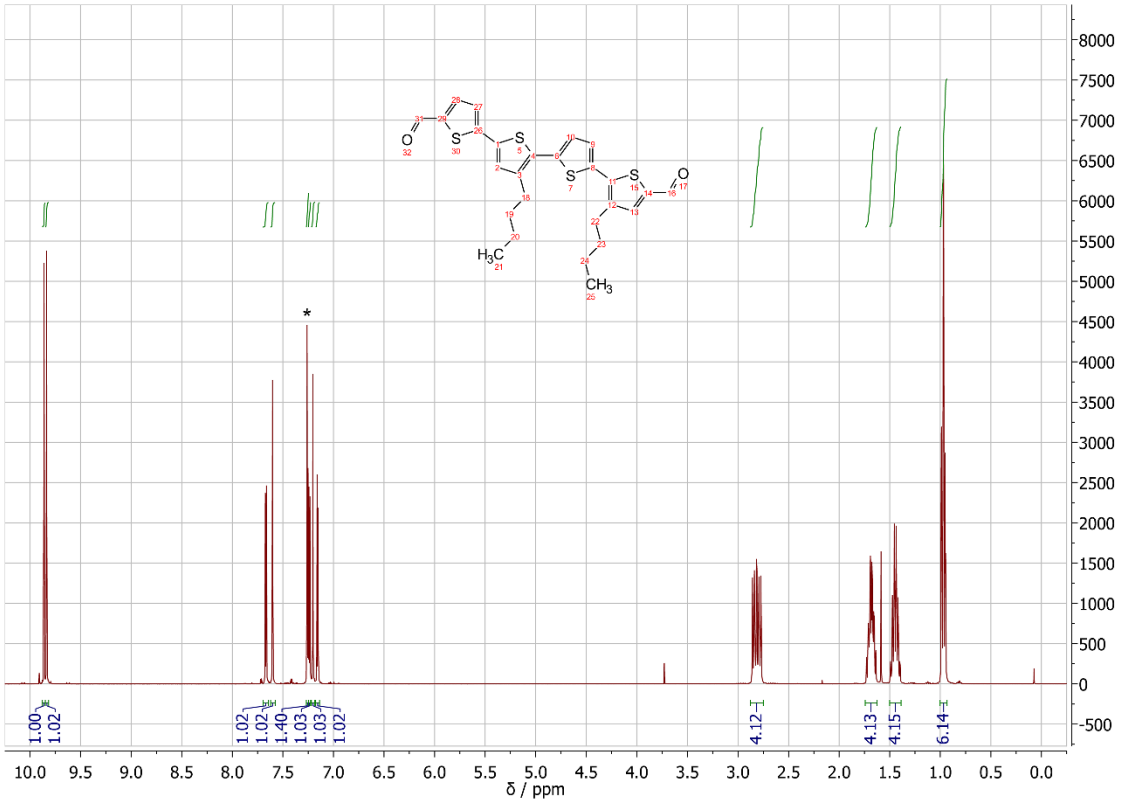
δ / ppm
1.00
1.02
1.02
1.02
1.40
1.03
1.03
1.02
4.12
4.13
4.15
6.14
*
H3C
CH3

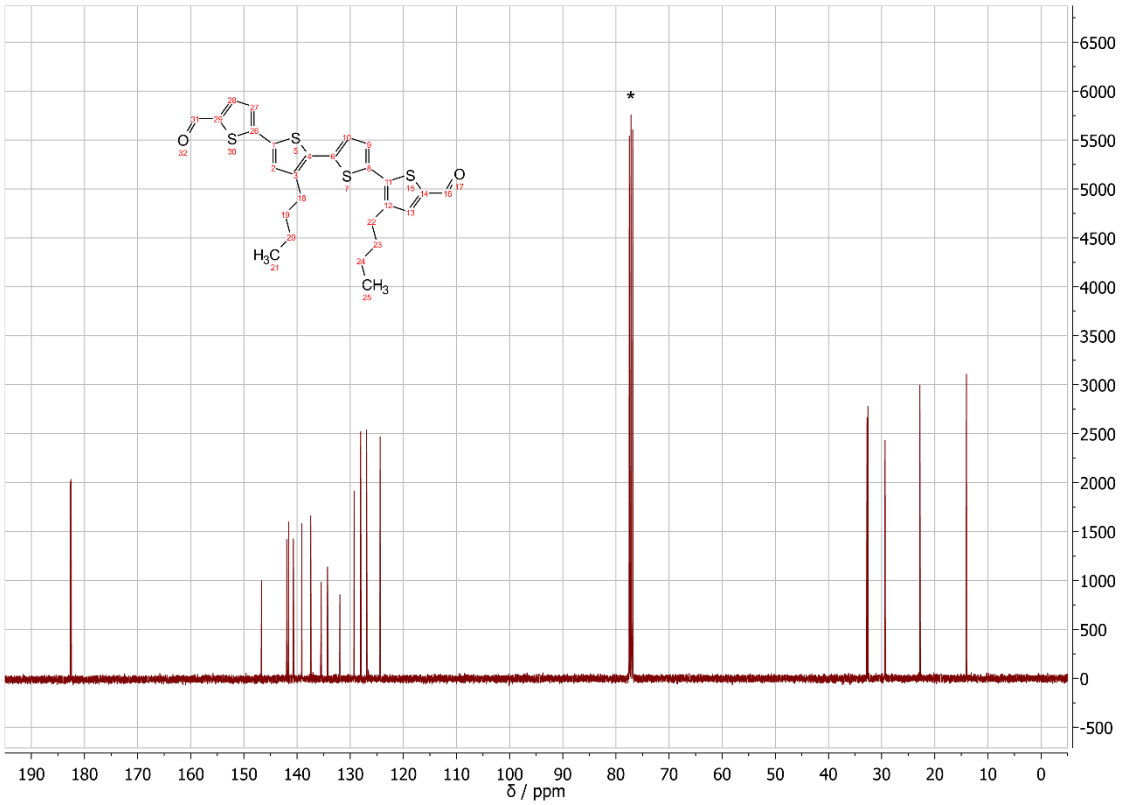
δ / ppm
*
H3C
CH3

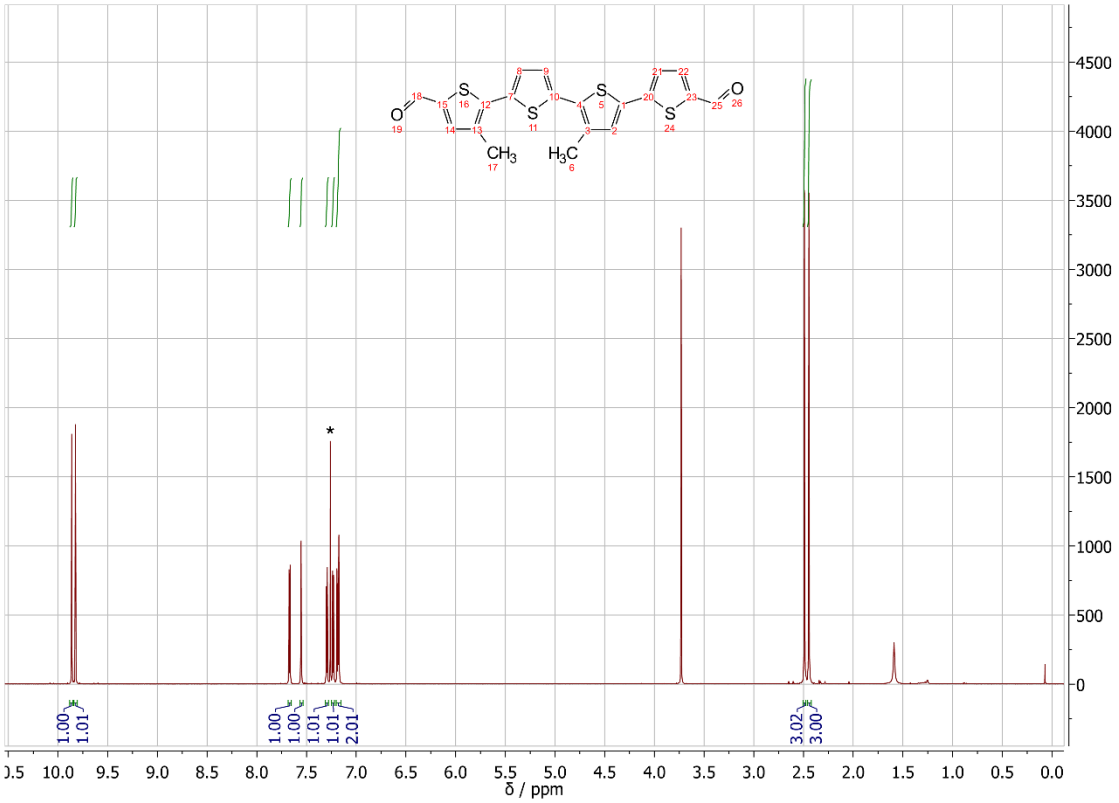
1.00
1.01
1.00
1.00
1.01
1.01
2.01
3.02
3.00
δ / ppm

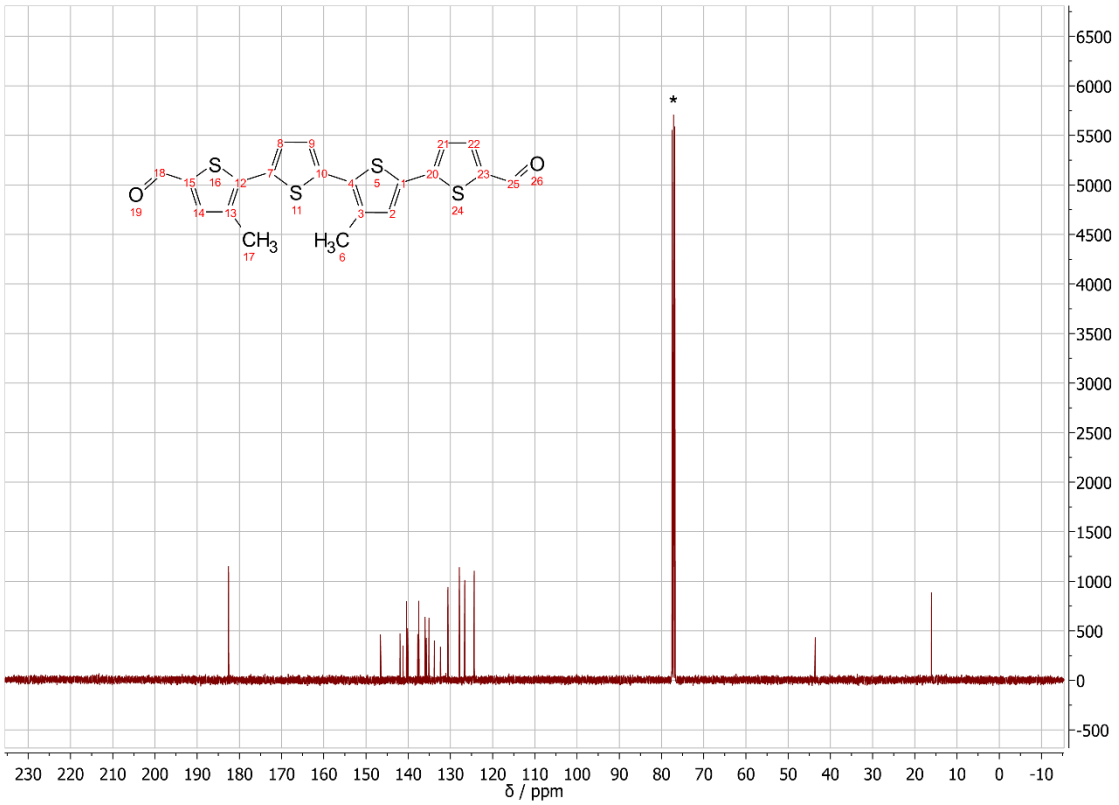
δ / ppm

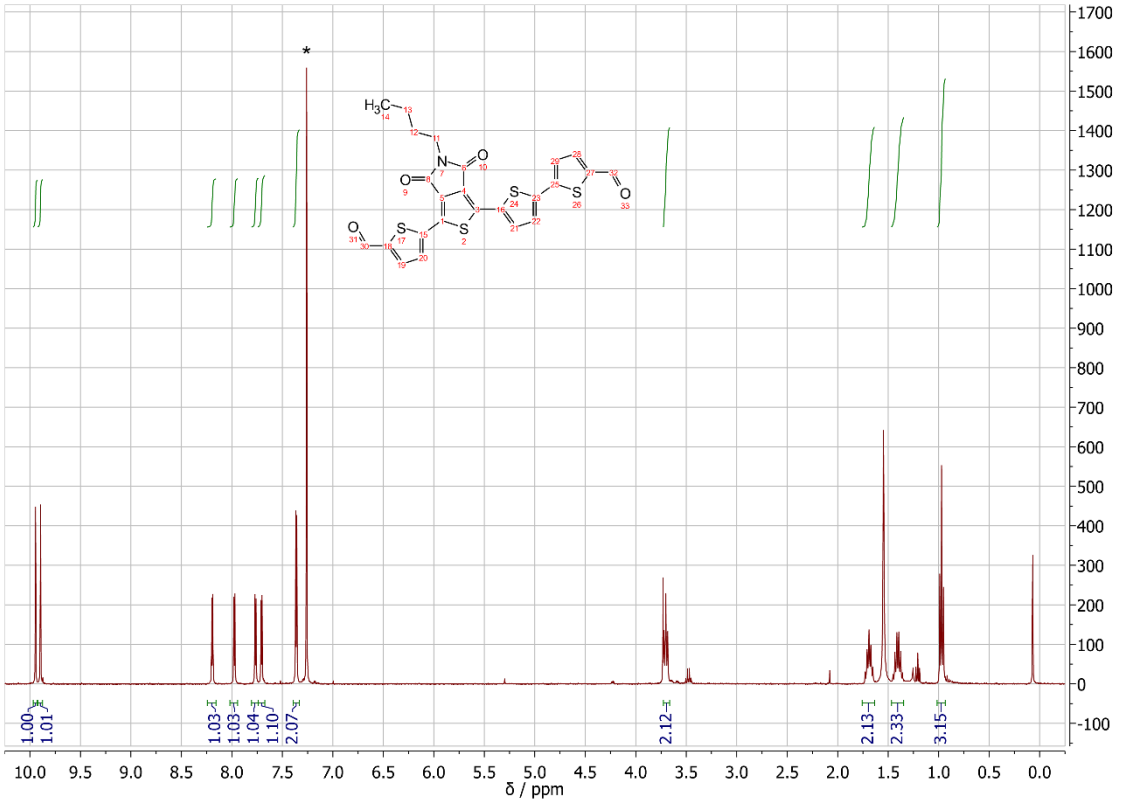
1.00
1.01
1.03
1.03
1.04
1.10
2.07
2.12
2.13
2.33
3.15
δ / ppm

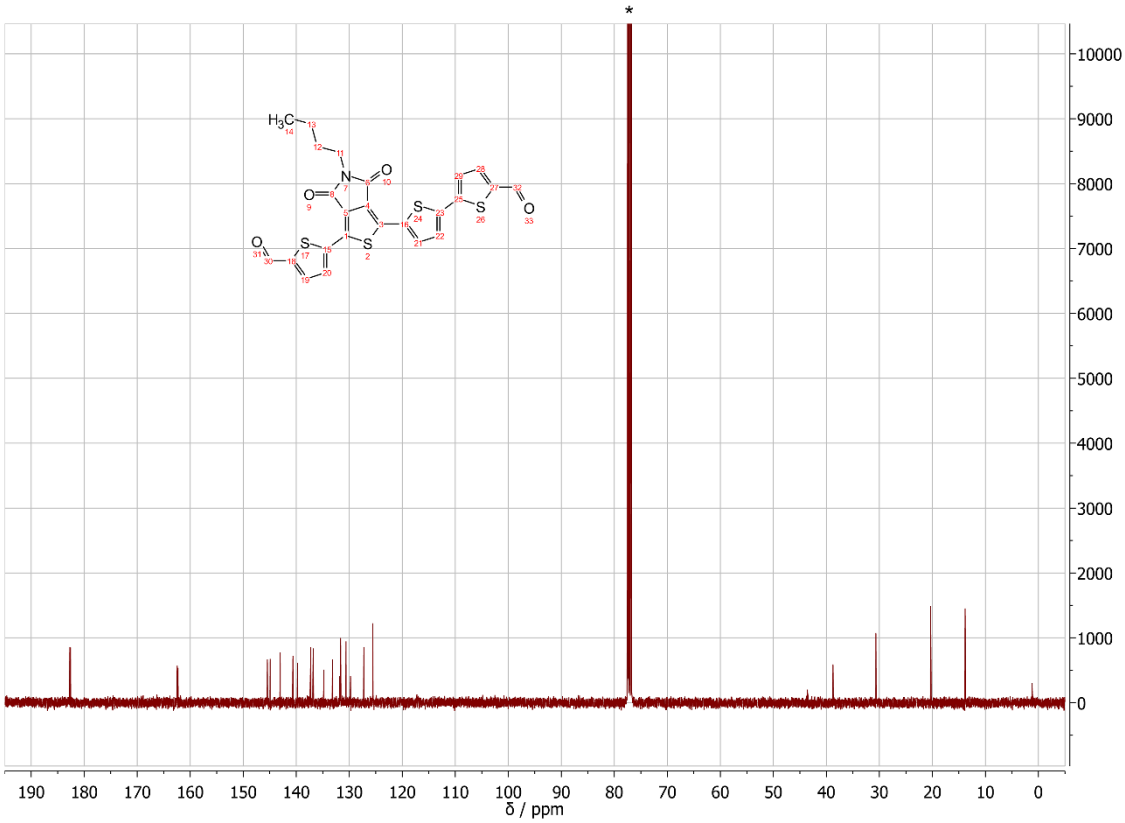
δ / ppm

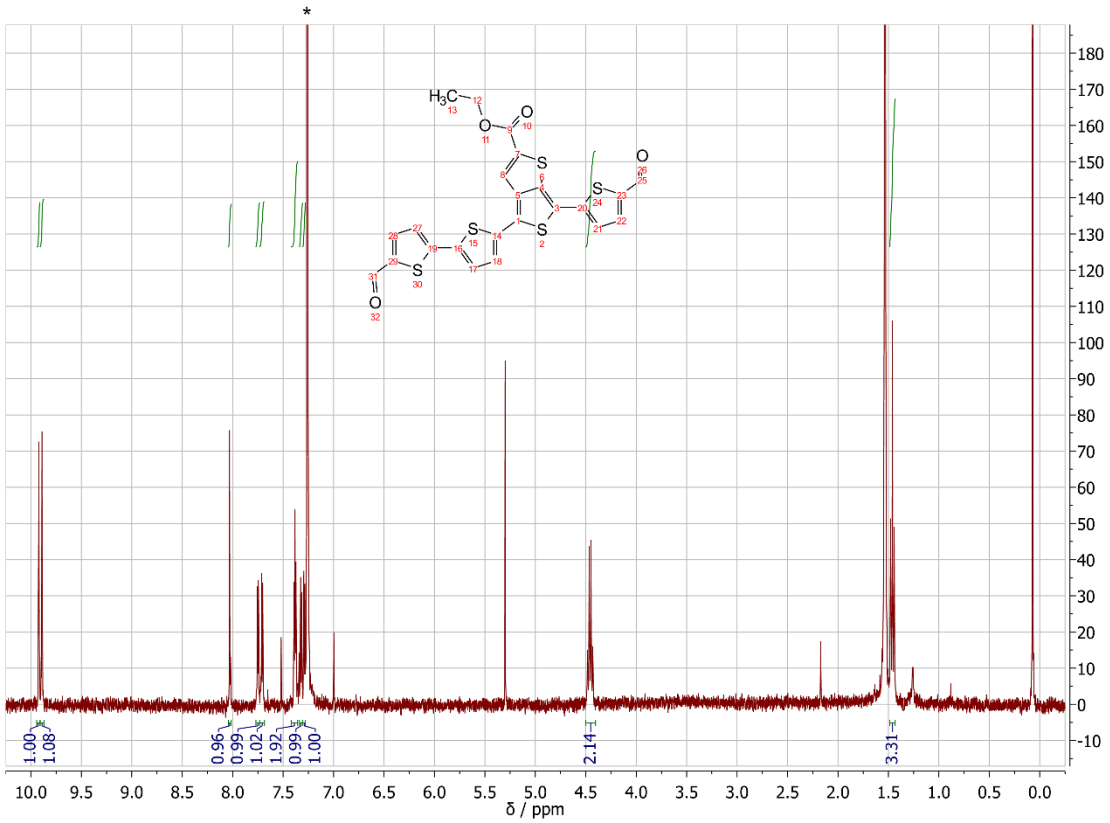
*
1.00
1.08
0.96
0.99
1.02
1.92
0.99
1.00
2.14
3.31
δ / ppm

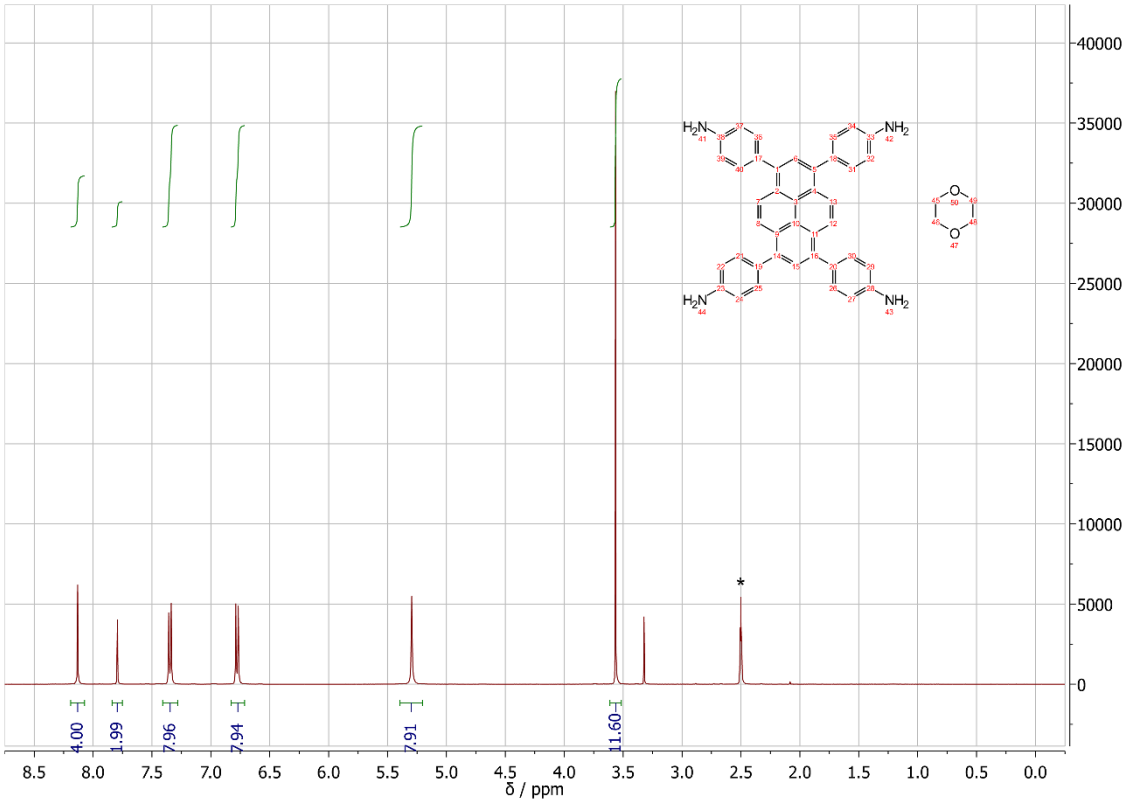
4.00
1.99
7.96
7.94
7.91
11.60
δ / ppm

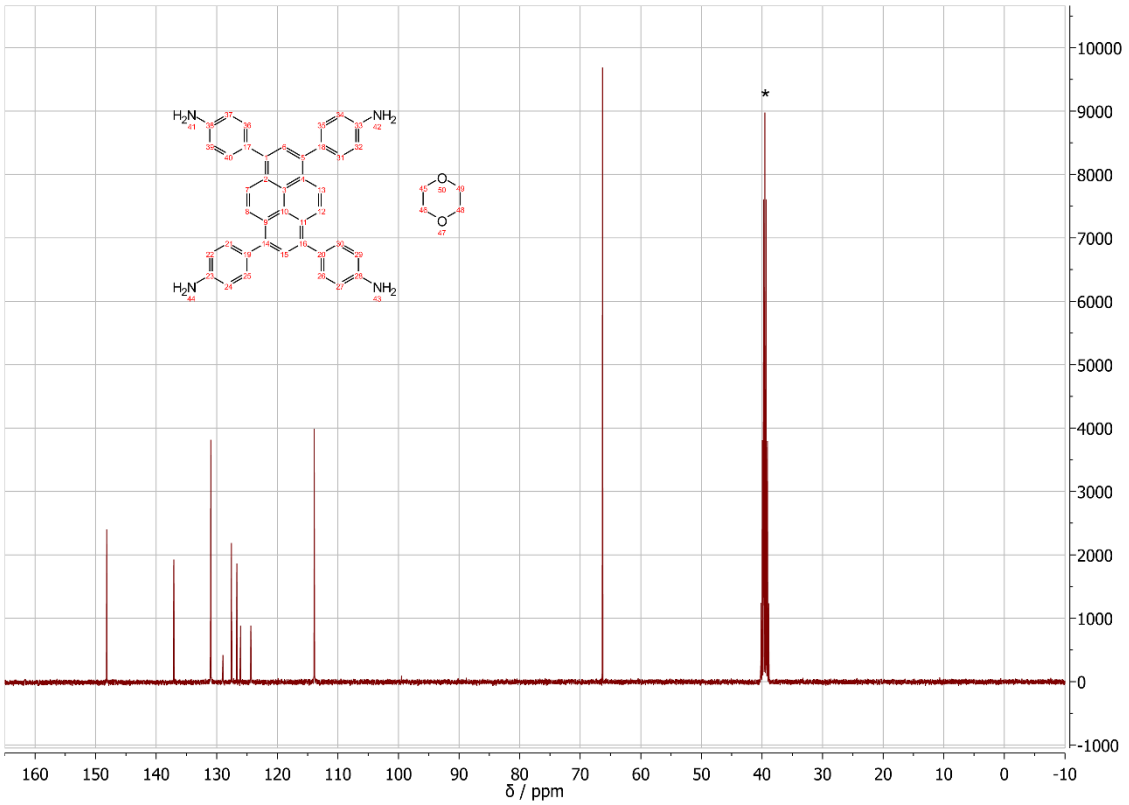
δ / ppm

5.5.5 High Resolution Mass Spectroscopy

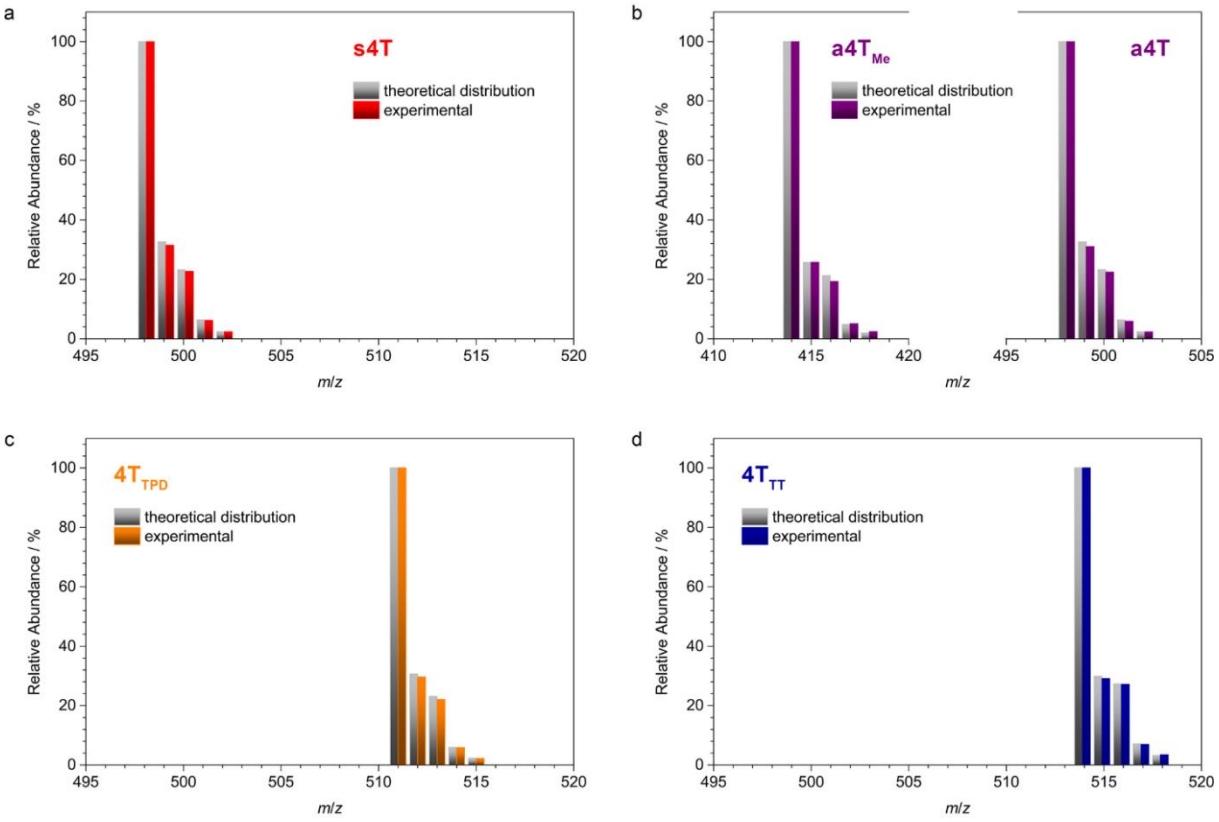

Figure 5.5: Comparison between the theoretical (grey) and the experimental (colored) HR-EI-MS patterns of the four quaterthiophene-derived building blocks. The patterns correspond to the respective singly positively charged molecules (M^+).

5.5.6 IR Spectroscopy

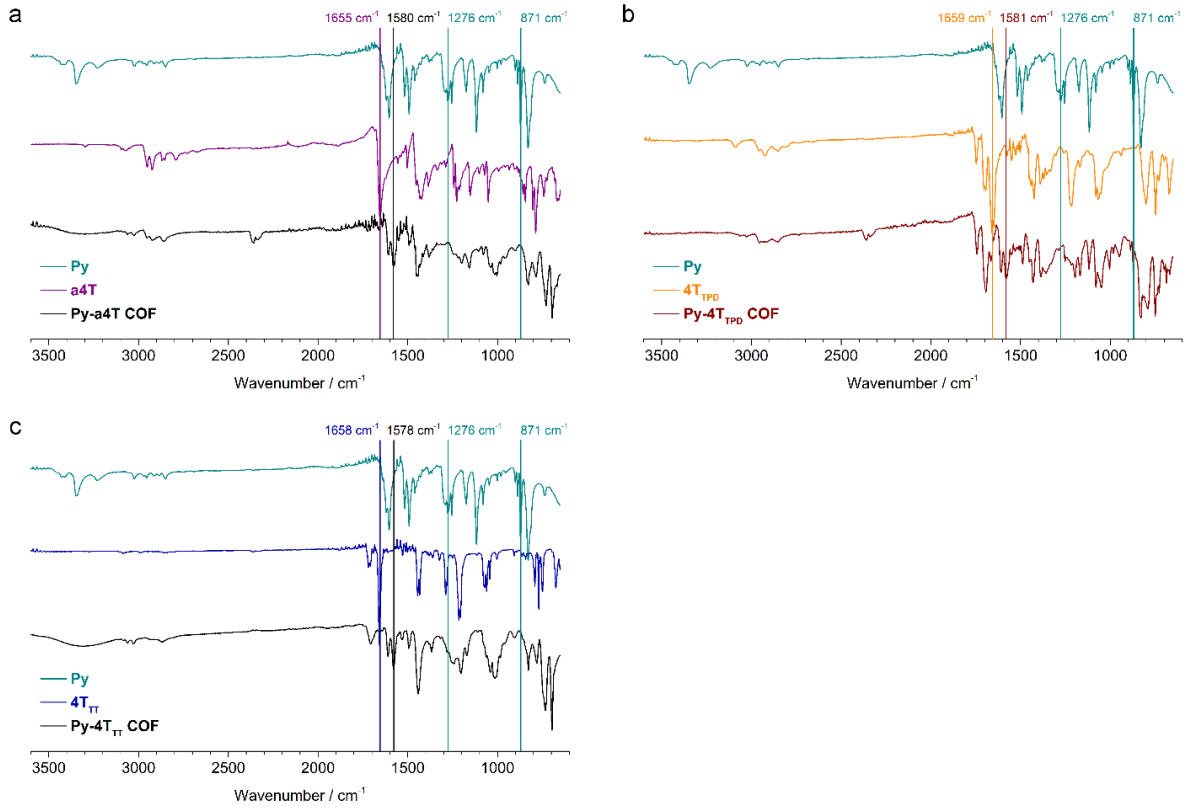

Figure 5.6: IR spectra of the building blocks and the quaterthiophene-based COFs.

Table 5.1: Assignments of the IR signals.

	Wavenumber / cm^{-1}	Vibration mode
Py	1276	C-N stretching mode
	871	N-H wag vibration
a4T	1655	C=O stretching vibration
Py-a4T COF	1580	C=N stretching mode
$4T_{TPD}$	1659	C=O stretching vibration
Py-$4T_{TPD}$ COF	1581	C=N stretching mode
$4T_{TT}$	1658	C=O stretching vibration
Py-$4T_{TT}$ COF	1578	C=N stretching mode

5.5.7 UV-vis Spectroscopy

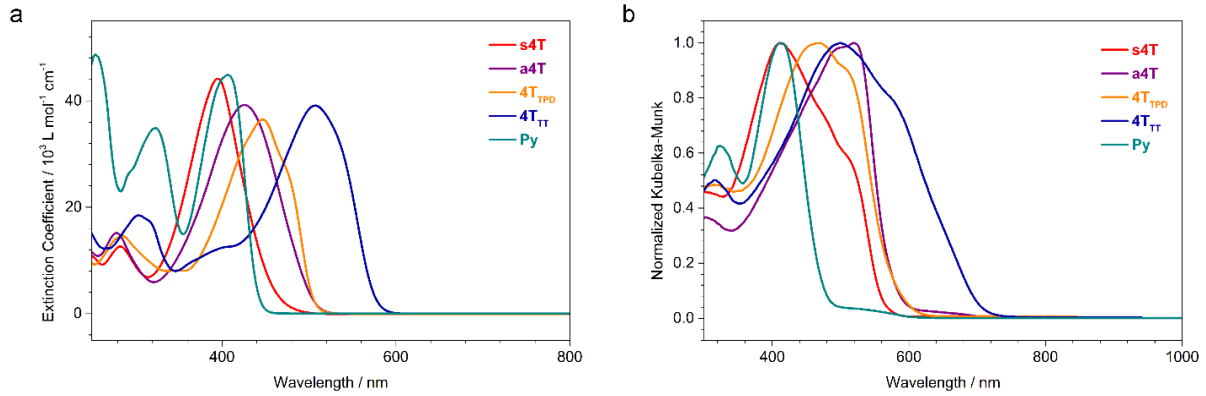

Figure 5.7: Comparison of the absorption spectra of the COF building blocks. (a) Transmission absorption spectra measured for 50 µM solutions in $CHCl_3$ (s4T, a4T, $4T_{TPD}$, $4T_{TT}$) or 1,4-dioxane (Py). (b) Corresponding diffuse reflectance spectra measured for the respective powders dispersed in $BaSO_4$.

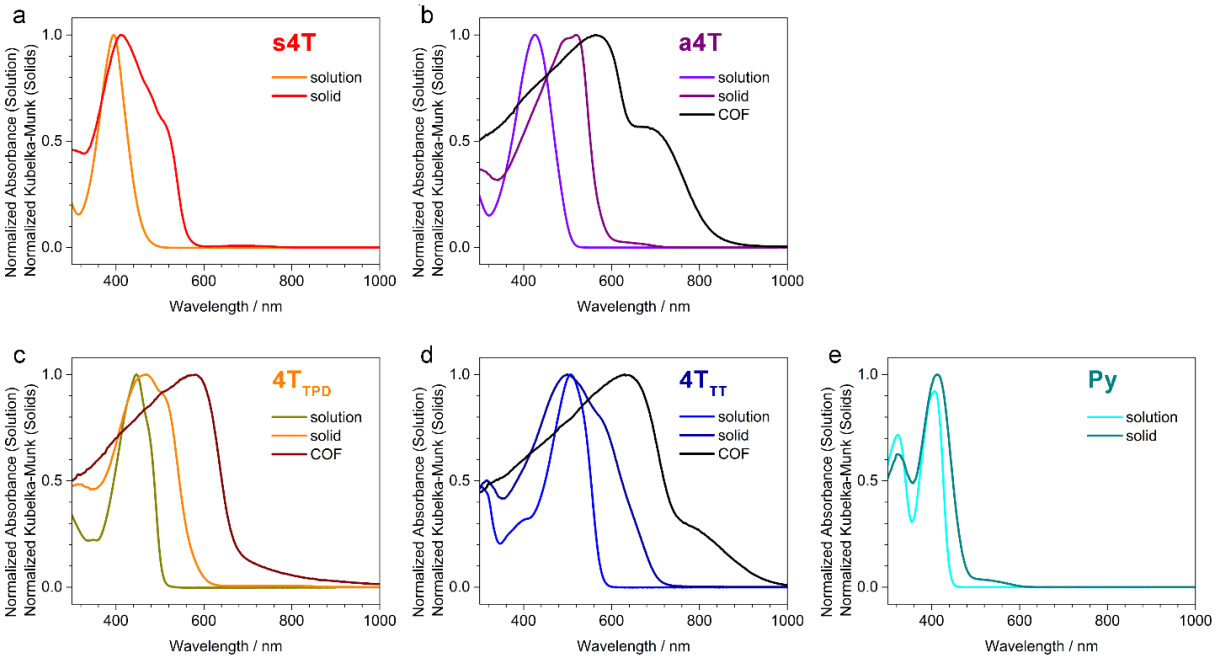

Figure 5.8: Comparison of the absorption and diffuse reflectance spectra of the building blocks in solution, as a solid, and (for a4T, $4T_{TPD}$, $4T_{TT}$) incorporated into the pyrene-linked COF.

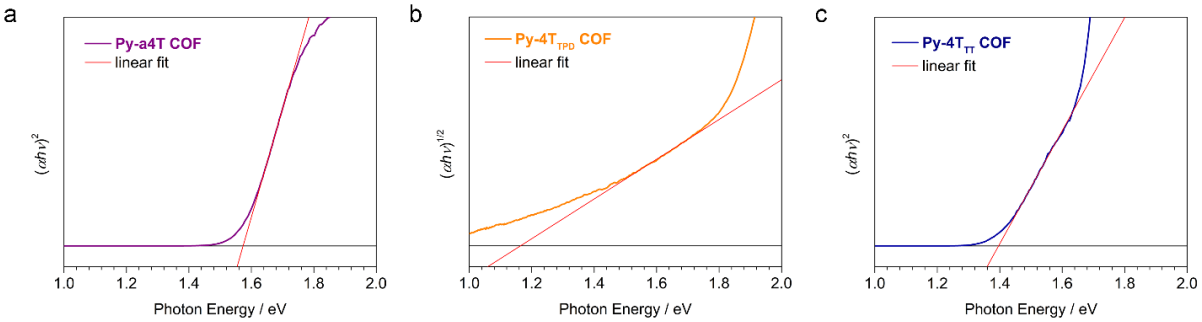

Figure 5.9: Tauc plots of the 4T-based COFs suggesting direct (Py-a4T and Py-4T$_{TT}$ COFs) and indirect optical bandgaps (Py-4T$_{TPD}$ COF).

5.5.8 Fluorescence Spectroscopy

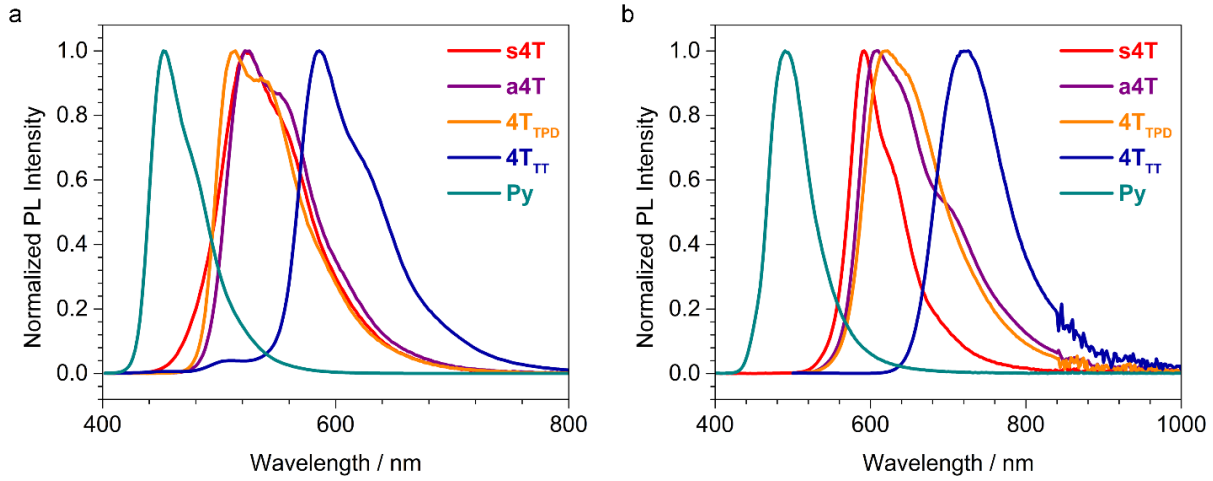

Figure 5.10: PL spectra of the COF building blocks measured (a) as 50 µM solutions in $CHCl_3$ (s4T, a4T, $4T_{TPD}$, $4T_{TT}$) or 1,4-dioxane (Py), and (b) as solids. λ_{exc} = 378 nm.

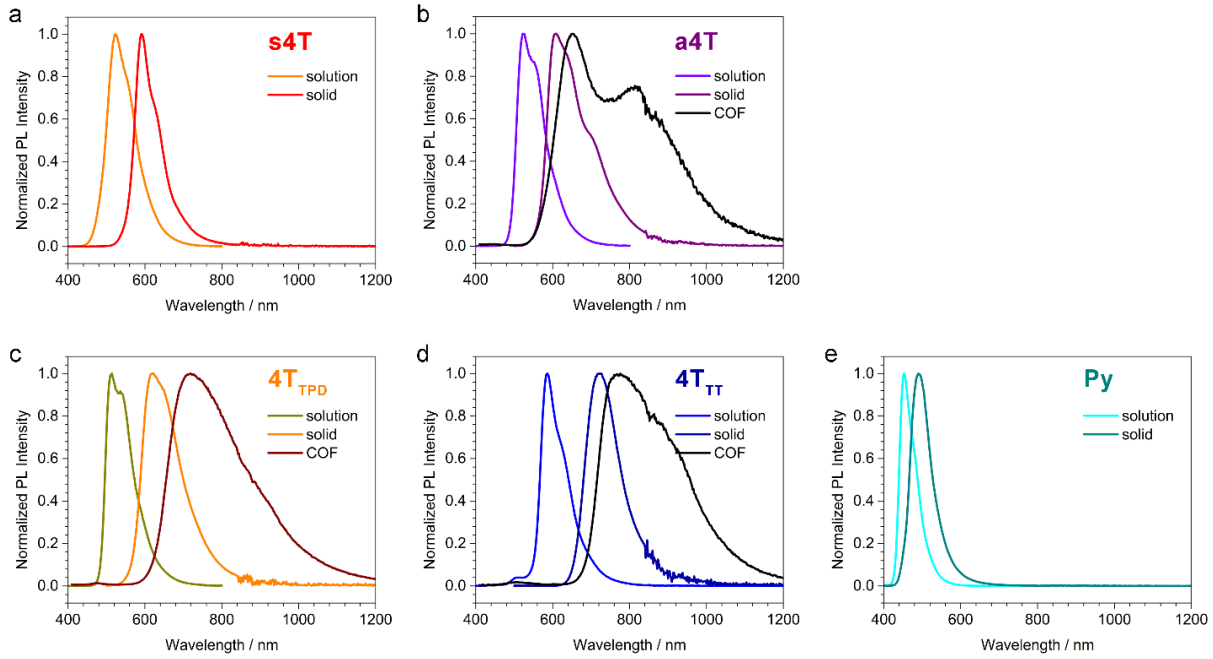

Figure 5.11: Comparison of the PL spectra of the building blocks in solution, as a solid, and (for a4T, $4T_{TPD}$, $4T_{TT}$) incorporated into the pyrene-linked COF. λ_{exc} = 378 nm.

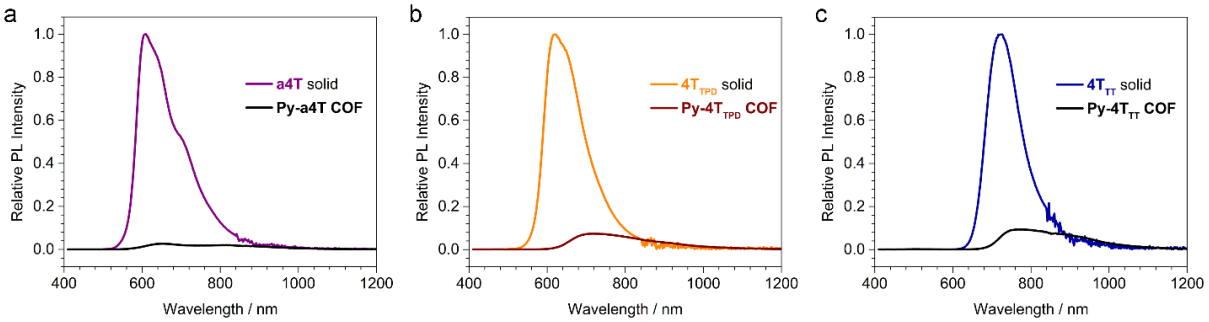

Figure 5.12: Comparison of the relative PL intensities of the 4T building blocks and the corresponding COFs.

5.5.9 Time-Correlated Single Photon Counting

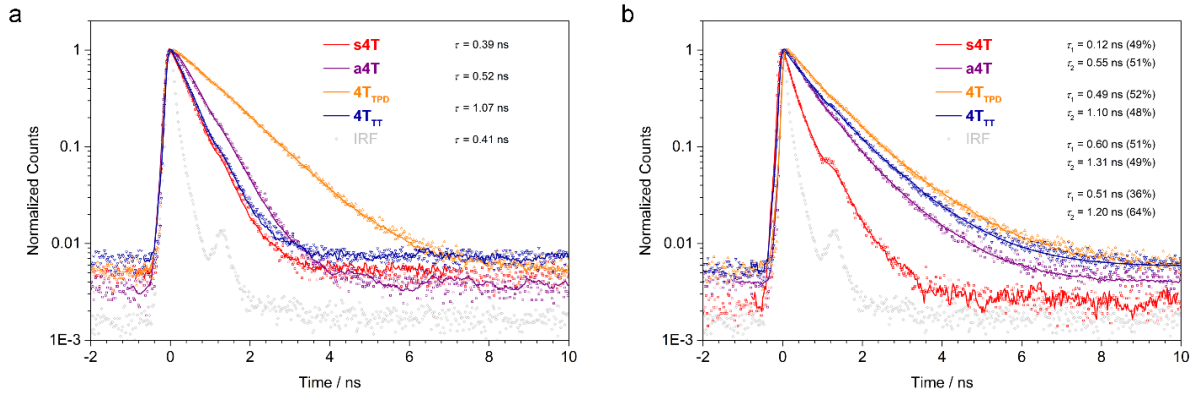

Figure 5.13: TCSPC traces of the building blocks (a) in 50 µM $CHCl_3$ solution and (b) as solids, recorded at their respective emission maximum. λ_{exc} = 378 nm. The lifetimes were obtained from exponential deconvolution fits (solid lines).

Table 5.2: PL decay times of the building blocks measured in 50 µM $CHCl_3$ solution.

		τ / ns	fractional intensity / %
s4T	τ	0.39	100
a4T	τ	0.52	100
$4T_{TPD}$	τ	1.07	100
$4T_{TT}$	τ	0.41	100

Table 5.3: PL decay times of the building blocks measured as solids.

		τ / ns	fractional intensity / %
s4T	τ_1	0.5512	51
	τ_2	0.12	49
a4T	τ_1	1.10	48
	τ_2	0.49	52
$4T_{TPD}$	τ_1	1.31	49
	τ_2	0.60	51
$4T_{TT}$	τ_1	1.20	64
	τ_2	0.51	36

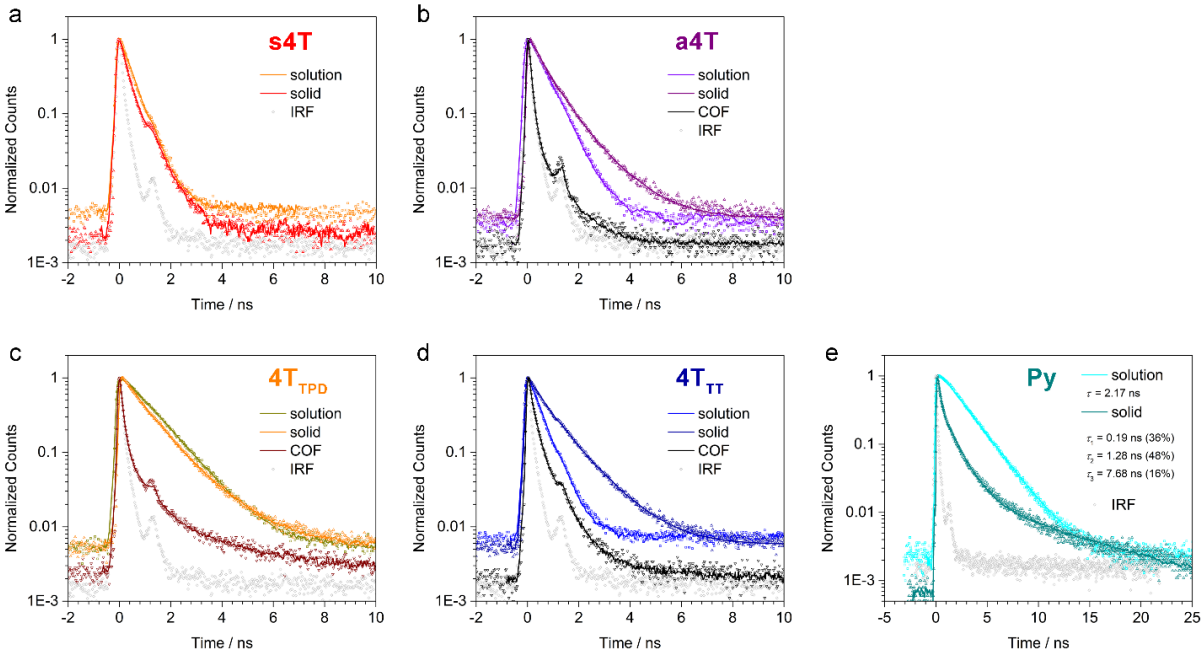

Figure 5.14: Comparison of the TCSPC traces of the building blocks in solution, as a solid, and (for a4T, $4T_{TPD}$, $4T_{TT}$) incorporated into the pyrene-linked COF.

5.5.10 Transmission Electron Microscopy

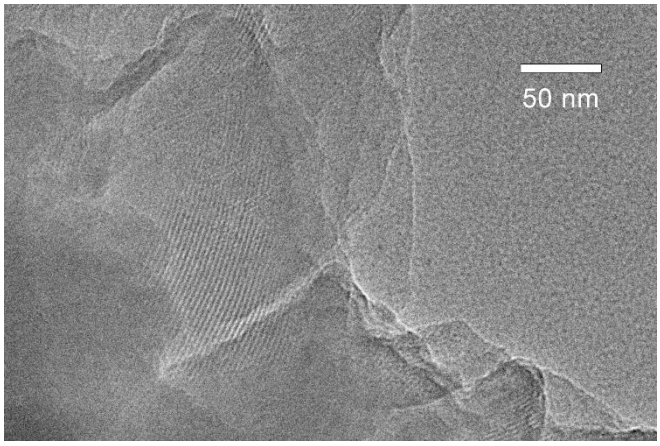

Figure 5.15: High-resolution TEM image of the Py-a4T COF. The parallel-aligned pores are visible for a number of individual COF crystallites (visibility depends on crystal orientation relative to the electron beam).

5.5.11 X-Ray Diffraction of Py-a4T$_{Me}$ COF

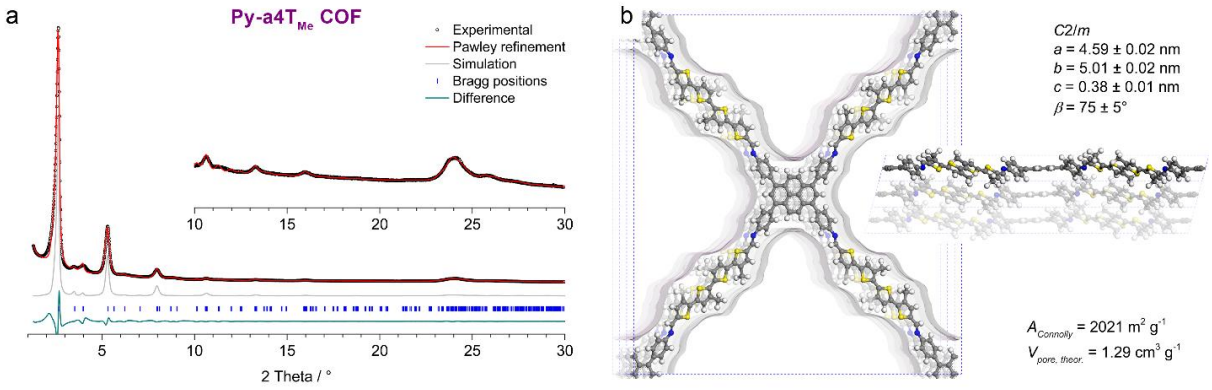

Figure 5.16: (a) Experimental PXRD pattern (black dots) of the short-chain Py-a4T$_{Me}$ COF. Pawley refinement (red line) in the space group *C*2/*m* provides an excellent fit to the experimental data. Inset, magnified view of the 2θ > 10° region. The simulated PXRD pattern (grey lines) based on the structure model shown in (b) agrees very well with the experimental and refined patterns of the framework. For the pattern simulation, the methyl groups were treated as a superposition of both possible orientations with 50% occupancy. The minimal differences in the peak intensities might stem from slight differences between the simulated and the actual COF structure. (b) The Py-a4T$_{Me}$ COF unit cell with the viewing direction normal to the *a*-*b* plane (left) and along *b* (right), and the Connolly surface calculated for a nitrogen-sized probe molecule

5.5.12 Nitrogen Sorption of Py-a4T$_{Me}$ COF

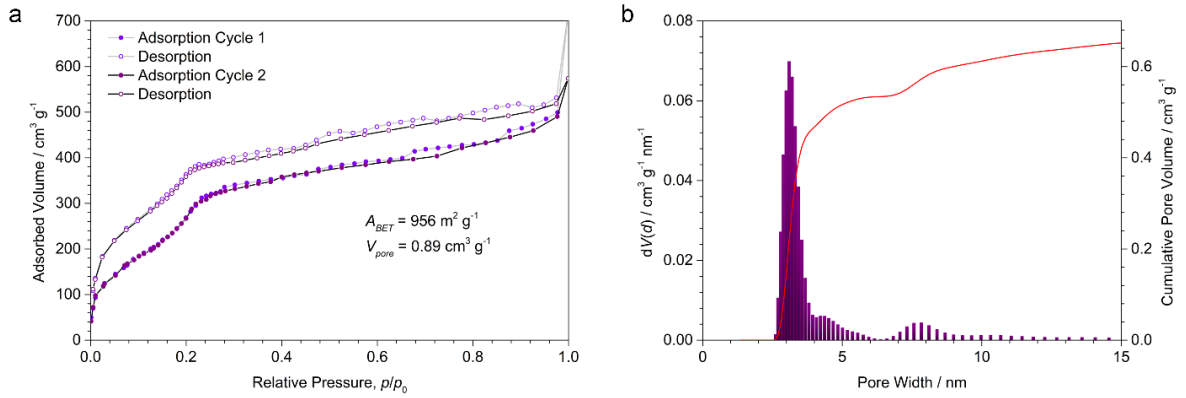

Figure 5.17: (a) Nitrogen sorption isotherms recorded at 77 K. Two adsorption-desorption cycles were recorded using the same sample to test the stability of the framework. (b) QSDFT calculation using the adsorption branch yields a narrow pore size distribution with a maximum at 3.1 nm, in excellent agreement with the pore diagonal of 3.06 nm in the Py-a4T$_{Me}$ COF structure.

The Py-a4T$_{Me}$ COF is porous with a BET surface close to 1000 m^2 g^{-1}, and the maximum of the pore size distribution agrees very well with the pore diagonal when taking into account the methyl groups.

Due to the length and inherent flexibility of the 4T based building blocks, the frameworks described in this study are quite fragile. Thus, the COFs bearing longer alkyl chains have a tendency to deform as a response to the adsorption of probe molecules during the nitrogen sorption experiments, leading to inconsistent isotherms. The shorter chains of the Py-a4T$_{Me}$ COF, however, seem to reduce the forces onto the COF walls during the sorption cycle and therefore this COF yields consistent and reproducible sorption results (Figure 5.17).

5.5.13 References

[1] Henderson, P. T.; Collard, D. M., Thiophene:alkylthiophene copolymers from substituted dialkyloligothiophenes. *Chem. Mater.* **1995,** *7* (10), 1879-1889.

[2] Yang, J.; Liu, S.; Zheng, J.-F.; Zhou, J., Room-Temperature Suzuki–Miyaura Coupling of Heteroaryl Chlorides and Tosylates. *Eur. J. Org. Chem.* **2012,** *2012* (31), 6248-6259.

[3] Grolleau, J.; Frère, P.; Gohier, F., Clean and Efficient Iodination of Thiophene Derivatives. *Synthesis* **2015,** *24* (47), 3901-3906.

[4] Song, Y.-T.; Lin, P.-H.; Liu, C.-Y., Copper-Catalyzed Direct C□H Arylation of Thieno[3,4-c]pyrrole-4,6-dione (TPD): Toward Efficient and Low-Cost Synthesis of π-Functional Small Molecules. *Adv. Synth. Catal.* **2014,** *356* (18), 3761-3768.

[5] Najari, A.; Beaupré, S.; Berrouard, P.; Zou, Y.; Pouliot, J.-R.; Lepage-Pérusse, C.; Leclerc, M., Synthesis and Characterization of New Thieno[3,4-c]pyrrole-4,6-dione Derivatives for Photovoltaic Applications. *Adv. Funct. Mater.* **2011,** *21* (4), 718-728.

[6] Nielsen, C. B.; Bjørnholm, T., New Regiosymmetrical Dioxopyrrolo- and Dihydropyrrolo-Functionalized Polythiophenes. *Org. Lett.* **2004,** *6* (19), 3381-3384.

[7] Baek, M.-J.; Lee, S.-H.; Zong, K.; Lee, Y.-S., Low band gap conjugated polymers consisting of alternating dodecyl thieno[3,4-b]thiophene-2-carboxylate and one or two thiophene rings: Synthesis and photovoltaic property. *Synth. Met.* **2010,** *160* (11), 1197-1203.

[8] Carsten, B.; Szarko, J. M.; Son, H. J.; Wang, W.; Lu, L.; He, F.; Rolczynski, B. S.; Lou, S. J.; Chen, L. X.; Yu, L., Examining the Effect of the Dipole Moment on Charge Separation in Donor–Acceptor Polymers for Organic Photovoltaic Applications. *J. Am. Chem. Soc.* **2011,** *133* (50), 20468-20475.

[9] Jin, S.; Sakurai, T.; Kowalczyk, T.; Dalapati, S.; Xu, F.; Wei, H.; Chen, X.; Gao, J.; Seki, S.; Irle, S.; Jiang, D., Two-Dimensional Tetrathiafulvalene Covalent Organic Frameworks: Towards Latticed Conductive Organic Salts. *Chem. - Eur. J.* **2014,** *20* (45), 14608-14613.

[10] Auras, F.; Ascherl, L.; Hakimioun, A. H.; Margraf, J. T.; Hanusch, F. C.; Reuter, S.; Bessinger, D.; Döblinger, M.; Hettstedt, C.; Karaghiosoff, K.; Herbert, S.; Knochel, P.; Clark, T.; Bein, T., Synchronized Offset Stacking: A Concept for Growing Large-Domain and Highly Crystalline 2D Covalent Organic Frameworks. *J. Am. Chem. Soc.* **2016,** *138* (51), 16703-16710.

6 Extension of Oligothiophene Backbones in Covalent Organic Frameworks

This chapter is based on the following manuscript:

Niklas Keller,[‡] Derya Bessinger,[‡] Andreas C. Jakowetz, Markus Döblinger, Thomas Bein, *to be submitted*.

[‡] These authors contributed equally.

The intriguing properties of oligothiophenes are of special interest for applications in organic optoelectronics. In this work, different types of oligothiophenes were embedded in the solid matrix defined by two-dimensional covalent organic frameworks (COFs). Due to challenges such as solubility of the molecular oligothiophene building blocks, modifications in form of alkyl chains were attached to the oligothiophene backbones. These modifications need to be carefully designed to avoid stability issues of the COFs in the presence of guest molecules. Herein, we developed a series of oligothiophene COFs regarding two aspects that need to be considered when designing these building blocks. Both the length of the alkyl chains attached to the thiophene bridges and the number of thiophene units coupled to form the oligothiophene building block were varied and their impact on the COFs' properties was examined. Hence, thiophene chains of three different lengths terminated with aldehyde groups were introduced into frameworks connected by co-condensation with 1,3,6,8-tetrakis(4-aminophenyl)pyrene (Py), leading to Py-2T, Py-4T and Py-6T COFs. For the quaterthiophene series, the side groups connected to the first and third thiophene ring were varied from hydrogen (4T) to methyl ($4T_{Me}$), ethyl ($4T_{Et}$) and butyl chains ($4T_{Bu}$). In combination with Py, all six different oligothiophenes led to covalent organic frameworks with pseudoquadratic pores. Our studies reveal a correlation between the nature of the inserted alkyl chains, the length of the oligothiophene bridge as well as the excited state dynamics of the COFs with increased lifetimes from 4.06 ns, 5.72 ns to 6.80 ns for Py-2T, Py-4T and Py-$6T_{Et}$, respectively. Further, crystalline COF films for Py-4T, Py-$4T_{Me}$ and Py-$4T_{Bu}$ need to be synthesized and investigations of the COF films can elucidate

processes involved in these frameworks which could lead to interesting optical characteristics and help to design functional oligothiophene-bridged COFs for optoelectronic applications.

6.1 Introduction

The potential of reticular chemistry becomes evident for covalent organic frameworks (COFs), a relatively new class of material. Building blocks (knots or bridges) are linked by slightly reversible condensation reactions to form 2D sheets that stack in the 3rd dimension leading to ordered, porous and light-weight material. The stacked sheets create columns of aggregated knots and bridges of the adjacent layers enabling electronic overlap of the COF layers that can allow charge carrier mobility along the stacks. The vast diversity of organic building blocks paves the way to tailor-made synthesis of molecular linkers that are designed specifically to meet the required properties of an application. But tailoring the properties of COFs is often still based on trial and error and becomes even more challenging when going beyond porous properties of the frameworks that are for example applicable for gas storage or separation,[1-3] as well as for insertion of guest molecules,[4-7] control of π-density,[8] and allowing access for postsynthetic treatments[9-10] or catalysis.[11-12] Therefore, it is highly desirable to obtain basic knowledge about critical COF construction rules. Using a well-defined and stable framework as a starting point and incorporating gradual changes into it, is expected to allow for valuable insights leading to general design rules for linker−structure−property relationships. By adjusting one structural feature at a time, the effect can be directly attributed to this modification. For example, the extension of building units to form larger pores is a straightforward example for a simple but well-developed design principle.[13-14] However, transferring one approach to other properties or a different system, i.e. proposing a comprehensive linker−structure−property relationship, has been challenging and often fails going beyond the specific system under study. The conductivity for sp^2-carbon conjugated bonds had been predicted to exceed COFs connected by less conjugated linkages, but the fully sp^2-carbon conjugated framework reported by the group of Jiang was identified as an insulator.[15] This example illustrates the general challenges still appearing in the field of COFs.

Boosting the electrical conductivity of COFs has been explored via the incorporation of thiophene, bithiophene and thienothiophene moieties, known as components of prominent molecular semiconductors in organic optoelectronics.[16] Another approach to utilize the conducting properties of thiophenes in this context is the creation of a host−guest system with 3,4-ethylenedioxythiophene (EDOT) insertion into the COF pores. Upon polymerization, PEDOT strands are formed throughout the pores forming electron-conducting pathways.[17-18] With the perspective to achieve high intrinsic charge carrier mobilities of both electrons and

holes, thiophene bridges in COFs were elongated to quaterthiophene-derivatives and successfully incorporated into COFs.[19]

Here, we investigate how the optoelectronic properties of oligothiophene-based COFs can be tuned by systematically modifying the nature of the oligothiophene building blocks. A series of bithiophene, quaterthiophene and sexithiophene building blocks was chosen to represent a comprehensive scope of oligothiophenes while still maintaining efficient handling and successful condensation to build the corresponding COFs. Both the impact of the number of condensed thiophene rings and the influence of attached alkyl chains of varying length on structural and optical properties was examined. Compared to previous work from our group,[19] the system was simplified to only the oligothiophene backbone without sterically demanding donor-acceptor moieties implemented but with attached alkyl chains due to the high crystallinity of the non-modified oligothiophene-based COFs. The series of building blocks also provided the same symmetry of the resulting COF structure for all linker molecules. Therefore, measurable deviations of the structure can be directly compared to the other frameworks in the series. The alkyl chains were introduced to shed light on the impact and interplay of their sterically demanding character regarding the assembly of the π-stacked 2D COFs, but also guiding functionalizations directing the adjacent layers on top of each other. Furthermore, the alkyl groups could be envisioned to serve as a facilitated tunneling pathway for incorporated guest molecules such as phenyl-C_{61}-butyric acid methyl ester (PCBM) to promote stronger electronic overlap between the framework and PCBM.

6.2 Results and Discussion

While pyrene linkers have been extensively studied as the tetragonal node in 2D COFs, oligothiophenes (nT) have only been applied in few reports as linear building blocks with a length of up to n = 4, denoted as 4T.[16, 19] Herein, we extend this concept to sexithiophenes (n = 6) and complete our series with 2T and 4T bridges, all containing dialdehyde termini. Upon condensation with the 1,3,6,8-tetrakis(4-aminophenyl)pyrene (Py) node, the resulting COFs form pseudoquadratic pores. In Figure 6.1, the scope of this work is schematically illustrated with the molecular building blocks and the chemical structures of the oligothiophene-bridged COFs.

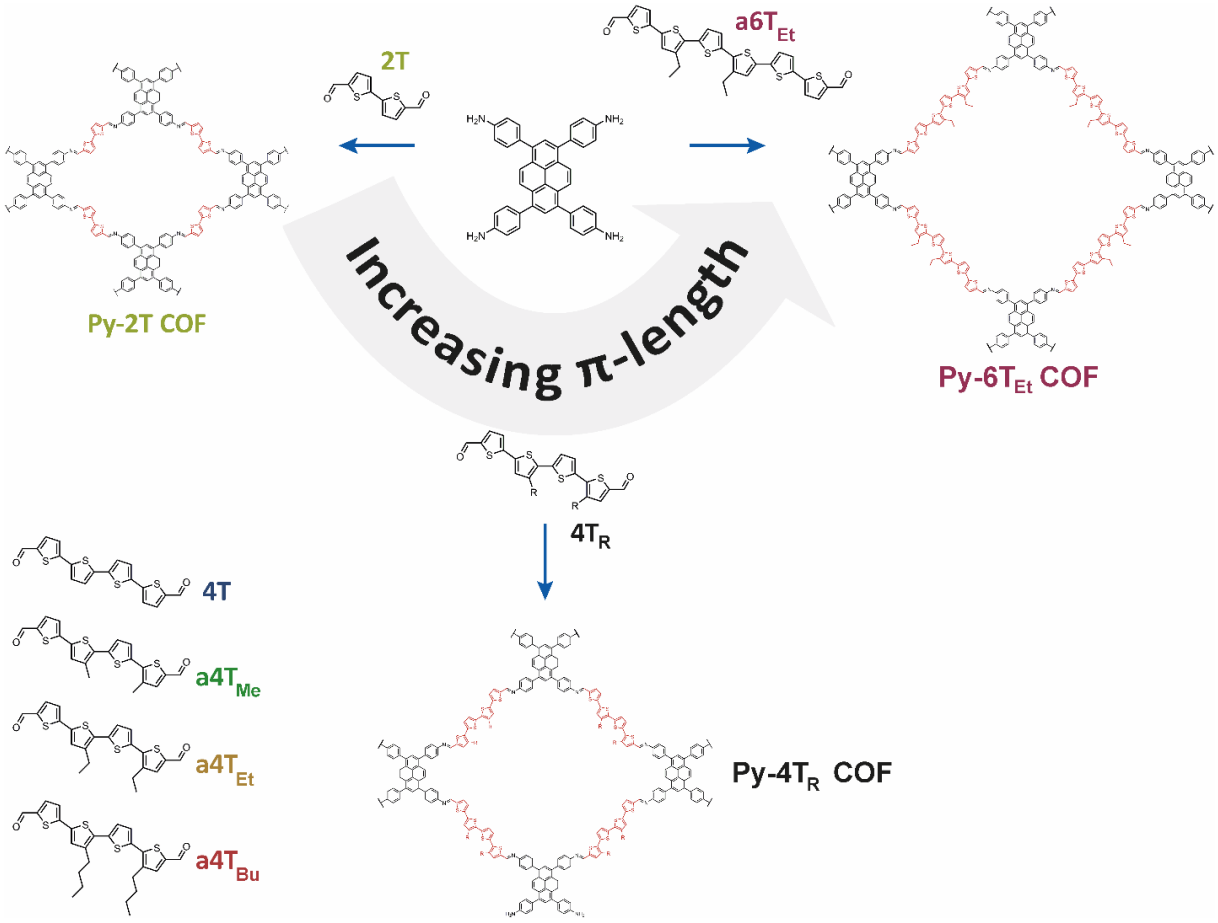

Figure 6.1: Overview of the oligothiophene-based COF series. Thiophene chains of three different lengths terminated with aldehyde groups were introduced into frameworks connected by co-condensation with 1,3,6,8-tetrakis(4-aminophenyl)pyrene (Py), leading to Py-2T, Py-4T and Py-6T COFs. For the quaterthiophene series, the side groups connected to the first and third thiophene ring were varied from hydrogen (4T) to methyl ($4T_{Me}$), ethyl ($4T_{Et}$) and butyl chains ($4T_{Bu}$). In combination with Py, all six different oligothiophenes led to covalent organic frameworks with pseudoquadratic pores.

The oligothiophenes were synthesized by following the asymmetric functionalization approach reported in literature[19] to allow for closely packed oligothiophene bridging units. Incorporated

into the crystalline framework, the steric repulsion of the alkyl chains is minimized by an alternating stacking behavior analogous to the a4T$_{Bu}$ COF (Figure 6.2). The 4T building blocks bear alkyl chains of methyl (4T$_{Me}$), ethyl (4T$_{Et}$) and butyl (4T$_{Bu}$) on the first and third thiophene, whereas the 6T linker was functionalized with ethyl chains on the second and fourth thiophene unit. Since solubility of the extended oligothiophenes is drastically lowered for longer oligomers, the 6T building block was not synthesized as a bare backbone. Studying the impact of increasing π-length is realized by comparing the 2T-, 4T- and 6T$_{Et}$-containing pyrene COFs (Figure 6.1).

The imine-linked oligothiophene-bridged COFs were synthesized via an acid-catalyzed solvothermal condensation with the pyrene node (for more details on the synthesis procedures see appendix).

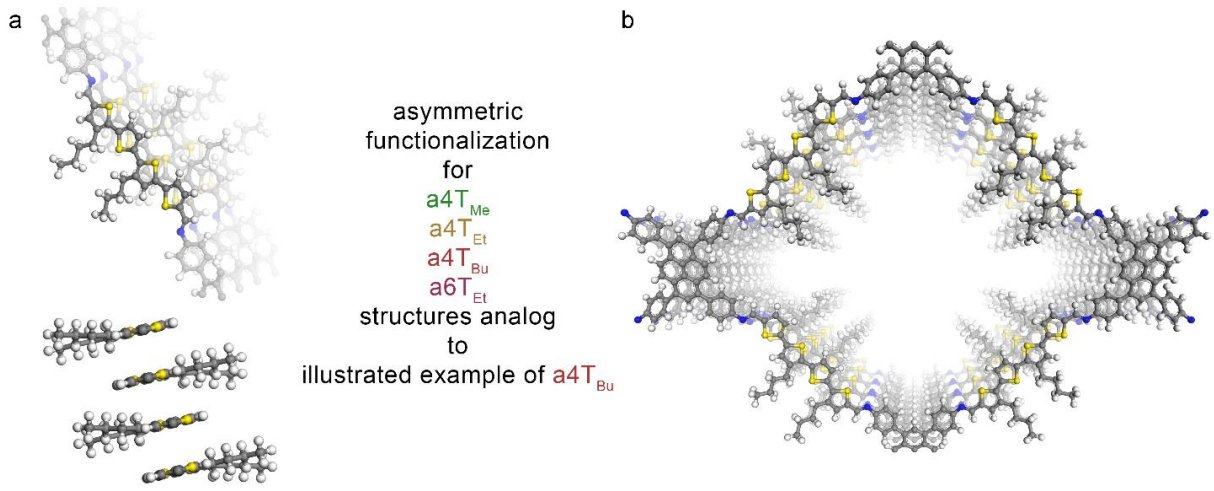

Figure 6.2: Exemplary illustration of asymmetric functionalization of the oligothiophenes with alkyl chains (model structure shown for the Py-4T$_{Bu}$ COF). The COFs with the listed oligothiophenes feature structures similar to the depicted structure. In the structural refinement analysis, the alkyl chains of the listed oligothiophene building blocks were treated as a superposition of both possible orientations with 50% occupancy each.

Powder X-ray diffraction patterns confirm the successful COF synthesis. The sharp reflections even in the higher-order region demonstrate the formation of highly crystalline structures upon condensation. Pawley refinement of the simulated COF structures revealed excellent fits with the experimental data. In order to simulate the oligothiophenes bearing alkyl chains in the space group *C*2/*m*, the alkyl chains were estimated to occupy both possible orientations with 50% probability each (Figure 6.3). Comparing the different numbers of connected thiophene units (2T, 4T and 6T), it is evident that the COF unit cells increase in directions *a* and *b* by about 1 nm for each two more thiophenes (see Chapter 6.5.5 for details). These findings correspond directly to the added bithiophene moieties (sized 0.75 nm) in each step. For each unit cell, two

bithiophene moieties are additionally introduced in the diagonal, leading to an increase of 1.5 nm in the diagonal and 1.0 nm in *a* and *b*. The impact of the alkyl chain length on the structural features is not as distinct. The lattice parameters *a* and *b* decrease slightly when introducing a methyl group and then increase when incorporating longer alkyl chains up to butyl groups. The stacking distance is simulated to be 0.382 nm for the Py-4T, Py-4T$_{Me}$ and Py-4T$_{Et}$ COFs and 0.388 nm for the Py-4T$_{Bu}$ COF, which is in good agreement with the experimental values for the complete series of thiophene-based COFs (see Table 6.1 in appendix for further details). These results show that direct (reticular) adjustment of the pore size while maintaining geometry and topology is possible by adding thiophene units to the chain, while additionally giving the possibility to slightly tune the stacking distance between the COF layers.

The ordered structure of the synthesized COFs was confirmed with transmission electron microscopy (TEM). Well-ordered crystalline domains are observed, with pore channels visible. The corresponding electron diffraction patterns show several reflection rings indicating the highly crystalline nature of the frameworks (see appendix).

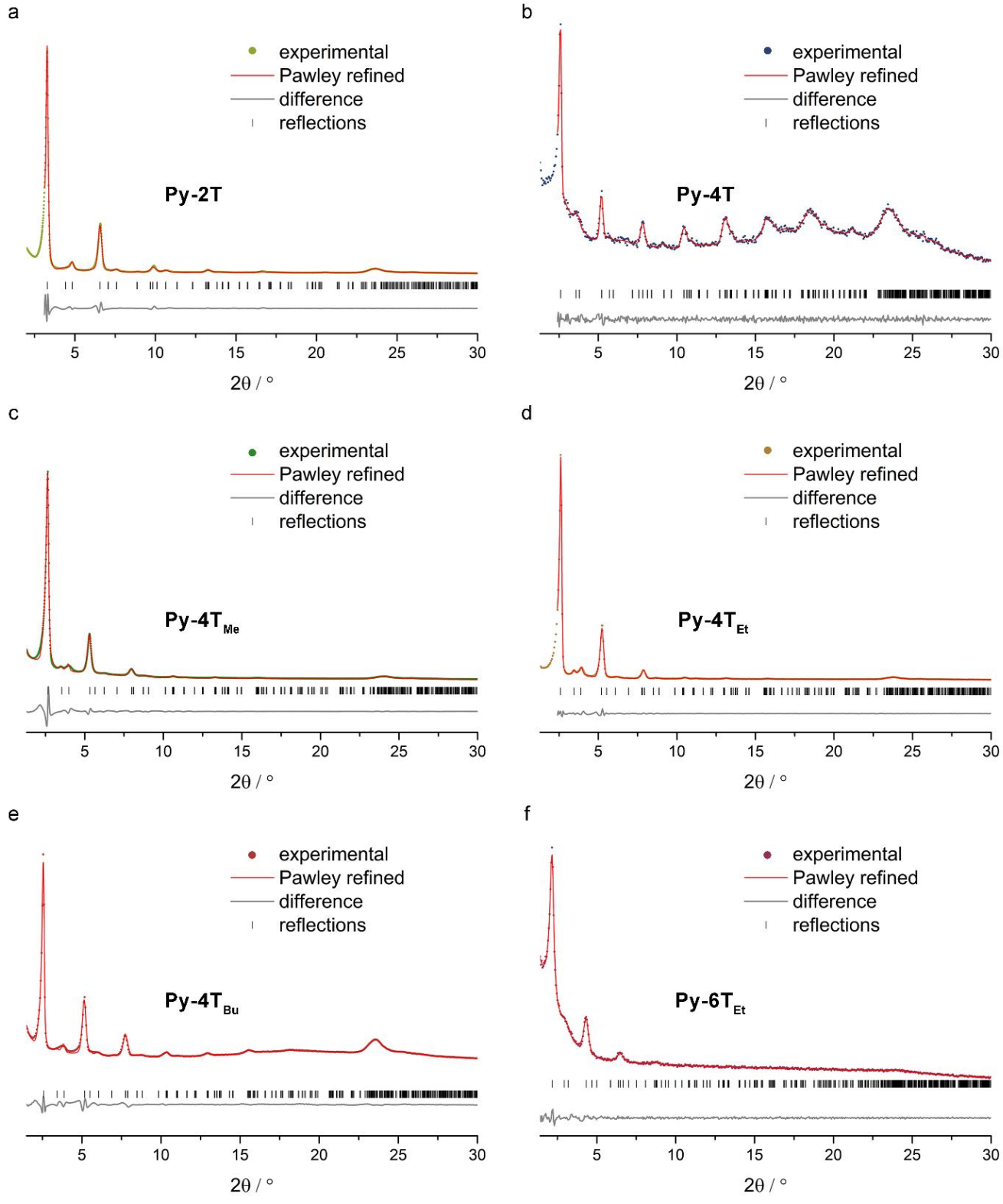

Figure 6.3: Experimental powder XRD data (dots) and structural refinements of the oligothiophene-bridged COF series.(a) Py-2T (b) Py-4T (c) Py-4TMe (d) Py-4TEt (e) Py-4TBu (f) Py-6T. Pawley refinement (red line) using the *C*2/*m* symmetric structure model shown in the appendix provides a very good fit to the experimental patterns with only minimal differences (grey line: difference between experimental and refined patterns). Bragg positions are indicated with black ticks.

In order to study the effect of the structural modifications in the framework on optical properties, UV-Vis absorption spectra of the COFs were recorded. Extending the 2T unit by another bithiophene moiety leads to a moderate red-shift of the absorption band, accompanied by an additional feature below the energy of the main π–π* transition (Figure 6.4a). This feature was attributed in a previous report to the generation of a charge transfer state.[19] Surprisingly, the addition of yet another bithiophene moiety did not lead to the expected bathochromic shift, but in contrast led to a blue shift compared to the Py-4T COF. At 544 nm, the absorption maximum of the Py-6T$_{Et}$ COF is in the same region as the Py-2T COF absorption maximum. These findings could indicate that the incorporation of the a6T$_{Et}$ linker into the framework might lead to smaller effective conjugation lengths, for example through a twist of the backbone. When moving to the quaterthiophene-based COF series with various alkyl chains attached, the absorption bands of the bulk materials can be influenced as well. The attached methyl and ethyl chains blue-shift the absorption maxima by more than 100 nm from 592 nm (Py-4T) to 484 nm and 458 nm for Py-4T$_{Me}$ and Py-4T$_{Et}$, respectively. In contrast, the further extension of the alkyl chains to the length of four carbon atoms red-shifts the absorption maximum of Py-4T$_{Bu}$ back to 564 nm, close to the peak of the Py-4T COF with the non-modified backbone. Furthermore, the charge transfer state is much more strongly pronounced in the Py-4T$_{Bu}$, observable as the strong band arising below the energy of the main π–π* transition at around 700 nm.

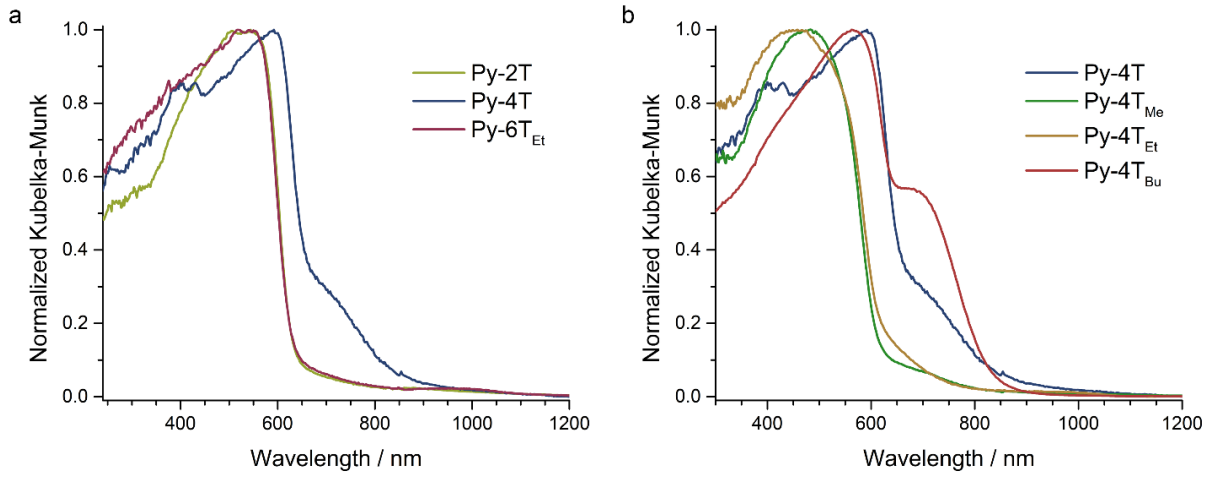

Figure 6.4: (a) Optical absorption spectra of Py-2T, Py-4T and Py-6T$_{Et}$ COFs and (b) of the Py-4T COFs, all measured with solid powders. Diffuse reflectance spectra were measured for the respective powders dispersed in $BaSO_4$ and transformed using the Kubelka-Munk equation.

Further characterization of COF film material could obtain valuable data to better understand the incorporation of oligothiophenes by directly measuring the transmission without approximation using the Kubelka-Munk equation. Film synthesis was challenging and only succeeded for Py-2T and Py-4T$_{Et}$ as seen in the GIWAXS data shown in Figure 6.5. Extensive screening of synthesis conditions and also different substrates led to successful film growth of COF thin films of Py-2T and Py-4T$_{Et}$. The other COFs in the series resulted in amorphous films on the different substrates examined (glass, ITO, fused SiO_2). The motivation behind the growth of oriented COF thin films is the potential to gather more information about the optoelectronic properties by demanding spectroscopic methods such as time-of-flight and time-resolved microwave conductivity for transport and transient absorption spectroscopy for exciton dynamics. Further development of COF-based devices requires also the processability as thin films.

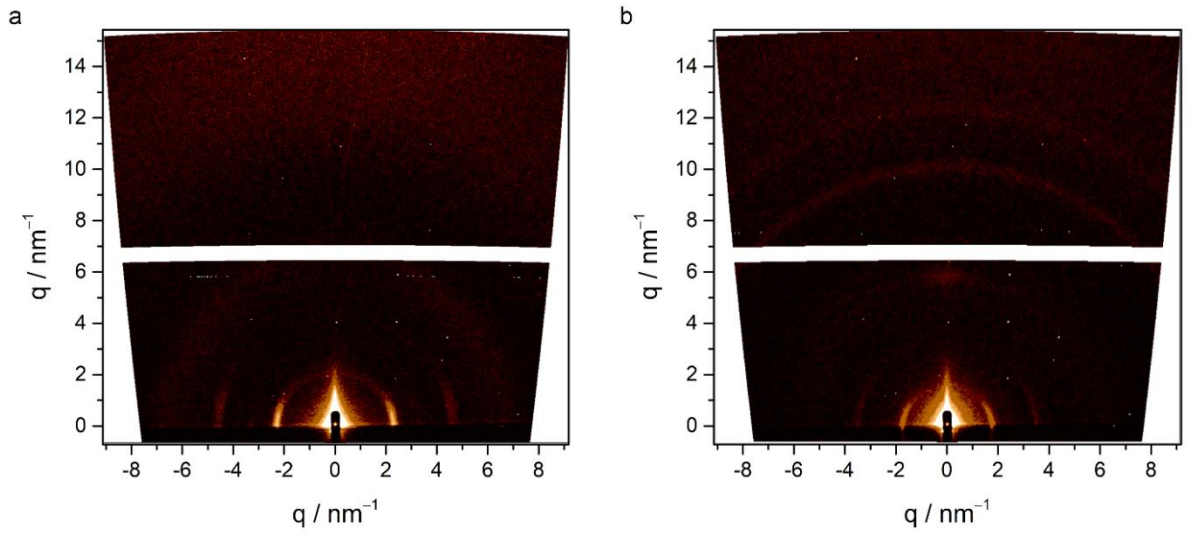

Figure 6.5: GIWAXS analysis of (a) Py-2T and (b) Py-4T$_{Et}$ thin films grown in an oriented and crystalline manner on ITO.

The photoluminescence (PL) of the oligothiophene-based COF series showed similar trends as found for absorption bands. For the bithiophene-containing COF Py-2T, the maximum emission was observed at 634 nm. The extension of the linear bridge to a quaterthiophene leads to a red-shift of the PL maximum to about 690 nm with a slight shoulder at lower energy at about 800 nm. When the linker was extended further to a6T$_{Et}$, the corresponding COF showed a more narrow emission peaking at about 680 nm (Figure 6.6). The Stokes shift was determined to be around 90 nm for Py-2T and Py-4T and over 130 nm for Py-6T$_{Et}$.

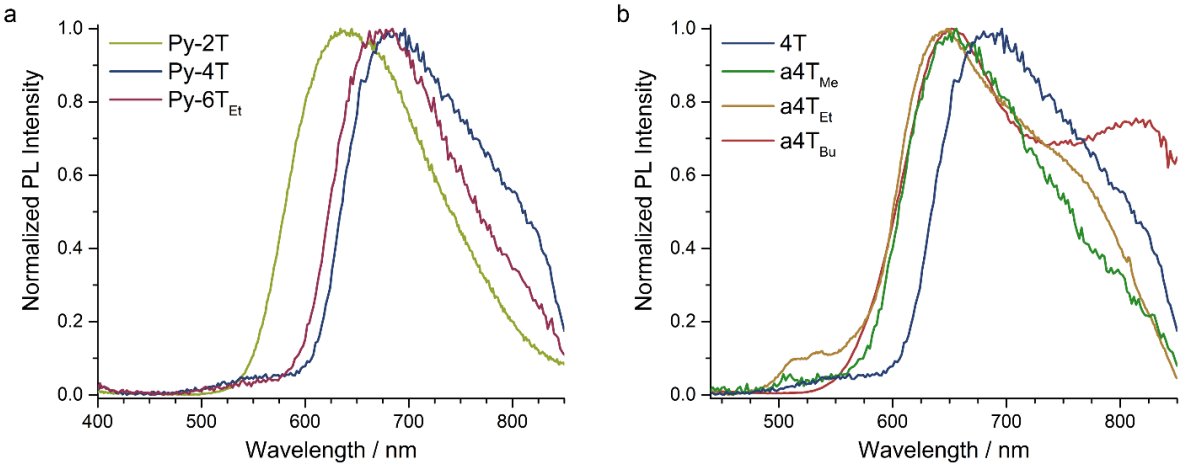

Figure 6.6: (a) Photoluminescence spectra of Py-2T, Py-4T and Py-6T$_{Et}$ and (b) of the Py-4T COFs measured as solids under inert atmosphere (λ_{exc} = 378 nm).

Regarding the impact of elongated alkyl chains, it would be interesting to confirm whether the PL trends found for the monomers (Figure 6.14) also translate to the corresponding COFs. An increasing chain length led to a slightly greater Stokes shift for the diluted monomers in solution, by blue-shifting the absorption maxima and red-shifting the emission maxima. However, for both absorption and photoluminescence, the spectroscopic data obtained from the COF bulk materials do not follow these trends. For closer comparison, the spectra of the solid monomers were also recorded (Figure 6.16). Intermolecular interactions changed the observed trend to the opposite, in a way that the elongation of the alkyl chain led to blue-shifted absorption maxima of the corresponding COFs. For the photoluminescence, it is evident that the small chain (methyl) has hardly any effect on the emission. When the chain is extended to ethyl, the emission band drastically differs and a second band arises. For the longest chain observed (butyl), no second emission peak occurs but two distinct shoulders arise at lower energy vs. the maximum emission.

We suggest that upon stacking in the COF the enforced proximity and relative spatial positioningleads to interactions of the chromophores within the frameworks that lead to changed optical profiles compared to both the monomers in solution and in powder form. To further shed light on the optical characteristics, it would be of great interest to investigate COF thin films. First measurements were performed on crystalline Py-4T$_{Et}$ COF thin films and compared to amorphous Py-4T, Py-4T$_{Me}$ and Py-4T$_{Bu}$ thin films (synthesis of crystalline films not possible yet). Measuring optical absorption directly and avoiding the approximation of Kubelka-Munk can lead to more reliable data from which the absorption bands and the quantitative absorption cross-section can be evaluated. For these thin films, the absorption

maxima were found to be around 450 nm but ultimately crystalline COF films need to be examined to derive conclusive results (Figure 6.19).

The PL decay histograms were recorded with time-correlated single photon counting (TCSPC) of the COF bulk materials under inert atmosphere. Considering the effect of the varied number of coupled thiophenes, a slight increase of the lifetimes can be observed. The long-time constants show a clear extension from 4.06 ns via 5.72 ns to 6.80 ns for Py-2T, Py-4T and Py-$6T_{Et}$, respectively. The faster decay components (τ_2 and τ_3) represent the larger fraction of the decay dynamics and do not clearly indicate extended lifetimes but reveal a larger contribution of the slower decay pathway of τ_2. The PL lifetimes of the oligothiophene monomers 2T, 4T and $6T_{Et}$ (measured in solution) increase with the number of thiophenes in the molecule, observable in the extended long-time constant and the intensity-weighted average lifetimes of 0.28 ns, 0.75 ns and 1.06 ns, respectively. Hence, integrating longer oligothiophenes into COFs results in stabilized excited singlet states in the framework.

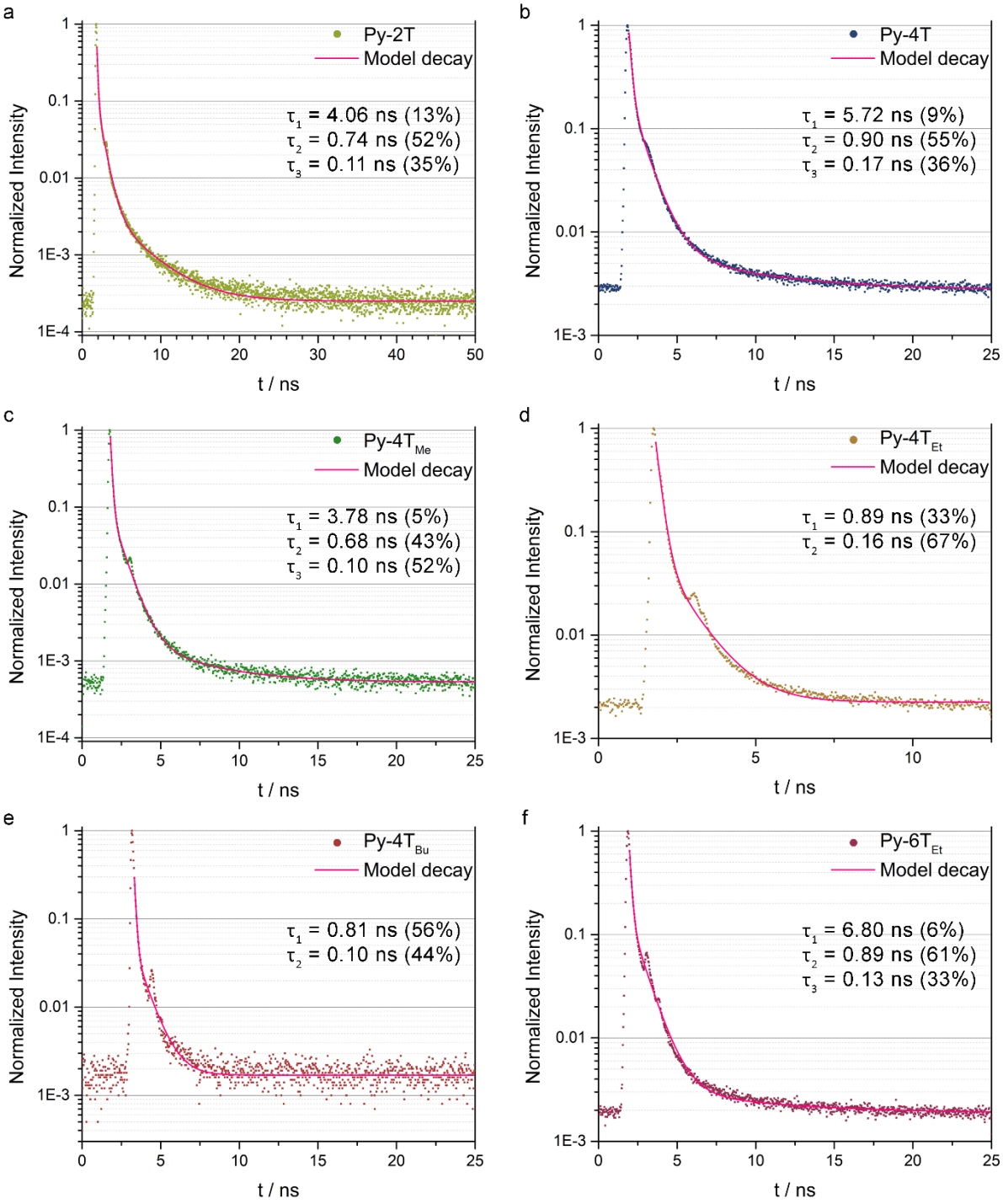

Figure 6.7: Photoluminescence decay of (a) Py-2T at 640 nm, (b) Py-4T at 690 nm, (c) Py-4T$_{Me}$ at 646 nm, (d) Py-4T$_{Et}$ at 650 nm, (e) Py-4T$_{Bu}$ at 654 nm and (f) Py-6T$_{Et}$ at 666 nm emission, respectively. The decays were recorded at the respective peaks of the PL spectra, using TCSPC with 378 nm excitation. Experimental decay: dots in respective color, tri-exponential or bi-exponential fit of the decay: pink line.

If we now change the perspective and track the influence of the alkyl length, a significant shift to faster decay channels was found. By introducing the methyl group, the excited singlet states relax faster leading to long-time decay constants of 3.78 ns for the Py-4T$_{Me}$ and an overall shift to faster decay times. Extending the alkyl chain to ethyl and butyl, the decay does not require a

tri-exponential fit but instead reveals two fast decay channels with lifetimes below 1 ns. Taking the PL decay traces from the monomers into consideration, these findings are in perfect agreement and show a consistent behavior for the excited state dynamics in COFs and monomers. The insertion of alkyl chains on quaterthiophene monomers results in a distinctly decreased long-time constant as well as slightly shorter fast-time constant (Figure 6.20). These insights can indicate a correlation between alkyl chain length at the quaterthiophene backbone and the photoluminescence lifetimes of the corresponding COFs. The longer alkyl chains might enhance non-radiative relaxation due to additional vibrational modes. Due to the slightly larger π-stacking distance for the COF with longer alkyl chains additional space for vibrational motion could possibly lead to a non-radiative decay pathway.

6.3 Conclusion

In this work, we developed an oligothiophene-based COF series for which we varied several structural parameters while keeping the overall geometry and topology of the COF intact. On the one hand, we developed the aldehyde-functionalized oligothiophene building blocks bithiophene, quaterthiophene and sexithiophene, and on the other hand we attached alkyl chains of different length to the quaterthiophene backbone. This way, the effect of the two factors on structural and optical properties could be studied in detail. We observed a correlation between the length of the oligothiophene used as bridging unit and the resulting singlet lifetimes in the COF. Furthermore, the length of the attached alkyl chains affected the excited state dynamics in the COF, in line with the behavior observed for the monomers in solution. The longer chains led to a faster PL decay, which could be attributed to additional non-radiative relaxation channels due to vibrational modes of the building blocks. As a result, we were able to elaborate design rules for tailoring the excited state dynamics in COFs due to the direct translation of the optoelectronic features of the monomers into the frameworks. However, such straightforward design rules could not be derived for absorption and emission characteristics of the COF, where additional aspects such as chain positioning in the pore might lead to changes or the application of the Kubelka-Munk approximation lost valuable information. But nevertheless, we could translate the excited state dynamics of the molecular building blocks into the the COF. This opens up another possibility to tune singlet lifetimes in the COF by the choice of oligothiophene backbone. Further investigation of COF films can therefore support these findings by methods such as transient absorption spectroscopy. We believe that this experimental design can be applied in a general manner to study yet unknown fundamental processes in COFs.

6.4 References

[1] Lee, G.-Y.; Lee, J.; Vo, H. T.; Kim, S.; Lee, H.; Park, T., Amine-Functionalized Covalent Organic Framework for Efficient SO2 Capture with High Reversibility. *Scientific Reports* **2017,** *7* (1), 557.

[2] Ding, S.-Y.; Wang, W., Covalent organic frameworks (COFs): from design to applications. *Chem. Soc. Rev.* **2013,** *42* (2), 548-568.

[3] Furukawa, H.; Yaghi, O. M., Storage of Hydrogen, Methane, and Carbon Dioxide in Highly Porous Covalent Organic Frameworks for Clean Energy Applications. *J. Am. Chem. Soc.* **2009,** *131* (25), 8875-8883.

[4] Dogru, M.; Handloser, M.; Auras, F.; Kunz, T.; Medina, D.; Hartschuh, A.; Knochel, P.; Bein, T., A Photoconductive Thienothiophene-Based Covalent Organic Framework Showing Charge Transfer Towards Included Fullerene. *Angew. Chem. Int. Ed.* **2013,** *52* (10), 2920-2924.

[5] Chen, L.; Furukawa, K.; Gao, J.; Nagai, A.; Nakamura, T.; Dong, Y.; Jiang, D., Photoelectric Covalent Organic Frameworks: Converting Open Lattices into Ordered Donor–Acceptor Heterojunctions. *J. Am. Chem. Soc.* **2014,** *136* (28), 9806-9809.

[6] Liao, Q.; Ke, C.; Huang, X.; Zhang, G.; Zhang, Q.; Zhang, Z.; Zhang, Y.; Liu, Y.; Ning, F.; Xi, K., Catalyst-free and efficient fabrication of highly crystalline fluorinated covalent organic frameworks for selective guest adsorption. *J. Mater. Chem. A* **2019**.

[7] Sun, J.; Zhou, X.; Lei, S., Host-guest architectures with a surface confined imine covalent organic framework as two-dimensional host networks. *Chem. Commun.* **2016**.

[8] Dalapati, S.; Addicoat, M.; Jin, S.; Sakurai, T.; Gao, J.; Xu, H.; Irle, S.; Seki, S.; Jiang, D., Rational design of crystalline supermicroporous covalent organic frameworks with triangular topologies. *Nat. Commun.* **2015,** *6*, 7786.

[9] Haase, F.; Troschke, E.; Savasci, G.; Banerjee, T.; Duppel, V.; Dörfler, S.; Grundei, M. M. J.; Burow, A. M.; Ochsenfeld, C.; Kaskel, S.; Lotsch, B. V., Topochemical conversion of an imine- into a thiazole-linked covalent organic framework enabling real structure analysis. *Nat. Commun.* **2018,** *9* (1), 2600.

[10] Waller, P. J.; AlFaraj, Y. S.; Diercks, C. S.; Jarenwattananon, N. N.; Yaghi, O. M., Conversion of Imine to Oxazole and Thiazole Linkages in Covalent Organic Frameworks. *J. Am. Chem. Soc.* **2018**.

[11] Stegbauer, L.; Schwinghammer, K.; Lotsch, B. V., A hydrazone-based covalent organic framework for photocatalytic hydrogen production. *Chem. Sci.* **2014,** *5* (7), 2789-2793.

[12] Sick, T.; Hufnagel, A. G.; Kampmann, J.; Kondofersky, I.; Calik, M.; Rotter, J. M.; Evans, A. M.; Döblinger, M.; Herbert, S.; Peters, K.; Boehm, D.; Knochel, P.; Medina, D. D.; Fattakhova-Rohlfing, D.; Bein, T., Oriented Films of Conjugated 2D Covalent Organic Frameworks as Photocathodes for Water Splitting. *J. Am. Chem. Soc.* **2017**.

[13] Spitler, E. L.; Colson, J. W.; Uribe-Romo, F. J.; Woll, A. R.; Giovino, M. R.; Saldivar, A.; Dichtel, W. R., Lattice Expansion of Highly Oriented 2D Phthalocyanine Covalent Organic Framework Films. *Angew. Chem. Int. Ed.* **2012,** *51* (11), 2623-2627.

[14] Ascherl, L.; Sick, T.; Margraf, J. T.; Lapidus, S. H.; Calik, M.; Hettstedt, C.; Karaghiosoff, K.; Döblinger, M.; Clark, T.; Chapman, K. W.; Auras, F.; Bein, T., Molecular docking sites designed for the generation of highly crystalline covalent organic frameworks. *Nat. Chem.* **2016,** *8* (4), 310-316.

[15] Jin, E.; Asada, M.; Xu, Q.; Dalapati, S.; Addicoat, M. A.; Brady, M. A.; Xu, H.; Nakamura, T.; Heine, T.; Chen, Q.; Jiang, D., Two-dimensional sp² carbon–conjugated covalent organic frameworks. *Science* **2017,** *357* (6352), 673-676.

[16] Bertrand, G. H. V.; Michaelis, V. K.; Ong, T.-C.; Griffin, R. G.; Dincă, M., Thiophene-based covalent organic frameworks. *Proceedings of the National Academy of Sciences* **2013,** *110* (13), 4923-4928.

[17] Mulzer, C. R.; Shen, L.; Bisbey, R. P.; McKone, J. R.; Zhang, N.; Abruña, H. D.; Dichtel, W. R., Superior Charge Storage and Power Density of a Conducting Polymer-Modified Covalent Organic Framework. *ACS Cent. Sci.* **2016**.

[18] Wu, Y.; Yan, D.; Zhang, Z.; Matsushita, M. M.; Awaga, K., Electron Highways into Nanochannels of Covalent Organic Frameworks for High Electrical Conductivity and Energy Storage. *ACS Appl. Mater. Interfaces* **2019,** *11* (8), 7661-7665.

[19] Keller, N.; Bessinger, D.; Reuter, S.; Calik, M.; Ascherl, L.; Hanusch, F. C.; Auras, F.; Bein, T., Oligothiophene-Bridged Conjugated Covalent Organic Frameworks. *J. Am. Chem. Soc.* **2017,** *139* (24), 8194-8199.

6.5 Appendix

6.5.1 Methods

Infrared (IR) spectra were recorded on a Perkin Elmer Spectrum BX II FT-IR system and a Thermo Scientific Nicolet™ 6700 FT-IR spectrometer in transmission mode. IR data are reported in wavenumbers (cm^{-1}).

The **nitrogen sorption** isotherms were recorded on a Quantachrome Autosorb 1 at 77 K in a pressure range from $p/p_0 = 0.001$ to 0.98. Prior to the measurement of the sorption isotherm, the sample was heated for 24 h at 120 °C under turbomolecular pump vacuum. For the evaluation of the surface area, the BET model was applied between 0.05 and 0.2 p/p_0. The calculation of the pore size distribution was done using the QSDFT equilibrium model with a carbon kernel for cylindrical pores on the adsorption branch. The Connolly surface area differs from the experimental data, usually due to the non-ideal composition and structure of the COF sample. Grain boundaries and the displacement of COF layers may also lead to defects in the crystalline structure and to blocked pores and thus lower experimental values. Residual, adsorbed molecular/oligomeric fragments may also decrease the accessible surface area.

Powder X-ray diffraction (PXRD) measurements were performed using a Bruker D8 Discover with Ni-filtered Cu K_α radiation and a LynxEye position-sensitive detector. **Two-dimensional grazing-incidence wide angle X-ray scattering (2D GIWAXS)** data were collected using an Anton-Paar SAXSpace system equipped with a Cu Kα microfocus source operated at 50 kV and 1 mA and an Eiger Dectris R 1M 2D detector.

Transmission electron microscopy (TEM) measurements were performed on a probe-corrected FEI Titan Themis 60-300 kV (FEI Company/Thermo Fisher Scientic Inc., USA) electron microscope equipped with a Super-X windowless EDX (four quadrant SDD EDX detection) and a X-FEG high-brightness gun with monochromator (energy spread <0.2 eV). **Scanning electron microscopy (SEM)** measurements were performed on an FEI Helios NanoLab G3 UC electron microscope (FEI Company/Thermo Fisher Scientic Inc., USA) with an X-MaxN EDX detector (Oxford Instruments, UK). The samples were mounted on sample carriers with a sticky carbon support and sputtered with carbon on a Bal-Tec MED 020 coating system.

UV-Vis spectra were recorded using a Perkin-Elmer Lambda 1050 spectrometer equipped with a 150 mm integrating sphere. **Diffuse reflectance spectra** were collected with a Praying Mantis (Harrick) accessory and were referenced to barium sulfate powder as white standard.

Photoluminescence (PL) measurements were performed using a home-built setup consisting of a Horiba Jobin Yvon iHR 320 monochromator equipped with a photomultiplier tube and a liquid N_2-cooled InGaAs detector. The samples were illuminated with a pulsed (83 Hz) 365 nm or 405 nm LED at a light intensity of 500 mW cm^{-2}.

Time-resolved PL measurements were acquired using a **time-correlated single photon counting (TCSPC)** setup (FluoTime 300, PicoQuant GmbH). The samples were photo-excited using lasers with suitable wavelengths according to the sample absorption, i.e. 378 nm, 403 nm or 507 nm wavelength (LDH-P-C-375, LDH-P-C-405, and LDH-P-C-510, respectively, all from PicoQuant GmbH) pulsed at 500 kHz, with a pulse duration of ~100 ps and fluence of ~300 nJcm^{-2}/pulse. The samples were exposed to the pulsed light source set at 0.3 µJcm^{-2}/pulse fluence for ~10 minutes prior to measurement to ensure stable sample emission. The PL was collected using a high-resolution monochromator and photomultiplier detector assembly (PMA-C 192-N-M, PicoQuant GmbH).

6.5.2 Building Block Syntheses

All reactions were carried out with magnetic stirring, and if moisture or air sensitive, under argon atmosphere using standard Schlenk techniques in oven-dried glassware. Liquid reagents and solvents were added by syringes or oven-dried stainless-steel cannulas through rubber septa. Chemicals were purchased from commercial suppliers and used without further purification. The solvents were of reagent grade or purified by distillation. Yields refer to isolated homogeneous and spectroscopically pure materials, unless otherwise specified.

Scheme 6.1: Synthesis of the oligothiophene series, **2T**, **4T**, **a4T$_{Me}$**, **a4T$_{et}$**, **a4T$_{Bu}$**, and **a6T$_{et}$**.

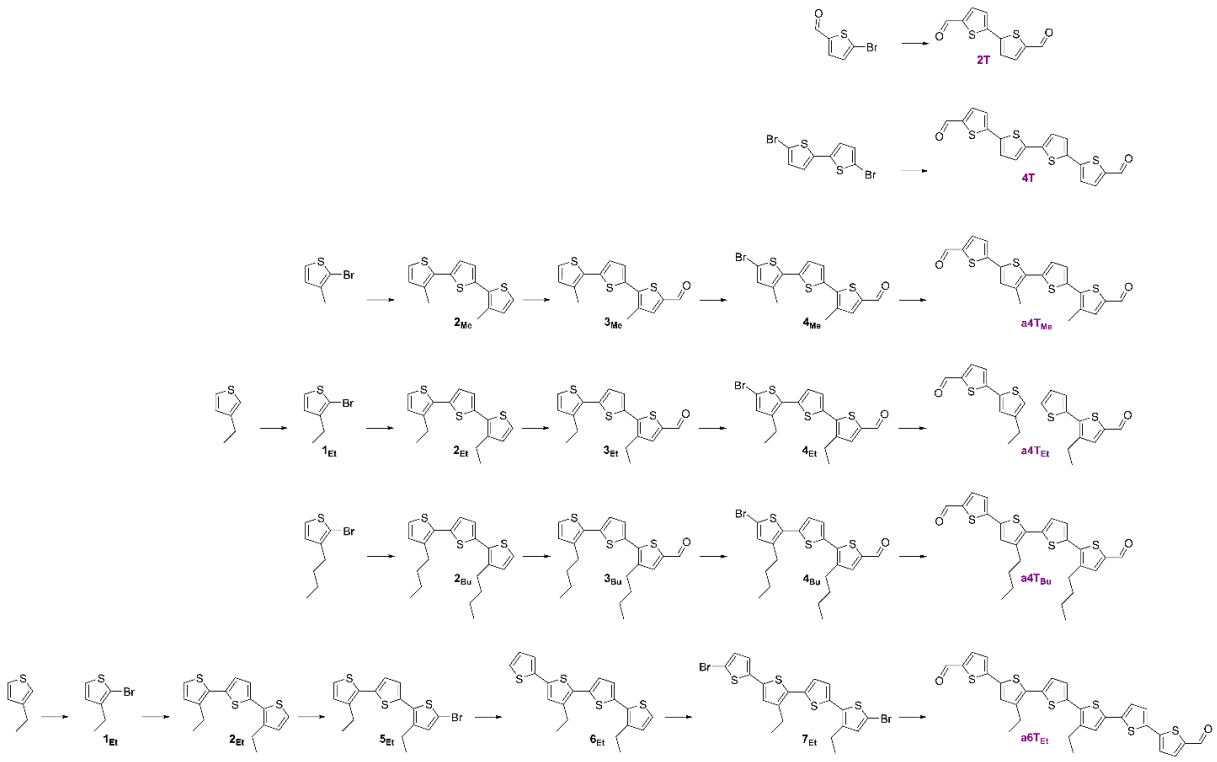

[2,2'-bithiophene]-5,5'-dicarbaldehyde (2T)

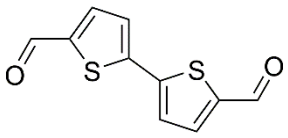

A solution of 5-bromo-2-thiophenecarboxaldehyde (1.910 g, 10 mmol, 1 eq), $Pd(OAc)_2$ (89.8 mg, 0.4 mmol, 0.04 eq), XPhos (228.8 mg, 0.48 mmol, 0.048 eq) in 56 mL 1-butanol was stirred for 15 min under argon at room temperature. Then a solution of $CsOH{\cdot}H_2O$ (3.358 g,

20 mmol, 2 eq.) in 14 mL water was prepared and added to the reaction suspension, followed by the addition of 5-formyl-2-thienylboronic acid (2.807 g, 18 mmol, 1.8 eq.). After stirring for 48 h at ambient conditions, the yellow-brown suspension was quenched by the addition of 400 mL of H_2O. The mixture was extracted with $CHCl_3$, dried over $MgSO_4$ and concentrated under reduced pressure. The crude product was purified via column chromatography (silica gel, DCM), yielding the title compound as a yellow powder (1.795 g, 8.1 mmol, 81%).

^{1}H NMR (400 MHz, $CDCl_3$): 9.92 (s, 2H), 7.72 (d, J = 4.0 Hz, 2H), 7.42 (d, J = 4.0 Hz, 2H).

^{13}C NMR (101 MHz, $CDCl_3$): 182.7, 145.0, 144.1, 137.0, 126.6.

[2,2':5',2'':5'',2'''-quaterthiophene]-5,5'''-dicarbaldehyde (4T)

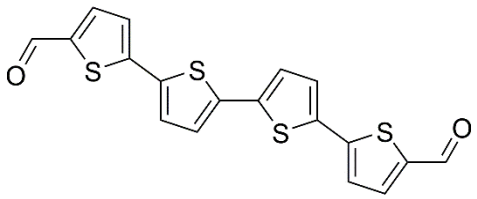

Following a procedure by Yang et al.,[1] 5,5'-dibromo-2,2'-bithiophene (1.0 g, 3.09 mmol, 1.0 eq.) was stirred with $Pd(OAc)_2$ (27.6 mg, 0.123 mmol, 4 mol%) and XPhos (70.6 mg, 0.148 mmol, 4.8 mol%) in 18 mL n-butanol for 15 min at room temperature. Next, a solution containing $CsOH{\cdot}H_2O$ (1.762 g, 10.5 mmol, 3.4 eq.) in 4.4 mL H_2O was added. Subsequently, 5-formyl-2-thienylboronic acid (1.444 g, 9.26 mmol, 3 eq.) was added and the resulting mixture was stirred for 48 h at room temperature. After completion, H_2O was added and the suspension was filtered and washed with *n*-hexane (100 mL) and $CHCl_3$ (20 mL). The organic phase was dried over $MgSO_4$ and concentrated under reduced pressure. The crude product was purified via recrystallization from THF and furnished the title compound as a dark red powder (754 mg, 1.95 mmol, 63%).

^{1}H NMR (400 MHz, DMSO-d_6): 9.90 (s, 2H), 8.02 (d, J = 4.0 Hz, 2H), 7.63 (d, J = 3.9 Hz, 2H), 7.60 (d, J = 4.0 Hz, 2H), 7.51 (d, J = 3.9 Hz, 2H).

HR-EI-MS: *m/z* 385.95 (M^+, calculated for $C_{26}H_{26}O_2S_4$: 385.95).

3,3''-dimethyl-2,2':5',2''-terthiophene (2_{Me})

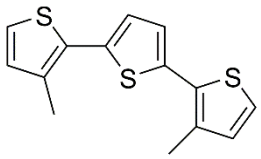

A Grignard reagent, prepared by sonication of 2-bromo-3-methylthiophene (5.06 g, 28.6 mmol, 2.9 eq.), 1,2-dibromoethane (5.38 g, 28.6 mmol, 2.9 eq.) and Mg (1.37 mg, 56.1 mmol, 5.7 eq.) in 85 mL of dry Et_2O, was slowly added to a solution containing 2,5-dibromothiophene (2.39 g, 10.0 mmol, 1.0 eq.) and Ni(dppp)Cl_2 (465.4 mg, 0.86 mmol, 3 mol%) in 57 mL dry Et_2O. The reaction mixture was heated to reflux for 40 h. Upon completion, the reaction was quenched by the addition of 2 M HCl (100 mL), extracted with DCM, washed with H_2O, dried over $MgSO_4$, and concentrated under reduced pressure. The crude product was purified via column chromatography (silica gel, *n*-pentane), yielding the title compound as yellow crystals (2.47 g, 6.84 mmol, 69%).

^{1}H NMR (400 MHz, $CDCl_3$): 7.15 (d, J = 5.1 Hz, 2H), 7.08 (s, 2H), 6.89 (d, J = 5.1 Hz, 2H), 2.42 (s, 6H).

^{13}C NMR (101 MHz, $CDCl_3$): 136.7, 134.5, 131.9, 131.3, 126.2, 123.8, 15.9.

3,3''-dimethyl-5-formyl-2,2':5',2''-terthiophene (3_{Me})

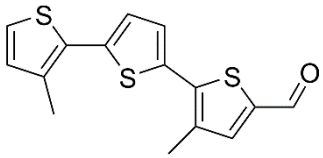

A Vilsmeier reagent, prepared by the addition of $POCl_3$ (1.39 g, 8.83 mmol, 1.3 eq.) to 6.6 mL of dry DMF, was added to a solution of compound **2_{Me}** (1.90 g, 6.87 mmol, 1.0 eq.) in 140 mL DCE. The reaction mixture was stirred overnight at 70 °C. Subsequently, H_2O (250 mL) was added and the pH was adjusted to 8.5-9 with 2 M NaOH. The product was extracted with DCM, dried over $MgSO_4$ and concentrated under reduced pressure. Purification via column chromatography (silica gel, $CHCl_3$) furnished the product as a yellow powder (1.72 g, 5.65 mmol, 82%).

^{1}H NMR (400 MHz, $CDCl_3$): 9.82 (s, 1H), 7.55 (s, 1H), 7.28 (d, J = 3.9 Hz, 1H), 7.19 (d, J = 5.1 Hz, 1H), 7.13 (d, J = 3.9 Hz, 1H), 6.91 (d, J = 5.1 Hz, 1H), 2.48 (s, 3H), 2.43 (s, 3H).

^{13}C NMR (101 MHz, $CDCl_3$): 182.5, 141.7, 140.5, 139.8, 139.0, 134.9, 134.9, 134.8, 131.8, 130.4, 127.8, 126.1, 124.2, 16.0, 15.7.

5-bromo-3,3''-dimethyl-5''-formyl-2,2':5',2''-terthiophene (4_{Me})

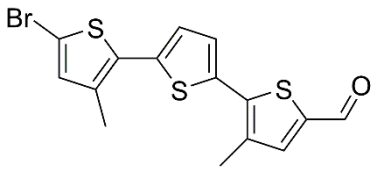

Compound $\mathbf{3_{Me}}$ (1.72 g, 5.6 mmol, 1.0 eq.) was dissolved in 55 mL $CHCl_3$ and cooled to 0 °C. NBS (1.10 mg, 6.2 mmol, 1.1 eq.) and glacial acetic acid (55 mL) were added and the solution was allowed to slowly warm up to room temperature. After stirring at room temperature for 2 d in the dark, the reaction mixture was poured onto H_2O, extracted with DCM, washed with saturated $NaHCO_3$ solution, dried over $MgSO_4$, and concentrated under reduced pressure. The crude product was purified by column chromatography (silica gel, n-hexane with 2% - 25% EtOAc), yielding an bright yellow solid (1.844 g, 4.81 mmol, 86%).

^{1}H NMR (400 MHz, $CDCl_3$): 9.82 (s, 1H), 7.55 (s, 1H), 7.26 (d, J = 3.8 Hz, 1H), 7.07 (d, J = 3.8 Hz, 1H), 6.88 (s, 1H), 2.47 (s, 3H), 2.37 (s, 3H).

^{13}C NMR (101 MHz, $CDCl_3$): 182.5, 141.3, 140.4, 140.1, 137.5, 135.4, 135.4, 135.0, 134.3, 131.9, 127.7, 126.5, 111.0, 16.0, 15.6.

3,3''-dimethyl-[2,2':5',5'':2'',2'''-quaterthiophene]-5,5'''-dicarbaldehyde ($a4T_{Me}$)

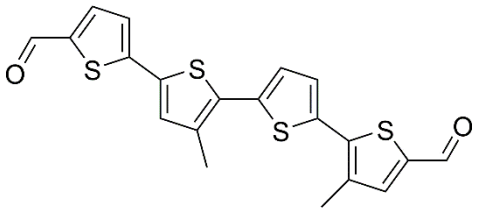

Following a procedure by Yang et al.,[1] compound $\mathbf{4_{Me}}$ (1.04 g, 2.7 mmol, 1.0 eq.) was stirred with $Pd(OAc)_2$ (12.2 mg, 0.05 mmol, 2 mol%) and XPhos (31.0 mg, 0.067 mmol, 2.4 mol%)

in 32 mL n-butanol (ca. 15 min). Next, a solution containing $CsOH \cdot H_2O$ (911.5 mg, 5.4 mmol, 2.0 eq.) in 7.8 mL H_2O was added, followed by the addition of 5-formyl-2-thienylboronic acid (170 mg, 1.09 mmol, 1.8 eq.). The resulting mixture was stirred for 3 d at room temperature. After completion, H_2O was added and the product was extracted with $CHCl_3$, washed with brine 3 times, dried over $MgSO_4$, and concentrated under reduced pressure. Purification via column chromatography (silica gel, chloroform/EtOAc 99:1) furnished the title compound as a bright red powder (205 mg, 0.494 mmol, 82%).

^{1}H NMR (400 MHz, $CDCl_3$): 9.86 (s, 1H), 9.83 (s, 1H), 7.67 (d, J = 4.0 Hz, 1H), 7.55 (s, 1H), 7.30 (d, J = 3.9 Hz, 1H), 7.23 (d, J = 4.0 Hz, 1H), 7.19 (d, J = 3.9 Hz, 1H), 7.18 (s, 1H), 2.49 (s, 3H), 2.45 (s, 3H).

^{13}C NMR (101 MHz, $CDCl_3$): 182.5, 146.6, 142.0, 141.2, 140.4, 140.2, 137.8, 137.5, 136.0, 135.8, 135.1, 133.9, 132.4, 130.6, 127.9, 126.7, 124.4, 16.1, 15.9.

HR-EI-MS: *m/z* 414.56 (M^+, calculated for $C_{20}H_{14}O_2S_4$: 414.57).

2-bromo-3-ethylthiophene (1_{Et})

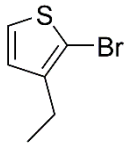

N-bromosuccinimide (8.3 g, 46.8 mmol, 1.05 eq.) was added to a solution of 2-ethylthiophene (5.0 g, 44.6 mmol, 1.0 eq.) in 47 mL $CHCl_3$. The reaction mixture was cooled to 0 °C, followed by the addition of 47 mL glacial acetic acid. The solution was allowed to warm to room temperature over the course of several hours and stirred for 2 d in the dark. The slightly yellow solution was poured onto 200 mL H_2O, extracted with DCM, washed with saturated $NaHCO_3$ solution, dried over $MgSO_4$, and concentrated under reduced pressure. High vacuum distillation (31 mbar, 33 °C) furnished the title compound as a colorless liquid (7.47 g, 39.1 mmol, 89%).

^{1}H NMR (400 MHz, CDCl3): 7.19 (d, J = 5.6 Hz, 1H), 6.82 (d, J = 5.6 Hz, 1H), 2.59 (q, J = 7.6 Hz, 2H), 1.19 (t, J = 7.6 Hz, 3H).

^{13}C NMR (101 MHz, $CDCl_3$): 143.3, 127.9, 125.4, 108.5, 23.0 (C-5), 14.3.

The consecutive compounds (**2$_{Et}$, 3$_{Et}$, 4$_{Et}$, a4T$_{Et}$, 2$_{Bu}$, 3$_{Bu}$, 4$_{Bu}$, a4T$_{Bu}$**) were synthesized analogous to the products listed above (**2$_{Me}$, 3$_{Me}$, 4$_{Me}$, a4T$_{Me}$**).

5-bromo-3,3''-diethyl-2,2':5',2''-terthiophene (5$_{Et}$)

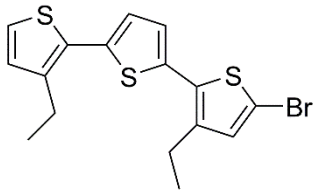

Compound **2$_{Et}$** (5.13 g, 16.8 mmol, 1.0 eq.) was dissolved in $CHCl_3$ (34 ml) and cooled to 0 °C. *N*-bromosuccinimide (3.15 g, 17.7 mmol, 1.05 eq.) and glacial acetic acid (34 ml) were added and the solution was allowed to slowly warm up to room temperature. After stirring at room temperature for 3 d in the dark, the reaction mixture was poured onto 100 mL water, extracted with CH2Cl2, washed with sat. $NaHCO_3$ solution, dried over $MgSO_4$, and concentrated under reduced pressure. The crude product was purified by flash column chromatography (silica, 2-methylpentane) yielding compound **5$_{Et}$** (3.667 g, 9.6 mmol, 57%) as a yellow oil.

^{1}H NMR (400 MHz, $CDCl_3$): 7.20 (d, J = 5.2 Hz, 1H), 7.05 (d, J = 3.7 Hz, 1H), 7.00 (d, J = 3.7 Hz, 1H), 6.97 (d, J = 5.2 Hz, 1H), 6.93 (s, 1H), 2.81 (q, J = 7.5 Hz, 2H), 2.75 (q, J = 7.5 Hz, 2H), 1.27 (t, J = 7.6 Hz, 3H), 1.25 (t, J = 7.6 Hz, 3H).

^{13}C NMR (101 MHz, $CDCl_3$): 141.5, 141.2, 136.7, 134.6, 132.2, 131.6, 129.8, 129.6, 126.5, 126.0, 124.1, 110.6, 22.5, 22.5, 15.1, 15.0.

HR-EI-MS: *m/z* 382.14 (M^+, calculated for $C_{16}H_{15}BrS_3$: 381.95).

3,3''-diethyl-2,2':5',2'':5'',2'''-quaterthiophene (6$_{Et}$)

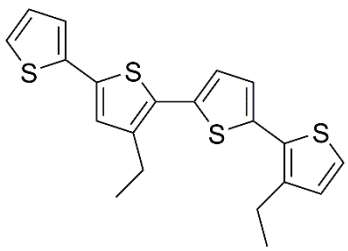

A solution of $CsOH \cdot H_2O$ (1.219 g, 7.26 mmol, 2 eq.) and water (5.1 ml) was added to a stirring suspension of compound **5Et** (1.391 g, 3.628 mmol, 1.0 eq.), palladium acetate (32.6 mg, 0.145 mmol, 4 mol%), XPhos (83.0 mg, 0.174 mmol, 4.8 mol%) and *n*-butanol (20 ml). After addition of 5-formyl-2-thienylboronic acid (836 mg, 6.53 mmol, 1.8 eq.) the slurry was stirred at room temperature for 2 d. Water (50 ml) and CH_2Cl_2 (100 ml) was added to the slurry. The aqueous phase was extracted by CH_2Cl_2 and the combined extracts were washed with sat. $NaHCO_3$ and brine. The solution was dried over Na_2SO_4 and concentrated under reduced pressure. The residue was purified by flash column chromatography (silica, 0% → 20% CH_2Cl_2 in *n*-pentane), yielding compound **6Et** (407 mg, 1.05 mmol, 29%) as an orange oil.

^{1}H NMR (400 MHz, $CDCl_3$): 7.22 (dd, J = 5.1, 1.1 Hz, 1H), 7.20 (d, J = 5.2 Hz, 1H), 7.17 (dd, J = 3.6, 1.1 Hz, 1H), 7.08 (d, J = 3.8 Hz, 1H), 7.06 (d, J = 3.8 Hz, 1H), 7.05 (s, 1H), 7.02 (dd, J = 5.1, 3.6 Hz, 1H), 6.98 (d, J = 5.2 Hz, 1H), 2.82 (p, J = 7.5 Hz, 4H), 1.31 (t, J = 7.6 Hz, 3H), 1.28 (t, J = 7.6 Hz, 3H).

HR-EI-MS: *m/z* 386.22 (M^+, calculated for $C_{20}H_{18}S_4$: 386.03).

5,5'''-dibromo-3,3''-diethyl-2,2':5',2'':5'',2'''-quaterthiophene (7Et)

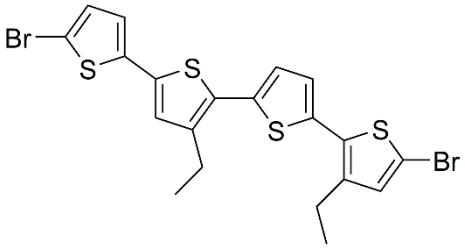

A solution of *N*-bromosuccinimide (439 mg, 2.46 mmol, 2.0 eq.) and dry DMF (3 ml) was added to a solution of compound **6Et** (477 mg, 1.23 mmol, 1.0 eq.) in DMF (13 ml) at 80 °C. After stirring at 80 °C for 3 h, the reaction mixture was poured onto water (100 ml), extracted with CH_2Cl_2, washed with water, dried over $MgSO_4$, and concentrated under reduced pressure. The crude product was purified by flash column chromatography (silica, 0% → 15% $CHCl_3$ in isohexane) yielding compound **7Et** (539 mg, 990 µmol, 80 %) as an orange solid.

^{1}H NMR (400 MHz, $CDCl_3$): 7.06 (d, J = 3.8 Hz, 1H), 7.01 (d, J = 3.8 Hz, 1H), 6.97 (s, 1H),6.97 (d, J = 3.9 Hz, 1H), 6.93 (s, 1H), 6.90 (d, J = 3.9 Hz, 1H), 2.78 (q, J = 7.6 Hz, 2H), 2.75 (q, J = 7.6 Hz, 2H), 1.29 (t, J = 7.6 Hz, 3H), 1.25 (t, J = 7.6 Hz, 3H).

^{13}C NMR (101 MHz, $CDCl_3$): 142.0, 141.8, 138.8, 136.1, 135.0, 134.6, 132.4, 131.6, 130.9, 129.5, 126.7, 126.5, 126.2, 123.9, 111.2, 110.9, 22.9, 22.7, 15.1, 15.0

HR-EI-MS: *m/z* 541.84 (M^+, calculated for $C_{20}H_{16}Br_2S_4$: 541.84).

3''',4'-diethyl-[2,2':5',2'':5'',2''':5''',2'''':5'''',2''''':5''''',2'''''-sexithiophene]-5,5'''''-dicarbaldehyde (a6T$_{Et}$)

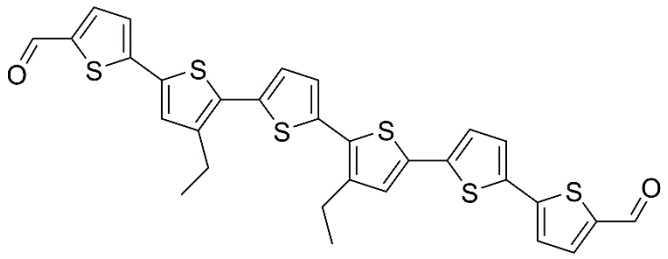

A solution of $CsOH \cdot H_2O$ (185 mg, 1.10 mmol, 2.0 eq.) and water (0.77 ml) was added to a stirring suspension of compound **7$_{Et}$** (300 mg, 551 µmol, 1.0 eq.), palladium acetate (5.0 mg, 22 µmol, 4 mol%), XPhos (12.6 mg, 27 µmol, 4.8 mol%) and *n*-butanol (6.2 ml). After addition of 5-formyl-2-thienylboronic acid (253 mg, 1.65 mmol, 3.0 eq.) the slurry was stirred at 50 °C for 2 d. Water (100 ml) and CH_2Cl_2 (200 ml) was added to the slurry. The aqueous phase was extracted by CH_2Cl_2 and the combined extracts were washed with sat. $NaHCO_3$ and brine. The organic layers were dried over Na_2SO_4 and concentrated under reduced pressure. Purification of the residue by flash column chromatography (silica, CH_2Cl_2) yielded 116 mg product (191 µmol, 35%). Recrystallization from DCE and vacuum drying afforded a6T$_{Et}$ (99 mg, 163 µmol, 30%) as deep dark purple crystals.

^{1}H NMR (400 MHz, $CDCl_3$): 9.90 (s, 2H), 8.02 (d, J = 2.4 Hz, 1H), 8.01 (d, J = 2.4 Hz, 1H), 7.61 (d, J = 3.9 Hz, 1H), 7.59 (s, 1H), 7.58 (d, J = 2.7 Hz, 1H), 7.57 (d, J = 2.7 Hz, 1H), 7.43 (s, 1H), 7.43 (d, J = 3.8 Hz, 1H), 7.34 (d, J = 3.9 Hz, 1H), 7.31 (d, J = 3.9 Hz, 1H), 2.81 (q, J = 7.5 Hz, 2H), 2.80 (q, J = 7.5 Hz, 2H), 1.28 (t, J = 7.5 Hz, 6H)

HR-EI-MS: *m/z* 605.99 (M^+, calculated for $C_{30}H_{22}O_2S_6$: 605.99).

1,3,6,8-tetrakis(4-aminophenyl)pyrene (Py)[2-3]

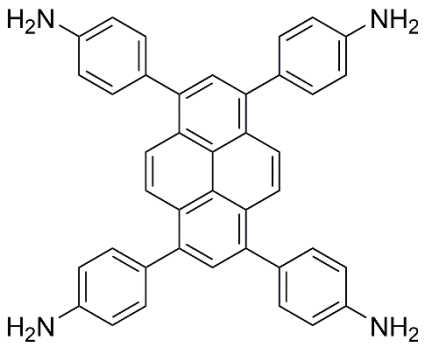

A reaction mixture containing 1,3,6,8-tetrabromopyrene (1482 mg, 2.86 mmol, 1.0 eq.), 4-aminophenylboronic acid pinacol ester (3010 mg, 13.7 mmol, 4.8 eq.), K_2CO_3 (2175 mg, 15.7 mmol, 5.5 eq.), and $Pd(PPh_3)_4$ (330 mg, 0.29 mmol, 10 mol%) in 32 mL 1,4-dioxane and 8 mL H_2O was heated to reflux (115 °C) for 3 d. After cooling to room temperature, H_2O was added. The resulting precipitate was collected via filtration and was washed with H_2O and MeOH. Recrystallization from 1,4-dioxane, followed by drying under high vacuum furnished the title compound, co-crystallized with approximately 1.5 dioxane molecules per formula unit, as a bright yellow powder (1792 mg, 2.56 mmol, 90%).

^{1}H NMR (400 MHz, DMSO-d_6): 8.13 (s, 4 H), 7.79 (s, 2 H), 7.34 (d, J = 8.4 Hz, 8 H), 6.77 (d, J = 8.5 Hz, 8 H), 5.30 (s, 8 H), 3.56 (s, 12 H, dioxane).

^{13}C NMR (100 MHz, DMSO-d_6): 148.2, 137.1, 131.0, 129.0, 127.6, 126.7, 126.1, 124.4, 113.9, 66.3 (dioxane).

6.5.3 COF Syntheses

COF bulk material syntheses were carried out under argon atmosphere in PTFE-sealed 6 mL glass tubes. High purity solvents and acetic acid were sourced from commercial suppliers and degassed and saturated with argon prior to use unless shipped under argon.

Py-2T

1,3,6,8-tetrakis(4-aminophenyl)pyrene dioxane adduct (Py; 7.0 mg, 10 µmol, 1.0 eq.) and [2,2'-bithiophene]-5,5'-dicarbaldehyde (2T; 4.5 mg, 20 µmol, 2.0 eq.) were filled into a reaction tube, followed by the addition of mesitylene (333 µl), benzyl alcohol (167 µl) and 6 M acetic acid (70 µL). The tube was sealed and the reaction mixture was heated at 120 °C for 3 d. After cooling to room temperature, the precipitate was collected by filtration, and extracted with supercritical CO_2 for 2 h, yielding the Py-2T as a red powder.

Py-4T

1,3,6,8-tetrakis(4-aminophenyl)pyrene dioxane adduct (Py; 10.5 mg, 15 µmol, 1.0 eq.) and [2,2':5',2":5",2"'-quaterthiophene]-5,5"'-dicarbaldehyde (4T; 11.6 mg, 30 µmol, 2.0 eq.) were filled into a reaction tube, followed by the addition of 1,2-dichlorobenzene (167 µl), benzyl alcohol (83 µl) and 6 M acetic acid (25 µL). The tube was sealed and the reaction mixture was heated at 120 °C for 3 d. After cooling to room temperature, the precipitate was collected by filtration, slowly dried in an argon atmosphere overnight, and extracted with supercritical CO_2 for 2 h, yielding the Py-4T as a dark red to black powder.

Py-4T$_{Me}$

1,3,6,8-tetrakis(4-aminophenyl)pyrene dioxane adduct (Py; 14.0 mg, 20 µmol, 1.0 eq.) and 3,3"-dimethyl-[2,2':5',5":2",2"'-quaterthiophene]-5,5"'-dicarbaldehyde (a4T$_{Me}$; 17 mg, 40 µmol, 2.0 eq.) were filled into a reaction tube, followed by the addition of mesitylene (333 µL), BnOH (167 µL), and 6 M acetic acid (50 µL). The tube was sealed and the reaction mixture was heated at 120 °C for 4 d. After cooling to room temperature, the precipitate was collected by filtration,

slowly dried in an argon atmosphere overnight, and extracted with supercritical CO_2 for 2 h, yielding the Py-a4T$_{Me}$ as a dark red powder.

Py-4T$_{Et}$

1,3,6,8-tetrakis(4-aminophenyl)pyrene dioxane adduct (Py; 7.0 mg, 10 µmol, 1.0 eq.) and 3,3"-diethyl-[2,2':5',5":2",2"'-quaterthiophene]-5,5"'-dicarbaldehyde (a4T$_{Et}$; 8.9 mg, 20 µmol, 2.0 eq.) were filled into a reaction tube, followed by the addition of mesitylene (187 µL), BnOH (63 µL), and 6 M acetic acid (50 µL). The tube was sealed and the reaction mixture was heated at 120 °C for 4 d. After cooling to room temperature, the precipitate was collected by filtration, slowly dried in an argon atmosphere overnight, and extracted with supercritical CO_2 for 2 h, yielding the Py-a4T$_{Me}$ as a dark red powder.

Py-4T$_{Bu}$

1,3,6,8-tetrakis(4-aminophenyl)pyrene dioxane adduct (Py; 14.0 mg, 20 µmol, 1.0 eq.) and 3,3"-dibutyl-[2,2':5',5":2",2"'-quaterthiophene]-5,5"'-dicarbaldehyde (a4T$_{Bu}$; 20 mg, 40 µmol, 2.0 eq.) were filled into a reaction tube, followed by the addition of mesitylene (133 µL), BnOH (67 µL), and 6 M acetic acid (20 µL). The tube was sealed and the reaction mixture was heated at 120 °C for 4 d. After cooling to room temperature, the precipitate was collected by filtration and slowly dried in air for 24 h, yielding the Py-a4T as a dark red powder (19 mg, 64%).

Py-6T$_{Et}$

1,3,6,8-tetrakis(4-aminophenyl)pyrene dioxane adduct (Py; 7.0 mg, 10 µmol, 1.0 eq.) and 3"',4'-diethyl-[2,2':5',2":5",2"':5"',2"":5"",2"""-sexithiophene]-5,5"""-dicarbaldehyde (a6T$_{Et}$; 12.1 mg, 20 µmol, 2.0 eq.) were filled into a reaction tube, followed by the addition of mesitylene (167 µL), BnOH (83 µL), and 6 M acetic acid (25 µL). The tube was sealed and the reaction mixture was heated at 120 °C for 3 d. After cooling to room temperature, the precipitate was collected by filtration and slowly dried in an argon atmosphere overnight, and extracted with supercritical CO_2 for 2 h, yielding the Py-a6T$_{Et}$ as a dark red powder.

COF thin film syntheses were carried out under argon atmosphere in PTFE-sealed 100 mL glass containers equipped with a glass liner. The COF films were grown on quartz substrates cleaned in Hellmanex solution, water and isopropanol. The substrates were placed in a PTFE holder in the reaction solution.

Py-2T thin film

1,3,6,8-tetrakis(4-aminophenyl)pyrene dioxane adduct (Py; 10.5 mg, 15 µmol, 1.0 eq.) and [2,2'-bithiophene]-5,5'-dicarbaldehyde (2T; 6.7 mg, 30 µmol, 2.0 eq.) were filled into a glass container, followed by the addition of mesitylene (1333 µl), benzyl alcohol (667 µl) and 6 M acetic acid (150 µL). The quartz substrate was placed in the reaction solution and the glass vessel was sealed and heated at 120 °C for 1 d. After cooling to room temperature, the substrate was cleaned with acetonitrile, and dried at 60 °C for 30 min, yielding the crystalline and oriented Py-2T as a red thin film.

Py-4T$_{Et}$ thin film

1,3,6,8-tetrakis(4-aminophenyl)pyrene dioxane adduct (Py; 14.0 mg, 20 µmol, 1.0 eq.) and 3,3"-diethyl-[2,2':5',5":2",2"'-quaterthiophene]-5,5"'-dicarbaldehyde (a4T$_{Et}$; 17 mg, 40 µmol, 2.0 eq.) were filled into a glass container, followed by the addition of mesitylene (1333 µl), benzyl alcohol (667 µl) and 6 M acetic acid (150 µL). The quartz substrate was placed in the reaction solution and the glass vessel was sealed and heated at 120 °C for 1 d. After cooling to room temperature, the substrate was cleaned with acetonitrile, and dried at 60 °C for 30 min, yielding the crystalline and oriented Py-4T$_{Et}$ as a red thin film.

Amorphous thin films of Py-4T, Py-4T$_{Me}$, Py-4T$_{Bu}$

1,3,6,8-tetrakis(4-aminophenyl)pyrene dioxane adduct (Py; 10.5 mg, 15 µmol, 1.0 eq.) and the corresponding quaterthiophene-dicarbaldehyde (4T, 4T$_{Me}$, 4T$_{Bu}$; 40 µmol, 2.0 eq.) were filled into a glass container, followed by the addition of mesitylene (1333 µl), benzyl alcohol (667 µl) and 6 M acetic acid (150 µL). The quartz substrate was placed in the reaction solution and the glass vessel was sealed and heated at 120 °C for 1-3 d. Extensive screening of the parameters did not yield a crystalline material yet, but resulted in amorphous Py-4T/-4T$_{Me}$/-4T$_{Bu}$ thin films.

6.5.4 NMR Spectroscopy

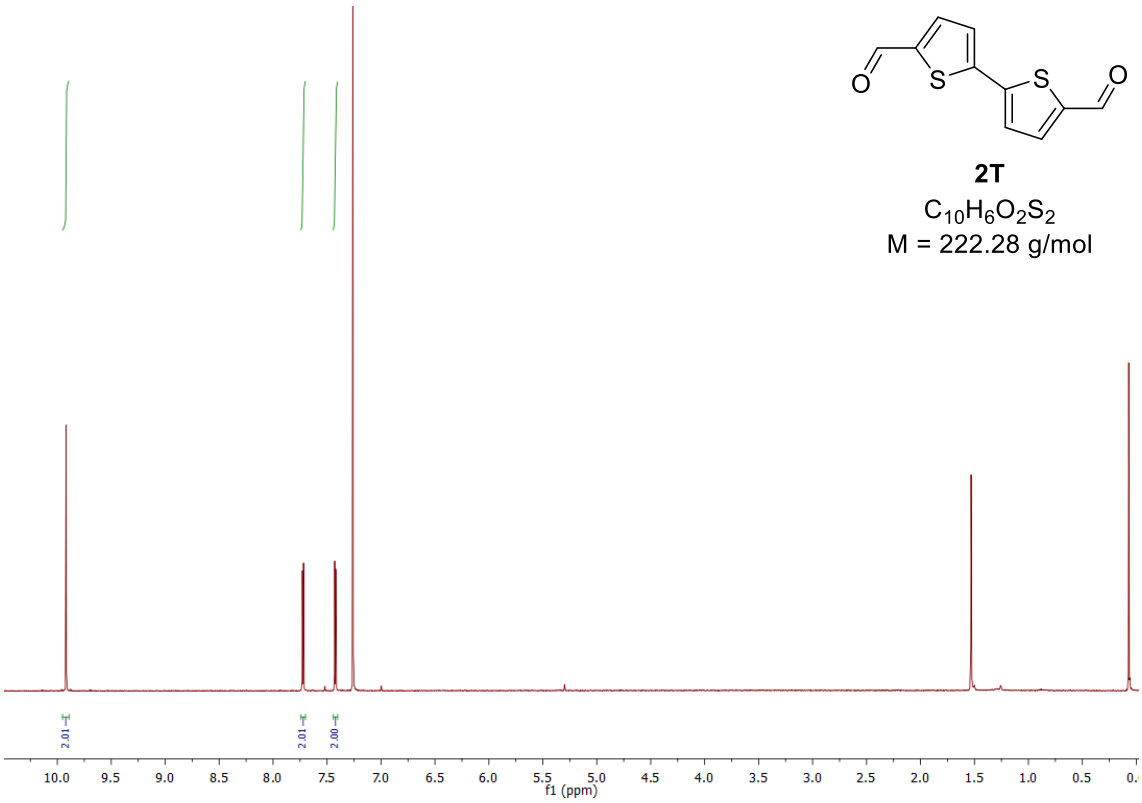

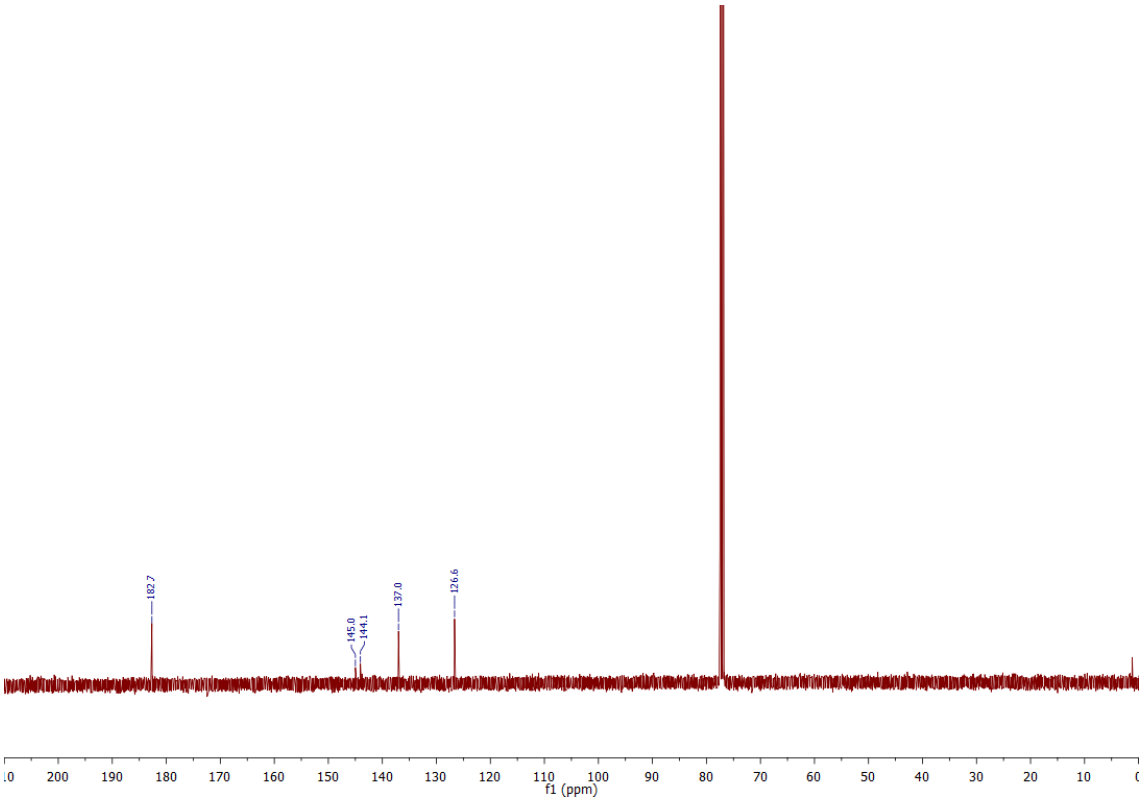

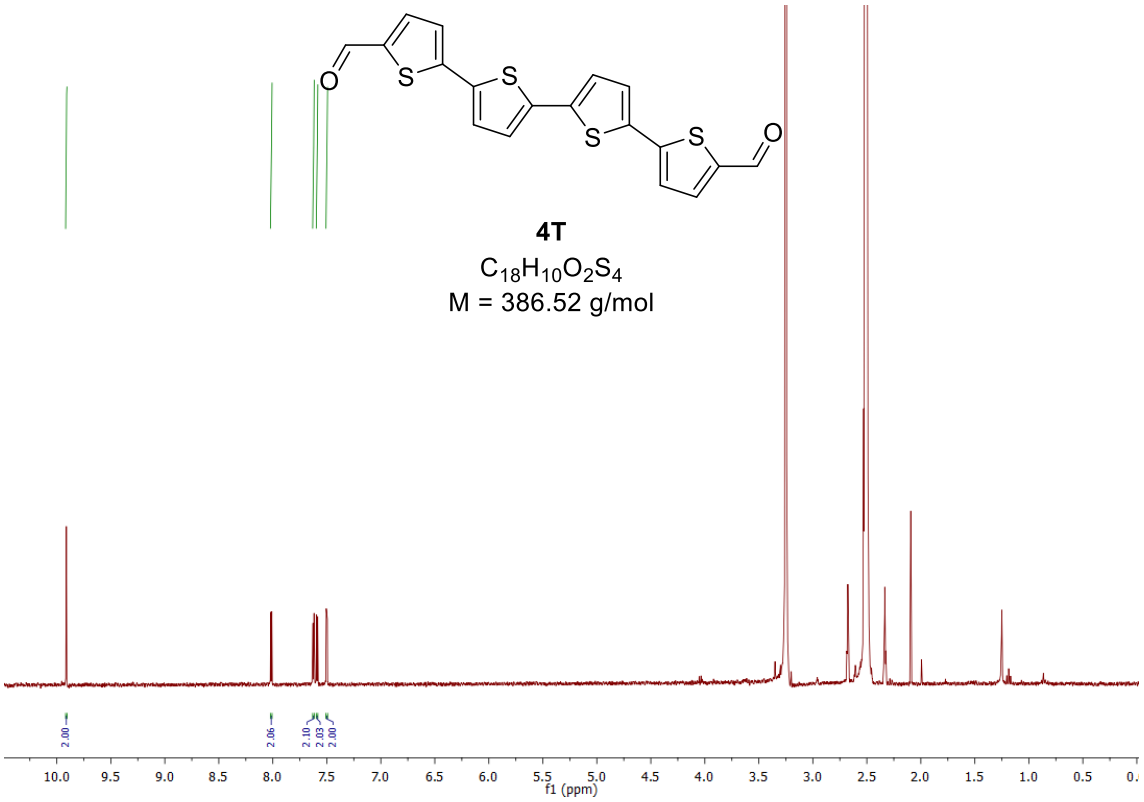
O
S
S
S
S
O
4T
C18H10O2S4
M = 386.52 g/mol
2.00
2.06
2.10
2.03
2.00
10.0
9.5
9.0
8.5
8.0
7.5
7.0
6.5
6.0
5.5
5.0
4.5
4.0
3.5
3.0
2.5
2.0
1.5
1.0
0.5
f1 (ppm)

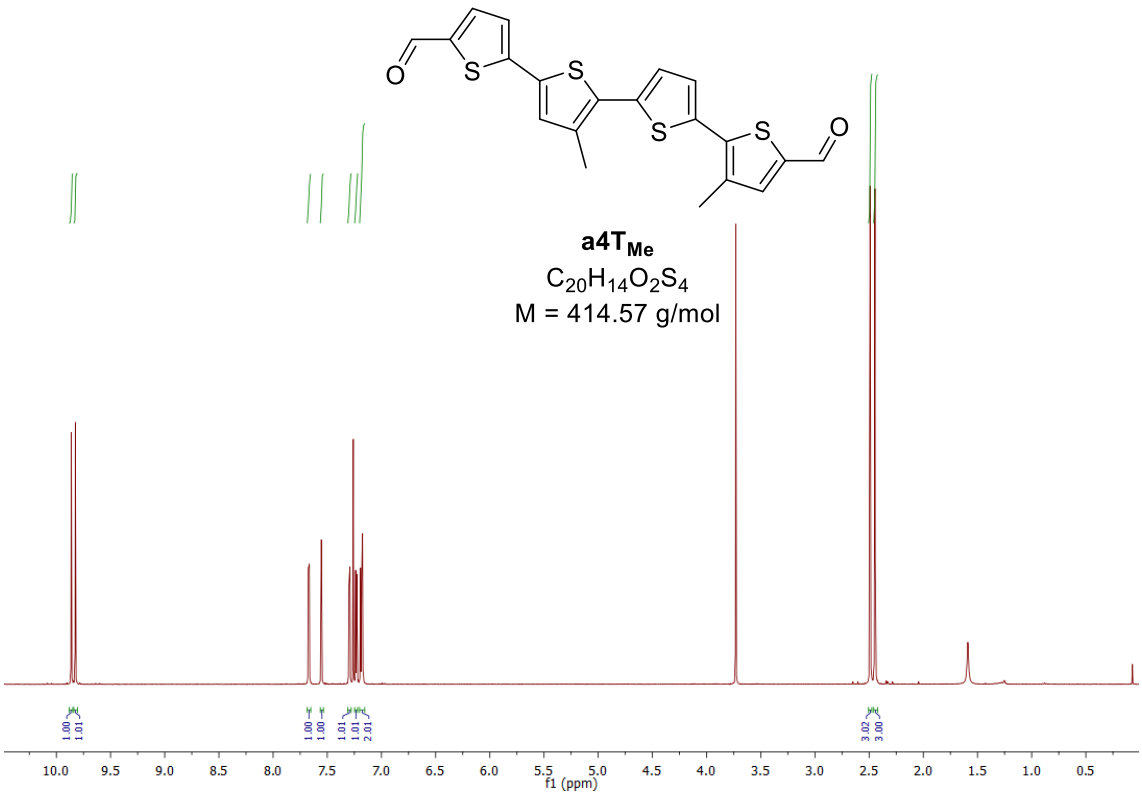
O
S
S
S
S
O
a4T$_{Me}$
$C_{20}H_{14}O_2S_4$
M = 414.57 g/mol
1.00
1.01
1.00
1.00
1.01
1.01
2.01
3.02
3.00
10.0
9.5
9.0
8.5
8.0
7.5
7.0
6.5
6.0
5.5
5.0
4.5
4.0
3.5
3.0
2.5
2.0
1.5
1.0
0.5
f1 (ppm)

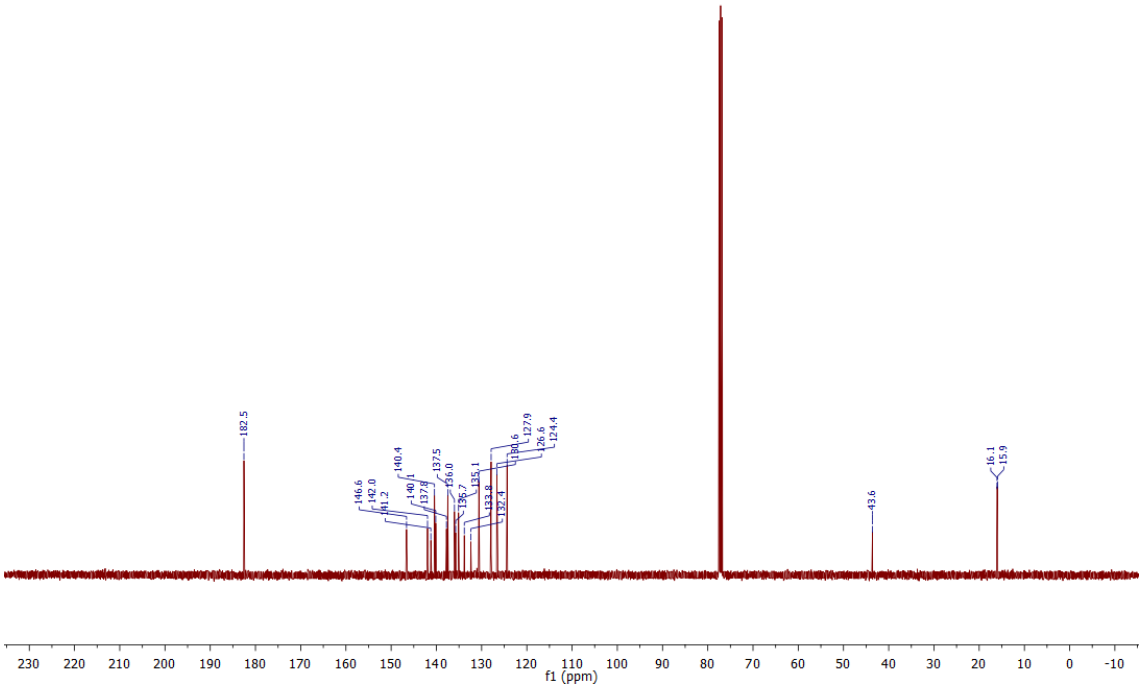
182.5
146.6
142.0
141.2
140.4
140.1
137.8
137.5
136.0
136.7
135.1
133.8
132.4
130.6
127.9
126.6
124.4
43.6
16.1
15.9
230
220
210
200
190
180
170
160
150
140
130
120
110
100
90
80
70
60
50
40
30
20
10
0
-10
f1 (ppm)

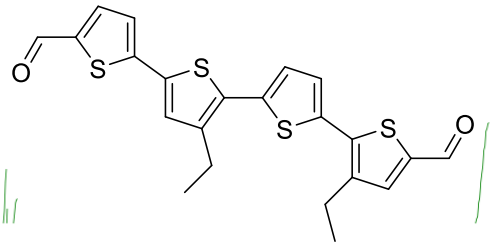

a4T$_{Et}$

$C_{22}H_{18}O_2S_4$

M = 442.62 g/mol

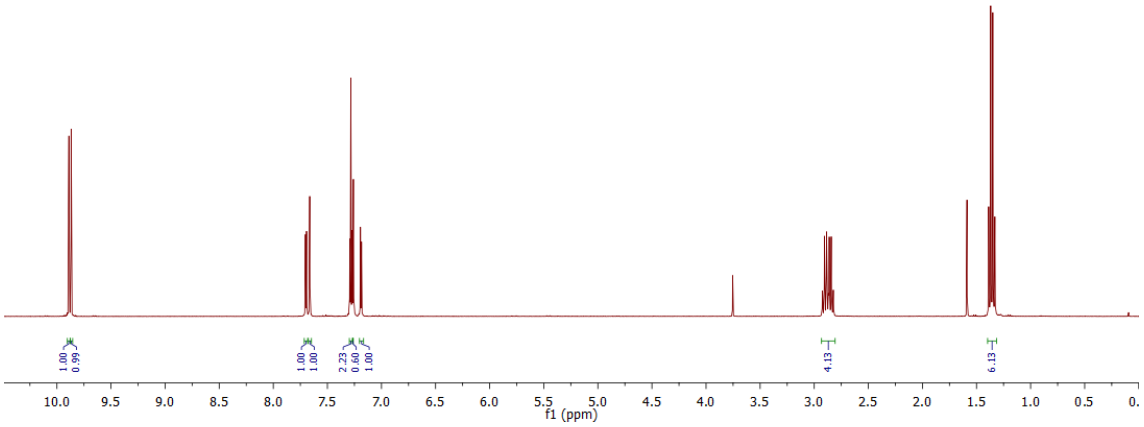

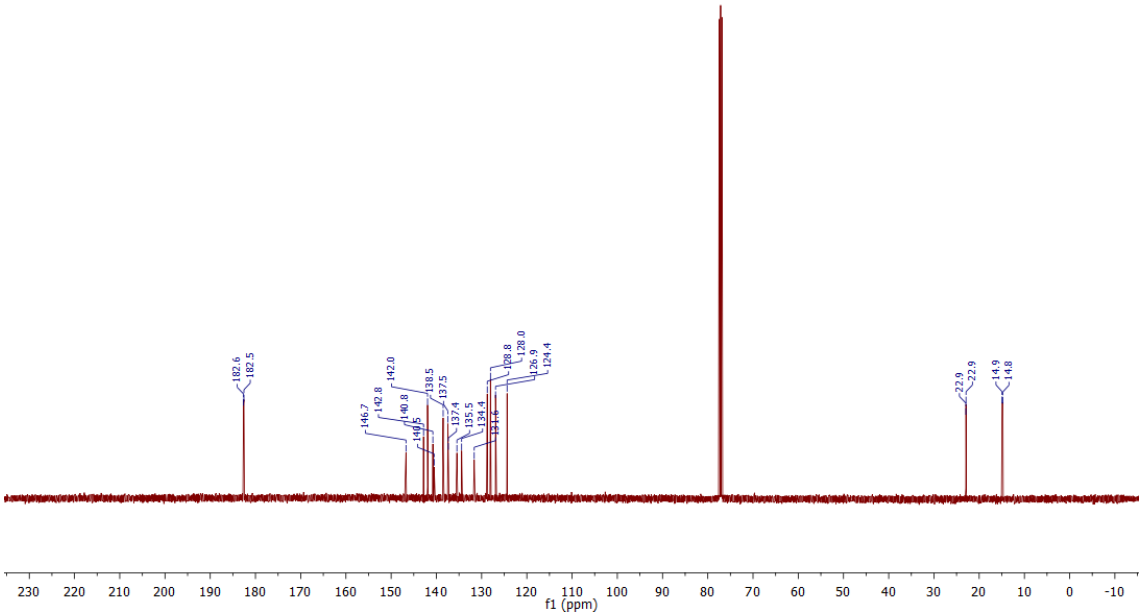

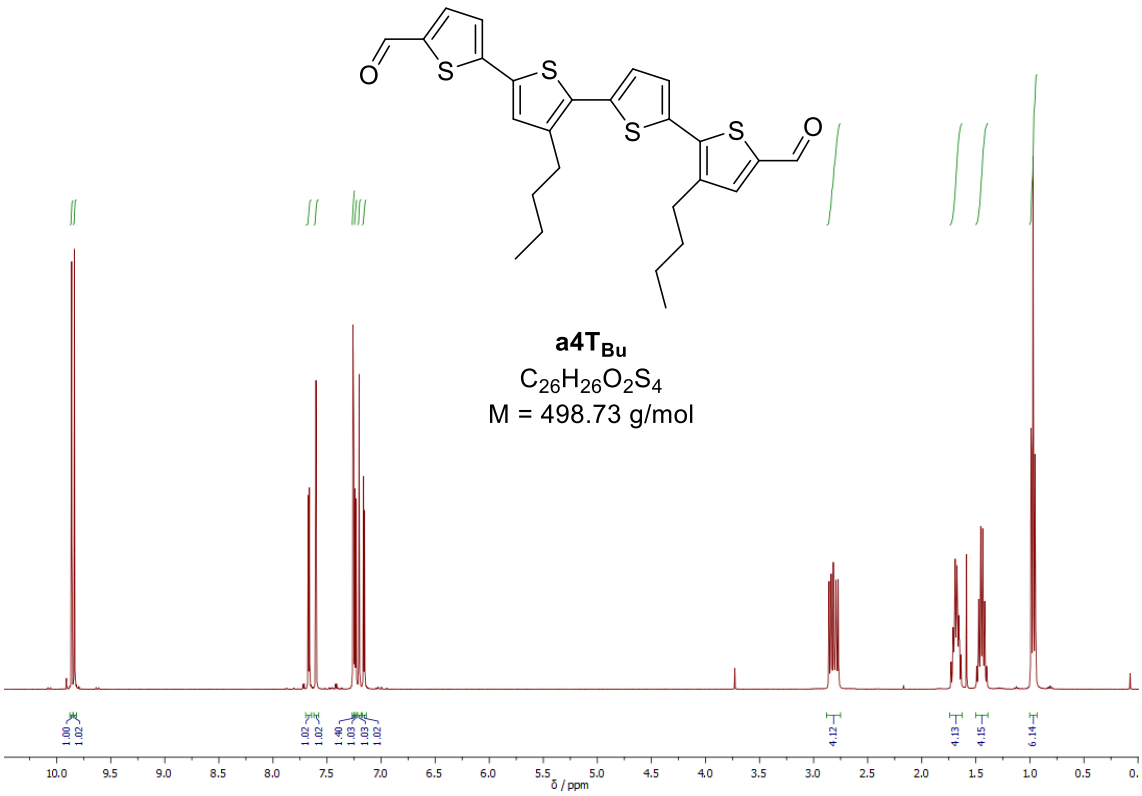
O
S
S
S
S
O
a4T$_{Bu}$
C$_{26}$H$_{26}$O$_2$S$_4$
M = 498.73 g/mol
1.00
1.02
1.02
1.02
1.40
1.03
1.03
1.02
4.12
4.13
4.15
6.14
10.0
9.5
9.0
8.5
8.0
7.5
7.0
6.5
6.0
5.5
5.0
4.5
4.0
3.5
3.0
2.5
2.0
1.5
1.0
0.5
δ / ppm

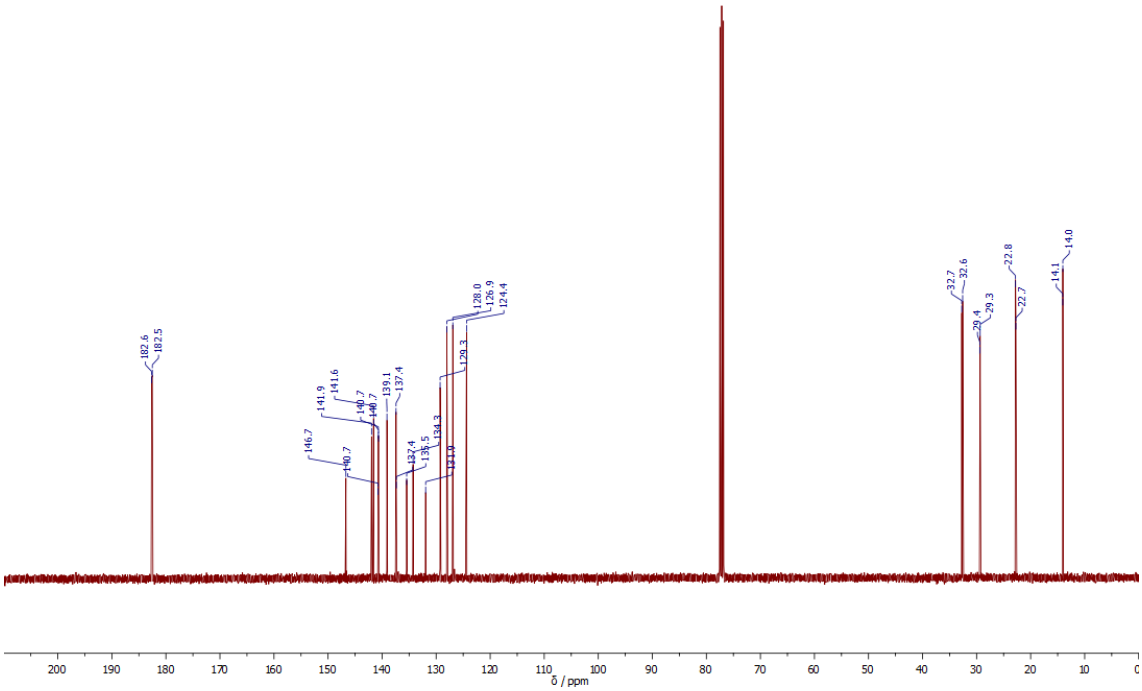
182.6
182.5
146.7
141.9
141.6
140.7
140.7
140.7
139.1
137.4
137.4
136.5
134.3
132.0
129.3
128.0
126.9
124.4
32.7
32.6
29.4
29.3
22.8
22.7
14.1
14.0
200
190
180
170
160
150
140
130
120
110
100
90
80
70
60
50
40
30
20
10
δ / ppm

Py

$C_{40}H_{30}N_4$

M = 566.71 g/mol

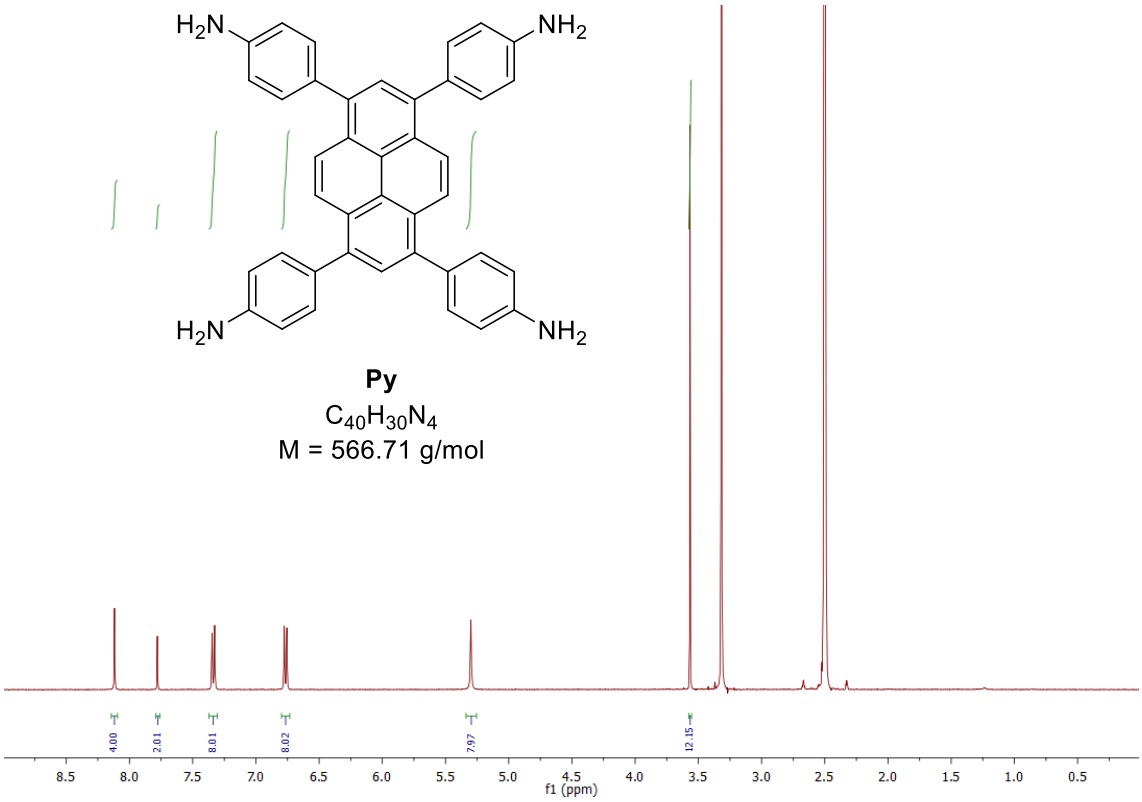

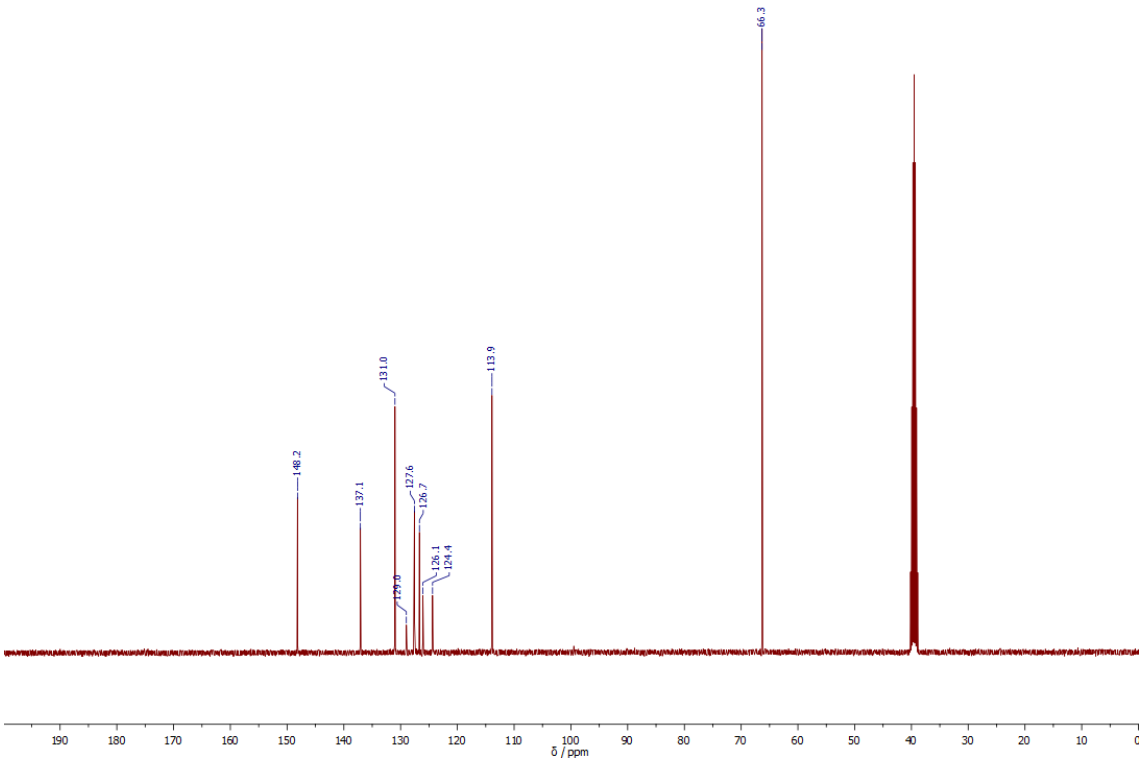

6.5.5 X-Ray Diffraction

It has to be noted that the oligothiophenes twist with the same angle as the phenylene of the pyrene core. This results in a planar bridge between adjacent pyrene knots.

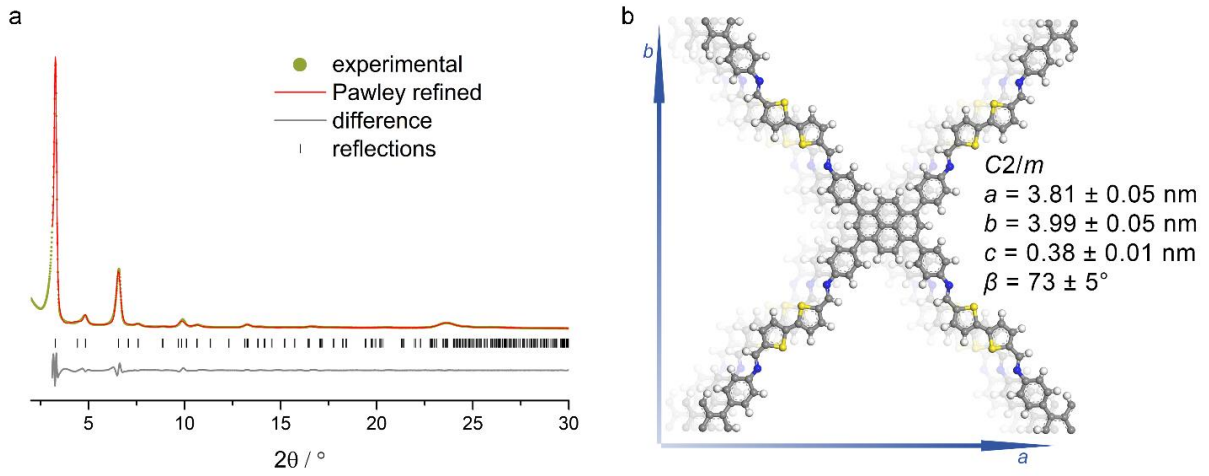

Figure 6.8: (a) Experimental PXRD data (light green dots) of Py-2T COF. Pawley refinement (red line) using the *C*2/*m* symmetric structure model shown in (b) provides a very good fit to the experimental pattern with only minimal differences (grey line: difference between experimental and refined patterns; R_{wp} = 8.2%, R_p = 6.3%). Bragg positions are indicated with black ticks.

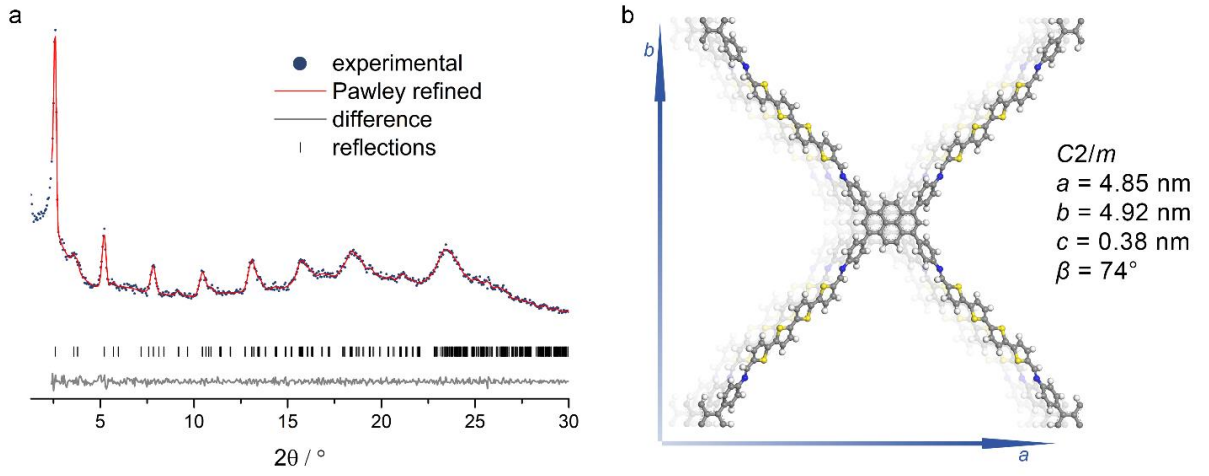

Figure 6.9: (a) Experimental PXRD data (blue dots) of Py-4T COF. Pawley refinement (red line) using the *C*2/*m* symmetric structure model shown in (b) provides a very good fit to the experimental pattern with only minimal differences (grey line: difference between experimental and refined patterns; R_{wp} = 3.5%, R_p = 2.8%). Bragg positions are indicated with black ticks.

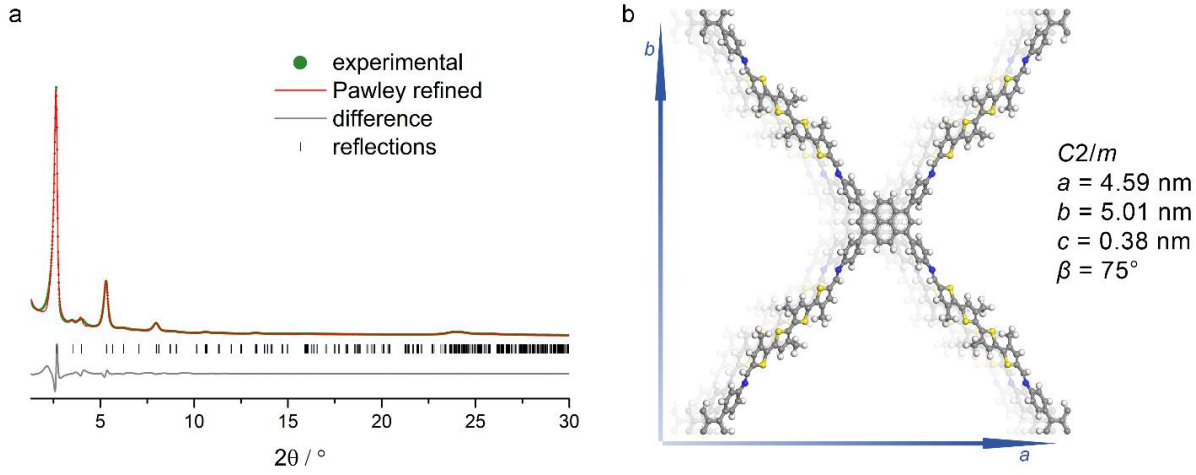

Figure 6.10: (a) Experimental PXRD data (green dots) of Py-4T$_{Me}$ COF. Pawley refinement (red line) using the *C*2/*m* symmetric structure model shown in (b) provides a very good fit to the experimental pattern with only minimal differences (grey line: difference between experimental and refined patterns; R_{wp} = 10.2%, R_p = 12.5%). Bragg positions are indicated with black ticks. The methyl groups of the a4T$_{Me}$ building block were treated in the refinement as a superposition of both possible orientations with 50% occupancy each (both shown in the figure).

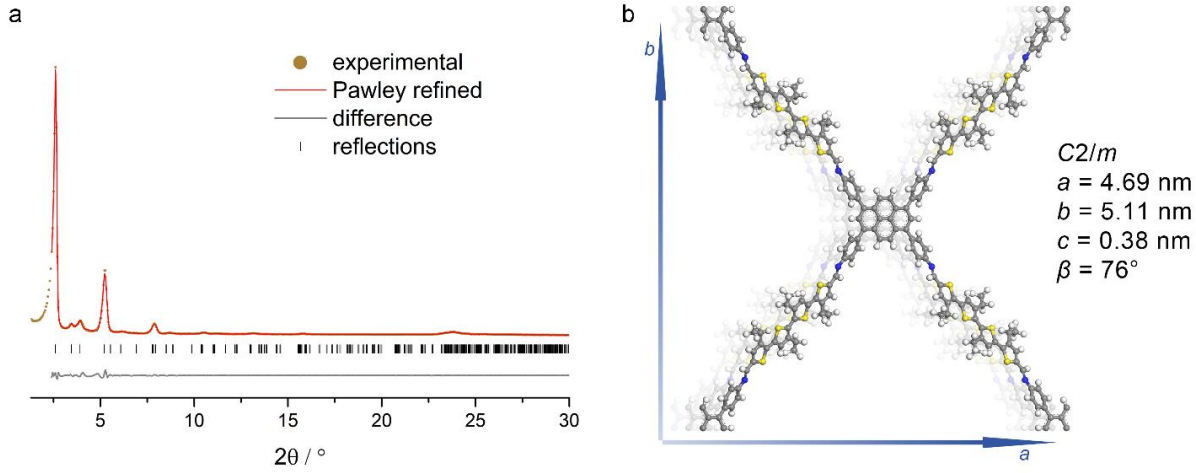

Figure 6.11: (a) Experimental PXRD data (brown dots) of Py-4T$_{Et}$ COF. Pawley refinement (red line) using the *C*2/*m* symmetric structure model shown in (b) provides a very good fit to the experimental pattern with only minimal differences (grey line: difference between experimental and refined patterns; R_{wp} = 5.8%, R_p = 3.9%). Bragg positions are indicated with black ticks. The alkyl chains of the a4T$_{Et}$ building block were treated in the refinement as a superposition of both possible orientations with 50% occupancy each (both shown in the figure).

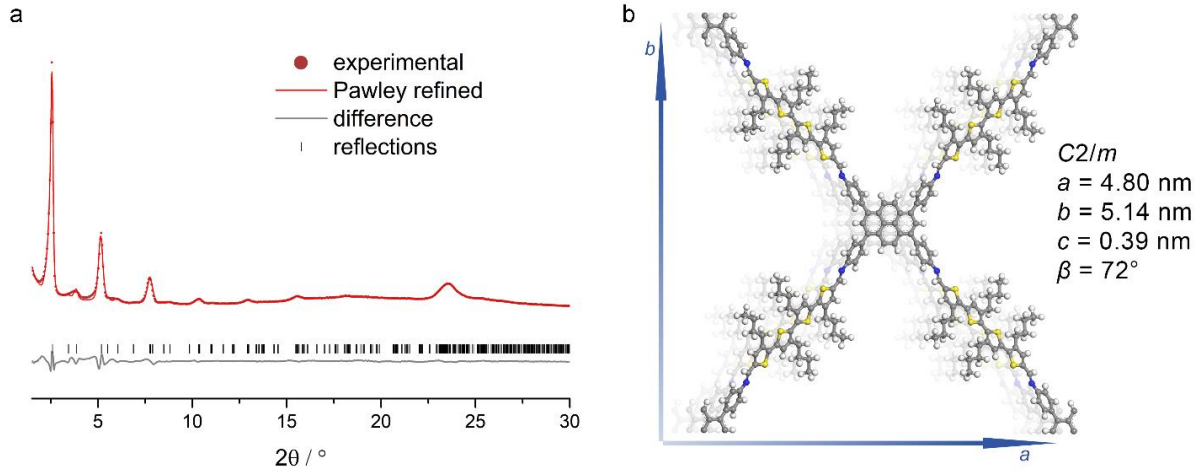

Figure 6.12: (a) Experimental PXRD data (red dots) of Py-4T$_{Bu}$ COF. Pawley refinement (red line) using the *C*2/*m* symmetric structure model shown in (b) provides a very good fit to the experimental pattern with only minimal differences (grey line: difference between experimental and refined patterns; R_{wp} = 7.5%, R_p = 13.4%). Bragg positions are indicated with black ticks. The alkyl chains of the a4T$_{Bu}$ building block were treated in the refinement as a superposition of both possible orientations with 50% occupancy each (both shown in the figure).

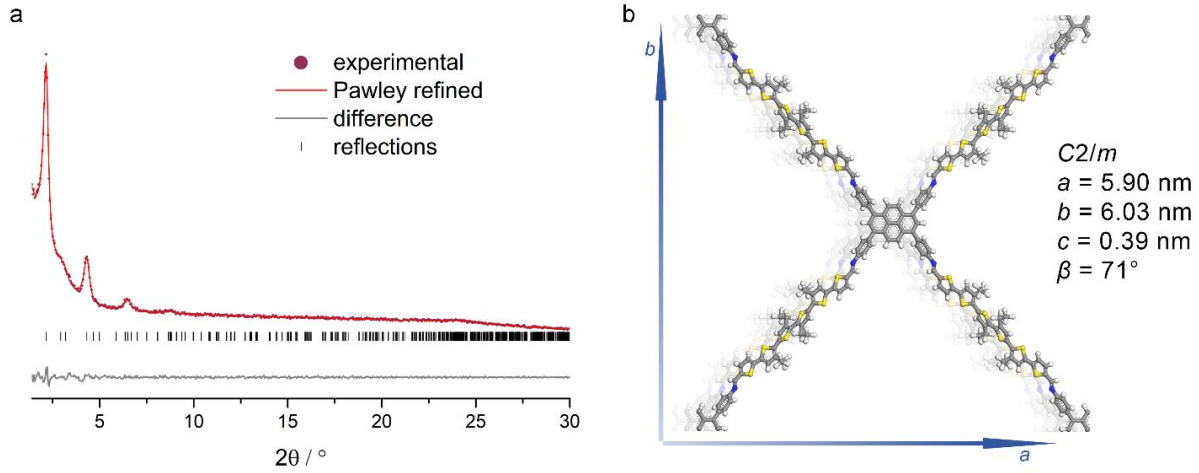

Figure 6.13: (a) Experimental PXRD data (dark red dots) of Py-6T$_{Et}$ COF. Pawley refinement (red line) using the *C*2/*m* symmetric structure model shown in (b) provides a very good fit to the experimental pattern with only minimal differences (grey line: difference between experimental and refined patterns; R_{wp} = 3.2%, R_p = 2.6%). Bragg positions are indicated with black ticks. The alkyl chains of the a6T$_{Et}$ building block were treated in the refinement as a superposition of both possible orientations with 50% occupancy each (both shown in the figure).

Table 6.1: Lattice parameter *c* which represents the stacking distance from Pawley refined structures.

	Lattice parameter *c* in Å
Py-2T	3.78
Py-4T	3.82
Py-4T$_{Me}$	3.82
Py-4T$_{Et}$	3.82
Py-4T$_{Bu}$	3.88
Py-6T$_{Et}$	3.90

6.5.6 UV-vis and Fluorescence Spectroscopy

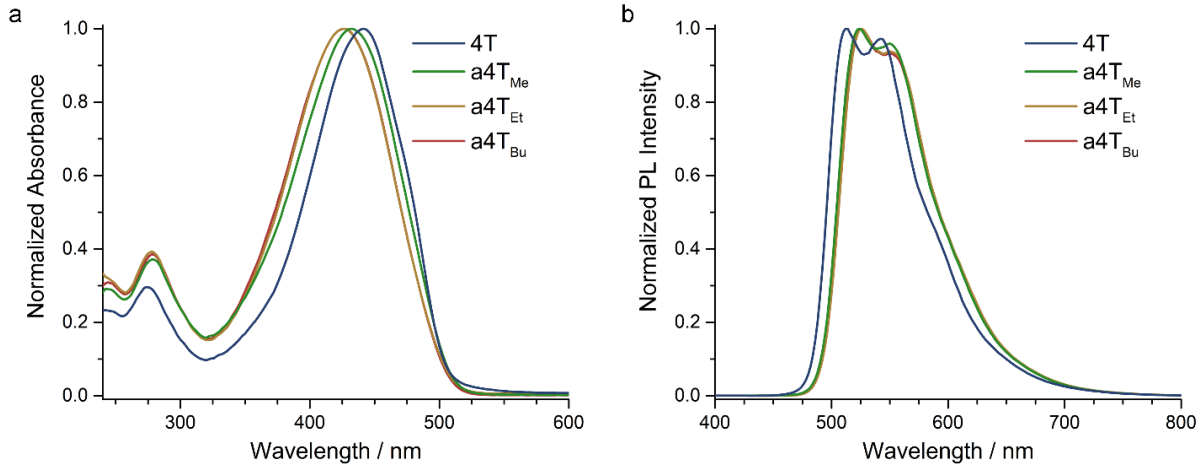

Figure 6.14: (a) Optical absorption spectra and (b) PL (λ_{exc} = 378 nm) spectra of the 4T monomers measured in solution (50 µM in $CHCl_3$).

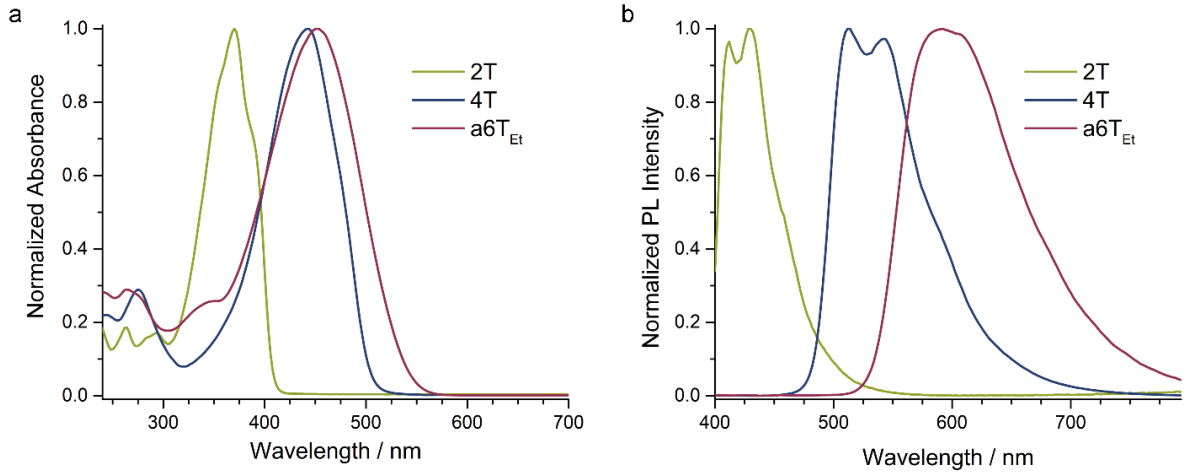

Figure 6.15: (a) Optical absorption spectra and (b) PL (λ_{exc} = 378 nm) spectra of 2T, 4T and a6T$_{Et}$ monomers measured in solution (50 µM in $CHCl_3$).

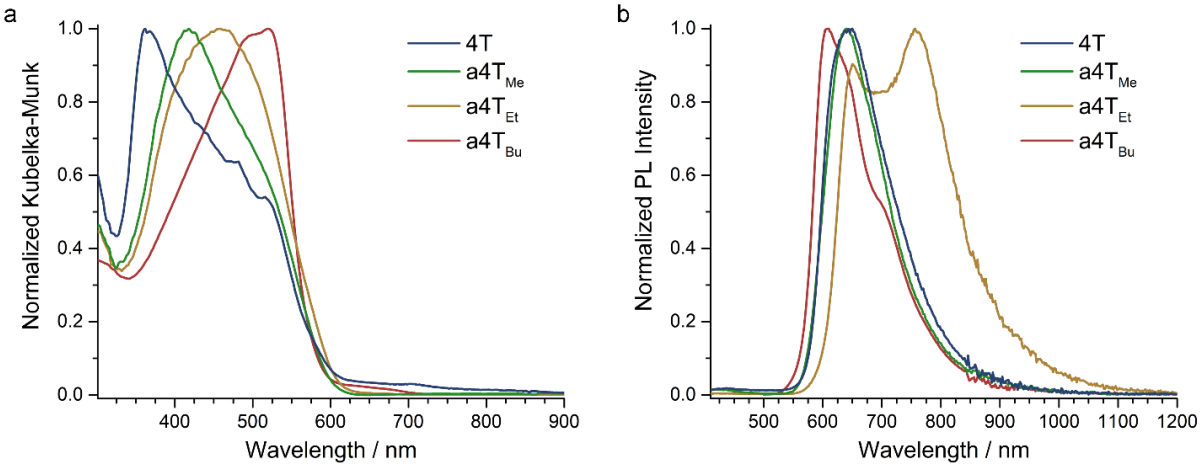

Figure 6.16: (a) Optical absorption spectra and (b) PL (λ_{exc} = 378 nm) spectra of the 4T monomers measured as solids. Diffuse reflectance spectra measured for the respective powders dispersed in $BaSO_4$.

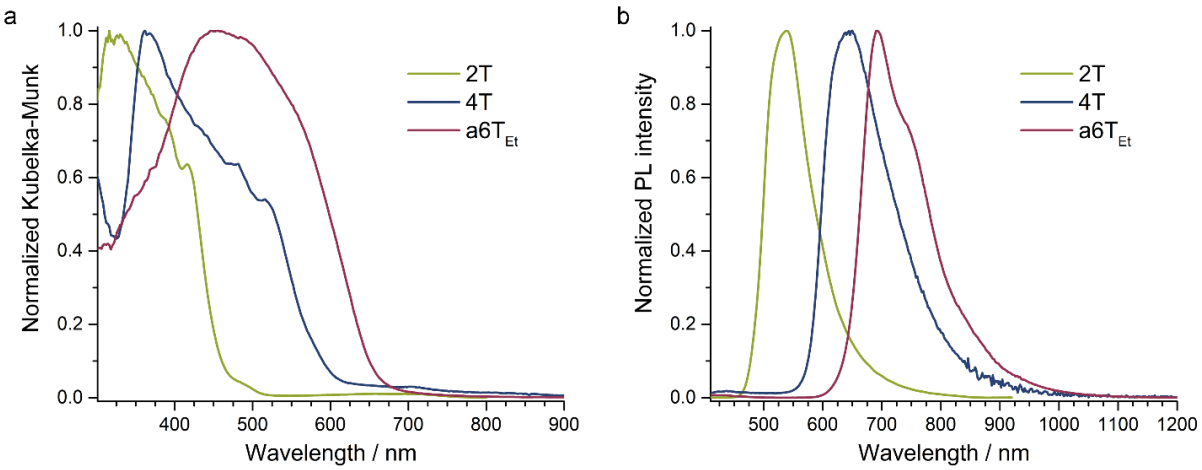

Figure 6.17: (a) Optical absorption spectra and (b) PL (λ_{exc} = 378 nm) spectra of 2T, 4T and a6T$_{Et}$ monomers measured as solids. Diffuse reflectance spectra measured for the respective powders dispersed in $BaSO_4$.

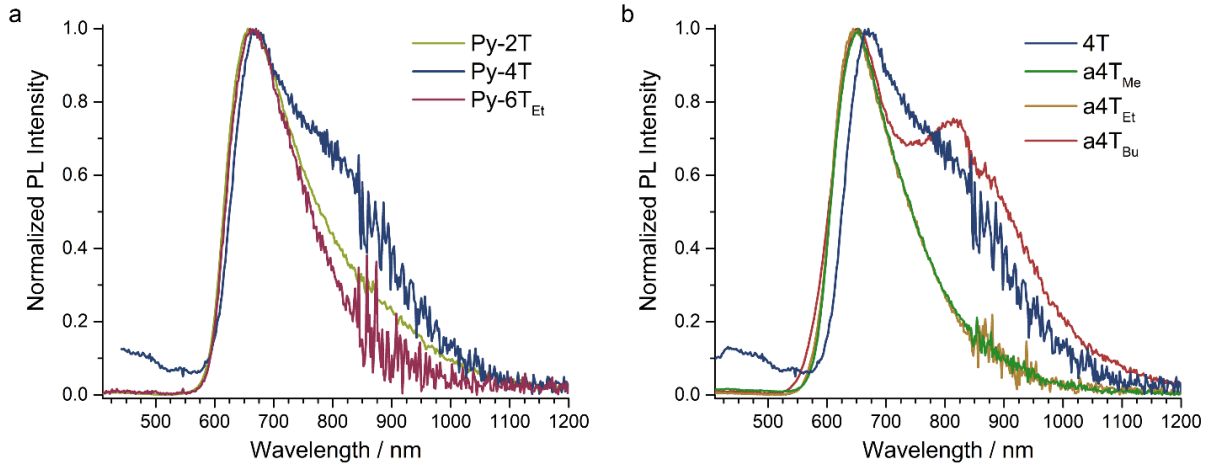

Figure 6.18: Photoluminescence spectra of the oligothiophene-based COF series (a,b) measured as solids under inert conditions and excited with an 365 nm LED (detector change at 860 nm).

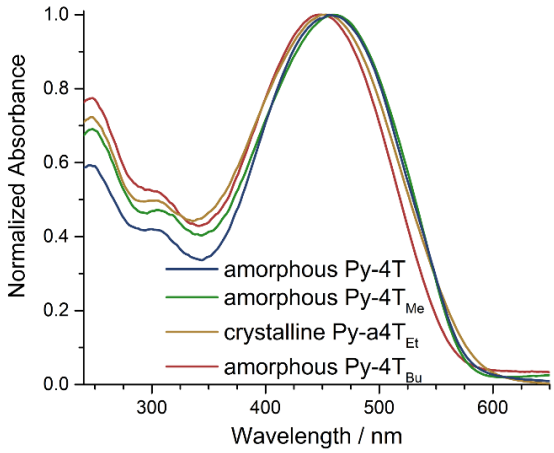

Figure 6.19: Optical absorption spectra of thin films of the 4T COF series. Since extensive screening did not result in crystalline and oriented thin films for all COFs, the spectra of Py-4T, Py-4T$_{Me}$ and Py-4T$_{Bu}$ were recorded from amorphous films. The similarity between the spectra for crystalline and amorphous frameworks is evident and could indicate that the absorption behavior in this series mainly depends on the short-range order in the framework.

6.5.7 Time-Correlated Single Photon Counting

Table 6.2: PL decay times of Py-2T shown in Figure 6.7 (bulk material). The given errors are uncertainties from the fit and hence do not reflect the real time-resolution of the setup. The latter is limited by the laser pulse duration of around 100 ps.

	τ / ns	error / ns	fractional intensity / %
τ_1	4.06	±0.16	13
τ_2	0.74	±0.01	52
τ_3	0.12	±0.003	35

Table 6.3: PL decay times of Py-4T shown in Figure 6.7 (bulk material). The given errors are uncertainties from the fit and hence do not reflect the real time-resolution of the setup. The latter is limited by the laser pulse duration of around 100 ps.

	τ / ns	error / ns	fractional intensity / %
τ_1	5.72	±0.39	9
τ_2	0.90	±0.01	55
τ_3	0.17	±0.004	36

Table 6.4: PL decay times of Py-4T_{Me} shown in Figure 6.7 (bulk material). The given errors are uncertainties from the fit and hence do not reflect the real time-resolution of the setup. The latter is limited by the laser pulse duration of around 100 ps.

	τ / ns	error / ns	fractional intensity / %
τ_1	3.78	±0.33	5
τ_2	0.68	±0.01	43
τ_3	0.10	±0.002	52

Table 6.5: PL decay times of Py-4T_{Et} shown in Figure 6.7 (bulk material). The given errors are uncertainties from the fit and hence do not reflect the real time-resolution of the setup. The latter is limited by the laser pulse duration of around 100 ps.

	τ / ns	error / ns	fractional intensity / %
τ_1	0.89	±0.02	33
τ_2	0.16	±0.003	67

Table 6.6: PL decay times of Py-4T_{Bu} shown in Figure 6.7 (bulk material). The given errors are uncertainties from the fit and hence do not reflect the real time-resolution of the setup. The latter is limited by the laser pulse duration of around 100 ps.

	τ / ns	error / ns	fractional intensity / %
τ_1	0.81	±0.04	56
τ_2	0.10	±0.007	44

Table 6.7: PL decay times of Py-6T_{Et} shown in Figure 6.7 (bulk material). The given errors are uncertainties from the fit and hence do not reflect the real time-resolution of the setup. The latter is limited by the laser pulse duration of around 100 ps.

	τ / ns	error / ns	fractional intensity / %
τ_1	6.80	±1.36	6
τ_2	0.89	±0.02	61
τ_3	0.13	±0.006	33

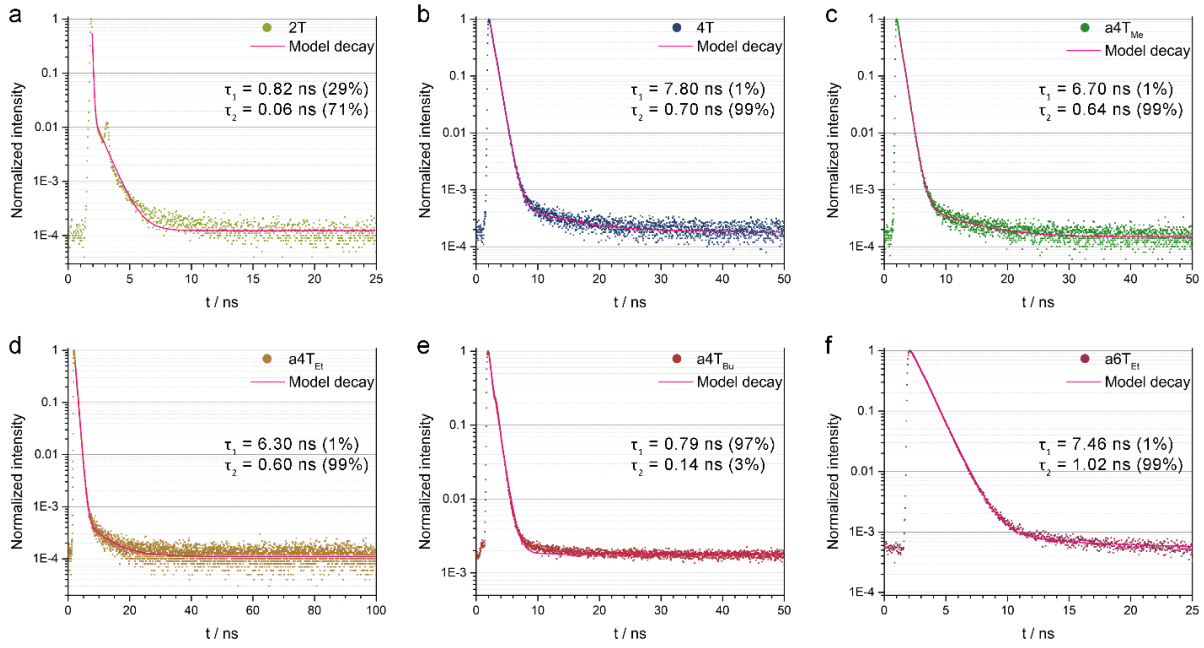

Figure 6.20: PL decay histograms of the monomers measured in solution (50 µM in $CHCl_3$). Excitation at 378 nm and emission recorded at the respective emission maximum. (a) 2T: emission at 430 nm. (b) 4T: emission at 512 nm. (c) $a4T_{Me}$: emission at 524 nm. (d) $a4T_{Et}$: emission at 526 nm. (e) $a4T_{Bu}$: emission at 525 nm. (f) $a6T_{Et}$: emission at 590 nm. Experimental decay: dots in respective color shown, bi-exponential fit of the decay: pink line.

Table 6.8: PL decay times of 2T shown above (monomers measured in solution). The given errors are uncertainties from the fit and hence do not reflect the real time-resolution of the setup. The latter is limited by the laser pulse duration of around 100 ps.

	τ / ns	error / ns	fractional intensity / %
τ_1	0.82	±0.04	29
τ_2	0.06	±0.002	71

Table 6.9: PL decay times of 4T shown above (monomers measured in solution). The given errors are uncertainties from the fit and hence do not reflect the real time-resolution of the setup. The latter is limited by the laser pulse duration of around 100 ps.

	τ / ns	error / ns	fractional intensity / %
τ_1	7.80	±0.8	1
τ_2	0.70	±0.003	99

Table 6.10: PL decay times of $a4T_{Me}$ shown above (monomers measured in solution). The given errors are uncertainties from the fit and hence do not reflect the real time-resolution of the setup. The latter is limited by the laser pulse duration of around 100 ps.

	τ / ns	error / ns	fractional intensity / %
τ_1	6.70	±0.6	1
τ_2	0.64	±0.003	99

Table 6.11: PL decay times of $a4T_{Et}$ shown above (monomers measured in solution). The given errors are uncertainties from the fit and hence do not reflect the real time-resolution of the setup. The latter is limited by the laser pulse duration of around 100 ps.

	τ / ns	error / ns	fractional intensity / %
τ_1	6.30	±0.7	1
τ_2	0.60	±0.004	99

Table 6.12: PL decay times of $a4T_{Bu}$ shown above (monomers measured in solution). The given errors are uncertainties from the fit and hence do not reflect the real time-resolution of the setup. The latter is limited by the laser pulse duration of around 100 ps.

	τ / ns	error / ns	fractional intensity / %
τ_1	0.79	±0.008	97
τ_2	0.14	±0.05	3

Table 6.13: PL decay times of $a6T_{Bu}$ shown above (monomers measured in solution). The given errors are uncertainties from the fit and hence do not reflect the real time-resolution of the setup. The latter is limited by the laser pulse duration of around 100 ps.

	τ / ns	error / ns	fractional intensity / %
τ_1	7.46	±1.0	1
τ_2	1.02	±0.003	99

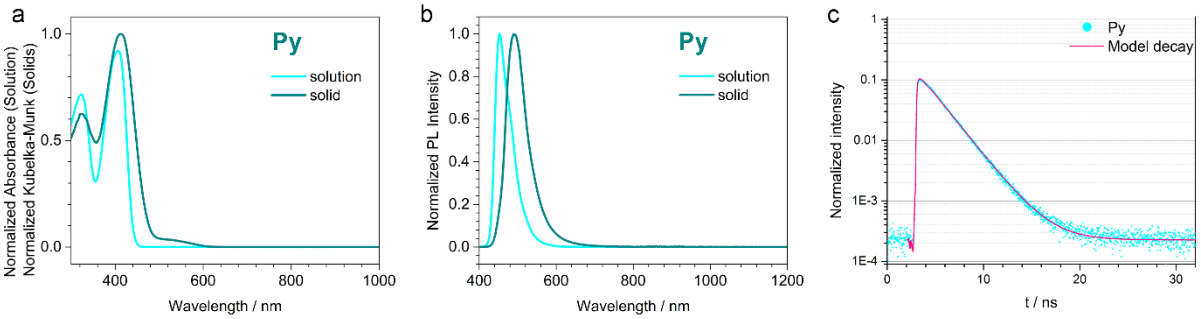

Figure 6.21: (a) Optical absorption spectra and (b) PL (λ_{exc} = 378 nm) spectra of the Py monomer measured in solution (50 µM in $CHCl_3$) and as solid. (c) PL decay histograms of Py measured in solution (50 µM in $CHCl_3$). Excitation at 378 nm and emission recorded at the emission maximum (455 nm). Experimental decay: dots in respective color, mono-exponential fit of the decay: pink line.

Table 6.14: PL decay time of Py shown above (monomers measured in solution). The given errors are uncertainties from the fit and hence do not reflect the real time-resolution of the setup. The latter is limited by the laser pulse duration of around 100 ps.

	τ / ns	error / ns	fractional intensity / %
τ_1	2.17	±0.01	100

6.5.8 Electron Microscopy

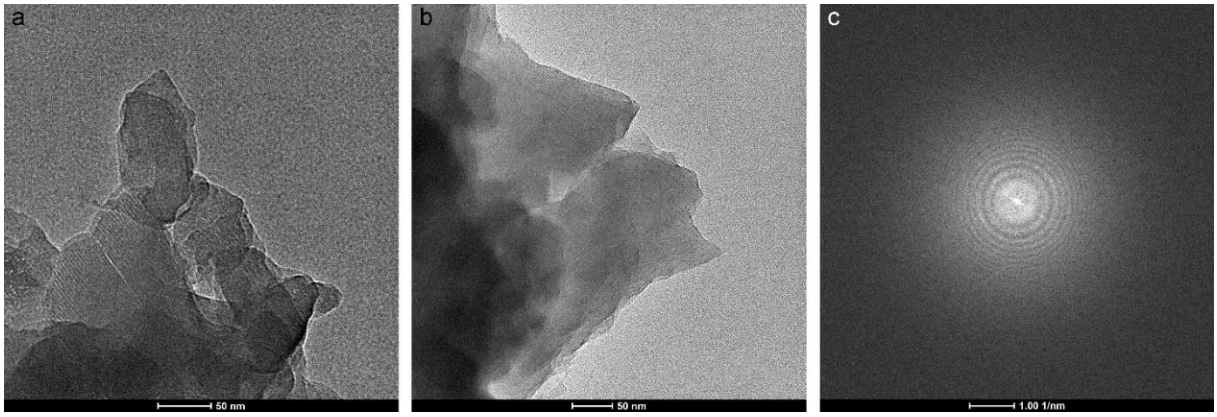

Figure 6.22: (a)-(b) Selection of TEM micrographs of Py-4T. (c) Fast Fourier transformation (FFT) from region depicted in (b).

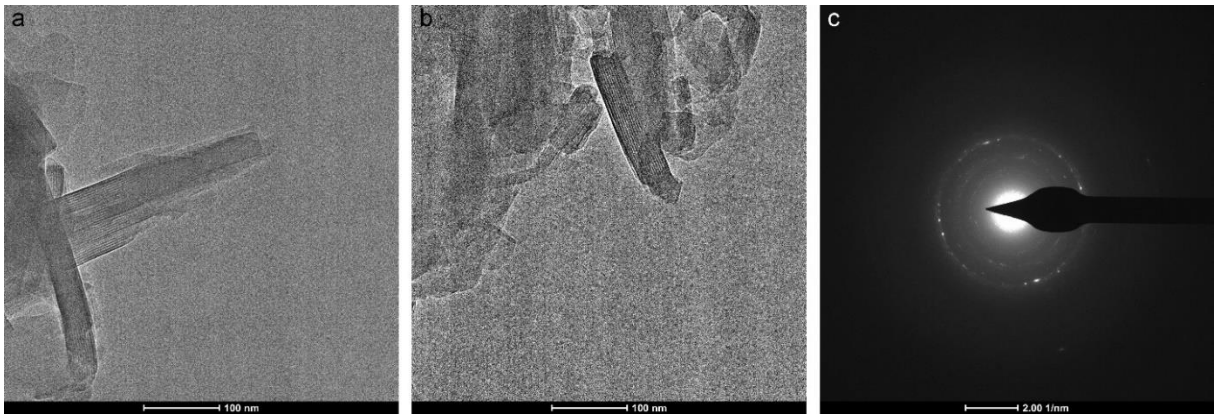

Figure 6.23: (a)-(b) Selection of TEM micrographs of Py-4T$_{Et}$. (c) Electron diffraction pattern of several Py-4T$_{Et}$ COF single crystals with distinct reflection spots.

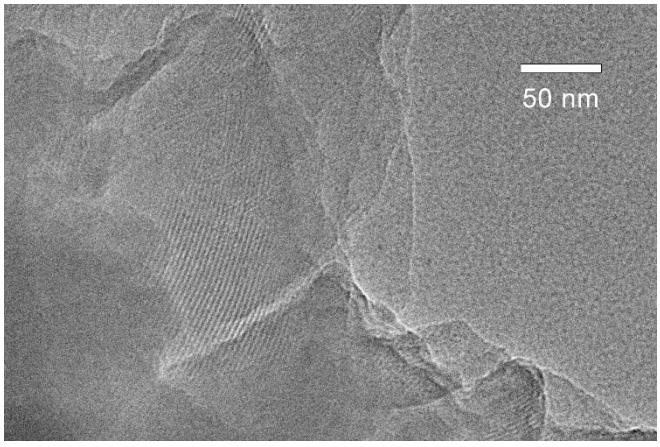

Figure 6.24: TEM image of Py-4T$_{Bu}$.

6.5.9 Nitrogen Sorption

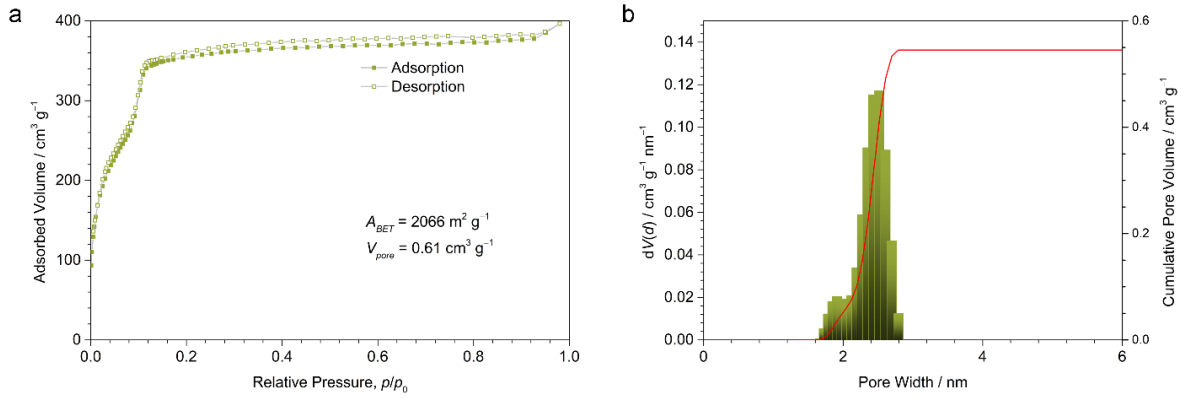

Figure 6.25: (a) Nitrogen sorption isotherms of Py-2T COF recorded at 77 K. (b) QSDFT calculation using the adsorption branch and desorption branch yields a pore size distribution with the maximum at 2.5 nm with a tail to smaller pore width, in excellent agreement with the pore diagonal of 2.47 nm in the Py-2T structure.

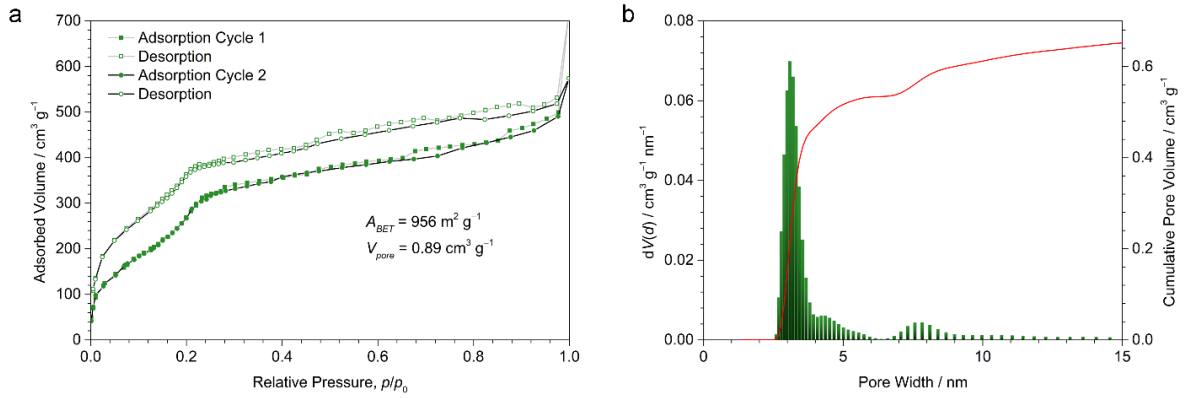

Figure 6.26: (a) Nitrogen sorption isotherms of Py-4T$_{Me}$ COF recorded at 77 K. Two adsorption-desorption cycles were recorded using the same sample to test the stability of the framework. (b) QSDFT calculation using the adsorption branch yields a narrow pore size distribution with a maximum at 3.1 nm, in excellent agreement with the pore diagonal of 3.06 nm in the Py-4T$_{Me}$ structure.

The other oligothiophene-bridged COFs from the series were also investigated with nitrogen sorption but it was not possible to generate reproducible data from these experiments. These issues have been observed in previous reports on oligothiophene-based COFs and are attributed to the fragile bridges bearing longer alkyl chains which seem to have a tendency to deform as a response to the adsorption of probe molecules during the nitrogen sorption experiments, leading to inconsistent isotherms.[4] Similarly, for the Py-4T COF without any alkyl chain modification, nitrogen sorption analysis did not produce reliable data. This can be also attributed to the interaction between the COF material and guest molecules, which can also be

observed after extraction with supercritical CO_2 leading to the loss of crystallinity and long-range order.

6.5.10 References

[1] Yang, J.; Liu, S.; Zheng, J.-F.; Zhou, J., Room-Temperature Suzuki–Miyaura Coupling of Heteroaryl Chlorides and Tosylates. *Eur. J. Org. Chem.* **2012,** *2012* (31), 6248-6259.

[2] Jin, S.; Sakurai, T.; Kowalczyk, T.; Dalapati, S.; Xu, F.; Wei, H.; Chen, X.; Gao, J.; Seki, S.; Irle, S.; Jiang, D., Two-Dimensional Tetrathiafulvalene Covalent Organic Frameworks: Towards Latticed Conductive Organic Salts. *Chem. - Eur. J.* **2014,** *20* (45), 14608-14613.

[3] Auras, F.; Ascherl, L.; Hakimioun, A. H.; Margraf, J. T.; Hanusch, F. C.; Reuter, S.; Bessinger, D.; Döblinger, M.; Hettstedt, C.; Karaghiosoff, K.; Herbert, S.; Knochel, P.; Clark, T.; Bein, T., Synchronized Offset Stacking: A Concept for Growing Large-Domain and Highly Crystalline 2D Covalent Organic Frameworks. *J. Am. Chem. Soc.* **2016,** *138* (51), 16703-16710.

[4] Keller, N.; Bessinger, D.; Reuter, S.; Calik, M.; Ascherl, L.; Hanusch, F. C.; Auras, F.; Bein, T., Oligothiophene-Bridged Conjugated Covalent Organic Frameworks. *J. Am. Chem. Soc.* **2017,** *139* (24), 8194-8199.

7 Heavy Atom Effect by Selective Exchange of Atoms on Optoelectronic Properties in Covalent Organic Frameworks

Niklas Keller, Michael Beetz, Andreas C. Jakowetz, Thomas Bein, *to be submitted*.

Covalent organic frameworks have been subject of extensive studies on the way towards promising applications. However, fundamental and generalized design principles that can directly translate into tailoring optical properties are still desired. We have created a series of COFs based on [2,2'-bithiophene]-5,5'-dicarbaldehyde (2T), 3,3'-dibromo-[2,2'-bithiophene]-5,5'-dicarbaldehyde (3,3'-$2T_{Br}$) and 4,4'-dibromo-[2,2'-bithiophene]-5,5'-dicarbaldehyde (4,4'-$2T_{Br}$) as linear building blocks and connected via 1,3,6,8-tetrakis(4-aminophenyl)pyrene (Py) knots with precise modifications at the atomic level achieved through insertion of bromine, aimed at investigating the heavy atom effect in COFs. While conserving the overall structure (geometry, symmetry, framework topology) to a large degree, the optical properties could be tuned such that the brominated COFs exhibited extended and stabilized excited singlet lifetimes, which corresponds to the heavy atom effect implemented in the frameworks of the COFs through the modified molecular building blocks. This design principle is envisioned to provide a general method for constructing COFs with tunable optical properties while retaining almost identical structural frameworks.

7.1 Introduction

Covalent organic frameworks are built from light-weight elements such as hydrogen, boron, carbon, nitrogen and oxygen. These elements are also considered to exhibit low spin−orbit coupling – a phenomenon which increases with atomic number Z. Incorporating elements with high Z can lead to an amplification of otherwise spin-forbidden processes such as phosphorescence, which is called the heavy atom effect.[1] Incorporating the heavy atom into a molecule is refered to as internal heavy atom effect and a heavy atom in the proximity of a molecule is denoted as external heavy atom effect. A well-known example is the observation of two emissive sodium D-lines which occurs due to spin−orbit splitting also known as the Zeeman effect. Organic chromophores such as octaethylporphyrin exhibit a heavy atom effect when Pt is coordinated into the macrocycle. Thereby, the fluorescence quenches drastically to around 1 ps and the phosphorescence lifetime reaches 91 µs with an room-temperature (rt) efficiency of 0.5.[2] This behavior was also reported for chromophores containing bromine atoms by the group of Kim.[3] The rt phosphorescence efficiency reached 55% when 2,5-dihexyloxy-1,4-dibromobenzene was co-crystallized with 1 w% of 2,5-dihexyloxy-4-bromobenzaldehyde with an additional aldehyde group instead of the bromine. With an increased phosphorescence efficiency these materials could be envisioned applicable in light-emitting diodes (LEDs). To control the crystal environment of brominated chromophores and enforce specific aggregation, covalent organic frameworks can be envisioned as potential solid matrix for chromophore aggregation which was already reported in literature.[4]

The first COF architecture exploiting this principle was reported by Dinca's group, based on the integration of heavier chalcogens such as sulfur, selenium and tellurium.[5] The approach was envisioned to reach higher charge carrier mobilities in COFs and a first promising indication was found in the increased conductivity for COFs containing heavier chalcogens. Heavy halogens have been integrated into COFs, but so far not to study the heavy atom effect, but rather to increase stacking energy or guest uptake.[6-7] With a view on potential applications of organic electronics such as LEDs, we designed a 2D COF system with incorporated bromines on two positions, respectively.

In order to investigate the heavy atom effect in the stable oligothiophene-based 2D COF system, we modified the [2,2'-bithiophene]-5,5'-dicarbaldehyde (2T) with bromine at the 3,3'- and 4,4'-positions of the thiophene units to yield 3,3'-dibromo-[2,2'-bithiophene]-5,5'-dicarbaldehyde (3,3'-$2T_{Br}$) and 4,4'-dibromo-[2,2'-bithiophene]-5,5'-dicarbaldehyde (4,4'-

$2T_{Br}$). With tetraphenyl-pyrene as tetravalent node, the imine-linked frameworks were envisioned to easily crystallize in the same fashion as the non-modified Py-2T COF due to the guided structure formation in pyrene frameworks.[8] Replacing hydrogen by bromine with its much greater atomic weight, the COFs were anticipated to exhibit enhanced phosphorescence and/or extended photoluminescence lifetimes. By integrating the small modifications discussed here into the COF, the framework's geometrical structure, symmetry and topology are all maintained. Therefore, conceptional conclusions might be drawn, associated with surgical modifications in the molecular building blocks and serving to predict similar effects in other modified COFs.

Herein, we successfully synthesized the brominated bithiophene dialdehydes, denoted as 3,3'-$2T_{Br}$ and 4,4'-$2T_{Br}$, for the construction of highly crystalline pyrene-connected COFs. With a larger atomic weight and atomic radius of the bromine substitution, the unit cell of the resulting COFs was expected to slightly increase. Surprisingly, instead the unit cell of the brominated analogues decreased. When studying the photoluminescence (PL) decay dynamics, extended lifetimes were found for the monomers (from 0.82 ns to 3.69 ns for 2T and 4,4'-$2T_{Br}$, respectively) and this effect could be transferred to the complete COF materials that exhibited an overall extension of lifetimes, although to a lesser extent (from 4.1 ns to 4.6 ns for Py-2T and Py-4,4'-$2T_{Br}$, respectively). We believe that these findings will be of importance for new design principles constructing tunable COFs using straightforward and efficient measures.

7.2 Results and Discussion

In order to enhance the fluorescence lifetimes, the bithiophene unit was modified with bromine atoms in two different positions. The 3,3'-2T_{Br} monomer was synthesized by lithiation of the 3,3',5,5'-tetrabromo-2,2'-bithiophene and subsequent quenching with dimethylformamide, whereas the 4,4'-2T_{Br} monomer was obtained by a halogen dance starting from the 5,5'-dibromo-2,2'-bithiophene (see appendix for further experimental details).

The three dialdehyde monomers with a 2T backbone were condensed with 1,3,6,8-tetrakis(4-aminophenyl)pyrene (Py) as the tetravalent node to form a series of 2T-derived COFs with a pseudoquadratic pore (Figure 7.1). The condensation reaction was performed under solvothermal and acid-catalyzed conditions (see appendix for details).

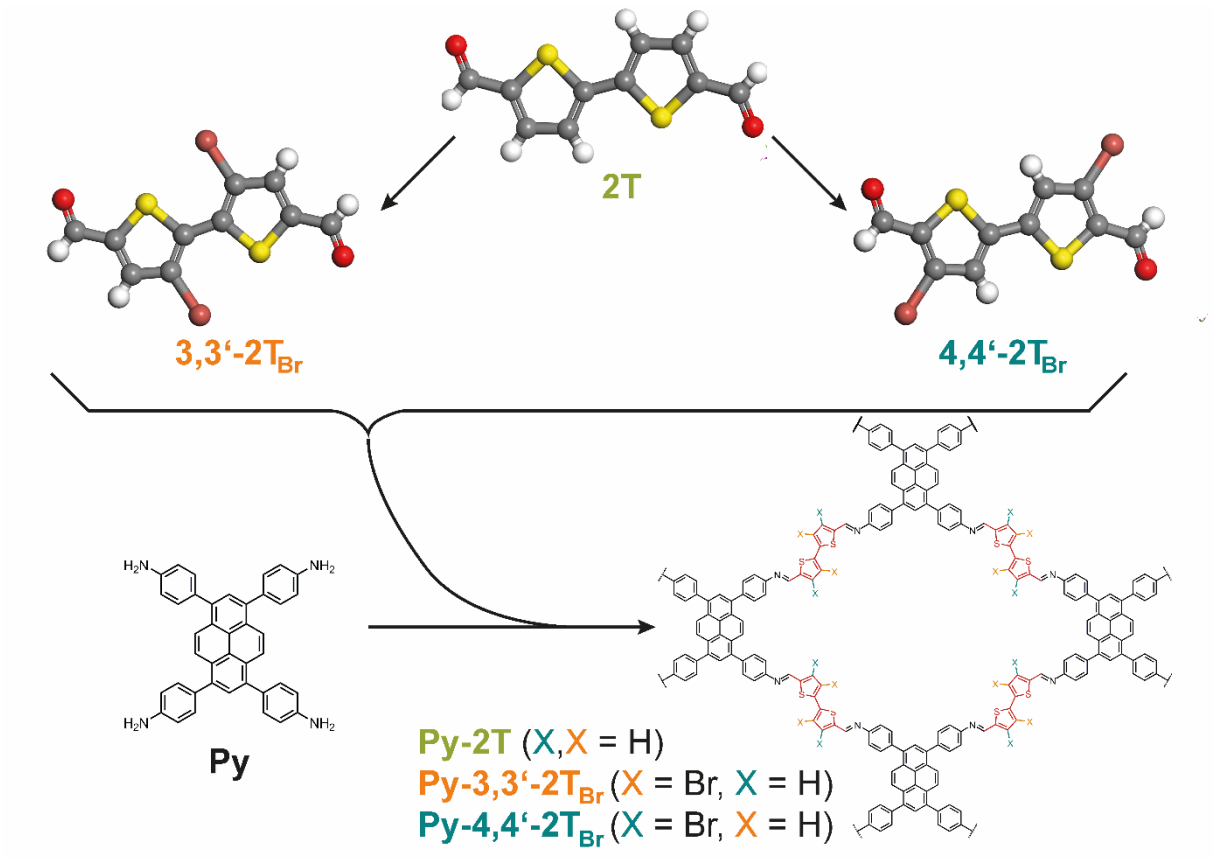

Figure 7.1: Overview of linear non-modified 2T and the bithiophene-derived brominated 3,3'-2T_{Br} and 4,4'-2T_{Br} dialdehyde building blocks (molecular structures from single crystal XRD) and general synthesis route with 1,3,6,8-tetrakis(4-aminophenyl)pyrene (Py) as tetravalent node resulting in a 2D COF with pseudoquadratic pores.

Powder X-ray diffraction reveals several sharp reflections also in the higher-order range confirming the synthesis of highly crystalline COF bulk material. Pawley refinement of the

COF structure simulated in the space group *C*2/*m* led to a very good fit with the experimental data (see Chapter 7.5.5). The influence of the inserted bromine atoms was evaluated for the PXRD data regarding the reflections 110, 020, 200, 220 (Figure 7.2a) and 001 (Figure 7.2b). The brominated linker molecules led to COFs with reflections shifted to higher 2θ values indicating a smaller unit cell compared to the COF synthesized from non-brominated 2T building units. Even though bromine insertion led to a significant atomic weight (79 times) and radius increase, which could be expected to be accompanied by a sterically impeded stacking behavior, the size of the unit cell decreases for Py-3,3'-2T_{Br} and even more for Py-4,4'-2T_{Br}. Similar observations such as the decrease of the unit cell have been made for COFs upon fluoro-substituted linker integration. The COF with equal shares of fluorinated and non-fluorinated building units led to enhanced crystallinity. The alternating stacking of the two different linker allowed for self-complementary π-electronic interactions which resulted in a minimized unit cell and increased total crystal stacking energy.[6]

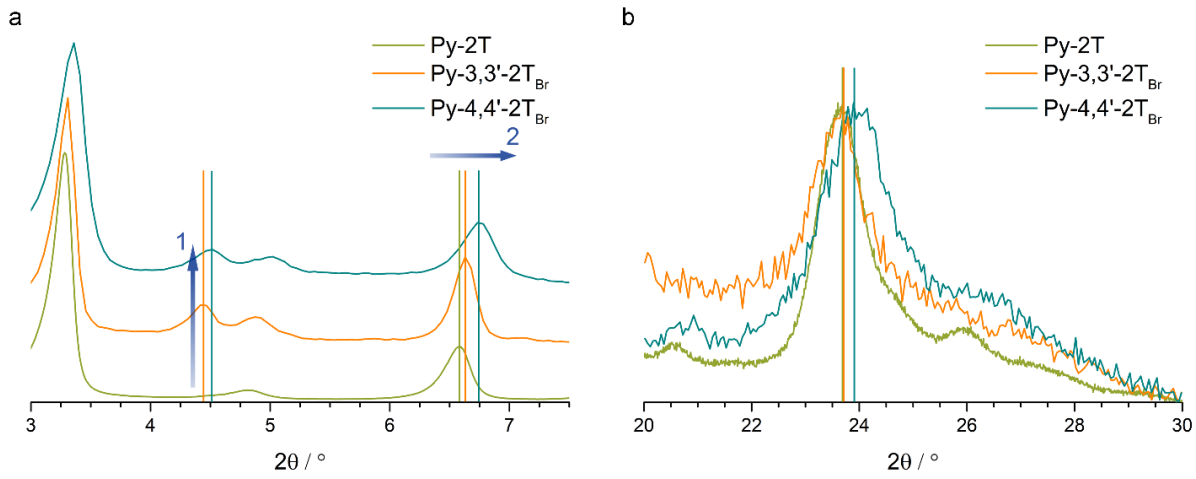

Figure 7.2: Experimental PXRD data of the three COFs Py-2T (green), Py-3,3'-2T_{Br} (orange) and Py-4,4'-2T_{Br} (blue) magnified for the regions (a) 3 – 8° 2θ and (b) 20 – 30° 2θ. The two arrows indicate (1) the appearance of a peak splitting for Py-3,3'-2T_{Br} (orange) and Py-4,4'-2T_{Br} (blue) and (2) the shift to higher 2θ values from Py-2T to Py-4,4'-2T_{Br}.

An alternating stacking of the asymmetric pyrene-4,5-dione with the dipole changing directions from layer to layer led to the same result of high crystallinity and surface area.[9] Transferring this knowledge to our COF system, the decreased size of the unit cell could be attributed to an alternating stacking of the brominated bithiophene bridges, for which the bridges are flipped from COF layer to COF layer.

The porosity was investigated using nitrogen sorption measurements which revealed surface areas of 2066, 1657 and 1618 $m^2\ g^{-1}$ for Py-2T, Py-3,3'-2T_{Br} and Py-4,4'-2T_{Br}, respectively

(Figure 7.17 – Figure 7.19). These values are in very good agreement with the theoretically obtained Connolly surface areas calculated for the simulated COF structures (Table 7.6). Furthermore, pore size distributions based on carbon with a QSDFT kernel for cylindrical pores are in excellent agreement with the pore sizes derived from structure simulations. The pore sizes from the fitted sorption measurements were determined to be 2.5 nm, 2.2 nm and 2.1 nm for Py-2T, Py-3,3'-2T_{Br} and Py-4,4'-2T_{Br}, respectively (Figure 7.17 – Figure 7.19).

Additional investigations with transmission electron microscopy (TEM) revealed spherical particles for Py-2T and Py-4,4'-2T_{Br}, whereas Py-3,3'-2T_{Br} exhibited mostly particles with a rectangular shape. The crystal fringes of the parallel-aligned pores and stacks are visible for the individual COF crystallites of the complete series, revealing the highly crystalline nature of the frameworks (Figure 7.14 – Figure 7.16).

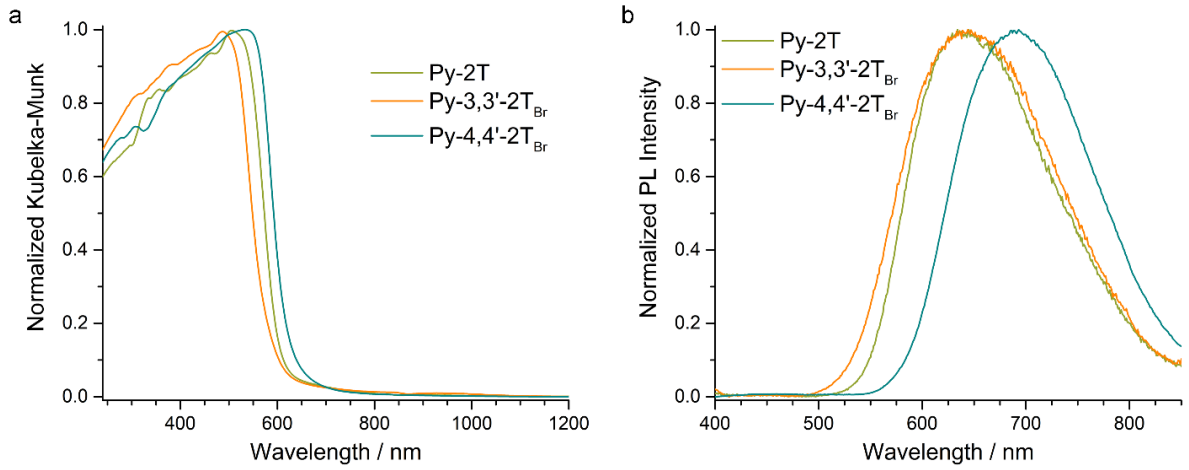

Figure 7.3: (a) Optical absorption spectra and (b) PL (λ_{exc} = 378 nm) spectra of the 2T-based COF series measured as solids. Diffuse reflectance spectra measured for the respective powders dispersed in $BaSO_4$. The PL was measured under nitrogen atmosphere.

An overview of the optical absorption and emission characteristics of the COF series is shown in (Figure 7.3). The Py-3,3'-2T_{Br} exhibits the bluest absorption band with its maximum at 488 nm, which resembles the monomer absorption behavior (Figure 7.11). Appearing at 506 nm and 532 nm, the maxima of Py-2T and Py-4,4'-2T_{Br} are almost 20 nm and 50 nm red-shifted, respectively (Figure 7.3). This corresponds to the data collected for the monomer absorption but the additional red-shift from the Py-4,4'-2T_{Br} cannot be conclusively explained by the monomer behavior. As reports in the literature have already shown, decreasing the π-stacking distance can correlate with lowering the bandgap.[10-11] Therefore, we attribute the red-shift in

the absorption spectrum to tighter stacking, which we observed for the Py-4,4'-2T_{Br} (Table 7.2) compared to the other two COFs.

Correspondingly, the photoluminescence (PL) peak of Py-4,4'-2T_{Br} is shifted to higher wavelengths (693 nm), whereas Py-2T and Py-3,3'-2T_{Br} feature PL maxima at 634 and 644 nm, respectively (Figure 7.3). It has to be noted that the maxima for Py-2T and Py-3,3'-2T_{Br} can hardly be distinguished due to the signal-to-noise ratio. Considering the sharpness of the PL signal at full width half maximum (FWHM), Py-4,4'-2T_{Br} presents the narrowest emission peak with 158 nm FWHM, followed by Py-2T and Py-3,3'-2T_{Br} with 160 and 176 nm FWHM, respectively.

To study time-resolved PL processes, the COFs were characterized under inert atmosphere using TCSPC analysis. After a pulsed laser excitation at 378 nm the emission was detected at the respective maximum for each COF and fitted with a tri-exponential function (Figure 7.4). The recorded histograms of the PL decay exhibit a distinct increase of the long-time decay constant when brominated bithiophene units are integrated into the framework. Furthermore, the fast decay

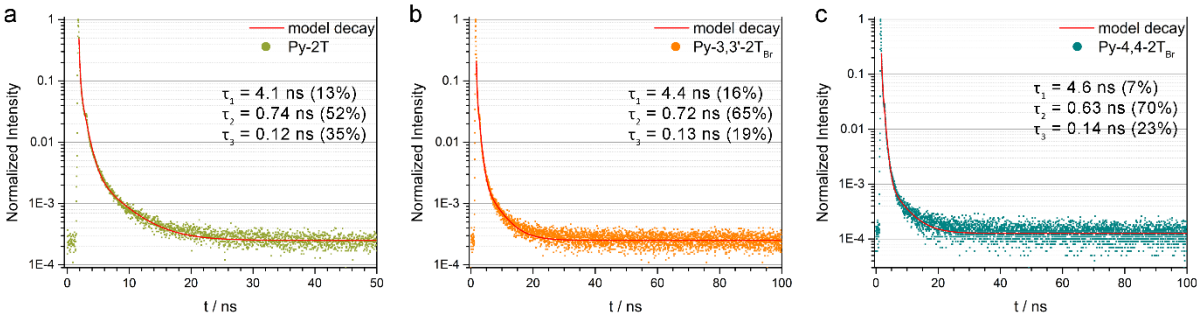

Figure 7.4: (b) PL decay curve of 2T-based COF series measured as solid under nitrogen atmosphere. The samples were excited at 378 nm with a pump fluence of ~0.99 nJ cm^{-2}; the emission was monitored at the respective PL maximum and the obtained histogram was fitted with three exponentials (model decay in red).

channel contribution decreases for Py-3,3'-2T_{Br} and Py-4,4'-2T_{Br} compared to the non-brominated Py-2T. The overall longest time constant was found for COF Py-4,4'-2T_{Br} with 4.6 ns, followed by Py-3,3'-2T_{Br} with 4.4 ns and Py-2T with 4.1 ns. The same trend can be observed for the TCSPC traces of the monomers (Figure 7.12). Here, the differences are more significant with an increase of the long-time constant and a drastic contribution gain of the long decay channels at the cost of the fast relaxation channels. The long-time decay constants and the overall contributions are 0.82 ns (29%), 1.56 ns (54%) and 3.69 ns (91%) for 2T, 3,3'-2T_{Br} and 4,4'-2T_{Br}, respectively. The effect could not be translated to the COF at the same scale, but

still the impact is evident and allows for the general design rule that the inserted bromine atoms can lead to elongated PL lifetimes. Additionally, the constructed frameworks stabilize the excited singlet states resulting in longer-living PL dynamics compared to the monomers. The contribution of the pyrene node to the extended lifetimes was considered but can be neglected due to a lifetime of 2.2 ns, which is only around 50% of the longest lifetime found in the COFs (Figure 7.13).

7.3 Conclusion

Herein, we have developed modified bithiophene-bridged 2D covalent organic frameworks with high crystallinity and porosity. The Py-2T was pushed from equilibrium by selective substitutions of hydrogen atoms with sterically more demanding bromine atoms. The effect of these small changes did not affect the crystallinity or porosity of the frameworks consisting of brominated bithiophene units, but small structural changes occurred, such as the decrease of the unit cell for both Py-3,3'-2T_{Br} and Py-4,4'-2T_{Br}. This behavior has yet to be studied further by methods such as pair distribution function (PDF) where near-order structure can be resolved. Additionally, the ordered π-stacked columns of 4,4'-2T_{Br} and pyrene moieties favored a denser packing with a slightly decreased π-stacking distance.

Interestingly, the observed trend of the heavy atom effect for optical properties of the molecular building units could be translated into the framework. The tunability of the absorption and emission bands by simply changing hydrogen to bromine was intriguing and could be enhanced by the additional factor of the stacking distance. Studying the PL dynamics revealed the extension of singlet lifetimes upon integration of brominated bridges into the COFs, in comparison to the respective molecular building blocks. We demonstrate that this approach provides a facile strategy for modifying the electronic properties of bithiophenes and simultaneously maintaining the overall structure of the basic scaffolding of the Py-2T COF.

This design principle is envisioned to provide a general method to construct COFs with tunable optical properties while maintaining almost identical structural networks.

7.4 References

[1] Verhoeven, J. W., Glossary of terms used in photochemistry (IUPAC Recommendations 1996). *Pure Appl. Chem.* **1996,** *68* (12), 2223-2286.

[2] Lower, S. K.; El-Sayed, M. A., The Triplet State and Molecular Electronic Processes in Organic Molecules. *Chem. Rev.* **1966,** *66* (2), 199-241.

[3] Bolton, O.; Lee, K.; Kim, H.-J.; Lin, K. Y.; Kim, J., Activating efficient phosphorescence from purely organic materials by crystal design. *Nat. Chem.* **2011,** *3* (3), 205-210.

[4] Keller, N.; Calik, M.; Sharapa, D.; Soni, H. R.; Zehetmaier, P. M.; Rager, S.; Auras, F.; Jakowetz, A. C.; Görling, A.; Clark, T.; Bein, T., Enforcing Extended Porphyrin J-Aggregate Stacking in Covalent Organic Frameworks. *J. Am. Chem. Soc.* **2018,** *140* (48), 16544-16552.

[5] Duhović, S.; Dincă, M., Synthesis and Electrical Properties of Covalent Organic Frameworks with Heavy Chalcogens. *Chem. Mater.* **2015,** *27* (16), 5487-5490.

[6] Chen, X.; Addicoat, M.; Irle, S.; Nagai, A.; Jiang, D., Control of Crystallinity and Porosity of Covalent Organic Frameworks by Managing Interlayer Interactions Based on Self-Complementary π-Electronic Force. *J. Am. Chem. Soc.* **2013,** *135* (2), 546-549.

[7] Hu, J.; Zhao, J.; Yan, T., Methane Uptakes in Covalent Organic Frameworks with Double Halogen Substitution. *J. Phys. Chem. C* **2015,** *119* (4), 2010-2014.

[8] Auras, F.; Ascherl, L.; Hakimioun, A. H.; Margraf, J. T.; Hanusch, F. C.; Reuter, S.; Bessinger, D.; Döblinger, M.; Hettstedt, C.; Karaghiosoff, K.; Herbert, S.; Knochel, P.; Clark, T.; Bein, T., Synchronized Offset Stacking: A Concept for Growing Large-Domain and Highly Crystalline 2D Covalent Organic Frameworks. *J. Am. Chem. Soc.* **2016,** *138* (51), 16703-16710.

[9] Salonen, L. M.; Medina, D. D.; Carbo-Argibay, E.; Goesten, M. G.; Mafra, L.; Guldris, N.; Rotter, J. M.; Stroppa, D. G.; Rodriguez-Abreu, C., A supramolecular strategy based on molecular dipole moments for high-quality covalent organic frameworks. *Chem. Commun.* **2016,** *52* (51), 7986-7989.

[10] Wang, M.; Ballabio, M.; Wang, M.; Lin, H.-H.; Biswal, B. P.; Han, X.; Paasch, S.; Brunner, E.; Liu, P.; Chen, M.; Bonn, M.; Heine, T.; Zhou, S.; Cánovas, E.; Dong, R.; Feng, X., Unveiling Electronic Properties in Metal–Phthalocyanine-Based Pyrazine-Linked Conjugated Two-Dimensional Covalent Organic Frameworks. *J. Am. Chem. Soc.* **2019,** *141* (42), 16810-16816.

[11] Keller, N.; Sick, T.; Bach, N.; Koszalkowski, A.; Rotter, J. M.; Medina, D. D.; Bein, T., Dibenzochrysene Enables Tightly Controlled Docking and Stabilizes Photoexcited States in Dual-Pore Covalent Organic Frameworks. *Nanoscale* **2019,** *11* (48), 23338-23345.

7.5 Appendix

7.5.1 Methods

Infrared (IR) spectra were recorded on a Perkin Elmer Spectrum BX II FT-IR system and a Thermo Scientific Nicolet™ 6700 FT-IR spectrometer in transmission mode. IR data are reported in wavenumbers (cm^{-1}).

The **nitrogen sorption** isotherms were recorded on a Quantachrome Autosorb 1 at 77 K in a pressure range from $p/p_0 = 0.001$ to 0.98. Prior to the measurement of the sorption isotherm, the sample was heated for 24 h at 120 °C under turbomolecular pump vacuum. For the evaluation of the surface area, the BET model was applied between 0.05 and 0.2 p/p_0. The calculation of the pore size distribution was done using the QSDFT equilibrium model with a carbon kernel for cylindrical pores on the adsorption branch. The Connolly surface area differs from the experimental data usually due to the non-ideal composition and structure of the COF sample. Grain boundaries and the displacement of COF layers may lead to defects in the crystalline structure and to blocked pores and thus lower experimental values. Adsorbed molecular fragments may also decrease the accessible surface area.

Powder X-ray diffraction (PXRD) measurements were performed using a Bruker D8 Discover with Ni-filtered Cu K_α radiation and a LynxEye position-sensitive detector.

Transmission electron microscopy (TEM) measurements were performed on a probe-corrected FEI Titan Themis 60-300 kV (FEI Company/Thermo Fisher Scientic Inc., USA) electron microscope equipped with a Super-X windowless EDX (four quadrant SDD EDX detection) and a X-FEG high-brightness gun with monochromator (energy spread <0.2 eV). **Scanning electron microscopy (SEM)** measurements were performed on a FEI Helios NanoLab G3 UC electron microscope (FEI Company/Thermo Fisher Scientic Inc., USA) with a X-MaxN EDX detector (Oxford Instruments, UK). The samples were mounted on sample carriers with a sticky carbon support and sputtered with carbon on a Bal-Tec MED 020 coating system.

UV-Vis spectra were recorded using a Perkin-Elmer Lambda 1050 spectrometer equipped with a 150 mm integrating sphere. **Diffuse reflectance spectra** were collected with a Praying Mantis (Harrick) accessory and were referenced to barium sulfate powder as white standard.

Photoluminescence (PL) measurements were performed using a home-built setup consisting of a Horiba Jobin Yvon iHR 320 monochromator equipped with a photomultiplier tube and a liquid N_2-cooled InGaAs detector. The samples were illuminated with a pulsed (83 Hz) 365 nm or 405 nm LED at a light intensity of 500 mW cm^{-2}.

Time-resolved PL measurements were acquired using a **time-correlated single photon counting (TCSPC)** setup (FluoTime 300, PicoQuant GmbH). The samples were photo-excited using lasers with suitable wavelengths according to the sample absorption, i.e. 378 nm, 403 nm or 507 nm wavelength (LDH-P-C-375, LDH-P-C-405, and LDH-P-C-510, respectively, all from PicoQuant GmbH) pulsed at 500 kHz, with a pulse duration of ~100 ps and fluence of ~300 nJcm^{-2}/pulse. The samples were exposed to the pulsed light source set at 0.3 μJcm^{-2}/pulse fluence for ~10 minutes prior to measurement to ensure stable sample emission. The PL was collected using a high-resolution monochromator and photomultiplier detector assembly (PMA-C 192-N-M, PicoQuant GmbH).

7.5.2 Building Block Syntheses

All reactions were carried out with magnetic stirring, and if moisture or air sensitive, under argon atmosphere using standard Schlenk techniques in oven-dried glassware. Liquid reagents and solvents were added by syringes or oven-dried stainless-steel cannulas through rubber septa. Chemicals were purchased from commercial suppliers and used without further purification. The solvents were of reagent grade or purified by distillation. Yields refer to isolated homogeneous and spectroscopically pure materials, unless otherwise specified.

Scheme 7.1: Synthesis of the 2T series, **2T**, **3,3'-2T$_{Br}$**, and **4,4'-2T$_{Br}$**.

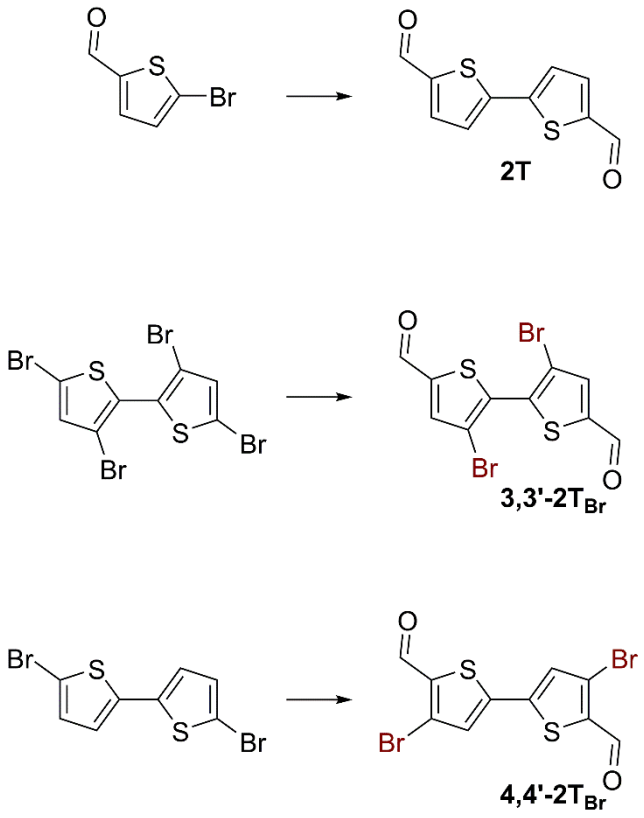

[2,2'-bithiophene]-5,5'-dicarbaldehyde (2T)

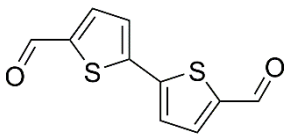

A solution of 5-bromo-2-thiophenecarboxaldehyde (1.910 g, 10 mmol, 1 eq), $Pd(OAc)_2$ (89.8 mg, 0.4 mmol, 0.04 eq), XPhos (228.8 mg, 0.48 mmol, 0.048 eq) in 56 mL 1-butanol was

stirred for 15 min under argon at room temperature. Then a solution of $CsOH \cdot H_2O$ (3.358 g, 20 mmol, 2 eq.) in 14 mL water was prepared and added to the reaction suspension, followed by the addition of 5-formyl-2-thienylboronic acid (2.807 g, 18 mmol, 1.8 eq.). After stirring for 48 h at ambient conditions, the yellow-brown suspension was quenched by the addition of 400 mL of H_2O. The mixture was extracted with $CHCl_3$, dried over $MgSO_4$ and concentrated under reduced pressure. The crude product was purified via column chromatography (silica gel, DCM), yielding the title compound as a yellow powder (1.795 g, 8.1 mmol, 81%).

^{1}H NMR (400 MHz, $CDCl_3$): 9.92 (s, 2H), 7.72 (d, J = 4.0 Hz, 2H), 7.42 (d, J = 4.0 Hz, 2H).

^{13}C NMR (101 MHz, $CDCl_3$): 182.7, 145.0, 144.1, 137.0, 126.6.

3,3'-dibromo-[2,2'-bithiophene]-5,5'-dicarbaldehyde (3,3'-2T$_{Br}$)[1]

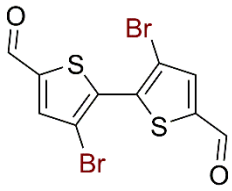

n-Butyllithium (2.33 ml, 2 M in cyclohexane, 4.67 mmol, 2.25 eq.) was added dropwise at −78 °C to a solution of 3,3',5,5'-tetrabromo-2,2'-bithiophene (1.0 g, 2.08 mmol, 1.0 eq.) in 20 mL anhydrous THF. After 2 h of stirring at −78 °C, anhydrous DMF (400 µl, 5.2 mmol, 2.5 eq.) was added. The solution was allowed to warm up to room temperature overnight. The reaction was quenched by the addition of 1 M HCl. The resulting solid was then filtered, washed with water and recrystallized in dichloroethane (DCE). The product was dissolved in DCM, washed with 2 M NaOH, dried over $MgSO_4$ and concentrated under reduced pressure to furnish the title compound as a yellow solid (521 mg, 1.37 mmol, 66%).

^{1}H NMR (400 MHz, $CDCl_3$): 9.92 (s, 2H), 7.77 (s, 2H)

^{13}C NMR (101 MHz, $CDCl_3$): 181.8, 143.9, 138.7, 136.9, 114.1.

HR-EI-MS: *m/z* 377.8019 (M^+, calculated for $C_{10}H_4Br_2O_2S_2$: 377.8014).

4,4'-dibromo-[2,2'-bithiophene]-5,5'-dicarbaldehyde (4,4‘-2T$_{Br}$)[2]

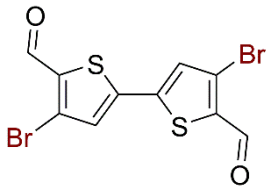

n-Butyllithium (3.86 ml, 2 M in cyclohexane, 7.71 mmol, 2.5 eq.) was added dropwise for 10 min to a solution of diisopropylamine (1081 µl, 7.71 mmol, 2.5 eq.) in 20 mL anhydrous THF at −40 °C. After 15 min, the generated lithiumdiisopropylamid LDA was added dropwise for 10 min to a suspension of 5,5’-dibromo-2,2’-bithiophene (1000 mg, 3.08 mmol, 1.0 eq.) in 10 mL THF at −20 °C. After stirring for 15 min at −20 °C, a solution of DMF (617 µl, 8.00 mmol, 2.6 eq.) in 5 mL THF was added at the same temperature. The solution was allowed to reach 0 °C, poured into water (50 ml) and extracted with $CHCl_3$. The combined organic layers were washed with water, dried over Na_2SO_4 and concentrated under reduced pressure. The crude product was purified by flash column chromatography (silica, DCM/*n*-pentane 1:1) and recrystallization from $CHCl_3$. The yellow powder was dissolved in DCM, washed with 2 M NaOH and dried over $MgSO_4$ to furnish the title compound as an orange powder (737 mg, 1.94 mmol, 63%).

^{1}H NMR (400 MHz, $CDCl_3$): 9.97 (s, 2H), 7.35 (s, 2H)

^{13}C NMR (101 MHz, $CDCl_3$): 182.7, 143.0, 137.5, 130.0, 120.8.

HR-EI-MS: *m/z* 377.8019 (M^+, calculated for $C_{10}H_4Br_2O_2S_2$: 377.8014).

1,3,6,8-tetrakis(4-aminophenyl)pyrene (Py)[3-4]

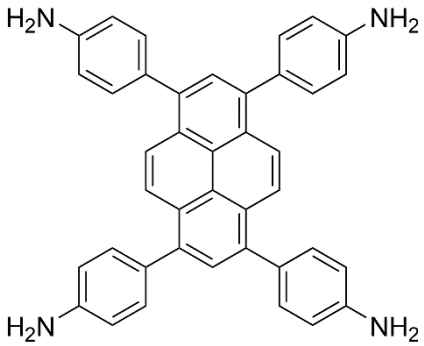

A reaction mixture containing 1,3,6,8-tetrabromopyrene (1482 mg, 2.86 mmol, 1.0 eq.), 4-aminophenylboronic acid pinacol ester (3010 mg, 13.7 mmol, 4.8 eq.), K_2CO_3 (2175 mg, 15.7 mmol, 5.5 eq.), and $Pd(PPh_3)_4$ (330 mg, 0.29 mmol, 10 mol%) in 32 mL 1,4-dioxane and

8 mL H_2O was heated to reflux (115 °C) for 3 d. After cooling to room temperature, H_2O was added. The resulting precipitate was collected via filtration and was washed with H_2O and MeOH. Recrystallization from 1,4-dioxane, followed by drying under high vacuum furnished the title compound, co-crystallized with approximately 1.5 dioxane molecules per formula unit, as a bright yellow powder (1792 mg, 2.56 mmol, 90%).

^{1}H NMR (400 MHz, DMSO-d_6): 8.13 (s, 4 H), 7.79 (s, 2 H), 7.34 (d, J = 8.4 Hz, 8 H), 6.77 (d, J = 8.5 Hz, 8 H), 5.30 (s, 8 H), 3.56 (s, 12 H, dioxane).

^{13}C NMR (100 MHz, DMSO-d_6): 148.2, 137.1, 131.0, 129.0, 127.6, 126.7, 126.1, 124.4, 113.9, 66.3 (dioxane).

7.5.3 COF Syntheses

COF bulk material syntheses were carried out under argon atmosphere in PTFE-sealed 6 mL glass tubes. High purity solvents and acetic acid were sourced from commercial suppliers and degassed and saturated with argon prior to use unless shipped under argon.

Py-2T COF

1,3,6,8-tetrakis(4-aminophenyl)pyrene dioxane adduct (Py; 7.0 mg, 10 µmol, 1.0 eq.) and [2,2'-bithiophene]-5,5'-dicarbaldehyde (2T; 4.5 mg, 20 µmol, 2.0 eq.) were filled into a reaction tube, followed by the addition of mesitylene (333 µl), benzyl alcohol (167 µl) and 6 M acetic acid (70 µL). The tube was sealed and the reaction mixture was heated at 120 °C for 3 d. After cooling to room temperature, the precipitate was collected by filtration, and extracted with supercritical CO_2 for 2 h, yielding the Py-2T COF as a red powder.

Py-3,3'-2T$_{Br}$ COF

1,3,6,8-tetrakis(4-aminophenyl)pyrene dioxane adduct (Py; 7.0 mg, 10 µmol, 1.0 eq.) and 3,3'-dibromo-[2,2'-bithiophene]-5,5'-dicarbaldehyde (3,3'-2T$_{Br}$; 7.60 mg, 20 µmol, 2.0 eq.) were filled into a sealed pressure tube, followed by the addition of benzyl alcohol (125 µl), mesitylen (375 µl) and acetic acid (70 µl, 6 M). The tube was sealed and the reaction mixture was heated at 120 °C for 3 d. After cooling to room temperature, the precipitate was collected by filtration, and extracted with supercritical CO_2, yielding the Py-3,3'-s2T$_{Br}$ COF as a red powder.

Py-4,4'-2T$_{Br}$ COF

1,3,6,8-tetrakis(4-aminophenyl)pyrene dioxane adduct (Py; 7.0 mg, 10 µmol, 1.0 eq.) and 4,4'-dibromo-[2,2'-bithiophene]-5,5'-dicarbaldehyde (4,4'-2T$_{Br}$; 7.60 mg, 20 µmol, 2.0 eq.) were filled into a sealed pressure tube, followed by the addition of benzyl alcohol (125 µl), mesitylen (375 µl) and acetic acid (50 µl, 6 M). The tube was sealed and the reaction mixture was heated at 120 °C for 3 d. After cooling to room temperature, the precipitate was collected by filtration, and extracted with supercritical CO_2, yielding the Py-4,4'-s2T$_{Br}$ COF as a dark red powder.

COF thin film syntheses were carried out under argon atmosphere in PTFE-sealed 100 mL glass containers equipped with a glass liner. The COF films were grown on quartz substrates cleaned in Hellmanex solution, water and isopropanol. The substrates were placed in a PTFE holder face down in the reaction solution.

Py-2T COF thin film

1,3,6,8-tetrakis(4-aminophenyl)pyrene dioxane adduct (Py; 10.5 mg, 15 μmol, 1.0 eq.) and [2,2'-bithiophene]-5,5'-dicarbaldehyde (2T; 6.7 mg, 30 μmol, 2.0 eq.) were filled into a glass container, followed by the addition of mesitylene (1333 μl), benzyl alcohol (667 μl) and 6 M acetic acid (150 μL). The quartz substrate was placed in the reaction solution and the glass vessel was sealed and heated at 120 °C for 1 d. After cooling to room temperature, the substrate was cleaned with acetonitrile, and dried at 60 °C for 30 min, yielding the Py-2T COF as a red thin film.

7.5.4 NMR Spectroscopy

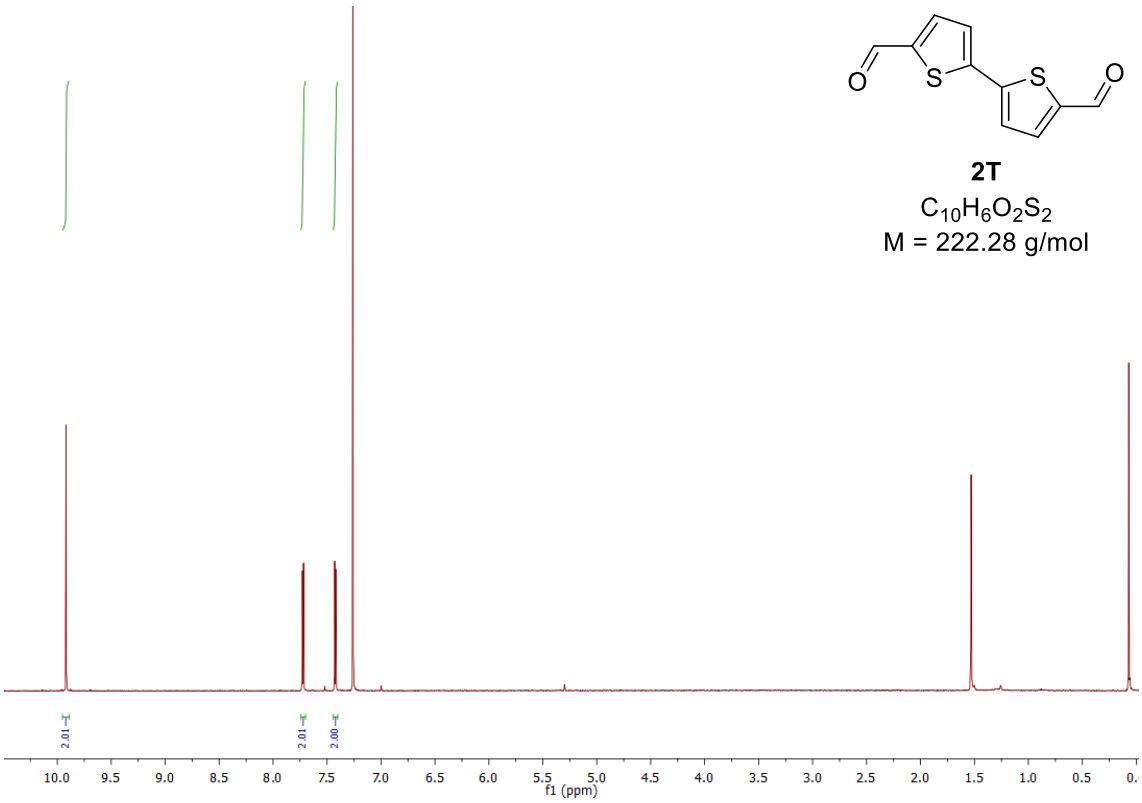

2T

$C_{10}H_6O_2S_2$

M = 222.28 g/mol

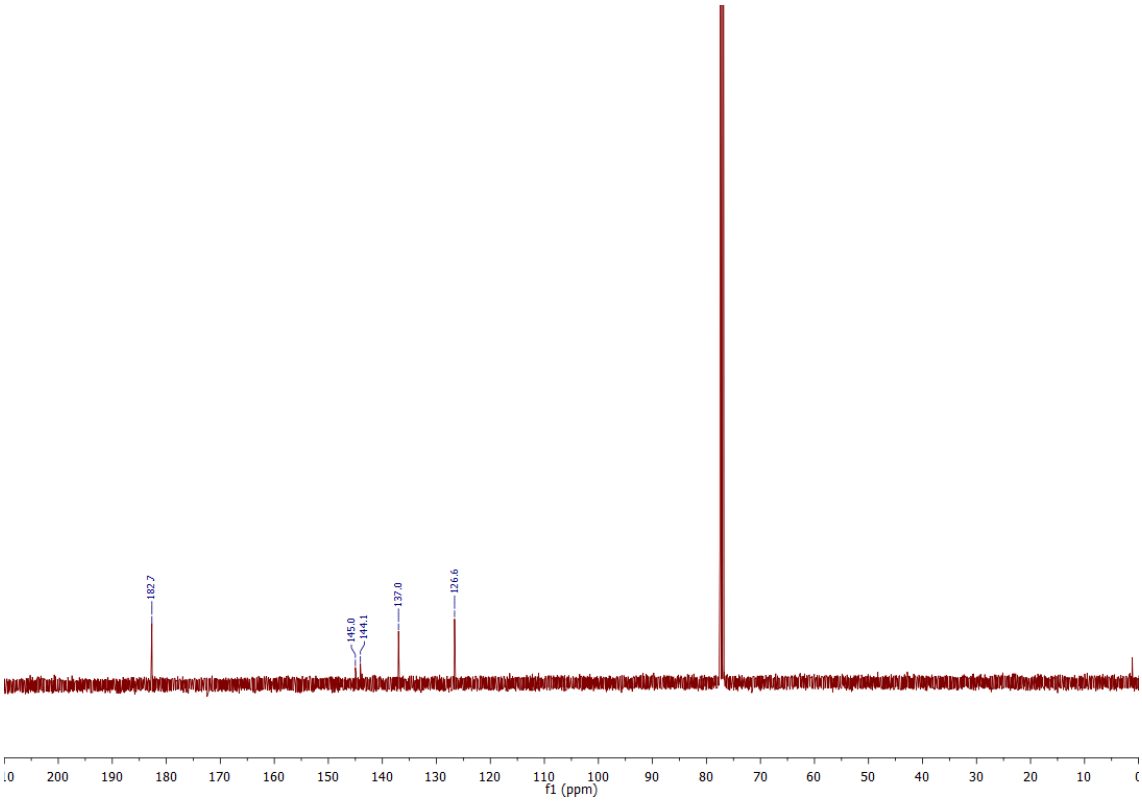

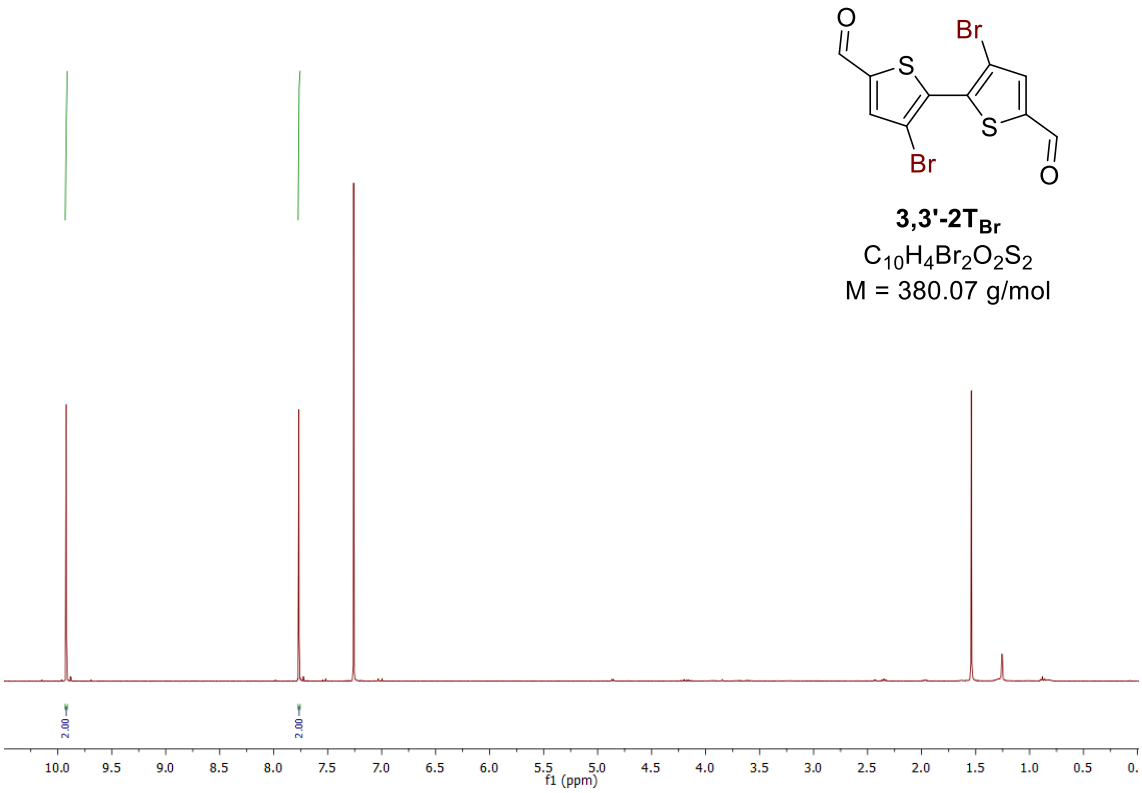
O
Br
S
S
Br
O
3,3'-2T$_{Br}$
$C_{10}H_4Br_2O_2S_2$
M = 380.07 g/mol
2.00
2.00
10.0 9.5 9.0 8.5 8.0 7.5 7.0 6.5 6.0 5.5 5.0 4.5 4.0 3.5 3.0 2.5 2.0 1.5 1.0 0.5 0.
f1 (ppm)

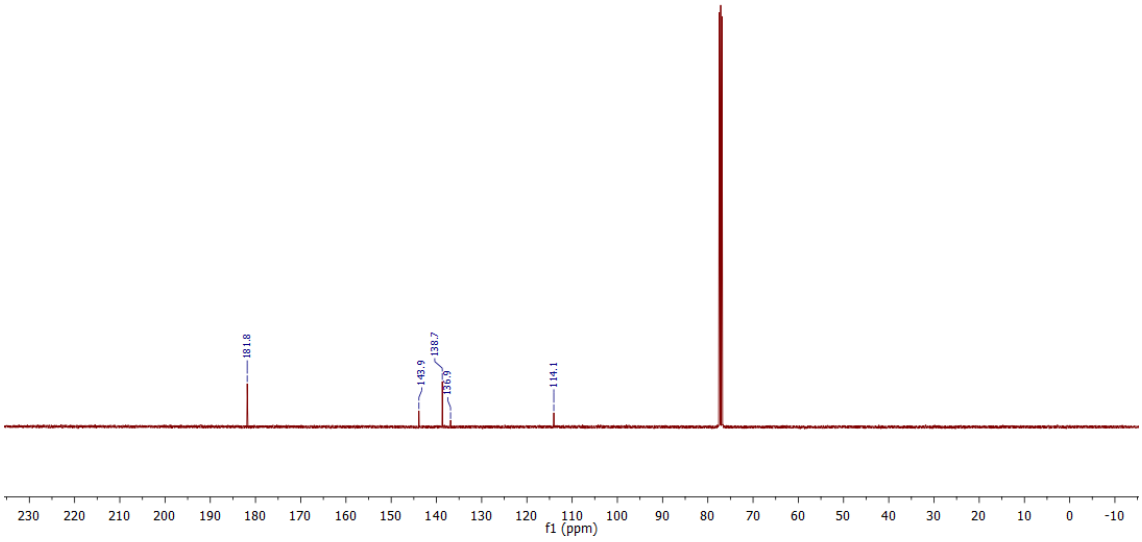
181.8
143.9
138.7
136.9
114.1
230 220 210 200 190 180 170 160 150 140 130 120 110 100 90 80 70 60 50 40 30 20 10 0 -10
f1 (ppm)

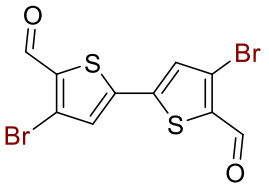

4,4'-2T$_{Br}$
$C_{10}H_4Br_2O_2S_2$
M = 380.07 g/mol

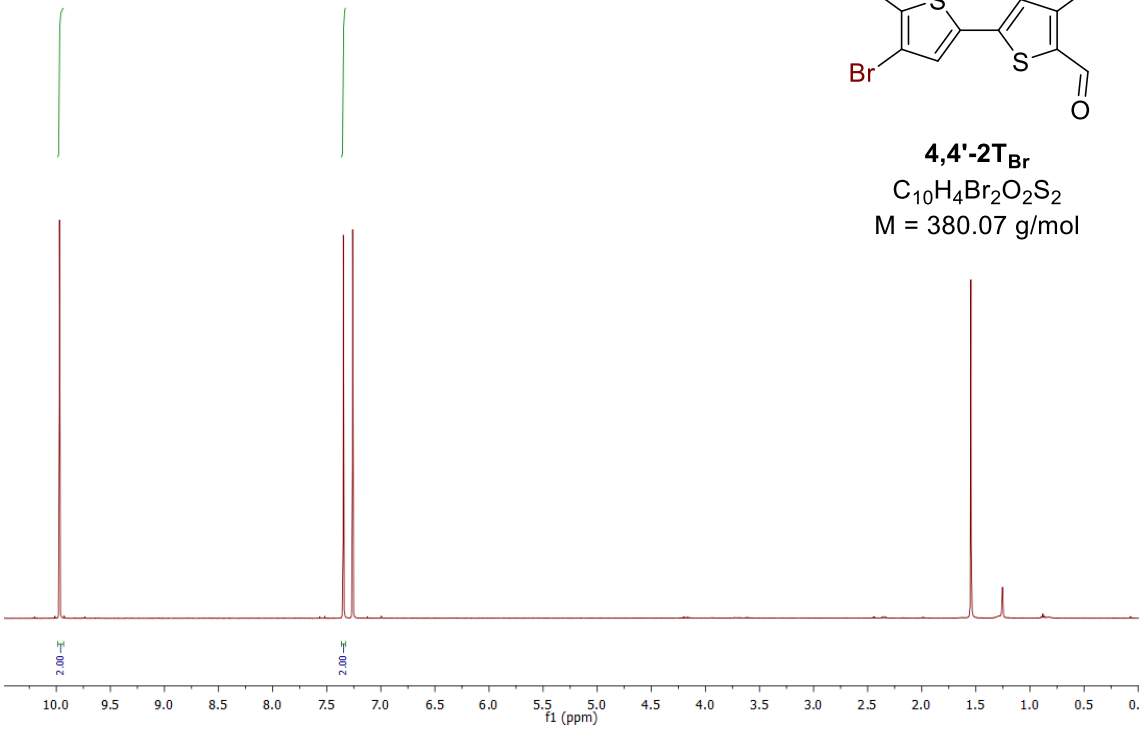

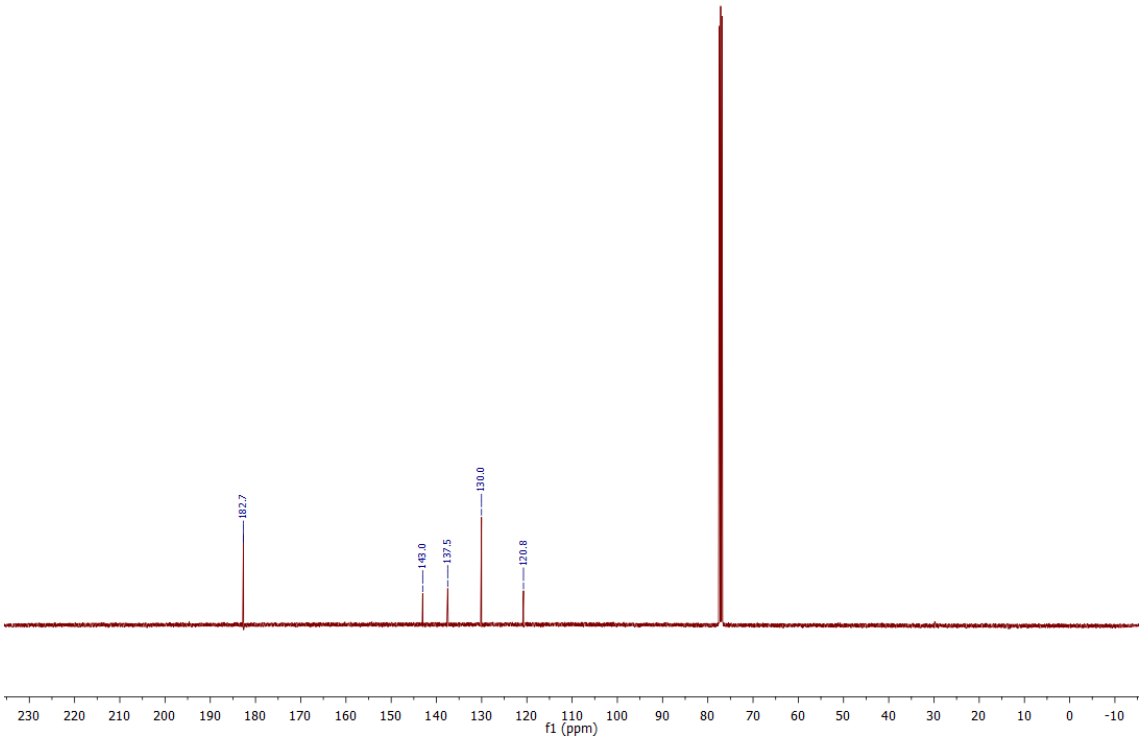

Py

$C_{40}H_{30}N_4$

M = 566.71 g/mol

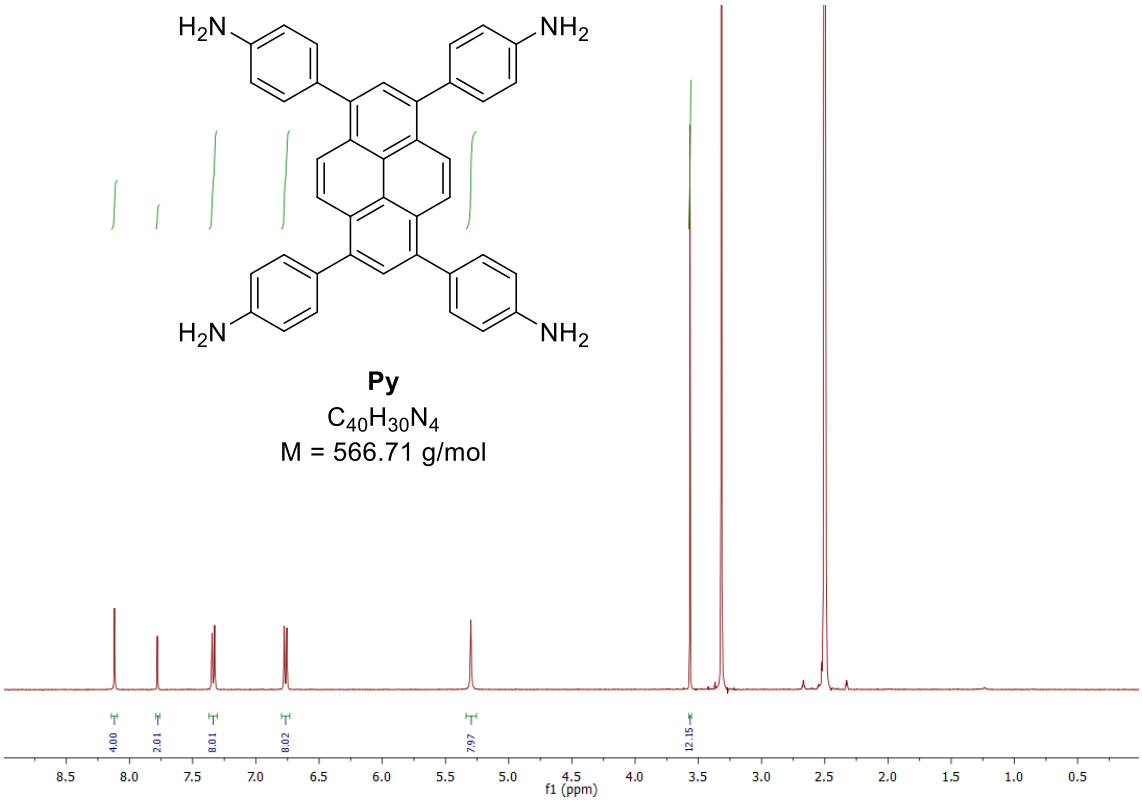

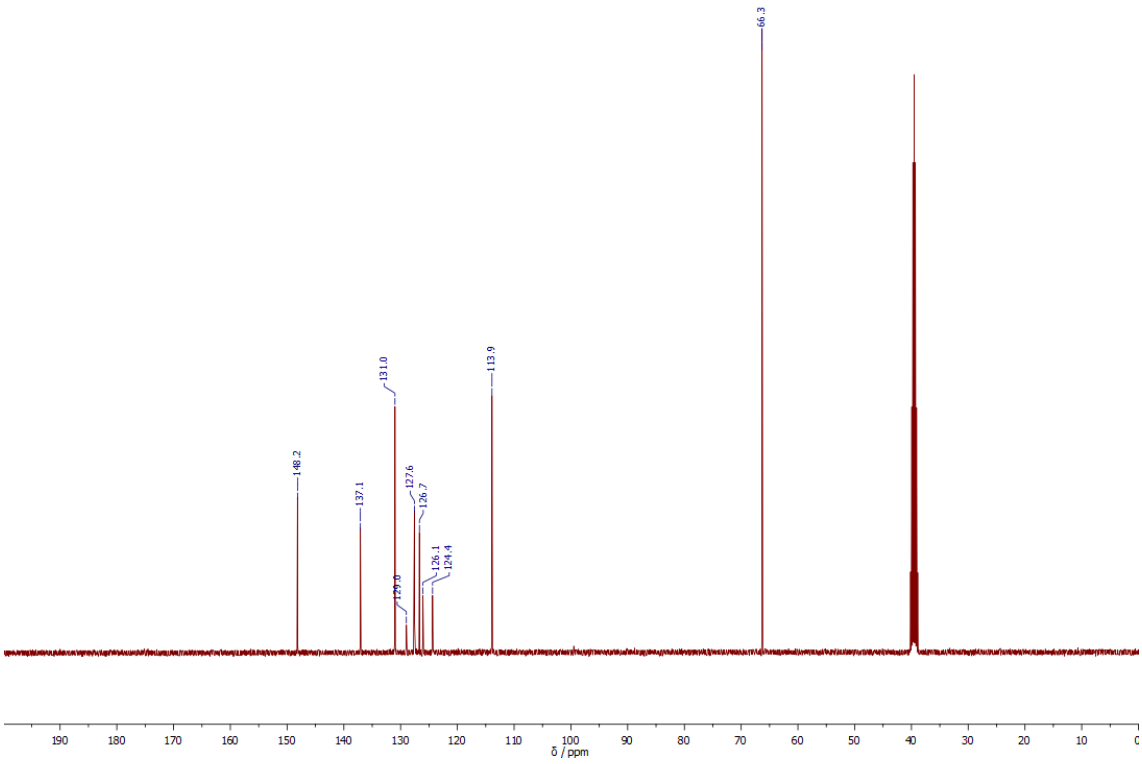

7.5.5 X-Ray Diffraction

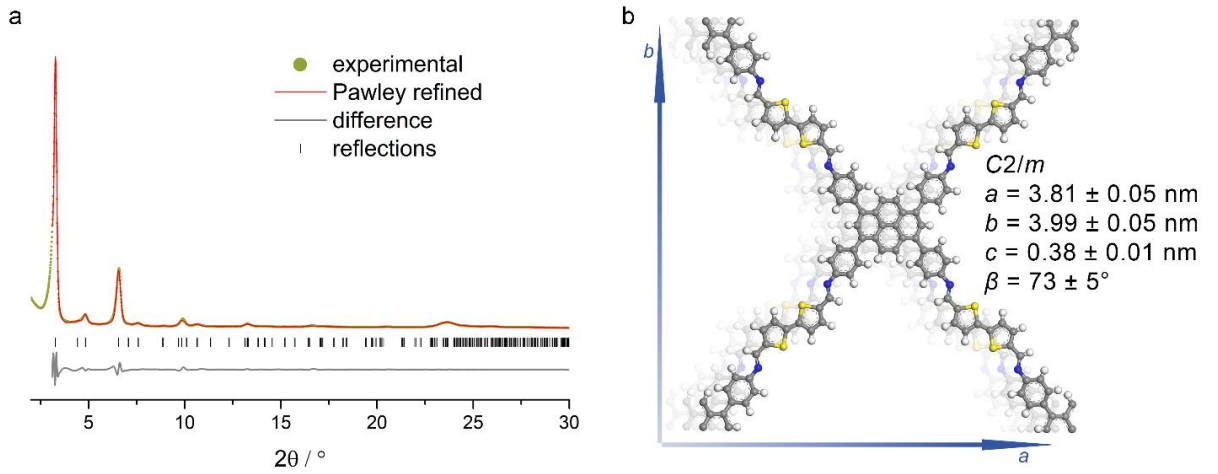

Figure 7.5: (a) Experimental PXRD data (light green dots) of Py-2T. Pawley refinement (red line) using the *C*2/*m* symmetric structure model shown in (b) provides a very good fit to the experimental pattern with only minimal differences (grey line: difference between experimental and refined patterns; R_{wp} = 8.2%, R_p = 6.3%). Bragg positions are indicated with black ticks.

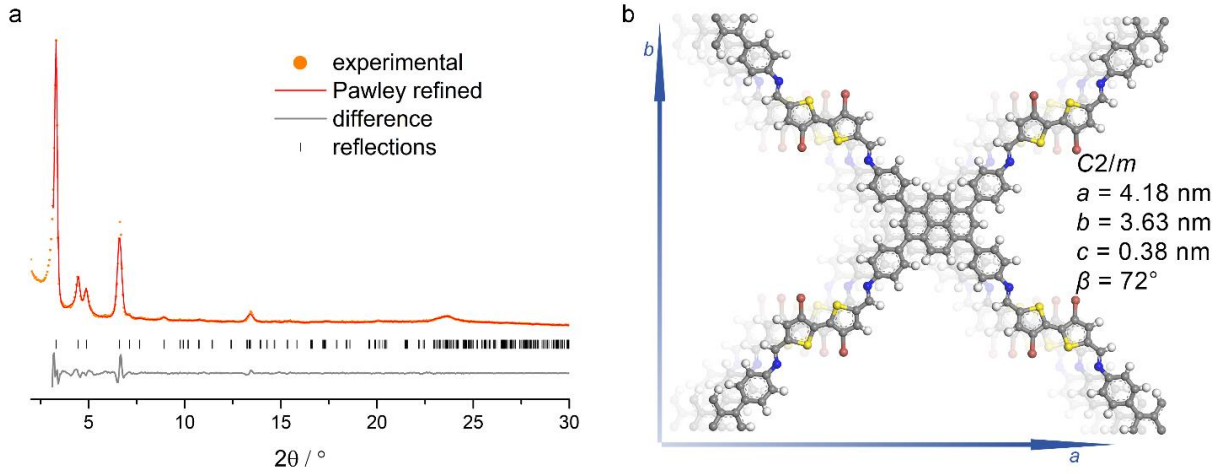

Figure 7.6: (a) Experimental PXRD data (orange dots) of Py-3,3'-2T_{Br}. Pawley refinement (red line) using the *C*2/*m* symmetric structure model shown in (b) provides a very good fit to the experimental pattern with only minimal differences (grey line: difference between experimental and refined patterns; R_{wp} = 6.9%, R_p = 5.0%). Bragg positions are indicated with black ticks.

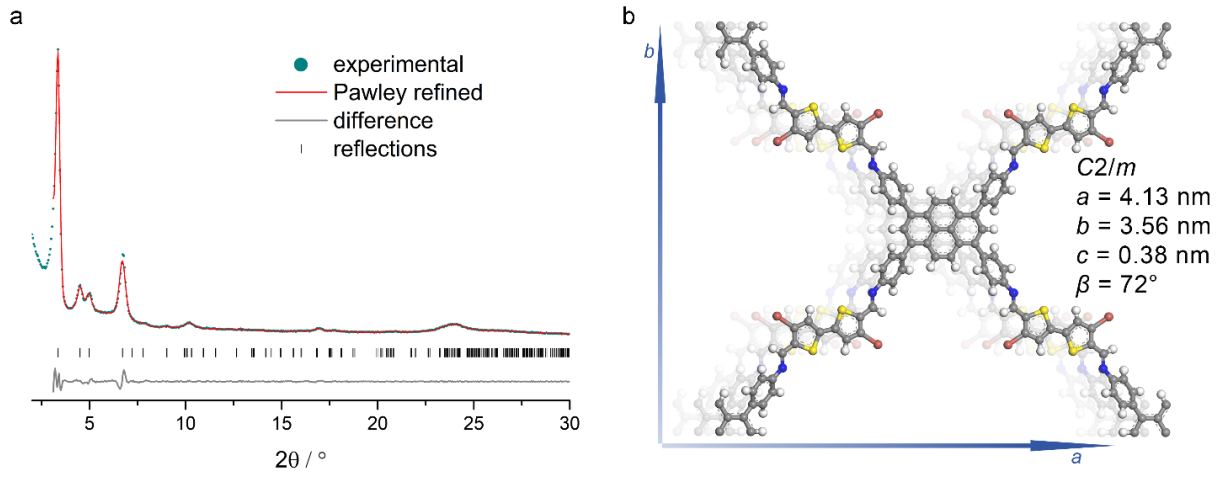

Figure 7.7: (a) Experimental PXRD data (blue dots) of Py-4,4'-2T$_{Br}$. Pawley refinement (red line) using the *C*2/*m* symmetric structure model shown in (b) provides a very good fit to the experimental pattern with only minimal differences (grey line: difference between experimental and refined patterns; $R_{wp} = 4.4\%$, $R_p = 3.3\%$). Bragg positions are indicated with black ticks.

Table 7.1: Positions of first Bragg reflections and the reflection 001 attributed to the π-stacking of the COF layers obtained from experimental PXRD data. The order of appearance in the table corresponds to the order of observed peaks in the PXRD pattern. The values are given in ° 2θ.

Reflection	110	020	200	220	001
Py-2T	3.28		4.83	6.58	23.69
Py-3,3'-2T$_{Br}$	3.31	4.42	4.87	6.63	23.69
Py-4,4'-2T$_{Br}$	3.36	4.52	5.02	6.73	23.89

Table 7.2: Corresponding *d*-spacing for reflection 001 attributed to the π-stacking distance of COF layers and calculated with the Bragg equation.

Reflection	001	*d*-spacing [Å]
Py-2T	23.69	3.75
Py-3,3'-2T$_{Br}$	23.69	3.75
Py-4,4'-2T$_{Br}$	23.89	3.72

7.5.6 Single Crystal Diffraction

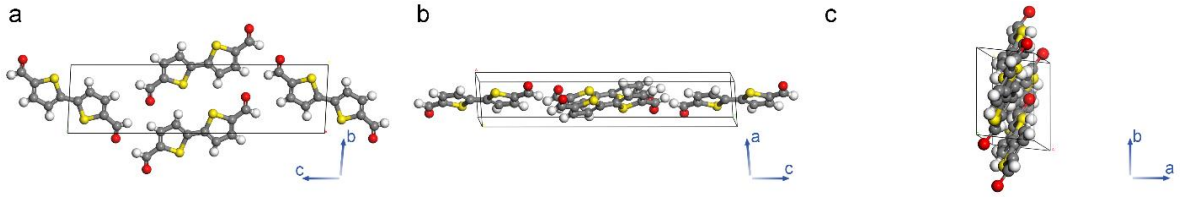

Figure 7.8: Crystal structure of 2T monomer obtained by single crystal diffraction. (a) view along *a*. (b) view along *b*. (c) view along *c*.

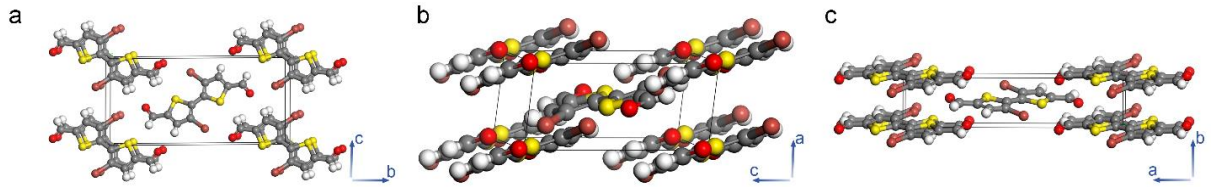

Figure 7.9: Crystal structure of 3,3'-2T_{Br} monomer obtained by single crystal diffraction. (a) view along *a*. (b) view along *b*. (c) view along *c*.

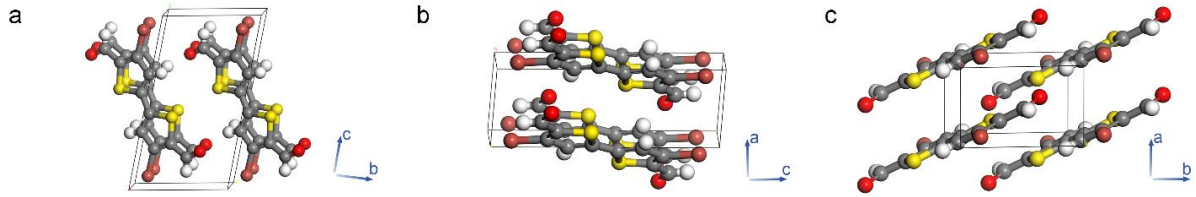

Figure 7.10: Crystal structure of 4,4'-2T_{Br} monomer obtained by single crystal diffraction. (a) view along *a*. (b) view along *b*. (c) view along *c*.

7.5.7 UV-vis and Fluorescence Spectroscopy

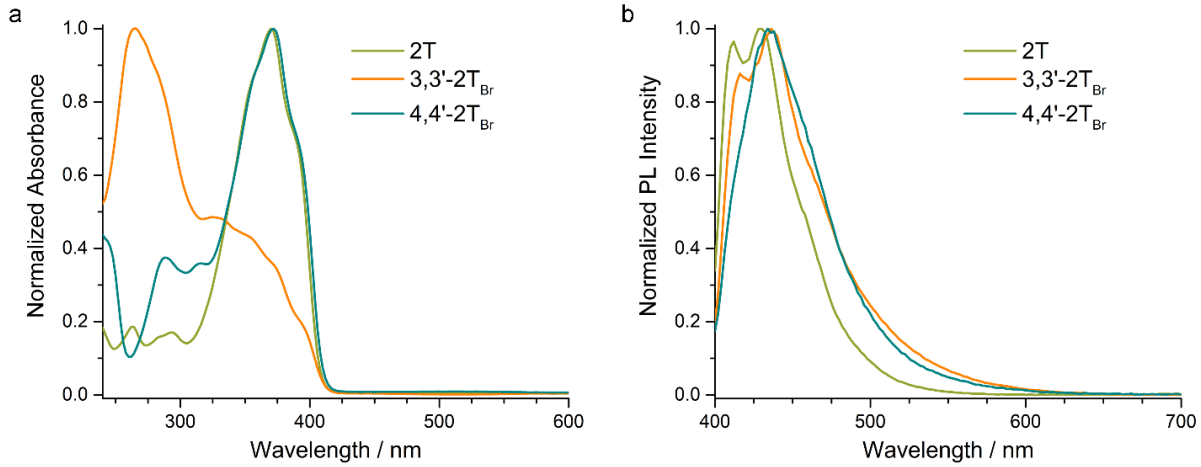

Figure 7.11: (a) Optical absorption spectra and (b) PL (λ_{exc} = 378 nm) spectra of the 2T, 3,3'-2T$_{Br}$ and 4,4'-2T$_{Br}$ monomers measured in solution (50 µM $CHCl_3$).

7.5.8 Time-Correlated Single Photon Counting

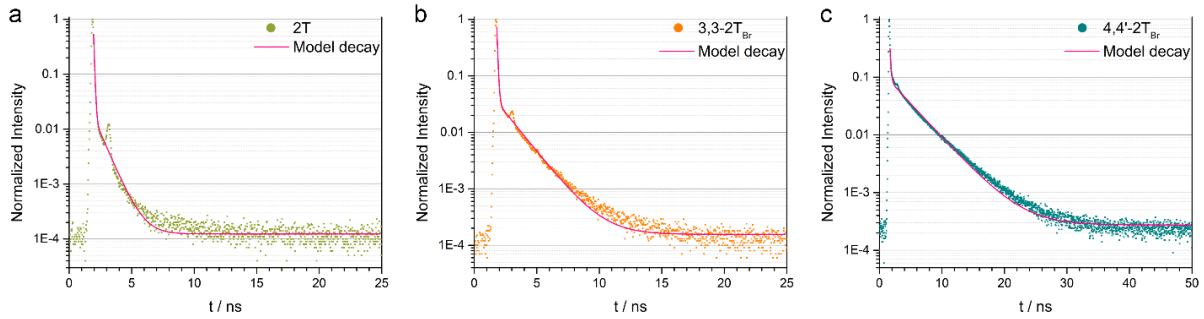

Figure 7.12: PL decay histograms of the monomers measured in solution (50 µM in $CHCl_3$). Excitation at 378 nm and emission recorded at the respective emission maximum. (a) 2T: emission at 430 nm. (b) 3,3'-2T_{Br}: emission at 438 nm. (c) 4,4'-T_{Br}: emission at 434 nm. Experimental decay: dots in respective color, bi-exponential fit of the decay: pink line.

Table 7.3: PL decay times of the three monomers 2T, 3,3'-2T_{Br} and 4,4'-2T_{Br} measured in solution (50 µM in $CHCl_3$). The given errors are uncertainties from the fit and hence do not reflect the real time-resolution of the setup. The latter is limited by the laser pulse duration of around 100 ps.

		τ / ns	error / ns	fractional intensity / %
2T	τ_1	0.82	±0.04	29
	τ_2	0.064	±0.002	71
3,3'-2T_{Br}	τ_1	1.56	±0.03	54
	τ_2	0.068	±0.002	46
4,4'-2T_{Br}	τ_1	3.69	±0.05	91
	τ_2	0.14	±0.01	9

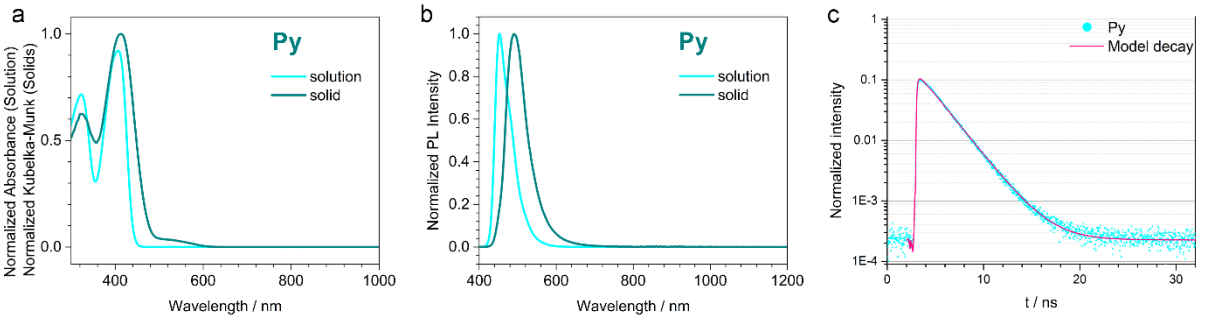

Figure 7.13: (a) Optical absorption spectra and (b) PL (λ_{exc} = 378 nm) spectra of the Py monomer measured in solution (50 µM in $CHCl_3$) and as solid. (c) PL decay histogram of Py measured in solution (50 µM in $CHCl_3$). Excitation at 378 nm and emission recorded at the emission maximum (455 nm). Experimental decay: dots in respective color, mono-exponential fit of the decay: pink line.

Table 7.4: PL decay time of Py shown above. The given error is the uncertainty from the fit and hence does not reflect the real time-resolution of the setup. The latter is limited by the laser pulse duration of around 100 ps.

	τ / ns	error / ns	fractional intensity / %
τ_1	2.17	±0.01	100

Table 7.5: PL decay times of the three COFs Py-2T, Py-3,3'-2T_{Br} and Py-4,4'-2T_{Br}. The given errors are uncertainties from the fit and hence do not reflect the real time-resolution of the setup. The latter is limited by the laser pulse duration of around 100 ps.

		τ / ns	error / ns	fractional intensity / %
Py-2T	τ_1	4.1	±0.2	13
	τ_2	0.74	±0.01	52
	τ_3	0.117	±0.003	35
Py-3,3'-2T_{Br}	τ_1	4.4	±0.3	16
	τ_2	0.72	±0.02	65
	τ_3	0.13	±0.01	19
Py-4,4'-2T_{Br}	τ_1	4.6	±0.4	7
	τ_2	0.63	±0.01	70
	τ_3	0.14	±0.01	23

7.5.9 Electron Microscopy

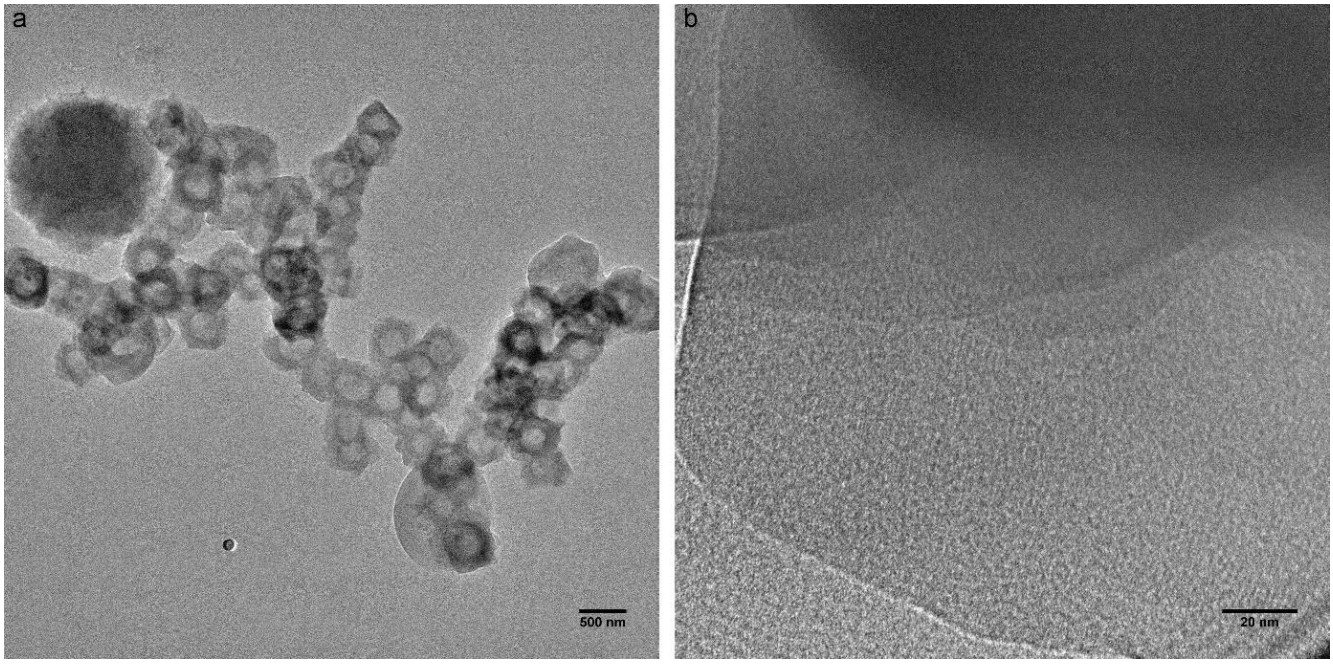

Figure 7.14: TEM image of Py-2T with (a) an overview of the hollow spheres and (b) the high resolution micrograph in which the crystal fringes of the COF crystallite.

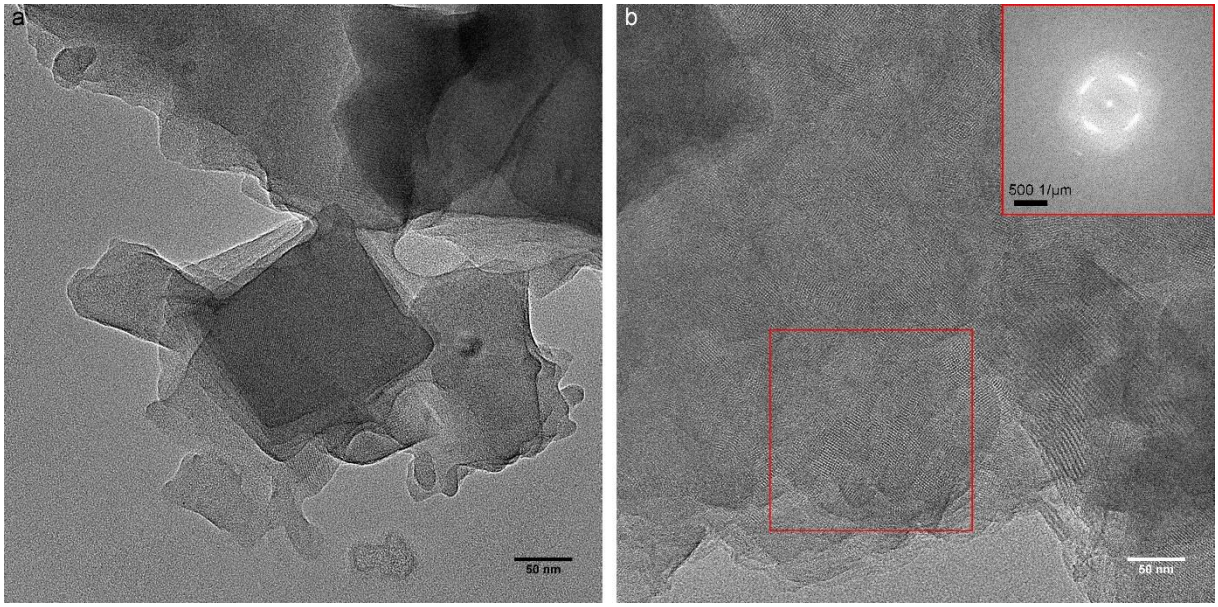

Figure 7.15: TEM image of Py-3,3'-2T_{Br} COF with (a) an overview of the rectangular particles and (b) the high resolution micrograph in which the crystal fringes of the pores are visible for the individual COF crystallites. The fast Fourier transform of the marked area is depicted in the inset on the top right. Maxima of Fourier transform of selected area: tetragonal crystal with lattice constants of around 2.18 nm.

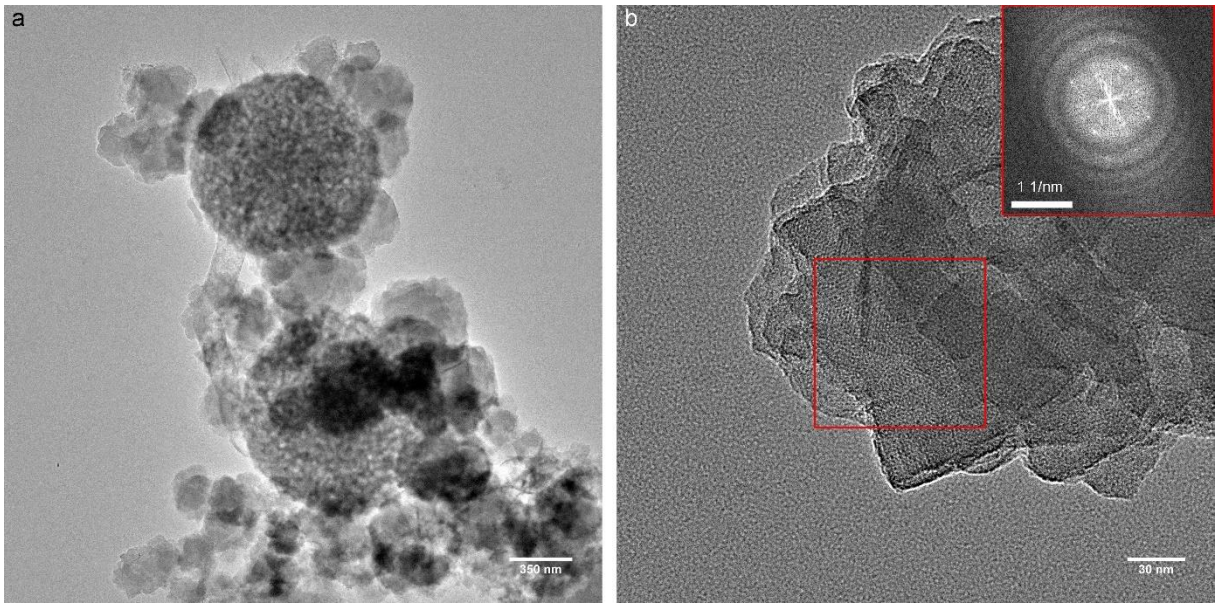

Figure 7.16: TEM image of Py-4,4'-2TBr with (a) an overview of the porous spheres and (b) the high resolution micrograph along the c-axis of the COF shows the periodic pore structure of the individual COF crystallites with pores visible. The fast Fourier transform of the marked area is depicted in the inset on the top right. Maxima of Fourier transform of selected area: tetragonal crystal with lattice constants of around 2.19 nm.

7.5.10 Nitrogen Sorption

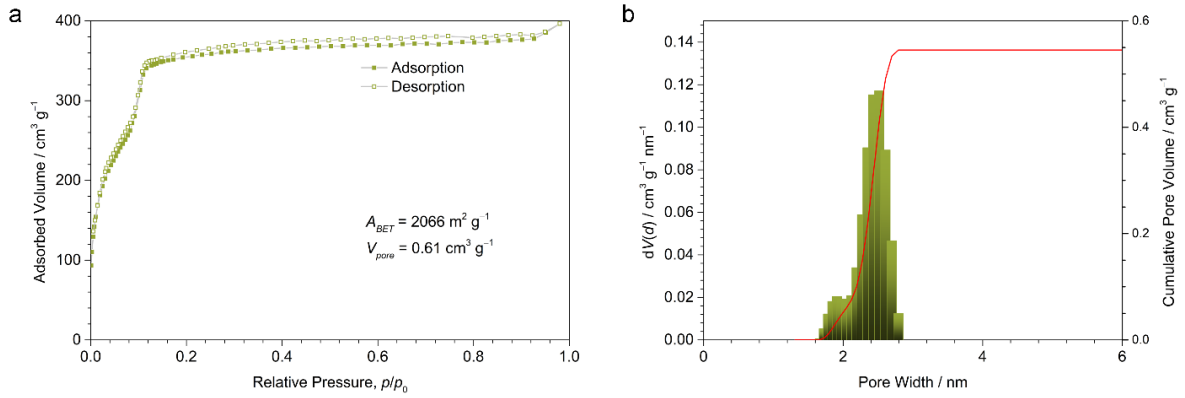

Figure 7.17: (a) Nitrogen sorption isotherms of Py-2T recorded at 77 K. (b) QSDFT calculation using the adsorption branch and desorption branch yields a pore size distribution with the maximum at 2.5 nm with a tail to smaller pore width, in excellent agreement with the pore diagonal of 2.47 nm in the Py-2T structure.

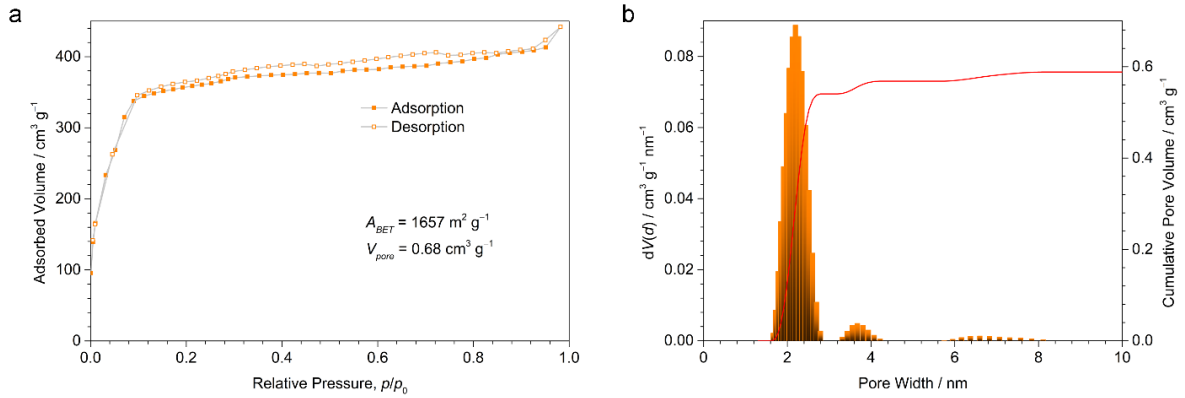

Figure 7.18: (a) Nitrogen sorption isotherms of Py-3,3'-2T$_{Br}$ recorded at 77 K. (b) QSDFT calculation using the adsorption branch and desorption branch yields a pore size distribution with the maximum at 2.2 nm, in excellent agreement with the pore diagonal of 2.15 nm in the Py-3,3'-2T$_{Br}$ structure.

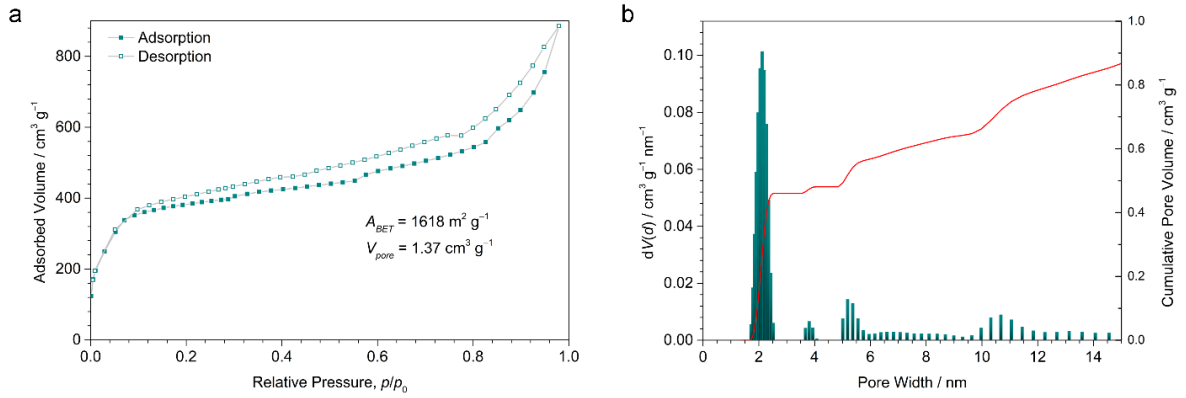

Figure 7.19: (a) Nitrogen sorption isotherms of Py-4,4'-2T_{Br} recorded at 77 K. (b) QSDFT calculation using the adsorption branch and desorption branch yields a pore size distribution with the maximum at 2.1 nm, in good agreement with the pore diagonal of 1.93 nm in the Py-4,4'-2T_{Br} structure.

Table 7.6: Comparison of experimentally derived BET surface area and calculated Connolly surface area from simulated COF structures, which reveals a good agreement of experimental and calculated values. We note that the difference of the surface area arises from the significantly increased weight of the brominated COF species.

	A_{BET} [m^2 g^{-1}]	$A_{Connolly}$ [m^2 g^{-1}]
Py-2T	2066	2164
Py-3,3'-2T_{Br}	1657	1708
Py-4,4'-2T_{Br}	1618	1700

7.5.11 References

[1] Bhuwalka, A.; Mike, J. F.; Intemann, J. J.; Ellern, A.; Jeffries-El, M., A versatile and efficient synthesis of bithiophene-based dicarboxaldehydes from a common synthon. *Org. Biomol. Chem.* **2015,** *13* (36), 9462-9470.

[2] Kano, S.; Yuasa, Y.; Yokomatsu, T.; Shibuya, S., Synthesis of 2-Substituted 3,5-Dibromothiophenes through Base-catalyzed Halogen Dance Reaction of 2,5-Dibromothiophene. *Heterocycles* **1983,** *20* (10), 2035-2037.

[3] Jin, S.; Sakurai, T.; Kowalczyk, T.; Dalapati, S.; Xu, F.; Wei, H.; Chen, X.; Gao, J.; Seki, S.; Irle, S.; Jiang, D., Two-Dimensional Tetrathiafulvalene Covalent Organic Frameworks: Towards Latticed Conductive Organic Salts. *Chem. - Eur. J.* **2014,** *20* (45), 14608-14613.

[4] Auras, F.; Ascherl, L.; Hakimioun, A. H.; Margraf, J. T.; Hanusch, F. C.; Reuter, S.; Bessinger, D.; Döblinger, M.; Hettstedt, C.; Karaghiosoff, K.; Herbert, S.; Knochel, P.; Clark, T.; Bein, T., Synchronized Offset Stacking: A Concept for Growing Large-Domain and Highly Crystalline 2D Covalent Organic Frameworks. *J. Am. Chem. Soc.* **2016,** *138* (51), 16703-16710.

8 On the lookout for new optically interesting molecules

This chapter is published as:

Jie Li,‡ Eric Tan,‡ Niklas Keller,‡ Yi-Hung Chen, Peter M. Zehetmaier, Andreas C. Jakowetz, Thomas Bein, and Paul Knochel, *J. Am. Soc. Chem.* **2019**, *141*, pp 98–103.

‡ These authors contributed equally.

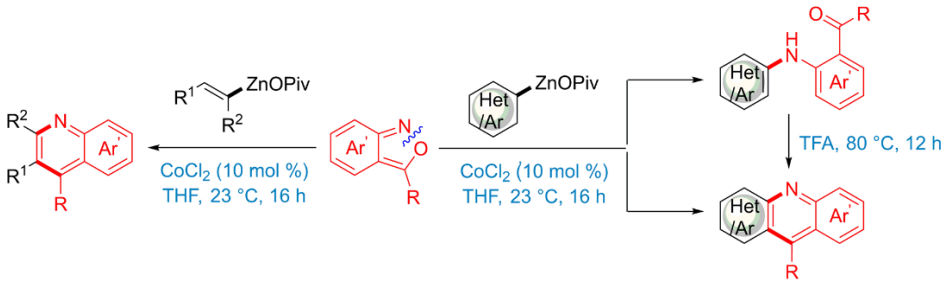

The reaction of various organozinc pivalates with anthranils provides anilines derivatives, which cyclize under acidic conditions providing condensed quinolines. Using alkenyl-zinc pivalates, electron-rich arylzinc pivalates or heterocyclic zinc pivalates produces directly the condensed quinolines of which several structures belong to new heterocyclic scaffolds. These N-heterocycles are of particular interest for organic light emitting diodes with their high photoluminescence quantum yields and long exciton lifetimes as well as for hole-transporting materials in methyl-ammonium lead iodide perovskites solar cells due to an optimal band alignment for holes and a large bandgap.

8.1 Introduction

Condensed N-heterocycles are important molecules for material science applications.[1-2] Although, several synthetic methods have been developed for the preparation of condensed N-heterocycles, there is a lack of generality in such methods, especially for the preparation of condensed quinolines of type **1**, which are of interest as new materials.[1-2] Organometallics reagents are very useful for constructing heterocyclic scaffolds,[3-8] especially organozinc reagents have found wide applications.[9-10] Organozinc pivalates are a class of zinc organometallics with enhanced air and moisture-stability, which can be stored for months as solids under argon.[11] Recently, we have reported a new cobalt-catalyzed electrophilic amination using the reaction of organozinc pivalates[12-16] with hydroxylamine benzoates.[17-33] Compared to Pd- or Ni-catalysts, the use of cobalt salts[34-36] was preferred for toxicity and price considerations.[37] This amination had a broad reaction scope and proceeded under mild reaction conditions. Herein, we report an extension of this amination using readily accessible anthranils[38-40] of type **2** as electrophilic reaction partner.

8.2 Results and Discussion

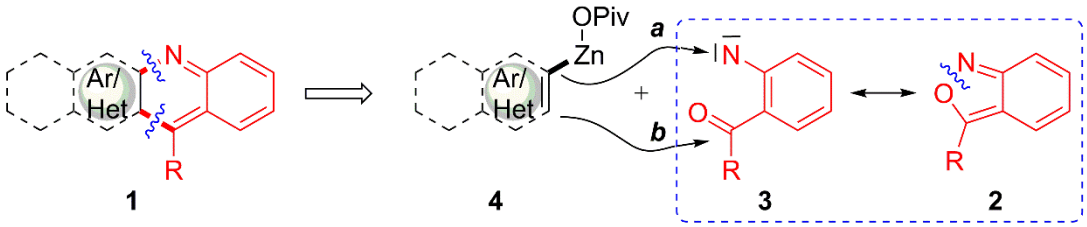

(1)

We envision that anthranils **2** could react (formally via resonance structure **3**, eq. 1) with alkenyl-, aryl- or heteroaryl-zinc pivalates **4** (step a) to provide after a Friedel-Crafts reaction (step b) condensed quinoline structures of type **1**. Preliminary experiments show that PhZnOPiv (**4a**) reacts best with anthranil (**2a**) in the presence of 10 mol % of $CoCl_2$ at 23 °C for 16 h to provide the amino-aldehyde **5a** in 65% isolated yield. Other transition-metal salts, such as $CrCl_2$, $MnCl_2$, $FeCl_2$ or $Fe(acac)_3$ gave no product (Table 8.1, entries 1–7).[41]

Table 8.1: Optimization for cobalt-catalyzed amination using anthranils (**2a**).[a]

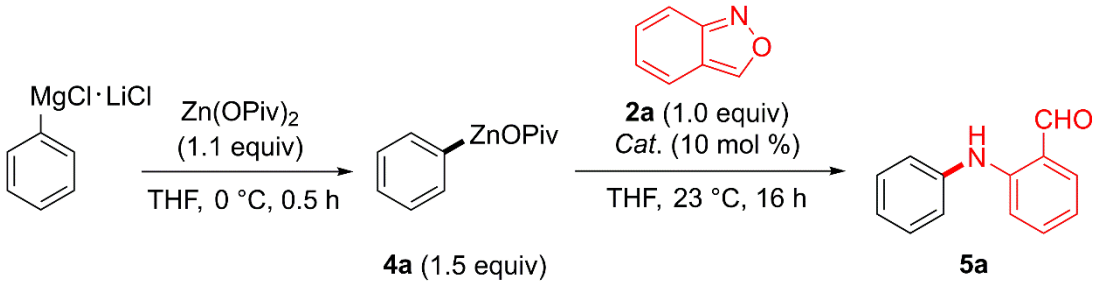

entry	[met] (10 mol %)	yield (%)[b]
1	$CoCl_2$	65
2	$MnCl_2$	0
3	$CrCl_2$	0
4	$FeCl_2$	0
5	$Fe(acac)_3$	0
6	--	0
7	CoCl2	0[c]

[a] Reaction conditions: **4a** (0.75 mmol), **2a** (0.50 mmol), [cat.] (10 mol %), THF (2.0 mL), 23 °C, N_2, 16 h. [b] Isolated yields. [c] PhMgCl (1.5 equiv) was used.

Using these conditions, we have prepared a range of amino-aldehydes (**5b–5f**) and amino-ketones (**5g–5k**) in 56–91% yields (Scheme 8.1). Organozinc pivalates were the best nucleophiles, although arylalanes of type $ArAlEt_2$ can also be used (see appendix for further

details). Also, heterocyclic zinc pivalates derived from the pyrazole and indole scaffolds produce the expected aniline derivatives **5l** and **5m** in 55–75% yields. Moreover, ferrocenylzinc pivalate, as well as methyl- or benzylzinc pivalates smoothly delivered the corresponding anilines **5n–5p** in 40–79% yields.

Scheme 8.1: Amino-aldehydes and amino-ketones of type **5** obtained by cobalt-catalyzed reaction of organozinc pivalates (**4**) with anthranils (**2**). [a] $PhAl(Et)_2$ (1.5 equiv) was used as nucleophile.

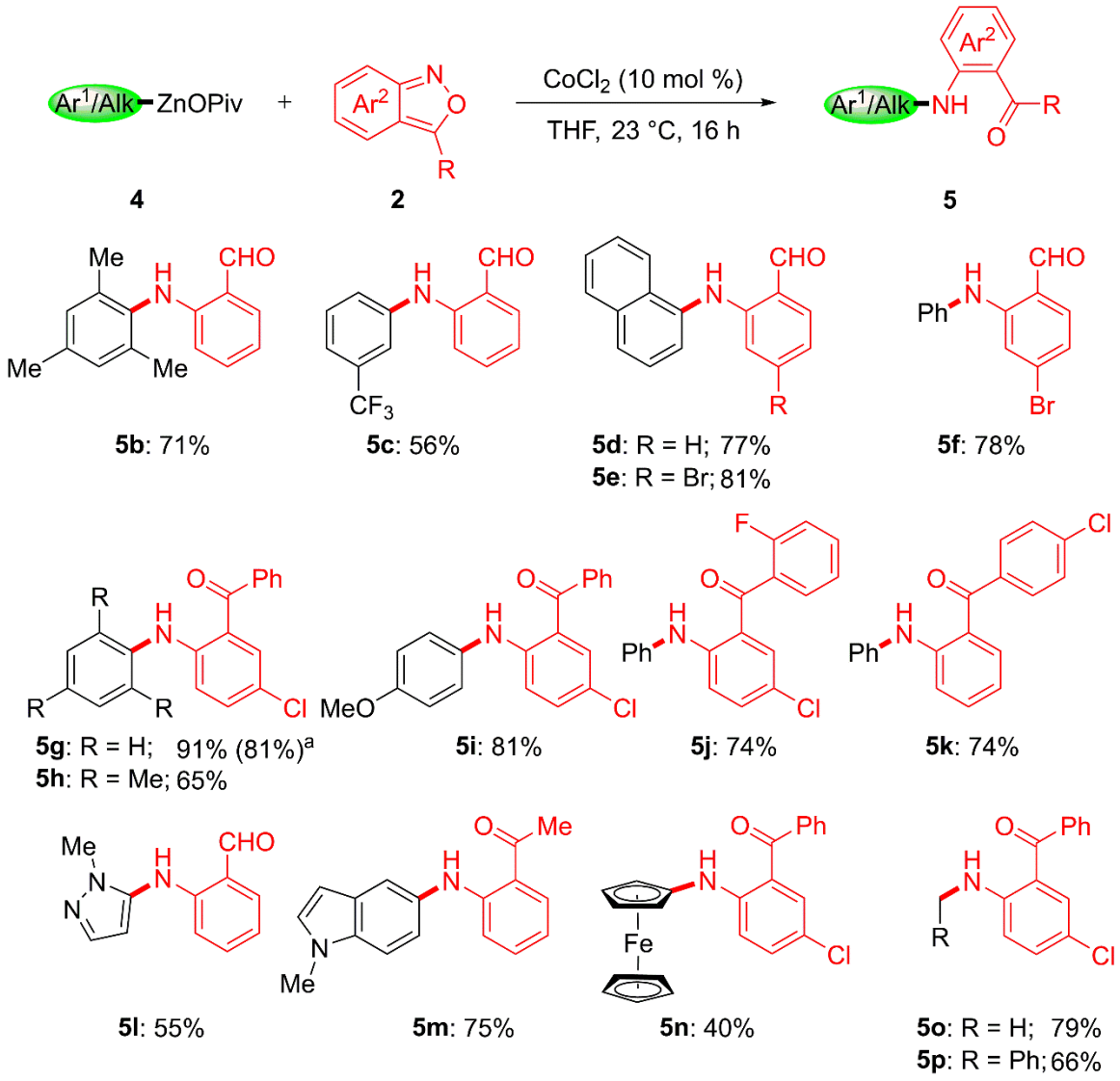

The treatment of aniline derivatives of type **5** in TFA for 12 h at 80 °C provides the corresponding acridines (**6a–6c**) in excellent yields (Scheme 8.2). We have extended this preparation of quinoline derivatives by treating various anthranils (**2**) with alkenylzinc pivalates[42] under our standard conditions. To our delight, we observed after the electrophilic amination step, a cycloisomerisation which in a one-pot procedure provided the quinolines **8a–8n** in 62–96% yields (Scheme 8.3).

Scheme 8.2: Condensed N-heterocycles prepared from anilines of type **5**.

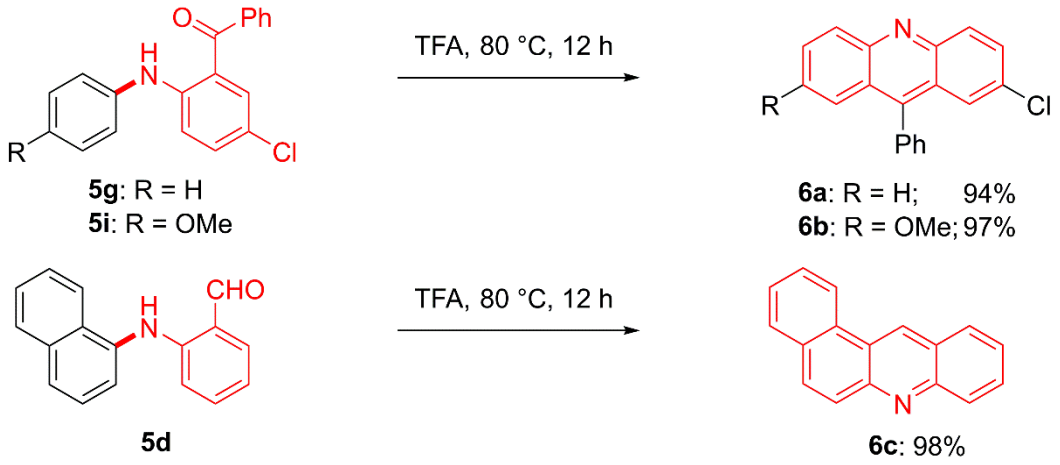

Scheme 8.3: Cobalt-catalyzed amination of alkenylzinc pivalates (7) with anthranils (2).

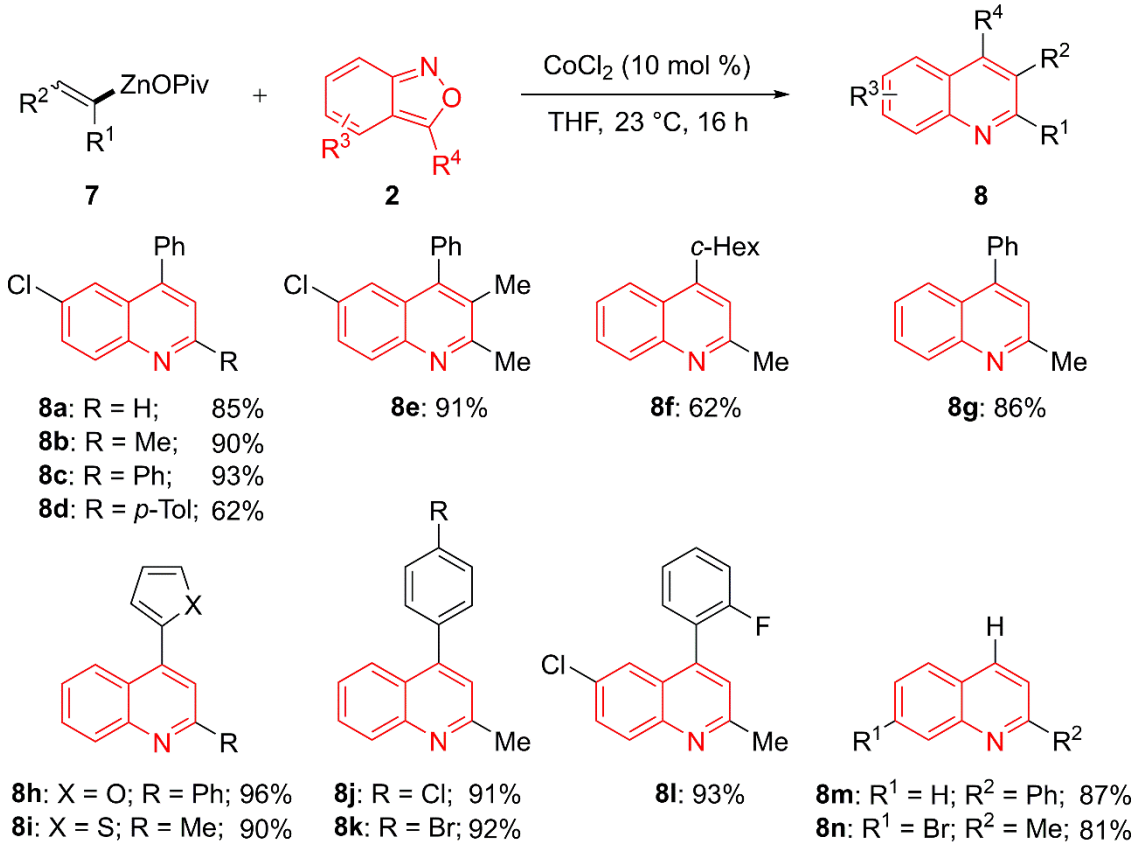

Furthermore, we have extended this new quinoline synthesis using aryl and heterocylic zinc pivalates **9**, which were prepared from the corresponding (hetero)aryl bromides by Mg-insertion in the presence of LiCl[43] (**9a–9g**), or by a directed metalation of heterocyclic substrates with TMP-bases (TMP = 2,2,6,6-tetramethylpiperidyl)[44-46] such as TMPZnOPiv·LiCl[14, 47-48] or TMPMgCl·LiCl[49-52] (**9h–9n**), followed by transmetalation with $Zn(OPiv)_2$. By using especially

electron-rich organozinc pivalates, we have observed using our standard conditions, that after amination a cyclization occurs (via A and B in Table 8.2) leading to various condensed N-heterocyclic derivatives **10a–10p**. In several cases, fully new types of heterocycles were ob-

Table 8.2: Substrate scope of (hetero)arylzinc pivalates **9** leading to condensed N-heterocycles type **10**.

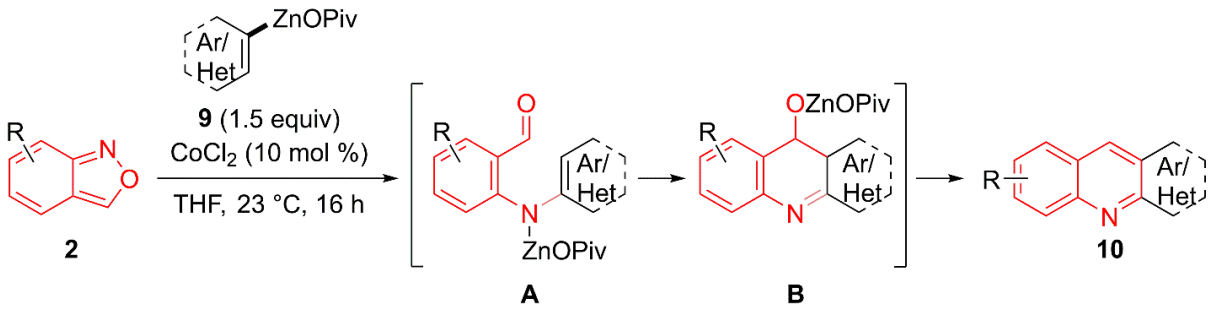

entry	(hetero) arvl-zinc pivalate of type **9**	anthranil **2**	product of type **10**[b]
1	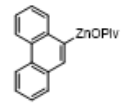 **9a**	 **2a**	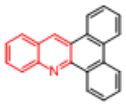 **10a**: 61%
2	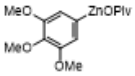 **9b**	**2a**	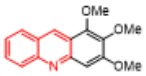 **10b**: 55%
3	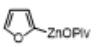 **9c**	**2a**	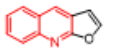 **10c**: 61%
4	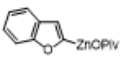 **9d**	**2a**	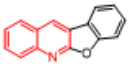 **10d**: 75%
5	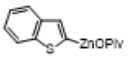 **9e**	**2a**	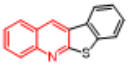 **10e**: 60%
6	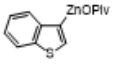 **9f**	**2a**	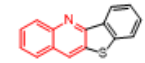 **10f**: 45%
7	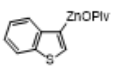 **9f**	**2b**	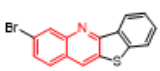 **10g**: 40%
8	 **9g**	**2a**	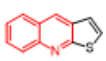 **10h**: 58%
9	 **9g**	**2b**	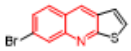 **10i**: 38%
10	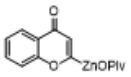 **9h**	**2a**	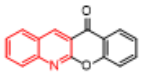 **10j**: 50%
11	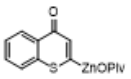 **9i**	**2a**	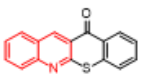 **10k**: 61%
12	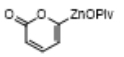 **9j**	**2a**	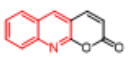 **10l**: 54%
13	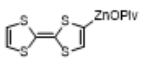 **9k**	**2a**	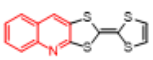 **10m**: 51%
14	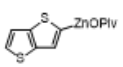 **9l**	**2a**	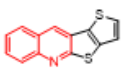 **10n**: 53%
15	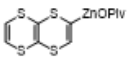 **9m**	**2a**	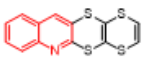 **10o**: 55%
16	 **9n**	**2a**	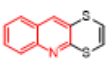 **10p**: 80%

tained (**10l–10p**). Of special interest for material applications may be the TTF-derived heterocycle[53-55] **10m** (entry 13), as well as the related sulfur-contained heterocycles[56-57] **10n** to **10p** (entries 14–16).

Furthermore, we have shown that some of these heterocycles can be further functionalized by metalation. Thus, the condensed heterocycles **10m** and **10f** were treated with TMPMgCl·LiCl at 23 °C for 16 h to give complete magnesiation (as shown by iodolysis, for further details see appendix).[49-52] Addition of $Zn(OPiv)_2$ followed by a Negishi cross-coupling using X-Phos[58] gave the arylated N-heterocycle bond.[15] Also a Buchwald–Hartwig amination[59] of **10g** provided the aminated thieno[2,3-*b*]quinoline **13** in 72% yield. Interestingly, the zinc pivalate derived from thieno[2,3-*b*]quinoline (**10f**) reacted again with anthranil (**4a**) in the presence of $CoCl_2$ (10 mol %) furnishing the new heterocycle **14** in 34% yield (Scheme 8.4).

Scheme 8.4: Late-stage functionalizations of N-heterocycles.

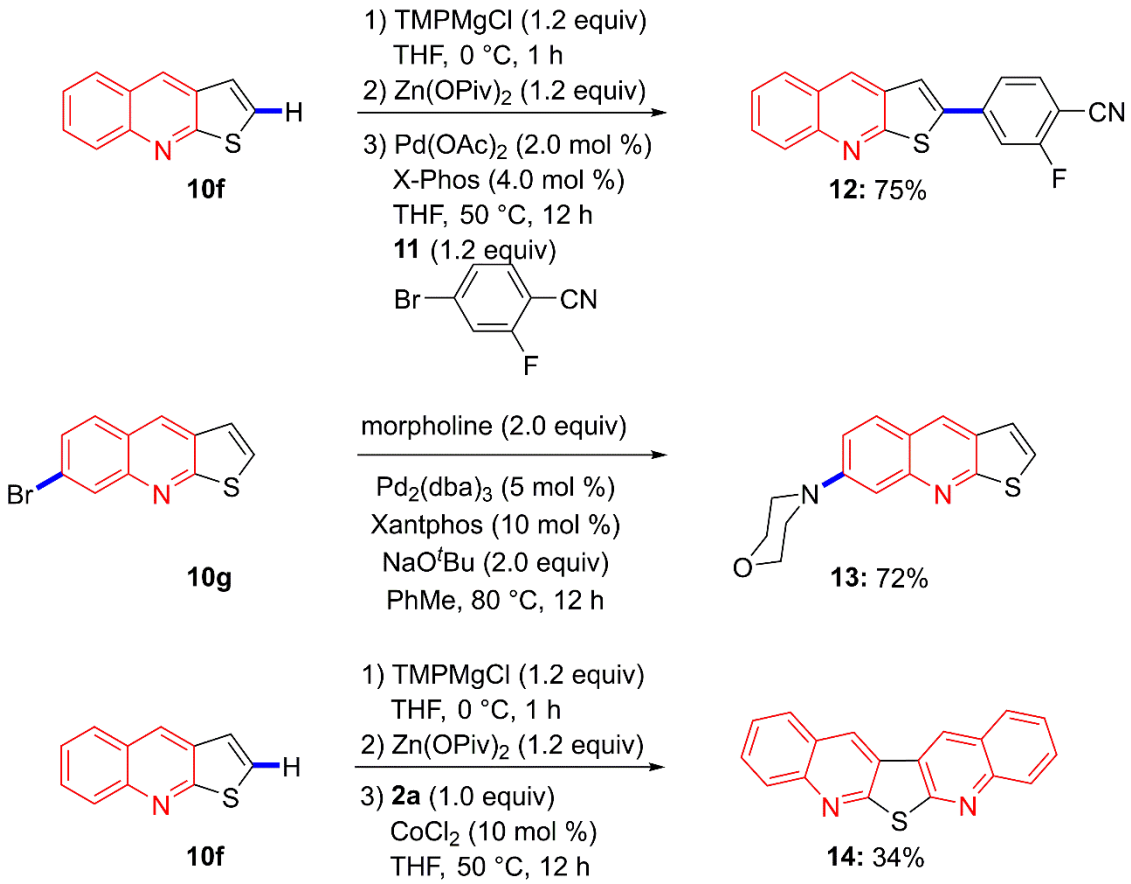

In order to gain insights about the electronic structures of these heterocycles, we analyzed the optical properties and performed in some cases additional cyclovoltammetry measurements. Studies about the optical features of these N-heterocycles can allow for the preparation of tailor-

made molecules with optimum optical properties. All compounds showed a strong absorption in the UV region whereas careful tuning or functionalization of the quinoline backbone allowed extending the absorption towards the visible range (see appendix for further details). This was achieved by simply increasing the size of the chromophore, exchanging the heteroatoms or inserting functional groups such as a methoxy group. In the case of **6a** and **6b**, it was noticed that the insertion of a methoxy group at the acridine body leads to a small red-shift and an increased absorption of wavelengths longer than 300 nm (Figure 8.1a). When comparing **10d**, **10e** and **10f**, or **10j** and **10k**, it was observed that the exchange of oxygen heteroatoms with sulfur leads to a red-shift of the absorption which results in a 0.3 eV reduced bandgap (see appendix).[60-61] This was explained by the higher electronegativity of oxygen which led to a more localized electron density and subsequently a loss of aromaticity of the heterocycles. For the sulfur containing heterocycles, the better aromaticity led to larger π-systems and thus absorption of longer wavelengths.

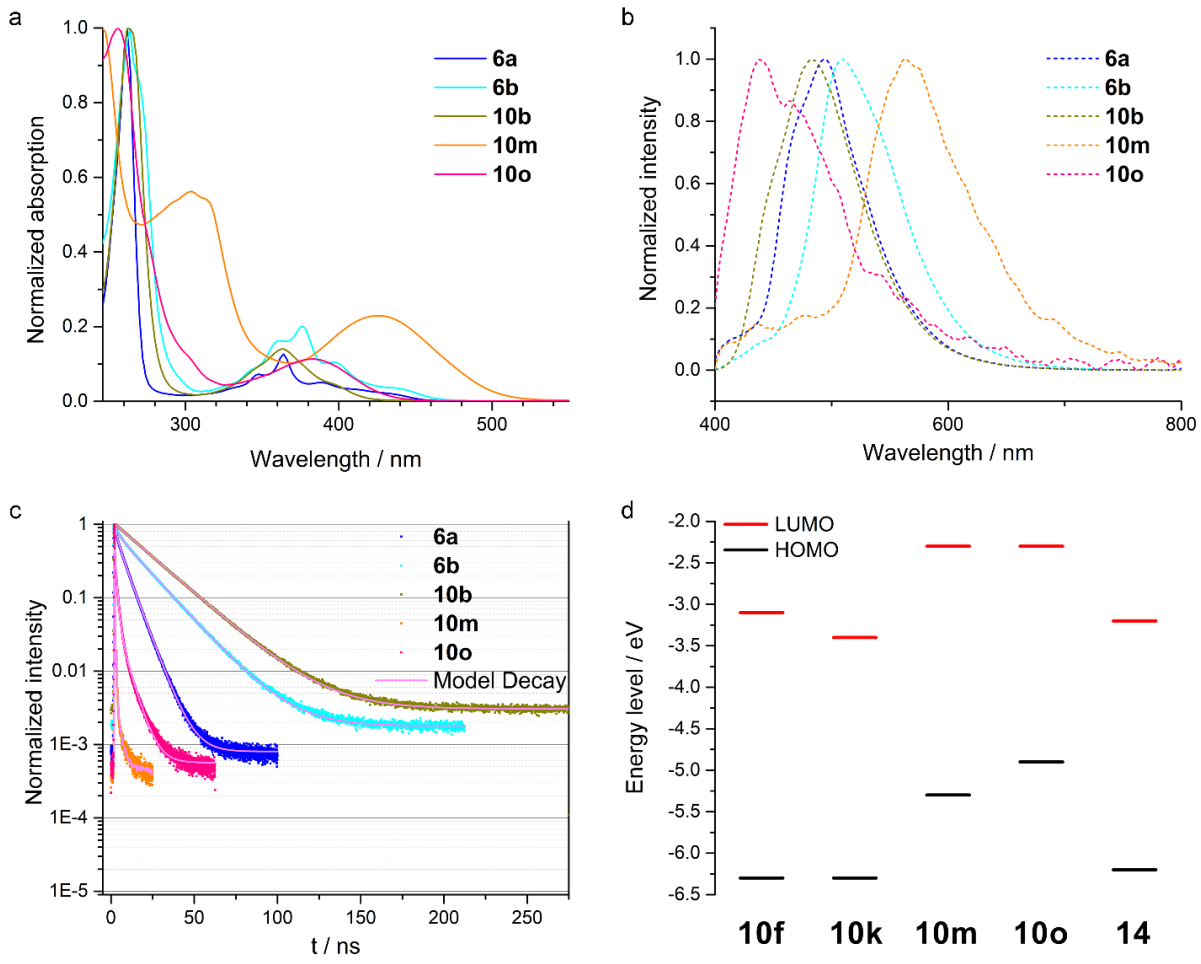

Figure 8.1: (a) Absorption spectra, (b) photoluminescence spectra and (c) time-correlated single photon counting in solution (50 µM in DCM). (d) Energy levels of selected condensed N-heterocycles obtained by CV measurements and optical bandgap.

Upon excitation at 378 nm the compounds showed photoluminescence (PL) in the range of 400 nm to 570 nm. The strongest emission was found for **6b** at 510 nm followed by **10b**, **10a**, **6a** and **14** with their maxima at 482 nm, 398 nm, 494 nm and 434 nm respectively. Additionally, a significant red-shift was observed for the PL maxima of **10m** compared to **10o** which was attributed to the larger π-system and the TTF-scaffold (Figure 8.1b). We measured the photoluminescence quantum yields (PLQY) of the heterocycles whereby the highest PLQY of 37% was observed for compound **6b**, followed by the other acridine containing heterocycles **10b** (26%) and 6a (15%). The other heterocycles showed only moderate PLQY below 5% (see appendix for further details). Interestingly, the compounds with the strongest PL were all containing an acridine core unit. Furthermore, by just flipping a thiophene unit in compound **10e**, i.e. the sulfur and nitrogen heteroatoms were not in neighbouring position but on opposite sites (**10f**), the PL position and intensity as well as the lifetimes did drastically change. In this fashion, it is possible to tune PL properties without changing the absorption bands and bandgap considerably (see appendix for further details). The longest PL decay times were measured on **10b** with an acridine core and three methoxy groups. Furthermore, the PL lifetimes of **6b** were more than doubled compared to **6a** which is missing a methoxy group. Also interesting was the that the TTF-scaffold in **10m** resulted in one of the fastest PL decays (Figure 8.1c). These results give an indication that the inserted methoxy groups are of great advantage to increase PL lifetimes. Regarding the overall emission properties of the studied N-heterocycles, applications in the field of OLEDs are promising. Materials for OLEDs require, among other properties, a long PL lifetime and high PL quantum yield, i.e. low nonradiative recombination loss, in order to provide high device efficiencies.[62-63] In our study, compound **6b** was found to be a promising candidate for OLEDs with a high PL quantum yield and long lifetimes. Our values are comparable with reports in the literature, particularly for materials based on singlet emission (fluorescence).[62, 64-66] On the basis of these results, one can even improve or tailor-design the desired features by adding new or different functional groups, such as methoxy groups, which would be part of further studies.

In order to investigate the energy levels of compounds **10f**, **10k**, **10m**, **10o** and **14**, we performed cyclic voltammetry (CV) measurements. The energy for the highest occupied molecular orbital (HOMO) was extracted from forward scans in an acetonitrile solution using the internal standard ferrocene with a potential of $E(Fc/Fc^+) = -4.8$ eV vs. E_{vac}.[67] The HOMO levels for **10f**, **10k** and **14** were found to be in the same region around −6.3 eV, whereas **10m** and **10o** exhibit significantly higher HOMO energies with −4.9 eV and −5.3 eV, respectively. The TTF-derived

heterocycle displayed the highest HOMO, which is in good agreement with results from the literature (Figure 8.1d).[55] Solely from the energy level of compound **10m** and **10o** the alignment would be suitable for an application as hole transporting material in organic photovoltaics (OPVs) or in the case of **10o** for perovskite solar cells. For the latter, not only the HOMO is in good alignment with the commonly used methylammonium lead iodide (MAPI) perovskite, but also the LUMO value is high enough to effectively block electrons. The large bandgap also implies that no visible light is absorbed which will hence not diminish the light to be absorbed by the active layer.[68]

8.3 Conclusion

In summary, we have reported a convenient cobalt-catalyzed amination using various anthranils and functionalized aryl-, heteroaryl-, alkenyl- and alkyl-zinc pivalates under mild reaction conditions. This method gives an access to condensed N-heterocycles, of which several are new heterocyclic scaffolds. The optical characterization of the condensed N-heterocycles revealed promising properties for applications such as organic light emitting diodes or hole transporting materials e.g. in perovskite solar cells. Further extensions of the method are currently underway in our laboratory and will provide a broad set of potential building blocks for new materials.

8.4 References

[1] Bunz, U. H. F.; Engelhart, J. U.; Lindner, B. D.; Schaffroth, M., Large N-heteroacenes: new tricks for very old dogs. *Angew. Chem., Int. Ed.* **2013,** *52*, 3810.

[2] Bunz, U. H. F., The larger linear N-heteroacenes. *Acc. Chem. Res.* **2015,** *48*, 1676.

[3] Eicher, T.; Hauptmann, S., *The Chemistry of Heterocycles*. 2003.

[4] Joule, J. A.; Mills, K., *Heterocyclic Chemistry*. 2000.

[5] Bartoli, G.; Palmieri, G.; Bosco, M.; Dalpozzo, R., The reaction of vinyl grignard reagents with 2-substituted nitroarenes: a new approach to the synthesis of 7-substituted indoles. *Tetrahedron Lett.* **1989,** *30*, 2129.

[6] Frischmuth, A.; Knochel, P., Preparation of functionalized indoles and azaindoles by the intramolecular copper-mediated carbomagnesiation of ynamides. *Angew. Chem., Int. Ed.* **2013,** *52*, 10084.

[7] Gati, W.; Couty, F.; Boubaker, T.; Rammah, M. M.; Rammah, M. B.; Evano, G., Intramolecular carbocupration of N-aryl-ynamides: a modular indole synthesis. *Org. Lett.* **2013,** *15*, 3122.

[8] Nickel, J.; Fernandez, M.; Klier, L.; Knochel, P., Synthesis of pyrrolo[2,3-d]pyrimidines by copper-mediated carbomagnesiations of N-sulfonyl ynamides and application to the preparation of rigidin A and a 7-azaserotonin derivative. *Chem. - Eur. J.* **2016,** *22*, 14397.

[9] Chen, Y. H.; Ellwart, M.; Malakhov, V.; Knochel, P., Solid organozinc pivalates: a new class of zinc organometallics with greatly enhanced air- and moisture-stability. *Synthesis* **2017,** *49*, 3215.

[10] Haas, D.; Hammann, J. M.; Greiner, R.; Knochel, P., Recent developments in Negishi cross-coupling eeactions. *ACS Catal.* **2016,** *6*, 1540.

[11] Hernán-Gómez, A.; Herd, E.; Hevia, E.; Kennedy, A. R.; Knochel, P.; Koszinowski, K.; Manolikakes, S. M.; Mulvey, R. E.; Schnegelsberg, C., Organozinc pivalate reagents: segregation, solubility, stabilization, and structural insights. *Angew. Chem., Int. Ed.* **2014,** *53*, 2706.

[12] Greshock, T. J.; Moore, K. P.; McClain, R. T.; Bellomo, A.; Chung, C. K.; Dreher, S. D.; Kutchukian, P. S.; Peng, Z.; Davies, I. W.; Vachal, P.; Ellwart, M.; Manolikakes, S. M.; Knochel, P.; Nantermet, P. G., Synthesis of complex druglike molecules by the sse of highly functionalized bench-stable organozinc reagents. *Angew. Chem., Int. Ed.* **2016,** *55*, 13714.

[13] Manolikakes, S. M.; Ellwart, M.; Stathakis, C. I.; Knochel, P., Air-stable solid aryl and heteroaryl organozinc pivalates: syntheses and applications in organic synthesis. *Chem. - Eur. J.* **2014,** *20*, 12289.

[14] Stathakis, C. I.; Manolikakes, S. M.; Knochel, P., TMPZnOPiv•LiCl: a new base for the preparation of air-stable solid zinc pivalates of sensitive aromatics and heteroaromatics. *Org. Lett.* **2013,** *15*, 1302.

[15] Colombe, J. R.; Bernhardt, S.; Stathakis, C.; Buchwald, S. L.; Knochel, P., Synthesis of solid 2-pyridylzinc reagents and their application in Negishi reactions. *Org. Lett.* **2013,** *15*, 5754.

[16] Stathakis, C. I.; Bernhardt, S.; Quint, V.; Knochel, P., Improved air-stable solid aromatic and heterocyclic zinc reagents by highly selective metalations for Negishi cross-couplings. *Angew. Chem., Int. Ed.* **2012,** *51*, 9428.

[17] Chen, Y. H.; Grassl, S.; Knochel, P., Cobalt-catalyzed electrophilic amination of aryl- and heteroarylzinc pivalates with N-hydroxylamine benzoates. *Angew. Chem., Int. Ed.* **2018,** *57*, 1108.

[18] Gao, H.; Zhou, Z.; Kwon, D. H.; Coombs, J.; Jones, S.; Behnke, N. E.; Ess, D. H.; Kürti, L., Rapid heteroatom transfer to arylmetals utilizing multifunctional reagent scaffolds. *Nat. Chem.* **2017,** *9*, 681.

[19] Zhou, Z.; Ma, Z.; Behnke, N. E.; Gao, H.; Kürti, L., Non-deprotonative primary and secondary amination of (hetero)arylmetals. *J. Am. Chem. Soc.* **2017,** *139*, 115.

[20] Liu, J.; Wu, K.; Shen, T.; Liang, Y.; Zou, M.; Zhu, Y.; Li, X.; Li, X.; Jiao, N., Fe-catalyzed amination of (hetero)arenes with a redox-active aminating reagent under mild conditions. *Chem. - Eur. J.* **2017,** *23*, 563.

[21] Hendrick, C. E.; Bitting, K. J.; Cho, S.; Wang, Q., Site-selective copper-catalyzed amination and azidation of arenes and heteroarenes via deprotonative zincation. *J. Am. Chem. Soc.* **2017,** *139*, 11622.

[22] Zhou, S.; Yang, Z.; Chen, X.; Li, Y.; Zhang, L.; Fang, H.; Wang, W.; Zhu, X.; Wang, S., Copper-catalyzed electrophilic amination of organoaluminum nucleophiles with O-benzoyl hydroxylamines. *J. Org. Chem.* **2015,** *80*, 6323.

[23] McDonald, S. L.; Hendrick, C. E.; Wang, Q., Copper-catalyzed electrophilic amination of heteroarenes and arenes by C-H zincation. *Angew. Chem., Int. Ed.* **2014,** *53*, 4667.

[24] Nguyen, M. H.; Smith, A. B., Copper-catalyzed electrophilic amination of organolithiums mediated by recoverable siloxane transfer agents. *Org. Lett.* **2013,** *15*, 4872.

[25] Qian, X.; Yu, Z.; Auffrant, A.; Gosmini, C., Cobalt-catalyzed electrophilic amination of arylzincs with N-chloroamines. *Chem. - Eur. J.* **2013,** *19*, 6225.

[26] Barker, T. J.; Jarvo, E. R., Titanium-mediated amination of Grignard reagents using primary and secondary amines. *Angew. Chem., Int. Ed.* **2011,** *50*, 8325.

[27] He, C.; Chen, C.; Cheng, J.; Liu, C.; Liu, W.; Li, Q.; Lei, A., Aryl halide tolerated electrophilic amination of arylboronic acids with N-chloroamides catalyzed by CuCl at room temperature. *Angew. Chem., Int. Ed.* **2008,** *47*, 6414.

[28] Kawano, T.; Hirano, K.; Satoh, T.; Miura, M., A new entry of amination reagents for heteroaromatic C–H bonds: copper-catalyzed direct amination of azoles with chloroamines at room temperature. *J. Am. Chem. Soc.* **2010,** *132*, 6900.

[29] Barker, T. J.; Jarvo, E. R., Umpolung amination: nickel-catalyzed coupling reactions of N,N-dialkyl-N-chloroamines with diorganozinc reagents. *J. Am. Chem. Soc.* **2009,** *131*, 15598.

[30] Campbell, M. J.; Johnson, J. S., Mechanistic studies of the copper-catalyzed electrophilic amination of diorganozinc reagents and development of a zinc-free protocol. *Org. Lett.* **2007,** *9*, 1521.

[31] Hendrick, C. E.; Wang, Q., Emerging developments using nitrogen-heteroatom bonds as amination reagents in the synthesis of aminoarenes. *J. Org. Chem.* **2017,** *82*, 839.

[32] Dong, X.; Liu, Q.; Dong, Y.; Liu, H., Transition-metal-catalyzed electrophilic amination: application of O-benzoylhydroxylamines in the construction of the C–N bond. *Chem. - Eur. J.* **2017,** *23*, 2481.

[33] Yan, X.; Yang, X.; Xi, C., Recent progress in copper-catalyzed electrophilic amination. *Catal. Sci. Technol.* **2014,** *4*, 4169.

[34] Knappke, C. E. I.; Grupe, S.; Gartner, D.; Corpet, M.; Gosmini, C.; Jacobi von Wangelin, A., Reductive cross-coupling reactions between two electrophiles. *Chem. - Eur. J.* **2014,** *20*, 6828.

[35] Cahiez, G.; Moyeux, A., Cobalt-catalyzed cross-coupling reactions. *Chem. Rev.* **2010,** *110*, 1435.

[36] Gosmini, C.; Begouin, J. M.; Moncomble, A., Cobalt-catalyzed cross-coupling reactions. *Chem. Commun.* **2008**, 3221.

[37] Egorova, K. S.; Ananikov, V. P., *Angew. Chem., Int. Ed.* **2016,** *55*, 12150.

[38] Yu, S.; Tang, G.; Li, Y.; Zhou, X.; Lan, Y.; Li, X., Anthranil: an aminating reagent leading to bifunctionality for both C(sp3)–H and C(sp2)–H under rhodium(III) catalysis. *Angew. Chem., Int. Ed.* **2016,** *55*, 8696.

[39] Zou, M.; Liu, J.; Tang, C.; Jiao, N., Rh-catalyzed N–O bond cleavage of anthranil: a C–H amination reagent for simultaneous incorporation of amine and a functional group. *Org. Lett.* **2016,** *18*, 3030.

[40] Wang, M.; Kong, L.; Wang, F.; Li, X., Rhodium-catalyzed amination and annulation of arenes with anthranils: C-H activation assisted by weakly coordinating amides. *Adv. Synth. Catal.* **2017,** *359*, 4411.

[41] Baum, J. S.; Condon, M. E.; Shook, D. A., Nickel-catalyzed transformations of 2,1-benzisoxazoles with organozinc reagents. *J. Org. Chem.* **1987,** *52*, 2983.

[42] Li, J.; Knochel, P., Cobalt-catalyzed cross-couplings between alkenyl acetates and aryl or alkenyl zinc pivalates. *Angew. Chem., Int. Ed.* **2018,** *57*, 11436.

[43] Piller, F. M.; Appukkuttan, P.; Gavryushin, A.; Helm, M.; Knochel, P., Convenient preparation of polyfunctional aryl magnesium reagents by a direct magnesium insertion in the presence of LiCl. *Angew. Chem., Int. Ed.* **2008,** *47*, 6802.

[44] Uzelac, M.; Kennedy, A. R.; Hevia, E.; Mulvey, R. E., Transforming LiTMP lithiation of challenging diazines through Gallium alkyl trans-metal-trapping. *Angew. Chem., Int. Ed.* **2016,** *55*, 13147.

[45] McLellan, R.; Uzelac, M.; Kennedy, A. R.; Hevia, E.; Mulvey, R. E., LiTMP trans-metal-trapping of fluorinated aromatic molecules: a comparative study of aluminum and Gallium carbanion traps. *Angew. Chem., Int. Ed.* **2017,** *56*, 9566.

[46] Davin, L.; Clegg, W.; Kennedy, A. R.; Probert, M. R.; McLellan, R.; Hevia, E., Structural and synthetic insights into pyridine homocouplings mediated by a β-diketiminato Magnesium amide complex. *Chem. - Eur. J.* **2018,** *24*, 14830.

[47] Klier, L.; Bresser, T.; Nigst, T. A.; Karaghiosoff, K.; Knochel, P., Lewis acid-triggered selective zincation of chromones, quinolones, and thiochromones: application to the preparation of natural flavones and isoflavones. *J. Am. Chem. Soc.* **2012,** *134*, 13584.

[48] Mosrin, M.; Knochel, P., TMPZnCl·LiCl: a new active selective base for the directed zincation of sensitive aromatics and heteroaromatics. *Org. Lett.* **2009,** *11*, 1837.

[49] Balkenhohl, M.; Greiner, R.; Makarov, I. S.; Heinz, B.; Karaghiosoff, K.; Zipse, H.; Knochel, P., Zn-, Mg-, and Li-TMP bases for the successive regioselective metalations of the 1,5-naphthyridine scaffold. *Chem. - Eur. J.* **2017,** *23*, 13046.

[50] Jaric, M.; Haag, B. A.; Unsinn, A.; Karaghiosoff, K.; Knochel, P., Highly selective metalations of pyridines and related heterocycles using new frustrated lewis pairs or tmp-Zinc and tmp-Magnesium bases with BF3·OEt2. *Angew. Chem., Int. Ed.* **2010,** *49*, 5451.

[51] Mosrin, M.; Bresser, T.; Knochel, P., Regio- and chemoselective multiple functionalization of chloropyrazine derivatives. application to the synthesis of coelenterazine. *Org. Lett.* **2009,** *11*, 3406.

[52] Krasovskiy, A.; Krasovskaya, V.; Knochel, P., Mixed Mg/Li amides of the type R2NMgCl·LiCl as highly efficient bases for the regioselective generation of functionalized aryl and heteroaryl magnesium compounds. *Angew. Chem., Int. Ed.* **2006,** *45*, 2958.

[53] Gorgues, A.; Hudhomme, P.; Sallé, M., Highly functionalized tetrathiafulvalenes: riding along the synthetic trail from electrophilic alkynes. *Chem. Rev.* **2004,** *104*, 5151.

[54] Lorcy, D.; Bellec, N.; Fourmigué, M.; Avarvari, N., Tetrathiafulvalene-based group XV ligands: synthesis, coordination chemistry and radical cation salts. *Coord. Chem. Rev.* **2009,** *253*, 1398.

[55] Nafe, J.; Auras, F.; Karaghiosoff, K.; Bein, T.; Knochel, P., Selective functionalization of tetrathiafulvalene using Mg- and Zn-TMP-bases: preparation of mono-, di-, tri-, and tetrasubstituted derivatives. *Org. Lett.* **2015,** *17*, 5356.

[56] Castelló-Micó, A.; Nafe, J.; Higashida, K.; Karaghiosoff, K.; Gingras, M.; Knochel, P., Selective metalations of 1,4-dithiins and condensed analogues using TMP-magnesium and -zinc bases. *Org. Lett.* **2017,** *19*, 360.

[57] Kunz, T.; Knochel, P., Selective multiple magnesiations of the thieno[3,2-b]thiophene scaffold. *Chem. - Eur. J.* **2011,** *17*, 866.

[58] Martin, R.; Buchwald, S. L., Palladium-catalyzed Suzuki–Miyaura cross-coupling reactions employing dialkylbiaryl phosphine ligands. *Acc. Chem. Res.* **2008,** *41*, 1461.

[59] Li, J.; Zhang, Z.; Tang, M.; Zhang, X.; Jin, J., Selective synthesis of isoquinolines by rhodium(III)-Catalyzed C–H/N–H functionalization with α-substituted ketones. *Org. Lett.* **2016,** *18*, 3898.

[60] Fernandez, S.; Ganiek, M. A.; Karpacheva, M.; Hanusch, F. C.; Reuter, S.; Bein, T.; Auras, F.; Knochel, P., Synthesis and reactivity of triazaphenanthrenes. *Org. Lett.* **2016,** *18*, 3158.

[61] Nafe, J.; Herbert, S.; Auras, F.; Karaghiosoff, K.; Bein, T.; Knochel, P., Functionalization of quinoxalines by using TMP bases: preparation of tetracyclic heterocycles with high photoluminescene quantum yields. *Chem. - Eur. J.* **2015,** *21*, 1102.

[62] Jou, J.-H.; Kumar, S.; Agrawal, A.; Li, T.-H.; Sahoo, S., Approaches for fabricating high efficiency organic light emitting diodes. *J. Mater. Chem. C* **2015,** *3* (13), 2974-3002.

[63] Yersin, H.; Finkenzeller, W. J., Triplet Emitters for Organic Light-Emitting Diodes: Basic Properties. In *Highly Efficient OLEDs with Phosphorescent Materials*, Yersin, H., Ed. WILEY-VCH Verlag GmbH & Co. KGaA: Weinheim, 2008.

[64] Yao, L.; Zhang, S.; Wang, R.; Li, W.; Shen, F.; Yang, B.; Ma, Y., Highly Efficient Near-Infrared Organic Light-Emitting Diode Based on a Butterfly-Shaped Donor–Acceptor Chromophore with Strong Solid-State Fluorescence and a Large Proportion of Radiative Excitons. *Angew. Chem., Int. Ed.* **2014,** *53*, 2119.

[65] Lo, M. Y.; Zhen, C.; Lauters, M.; Jabbour, G. E.; Sellinger, A., Organic–Inorganic Hybrids Based on Pyrene Functionalized Octavinylsilsesquioxane Cores for Application in OLEDs. *J. Am. Chem. Soc.* **2007,** *129*, 5808.

[66] Hughes, G.; Bryce, M. R., Electron-transporting materials for organic electroluminescent and electrophosphorescent devices. *J. Mater. Chem.* **2005,** *15*, 94.

[67] Frost, J. M.; Faist, M. A.; Nelson, J., Energetic disorder in higher fullerene adducts: a quantum chemical and voltammetric study. *Adv. Mater.* **2010,** *22*, 4881.

[68] Petrus, M. L.; Music, A.; Closs, A. C.; Bijleveld, J. C.; Sirtl, M. T.; Hu, Y.; Dingemans, T. J.; Bein, T.; Docampo, P., Design rules for the preparation of low-cost hole transporting materials for perovskite solar cells with moisture barrier properties. *J. Mater. Chem. A* **2017,** *5*, 25200.

8.5 Appendix I

8.5.1 Methods

UV-VIS-NIR spectra were recorded using a Perkin-Elmer Lambda 1050 spectrometer equipped with a 150 mm integrating sphere and photomultiplier tube (PMT) and InGaAs detectors.

Steady-state photoluminescence (PL) measurements and **time-correlated single photon counting** (TCSPC) measurements were performed using a PicoQuant FluoTime 300 spectrometer equipped with a 378 nm picosecond diode laser (pulse power 0.99 nJ cm^{-2}, pulse rate 40 MHz).

Cyclic voltammetry measurements were measured using 100 μM or 200 μM solutions of the condensed N-heterocycles in acetonitrile, with 0.2 M tetrabutylammonium hexafluorophosphate as electrolyte and 0.2 mM ferrocene as internal reference and external reference. Measurements were performed with a Metrohm Autolab PGSTAT302N potentiostat, using Pt wires as the working electrode and counter electrode and an Ag wire as reference electrode. The potential window was from −1.6 V up to 2.6 V with a scan speed of 50 mV s^{-1}.

8.5.2 UV-vis Spectroscopy and Photoluminescence Spectroscopy

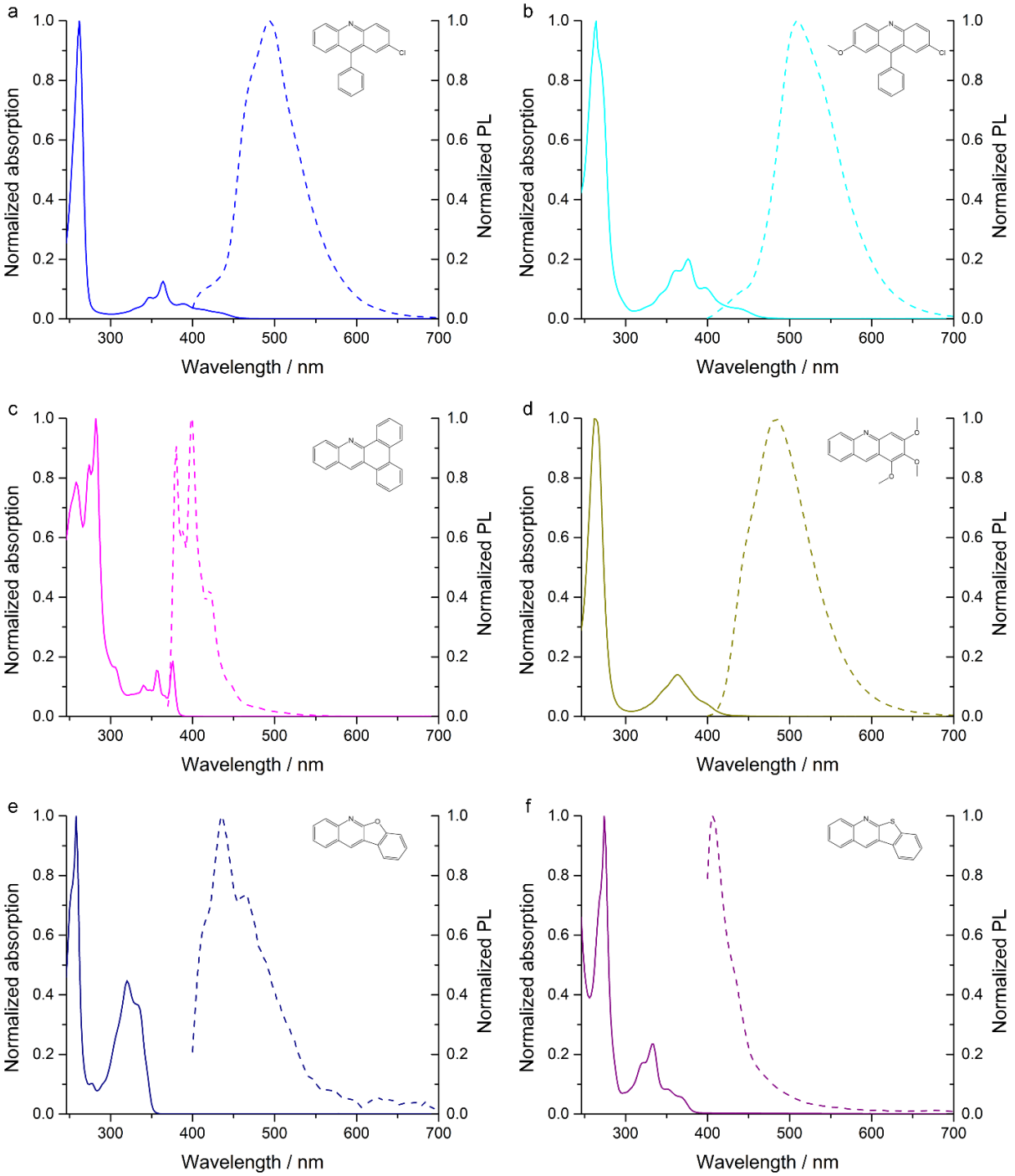

Figure 8.2: Normalized absorption and photoluminescence spectrum of compound **6a**, **6b**, **10a**, **10b**, **10d**, and **10e** in solution (50 µM in $CHCl_3$).

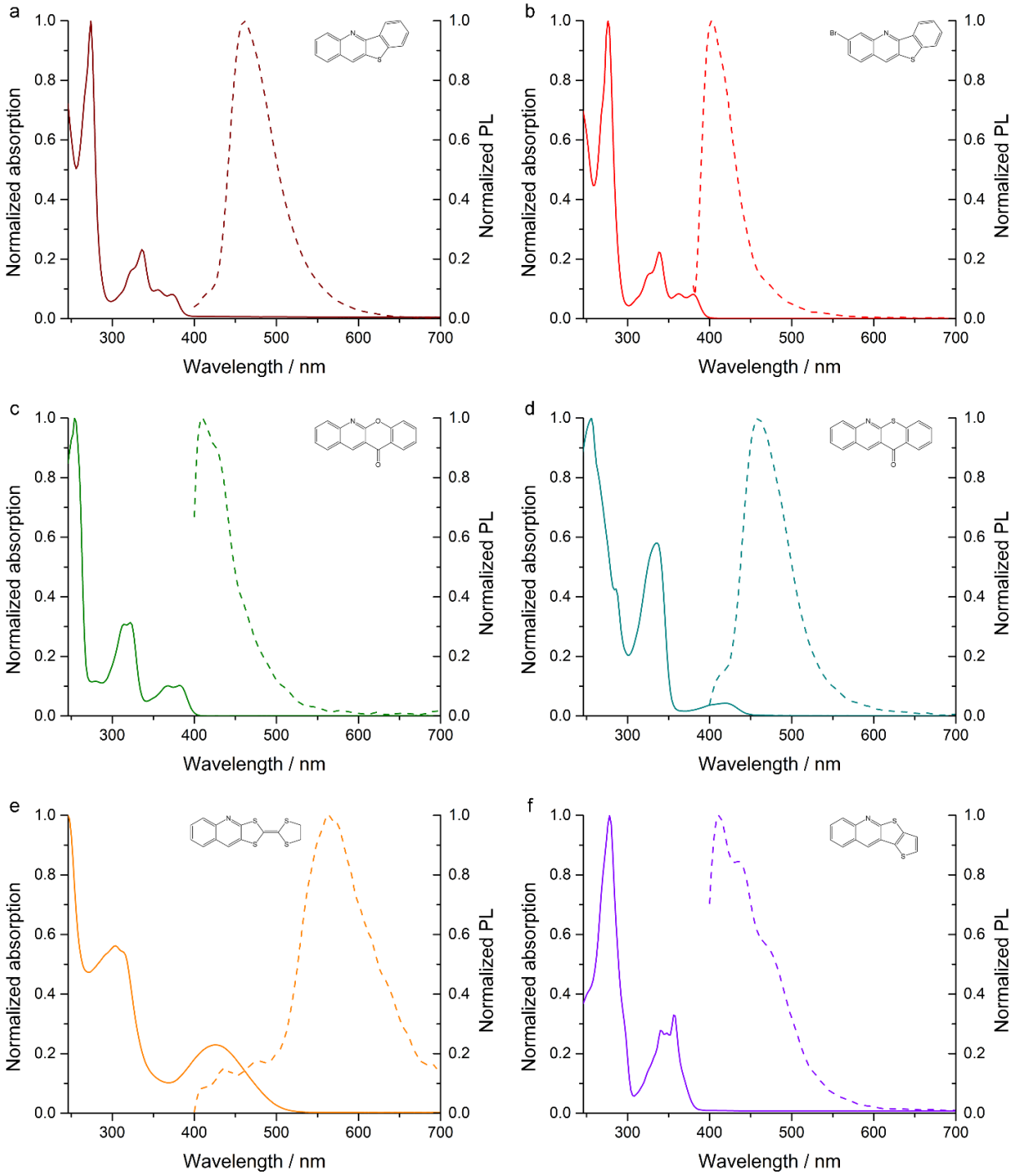

Figure 8.3: Normalized absorption and photoluminescence spectrum of compound **10f**, **10g**, **10j**, **10k**, **10m** and **10n** in solution (50 µM in $CHCl_3$).

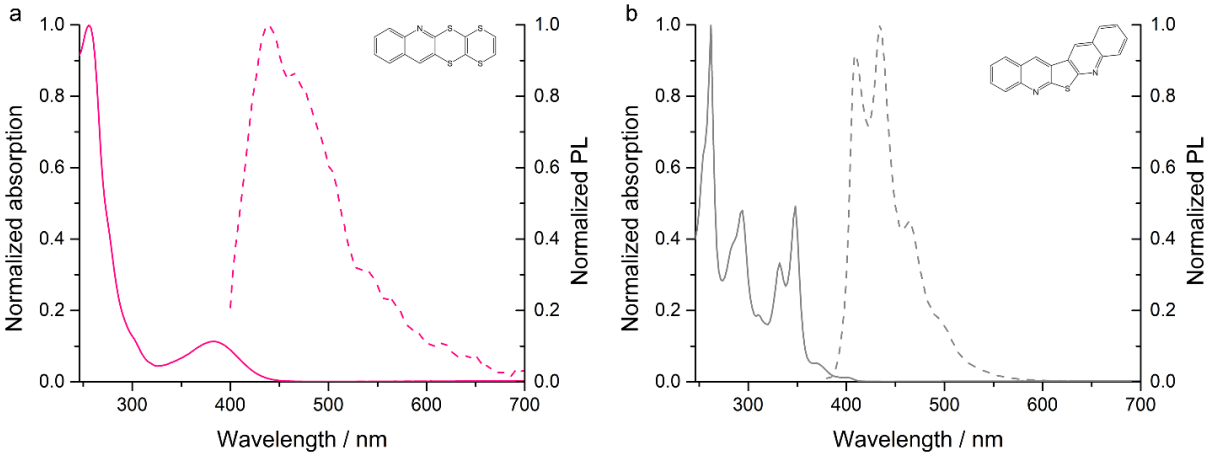

Figure 8.4: Normalized absorption and photoluminescence spectrum of compound **10o** and **14** in solution (50 µM in $CHCl_3$).

8.5.3 Tauc Plots

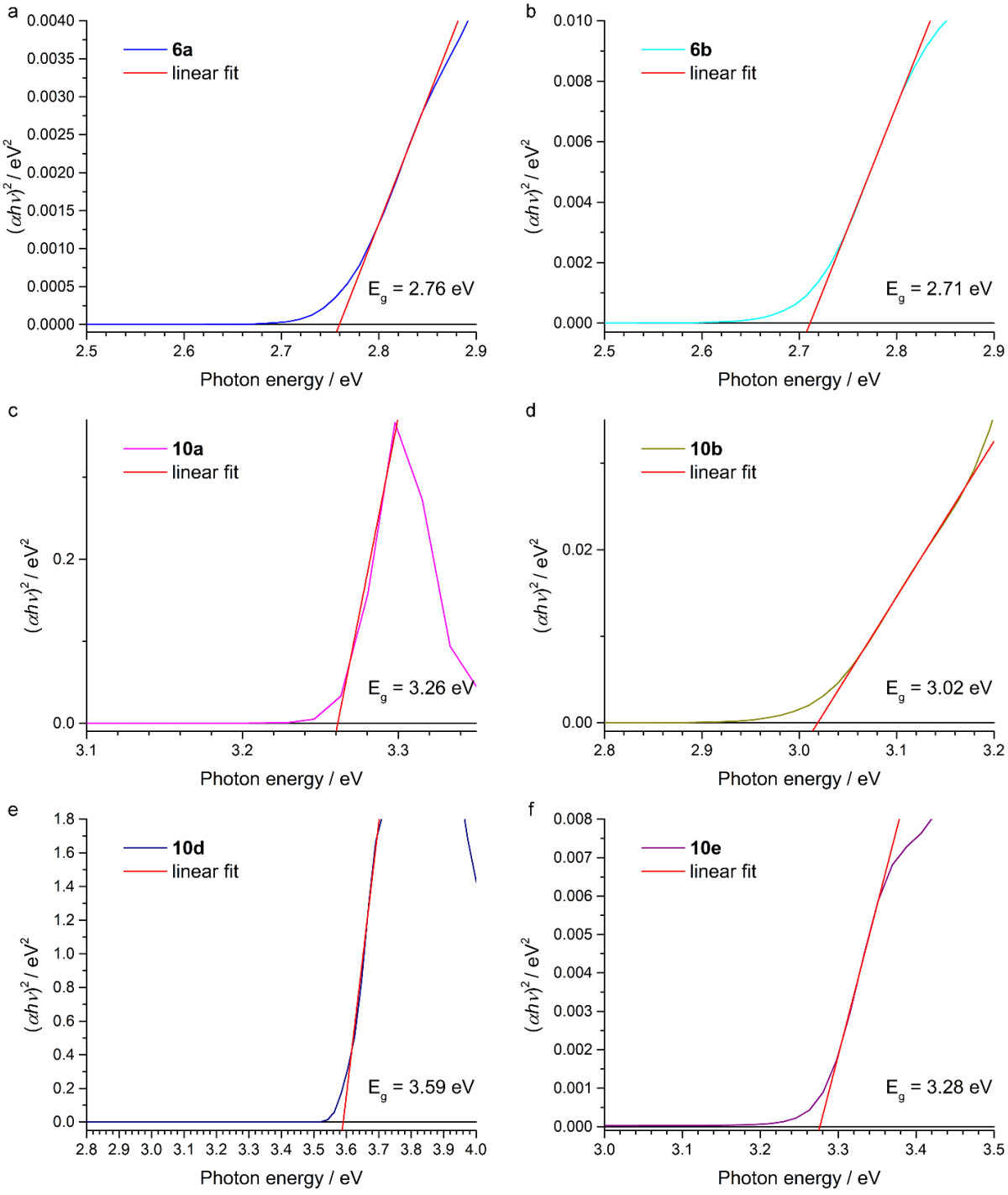

Figure 8.5: Tauc plots generated from optical absorption spectra of selected condensed N-heterocycles and linear fits for direct bandgaps (red). The energy of the bandgap is shown in each graph on the bottom right.

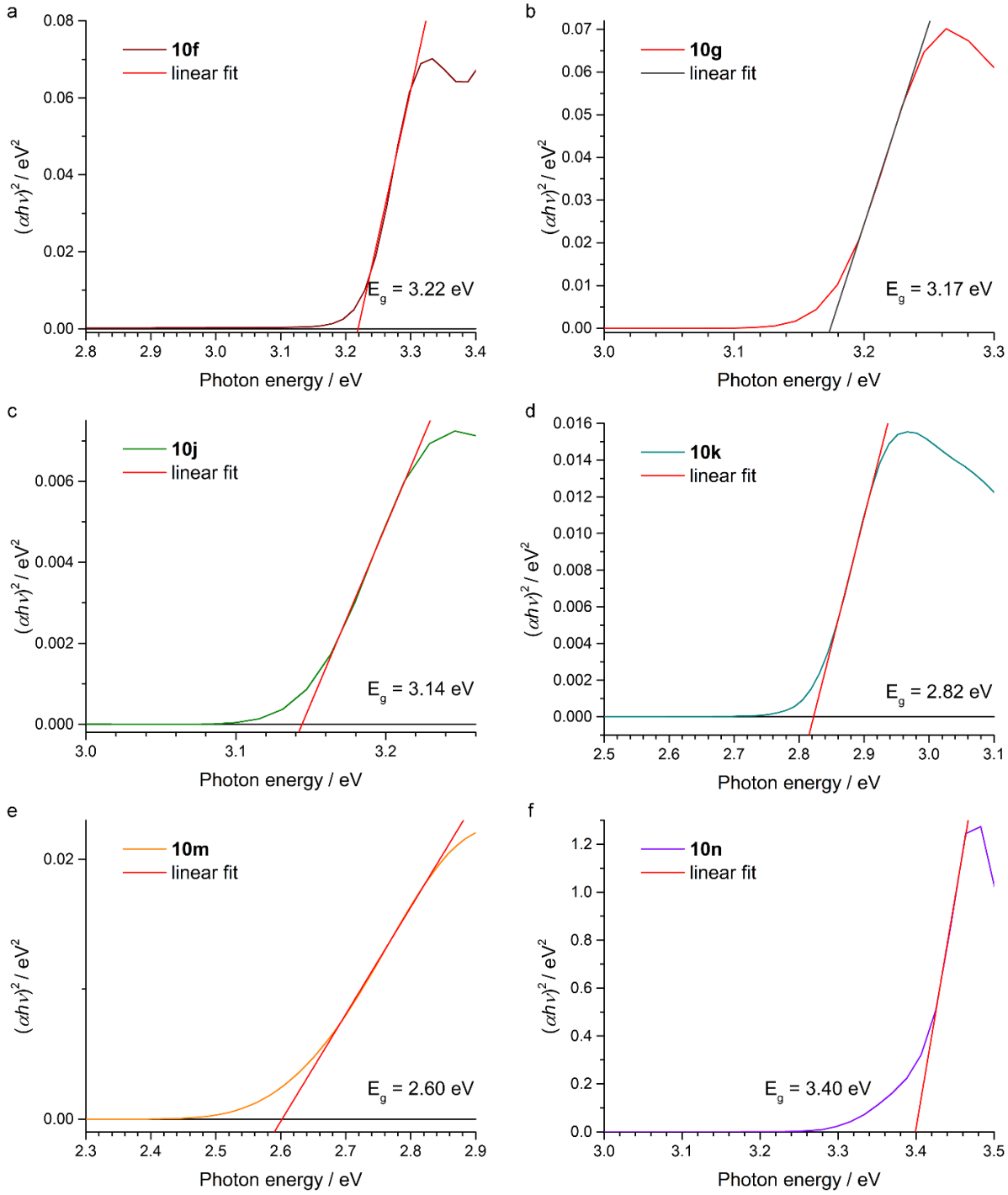

Figure 8.6: Tauc plots generated from optical absorption spectra of selected condensed N-heterocycles and linear fits for direct bandgaps (red, except (b) in grey). The energy of the bandgap is shown in each graph on the bottom right.

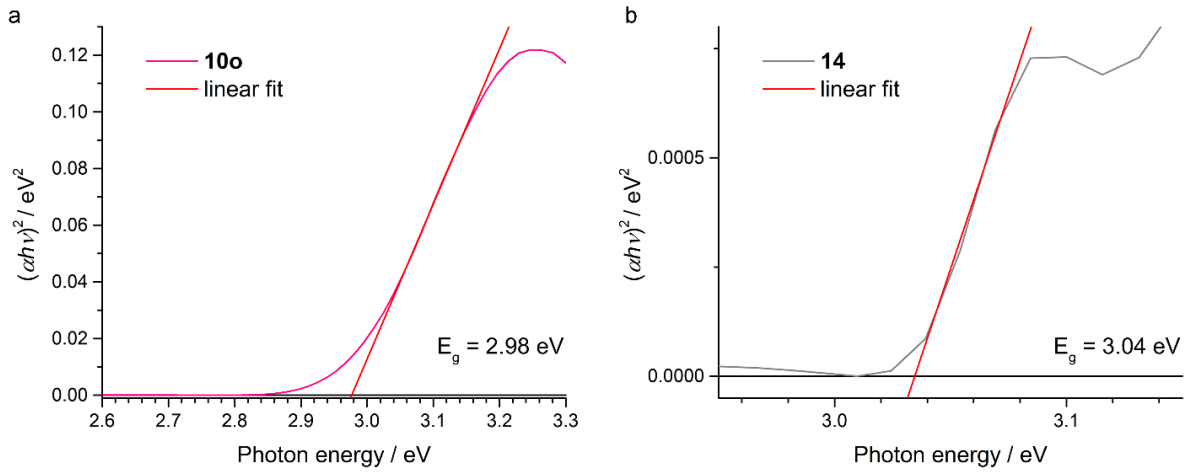

Figure 8.7: Tauc plots generated from optical absorption spectra of selected condensed N-heterocycles and linear fits for direct bandgaps (red). The energy of the bandgap is shown in each graph on the bottom right.

8.5.4 Photoluminescence Quantum Yield (PLQY)

We measured the photoluminescence quantum yield PLQY using a PicoQuant FluoTime 300 spectrometer and the software *easytau*.

Compound	PLQY / %
6b	37.32
10b	26.35
6a	15.31
10a	4.89
14	3.39
10k	2.13
10n	1.56
10e	1.13
10f	0.87
10g	0.39
10j	0.17
10d	0
10m	0
10o	0

8.5.5 Time-Correlated Single Photon Counting

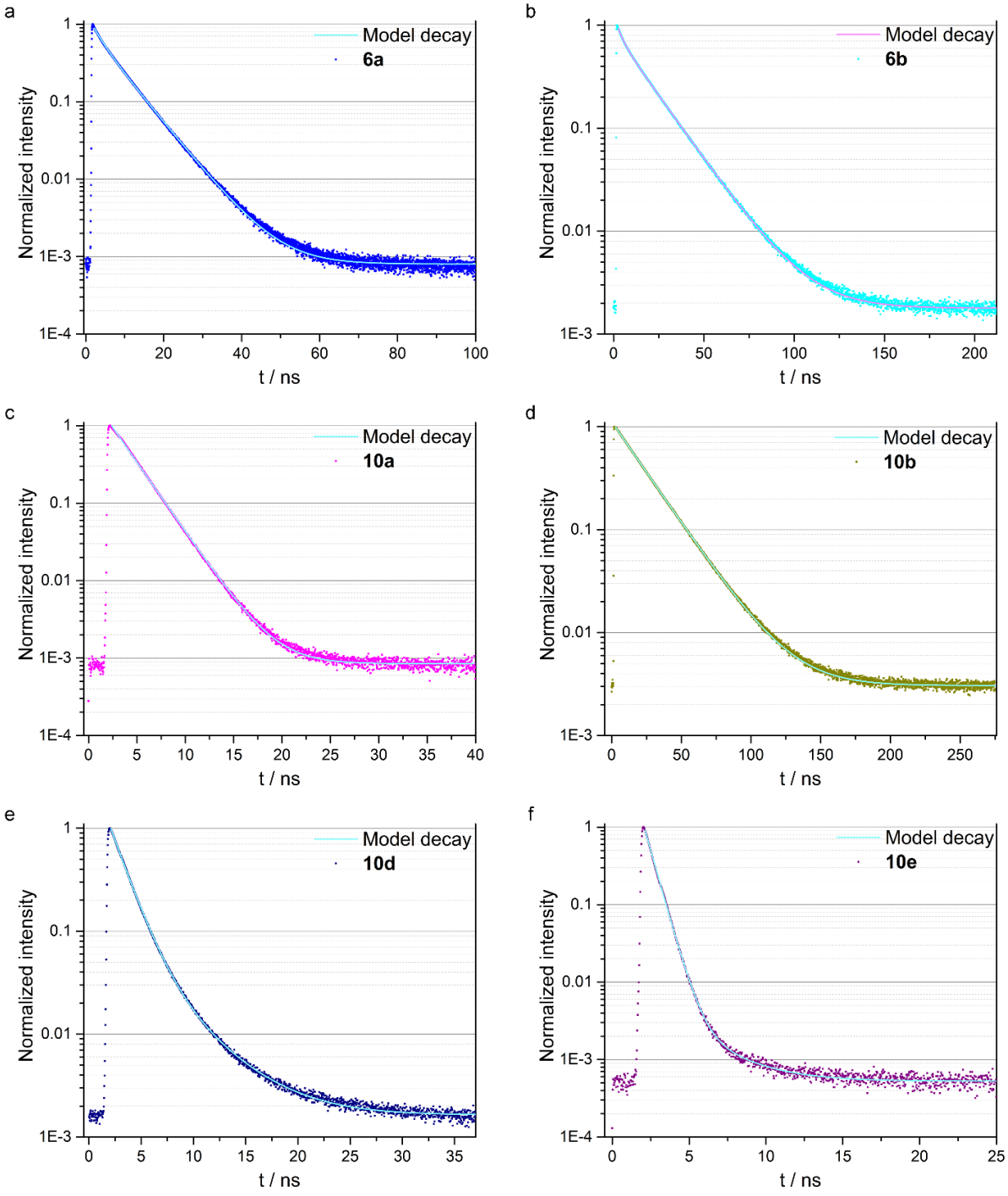

Figure 8.8: PL decay of selected condensed N-heterocycles excited at 378 nm and measured at the corresponding maxima of the PL emissions. All samples were measured in solution (50 µM in $CHCl_3$). Experimental decay is shown in dots and the corresponding mono- or bi-exponential fit of the decay as light cyan line.

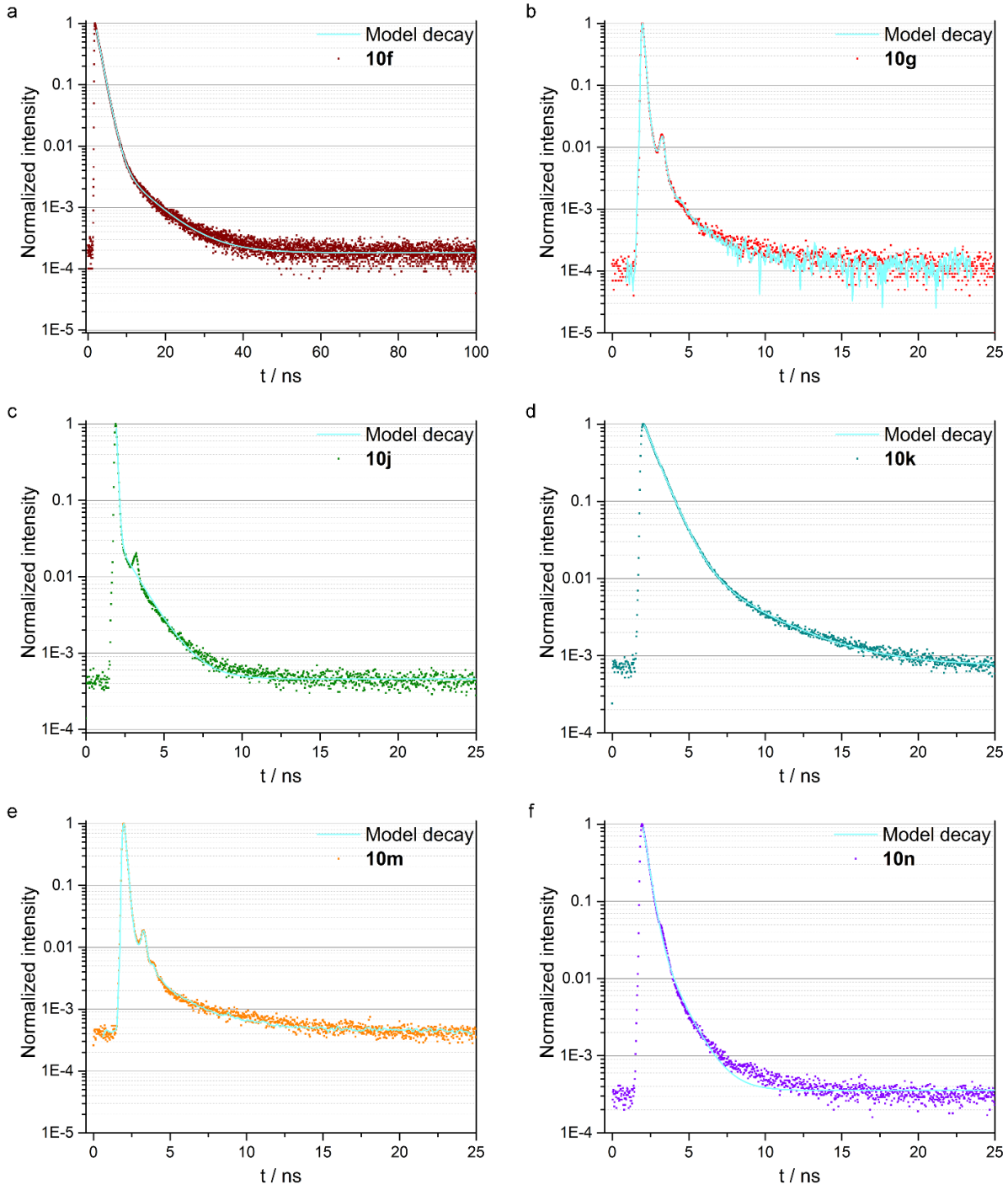

Figure 8.9: PL decay of selected condensed N-heterocycles excited at 378 nm and measured at the corresponding maxima of the PL emissions. All samples were measured in solution (50 µM in $CHCl_3$). Experimental decay is shown in dots and the corresponding mono- or bi-exponential fit of the decay as light cyan line. The additional peak in the decay is due to the instrument response function that can be observed for fast decays (b, c, e).

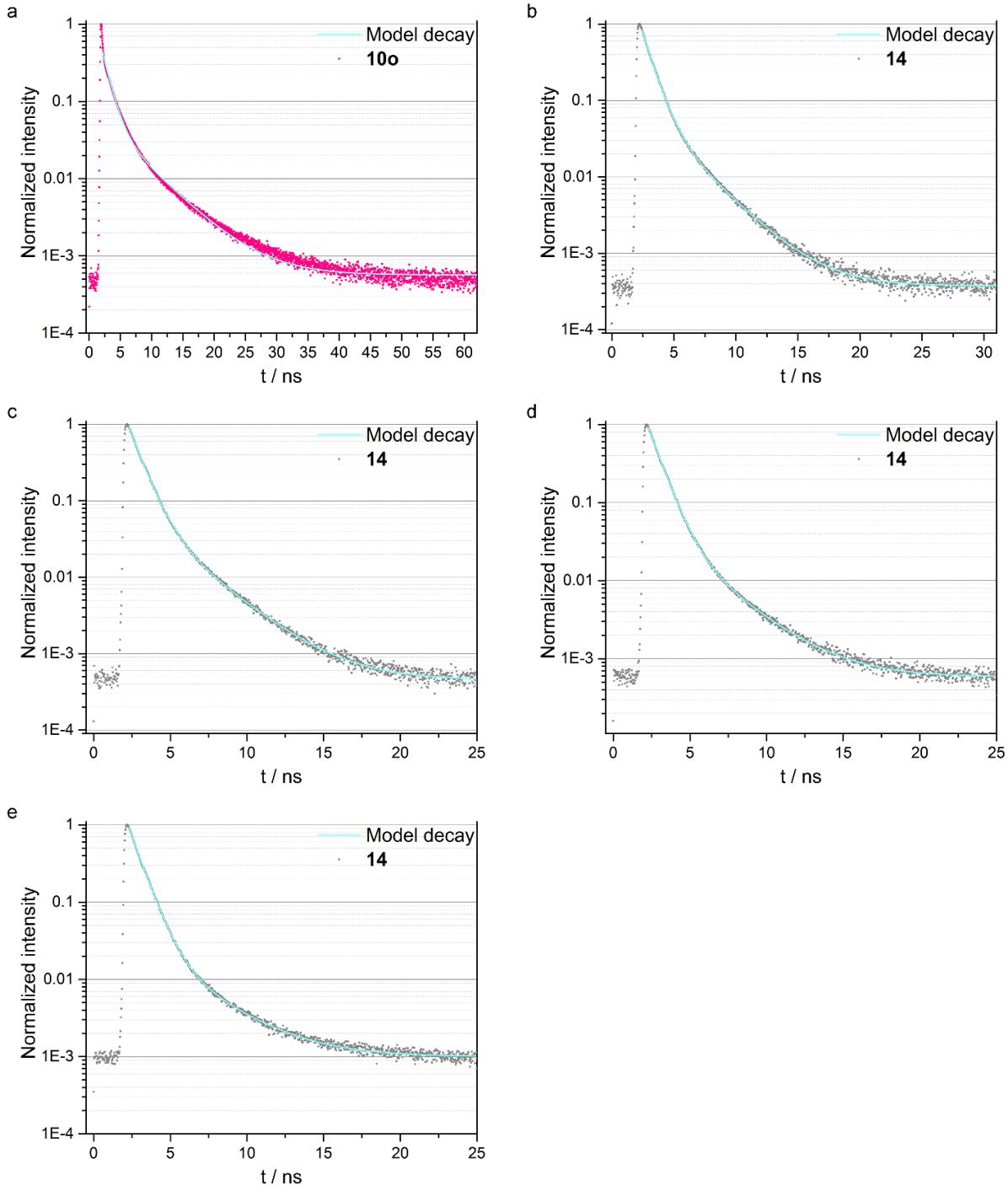

Figure 8.10: PL decay of selected condensed N-heterocycles excited at 378 nm and measured at the corresponding maxima of the PL emissions. All samples were measured in solution (50 µM in $CHCl_3$). Experimental decay is shown in dots and the corresponding mono- or bi-exponential fit of the decay as light cyan line. For compound 14 the decay traces have been recorded at different emission wavelength of the four maxima in the PL spectrum: (b) 410 nm, (c) 434 nm, (d) 464 nm, (e) 494 nm.

Table 8.3: PL decay times of compounds shown above. The given errors are uncertainties from the fit and hence do not reflect the real time-resolution of the setup. The latter is limited by the laser pulse duration of around 100 ps.

		τ / ns	error / ns	fractional intensity / %
6a	τ_1	7.08	±0.02	75.7
	τ_2	2.61	±0.06	24.3
6b	τ_1	17.51	±0.05	80.3
	τ_2	3.2	±0.2	19.7
10a	τ_1	2.414	±0.007	100
10b	τ_1	22.00	±0.06	100
10d	τ_1	1.478	±0.004	92.8
	τ_2	4.27	±0.03	7.2
10e	τ_1	2.7	±0.1	0.6
	τ_2	0.615	±0.002	99.4
10f	τ_1	7.2	±0.1	1.1
	τ_2	1.305	±0.005	98.9
10g	τ_1	1.10	±0.09	0.2
	τ_2	0.0670	±0.0008	99.8
10j	τ_1	1.23	±0.03	3.3
	τ_2	0.085	±0.002	96.7
10k	τ_1	3.59	±0.04	2.6
	τ_2	0.849	±0.002	97.4
10m	τ_1	2.1	±0.1	0.2
	τ_2	0.1225	±0.0007	99.8
10n	τ_1	1.06	±0.02	5.9
	τ_2	0.315	±0.003	94.1
10o	τ_1	5.5	±0.1	12.2
	τ_2	1.19	±0.02	87.8

14 (λ_{em} = 410 nm)	τ_1	2.72	±0.02	8.6
	τ_2	0.789	±0.003	91.4
14 (λ_{em} = 434 nm)	τ_1	2.71	±0.02	7.7
	τ_2	0.791	±0.003	92.3
14 (λ_{em} = 464 nm)	τ_1	2.74	±0.02	5.1
	τ_2	0.776	±0.002	94.9
14 (λ_{em} = 494 nm)	τ_1	3.03	±0.03	3.5
	τ_2	0.767	±0.002	96.5

8.5.6 Cyclic Voltammetry and Energy Levels of HOMO and LUMO

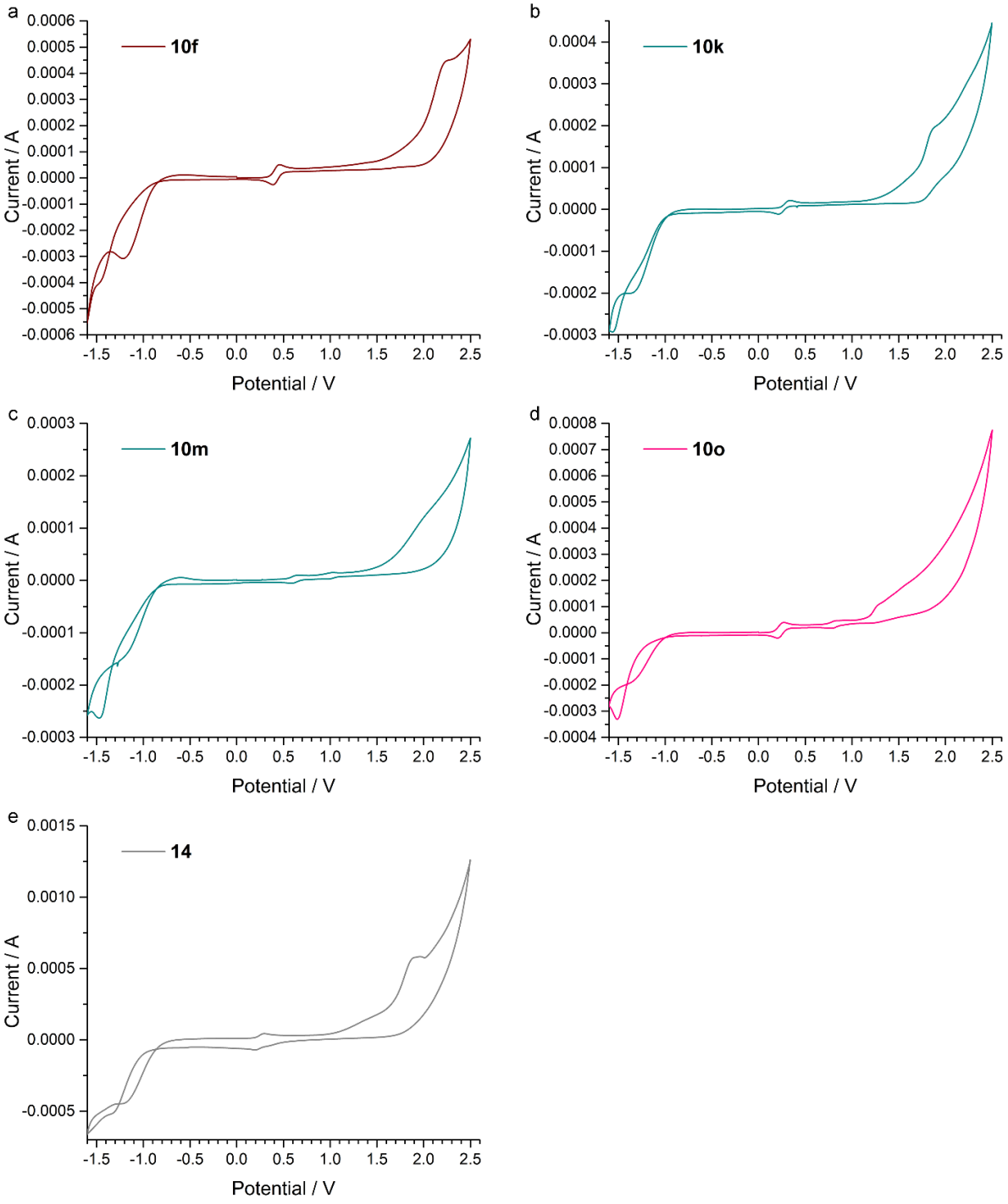

Figure 8.11: CV measurements of compounds **10f**, **10k**, **10m**, **10o**, and **14**. All samples were measured according to the procedure described before. Below the potential of −1.0 V the redox behavior of the electrolyte can be observed. An external reference was used for **10m** due to the overlap of the signals.

Compound	HOMO / eV	LUMO / eV
6b	−6.3	−3.1
10b	−6.3	−3.4
6a	−4.9	−2.3
10a	−5.3	−2.3
14	−6.2	−3.2

8.6 Appendix II

8.6.1 General Remarks

Unless otherwise indicated, all reactions were carried out with magnetic stirring and in flame-dried glassware under argon. Syringes used to transfer reagents and solvents were purged with N_2 prior to use. The following starting materials were synthesized according to previously described methods: Anthranils **2**.[1-2] Other chemicals were obtained from commercial sources and were used without further purification. Yields refer to isolated compounds, estimated to be >95% pure as determined by ^{1}H-NMR and GC-analysis. Reactions were monitored by gas chromatography (GC and GC-MS) or thin layer chromatography (TLC). TLC were performed using aluminum plates covered with SiO_2 (Merck 60, F-254) and visualized by UV detection. Purification *via* column chromatography was performed using Merck silica gel 60 (40–63 mm 230–400 mesh ASTM from Merck). THF was continuously refluxed and freshly distilled from sodium benzophenone ketyl under nitrogen. Melting points were measured using a Büchi B-540 apparatus and are uncorrected. NMR spectra were recorded in $CDCl_3$ and chemical shifts (δ) are reported in parts per million (ppm). Mass spectra and highresolution mass spectra (HR-MS) were recorded using electro ionization (EI) except where otherwise noted. GCs were recorded on machines of the type Hewlett-Packard 6890 (Hewlett Packard, 5% phenylmethylpolysiloxane; length: 15 m, diameter: 0.25 mm; film thickness: 0.25 μm).

Table 8.4: Optimization for cobalt-catalyzed amination using anthranils (**2a**).[a]

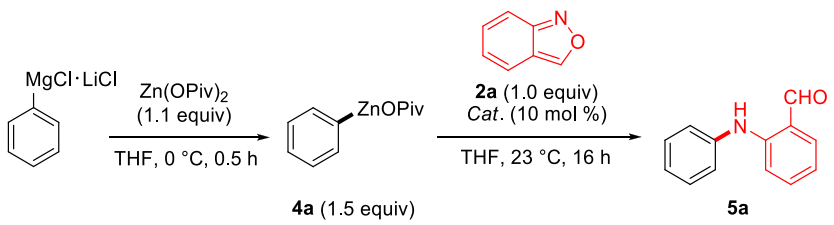

entry	[met] (10 mol %)	yield (%)[b]
1	$CoCl_2$	65
2	$MnCl_2$	0
3	$CrCl_2$	0
4	$FeCl_2$	0
5	$Fe(acac)_3$	0
6	--	0
7	$CoCl_2$	0[c]

[a] Reaction conditions: **4a** (0.75 mmol), **2a** (0.50 mmol), [Cat.] (10 mol %), THF (2.0 mL), 23 °C, N, 16 h. [b] Isolated yields. [c] PhMgCl (1.5 equiv) instead of PhZnOPiv.

Table 8.5: Optimization for cobalt-catalyzed amination using organoaluminun reagents.

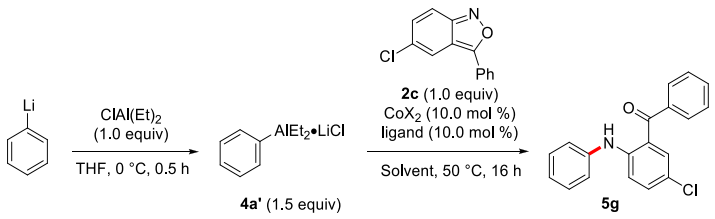

entry	[Co]	ligand (10 mol %)	solvent	yield (%)[b]
1	$CoBr_2$	--	THF-Tol (1:1)	36
2	$CoBr_2$	bpy	THF-Tol (1:1)	75
3	$CoBr_2$	bpy	THF-Tol (1:1)	14 (25 °C)
4	$CoBr_2$	Xantphos	THF-Tol (1:1)	46
5	$CoBr_2$	dppbz	THF-Tol (1:1)	57
6	$CoBr_2$	IMesHCl	THF-Tol (1:1)	54
7	$CoBr_2$	IMesHCl	MeCN-Tol (1:1)	21
8	$CoBr_2$	dttbpy	THF-Tol (1:1)	74

9	$CoCl_2$	bpy	THF-Tol (1:1)	77
10	**$Co(acac)_2$**	**bpy**	**THF-Tol (1:1)**	**81**
11	--	bpy	THF-Tol (1:1)	0
12	$Co(acac)_2$	bpy	THF-Tol (1:1)	34 (40 °C)
13	$Co(acac)_2$	bpy	THF	53
14	$Co(acac)_2$	bpy	THF	51[c]
15	$Co(acac)_2$	bpy	THF	12[d]
16	$CoBr_2$bpy	--	THF-Tol (1:1)	56
17	$Co(acac)_2$	bpy	THF-Tol (1:1)	0[e]
18	$Co(acac)_2$	bpy	THF-Tol (1:1)	23[f]

[c] 5.0 mol % of [Co] and bpy were used. [d] **1a** was prepared from PhMgCl•LiCl. [e] 1.5 equiv of $PhAlCl_2$ was used. [f] 1.5 equiv of PhAlEtCl was used.

8.6.2 Additional Experiments

a) Cobalt-catalyzed electrophilic amination using $ArAl(Et)_2$•LiCl:

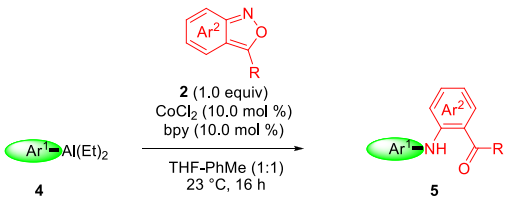

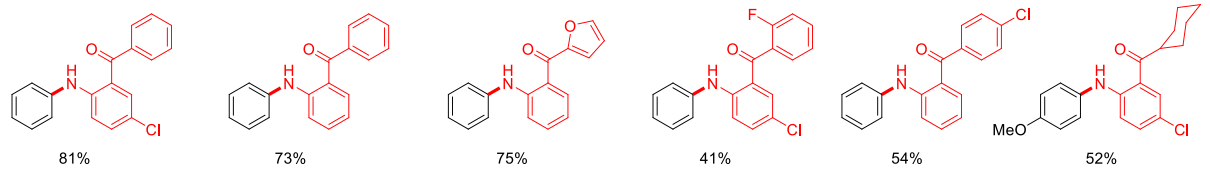

b) Selective C–H metalation by TMPMgCl:

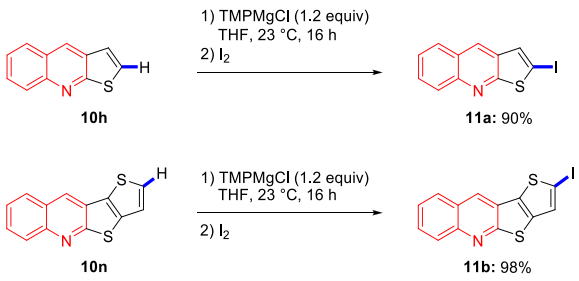

c) Other aminating reagents:

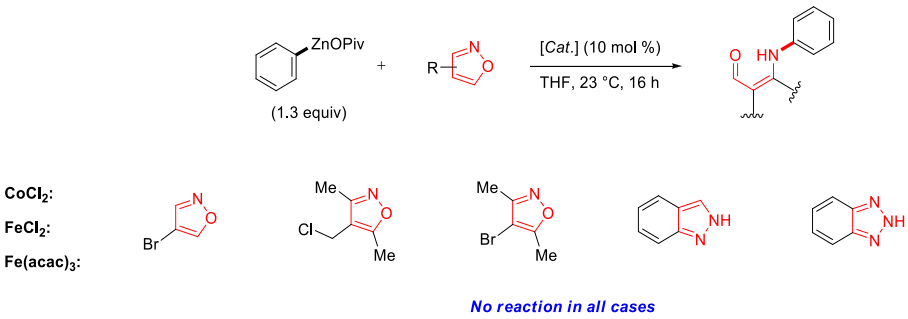

8.6.3 Representative Procedures

Preparation of $Zn(OPiv)_2$:

Pivalic acid (20.4 g, 22.6 mL, 200 mmol) was placed in a dry and argon-flushed 500 mL three-necked roundbottom flask, equipped with a magnetic stirring bar, a septum and a pressure equalizer, and was dissolved in dry THF (120 mL). The mixture was cooled to 0 °C, and a solution of Et_2Zn (13.0 g, 10.8 mL, 105 mmol) in dry THF (120 mL) was added over a period of 30 min under vigorous stirring. Then, the ice-bath was removed and stirring was continued at 25 °C for one additional hour at which point bubbling was ceased (a thick slurry was formed). The solvent was removed *in vacuo* and the solid residue was dried for at least 4 h longer. $Zn(OPiv)_2$ was obtained in quantitative yield, as a puffy amorphous white solid.

Typical procedure 1 (TP1) for the preparation of organozinc pivalates:

LiCl (1.5 equiv) was dried under high vacuum and allowed to cool to room temperature, then Mg turnings (1.2 equiv) and THF (1 M solution relating to the aryl bromide) were added. The reaction mixture was cooled to 0 °C and the corresponding aryl bromide (1.0 equiv) was then added. The reaction was stirred at room temperature until iodolysis and protolysis of a reaction aliquot indicated full consumption of the starting material. $Zn(OPiv)_2$ (1.1 equiv) is then added to afford a solution of the corresponding zinc reagent.

Typical procedure 2 (TP2) for the preparation of organozinc pivalates:

TMPMgCl·LiCl (1.1 equiv, 1.2 M) is added dropwise to a solution of aromatic substrate in THF at the indicated temperature. The reaction was stirred until iodolysis of a reaction aliquot indicated full consumption of the starting material. $Zn(OPiv)_2$ (1.1 equiv) is then added to afford a solution of the corresponding zinc reagent.

Typical procedure 3 (TP3) for the preparation of organozinc pivalates:

TMPZnCl·$Mg(OPiv)_2$·LiCl (1.1 equiv, 1.2 M) is added dropwise to a solution of aromatic substrate in THF at the indicated temperature. The reaction mixture was stirred until iodolysis of a reaction aliquot indicated full consumption of the starting material.

Typical procedure 4 (TP4) for the preparation of organozinc pivalates:

$Zn(OPiv)_2$ (1.1 equiv) is added to a solution of the corresponding commercial Grignard reagent.

Typical procedure 5 (TP5) for the preparation of organozinc pivalates:

i-PrMgCl.LiCl (1.1 equiv, 1.267 M) was added dropwise to a 1.0 M solution of aryl bromide in THF. The reaction was stirred until iodolysis and protolysis of a reaction aliquot indicated full consumption of the starting material. $Zn(OPiv)_2$ (1.1 equiv) is then added to afford a solution of the corresponding zinc reagent.

Typical procedure 6 (TP6) for the preparation of alkenylzinc pivalates:

Mg turnings (1.2 equiv), catalytic amount of I_2 (10 mol %), THF (1.0 M solution relating to the alkenyl bromide) and the corresponding alkenyl bromide (1.0 equiv) were added. The reaction mixture was refluxed at 80 °C for 3–6 h. The reaction was stirred until protolysis of a reaction aliquot indicated full consumption of the starting material. $Zn(OPiv)_2$ (1.1 equiv) is then added to afford a solution of the corresponding zinc reagent.

Typical procedure 7 (TP7) for the cobalt-catalyzed electrophilic amination of organozinc pivalate with anthranil derivatives:

Organozinc pivalates (0.45 mmol, 1.5 equiv) prepared from (TP1-TP6) is added to a solution of anthranil 2 (0.3 mmol, 1.0 equiv) and $CoCl_2$ (2.6 mg, 10 mol %) in THF (1.5 mL). The reaction mixture is stirred for 16 h at room temperature. The reaction mixture was quenched with water (2 drops), diluted with ethyl acetate and concentrated under vacuo. The residue was

purified by column chromatography using a gradient of 100% *iso*-hexane to 100% ethyl acetate as eluent to yield the title compound.

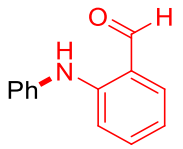

2-(Phenylamino)benzaldehyde (5a)[3]

The general procedure **TP7** was followed using benzo[*c*]isoxazole (60 mg, 0.5 mmol) and oxo(phenyl)(pivaloyl)zinc **(**prepared from **TP4**, 0.75 mmol) for 16 h. Purification by column chromatography (*n*-hexane/EtOAc 15:1) yielded **5a** (64 mg, 65%) as a white solid. **M.p.**: 74–76 °C. **^{1}H-NMR (400 MHz, CDCl$_3$)** δ = 9.94 (s, 1H), 9.83 (s, 1H), 7.49 (dd, *J* = 7.8, 1.8 Hz, 1H), 7.29 (qd, *J* = 8.2, 7.3, 1.8 Hz, 3H), 7.23 – 7.13 (m, 3H), 7.07 (td, *J* = 7.3, 1.3 Hz, 1H), 6.78 – 6.72 (m, 1H). **^{13}C-NMR (100 MHz, CDCl$_3$)** δ = 194.3, 147.8, 139.7, 136.6, 135.6, 129.4, 124.4, 123.2, 119.4, 117.1, 112.9. **IR (Diamond-ATR, neat):** ν / cm = 3279, 2921, 2848, 2835, 2755, 1648, 1589, 1570, 1518, 1492, 1450, 1422, 1397, 1321, 1314, 1245, 1199, 1184, 1154, 1117, 1079, 1041, 1028, 1004, 1004, 940, 898, 821, 808, 750, 697, 662. **MS (EI, 70 eV):** m/z (%) = 197 (41), 196 (51), 179 (57), 178 (17), 169 (13), 168 (100), 167 (47). **HR-MS (EI, 70 eV)** : [$C_{13}H_{10}ON$], [M-H], calcd.: 197.0841; found: 197.0757.

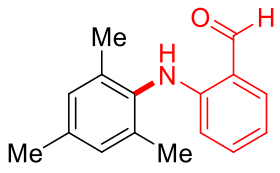

2-(Mesitylamino)benzaldehyde (5b)

The general procedure **TP7** was followed using benzo[*c*]isoxazole (36 mg, 0.3 mmol) and mesityl(oxo)(pivaloyl)zinc (prepared from **TP1**, 0.45 mmol) for 16 h. Purification by column chromatography (*n*-hexane/EtOAc 15:1) yielded **5b** (51 mg, 71%) as a white solid. **M.p.**: 54–56 °C. **^{1}H-NMR (400 MHz, CDCl$_3$)** δ = 9.99 (s, 1H), 9.53 (s, 1H), 7.58 (dd, *J* = 7.8, 1.7 Hz, 1H), 7.28 (ddd, *J* = 8.6, 7.0, 1.7 Hz, 1H), 7.00 (s, 2H), 6.76 (ddd, *J* = 7.8, 7.1, 1.0 Hz, 1H), 6.27 (d, *J* = 8.6 Hz, 1H), 2.36 (s, 3H), 2.18 (s, 6H). **^{13}C-NMR (100 MHz, CDCl$_3$)** δ = 194.3, 149.9,

136.6, 136.4, 136.3, 135.7, 133.6, 129.2, 118.3, 115.8, 112.3, 21.0, 18.2. **IR (Diamond-ATR, neat):** ν / cm = 3293, 2914, 2853, 2815, 2745, 1654, 1650, 1602, 1566, 1495, 1454, 1395, 1372, 1331, 1322, 1303, 1236, 1216, 1201, 1186, 1154, 1115, 1034, 1011, 888, 854, 800, 750, 712, 658. **MS (EI, 70 eV):** m/z (%) = 240 (17), 239 (100), 238 (19), 224 (42), 222 (15), 211 (10), 210 (34), 209 (10), 208 (18), 196 (51), 195 (17), 194 (27), 193 (11), 181 (42), 180 (32), 179 (11), 134 (16), 120 (11), 119 (33), 91 (12). **HR-MS (EI, 70 eV)** : [$C_{16}H_{17}NO$], calcd: 265.0714; found: 265.0704.

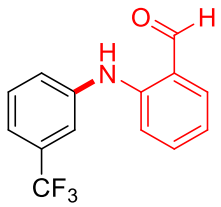

2-{[3-(Trifluoromethyl)phenyl]amino}benzaldehyde (5c)

The general procedure **TP7** was followed using benzo[*c*]isoxazole (36 mg, 0.3 mmol) and oxo(pivaloyl)(3-(trifluoromethyl)phenyl)zinc (prepared from **TP5**, 0.45 mmol) for 16 h. Purification by column chromatography (*n*-hexane/EtOAc 15:1) yielded **5c** (48 mg, 56%) as a yellow oil. **^{1}H-NMR (400 MHz, $CDCl_3$)** δ = 10.03 (s, 1H), 9.83 (s, 1H), 7.53 (dd, J = 7.7, 1.7 Hz, 1H), 7.45 (m, 1H), 7.41 – 7.25 (m, 4H), 7.17 (m, 1H), 6.86 – 6.80 (m, 1H). **^{13}C-NMR (100 MHz, $CDCl_3$)** δ = 194.0, 146.6, 140.5, 136.8, 135.7, 131.9 (q, J = 32 Hz), 130.0, 125.54, 123.8 (q, J = 270 Hz), 120.6 (q, J = 4 Hz), 119.94, 119.0 (q, J = 4 Hz), 118.25, 112.89. **^{19}F-NMR (376 MHz, $CDCl_3$)** δ = -62.78. **MS (EI, 70 eV):** m/z (%) = 265 (61), 264 (29), 237 (13), 236 (100), 216 (60), 196 (16), 168 (11), 167 (64), 166 (11). **HR-MS (EI, 70 eV)** : [$C_{14}H_{10}F_3NO$], calcd: 265.0714; found: 265.0704.

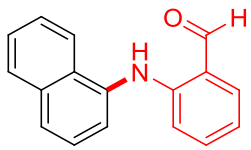

2-(Naphthalen-1-ylamino)benzaldehyde (5d)

The general procedure **TP7** was followed using benzo[*c*]isoxazole (36 mg, 0.3 mmol) and naphthalen-1-yl(oxo)(pivaloyl)zinc (prepared from **TP1**, 0.45 mmol) for 16 h. Purification by

column chromatography (*n*-hexane/EtOAc 15:1) yielded **5d** (57 mg, 77%) as a yellow solid. **M.p.**: 115–117 °C. **^{1}H-NMR (400 MHz, $CDCl_3$)** δ = 10.44 (s, 1H), 10.06 (s, 1H), 8.18 – 8.12 (m, 1H), 7.96 (dd, *J* = 8.0, 1.7 Hz, 1H), 7.81 (d, *J* = 8.0 Hz, 1H), 7.65 (dd, *J* = 8.0, 1.7 Hz, 1H), 7.62 – 7.51 (m, 4H), 7.32 (ddd, *J* = 8.6, 7.0, 1.7 Hz, 1H), 6.97 (d, *J* = 8.6 Hz, 1H), 6.89 – 6.82 (m, 1H). **^{13}C-NMR** (100 MHz, $CDCl_3$) δ = 194.6, 149.3, 136.5, 135.7, 135.6, 134.8, 129.7, 128.5, 126.5, 126.5, 126.0, 125.8, 122.7, 121.8, 119.3, 117.0, 113.4. **IR (Diamond-ATR, neat):** ν / cm = 3273, 3047, 2833, 2742, 1651, 1626, 1607, 1594, 1572, 1515, 1499, 1455, 1420, 1392, 1314, 1269, 1224, 1197, 1154, 1119, 1082, 1037, 1015, 965, 900, 856, 785, 769, 731, 693, 659. **MS (EI, 70 eV):** m/z (%) = 247 (25), 246 (12), 230 (18), 229 (100), 228 (34), 227 (11), 218 (25), 217 (28), 114 (13). **HR-MS (EI, 70 eV)**: [$C_{17}H_{13}ON$], calcd.: 247.0997; found: 247.0989.

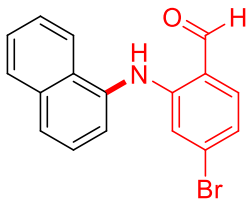

4-Bromo-2-(naphthalen-1-ylamino)benzaldehyde (5e)

The general procedure **TP7** was followed using 6-bromobenzo[*c*]isoxazole (60 mg, 0.3 mmol) and naphthalen-1-yl(oxo)(pivaloyl)zinc (prepared from **TP1**, 0.45 mmol) for 16 h. Purification by column chromatography (*n*-hexane/EtOAc 15:1) yielded **5e** (81 mg, 81%) as a white solid. **M.p.**: 157–159 °C. **^{1}H-NMR (400 MHz, $CDCl_3$)** δ = 10.26 (s, 1H), 9.84 (d, *J* = 3.0 Hz, 1H), 7.95 – 7.86 (m, 1H), 7.83 – 7.77 (m, 1H), 7.69 (dt, *J* = 6.9, 3.0 Hz, 1H), 7.42 (m, 4H), 7.33 (dd, *J* = 8.2, 3.0 Hz, 1H), 6.91 (d, *J* = 2.0 Hz, 1H), 6.82 (dt, *J* = 8.5, 2.0 Hz, 1H). **^{13}C-NMR (100 MHz, $CDCl_3$)** δ = 193.7, 150.1, 137.6, 134.8, 134.6, 131.5, 129.7, 128.5, 126.8, 126.7, 126.7, 125.8, 122.5, 122.4, 120.3, 117.9, 116.0. **IR (Diamond-ATR, neat):** ν / cm = 3263, 3050, 2834, 2742, 1648, 1594, 1562, 1492, 1424, 1382, 1324, 1277, 1219, 1187, 1123, 1072, 1016, 915, 871, 861, 851, 829, 788, 727, 685. **MS (EI, 70 eV):** m/z (%) = 309 (87), 307 (91), 228 (57), 226 (63), 217 (100), 114 (44). **HR-MS (EI, 70 eV)**: [$C_{17}H_{12}ONBr$], calcd.: 325.0102; found: 325.0096.

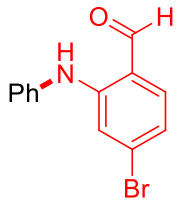

4-Bromo-2-(phenylamino)benzaldehyde (5f)

The general procedure **TP7** was followed using 6-bromobenzo[*c*]isoxazole (60 mg, 0.3 mmol) and oxo(phenyl)(pivaloyl)zinc (prepared from **TP4**, 0.45 mmol) for 16 h. Purification by column chromatography (*n*-hexane/EtOAc 15:1) yielded **5f** (64 mg, 78%) as an oil. **^{1}H-NMR (400 MHz, $CDCl_3$)** δ = 10.08 (s, 1H), 9.87 (d, *J* = 0.5 Hz, 1H), 7.47 – 7.40 (m, 3H), 7.35 (d, *J* = 1.5 Hz, 1H), 7.29 (dd, *J* = 5.6, 1.9 Hz, 2H), 7.26 – 7.20 (m, 1H), 6.96 (dd, *J* = 8.3, 1.7 Hz, 1H). **^{13}C-NMR (100 MHz, $CDCl_3$)** δ = 193.4, 148.7, 138.8, 137.7, 131.4, 129.7, 125.3, 123.8, 120.4, 118.0, 115.6. **IR (Diamond-ATR, neat):** ν / cm = 3274, 2835, 1656, 1482, 1241, 1018. **MS (EI, 70 eV):** m/z (%) = 274 (30), 257 (100), 255 (35). **HR-MS (EI, 70 eV)**: [$C_{13}H_{10}BrNO$], calcd.: 274.9946; found: 274.9942.

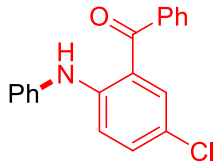

[5-Chloro-2-(phenylamino)phenyl](phenyl)methanone (5g)

The general procedure **TP7** was followed using 5-chloro-3-phenylbenzo[*c*]isoxazole (69 mg, 0.3 mmol) and oxo(phenyl)(pivaloyl)zinc (prepared from **TP4**, 0.45 mmol) for 16 h. Purification by column chromatography (*n*-hexane/EtOAc 15:1) yielded **5g** (84 mg, 91%) as a yellow oil. **^{1}H-NMR (400 MHz, $CDCl_3$)** δ = 9.92 (s, 1H), 7.64 – 7.59 (m, 2H), 7.52 – 7.47 (m, 1H), 7.45 – 7.38 (m, 3H), 7.28 (m, 2H), 7.22 – 7.15 (m, 4H), 7.03 (t, *J* = 7.3 Hz, 1H). **^{13}C-NMR (100 MHz, $CDCl_3$)** δ = 198.0, 146.6, 140.1, 139.0, 134.1, 133.6, 131.8, 129.5, 129.4, 128.4, 124.0, 122.3, 121.0, 120.5, 116.3. **IR (Diamond-ATR, neat):** ν / cm = 3279, 3059, 2921, 2849, 1626, 1587, 1565, 1500, 1454, 1401, 1304, 1243, 1227, 1153, 1120, 1075, 1026, 847, 897, 812, 802, 773, 738, 670, 655. **MS (EI, 70 eV):** m/z (%) = 308 (31), 307 (26), 306 (100), 271 (17), 254 (13), 195 (11), 167 (15), 166 (14), 77 (12). **HR-MS (EI, 70 eV)**: [$C_{19}H_{13}ONCl$], [M-H], calcd.: 306.0764; found: 306.0681.

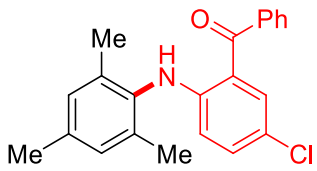

[5-Chloro-2-(mesitylamino)phenyl](phenyl)methanone (5h)

The general procedure **TP7** was followed using 5-chloro-3-phenylbenzo[*c*]isoxazole (69 mg, 0.3 mmol) and mesityl(oxo)(pivaloyl)zinc (prepared from **TP6**, 0.45 mmol) for 16 h. Purification by column chromatography (*n*-hexane/EtOAc 15:1) yielded **5h** (68 mg, 65%) as a colorless oil. **^{1}H-NMR (400 MHz, $CDCl_3$)** δ = 9.59 (s, 1H), 7.64 – 7.59 (m, 2H), 7.48 (m, 1H), 7.45 – 7.40 (m, 3H), 7.07 (dd, *J* = 9.1, 2.5 Hz, 1H), 6.89 (s, 2H), 6.19 (d, *J* = 9.1 Hz, 1H), 2.24 (s, 3H), 2.10 (s, 6H). **^{13}C-NMR** (100 MHz, $CDCl_3$) δ = 198.5, 149.4, 139.6, 136.6, 136.2, 134.7, 133.8, 131.4, 129.4, 129.3, 129.2, 128.4, 119.2, 117.9, 114.8, 21.0, 18.3. **IR (Diamond-ATR, neat):** ν / cm = 3289, 3057, 2916, 2854, 1625, 1561, 1500, 1444, 1430, 1327, 1311, 1298, 1237, 1217, 1177, 1152, 1118, 1098, 1053, 1025, 1011, 999, 947, 928, 906, 850, 808, 803, 770, 737, 730, 699, 679, 664. **MS (EI, 70 eV):** m/z (%) = 351 (15), 350 (11), 350 (32), 349 (52), 348 (100), 208 (12), 207 (11), 105 (13), 77 (15). **HR-MS (EI, 70 eV)**: [$C_{22}H_{19}ONCl$], [M-H], calcd.: 348.1233; found: 348.1147.

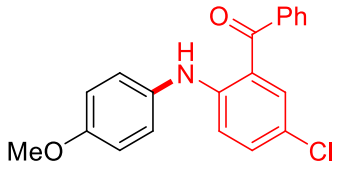

{5-Chloro-2-[(4-methoxyphenyl)amino]phenyl}(phenyl)methanone (5i)

The general procedure **TP7** was followed using 5-chloro-3-phenylbenzo[*c*]isoxazole (69 mg, 0.3 mmol) and (4-methoxyphenyl)(oxo)(pivaloyl)zinc (prepared from **TP5**, 0.45 mmol) for 16 h. Purification by column chromatography (*n*-hexane/EtOAc 10:1) yielded **5i** (80 mg, 81%) as a red solid. **M.p.**: 104–106 °C. **^{1}H-NMR (400 MHz, $CDCl_3$)** δ = 10.04 (s, 1H), 7.74 – 7.70 (m, 2H), 7.60 (t, *J* = 6.7 Hz, 1H), 7.56 – 7.49 (m, 3H), 7.27 – 7.21 (m, 3H), 7.08 (m, 1H), 6.99 – 6.94 (m, 2H), 3.85 (s, 3H). **^{13}C-NMR (100 MHz, $CDCl_3$)** δ = 198.1, 157.0, 148.5, 139.4, 134.4, 133.8, 132.7, 131.6, 129.3, 128.4, 125.7, 120.0, 119.2, 115.6, 114.8, 55.5.

IR (Diamond-ATR, neat): ν / cm = 3258, 3083, 3067, 3002, 2844, 1622, 1588, 1568, 1510, 1444, 1466, 1411, 1496, 1331, 1294, 1250, 1238, 1153, 1098, 1024, 946, 923, 816, 801, 773,

674, 667. **MS (EI, 70 eV):** m/z (%) = 339 (21), 338 (30), 337 (75), 336 (100), 322 (22), 319 (23), 216 (27), 188 (23), 105 (21), 77 (20). **HR-MS (EI, 70 eV)**: [$C_{20}H_{15}O_2NCl$], [M-H], calcd.: 336.0870; found: 336.0764.

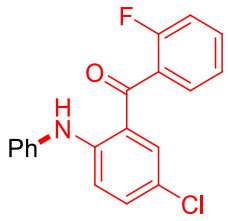

[5-Chloro-2-(phenylamino)phenyl](2-fluorophenyl)methanone (5j)

The general procedure **TP7** was followed using 5-chloro-3-(2-fluorophenyl)benzo[*c*]isoxazole (74 mg, 0.3 mmol) and oxo(phenyl)(pivaloyl)zinc (prepared from **TP4**, 0.45 mmol) for 16 h. Purification by column chromatography (*n*-hexane/EtOAc 15:1) yielded **5j** (71 mg, 74%) as a white solid. **M.p.**: 165–167 °C. **^{1}H-NMR (400 MHz, $CDCl_3$)** δ = 10.46 (s, 1H), 7.55 (dddd, *J* = 8.3, 7.3, 5.2, 1.8 Hz, 1H), 7.49 (td, *J* = 7.4, 1.8 Hz, 1H), 7.41 (ddd, *J* = 6.8, 6.1, 2.1 Hz, 3H), 7.36 – 7.29 (m, 3H), 7.28 (dd, *J* = 3.8, 1.4 Hz, 2H), 7.26 – 7.17 (m, 2H). **^{13}C-NMR (100 MHz, $CDCl_3$)** δ = 194.7, 159.2 (d, J_{C-F} = 250.7 Hz), 147.5, 139.6, 135.2, 133.7 (d, J_{C-F} = 1.8 Hz), 132.5 (d, J_{C-F} = 8.2 Hz), 129.9 (d, J_{C-F} = 3.0 Hz), 129.6, 127.8 (d, J_{C-F} = 15.9 Hz), 124.7, 124.4 (d, J_{C-F} = 3.6 Hz), 123.4, 120.9, 119.8, 116.4 (d, J_{C-F} = 21.5 Hz), 115.8. **IR (Diamond-ATR, neat):** ν / cm = 3262, 1635, 1519, 1264, 946. **MS (EI, 70 eV):** m/z (%) = 325 (15), 324 (100), 308 (45), 306 (20). **HR-MS (EI, 70 eV)**: [$C_{19}H_{13}ClFNO$], calcd.: 325.0670; found: 325.0664.

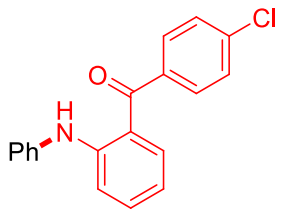

(4-Chlorophenyl)[2-(phenylamino)phenyl]methanone (5k)

The general procedure **TP7** was followed using 5-chloro-3-(2-fluorophenyl)benzo[*c*]isoxazole (69 mg, 0.3 mmol) and oxo(phenyl)(pivaloyl)zinc (prepared from **TP4**, 0.45 mmol) for 16 h. Purification by column chromatography (*n*-hexane/EtOAc 15:1) yielded **5k** (68 mg, 74%) as a

white solid. **M.p.**: 147–149 °C. **^{1}H-NMR (400 MHz, $CDCl_3$)** δ = 10.08 (s, 1H), 7.72 – 7.65 (m, 2H), 7.55 – 7.46 (m, 3H), 7.42 – 7.34 (m, 4H), 7.34 – 7.29 (m, 2H), 7.17 – 7.09 (m, 1H), 6.78 – 6.70 (m, 1H). **^{13}C-NMR (100 MHz, $CDCl_3$)** δ = 197.8, 148.2, 140.4, 138.1, 137.7, 134.7, 134.5, 130.9, 129.4, 128.5, 123.7, 122.3, 119.4, 116.7, 114.8. **IR (Diamond-ATR, neat):** ν / cm = 3258, 1641, 1509, 1247, 946. **MS (EI, 70 eV):** m/z (%) = 307 (10), 306 (45), 290 (100), 288 (40). **HR-MS (EI, 70 eV)**: [$C_{19}H_{14}ClNO$], calcd.: 307.0764; found: 307.0758.

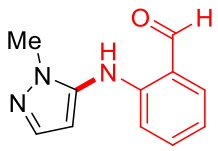

2-[(1-Methyl-1*H*-pyrazol-5-yl)amino]benzaldehyde (5l)

The general procedure **TP7** was followed using benzo[*c*]isoxazole (37 mg, 0.3 mmol) and (1-methyl-1*H*-pyrazol-5-yl)(oxo)(pivaloyl)zinc (prepared from **TP2**, metalation at room temperature, 0.45 mmol) for 16 h. Purification by column chromatography (*n*-hexane/EtOAc 15:1) yielded **5l** (33 mg, 55%) as a yellow oil. **^{1}H-NMR (400 MHz, $CDCl_3$)** δ = 9.96 (s, 1H), 9.77 (s, 1H), 7.64 (dd, *J* = 7.6, 1.6 Hz, 1H), 7.53 (s, 1H), 7.44 (ddd, *J* = 8.6, 7.1, 1.6 Hz, 1H), 6.95 (td, *J* = 7.6, 1.0 Hz, 1H), 6.83 (d, *J* = 8.6 Hz, 1H), 6.20 – 6.14 (m, 1H), 3.77 (s, 3H). **^{13}C-NMR (100 MHz, $CDCl_3$)** δ = 194.8, 147.5, 138.8, 138.0, 136.3, 136.1, 119.5, 118.4, 113.3, 100.0, 35.1. **IR (Diamond-ATR, neat):** ν / cm = 3275, 3071, 2919, 1631, 1601, 1567, 1545, 1491, 1454, 1421, 1318, 1321, 1241, 1161, 1099, 1038, 1009, 951, 880, 848, 791, 745, 715, 700, 665. **MS (EI, 70 eV):** m/z (%) = 201 (14), 184 (11), 183 (96), 182 (100), 173 (14), 155 (13), 129 (25), 128 (20), 117 (11). **HR-MS (EI, 70 eV)**: [$C_{11}H_{11}N_3O$], calcd.: 201.0902; found: 201.0895.

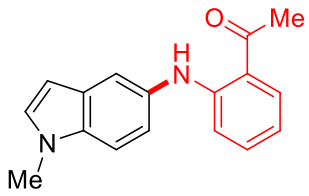

1-{2-[(1-Methyl-1*H*-indol-5-yl)amino]phenyl}ethan-1-one (5m)

The general procedure **TP7** was followed using methylbenzo[*c*]isoxazole (40 mg, 0.3 mmol)

and (1-methyl-1*H*-indol-5-yl)(oxo)(pivaloyl)zinc (prepared from **TP1**, 0.45 mmol) for 16 h. Purification by column chromatography (*n*-hexane/EtOAc 10:1) yielded **5m** (59 mg, 75%) as a colorless liquid. **^{1}H-NMR (400 MHz, $CDCl_3$)** δ = 10.60 (s, 1H), 7.87 – 7.81 (m, 1H), 7.57 (s, 1H), 7.36 (d, J = 8.6 Hz, 1H), 7.31 – 7.25 (m, 1H), 7.18 (dd, J = 8.6, 1.5 Hz, 1H), 7.12 (d, J = 3.0 Hz, 1H), 7.08 (d, J = 8.6 Hz, 1H), 6.69 (t, J = 7.5 Hz, 1H), 6.51 (d, J = 3.0 Hz, 1H), 3.84 (s, 3H), 2.71 (s, 3H). **^{13}C-NMR (100 MHz, $CDCl_3$)** δ = 201.0, 150.5, 134.6, 132.5, 132.0, 129.8, 129.1, 120.4, 117.9, 117.4, 115.2, 113.9, 110.0, 100.9, 33.1, 28.1. **IR (Diamond-ATR, neat):** ν / cm = 3265, 3070, 2919, 1631, 1602, 1566, 1505, 1490, 1444, 1420, 1358, 1321, 1241, 1160, 1079, 1038, 1009, 950, 880, 847, 794, 742, 715, 699, 666. **MS (EI, 70 eV):** m/z (%) = 265 (18), 264 (100), 249 (13), 246 (19), 234 (21), 221 (26), 206 (49), 205 (12), 144 (50), 120 (17). **HR-MS (EI, 70 eV)**: [$C_{17}H_{16}ON_2$], calcd.: 264.1263; found: 264.1259.

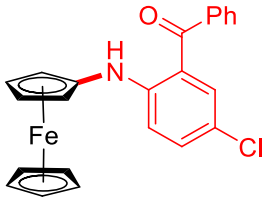

[5-Chloro-2-(ferrocenylamino)phenyl](phenyl)methanone (5n)

The general procedure **TP7** was followed using 5-chloro-3-phenylbenzo[*c*]isoxazole (69 mg, 0.3 mmol) and oxo(ferrocenyl)(pivaloyl)zinc (prepared from **TP1**, 0.45 mmol) for 16 h. Purification by column chromatography (*n*-hexane/EtOAc 10:1) yielded **5n** (50 mg, 40%) as an orange solid. **M.p.**: 114–116 °C. **^{1}H-NMR (400 MHz, $CDCl_3$)** δ = 9.72 (s, 1H), 7.73 – 7.65 (m, 2H), 7.60 (m, 1H), 7.56 – 7.48 (m, 3H), 7.31 – 7.26 (m, 1H), 7.11 (m, 1H), 4.39 (s, 2H), 4.29 (s, 5H), 4.17 (s, 2H). **^{13}C-NMR (100 MHz, $CDCl_3$)** δ = 198.5, 149.7, 139.5, 134.4, 133.6, 131.5, 129.1, 128.4, 119.6, 118.4, 115.8, 95.5, 69.5, 65.8, 65.1. **IR (Diamond-ATR, neat):** ν / cm = 3299, 3082, 2922, 1622, 1597, 1563, 1497, 1444, 1406, 1324, 1304, 1233, 1204, 1178, 1151, 1104, 1026, 999, 949, 934, 906, 814, 801, 768, 729, 710, 666. **MS (EI, 70 eV):** m/z (%) = 417 (29), 416 (24), 415 (100), 350 (14), 77 (12). **HR-MS (EI, 70 eV):** [$C_{23}H_{18}ClFeNO$], calcd: 415.0426.1052; found: 415.0420.

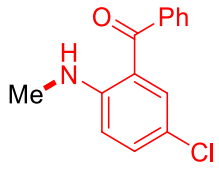

[5-Chloro-2-(methylamino)phenyl](phenyl)methanone (5o)

The general procedure **TP7** was followed using 5-chloro-3-phenylbenzo[*c*]isoxazole (69 mg, 0.3 mmol) and methyl(oxo)(pivaloyl)zinc (prepared from **TP4**, 0.45 mmol) for 16 h. Purification by column chromatography (*n*-hexane/EtOAc 15:1) yielded **5o** (58 mg, 79%) as a yellow solid. **M.p.**: 89–91 °C. **^{1}H-NMR (400 MHz, $CDCl_3$)** δ = 8.38 (s, 1H), 7.52 – 7.47 (m, 2H), 7.45 – 7.41 (m, 1H), 7.40 – 7.33 (m, 3H), 7.24 (dd, J = 9.0, 2.5 Hz, 1H), 6.61 (d, J = 9.0 Hz, 3H). **^{13}C-NMR (100 MHz, $CDCl_3$)** δ = 198.3, 151.2, 139.8, 134.9, 134.1, 131.2, 129.0, 128.3, 118.2, 117.9, 112.8, 29.6. **IR (ATR):** 3328, 1618, 1613, 1561, 1555, 1508, 1503, 1466, 1441, 1397, 1340, 1238, 1170, 1101, 1078, 945, 939, 892, 813, 809, 800, 754, 737, 700, 660. **MS (EI, 70 eV):** m/z (%) = 247 (14), 246 (32), 245 (46), 244 (100), 230 (11), 228 (34), 209 (18), 193 (48), 168 (11), 133 (14), 77 (19). **HR-MS (EI)**: [$C_{14}H_{11}ONCl$], [M-H], calcd.: 245.0607; found: 245.0523.

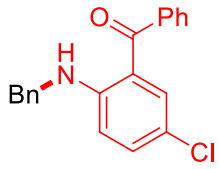

[2-(Benzylamino)-5-chlorophenyl](phenyl)methanone (5p)

The general procedure **TP7** was followed using 5-chloro-3-phenylbenzo[*c*]isoxazole (69 mg, 0.3 mmol) and benzyl(oxo)(pivaloyl)zinc (prepared from **TP4**, 0.45 mmol) for 16 h. Purification by column chromatography (*n*-hexane/EtOAc 15:1) yielded **5p** (64 mg, 66%) as a yellow solid. **M.p.**: 69–71 °C. **^{1}H-NMR (400 MHz, $CDCl_3$)** δ = 8.84 (s, 1H), 7.54 – 7.49 (m, 2H), 7.44 (m, 1H), 7.40 – 7.33 (m, 3H), 7.29 – 7.22 (m, 4H), 7.17 (m, 3H), 6.57 (d, J = 9.1 Hz, 1H), 4.37 (s, 2H). **^{13}C-NMR (100 MHz, $CDCl_3$)** δ = 198.3, 150.0, 140.6, 138.00, 134.7, 134.0, 131.2, 129.0, 128.7, 128.2, 127.3, 127.0, 118.7, 118.2, 113.6, 47.0. **IR (ATR):** 3356, 3239, 3059, 2921, 2849, 1626, 1587, 1465, 1506, 1454, 1401, 1304, 1243, 1227, 1153, 1130, 1075, 1026, 847, 897, 812, 802, 753, 738, 670, 655. **MS (EI):** m/z (%) = 323 (21), 321 (67), 320 (29), 304 (46), 303 (22), 290 (29), 214 (28), 152 (23), 106 (45), 105 (20), 91 (100), 77 (24). **HR-MS**

(EI, 70 eV): [$C_{20}H_{16}ONCl$], calcd.: 321.0920; found: 321.0914.

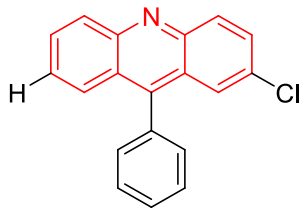

2-Chloro-9-phenylacridine (**6a**)

A suspension of compound **5g** (61 mg, 0.2 mmol) in TFA (2.0 mL) was stirred at 80 ℃ for 12 h under an atmosphere of N_2.[4] At ambient temperature, the reaction mixture was extracted with DCM (3 × 20 mL) and the combined organic layers were washed with saturated $NaHCO_3$ and brine, and dried over Na_2SO_4. The solvent was evaporated *in vacuo* and the remaining residue was purified by column chromatography on silica gel (*n*-hexane/EtOAc 5:1) to yield product **6a** (54 mg, 94%) as a colorless solid. **M.p.** = 197−200 °C. **^{1}H-NMR (400 MHz, $CDCl_3$)** δ = 8.82 (d, *J* = 9.3 Hz, 1H), 8.78 (d, *J* = 8.8 Hz, 1H), 8.14 (dd, *J* = 11.2, 4.2 Hz, 1H), 8.07 – 7.98 (m, 1H), 7.95 – 7.88 (m, 1H), 7.86 (d, *J* = 2.2 Hz, 1H), 7.80 – 7.69 (m, 4H), 7.55 – 7.43 (m, 2H). **^{13}C-NMR (100 MHz, $CDCl_3$)** δ = 156.8, 141.2, 139.5, 136.7, 136.2, 134.2, 132.8, 130.4, 129.8, 129.2, 128.4, 127.8, 125.9, 125.8, 125.8, 124.0, 122.3. **IR (Diamond-ATR, neat):** ν / cm = 3325, 1715, 1564, 1252, 927. **MS (EI, 70 eV):** m/z (%) = 289 (35), 254 (100). **HR-MS (EI, 70 eV)**: [$C_{19}H_{12}ClN$], calcd.: 289.0658; found: 289.0653.

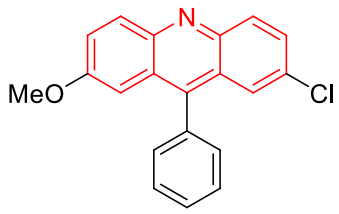

2-Chloro-7-methoxy-9-phenylacridine (**6b**)

A suspension of compound **5i** (67 mg, 0.2 mmol) in TFA (2.0 mL) was stirred at 80 ℃ for 12 h under an atmosphere of N_2.[3]. At ambient temperature, the reaction mixture was extracted with DCM (3 × 20 mL) and the combined organic layers were washed with saturated $NaHCO_3$ and brine, and dried over Na_2SO_4. The solvent was evaporated *in vacuo* and the remaining residue

was purified by column chromatography on silica gel (*n*-hexane/EtOAc 5:1) to yield product **6b** (62 mg, 97%) as a colorless solid. **M.p.** = 221−223 °C. **^{1}H-NMR (400 MHz, CDCl$_3$)** δ = 8.81 – 8.73 (m, 1H), 8.71 (d, J = 9.5 Hz, 1H), 7.90 (dd, J = 9.2, 2.1 Hz, 1H), 7.81 – 7.70 (m, 5H), 7.53 – 7.43 (m, 2H), 6.93 (d, J = 2.6 Hz, 1H), 3.80 (s, 3H). **^{13}C-NMR (100 MHz, CDCl$_3$)** δ = 158.8, 152.4, 138.8, 138.3, 134.8, 134.0, 133.5, 130.6, 130.1, 129.5, 129.4, 127.4, 126.0, 125.2, 124.5, 124.4, 102.6, 55.7. **IR (Diamond-ATR, neat):** ν / cm = 3319, 1721, 1557, 1248, 1046. **MS (EI, 70 eV):** m/z (%) = 319 (25), 304 (75), 288 (100), 284 (20). **HR-MS (EI, 70 eV)**: [$C_{20}H_{14}ClNO$], calcd.: 319.0764; found: 319.0761.

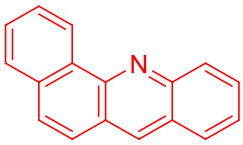

Benzo[*c*]acridine (6c)

A suspension of compound **5d** (49 mg, 0.2 mmol) in TFA (2.0 mL) was stirred at 80 ℃ for 12 h under an atmosphere of N_2.[3]. At ambient temperature, the reaction mixture was extracted with DCM (3 × 20 mL) and the combined organic layers were washed with saturated $NaHCO_3$ and brine, and dried over Na_2SO_4. The solvent was evaporated *in vacuo* and the remaining residue was purified by column chromatography on silica gel (*n*-hexane/EtOAc 5:1) to yield product **6c** (45 mg, 97%) as a colorless solid. **M.p.** = 179−182 °C. **^{1}H-NMR (400 MHz, CDCl$_3$)** δ = 9.61 – 9.50 (m, 1H), 8.66 (s, 1H), 8.42 (dd, J = 8.7, 0.8 Hz, 1H), 8.09 – 8.01 (m, 1H), 7.90 (dd, J = 7.7, 1.4 Hz, 1H), 7.88 – 7.70 (m, 5H), 7.62 (ddd, J = 8.0, 6.7, 1.1 Hz, 1H). **^{13}C-NMR (100 MHz, CDCl$_3$)** δ = 147.8, 147.8, 135.0, 134.0, 131.6, 129.8, 129.7, 129.1, 127.9, 127.8, 127.7, 127.3, 127.1, 125.9, 125.8, 125.3, 125.2. **IR (Diamond-ATR, neat):** ν / cm = 3323, 1691, 1536, 1268, 1046. **MS (EI, 70 eV):** m/z (%) = 229 (100). **HR-MS (EI, 70 eV)**: [$C_{17}H_{11}N$], calcd.: 229.0891; found: 229.0893.

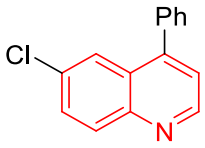

6-Chloro-4-phenylquinoline (8a)

The general procedure **TP7** was followed using 5-chloro-3-phenylbenzo[*c*]isoxazole (69 mg, 0.3 mmol) and oxo(pivaloyl)(vinyl)zinc (prepared from **TP4**, 0.45 mmol) for 16 h. Purification by column chromatography (*n*-hexane/EtOAc 8:1) yielded **8a** (61 mg, 85%) as a white solid. **M.p.**: 134–135 °C. **^{1}H-NMR (400 MHz, $CDCl_3$)** δ = 8.93 (d, J = 4.4 Hz, 1H), 8.12 (d, J = 9.0 Hz, 1H), 7.90 (d, J = 2.3 Hz, 1H), 7.66 (dd, J = 9.0, 2.3 Hz, 1H), 7.57 – 7.45 (m, 5H), 7.35 (d, J = 4.4 Hz, 1H). **^{13}C-NMR (100 MHz, $CDCl_3$)** δ = 150.2, 147.7, 147.1, 137.3, 132.6, 131.5, 130.3, 129.4, 128.8, 128.7, 127.5, 124.7, 122.1. **IR (Diamond-ATR, neat):** ν / cm = 3054, 3024, 2963, 1601, 1583, 1571, 1561, 1498, 1486, 1449, 1434, 1420, 1353, 1151, 1125, 1074, 1054, 1028, 970, 880, 854, 824, 780, 758, 730, 710, 700, 665. **MS (EI, 70 eV):** m/z (%) = 239 (55), 238 (15), 205 (15), 204 (100), 203 (23), 176 (25), 88 (13). **HR-MS (EI, 70 eV)**: [$C_{15}H_{10}NCl$], calcd: 239.0502; found: 239.0494.

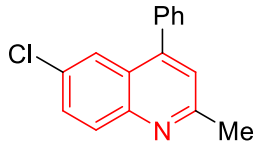

6-Chloro-2-methyl-4-phenylquinoline (8b)

The general procedure **TP7** was followed using 5-chloro-3-phenylbenzo[*c*]isoxazole (69 mg, 0.3 mmol) and oxo(pivaloyl)(prop-1-en-2-yl)zinc (prepared from **TP4**, 0.45 mmol) for 16 h. Purification by column chromatography (*n*-hexane/EtOAc 8:1) yielded **8b** (68 mg, 90%) as a white solid. **M.p.**: 138–140 °C. **^{1}H-NMR (600 MHz, $CDCl_3$)** δ = 8.01 (d, J = 9.0 Hz, 1H), 7.82 (d, J = 2.3 Hz, 1H), 7.62 (dd, J = 9.0, 2.3 Hz, 1H), 7.57 – 7.49 (m, 3H), 7.49 – 7.45 (m, 2H), 7.25 (s, 1H), 2.77 (s, 3H). **^{13}C-NMR (150 MHz, $CDCl_3$)** δ = 158.8, 147.8, 146.8, 137.5, 131.6, 130.6, 130.1, 129.3, 128.7, 128.6, 125.8, 124.5 (d, J = 2.7 Hz), 123.0 (d, J = 5.8 Hz). **IR (Diamond-ATR, neat):** ν / cm = 3048, 1607, 1578, 1349, 1075, 963. **MS (EI, 70 eV):** m/z (%) = 253 (45), 252 (15), 238 (55), 218 (100). **HR-MS (EI, 70 eV)**: [$C_{16}H_{12}NCl$], calcd: 253.0658; found: 253.0654.

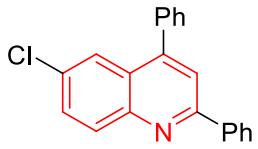

6-Chloro-2,4-diphenylquinoline (8c)

The general procedure **TP7** was followed using 5-chloro-3-phenylbenzo[*c*]isoxazole (69 mg, 0.3 mmol) and oxo(1-phenylvinyl)(pivaloyl)zinc (prepared from **TP6**, 0.45 mmol) for 16 h. Purification by column chromatography (*n*-hexane/EtOAc 8:1) yielded **8c** (88 mg, 93%) as a white solid. **M.p.**: 138–140 °C. **^{1}H-NMR (400 MHz, $CDCl_3$)** δ = 8.25 – 8.18 (m, 3H), 7.90 (d, *J* = 2.3 Hz, 1H), 7.87 (s, 1H), 7.69 (dd, *J* = 9.0, 2.3 Hz, 1H), 7.64 – 7.47 (m, 8H). **^{13}C-NMR (100 MHz, $CDCl_3$)** δ = 157.1, 148.5, 147.3, 139.2, 137.8, 132.2, 131.8, 130.5, 129.6, 129.5, 128.9, 128.8, 128.7, 127.6, 126.5, 124.5, 120.1. **IR (Diamond-ATR, neat):** ν / cm = 3051, 1614, 1582, 1354, 1067, 963. **MS (EI, 70 eV):** m/z (%) = 315 (25), 314 (10), 280 (100). **HR-MS (EI, 70 eV)**: [$C_{21}H_{14}NCl$], calcd: 315.0815; found: 315.0819.

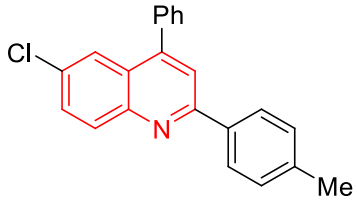

6-Chloro-4-phenyl-2-p-tolylquinoline (8d)

The general procedure **TP7** was followed using 5-chloro-3-phenylbenzo[*c*]isoxazole (69 mg, 0.3 mmol) and oxo(pivaloyl)(1-*p*-tolylvinyl)zinc (prepared from **TP6**, 0.45 mmol) for 16 h. Purification by column chromatography (*n*-hexane/EtOAc 10:1) yielded **8d** (61 mg, 62%) as a white solid. **M.p.**: 151–153 °C. **^{1}H-NMR (400 MHz, $CDCl_3$)** δ = 8.18 (d, *J* = 9.0 Hz, 1H), 8.15 – 8.09 (m, 2H), 7.88 (t, *J* = 4.0 Hz, 1H), 7.85 (d, *J* = 4.0 Hz, 1H), 7.72 – 7.65 (m, 1H), 7.64 – 7.53 (m, 5H), 7.35 (t, *J* = 8.8 Hz, 2H), 2.46 (s, 3H). **^{13}C-NMR (100 MHz, $CDCl_3$)** δ = 157.1, 148.3, 147.2, 139.8, 137.8, 136.4, 132.0, 131.7, 130.4, 129.7, 129.5, 128.8, 128.7, 127.4, 126.4, 124.5, 119.9, 21.4. **IR (Diamond-ATR, neat):** ν / cm = 3052, 1621, 1575, 1361, 1066, 967. **MS (EI, 70 eV):** m/z (%) = 329 (20), 328 (5), 314 (35), 294 (100). **HR-MS (EI, 70 eV)**: [$C_{22}H_{16}NCl$], calcd: 329.0971; found: 329.0973.

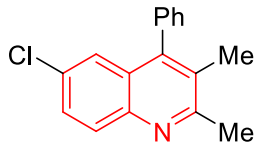

6-Chloro-2,3-dimethyl-4-phenylquinoline (8e)

The general procedure **TP7** was followed using 5-chloro-3-phenylbenzo[*c*]isoxazole (69 mg, 0.3 mmol) and but-2-en-2-yl(oxo)(pivaloyl)zinc (prepared from **TP4**, 0.45 mmol) for 16 h. Purification by column chromatography (*n*-hexane/EtOAc 9:1) yielded **8e** (73 mg, 91%) as a white solid. **M.p.**: 127–130 °C. **^{1}H-NMR (400 MHz, $CDCl_3$)** δ = 7.98 (d, *J* = 8.9 Hz, 1H), 7.60 – 7.48 (m, 4H), 7.30 (d, *J* = 2.3 Hz, 1H), 7.27 – 7.21 (m, 2H), 2.77 (s, 3H), 2.20 (s, 3H). **^{13}C-NMR (100 MHz, $CDCl_3$)** δ = 159.3, 145.6, 144.5, 136.9, 131.3, 130.1, 129.3, 129.1, 128.8, 128.6, 128.1, 127.7, 124.9, 24.5, 17.1. **IR (Diamond-ATR, neat):** ν / cm = 3035, 1619, 1571, 1349, 1062, 952. **MS (EI, 70 eV):** m/z (%) = 267 (20), 252 (45), 232 (100). **HR-MS (EI, 70 eV)**: [$C_{17}H_{14}NCl$], calcd: 267.0815; found: 267.0812.

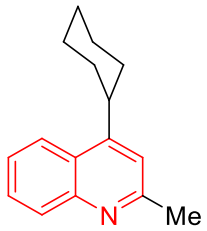

4-Cyclohexyl-2-methylquinoline (8f)

The general procedure **TP7** was followed using 3-cyclohexylbenzo[*c*]isoxazole (60 mg, 0.3 mmol) and oxo(pivaloyl)(prop-1-en-2-yl)zinc (prepared from **TP4**, 0.45 mmol) for 16 h. Purification by column chromatography (*n*-hexane/EtOAc 9:1) yielded **8f** (42 mg, 62%) as a yellow oil. **^{1}H-NMR (400 MHz, $CDCl_3$)** δ = 8.05 (d, *J* = 8.9 Hz, 2H), 7.67 (ddd, *J* = 8.4, 6.9, 1.3 Hz, 1H), 7.50 (ddd, *J* = 8.2, 6.9, 1.3 Hz, 1H), 7.19 (s, 1H), 3.31 (ddd, *J* = 11.2, 8.3, 3.1 Hz, 1H), 2.74 (s, 3H), 2.08 – 1.81 (m, 5H), 1.65 – 1.48 (m, 4H), 1.43 – 1.30 (m, 1H). **^{13}C-NMR (125 MHz, $CDCl_3$)** δ = 158.8, 153.3, 148.2, 129.6, 128.8, 125.3, 125.2, 122.8, 118.3, 38.8, 33.6, 27.0, 26.3, 25.6. **IR (Diamond-ATR, neat):** ν / cm = 3021, 1643, 1514, 1354, 1057, 951. **MS (EI, 70 eV):** m/z (%) = 225 (55), 224 (15), 210 (100). **HR-MS (EI, 70 eV)**: [$C_{16}H_{19}N$], calcd: 225.1517; found: 225.1519

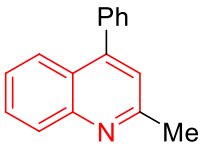

2-Methyl-4-phenylquinoline (8g)

The general procedure **TP7** was followed using 3-phenylbenzo[*c*]isoxazole (59 mg, 0.3 mmol) and oxo(pivaloyl)(prop-1-en-2-yl)zinc (prepared from **TP4**, 0.45 mmol) for 16 h. Purification by column chromatography (*n*-hexane/EtOAc 9:1) yielded **8g** (57 mg, 86%) as a white solid. **M.p.**: 121–123 °C. **^{1}H-NMR (400 MHz, CDCl$_3$)** δ = 8.11 (dd, *J* = 8.5, 0.6 Hz, 1H), 7.88 (dd, *J* = 8.4, 1.0 Hz, 1H), 7.71 (ddd, *J* = 8.4, 6.9, 1.4 Hz, 1H), 7.58 – 7.50 (m, 5H), 7.46 (ddd, *J* = 8.2, 6.9, 1.2 Hz, 1H), 7.26 (s, 1H), 2.81 (s, 3H). **^{13}C-NMR (100 MHz, CDCl$_3$)** δ = 158.5, 148.6, 148.4, 138.2, 129.5, 129.3, 129.0, 128.5, 128.3, 125.8, 125.7, 125.1, 122.3, 25.4. **IR (Diamond-ATR, neat):** ν / cm = 3051, 1624, 1601, 1351, 1066, 967. **MS (EI, 70 eV):** m/z (%) = 219 (25), 218 (10), 204 (100). **HR-MS (EI, 70 eV)**: [$C_{16}H_{13}N$], calcd: 219.1048; found: 219.1043.

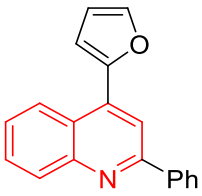

4-(Furan-2-yl)-2-phenylquinoline (8h)

The general procedure **TP7** was followed using 3-(furan-2-yl)benzo[*c*]isoxazole (56 mg, 0.3 mmol) and oxo(1-phenylvinyl)(pivaloyl)zinc (prepared from **TP6**, 0.45 mmol) for 16 h. Purification by column chromatography (*n*-hexane/EtOAc 9:1) yielded **8h** (78 mg, 96%) as a slight yellow solid. **M.p.**: 117–119 °C. **^{1}H-NMR (600 MHz, CDCl$_3$)** δ = 8.48 (dd, *J* = 8.5, 0.7 Hz, 1H), 8.25 – 8.19 (m, 3H), 8.12 (s, 1H), 7.75 (qd, *J* = 6.6, 3.1 Hz, 1H), 7.73 – 7.70 (m, 1H), 7.58 (ddd, *J* = 8.2, 6.8, 1.3 Hz, 1H), 7.55 (dd, *J* = 10.3, 4.8 Hz, 2H), 7.51 – 7.46 (m, 1H), 7.04 (dd, *J* = 6.1, 2.9 Hz, 1H), 6.67 (dd, *J* = 3.4, 1.8 Hz, 1H). **^{13}C-NMR (150 MHz, CDCl$_3$)** δ = 157.1, 151.3, 149.2, 143.8, 143.8, 139.6, 136.4, 130.4, 129.5, 129.4 (d, *J* = 2.0 Hz), 128.8, 127.6 (d, *J* = 13.6 Hz), 126.7 (d, *J* = 1.9 Hz), 125.1, 123.5, 116.7 (t, *J* = 6.7 Hz), 112.0 (d, *J* = 2.0 Hz). **IR (Diamond-ATR, neat):** ν / cm = 3031, 1647, 1589, 1344, 1106, 962. **MS (EI, 70 eV):** m/z (%) = 271 (100), 270 (15). **HR-MS (EI, 70 eV)**: [$C_{19}H_{13}NO$], calcd: 271.0997; found: 271.0996.

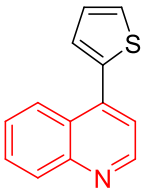

4-(Thiophen-2-yl)quinoline (8i)

The general procedure **TP7** was followed using 3-(thiophen-2-yl)benzo[*c*]isoxazole (60 mg, 0.3 mmol) and oxo(pivaloyl)(vinyl)zinc (prepared from **TP4**, 0.45 mmol) for 16 h. Purification by column chromatography (*n*-hexane/EtOAc 9:1) yielded **8i** (57 mg, 90%) as a red solid. **M.p.**: 105–108 °C. **^{1}H-NMR (400 MHz, $CDCl_3$)** δ = 8.94 (d, *J* = 4.5 Hz, 1H), 8.33 (dd, *J* = 8.5, 1.0 Hz, 1H), 8.20 (d, *J* = 8.0 Hz, 1H), 7.78 (ddd, *J* = 8.4, 6.9, 1.4 Hz, 1H), 7.60 (ddd, *J* = 8.3, 6.9, 1.3 Hz, 1H), 7.56 (dt, *J* = 4.4, 2.2 Hz, 1H), 7.49 (dd, *J* = 8.1, 2.9 Hz, 1H), 7.42 (dd, *J* = 3.6, 1.1 Hz, 1H), 7.26 (dd, *J* = 5.1, 3.6 Hz, 1H). **^{13}C-NMR (100 MHz, $CDCl_3$)** δ = 149.9, 148.9, 140.9, 138.9, 130.0, 129.6, 128.6, 127.8, 127.3, 127.0, 126.5, 125.6, 121.7. **IR (Diamond-ATR, neat):** ν / cm = 3029, 1650, 1571, 1341, 1124, 957. **MS (EI, 70 eV):** m/z (%) = 211 (100), 270 (5). **HR-MS (EI, 70 eV)**: [$C_{13}H_9NS$], calcd: 211.0456; found: 211.0461.

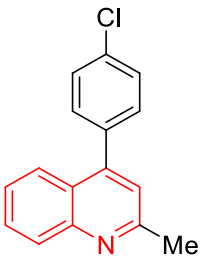

4-(4-Chlorophenyl)-2-methylquinoline (8j)

The general procedure **TP7** was followed using 3-(4-chlorophenyl)benzo[*c*]isoxazole (69 mg, 0.3 mmol) and oxo(pivaloyl)(prop-1-en-2-yl)zinc (prepared from **TP4**, 0.45 mmol) for 16 h. Purification by column chromatography (*n*-hexane/EtOAc 9:1) yielded **8j** (69 mg, 91%) as a white solid. **M.p.**: 135–137 °C. **^{1}H-NMR (600 MHz, $CDCl_3$)** δ = 8.11 – 8.07 (m, 1H), 7.82 – 7.77 (m, 1H), 7.69 (ddd, *J* = 8.3, 6.9, 1.3 Hz, 1H), 7.52 – 7.47 (m, 2H), 7.47 – 7.41 (m, 3H), 7.20 (s, 1H), 2.78 (s, 3H). **^{13}C-NMR (150 MHz, $CDCl_3$)** δ = 158.5, 148.3, 147.2, 136.5, 134.4 (d, *J* = 33.7 Hz), 130.8 (dd, *J* = 10.0, 5.5 Hz), 129.5 (d, *J* = 2.6 Hz), 129.1, 128.8 – 128.7 (m), 125.9 (d, *J* = 7.9 Hz), 125.3 – 125.2 (m), 124.8, 122.1 (d, *J* = 9.3 Hz), 25.3 (q, *J* = 6.9 Hz). **IR (Diamond-ATR, neat):** ν / cm = 3027, 1649, 1579, 1343, 1126, 957. **MS (EI, 70 eV):** m/z (%)

= 253 (30), 252 (10), 238 (25), 218 (100). **HR-MS (EI, 70 eV)**: [$C_{16}H_{12}ClN$], calcd: 253.0658; found: 253.0655.

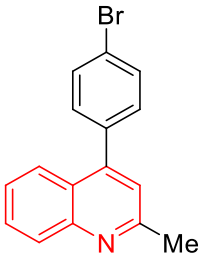

4-(4-Bromophenyl)-2-methylquinoline (8k)

The general procedure **TP7** was followed using 3-(4-bromophenyl)benzo[*c*]isoxazole (82 mg, 0.3 mmol) and oxo(pivaloyl)(prop-1-en-2-yl)zinc (prepared from **TP4**, 0.45 mmol) for 16 h. Purification by column chromatography (*n*-hexane/EtOAc 9:1) yielded **8k** (82 mg, 92%) as a white solid. **M.p.**: 135–137 °C. **^{1}H-NMR (400 MHz, $CDCl_3$)** δ = 8.11 (d, J = 8.4 Hz, 1H), 7.81 (dd, J = 8.4, 1.0 Hz, 1H), 7.75 – 7.69 (m, 1H), 7.69 – 7.64 (m, 2H), 7.50 – 7.44 (m, 1H), 7.43 – 7.36 (m, 2H), 7.22 (s, 1H), 2.80 (s, 3H). **^{13}C-NMR (100 MHz, $CDCl_3$)** δ = 158.5, 148.4, 147.3, 137.0, 131.8, 131.1, 129.5, 129.1, 126.0, 125.3, 124.8, 122.7, 122.1, 25.4. **IR (Diamond-ATR, neat):** ν / cm = 3029, 1653, 1581, 1342, 1131, 943. **MS (EI, 70 eV):** m/z (%) = 299 (45), 297 (45), 284 (30), 282 (30), 218 (100). **HR-MS (EI, 70 eV)**: [$C_{16}H_{12}BrN$], calcd: 297.0153; found: 297.0151.

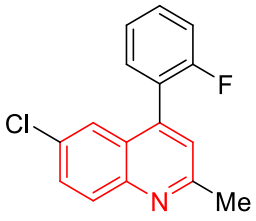

6-Chloro-4-(2-fluorophenyl)-2-methylquinoline (8l)

The general procedure **TP7** was followed using 5-chloro-3-(2-fluorophenyl)benzo[*c*]isoxazole (74 mg, 0.3 mmol) and oxo(pivaloyl)(prop-1-en-2-yl)zinc (prepared from **TP4**, 0.45 mmol) for 16 h. Purification by column chromatography (*n*-hexane/EtOAc 9:1) yielded **8l** (76 mg, 93%) as a white solid. **M.p.**: 136–137 °C. **^{1}H-NMR (400 MHz, $CDCl_3$)** δ = 8.04 (d, J = 8.9 Hz, 1H), 7.65 (dd, J = 8.9, 2.3 Hz, 1H), 7.60 (t, J = 2.1 Hz, 1H), 7.53 (dddd, J = 8.2, 7.2, 5.2, 2.0 Hz,

1H), 7.39 (td, J = 7.4, 2.0 Hz, 1H), 7.36 – 7.25 (m, 3H), 2.80 (s, 3H). **^{13}C-NMR (100 MHz, $CDCl_3$)** δ = 159.6 (d, J_{C-F} = 248.3 Hz), 158.8, 146.6, 141.9, 131.8, 131.6 (d, J_{C-F} = 3.1 Hz), 130.8 (d, J_{C-F} = 8.0 Hz), 130.7, 130.4, 126.0, 124.9 (d, J_{C-F} = 16.0 Hz), 124.5 (d, J_{C-F} = 3.7 Hz), 124.4 (d, J_{C-F} = 1.4 Hz), 123.9, 116.2 (d, J_{C-F} = 21.8 Hz), 25.3. **^{19}F-NMR (376 MHz, $CDCl_3$)** δ = -111.56 – -115.41 (m). **IR (Diamond-ATR, neat):** ν / cm = 3137, 1649, 1573, 1350, 1135, 961. **MS (EI, 70 eV):** m/z (%) = 299 (45), 297 (45), 284 (30), 282 (30), 218 (100). **HR-MS (EI, 70 eV)**: [$C_{16}H_{11}ClFN$], calcd: 271.0564; found: 271.0563.

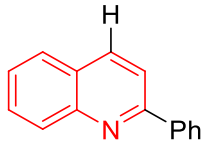

2-Phenylquinoline (8m)

The general procedure **TP7** was followed using benzo[*c*]isoxazole (37 mg, 0.3 mmol) and oxo(1-phenylvinyl)(pivaloyl)zinc (prepared from **TP6**, 0.45 mmol) for 16 h. Purification by column chromatography (*n*-hexane/EtOAc 9:1) yielded **8m** (54 mg, 87%) as a white solid. **M.p.**: 123–124 °C. **^{1}H-NMR (400 MHz, $CDCl_3$)** δ = 8.25 (d, J = 8.6 Hz, 1H), 8.23 – 8.15 (m, 3H), 7.91 (d, J = 8.6 Hz, 1H), 7.86 (dd, J = 8.1, 1.2 Hz, 1H), 7.76 (ddd, J = 8.4, 6.9, 1.5 Hz, 1H), 7.56 (tdd, J = 3.5, 2.5, 1.4 Hz, 3H), 7.53 – 7.46 (m, 1H). **^{13}C-NMR (125 MHz, $CDCl_3$)** δ = 157.4, 148.3, 139.7, 136.8, 129.8, 129.7, 129.3, 128.9, 127.6, 127.5, 127.2, 126.3, 119.0. **IR (Diamond-ATR, neat):** ν / cm = 3027, 1647, 1570, 1348, 1207, 957. **MS (EI, 70 eV):** m/z (%) = 205 (100). **HR-MS (EI, 70 eV)**: [$C_{15}H_{11}N$], calcd: 205.0891; found: 205.0887.

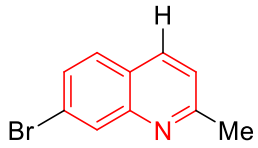

7-Bromo-2-methylquinoline (8n)

The general procedure **TP7** was followed using 5-bromobenzo[*c*]isoxazole (59 mg, 0.3 mmol) and oxo(pivaloyl)(prop-1-en-2-yl)zinc (prepared from **TP4**, 0.45 mmol) for 16 h. Purification by column chromatography (*n*-hexane/EtOAc 9:1) yielded **8n** (54 mg, 81%) as a colorless oil. **^{1}H-NMR (400 MHz, $CDCl_3$)** δ = 8.22 (d, J = 1.7 Hz, 1H), 8.01 (d, J = 8.4 Hz, 1H), 7.63 (d, J

= 8.6 Hz, 1H), 7.56 (dd, *J* = 8.6, 1.9 Hz, 1H), 7.30 (d, *J* = 8.5 Hz, 1H), 2.75 (s, 3H). **^{13}C-NMR (100 MHz, $CDCl_3$)** δ = 160.2, 148.4, 136.0, 131.0, 129.2, 128.7, 125.1, 123.5, 122.4, 25.3. **IR (Diamond-ATR, neat):** ν / cm = 3023, 1658, 1566, 1347, 1212, 947. **MS (EI, 70 eV):** m/z (%) = 223 (25), 221 (25), 208 (100), 206 (100), 142 (40). **HR-MS (EI, 70 eV)**: [$C_{15}H_{11}N$], calcd: 220.9840; found: 220.9847.

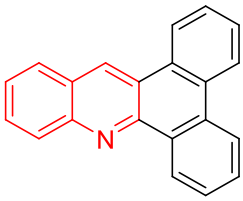

Dibenzo[*a*,*c*]acridine (10a)

The general procedure **TP7** was followed using benzo[*c*]isoxazole (37 mg, 0.3 mmol) and Oxo(phenanthren-9-yl)(pivaloyl)zinc (prepared from **TP1**, 0.45 mmol) for 16 h. Purification by column chromatography (*n*-hexane/EtOAc 10:1) yielded **10a** (51 mg, 61%) as a white solid. **M.p.**: 204–205 °C. **^{1}H-NMR (400 MHz, $CDCl_3$)** δ = 9.58 – 9.50 (m, 1H), 9.24 (s, 1H), 8.67 – 8.61 (m, 1H), 8.60 – 8.51 (m, 2H), 8.34 (d, *J* = 8.5 Hz, 1H), 8.07 – 8.00 (m, 1H), 7.83 (ddd, *J* = 8.5, 6.7, 1.4 Hz, 1H), 7.79 – 7.74 (m, 2H), 7.70 – 7.58 (m, 3H). **^{13}C-NMR (100 MHz, $CDCl_3$)** δ = 147.6, 147.5, 132.0, 131.1, 130.2, 129.8, 129.6, 129.4, 129.1, 128.1, 128.0, 127.7, 127.6, 127.1, 126.3, 126.2, 123.6, 123.5, 123.4, 122.7. **IR (Diamond-ATR, neat):** ν / cm = 2921, 2849, 1736, 1724, 1710, 1697, 1691, 1596, 1502, 1491, 1466, 1440, 1410, 1379, 1341, 1236, 1127, 1035, 949, 902, 853, 800, 753, 720, 699, 682. **MS (EI, 70 eV):** m/z (%) = 279 (100), 280 (17), 278 (19), 139 (10). **HR-MS (EI, 70 eV):** [$C_{21}H_{13}N$], calcd: 279.1048; found: 279.1047.

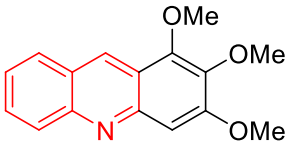

1,2,3-Trimethoxyacridine (10b)

The general procedure **TP7** was followed using benzo[*c*]isoxazole (24 mg, 0.2 mmol) and oxo(pivaloyl)(3,4,5-trimethoxyphenyl)zinc (prepared from **TP6**, 0.40 mmol) for 16 h. Purification by column chromatography (*n*-hexane/EtOAc 7:1) yielded **10b** (30 mg, 55%) as a

colorless oil. **^{1}H-NMR (400 MHz, $CDCl_3$)** δ = 8.86 (s, 1H), 8.05 (dd, J = 8.7, 1.1 Hz, 1H), 7.91 (dt, J = 8.4, 1.1 Hz, 1H), 7.66 (ddd, J = 8.7, 6.6, 1.5 Hz, 1H), 7.41 (ddd, J = 8.1, 6.6, 1.1 Hz, 1H), 7.23 (s, 1H), 4.09 (s, 3H), 3.99 (s, 3H), 3.95 (s, 3H). **^{13}C-NMR (100 MHz, $CDCl_3$)** δ = 157.5, 148.5, 147.3, 146.1, 140.1, 130.6, 130.1, 128.4, 125.2, 124.8, 119.5, 102.3, 61.6, 61.4, 56.3. **IR (Diamond-ATR, neat):** ν / cm = 2934, 1630, 1612, 1562, 1476, 1462, 1430, 1352, 1314, 1301, 1232, 1208, 1180, 1131, 1094, 1034, 998, 913, 829, 748. **MS (EI, 70 eV):** m/z (%) = 269 (100), 254 (64), 226 (81), 211 (68), 207 (39), 183 (35), 182 (33), 140 (64). **HR-MS (EI, 70 eV):** [$C_{16}H_{15}NO_3$], calcd: 269.1052; found: 269.1048.

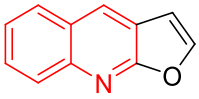

Furo[2,3-*b*]quinoline (10c)

The general procedure **TP7** was followed using benzo[*c*]isoxazole (37 mg, 0.3 mmol) and furan-2-yl(oxo)(pivaloyl)zinc (prepared from **TP2**, metalation at room temperature, 0.45 mmol) for 16 h. Purification by column chromatography (*n*-hexane/EtOAc 10:1) yielded **10c** (31 mg, 61%) as a white solid. **M.p.**: 74–76 °C. **^{1}H-NMR (400 MHz, $CDCl_3$)** δ = 8.22 (d, J = 1.9 Hz, 1H), 8.10 (d, J = 8.5 Hz, 1H), 7.83 (d, J = 8.2 Hz, 1H), 7.71 (d, J = 2.6 Hz, 1H), 7.65 (ddd, J = 8.5, 6.8, 1.5 Hz, 1H), 7.44 (dd, J = 8.5, 6.8 Hz, 1H), 6.76 (t, J = 1.9 Hz, 1H). **^{3}C-NMR (100 MHz, $CDCl_3$)** δ = 161.5, 146.9, 144.8, 129.3, 128.9, 128.3, 127.9, 126.2, 124.7, 119.8, 105.7. **IR (Diamond-ATR, neat):** ν / cm = 3103, 1587, 1537, 1504, 1387, 1329, 1244, 1129, 1098, 1014, 912, 907, 774, 764, 754, 745, 730. **MS (EI, 70 eV):** m/z (%) = 170 (12), 169 (100), 141 (34), 140 (36), 114 (26), 113 (12). **HR-MS (EI, 70 eV)**: [$C_{11}H_7NO$], calcd: 169.0528; found: 169.0522.

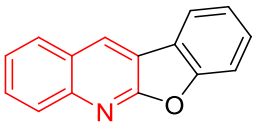

Benzofuro[2,3-*b*]quinoline (10d)

The general procedure **TP7** was followed using benzo[*c*]isoxazole (37 mg, 0.3 mmol) and benzofuran-2-yl(oxo)(pivaloyl)zinc (prepared from **TP1**, 0.45 mmol) for 16 h. Purification by

column chromatography (*n*-hexane/EtOAc 10:1) yielded **10d** (49 mg, 75%) as a white solid. **M.p.**: 190–192 °C. **^{1}H-NMR (400 MHz, CDCl$_3$)** δ = 8.38 (s, 1H), 7.99 (d, J = 8.3 Hz, 1H), 7.81 – 7.75 (m, 2H), 7.58 (ddd, J = 8.3, 6.7, 1.5 Hz, 1H), 7.43 (d, J = 8.3 Hz, 1H), 7.36 (t, J = 7.6 Hz, 2H), 7.20 (t, J = 7.6 Hz, 1H). **^{13}C-NMR (100 MHz, CDCl$_3$)** δ = 162.5, 155.8, 145.9, 129.6, 129.3, 129.0, 128.4, 128.1, 126.0, 125.0, 123.4, 122.1, 121.7, 117.6, 111.9. **IR (Diamond-ATR, neat):** ν / cm =3048, 1593, 1582, 1508, 1465, 1452, 1388, 1349, 1333, 1198, 1173, 1146, 1119, 1098, 1013, 984, 907, 864, 784, 754, 750, 720, 712, 666. **MS (EI, 70 eV):** m/z (%) = 220 (16), 219 (100), 190 (23). **HR-MS (EI, 70 eV)**: [$C_{15}H_9NO$], calcd: 219.0684; found: 219.0676.

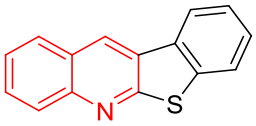

Benzo[4,5]thieno[2,3-*b*]quinoline (10e)

The general procedure **TP7** was followed using benzo[*c*]isoxazole (37 mg, 0.3 mmol) and benzo[*b*]thiophen-2-yl(oxo)(pivaloyl)zinc (prepared from **TP1**, 0.45 mmol) for 16 h. Purification by column chromatography (*n*-hexane/EtOAc 10:1) yielded **10e** (41 mg, 60%) as a white solid. **M.p.**: 140–142 °C. **^{1}H-NMR (400 MHz, CDCl$_3$)** δ = 8.68 (s, 1H), 8.18 – 8.11 (m, 2H), 7.97 (dd, J = 8.3, 1.5 Hz, 1H), 7.84 – 7.79 (m, 1H), 7.76 (ddd, J = 8.3, 6.8, 1.5 Hz, 1H), 7.59 – 7.43 (m, 3H). **^{13}C-NMR (101 MHz, CDCl$_3$)** δ = 163.2, 147.7, 138.3, 132.4, 129.7, 128.7, 128.4, 128.4, 128.1, 127.8, 125.6, 125.4, 125.0, 123.1, 122.2. **IR (Diamond-ATR, neat):** ν / cm = 3048, 2922, 2849, 1584, 1552, 1490, 1450, 1339, 1132, 1093, 1065, 1020, 954, 908, 862, 779, 760, 752, 740, 700, 689, 666. **MS (EI, 70 eV):** m/z (%) = 236 (15), 235 (100). **HR-MS (EI, 70 eV)**: [$C_{15}H_9NS_2$], calcd: 235.0456; found: 235.0450.

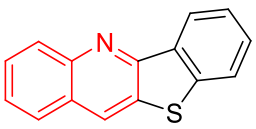

Benzo[4,5]thieno[3,2-*b*]quinoline (10f)

The general procedure **TP7** was followed using benzo[*c*]isoxazole (357 mg, 3 mmol) and benzo[*b*]thiophen-3-yl(oxo)(pivaloyl)zinc (prepared from **TP1**, 4.5 mmol) for 16 h.

Purification by column chromatography (*n*-hexane/EtOAc 10:1) yielded **10f** (318 mg, 45%) as a red solid. **M.p.**: 175–177 °C. **^{1}H-NMR (400 MHz, CDCl$_3$)** δ = 8.74 – 8.68 (m, 1H), 8.62 (s, 1H), 8.34 (d, *J* = 8.5 Hz, 1H), 7.94 (dd, *J* = 8.5, 1.4 Hz, 1H), 7.90 – 7.86 (m, 1H), 7.80 (ddd, *J* = 8.5, 6.8, 1.4 Hz, 1H), 7.68 – 7.56 (m, 3H). **^{13}C-NMR (100 MHz, CDCl$_3$)** δ = 154.0, 146.4, 141.3, 134.1, 131.7, 130.0, 129.4, 129.2, 129.0, 127.1, 126.6, 126.3, 125.1, 124.1, 123.1. **IR (Diamond-ATR, neat):** ν / cm = 3103, 1587, 1537, 1504, 1387, 1329, 1244, 1129, 1098, 1014, 912, 907, 774, 764, 754, 745, 730. **MS (EI, 70 eV):** m/z (%) = 281 (13), 236 (16), 235 (100), 207 (60), 191 (14). **HR-MS (EI, 70 eV)**: [$C_{15}H_9NS$], calcd: 235.0456; found: 235.0449.

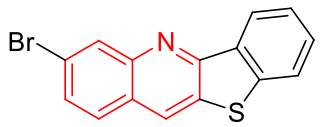

3-Bromobenzo[4,5]thieno[3,2-*b*]quinoline (10g)

The general procedure **TP7** was followed using 5-bromobenzo[*c*]isoxazole (59 mg, 0.3 mmol) and benzo[*b*]thiophen-3-yl(oxo)(pivaloyl)zinc (prepared from **TP1**, 0.45 mmol) for 16 h. Purification by column chromatography (*n*-hexane/EtOAc 10:1) yielded **10g** (39 mg, 40%) as a white solid. **M.p.**: 189–191 °C. **^{1}H-NMR (400 MHz, CDCl$_3$)** δ = 8.67 (d, *J* = 7.9 Hz, 1H), 8.59 (s, 1H), 8.52 (d, *J* = 1.8 Hz, 1H), 7.89 (dt, *J* = 7.9, 1.0 Hz, 1H), 7.81 (d, *J* = 8.8 Hz, 1H), 7.71 – 7.65 (m, 2H), 7.61 (td, *J* = 7.5, 1.0 Hz, 1H). **^{13}C-NMR (100 MHz, CDCl$_3$)** δ = 154.6, 146.9, 141.4, 133.8, 132.0, 131.7, 130.3, 129.7, 129.0, 128.3, 125.3, 125.1, 124.2, 123.1, 122.8. **IR (Diamond-ATR, neat):** ν / cm = 3051, 1603, 1591, 1546, 1476, 1445, 1338, 1168, 1078, 1054, 906, 888, 868, 799, 760, 754, 734, 740, 699, 684, 665. **MS (EI, 70 eV):** m/z (%) = 316 (15), 315 (97), 314 (15), 313 (100), 234 (35), 233 (27), 207 (26), 190 (23), 157 (12), 156 (11), 117 (16), 103 (10). **HR-MS (EI, 70 eV)**: [$C_{15}H_8BrNS$], calcd: 312.9561; found: 312.9556.

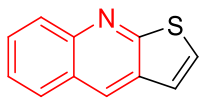

Thieno[2,3-*b*]quinoline (10h)

The general procedure **TP7** was followed using benzo[*c*]isoxazole (37 mg, 0.3 mmol) and oxo(pivaloyl)(thiophen-2-yl)zinc (prepared from **TP1**, metalation at room temperature,

0.45 mmol) for 16 h. Purification by column chromatography (*n*-hexane/EtOAc 10:1) yielded **10h** (32 mg, 58%) as a white solid. **M.p.**: 77–79 °C. **^{1}H-NMR (400 MHz, $CDCl_3$)** δ = 8.57 (s, 1H), 8.18 (dd, *J* = 8.6, 0.7 Hz, 1H), 8.03 – 7.96 (m, 1H), 7.77 (ddd, *J* = 8.5, 5.2, 1.4 Hz, 1H), 7.61 (d, *J* = 6.2 Hz, 1H), 7.58 (ddd, *J* = 8.1, 5.6, 1.1 Hz, 1H), 7.39 (d, *J* = 6.2 Hz, 1H). **^{13}C-NMR (100 MHz, $CDCl_3$)** δ = 163.3, 146.7, 131.5, 130.2, 129.3, 128.6, 128.4, 128.3, 125.6, 125.5, 121.2. **IR (Diamond-ATR, neat):** ν / cm = 3047, 1611, 1549, 1443, 1082, 973, 679. **MS (EI, 70 eV):** m/z (%) = 185 (100). **HR-MS (EI, 70 eV)**: [$C_{11}H_7NS$], calcd: 185.0299; found: 185.0293.

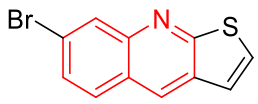

7-Bromothieno[2,3-*b*]quinoline (10i)

The general procedure **TP7** was followed using 5-bromobenzo[*c*]isoxazole (59 mg, 0.3 mmol) and oxo(pivaloyl)(thiophen-2-yl)zinc (prepared from **TP1**, metalation at room temperature, 0.45 mmol) for 16 h. Purification by column chromatography (*n*-hexane/EtOAc 10:1) yielded **10i** (30 mg, 38%) as a white solid. **M.p.**: 64–67 °C. **^{1}H-NMR (400 MHz, $CDCl_3$)** δ = 8.47 (s, 1H), 8.31 (d, *J* = 1.9 Hz, 1H), 7.80 (d, *J* = 8.8 Hz, 1H), 7.64 – 7.56 (m, 2H), 7.33 (d, *J* = 6.2 Hz, 1H). **^{13}C-NMR (100 MHz, $CDCl_3$)** δ = 164.1, 146.9, 131.6, 130.6, 130.0, 129.4, 129.1, 129.0, 124.0, 123.3, 121.1. **IR (Diamond-ATR, neat):** ν / cm = 3046, 1617, 1553, 1439, 1087, 954, 682. **MS (EI, 70 eV):** m/z (%) = 265 (30), 263 (30), 184 (100). **HR-MS (EI, 70 eV)**: [$C_{11}H_6BrNS$], calcd: 262.9404; found: 262.9401.

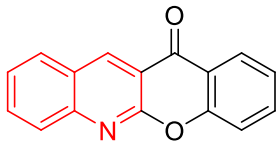

12*H*-Chromeno[2,3-*b*]quinolin-12-one (10j)

The general procedure **TP7** was followed using benzo[*c*]isoxazole (37 mg, 0.3 mmol) and benzo[*c*]isoxazole and oxo(4-oxo-4*H*-chromen-2-yl)(pivaloyl)zinc (prepared from **TP3**, metalation at −30 °C, 0.45 mmol) for 16 h. Purification by column chromatography (*n*-hexane/EtOAc 10:1) yielded **10j** (38 mg, 51%) as a white solid. **M.p.**: 240–242 °C. **^{1}H-NMR**

(400 MHz, $CDCl_3$) δ = 9.26 (s, 1H), 8.32 (dd, J = 7.9, 1.7 Hz, 1H), 8.11 – 8.03 (m, 2H), 7.89 (ddd, J = 8.5, 7.0, 1.4 Hz, 1H), 7.79 (ddd, J = 8.5, 7.0, 1.7 Hz, 1H), 7.64 – 7.56 (m, 2H), 7.45 – 7.37 (m, 1H). **^{13}C-NMR (100 MHz, $CDCl_3$)** δ = 178.1, 157.4, 156.2, 149.3, 140.0, 136.1, 133.5, 129.6, 128.1, 127.0, 126.4, 126.2, 124.4, 120.9, 118.4, 116.4. **IR (Diamond-ATR, neat):** ν / cm = 1670, 1618, 1599, 1494, 1466, 1414, 1402, 1378, 1331, 1299, 1258, 1215, 1118, 1025, 956, 934, 859, 800, 774, 750, 719, 687, 652. **MS (EI, 70 eV):** m/z (%) = 248 (17), 247 (100), 219 (38), 190 (22). **HR-MS (EI, 70 eV)**: [$C_{16}H_9NO_2$], calcd: 247.0633; found: 247.0628.

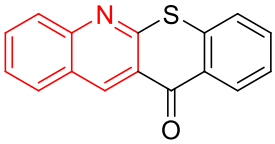

12*H*-Thiochromeno[2,3-*b*]quinolin-12-one (10k)

The general procedure **TP7** was followed using benzo[*c*]isoxazole (37 mg, 0.3 mmol) and benzo[*c*]isoxazole and oxo(4-oxothiochroman-2-yl)(pivaloyl)zinc (prepared from **TP3**, metalation at −40 °C, with 1.2 equiv of TMPZnOPiv; 0.45 mmol) for 16 h. Purification by column chromatography (*n*-hexane/EtOAc 10:1) yielded **10k** (48 mg, 61%) as a white solid. **M.p.**: 251–252 °C. **^{1}H-NMR (400 MHz, $CDCl_3$)** δ = 9.42 (s, 1H), 8.63 (dd, J = 8.0, 0.8 Hz, 1H), 8.11 (d, J = 8.7 Hz, 1H), 8.08 (d, J = 8.1 Hz, 1H), 7.91 (ddd, J = 8.5, 6.9, 1.4 Hz, 1H), 7.75 – 7.59 (m, 3H), 7.53 (ddd, J = 8.2, 6.7, 1.6 Hz, 1H). **^{13}C-NMR (100 MHz, $CDCl_3$)** δ = 181.3, 156.8, 149.6, 140.0, 137.7, 133.4, 133.3, 130.2, 129.9, 128.4, 127.9, 126.8, 126.5, 126.4, 126.3, 124.3. **IR (Diamond-ATR, neat):** ν / cm = 3116, 1727, 1549, 1417, 1078, 967, 672. **MS (EI, 70 eV):** m/z (%) = 263 (25), 262 (100). **HR-MS (EI, 70 eV)**: [$C_{16}H_9NOS$], calcd: 263.0405; found: 263.0403.

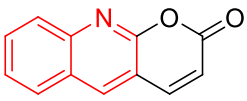

2*H*-Pyrano[2,3-*b*]quinolin-2-one (10l)

The general procedure **TP7** was followed using benzo[*c*]isoxazole (37 mg, 0.3 mmol) and oxo(2-oxo-2*H*-pyran-6-yl)(pivaloyl)zinc (prepared from **TP3**, metalation at −40 °C for 15 min, with 1.2 equiv of TMPMgCl and $Zn(OPiv)_2$; 0.45 mmol) for 16 h. Purification by column

chromatography (*n*-hexane/EtOAc 10:1) yielded **10l** (32 mg, 55%) as a white solid. **M.p.**: 161–163 °C. **^{1}H-NMR (400 MHz, $CDCl_3$)** δ = 8.40 (s, 1H), 8.10 (d, J = 8.6 Hz, 1H), 7.95 (dd, J = 8.4, 1.0 Hz, 1H), 7.90 – 7.82 (m, 2H), 7.62 (ddd, J = 8.1, 6.9, 1.1 Hz, 1H), 6.57 (d, J = 9.5 Hz, 1H). **^{13}C-NMR (100 MHz, $CDCl_3$)** δ = 1160.0, 156.2, 147.2, 141.8, 138.0, 132.3, 128.7, 128.1, 126.7, 126.3, 118.4, 114.0. **IR (Diamond-ATR, neat):** ν / cm = 3109, 1723, 1527, 1394, 1082, 958, 668. **MS (EI, 70 eV):** m/z (%) = 198 (20), 197 (100). **HR-MS (EI, 70 eV)**: [$C_{12}H_7NO_2$], calcd: 197.0477; found: 197.0483.

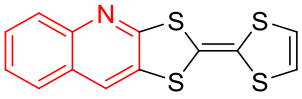

2-(1,3-Dithiol-2-ylidene)-[1,3]dithiolo[4,5-*b*]quinoline (10m)

The general procedure **TP7** was followed using benzo[*c*]isoxazole (37 mg, 0.3 mmol) and TTF-ZnOPiv (prepared from **TP3**, metalation at room temperature for 1 h, with 1.2 equiv of TMPMgCl and $Zn(OPiv)_2$; 0.45 mmol) for 16 h. Purification by column chromatography (*n*-hexane/EtOAc 10:1) yielded **10m** (47 mg, 51%) as a yellow solid. **M.p.**: 147–149 °C. **^{1}H-NMR (400 MHz, $CDCl_3$)**: δ = 7.88 (d, J = 8.0 Hz, 1H), 7.84 (s, 1H), 7.68 – 7.59 (m, 2H), 7.47 (ddd, J = 8.1, 7.0, 1.2 Hz, 1H), 6.43 – 6.36 (m, 2H). **^{13}C-NMR (100 MHz, $CDCl_3$)**: δ = 162.7, 146.1, 131.9, 129.3, 127.9, 126.7, 126.6, 125.9, 125.8, 125.8, 118.8, 118.6. **IR (Diamond-ATR, neat):** ν / cm = 3101, 1472, 1399, 1088, 907, 671. **MS (EI, 70 eV):** m/z (%) = 305 (15), 304 (100). **HR-MS (EI, 70 eV)**: [$C_{13}H_7NS_4$], calcd: 304.9461; found: 304.9466.

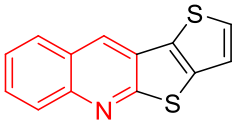

Thieno[2',3':4,5]thieno[2,3-*b*]quinoline (10n)

The general procedure **TP7** was followed using benzo[*c*]isoxazole (37 mg, 0.3 mmol) and oxo(pivaloyl)(thieno[3,2-*b*]thiophen-2-yl)zinc (prepared from **TP2**, metalation at room temperature; 0.9 mmol) for 16 h. Purification by column chromatography (*n*-hexane/EtOAc 10:1) yielded **10n** (38 mg, 53%) as a yellow solid. **M.p.**: 164–166 °C. **^{1}H-NMR (400 MHz, $CDCl_3$)** δ = 8.44 (s, 1H), 8.06 (d, J = 8.5 Hz, 1H), 7.89 (dd, J = 8.3, 1.5 Hz, 1H), 7.67 (ddd, J

= 8.3, 6.9, 1.5 Hz, 1H), 7.55 (d, *J* = 5.1 Hz, 1H), 7.49 (ddd, *J* = 8.3, 6.9, 1.2 Hz, 1H), 7.31 (dd, *J* = 5.1, 0.9 Hz, 1H). **^{13}C-NMR (100 MHz, $CDCl_3$)** δ = 165.8, 146.0, 137.5, 130.5, 129.3, 129.2, 128.3, 128.1, 126.4, 126.2, 125.9, 125.5, 121.3. **IR (Diamond-ATR, neat):** ν / cm = 3108, 3054, 1554, 1477, 1412, 1379, 1330, 1320, 1127, 1074, 904, 898, 778, 753, 720, 715, 666. **MS (EI, 70 eV):** m/z (%) = 242 (13), 241 (100), 196 (11). **HR-MS (EI, 70 eV)** : [$C_{13}H_7NS_2$], calcd: 241.0020; found: 241.0012.

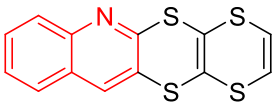

Compound (10o)

The general procedure **TP7** was followed using benzo[*c*]isoxazole (37 mg, 0.3 mmol) and [1,4]dithiino[2,3-*b*][1,4]dithiin-2-yl(oxo)(pivaloyl)zinc (prepared from **TP2**, metalation at -40 °C, with 1.2 equiv of TMPZnOPiv; 0.9 mmol) for 16 h. Purification by column chromatography (*n*-hexane/EtOAc 10:1) yielded **10o** (50 mg, 55%) as a yellow solid. **M.p.**: 157–159 °C. **^{1}H-NMR (400 MHz, $CDCl_3$)** δ = 8.04 (s, 1H), 8.02 – 7.95 (m, 1H), 7.76 – 7.68 (m, 2H), 7.59 – 7.50 (m, 1H), 6.54 (s, 2H). **^{13}C-NMR (100 MHz, $CDCl_3$)** δ = 157.4, 146.9, 134.6, 130.6, 128.7, 127.6, 127.2, 126.9, 126.5, 126.4, 126.4, 125.4, 121.0, 119.3. **IR (Diamond-ATR, neat):** ν / cm = 3099, 1475, 1411, 1097, 913, 665. **MS (EI, 70 eV):** m/z (%) = 305 (30), 304 (100). **HR-MS (EI, 70 eV)**: [$C_{13}H_7NS_4$], calcd: 304.9461; found: 304.9466.

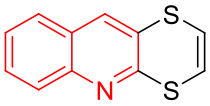

[1,4]Dithiino[2,3-*b*]quinoline (10p)

The general procedure **TP7** was followed using benzo[*c*]isoxazole (37 mg, 0.3 mmol) and [1,4]dithiino[2,3-*b*][1,4]dithiin-2-yl(oxo)(pivaloyl)zinc (prepared from **TP2**, metalation at – 30 °C; 0.45 mmol) for 16 h. Purification by column chromatography (*n*-hexane/EtOAc 10:1) yielded **10p** (52 mg, 80%) as a slight yellow solid. **M.p.**: 95–97 °C. **^{1}H-NMR (400 MHz, $CDCl_3$)** δ = 7.82 – 7.77 (m, 1H), 7.70 (s, 1H), 7.55 – 7.47 (m, 2H), 7.37 – 7.29 (m, 1H), 6.40 (d, *J* = 8.1 Hz, 1H), 6.25 (d, *J* = 8.1 Hz, 1H). **^{13}C-NMR (100 MHz, $CDCl_3$)** δ = 155.5, 146.8,

133.2, 130.0, 128.3, 127.3, 126.9, 126.9, 124.7, 122.2, 119.6. **IR (Diamond-ATR, neat):** ν / cm = 3026, 2963, 2921, 2866, 1612, 1577, 1553, 1483, 1377, 1362, 1319, 1295, 1198, 1150, 1135, 1119, 1015, 985, 951, 900, 855, 803, 774, 750, 660. **MS (EI, 70 eV):** m/z (%) = 218 (12), 217 (100), 215 (20), 185 (27), 173 (24), 172 (11), 141 (21), 140 (15). **HR-MS (EI, 70 eV)**: [$C_{11}H_7NS_2$], calcd: 217.0020; found: 217.009.

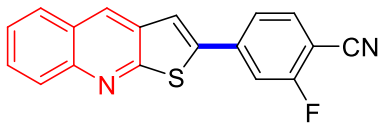

2-Fluoro-4-(thieno[2,3-*b*]quinolin-2-yl)benzonitrile (12)

To a suspension of compound **10h** (37 mg, 0.2 mmol) in anhydrous THF (1.0 mL) was added a solution of TMPMgCl·LiCl (1.2 equiv, 1.07 M) at 0 ℃ under an atmosphere of N_2. The mixture was stirred at the same temperature for 1 h, then $Zn(OPiv)_2$ (64 mg, 0.24 mmol, 1.2 equiv) was added and the mixture stirred for another 15 min. 4-Bromo-2-fluorobenzonitrile (48 mg, 0.24 mmol), $Pd(OAc)_2$ (0.9 mg, 2 mol %) and X-phos (4.0 mg, 4 mol %) were added, and the reaction mixture was stirred at 50 ℃ for another 12 h.[5] At ambient temperature, the reaction mixture was extracted with DCM (3 × 20 mL) and the combined organic layers were washed with brine, and dried over Na_2SO_4. The solvent was evaporated *in vacuo* and the remaining residue was purified by column chromatography on silica gel (*n*-hexane/EtOAc/DCM 6:1:1) to yield product **12** (46 mg, 75%) as a colorless solid. **M.p.** = 227−229 °C. **^{1}H-NMR (400 MHz, $CDCl_3$)** δ = 8.58 (s, 1H), 8.17 (d, J = 8.6 Hz, 1H), 8.00 (d, J = 8.2 Hz, 1H), 7.81 (ddd, J = 8.5, 6.8, 1.4 Hz, 1H), 7.77 – 7.70 (m, 2H), 7.67 (dd, J = 8.1, 1.6 Hz, 1H), 7.65 – 7.58 (m, 2H). **^{13}C-NMR (100 MHz, $CDCl_3$)** δ = 163.4 (d, J_{C-F} = 259.6 Hz), 162.6, 147.3, 141.5 (d, J_{C-F} = 2.5 Hz), 140.8 (d, J_{C-F} = 8.4 Hz), 134.1, 132.5, 131.1, 130.2, 128.5, 126.1, 122.8 (d, J_{C-F} = 3.4 Hz), 119.7, 114.2 (d, J_{C-F} = 21.3 Hz), 113.7, 101.2 (d, J_{C-F} = 15.8 Hz). ^{19}F-NMR ($CDCl_3$, 377 MHz): δ = -105.33 (dd, J = 9.8, 6.5 Hz). **IR (Diamond-ATR, neat):** ν / cm = 3119, 1805, 1521, 1433, 1127, 917. **MS (EI, 70 eV):** m/z (%) = 305 (25), 304 (100). **HR-MS (EI, 70 eV)**: [$C_{18}H_9FN_2S$], calcd: 304.0470; found: 304.0474.

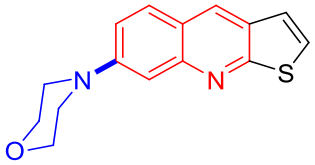

4-(Thieno[2,3-*b*]quinolin-7-yl)morpholine (13)

A suspension of compound **10h** (37 mg, 0.2 mmol) and $Pd_2(dba)_3$ (9.2 mg, 5 mol %), Xantphos (11.6 mg, 10 mol %), NaO^{t}Bu (38.4 mg, 2.0 equiv), morpholine (35.0 mg, 2.0 equiv) in anhydrous PhMe (2.0 mL) was stirred at 80 °C for 12 under an atmosphere of N_2.[6] At ambient temperature, the reaction mixture was extracted with DCM (3 × 20 mL) and the combined organic layers were washed with brine, and dried over Na_2SO_4. The solvent was evaporated *in vacuo* and the remaining residue was purified by column chromatography on silica gel (*n*-hexane/EtOAc 7:1) to yield product **13** (39 mg, 72%) as a colorless solid. **M.p.** = 136−139 °C. **^{1}H-NMR (400 MHz, $CDCl_3$)** δ = 8.37 (s, 1H), 7.80 (d, J = 9.1 Hz, 1H), 7.41 (d, J = 6.1 Hz, 1H), 7.35 (d, J = 2.1 Hz, 1H), 7.30 (dd, J = 9.2, 2.5 Hz, 1H), 7.27 (d, J = 6.2 Hz, 1H), 3.96 – 3.86 (m, 4H), 3.40 – 3.31 (m, 4H). **^{13}C-NMR (100 MHz, $CDCl_3$)** δ = 163.8, 151.8, 148.4, 129.6, 129.5, 128.9, 126.1, 121.3, 120.5, 118.3, 109.1, 66.7, 48.9. **IR (Diamond-ATR, neat):** ν / cm = 3312, 1655, 1519, 1439, 1136, 918. **MS (EI, 70 eV):** m/z (%) = 271 (35), 270 (100). **HR-MS (EI, 70 eV)**: [$C_{15}H_{14}N_2OS$], calcd: 270.0827; found: 270.0832.

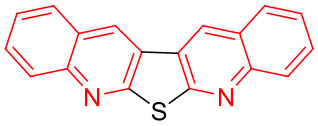

Compound (14)

To a suspension of compound **10h** (56 mg, 0.3 mmol) in anhydrous THF (1.0 mL) was added a solution of TMPMgCl·LiCl (1.2 equiv, 1.07 M) at 0 °C under an atmosphere of N_2. The mixture was stirred at the same temperature for 1 h, then $Zn(OPiv)_2$ (96 mg, 0.36 mmol, 1.2 equiv) was added and the mixture stirred for another 15 min. Anthranil (24 mg, 0.2 mmol) and $CoCl_2$ (2.6 mg, 10 mol %) were added, and the reaction mixture was stirred at room temperature for another 16 h. At ambient temperature, the reaction mixture was extracted with DCM (3 × 20 mL) and the combined organic layers were washed with brine, and dried over Na_2SO_4. The solvent was evaporated *in vacuo* and the remaining residue was purified by column chromatography on silica gel (*n*-hexane/EtOAc/DCM 15:1:10) to yield product **14** (20 mg, 34%) as a slight yellow

solid. **M.p.** = 261−264 °C. **^{1}H-NMR (400 MHz, $CDCl_3$)** δ = 8.82 (s, 2H), 8.17 (d, J = 8.5 Hz, 2H), 8.03 (d, J = 8.1 Hz, 2H), 7.81 (ddd, J = 8.3, 6.9, 1.4 Hz, 2H), 7.65 – 7.59 (m, 2H). **^{13}C-NMR (100 MHz, $CDCl_3$)** δ = 161.9, 148.3, 130.5, 128.5, 128.4, 128.4, 126.6, 126.2, 125.8. **IR (Diamond-ATR, neat):** ν / cm = 3132, 1541, 1421, 1098, 677. **MS (EI, 70 eV):** m/z (%) = 287 (15), 286 (100). **HR-MS (EI, 70 eV)**: [$C_{18}H_{10}N_2S$], calcd: 286.0565; found: 286.0571.

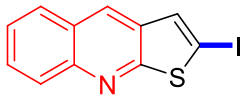

2-Iodothieno[2,3-*b*]quinoline (11a)

To a suspension of compound **10h** (28 mg, 0.15 mmol) in anhydrous THF (1.0 mL) was added a solution of TMPMgCl·LiCl (1.2 equiv, 1.07 M) under an atmosphere of N_2. The mixture was stirred at room temperature for 16 h, then a soultion of I_2 (76 mg, 0.3 mmol, 0.3 M) was added and the mixture stirred for another 30 min. At ambient temperature, the reaction mixture was extracted with DCM (2 × 10 mL) and the combined organic layers were washed with brine, and dried over Na_2SO_4. The solvent was evaporated *in vacuo* and the remaining residue was purified by column chromatography on silica gel (*n*-hexane/EtOAc 15:1) to yield product **11a** (42 mg, 90%) as a slight yellow solid. **M.p.** = 107−109 °C. **^{1}H-NMR (400 MHz, $CDCl_3$)** δ = 8.44 (s, 1H), 8.12 (dd, J = 8.6, 0.7 Hz, 1H), 8.00 – 7.94 (m, 1H), 7.78 (ddd, J = 8.5, 6.8, 1.4 Hz, 1H), 7.66 (s, 1H), 7.57 (ddd, J = 11.1, 6.1, 2.7 Hz, 1H). **^{13}C-NMR (125 MHz, $CDCl_3$)** δ = 166.5, 146.2, 133.0, 131.1, 129.8, 128.4, 128.3, 126.0, 125.6, 82.7. **R (Diamond-ATR, neat):** ν / cm = 3102, 1569, 1472, 1156, 711. **MS (EI, 70 eV):** m/z (%) = 312 (10), 311 (100), 184 (35). **HR-MS (EI, 70 eV)**: [$C_{11}H_6INS$], calcd: 310.9266; found: 310.9274.

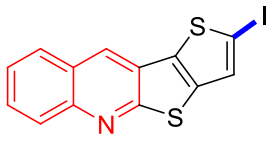

Compound (11b)

To a suspension of compound **10n** (35 mg, 0.15 mmol) in anhydrous THF (1.0 mL) was added a solution of TMPMgCl·LiCl (1.2 equiv, 1.07 M) under an atmosphere of N_2. The mixture was stirred at room temperature for 16 h, then a soultion of I_2 (76 mg, 0.3 mmol, 0.3 M) was added

and the mixture stirred for another 30 min. At ambient temperature, the reaction mixture was extracted with DCM (2 × 10 mL) and the combined organic layers were washed with brine, and dried over Na_2SO_4. The solvent was evaporated *in vacuo* and the remaining residue was purified by column chromatography on silica gel (*n*-hexane/EtOAc 15:1) to yield product **11b** (54 mg, 98%) as a slight yellow solid. **M.p.** = 128−130 °C. **^{1}H-NMR (400 MHz, $CDCl_3$)** δ = 8.44 (s, 1H), 8.13 (d, *J* = 8.6 Hz, 1H), 7.96 (d, *J* = 8.3 Hz, 1H), 7.75 (dd, *J* = 11.3, 4.1 Hz, 1H), 7.62 – 7.55 (m, 1H), 7.53 (s, 1H). **^{13}C-NMR (100 MHz, $CDCl_3$)** δ = 164.9, 146.0, 137.8, 135.6, 130.3, 129.5, 128.3, 128.1, 126.7, 126.1, 125.4, 125.4. **IR (Diamond-ATR, neat):** ν / cm = 3092, 1572, 1419, 1106, 692. **MS (EI, 70 eV):** m/z (%) = 368 (15), 367 (100), 240 (60). **HR-MS (EI, 70 eV)**: [$C_{13}H_6INS_2$], calcd: 366.8986; found: 366.8995.

8.6.4 References

[1] Jin, H.; Huang, L.; Xie, J.; Rudolph, M.; Rominger, F.; Hashmi, A. S. K., Gold-Catalyzed C□H Annulation of Anthranils with Alkynes: A Facile, Flexible, and Atom-Economical Synthesis of Unprotected 7-Acylindoles. *Angew. Chem. Int. Ed.* **2016,** *55* (2), 794-797.

[2] Zhao, D.; Shen, Q.; Li, J.-X., Potassium Iodide-Catalyzed Three-Component Synthesis of 2-Arylquinazolines via Amination of Benzylic C□H Bonds of Methylarenes. *Adv. Synth. Catal.* **2015,** *357* (2-3), 339-344.

[3] Baum, J. S.; Condon, M. E.; Shook, D. A., Nickel-catalyzed transformations of 2,1-benzisoxazoles with organozinc reagents. *J. Org. Chem.* **1987,** *52* (14), 2983-2988.

[4] Wang, M.; Kong, L.; Wang, F.; Li, X., Rhodium-Catalyzed Amination and Annulation of Arenes with Anthranils: C-H Activation Assisted by Weakly Coordinating Amides. *Adv. Synth. Catal.* **2017,** *359* (24), 4411-4416.

[5] Colombe, J. R.; Bernhardt, S.; Stathakis, C.; Buchwald, S. L.; Knochel, P., Synthesis of Solid 2-Pyridylzinc Reagents and Their Application in Negishi Reactions. *Org. Lett.* **2013,** *15* (22), 5754-5757.

[6] Li, J.; Zhang, Z.; Tang, M.; Zhang, X.; Jin, J., Selective Synthesis of Isoquinolines by Rhodium(III)-Catalyzed C–H/N–H Functionalization with α-Substituted Ketones. *Org. Lett.* **2016,** *18* (15), 3898-3901.

9 Conclusion and Outlook

In conclusion, the scope of this thesis was focused on the construction and investigation of design rules for tailor-made two-dimensional COFs with novel and tunable optoelectronic properties. This work can be divided into three sections, which elucidate the behavior of the tetravalent node (chapter 3 – 4) and the linear bridge (chapter 5 – 7), and the search for new interesting organic moieties in the linker synthesis (chapter 8).

In the first section, two different COF systems were developed with an intriguing stacking fashion and the resulting structural and optical characteristics were analyzed. In chapter 3, we describe a newly designed tetravalent node which generally assumes a sterically demanding shape with out-of-plane rotated phenyl rings. Our design led to the modified version, namely dibenzo[*g*,*p*]chrysene (DBC), which adapted a more planar conformation by generating only two new intramolecular C−C bonds. The condensation of the DBC node with terephthalaldehyde (TA), biphenyl (Biph), and thienothiophene (TT) resulted in highly crystalline and porous covalent organic frameworks. The modified building unit DBC led to a new docking site for successive layers and allowed for conjugation in the *a*,*b*-plane and a tighter packing of adjacent COF layers due to less steric hindrance compared to the non-modified ETTA (tetraphenylethylene) node. Further characterization elucidated the differences arising from the decreased π-stacking distance for the DBC-COFs compared to the analogous ETTA-COFs. Both COFs exhibit a hexagonal dual-pore kagome geometry but with significantly different interlayer distances from about 4.6 Å in ETTA-COFs to about 3.6 Å in DBC-COFs. The striking crystallinity of the DBC-COFs was also observed in well-defined hexagonally faceted single crystals sized about 50-100 nm. Studying the optical response, the DBC-COFs exhibited broad light absorption covering large parts of the visible spectrum with a distinct red-shift and thus gain in solar light-harvesting compared to the ETTA-COFs. Further time-resolved PL studies revealed extraordinary excited state lifetimes exceeding 10 ns, being much longer than for the analogous ETTA-COFs. In combination with the large number of recently developed linear conjugated building blocks, the new DBC tetra-connected node is expected to enable the synthesis of a large family of strongly π-stacked, highly ordered 2D COFs with promising optoelectronic properties.

Chapter 4 emphasizes the importance of understanding and controlling the self-assembled aggregation behavior of COFs. Herein, we integrated tetravalent porphyrin nodes (of great interest in many studies in biology and chemistry) with a view on the promising features especially in the field of electroactive materials. Implementation into COF structures led to unparalleled stacking behavior due to their nonplanar configuration and strong electrostatic interactions between the heterocyclic porphyrin centers. Specifically, the combination with thieno[3,2-*b*]thiophene-2,5-dicarboxaldehyde led to the formation of extended slipped J-aggregate stacks. Steady-state and time-resolved optical spectroscopy techniques confirmed the realization of the first porphyrin J-aggregates on a > 50 nm length scale with strongly red-shifted Q-bands and strongly increased absorption strength in the visible. Using the COF as a structural template, we were thus able to force the porphyrins into a covalently embedded J-aggregate arrangement. This approach could be transferred to other chromophores; hence, these COFs are promising model systems for applications in photocatalysis and solar light harvesting, as well as for potential applications in medicine and biology.

In the second section of this thesis, the structural and optical effects of small modifications on novel oligothiophene-based bridging units were elaborated and discussed. With a view toward the application of these materials in organic electronics and optoelectronics, the construction of oligothiophene-based COFs is highly desirable. The realization of such materials, however, has remained a challenge, in particular with respect to laterally conjugated imine-linked COFs. In order to overcome these issues, we have designed a series of functionalized quaterthiophene linkers for the construction of COFs, discussed in Chapter 5. An asymmetric modification on an otherwise symmetric backbone allowed for an alternating stacking behavior of the linear bridges, minimizing repulsive interactions and enabling the synthesis of highly crystalline quaterthiophene-derived COFs with tunable electronic properties. For these COF systems, we observed for the first time a charge transfer state across the imine bond between the electron-rich pyrene and the more electron-deficient quaterthiophene bridge. We believe that this asymmetric design provides a general approach for the construction of crystalline COFs from various extended building blocks, thus greatly expanding the range of suitable molecules.

Connected to the theme of Chapter 5, the scope of the study was extended to thiophene-based backbones of various length and differently alkylated backbones with either methyl, ethyl, butyl or without any alkyl. Developing this COF series, described in Chapter 6, allowed for the investigation of simple point-like modifications since only few structural parameters were changed while the overall framework structure and symmetry was maintained. Hence, we could

observe a correlation between the length of the bridging oligothiophene units and the resulting singlet lifetimes in the COF, leading to extended lifetimes for a greater number of thiophenes in the bridge. Furthermore, the length of the attached alkyl chains affected the excited state dynamics in the COF in the same fashion as observed for the monomers. The longer chains led to a faster PL decay, which might be attributed to enhanced non-radiative relaxation due to additional vibrational modes. Summarizing, we were able to derive design rules for tailoring the excited state dynamics in COFs due to the direct translation of the monomer properties into the framework. While straightforward design rules for tuning absorption and emission bands could not yet be derived in this series of COFs, it is hoped that additional in-depth characterization of the charge-carrier dynamics enabled by the growth of thin films will help to reach a detailed understanding of these fundamental processes in COFs.

In chapter 7, a simplified thiophene-bridged system based on bithiophene linkers was developed in order to study the heavy atom effect introduced by bromine substitution. Again point-wise modifications maintained the overall structure and symmetry of the COFs but enabled tracking of the investigated parameters. Interestingly, the crystallinity and porosity were not affected by implementation of the brominated bithiophene bridges, but slight changes of the unit cell dimensions were observed. For both Py-3,3'-2T_{Br} and Py-4,4'-2T_{Br}, the unit cell slightly shrunk and the ordered π-stacked columns of Py-4,4'-2T_{Br} favored a denser packing expressed in the decreased π-stacking distance. Optical analysis showed that the heavy atom effect seen in the monomers could be translated into the COF. The tunability of the absorption and emission features by simple bromine substitution could be enhanced by the additional factor of the different stacking distance. Studying the PL dynamics revealed the extension of singlet lifetimes upon integration of brominated bridges, as also measured for the molecular building blocks. We demonstrate that this approach provides a facile strategy for modifying the electronic properties of bithiophenes and simultaneously maintaining the overall structure of the fundamental scaffolding of the Py-2T COF.

The last section of this thesis focuses on the importance of the continuing search for building blocks and motifs and their prior characterization. Herein, the group of Knochel developed a direct route to produce condensed quinolines of which several structures belong to new heterocyclic scaffolds. These N-heterocycles are of particular interest for COFs due to their high photoluminescence quantum yields and long exciton lifetimes. These scaffolds could be envisioned as building units in COFs where the monomer characterization might help to predict and categorize the properties of the future frameworks. Furthermore, the investigation of N-

heterocycles revealed candidates for organic light emitting diodes as well as for hole-transporting materials in methylammonium lead iodide perovskite solar cells due to an optimal band alignment for holes and a large bandgap.

In conclusion, this thesis evaluates different approaches to predict and hence tailor the properties of COFs by detailed and comprehensive characterization of newly developed building blocks. It could be shown that in 2D COFs the tetragonal node and the corresponding stacking behavior drastically affects the optical properties of resulting COFs such as absorption, emission and singlet lifetimes. This allows for the construction of materials with large solar light harvesting capabilities and might lead to a better understanding of charge migration and separation in future studies. Further, COF systems with thiophene-based bridges could be significantly modified while maintaining the overall COF symmetry. This design strategy provided a general method for constructing COFs with tunable optical properties but almost identical structural networks. This facilitates the comparison and optimization of single parameters in different systems by keeping most parameters fixed. Transferred to other COF systems, this approach is anticipated to be beneficial for the development of fundamental and general design rules. These insights are believed to be of relevance for applications of COFs in sensors, photocatalysts and pseudocapacitors where a promising future for COFs lies ahead. In addition, further research needs to evaluate the impact of structure and topology on electrical conductivity and charge carrier mobility since these are some of the most challenging and crucial properties that still limit the use of COFs in optoelectronic applications such as organic photovoltaics.

10 Publications and Presentations

10.1 Publications

1 Dibenzochrysene Enables Tightly Controlled Docking and Stabilizes Photoexcited States in Dual-Pore Covalent Organic Frameworks

N. Keller,‡ T. Sick,‡ N. N. Bach, A. Koszalkowski, J. M. Rotter, D. D. Medina and T. Bein, *Nanoscale* **2019**, *11*, 23338–23345..

2 Cobalt-Catalyzed Electrophilic Aminations with Anthranils: An Expedient Route to Condensed Quinolines

J. Li,‡ E. Tan,‡ N. Keller,‡ Y.-H. Chen, P. M. Zehetmaier, A. C. Jakowetz, T. Bein and P. Knochel, *J. Am. Chem. Soc.* **2019**, *141*, 98–103.

3 Enforcing Extended Porphyrin J-Aggregate Stacking in Covalent Organic Frameworks

N. Keller, M. Calik, D. Sharapa, H. R. Soni, P. M. Zehetmaier, S. Rager, F. Auras, A. C. Jakowetz, A. Görling, T. Clark, T. Bein, *J. Am. Chem. Soc.* **2018,** *140*, 16544–16552.

4 Oligothiophene-Bridged Conjugated Covalent Organic Frameworks

N. Keller, D. Bessinger, S. Reuter, M. Calik, L. Ascherl, F. C. Hanusch, F. Auras and T. Bein, *J. Am. Chem. Soc.* **2017,** *139*, 8194–8199.

5 Optoelectronic Processes in Covalent Organic Frameworks

N. Keller and T. Bein, *Nanoscale*, 2020, *to be submitted*.

‡ These authors contributed equally.

10.2 Oral Presentations

1 Enforcing Extended Porphyrin J-Aggregate Stacking in Covalent Organic Frameworks

Deutsche Zeolith Tagung (DZT) **2019**, Dresden, Germany.

2 Oligothiophene-Bridged Conjugated Covalent Organic Frameworks

Materials Research Society (MRS) Spring Meeting **2019**, Phoenix, United States of America.

3 Oligothiophene-Bridged Conjugated Covalent Organic Frameworks

EuroMOF **2017**, Delft, Netherlands.

10.3 Poster Presentations

1 Enforcing Extended Porphyrin J-Aggregate Stacking in Covalent Organic Frameworks

EuroMOF **2019**, Paris, France.

2 Enforcing Extended Porphyrin J-Aggregate Stacking in Covalent Organic Frameworks

SolTech Meeting **2019**, Nürnberg, Germany.

3 Enforcing Extended Porphyrin J-Aggregate Stacking in Covalent Organic Frameworks

IUPAC 47th Chemistry Congress **2019**, Paris, France.

4 Oligothiophene-Bridged Conjugated Covalent Organic Frameworks

SolTech Meeting **2018**, Würzburg, Germany.

5 Oligothiophene-Bridged Conjugated Covalent Organic Frameworks

Nanosystems Initiative Munich (NIM) Conference **2018**, Tutzing, Germany.

6 Oligothiophene-Bridged Conjugated Covalent Organic Frameworks

Deutsche Zeolith Tagung (DZT) **2018**, Kiel, Germany.

7 Oligothiophene-Bridged Conjugated Covalent Organic Frameworks

Center for NanoScience (CeNS) Workshop **2017**, Venice, Italy.

8 Insights into the Unique Stacking Behavior of a Porphyrin Containing Covalent Organic Framework

Federation of European Zeolite Associations (FEZA) **2017***,* Sofia, Bulgaria.

9 Insights into the Unique Stacking Behavior of a Porphyrin Containing Covalent Organic Framework

Deutsche Zeolith Tagung **2017**, Frankfurt, Germany.